

Astrophysics and Space Science Library 392



Boris V. Somov

# Plasma Astrophysics, Part II

Reconnection and Flares

*Second Edition*

As  
SL

 Springer

# Plasma Astrophysics, Part II

# Astrophysics and Space Science Library

---

## EDITORIAL BOARD

### *Chairman*

W. B. BURTON, *National Radio Astronomy Observatory, Charlottesville, Virginia, U.S.A.*  
*([bburton@nrao.edu](mailto:bburton@nrao.edu)); University of Leiden, The Netherlands*  
*([burton@strw.leidenuniv.nl](mailto:burton@strw.leidenuniv.nl))*

F. BERTOLA, *University of Padua, Italy*  
J. P. CASSINELLI, *University of Wisconsin, Madison, U.S.A.*  
C. J. CESARSKY, *Commission for Atomic Energy, Saclay, France*  
P. EHRENFREUND, *Leiden University, The Netherlands*  
O. ENGVOLD, *University of Oslo, Norway*  
A. HECK, *Strasbourg Astronomical Observatory, France*  
E. P. J. VAN DEN HEUVEL, *University of Amsterdam, The Netherlands*  
V. M. KASPI, *McGill University, Montreal, Canada*  
J. M. E. KUIJPERS, *University of Nijmegen, The Netherlands*  
H. VAN DER LAAN, *University of Utrecht, The Netherlands*  
P. G. MURDIN, *Institute of Astronomy, Cambridge, UK*  
F. PACINI, *Istituto Astronomia Arcetri, Firenze, Italy*  
V. RADHAKRISHNAN, *Raman Research Institute, Bangalore, India*  
B. V. SOMOV, *Astronomical Institute, Moscow State University, Russia*  
R. A. SUNYAEV, *Space Research Institute, Moscow, Russia*

For further volumes:  
<http://www.springer.com/series/5664>

Boris V. Somov

# Plasma Astrophysics, Part II

Reconnection and Flares

Second Edition



Springer

Boris V. Somov  
Astronomical Institute and Faculty  
of Physics  
M.V. Lomonosov Moscow State University  
Universitetskij Prospekt 13  
119991 Moskva, Russia

ISSN 0067-0057

ISBN 978-1-4614-4294-3

ISBN 978-1-4614-4295-0 (eBook)

DOI 10.1007/978-1-4614-4295-0

Springer New York Heidelberg Dordrecht London

Library of Congress Control Number: 2012940742

© Springer Science+Business Media New York 2013

This work is subject to copyright. All rights are reserved by the Publisher, whether the whole or part of the material is concerned, specifically the rights of translation, reprinting, reuse of illustrations, recitation, broadcasting, reproduction on microfilms or in any other physical way, and transmission or information storage and retrieval, electronic adaptation, computer software, or by similar or dissimilar methodology now known or hereafter developed. Exempted from this legal reservation are brief excerpts in connection with reviews or scholarly analysis or material supplied specifically for the purpose of being entered and executed on a computer system, for exclusive use by the purchaser of the work. Duplication of this publication or parts thereof is permitted only under the provisions of the Copyright Law of the Publisher's location, in its current version, and permission for use must always be obtained from Springer. Permissions for use may be obtained through RightsLink at the Copyright Clearance Center. Violations are liable to prosecution under the respective Copyright Law.

The use of general descriptive names, registered names, trademarks, service marks, etc. in this publication does not imply, even in the absence of a specific statement, that such names are exempt from the relevant protective laws and regulations and therefore free for general use.

While the advice and information in this book are believed to be true and accurate at the date of publication, neither the authors nor the editors nor the publisher can accept any legal responsibility for any errors or omissions that may be made. The publisher makes no warranty, express or implied, with respect to the material contained herein.

*Cover illustration:* Total solar eclipse on 2006 March 29 in Turkey. The shape of the corona reveals the global structure of the dipole-like magnetic field with open field lines at the poles. Out of the poles, the so-called coronal streamers are the spectacular manifestations of the solar wind interaction with magnetic field. Here magnetic reconnection detaches the solar magnetic field from the Sun.

Photograph reproduced with kind permission by Hanna Druckmüllerová and Miloslave Druckmüller (<http://www.zam.fme.vutbr.cz/~druck/Eclipse>).

Printed on acid-free paper

Springer is part of Springer Science+Business Media ([www.springer.com](http://www.springer.com))

Lebedev Institute, Moscow (1959)



Photo from Syrovatskii's family archive

*At that time  
the magnetic reconnection  
was a new idea...*



# Reconnection and Flares

## *Introduction*

Magnetic fields are easily generated in astrophysical plasma owing to its high conductivity. Magnetic fields, having strengths of order few  $10^{-6}$  G, correlated on several kiloparsec scales are seen in spiral galaxies. Their origin could be due to amplification of a small seed field by a turbulent galactic dynamo. In several galaxies, like the famous M51, magnetic fields are well correlated (or anti-correlated) with the optical spiral arms. These are the weakest large-scale fields observed in cosmic space. The strongest magnets in space are presumably the so-called *magnetars*, the highly magnetized (with the strength of the field of about  $10^{15}$  G) young *neutron stars* (Duncan and Thompson 1992; Becker 2009) formed in the supernova explosions.

The energy of magnetic fields is accumulated in astrophysical plasma, and the sudden release of this energy – an original electrodynamical ‘burst’ or ‘explosion’ – takes place under definite but quite general conditions (Peratt 1992; Sturrock 1994; Kivelson and Russell 1995; Rose 1998; Priest and Forbes 2000; Somov 2000; Kundt 2001; Hurley et al. 2005). Such a ‘flare’ in astrophysical plasma is accompanied by fast directed ejections (jets) of plasma, powerful flows of heat and hard electromagnetic radiation as well as by impulsive acceleration of charged particles to high energies.

This phenomenon is quite a widespread one. It can be observed in flares on the Sun and other stars (Haisch et al. 1991), in the Earth’s magnetosphere as **magnetic storms** and substorms (Nishida and Nagayama 1973; Tsurutani et al. 1997; Kokubun and Kamide 1998; Nagai et al. 1998; Nishida et al. 1998), in coronae of accretion disks of cosmic X-ray sources (Galeev et al. 1979; Somov et al. 2003a), in nuclei of active galaxies and quasars (Ozernoy and Somov 1971; Begelman et al. 1984). However this process, while being typical of astrophysical plasma, can be directly and fully studied on the Sun.

The Sun is the only star that can be imaged with spatial resolution high enough to reveal its key (fine as well as large-scale) structures and their dynamic behaviors. This simple fact makes the Sun one of the most important objectives in astronomy. The solar atmosphere can be regarded as a natural ‘laboratory’ of

astrophysical plasmas in which we can study the physical processes involved in cosmic **electrodynamical explosions**.

We observe how magnetic fields are generated (strictly speaking, how they come to the surface of the Sun, called the photosphere). We observe the development of **solar flares** (e.g., Strong et al. 1999) and other non-stationary large-scale phenomena, such as a gigantic arcade formation, coronal transients, coronal mass ejections into the interplanetary medium (see Crooker et al. 1997), by means of ground observatories (in radio and optical wavelength ranges) and spaceships (practically in the whole electromagnetic spectrum).

As a very good example, on board the *Yohkoh* satellite (Ogawara et al. 1991; Acton et al. 1992), two telescopes worked in soft and hard X-ray bands (Tsuneta et al. 1991; Kosugi et al. 1991) during 10 years and allowed us to study the creation and development of non-steady processes in the solar atmosphere (Ichimoto et al. 1992; Tsuneta et al. 1992; Tsuneta 1993), acceleration of electrons in flares. Of particular interest to the acceleration process in solar flares were the hard X-ray emissions from the so-called chromospheric ribbons produced by accelerated electrons with energy  $\gtrsim 10$  keV (Masuda et al. 2001).

The LASCO experiment on board the *Solar and Heliospheric Observatory*, *SOHO* (Domingo et al. 1995) makes observations of such events in the solar corona out to 30 solar radii. Moreover *SOHO* is equipped with an instrument, the full disk magnetograph MDI (Scherrer et al. 1995), for observing the surface magnetic fields of the Sun. Following *SOHO*, the satellite *Transition Region and Coronal Explorer* (*TRACE*) was launched to obtain high spatial resolution X-ray images (see Golub et al. 1999). With the solar maximum of 2000, we had an unprecedented opportunity to use the three satellites for coordinated observations and study of solar flares.

The *Reuven Ramaty High-Energy Solar Spectroscopic Imager* (*RHESSI*) was launched in 2002 and observes solar hard X-rays and gamma-rays from 3 keV to 17 MeV with spatial resolution as high as 2.3 arcsec (Lin et al. 2002, 2003a). Imaging of gamma-ray lines, produced by nuclear collisions of energetic ions with the solar atmosphere, provided direct information of the spatial properties of the ion acceleration in solar flares (Hurford et al. 2003). *RHESSI* observations allowed us to investigate physical properties of solar flares in many details (e.g., Fletcher and Hudson 2002; Krucker et al. 2003).

Three experiments are flown on the *Hinode* mission (Kosugi et al. 2007) launched in 2006. The primary objective of *Hinode* is to study the origin of the corona and the coupling between the fine magnetic structure in the photosphere and the dynamic processes occurring in the corona. *Hinode* has three high-resolution telescopes in visible light, soft X-ray, and extreme ultra-violet (EUV) wavelengths: (a) a 50-cm optical telescope, the *Solar Optical Telescope* (SOT), (b) an X-ray telescope (XRT) for imaging the high-temperature coronal plasma with angular resolution  $\sim 1$  arcsec, (c) an EUV imaging spectrometer (EIS) for diagnosing events observed.

The telescope SOT (Tsuneta et al. 2008) gives measurements of the magnetic fields in features as small as 100 km in size thereby providing ten times better resolution than other space- and ground-based magnetic field measurements. So the SOT instrument gives opportunity to observe the Sun continuously with the level of

resolution that ground-based observations can match only under exceptionally good conditions. SOT aims at measuring the magnetic field and the Doppler velocity field in the photosphere.

New space-borne observations of the Sun from *Hinode*, *RHESSI*, *Solar Dynamics Observatory (SDO)* (Tarbell and AIA Team 2011), and *Solar Terrestrial Relations Observatory (STEREO)* have produced stunning results, invigorated solar research and challenged existing theoretical models.

The link between the solar flares observed and **topology** of the magnetic field in *active regions*, in which these flares occurred, was investigated by Gorbachev and Somov (1989, 1990). They developed the first topological model of an actual flare, the flare on 1980, November 5, and have shown that

all large-scale characteristic features of a flare can be explained by the presence of a current layer formed on the so-called *separator* which is the intersection of the separatrix surfaces.

In particular, the flare ribbons in the chromosphere as well as the ‘intersecting’ soft X-ray loops in the corona are the consequences of a topological structure of a magnetic field near the separator.

An increasing number of investigations clearly relates the location of a ‘chromospheric flare’ – the flare’s manifestation in the solar chromosphere – with the topological magnetic features of active regions (Mandrini et al. 1991, 1993; Démoulin et al. 1993; Bagalá et al. 1995; Longcope and Silva 1998). In all these works it was confirmed that the solar flares can be considered as a result of the interaction of large-scale magnetic structures; the authors derived the location of the separatrices – surfaces that separate cells of different field line connectivities – and of the separator.

These studies strongly supported the concept of **magnetic reconnection** in solar flares (Giovanelli 1946; Dungey 1958; Sweet 1958). Solar observations with the Hard X-ray Telescope (HXT) and the Soft X-ray Telescope (SXT) on board the *Yohkoh* satellite clearly showed that

the magnetic reconnection effect is common to impulsive (compact) and gradual (large scale) solar flares

(Masuda et al. 1994, 1995). However, in the interpretation of the *Yohkoh* data, the basic physics of magnetic reconnection in the solar atmosphere remained uncertain (see Kosugi and Somov 1998). Significant parts of the book in your hands are devoted to the physics of the reconnection process, a fundamental feature of astrophysical and laboratory plasmas.

Solar flares and *coronal mass ejections* (CMEs) strongly influence the interplanetary and terrestrial space by virtue of shock waves, hard electromagnetic radiation and accelerated particles (Kivelson and Russell 1995; Miroshnichenko 2001). That is why the problem of ‘weather and climate’ prediction in the *near space* becomes more and more important. The term ‘*near space*’ refers to the space that is within the reach of orbiting stations, both manned and automated. The number of satellites

(meteorological, geophysical, navigational ones) with electronic systems sensitive to the ionizing radiation of solar flares is steadily growing.

It has been established that adverse conditions in the space environment can cause disruption of satellite operations, communications, and electric power distribution grids, thereby leading to socioeconomic losses ([Wright 1997](#)). **Space weather** ([Hanslmeier 2007](#); [Lilensten 2007](#)) is of growing importance to the scientific community and refers to conditions at a particular place and time on the Sun and in the *solar wind*, magnetosphere, ionosphere, and thermosphere that can influence the performance and reliability of spaceborne and ground-based technological systems and can affect human life or health.

It is no mere chance that solar flares and coronal mass ejections are of interest to physicians, biologists and climatologists. Flares influence not only *geospace* – the terrestrial magnetosphere, ionosphere and upper atmosphere ([Hargreaves 1992](#); [Horwitz et al. 1998](#); [de Jager 2005](#)) but also the biosphere and the atmosphere of the Earth. They are therefore not only of pure scientific importance; they also have an applied or **practical relevance**. For this reason, the coming years promise to be the gold era of solar and heliospheric physics.

The latter aspect is, however, certainly beyond the scope of this text, the second volume of the book “Plasma Astrophysics”, lectures given the students of the Astronomical Division of the Faculty of Physics at the Moscow State University in spring semesters over the years after 2000. The subject of the present book “Plasma Astrophysics. Part II. Reconnection and Flares” is the basic physics of the magnetic reconnection phenomenon and the reconnection related flares in astrophysical plasmas. The first volume of the book, “Plasma Astrophysics. Part I. Fundamentals and Practice” ([Somov 2012a](#), referred in the text as Part I), is unique in covering the main principles and practical tools required for understanding and work in modern plasma astrophysics.

**Magnetic reconnection** is a fundamental process in plasmas by which magnetic field topology changes and connections of plasma particles with the magnetic field are re-arranged. Reconnection plays a key role in explosive energy release events, flares in astrophysical plasma. However a direct observations of 3D geometry of magnetic reconnection in space was never able to make until launching of ESA *Cluster* constellation. The *Cluster* mission provides the first opportunity to detect the 3D magnetic structure through 4-point measurement as the spacecraft traverse the heart of a reconnection region.

In addition, the *Cluster* observations coordinated with other satellites enable us to see the evolution of structures at small scales within the *Cluster* tetrahedron, and also at large scales with other satellites. These measurements make it possible to observe the global pattern of reconnection at the magnetopause and in the magnetotail of the Earth (e.g., [Xiao et al. 2007](#)). In situ evidence of the full 3D reconnection geometry and associated dynamics provides an important step towards establishing an observational framework of 3D reconnection.

In the past half a century, great progresses in understanding of the magnetic reconnection effect has been gained through theoretical analysis, numerical simulations, and experimental and satellite observations. We would like to see these progresses, stated most simply.

# Acknowledgements

This textbook has grown out of lectures; and, first of all, I want to thank my students. During many years of my teaching at the Moscow Institute of Physics and Technics (the ‘fiz-tekh’) and later-on at the Moscow State University, they were never silent if something was not or seemed to be not crystal clear immediately. The students forced me to write down this book; they read the Chapters (included in a program of exams) as well as they suggested critical comments and corrections.

I am grateful to my colleagues: Ester Antonucci, Sergei I. Bezrodnykh, Sergei A. Bogachev, Cornelis de Jager, O.G. Den, Sergei V. Diakonov, Andre Duijveman, Pavel A. Gritsyk, Jean-Claude Hénoux, Hugh S. Hudson, Irina A. Kovalenko, Victor A. Kovalev, Takeo Kosugi, Pankaj Kumar, Leonid S. Ledentsov, Yuri E. Litvinenko, Marcos E. Machado, Satoshi Masuda, Sergei A. Markovskii, Elena Yu. Merenkova, Anna V. Oreshina, Inna V. Oreshina, Alexandr I. Podgornii, Olga V. Ptitsina, David M. Rust, Taro Sakao, Yuri I. Skrynnikov, Andrei R. Spektor, Abhishek Srivastava, Zdeněk Švestka, Igor P. Tindo, Vyacheslav S. Titov, Alexandr I. Verneta, and Vladimir I. Vlasov for the pleasure of working together, for generous help and valuable remarks. I am also happy to acknowledge helpful discussions with many of my colleagues and friends in the world. There is no way to adequately express how much I owed to my wife, Irina Konstantinovna Somova, for her love and patience.

This work was supported by the Russian Foundation for Fundamental Research, grants Nos. 04-02-16125-a, 08-02-01033-a and 11-02-00843-a.

Moscow

Boris V. Somov



# Contents

<b>1</b>	<b>Magnetic Reconnection .....</b>	1
1.1	What Is Magnetic Reconnection? .....	1
1.1.1	Neutral Points of a Magnetic Field .....	1
1.1.2	Reconnection in Vacuum .....	3
1.1.3	Reconnection in Plasma .....	4
1.1.4	Three Stages in the Reconnection Process .....	7
1.2	Acceleration in Current Layer, Why and How? .....	9
1.2.1	Simplified Consideration .....	9
1.2.2	The Origin of Particle Acceleration .....	11
1.2.3	Acceleration in a Neutral Current Layer .....	11
1.3	Practice: Exercises and Answers .....	15
<b>2</b>	<b>Reconnection in a Strong Magnetic Field .....</b>	19
2.1	Small Perturbations Near a Neutral Line .....	19
2.1.1	Historical Comments .....	19
2.1.2	Basic Equation of the 2D Ideal MHD .....	20
2.1.3	The Strong Magnetic Field Approximation .....	21
2.1.4	Formation of a Current Layer .....	22
2.1.5	Classical Formulation of a Problem .....	23
2.1.6	A Linearized Problem for Small Perturbations .....	25
2.1.7	Converging Waves and the Cumulative Effect .....	26
2.2	Large Perturbations Near a Neutral Line .....	28
2.2.1	Magnetic Field Line Deformations .....	29
2.2.2	Plasma Density Variations .....	32
2.3	Dynamic Dissipation of Magnetic Field .....	33
2.3.1	Conditions of Appearance .....	33
2.3.2	The Physical Meaning of Dynamic Dissipation .....	35
2.4	Nonstationary Analytical Models of RCL .....	36
2.4.1	Self-similar 2D MHD Solutions .....	36
2.4.2	Magnetic Collapse at the Zeroth Point .....	39

2.4.3	From Collisional to Collisionless Reconnection .....	42
2.4.4	Hall Currents in a Reconnecting Current Layer .....	44
<b>3</b>	<b>Generalized Analytical Models of Reconnection .....</b>	<b>47</b>
3.1	Two Classical Models of Reconnection .....	47
3.2	Generalized Models of Syrovatskii's Current Layer .....	49
3.3	Approach to Finding the Magnetic Field .....	51
3.4	Current Layer with Attached Discontinuities .....	53
3.4.1	Magnetic Field Pattern .....	53
3.4.2	Character of Shock Waves .....	55
3.4.3	Changes of a Shock-Wave Type .....	57
3.5	Current Layers in Collisionless Plasma .....	59
3.6	Disrupting Current Layers .....	60
3.7	Practice: Exercises and Answers .....	63
<b>4</b>	<b>Evidence of Reconnection in Solar Flares .....</b>	<b>67</b>
4.1	The Role of Magnetic Fields .....	67
4.1.1	Basic Questions .....	67
4.1.2	Concept of Magnetic Reconnection .....	68
4.1.3	Some Results of Observations .....	70
4.2	The Simple Topological Model of an Active Region .....	71
4.2.1	The Potential Magnetic Field Approximation .....	71
4.2.2	Classification of Zeroth Points .....	73
4.2.3	The Number of Zeroth Points .....	74
4.2.4	The Electric Currents Needed .....	77
4.2.5	The Longitudinal Magnetic Field .....	78
4.3	The Solar Flare on 1980 November 5 .....	79
4.3.1	Observed and Model Magnetograms .....	79
4.3.2	Topological Portrait of the Active Region .....	83
4.3.3	Features of the Flare Topological Model .....	85
4.3.4	Complexity of a Topological Model .....	87
4.3.5	The S-Like Morphology and Eruptive Activity .....	88
<b>5</b>	<b>Reconnection in Action .....</b>	<b>91</b>
5.1	A Current Layer as the Source of Energy .....	91
5.1.1	Pre-flare Accumulation of Energy .....	91
5.1.2	Flare Energy Release .....	92
5.1.3	The RCL as a Part of an Electric Circuit .....	94
5.2	Solar Flares of the Syrovatskii Type .....	96
5.2.1	General Definitions .....	96
5.2.2	Accumulation of Flare Energy .....	97
5.2.3	Stationary Heating of a Current Layer .....	98
5.2.4	Particle Acceleration .....	100
5.2.5	3D Models of the Syrovatskii Type .....	101
5.3	Different Types of Solar Flares .....	102
5.3.1	The Sakao-Type Flares .....	102

5.3.2	New Topological Models .....	105
5.3.3	Reconnection Between Active Regions .....	106
<b>6</b>	<b>The Bastille Day Flare and Similar Solar Flares .....</b>	<b>109</b>
6.1	Observational Properties of the Bastille Day Flare .....	109
6.1.1	General Characteristics of the Flare .....	109
6.1.2	Overlay HXR Images on Magnetograms .....	111
6.1.3	Questions of Interpretation .....	114
6.1.4	Motion of the HXR Kernels .....	115
6.1.5	Magnetic Field Evolution .....	116
6.1.6	The HXR Kernels and Field Evolution .....	117
6.2	Simplified Topological Model .....	118
6.2.1	Photospheric Field Model. Topological Portrait .....	118
6.2.2	Coronal Field Model: Separators .....	119
6.2.3	Chromospheric Ribbons and Kernels .....	121
6.2.4	Reconnected Magnetic Flux .....	123
6.2.5	Electric Field .....	126
6.2.6	Discussion of Topological Model .....	127
6.3	Topological Trigger for Solar Flares .....	129
6.3.1	What Is That? .....	129
6.3.2	How Does the Topological Trigger Work? .....	131
6.4	The Topological Trigger Does Work .....	135
6.4.1	The Geoeffective Flares on 2003 November 18 .....	135
6.4.2	Modeling the Photospheric Magnetograms .....	136
6.4.3	Separators and Separatrix Surfaces .....	137
6.4.4	Evolution of Magnetic Field Topology .....	138
6.4.5	Topologically Critical State .....	140
<b>7</b>	<b>Electric Currents Related to Reconnection .....</b>	<b>143</b>
7.1	Plane Reconnection as a Starting Point .....	143
7.1.1	Pre-flare Evolution and Energy Accumulation .....	143
7.1.2	Flare Energy Release .....	147
7.1.3	Three-Component 2D and 3D Reconnection .....	149
7.2	Photospheric Shear and Coronal Reconnection .....	151
7.2.1	Accumulation of Magnetic Energy .....	151
7.2.2	Flare Energy Release and CMEs .....	153
7.2.3	Flare and HXR Footpoints .....	155
7.3	Shear Flows and Photospheric Reconnection .....	158
7.4	Motions of the HXR Footpoints in Flares .....	160
7.4.1	The Footpoint Motions in Some Flares .....	160
7.4.2	Statistics of the Footpoint Motions .....	161
7.4.3	The FP Motions Orthogonal to the SNL .....	162
7.4.4	The FP Motions Along the SNL .....	163
7.4.5	Discussion of Statistical Results .....	165

7.5	Motions of the Coronal HXR Sources .....	169
7.5.1	Observational Background .....	169
7.5.2	Theoretical Interpretation .....	169
7.6	Open Issues and Some Conclusions .....	174
<b>8</b>	<b>Models of Reconnecting Current Layers.....</b>	<b>177</b>
8.1	Magnetically Neutral Current Layers .....	177
8.1.1	The Simplest MHD Model .....	177
8.1.2	The Current Layer by Syrovatskii .....	179
8.1.3	Simple Scaling Laws .....	182
8.2	Magnetically Non-neutral RCL.....	184
8.2.1	Transversal Magnetic Fields .....	184
8.2.2	The Longitudinal Magnetic Field .....	185
8.3	Basic Physics of the SHTCL.....	187
8.3.1	A General Formulation of the Problem .....	187
8.3.2	Problem in the Strong Field Approximation .....	190
8.3.3	Basic Local Parameters of the SHTCL .....	191
8.3.4	The General Solution of the Problem .....	192
8.4	Plasma Turbulence Inside the SHTCL .....	194
8.4.1	Marginal and Saturation Regimes .....	194
8.4.2	Formulae for the Basic Parameters of the SHTCL .....	196
8.4.3	The Applicability of the Model .....	197
8.4.4	The SHTCL with a Small Transverse Field .....	200
8.5	SHTCL in Solar Flares.....	201
8.5.1	Why Are Flares So Different But Similar? .....	201
8.5.2	Magnetic-Field Gradient Effects .....	203
8.5.3	The Role of the Plasma Density .....	204
8.5.4	Super-Hot Plasma Production .....	205
8.5.5	Before and After <i>Yohkoh</i> .....	206
8.5.6	On the Particle Acceleration in a SHTCL .....	207
8.6	Open Issues of Reconnection in Flares .....	208
8.7	Practice: Exercises and Answers .....	210
<b>9</b>	<b>Collapsing Magnetic Traps in Solar Flares .....</b>	<b>213</b>
9.1	Coronal HXR Sources in Flares .....	213
9.1.1	General Properties and Observational Problems .....	213
9.1.2	Upward Motion of Coronal HXR Sources .....	215
9.1.3	<i>Yohkoh</i> Data on Average Upward Velocity .....	216
9.1.4	RHESSI Observation of Coronal X-Ray Sources .....	219
9.2	The Collapsing Trap Effect in Solar Flares .....	220
9.2.1	Fast Electrons in Coronal HXR Sources .....	220
9.2.2	Fast Plasma Outflows and Shocks .....	221
9.2.3	Particle Acceleration in Collapsing Trap .....	222
9.2.4	The Upward Motion of Coronal HXR Sources .....	225
9.2.5	Trap Without a Shock Wave .....	227

9.3	Acceleration Mechanisms in Traps .....	228
9.3.1	Fast and Slow Reconnection .....	228
9.3.2	The First-Order Fermi-Type Acceleration .....	231
9.3.3	The Betatron Acceleration in a Collapsing Trap .....	232
9.3.4	The Betatron Acceleration in a Shockless Trap .....	234
9.4	Main Properties of Trapped Particles .....	235
9.4.1	Dominant Mechanism of Acceleration .....	235
9.4.2	Anisotropy of Trapped Particles .....	238
9.4.3	The Number of Trapped Particles .....	240
9.4.4	Density of Trapped Particles .....	242
9.4.5	Total Energy of Trapped Particles .....	245
9.5	Diagnostics of Collapsing Traps .....	248
9.5.1	Spectrum of Trapped Particles .....	248
9.5.2	The Emission Measure of HXR Bremsstrahlung .....	253
9.5.3	The Spectrum of HXR Bremsstrahlung .....	255
9.6	Coulomb Collisions in Collapsing Traps .....	259
9.6.1	Qualitative Description of Expected Effects .....	259
9.6.2	Isotropization Effect of Scattering .....	260
9.6.3	Particle Confinement .....	262
9.6.4	Spectrum of Trapped Particles .....	263
9.6.5	Particle Braking and Confinement .....	265
9.7	Final Remarks About Collapsing Traps .....	266
9.8	Practice: Exercises and Answers .....	268
10	<b>Solar-Type Flares in Laboratory and Space .....</b>	275
10.1	Solar Flares in Laboratory .....	275
10.1.1	Turbulent Heating in Toroidal Devices .....	275
10.1.2	Current-Driven Turbulence in Current Layers .....	277
10.1.3	Parameters of a Current Layer with CDT .....	279
10.1.4	The SHTCL with Anomalous Heat Conduction .....	280
10.2	Reconnection in the Earth Magnetosphere .....	281
10.2.1	Magnetospheric Physics Problems .....	281
10.2.2	Origin of Magnetospheric Reconnection .....	282
10.2.3	MHD Simulations of Space Weather .....	284
10.3	Flares in Accretion Disk Coronae .....	285
10.3.1	Introductory Comments .....	285
10.3.2	Models of the Star Magnetosphere .....	286
10.3.3	Power of Energy Release in the Disk Coronae .....	289
10.4	The Giant Flares .....	291
11	<b>Particle Acceleration in Current Layers .....</b>	293
11.1	Magnetically Non-neutral RCLs .....	293
11.1.1	An Introduction in the Problem .....	293
11.1.2	Dimensionless Parameters and Equations .....	294
11.1.3	An Iterative Solution of the Problem .....	297

11.1.4	The Maximum Energy of an Accelerated Particle .....	300
11.1.5	The Non-adiabatic Thickness of Current Layer .....	302
11.2	Regular Versus Chaotic Acceleration .....	303
11.2.1	Reasons for Chaos .....	303
11.2.2	The Stabilizing Effect of the Longitudinal Field .....	305
11.2.3	Characteristic Times of Processes .....	306
11.2.4	Dynamics of Accelerated Electrons in Solar Flares.....	307
11.2.5	Initial Conditions of Motion .....	308
11.2.6	Particle Simulations of Collisionless Reconnection .....	308
11.3	Ion Acceleration in Current Layers.....	309
11.3.1	Ions Are Much Heavier Than Electrons .....	309
11.3.2	Electrically Non-neutral Current Layers .....	310
11.3.3	Maximum Particle Energy and Acceleration Rates .....	312
11.4	How Are Solar Particles Accelerated? .....	315
11.4.1	Place of Acceleration .....	315
11.4.2	Time of Acceleration .....	317
11.4.3	Spectrum of Accelerated Particles .....	318
11.5	Cosmic Rays and Cosmic Gamma-Rays .....	319
12	<b>Structural Instability of Reconnecting Current Layers .....</b>	321
12.1	Some Properties of Current Layers .....	321
12.1.1	Current Layer Splitting .....	321
12.1.2	Evolutionarity of Reconnecting Current Layers .....	323
12.1.3	Magnetic Field Near the Current Layer .....	324
12.1.4	Reconnecting Current Layer Flows .....	325
12.1.5	Additional Simplifying Assumptions .....	326
12.2	Small Perturbations Outside the RCL .....	327
12.2.1	Basic Assumptions .....	327
12.2.2	Propagation of Perturbations Normal to a RCL .....	328
12.2.3	The Inclined Propagation of Perturbations .....	329
12.3	Perturbations Inside the RCL .....	333
12.3.1	Linearized Dissipative MHD Equations .....	333
12.3.2	Boundary Conditions .....	334
12.3.3	Dimensionless Equations and Small Parameters .....	336
12.3.4	Solution of the Linearized Equations .....	337
12.4	Solution on the Boundary of the RCL .....	340
12.5	The Criterion of Evolutionarity .....	343
12.5.1	One-Dimensional Boundary Conditions .....	343
12.5.2	Solutions of the Boundary Equations .....	344
12.5.3	Evolutionarity and Splitting of Current Layers .....	347
12.6	Practice: Exercises and Answers .....	348
13	<b>Tearing Instability of Reconnecting Current Layers .....</b>	351
13.1	The Origin of the Tearing Instability .....	351
13.1.1	Two Necessary Conditions .....	351
13.1.2	Historical Comments .....	352

<b>13.2</b>	<b>The Simplest Problem and Its Solution .....</b>	354
13.2.1	The Model and Equations for Small Disturbances .....	354
13.2.2	The External Non-dissipative Region .....	356
13.2.3	The Internal Dissipative Region .....	357
13.2.4	Matching of the Solutions and the Dispersion Relation ..	359
<b>13.3</b>	<b>Physical Interpretation of the Instability .....</b>	360
13.3.1	Acting Forces of the Tearing Instability .....	360
13.3.2	Dispersion Equation for Tearing Instability .....	362
<b>13.4</b>	<b>The Stabilizing Effect of Transversal Field .....</b>	363
<b>13.5</b>	<b>Compressibility and a Longitudinal Field .....</b>	366
13.5.1	Neutral Current Layers .....	366
13.5.2	Non-neutral Current Layers .....	368
<b>13.6</b>	<b>The Kinetic Approach.....</b>	369
13.6.1	The Tearing Instability of Neutral Layer .....	369
13.6.2	Stabilization by the Transversal Field .....	373
13.6.3	The Tearing Instability of the Geomagnetic Tail .....	374
<b>14</b>	<b>Magnetic Reconnection and Turbulence .....</b>	377
<b>14.1</b>	<b>Reconnection and Magnetic Helicity .....</b>	377
14.1.1	General Properties of Complex MHD Systems .....	377
14.1.2	Two Types of MHD Turbulence .....	379
14.1.3	Helical Scaling in MHD Turbulence .....	381
14.1.4	Large-Scale Solar Dynamo .....	382
<b>14.2</b>	<b>Coronal Heating and Flares .....</b>	383
14.2.1	Coronal Heating in Solar Active Regions .....	383
14.2.2	Helicity and Reconnection in Solar Flares .....	384
<b>14.3</b>	<b>Stochastic Acceleration in Solar Flares .....</b>	386
14.3.1	Stochastic Acceleration of Electrons .....	386
14.3.2	Acceleration of Protons and Heavy Ions .....	388
14.3.3	Acceleration of $^3\text{He}$ and $^4\text{He}$ in Solar Flares .....	389
14.3.4	Electron-Dominated Solar Flares .....	389
<b>14.4</b>	<b>Mechanisms of Coronal Heating .....</b>	392
14.4.1	Heating of the Quiet Solar Corona .....	392
14.4.2	Coronal Heating in Active Regions .....	394
<b>14.5</b>	<b>Practice: Exercises and Answers .....</b>	395
<b>15</b>	<b>Reconnection in Weakly-Ionized Plasma .....</b>	397
<b>15.1</b>	<b>Early Observations and Classical Models .....</b>	397
<b>15.2</b>	<b>Model of Reconnecting Current Layer .....</b>	398
15.2.1	Simplest Balance Equations .....	398
15.2.2	Solution of the Balance Equations .....	400
15.2.3	Characteristics of the Reconnecting Current Layer .....	400
<b>15.3</b>	<b>Reconnection in Solar Prominences .....</b>	403
<b>15.4</b>	<b>Element Fractionation by Reconnection .....</b>	404
<b>15.5</b>	<b>The Photospheric Dynamo .....</b>	406
15.5.1	Current Generation Mechanisms .....	406

15.5.2	Physics of Thin Magnetic Flux Tubes .....	407
15.5.3	FIP Fractionation Theory.....	409
15.6	Practice: Exercises and Answers .....	410
<b>16</b>	<b>Magnetic Reconnection of Electric Currents .....</b>	<b>415</b>
16.1	Introductory Comments .....	415
16.2	Flare Energy Storage and Release .....	416
16.2.1	From Early Models to Future Investigations .....	416
16.2.2	Some Alternative Trends in the Flare Theory .....	419
16.2.3	Current Layers at Separatrices .....	421
16.3	Current Layer Formation Mechanisms .....	421
16.3.1	Magnetic Footpoints and Their Displacements .....	421
16.3.2	Classical 2D Reconnection .....	423
16.3.3	Creation of Current Layers by Shearing Flows .....	425
16.3.4	Antisymmetrical Shearing Flows .....	426
16.3.5	The Third Class of Displacements .....	428
16.4	The Shear and Reconnection of Currents .....	429
16.4.1	Physical Processes Related to Shear and Reconnection ..	429
16.4.2	Topological Interruption of Electric Currents .....	431
16.4.3	The Inductive Change of Energy.....	431
16.5	Potential and Non-potential Fields .....	433
16.5.1	Properties of Potential Fields .....	433
16.5.2	Classification of Non-potential Fields .....	434
16.6	Observations by <i>Hinode</i> .....	435
<b>17</b>	<b>Fast Particles in Solar Flares .....</b>	<b>439</b>
17.1	Hard X-Ray Radiation from Fast Electrons .....	439
17.2	Electron Spectrum and Choice of a Model.....	440
17.2.1	Injection Spectrum.....	440
17.2.2	Electron Spectrum and Choice of a Model .....	441
17.2.3	Thin Target .....	442
17.2.4	Thick Target .....	444
17.2.5	Intermediate Cases .....	445
17.3	Thick Target and Other Models .....	446
17.3.1	The Flux of Injected Electrons .....	446
17.3.2	Some Combined Models .....	448
17.4	Flare Heating of the Chromosphere .....	449
17.4.1	Chromospheric Heating by Electrons .....	449
17.4.2	Protons or Electrons Heat White-Light Flares? .....	452
17.5	Practice: Exercises and Answers .....	455
<b>Epilogue .....</b>	<b>459</b>	
<b>A Acronyms .....</b>	<b>461</b>	
<b>B Notation .....</b>	<b>463</b>	

Contents	xxi
<b>C    Useful Formulae .....</b>	<b>465</b>
<b>D    Constants .....</b>	<b>469</b>
<b>Bibliography .....</b>	<b>471</b>
<b>Index .....</b>	<b>497</b>



# Chapter 1

## Magnetic Reconnection

**Abstract** Magnetic reconnection is a fundamental feature of astrophysical and laboratory plasmas, which takes place under definite but quite general conditions and creates a sudden release of magnetic energy, an original electrodynamic explosion or *flare*. Surprisingly, the simplest approximation – a single particle in given force fields – gives us clear approach to several facets of reconnection and particle acceleration.

### 1.1 What Is Magnetic Reconnection?

#### 1.1.1 Neutral Points of a Magnetic Field

The so-called *zeroth* or *neutral* points, lines and surfaces of magnetic field, which are the regions where magnetic field equals zero:

$$\mathbf{B} = 0, \quad (1.1)$$

play the important role in plasma astrophysics since [Giovanelli \(1946\)](#). They are of interest for the following reasons. First, **plasma behavior is quite specific** in the vicinity of such regions ([Dungey 1958](#)). Second, they predetermine a large number of astrophysical phenomena. We shall be primarily concerned with non-stationary phenomena in the solar atmosphere (such as flares, coronal transients, coronal mass ejections), accompanied by particle acceleration to high energies. Analogous phenomena take place on other stars, in planetary magnetospheres, and pulsars.

Neutral points of magnetic field most commonly appear in places of the interaction of magnetic fluxes.

The simplest way to recognize this is to consider the emerging flux in the solar atmosphere.

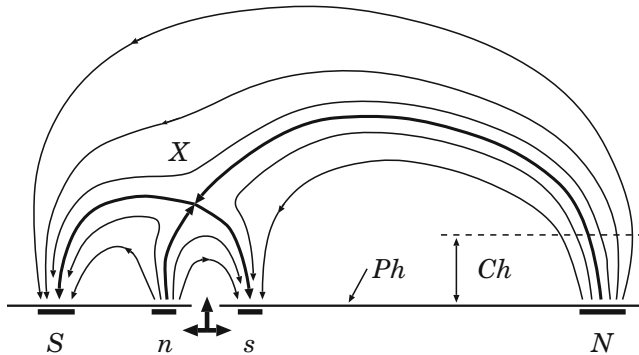


**Fig. 1.1** The emergence of a new magnetic flux ( $n, s$ ) from under the photosphere  $Ph$  inside an active region whose magnetic field is determined by the sources  $S$  and  $N$

**Fig. 1.2** A hyperbolic zeroth point (the line along the axis  $z$  of the Cartesian coordinates  $x, y, z$ ) of a potential magnetic field  $\mathbf{B}$

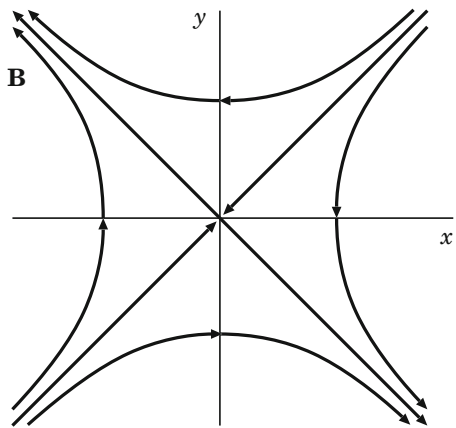
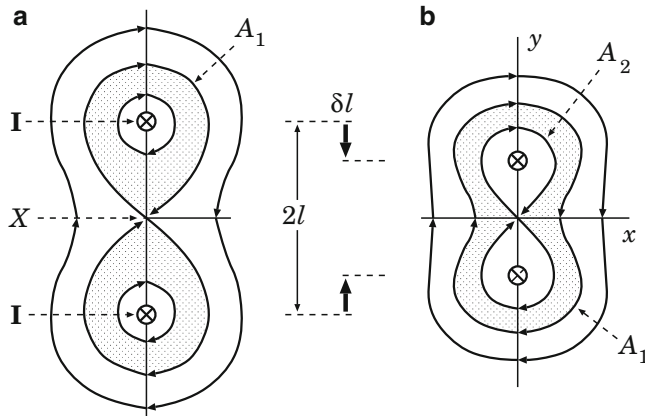


Figure 1.1 shows the sources  $N$  and  $S$  corresponding to the active region's magnetic field. The sources  $n$  and  $s$  play the role of a new flux emerging from under the photosphere  $Ph$ . The chromosphere is shown by the dashed line  $Ch$ . We consider an arrangement of the sources along a straight line, although the treatment can well be generalized (Sect. 4.2.1) to consider arbitrary configurations of the four sources in the photosphere.

Obviously a point can be found above the emerging flux, where oppositely directed but equal in magnitude magnetic fields ‘meet’. Here the total field, that is the sum of the old and the new ones, is zero. Let us denote this point by  $X$ , bearing in mind that the field in its vicinity has the hyperbolic structure shown in Fig. 1.2.

In order to convince oneself that this is the case, we can consider the magnetic field in the simplest approach which is the *potential* approximation (see Part I, Sect. 13.1.3). This will be done, for example, in Sect. 1.1.4. However, at first, we shall recall and illustrate the basic definitions related to the magnetic reconnection effect considering the simplest situations.



**Fig. 1.3** The potential field of two parallel currents **I**: (a) the initial state,  $2l$  is a distance between the currents; (b) the final state after they have been drawn nearer by a driven displacement  $\delta l$ . Note that here the electric currents are antiparallel to the axis  $z$  of the Cartesian coordinates

### 1.1.2 *Reconnection in Vacuum*

The X-type points constitute the most important topological peculiarity of a magnetic field. They are the places where redistribution of magnetic fluxes occurs, which changes the connectivity of field lines. Let us illustrate such a process by the simplest example of two parallel electric currents **I** of equal magnitude  $I$  in vacuum as shown in Fig. 1.3.

The magnetic field of these currents forms three different fluxes in the plane ( $x$ ,  $y$ ). Two of them belong to the upper and the lower currents, respectively, and are situated inside the *separatrix* field line  $A_1$  which forms the eight-like curve with a zeroth X-point. The third flux situated outside this curve belongs to both currents and is situated outside the separatrix.

If the currents are displaced in the direction of each other, then the following redistribution of a magnetic flux will take place. The current's proper fluxes will diminish by the quantity  $\delta A$  (shown by two shadowed rings in Fig. 1.3a), while their common flux will increase by the same quantity (shown by the shadowed area in Fig. 1.3b). So the field line  $A_2$  will be the separatrix of the final state.

This process is realized as follows. Two field lines approach the X-point, merge there, forming a separatrix, and then they *reconnect* forming a field line which encloses both currents. Such a process is termed reconnection of field lines or *magnetic reconnection*.  $A_2$  is the last reconnected field line.

Reconnection is of fundamental importance for the nature of many non-stationary phenomena in astrophysical plasma. We shall discuss the physics of this process more fully in Chaps. 2–16. Suffice it to note that

the magnetic reconnection process is inevitably associated with electric field generation in the vicinity of a neutral point.

This field is the inductive one, since

$$\mathbf{E} = -\frac{1}{c} \frac{\partial \mathbf{A}}{\partial t}, \quad (1.2)$$

where  $\mathbf{A}$  is the vector potential of magnetic field,

$$\mathbf{B} = \text{rot } \mathbf{A}. \quad (1.3)$$

In the above example the electric field is directed along the  $z$  axis. It is clear that, if  $\delta t$  is the characteristic time of the reconnection process shown in Fig. 1.3, then according to (1.2)

$$E \approx \frac{1}{c} \frac{\delta A}{\delta t} \approx \frac{1}{c} \frac{A_2 - A_1}{\delta t}; \quad (1.4)$$

the last equality is justified in Part I, Sect. 14.2.

**Reconnection in vacuum is a real physical process:** magnetic field lines move to the X-type neutral point and reconnect in it as well as

the electric field is induced and can accelerate a charged particle or particles in the vicinity of the neutral point.

In this sense, a *collisionless* reconnection – the physical process in a high-temperature *rarefied* plasma such as the solar corona, geomagnetic tail, fusion plasmas, and so on – is simpler for understanding than reconnection in a highly-conducting collisional astrophysical plasma.

### 1.1.3 Reconnection in Plasma

Let us try to predict plasma behavior near the X-point as reconnection proceeds on the basis of our knowledge about the motion of a charged particle in given magnetic and electric fields (see Part I, Chap. 5).

The first obvious fact is that, given the non-zero electric field  $\mathbf{E}$ , the plasma begins to drift in the magnetic field  $\mathbf{B}$  (Part I, Sect. 5.1.5), in a way shown in Fig. 1.4a. The *electric drift velocity*

$$\mathbf{v}_d = c \frac{\mathbf{E} \times \mathbf{B}}{B^2} \quad (1.5)$$

is shown in four points. The magnetic field is considered as a uniform field in the vicinity of these points.

The second fact consists of the inapplicability of the *adiabatic drift approximation* (Part I, Sect. 5.2) near the zeroth point, since the Larmor radius (see Appendix 3)

$$r_L = \frac{cp_\perp}{eB} \quad (1.6)$$

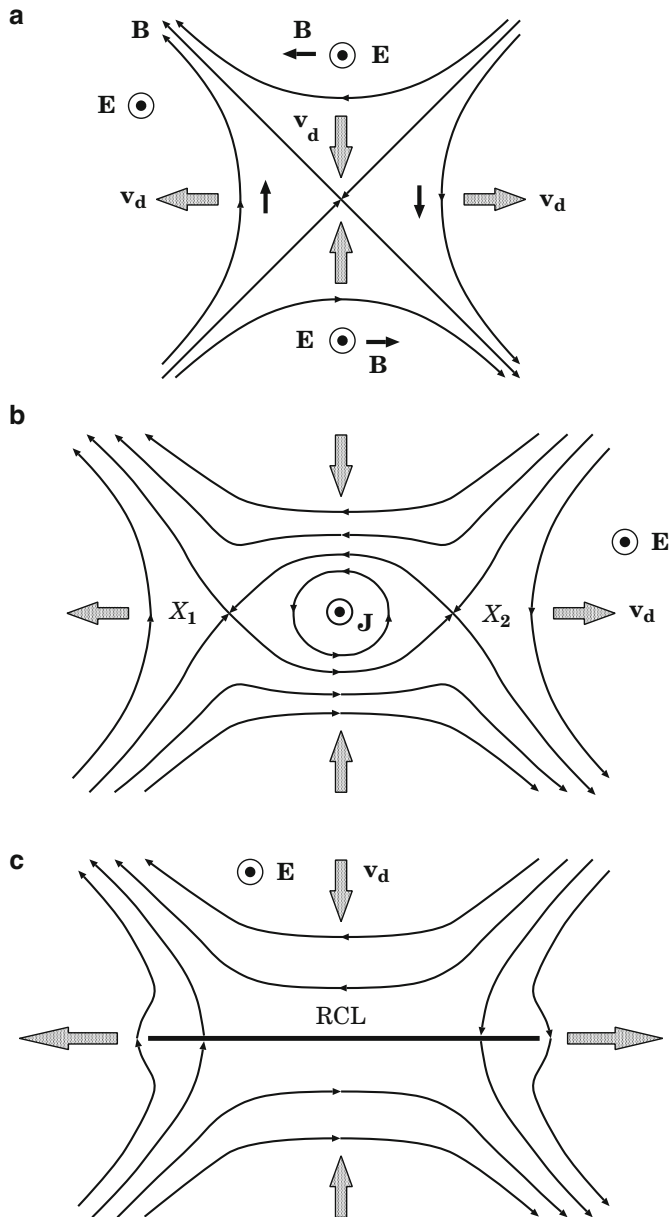


**Fig. 1.4** (a) Plasma flows owing to the electric drift in the vicinity of a zeroth point. (b) The appearance of secondary X-points – bifurcation of the initial zeroth line, given the current  $\mathbf{J}$  flowing along it. (c) A thin reconnecting current layer (RCL)

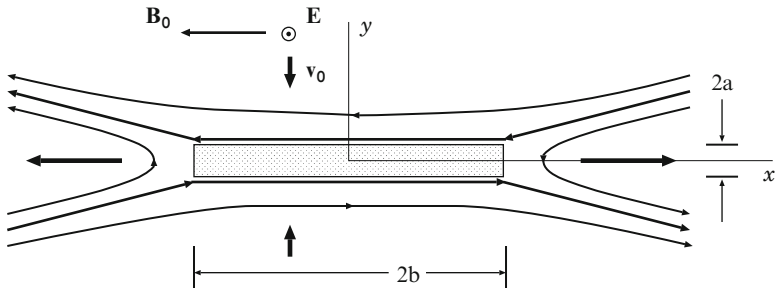


**Fig. 1.5** The simplest model of a RCL – the neutral layer

increases indefinitely as  $B \rightarrow 0$ . We have to solve the exact equations of motion. This will be done later on. However we see at once that in this region an electric current  $\mathbf{J}$  can flow along the  $z$  axis. The proper magnetic field of the current changes the initial field topology, so that there will be two symmetric zeroth points  $X_1$  and  $X_2$  on the  $x$  axis in Fig. 1.4b instead of one X-point.

The same arguments concerning drift flows and X-point *bifurcation* are applicable to the new X-points. We easily guess that

the result of the interaction of line currents with the external hyperbolic field is a *current layer* in the region of reconnection.

The **reconnecting current layer** (RCL) is shown by thick solid straight line in Fig. 1.4c. Note that the direction of the electric current can change at the external edges of the layer. Here the currents can flow in the opposite direction (the *reverse currents*) with respect to the main current (the *direct current*) in the central part.

RCLs are, in general, at least *two-dimensional* and *two-scale* formations. The former means that one-dimensional models are in principle inadequate for describing the RCL: both plasma inflow in the direction perpendicular to the layer and plasma outflow along the layer, along the  $x$  axis in Fig. 1.5, have to be taken into account.

The existence of two scales implies that usually (for a sufficiently strong field and high conductivity like in the solar corona) the RCL width  $2b$  is much greater than its thickness  $2a$ . This is essential since

the wider the reconnecting current layer, the larger the magnetic energy which is accumulated

in the region of reconnecting fluxes interaction. On the other hand, a small thickness is responsible for the high rate of accumulated energy dissipation, as well as for the possibility of non-stationary processes (for instance, *tearing instability*) in the RCL. It is generally believed, on a very serious basis (see Chap. 4), that the solar flares and similar phenomena in astrophysical plasma result from the fast conversion of the excess magnetic energy into heat and bulk plasma motions as well as the kinetic energy of accelerated particles.

### 1.1.4 Three Stages in the Reconnection Process

Now we come back to the example of magnetic reconnection considered in Sect. 1.1.2. Let the parallel electric currents  $\mathbf{I}$  move to each other with velocity  $2\mathbf{u}$  as shown in Fig. 1.3. Let us describe the electric field induced in the space between the currents.

The magnetic field of two parallel currents is expressed with the aid of the vector-potential  $\mathbf{A}$  having only the  $z$  component:

$$\mathbf{A} = \{0, 0, A(x, y, t)\}. \quad (1.7)$$

The magnetic field  $\mathbf{B}$  is defined by the  $z$  component of the vector-potential:

$$\mathbf{B} = \text{rot } \mathbf{A} = \left\{ \frac{\partial A}{\partial y}, -\frac{\partial A}{\partial x}, 0 \right\}. \quad (1.8)$$

The scalar function  $A(x, y, t)$  is termed the *vector potential*. In the case under consideration

$$A(x, y, t) = \frac{I}{c} \{ \ln [x^2 + (y - l(t))^2] + \ln [x^2 + (y + l(t))^2] \}. \quad (1.9)$$

Note that here the electric currents are antiparallel to the axis  $z$  of the Cartesian coordinates  $x, y, z$ .

For a sake of simplicity, near the zeroth line of the magnetic field, situated on the  $z$  axis, formula (1.9) may be expanded in a Teylor series, the zeroth order and square terms of the expansion being sufficient for our purposes:

$$A(x, y, t) = A(0, 0, t) + \frac{2I}{c} (x^2 - y^2). \quad (1.10)$$

Here

$$A(0, 0, t) = \frac{4I}{c} \ln l(t) = A(t) \quad (1.11)$$

is the time-dependent part of the vector potential.

From formula (1.11) the electric field induced along the zeroth line and in its vicinity can be found

$$\mathbf{E} = -\frac{1}{c} \frac{\partial \mathbf{A}}{\partial t} = -\frac{4I}{c} \frac{1}{l} \frac{dl}{dt} \mathbf{e}_z, \quad (1.12)$$

where the half-distance between currents  $l = l_0 - ut$  with  $u = |\mathbf{u}|$ . Hence

$$\mathbf{E} = \frac{4I}{c} \frac{1}{l} u \mathbf{e}_z. \quad (1.13)$$

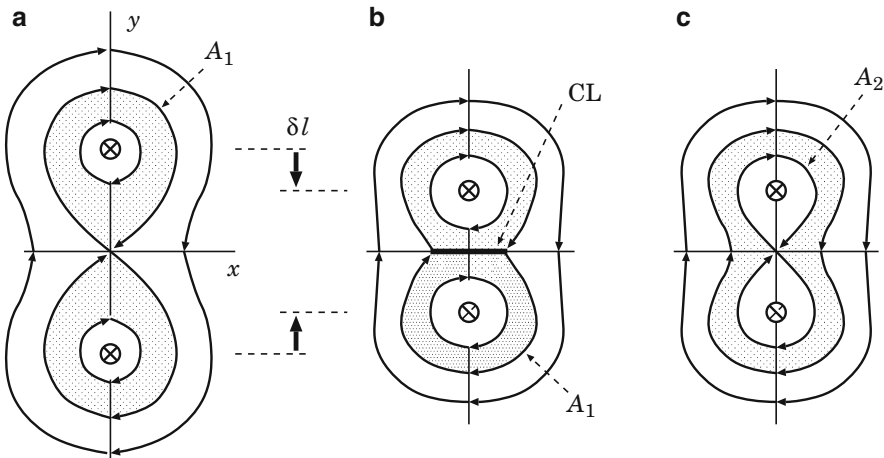


**Fig. 1.6** Three states of magnetic field: (a) the initial state; (b) the *pre-reconnection* state with a ‘non-reconnecting’ current layer  $CL$ ; (c) the final state after reconnection

Therefore

the electric field induced between two parallel currents, that move to each other, is antiparallel to these electric currents and induces the current layer in plasma

as shown in Fig. 1.6.

So two parallel currents are displaced from the initial state (a) in Fig. 1.6 to the final state (c) in plasma, which is the same as the state (b) in Fig. 1.3. However, contrary to the case of reconnection in vacuum, in astrophysical plasma of *low resistivity* we have to add an intermediate state. We call it the *pre-reconnection state*.

At this state, coming between the initial and final one, the electric currents have been displaced to the final positions, but the magnetic field lines have not started to reconnect yet, if the plasma conductivity can be considered as *infinite*.

The ‘non-reconnecting’ current layer along the X-type neutral line protects the interacting magnetic fluxes from reconnection in a plasma of ‘infinite’ conductivity.

The energy of this interaction called the *free magnetic energy* is just the energy of the magnetic field of the current layer.

Because of the *finite* conductivity of astrophysical plasma, magnetic reconnection proceeds slowly (or rapidly) depending on how high (or low) the conductivity of plasma is. Anyway, the final state (c) after reconnection is the same as the state (b) in Fig. 1.3 with the field line  $A_2$  as the separatrix of the final state or the last reconnected line.

The following analogy in everyday life is appropriate to the magnetic reconnection process under discussion. A glass of hot water will invariably cool from a given

temperature (the initial state) to a room temperature (the final state), independently of the mechanism of heat conductivity, i.e. the heat exchange with the surrounding air; the mechanism determines only the rate of cooling.

## 1.2 Acceleration in Current Layer, Why and How?

### 1.2.1 Simplified Consideration

The formation and properties of reconnecting current layers will be considered in detail later on in Chaps. 2–16 in different approximations. However one property which is fundamentally important from the standpoint of astrophysical applications can be understood just now by considering the motion of a charged particle in given magnetic and electric fields (see Part I, Chap. 5). This property is *particle acceleration*.

In accordance with Fig. 1.5, let the magnetic field  $\mathbf{B}$  be directed along the  $x$  axis, changing the sign at  $y = 0$  (the current layer plane). That is why the  $y = 0$  plane is called the *neutral surface* (or neutral plane) and the model under consideration is called the *neutral current layer*. Certainly this simplest model is not well justified from physical point of view but mathematically convenient. Moreover, even being a strong idealization, the model allows us to understand why particles are accelerated in a *reconnecting current layer*.

The electric field  $\mathbf{E}$  is directed along the  $z$  axis, to the right in Fig. 1.7, being constant and homogeneous. Thus, inside the current layer, let us put

$$\mathbf{B} = \{-hy, 0, 0\}, \quad \mathbf{E} = \{0, 0, E\}, \quad (1.14)$$

where  $h$  and  $E$  are constants. We assume that the magnetic field changes its value gradually inside the current layer with a gradient  $h = |\nabla B|$ .

Let us consider the particle motion in such crossed fields. At sufficiently large distances from the neutral plane  $y = 0$ , the motion is a sum of electric and gradient drifts (see Part I, Sect. 5.2.5).

**|** The *electric drift* makes a particle move to the neutral plane from both sides of this plane.

So the electric drift creates some confinement of a particle near the neutral plane.

The *gradient drift* velocity

$$\mathbf{v}_d = \frac{\mathcal{M}c}{eB^2} \mathbf{B} \times \nabla B, \quad (1.15)$$

where

$$\mathcal{M} = \frac{1}{2\pi} \frac{e^2}{mc^2} B \pi r_L^2 \quad (1.16)$$

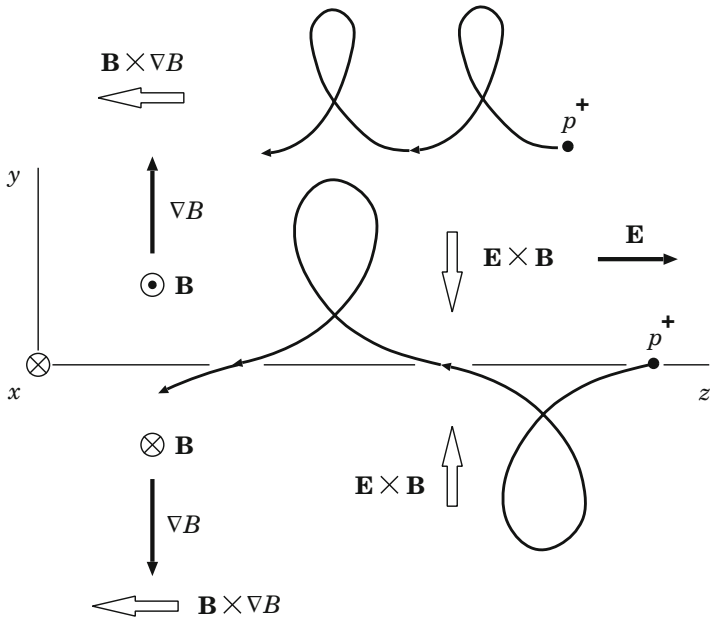


**Fig. 1.7** The drift motions of a positively charged particle (an ion) near the neutral plane  $y = 0$  in a reconnecting current layer. The electric field  $\mathbf{E}$  induces a particle drift towards the neutral plane from both above and below. The case of the slow gradient drift is shown high above the plane and for a particle crossing the plane

is the *magnetic moment* of a particle on the Larmor orbit. Therefore

| the gradient drift drives positively charged particles (protons and ions) in the direction opposite to the electric field  $\mathbf{E}$ ,

i.e. along the negative direction of the  $z$  axis, to the left in Fig. 1.7. Hence the energy of an ion decreases. A negatively charged particle (an electron) moves in opposite direction to the ion's drift, i.e. along the electric field; so its energy also decreases due to the gradient drift.

Note that the electric current generated by gradient drift flows in the direction opposite to the electric field  $\mathbf{E}$  too. That is why, in collisionless magnetic reconnection,

| the electric current generated by the electric field  $\mathbf{E}$  and concentrated in the center of a reconnecting current layer is partially balanced by reverse currents in the gradient region

(see, e.g., Scholer et al. 2003).

All these properties are very clear in the case when a particle does not cross the neutral plane.

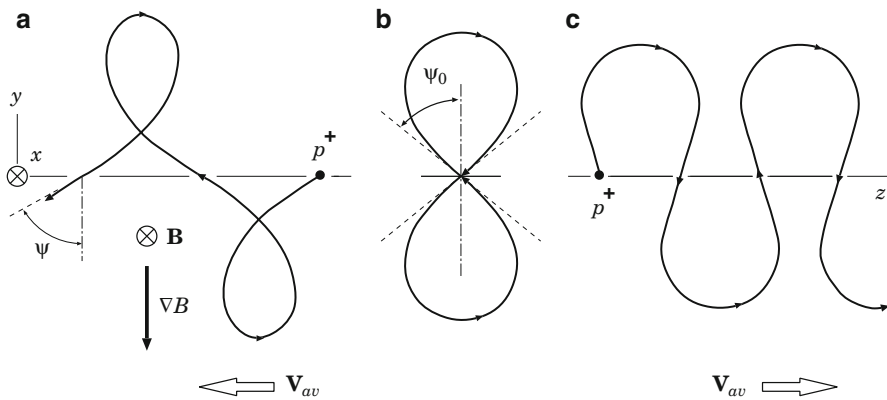


**Fig. 1.8** The serpentine-type orbits of a positively charged particle crossing the neutral plane  $y = 0$ . An ion can ‘drift’ (move in average) to the *left* or to the *right* depending on the angle at which it crosses the neutral plane.  $\mathbf{v}_{av}$  is the velocity of net motion

### 1.2.2 The Origin of Particle Acceleration

Particles that cross the neutral plane have more complex orbits.

An ion can drift to the left, as shown in Fig. 1.8a, or to the right, as shown in Fig. 1.8c, depending on the angle at which it crosses the neutral plane. There is only one angle  $\psi_0$  for which the ion moves in a figure-eight pattern (Fig. 1.8b) and has no net motion. It stays (in the absence of electric field along the plane, of course).

Any ion that crosses the plane with a velocity vector closer to the normal than the ion which stays still, will drift to the right

(Cowley 1986). Such ions moving along the electric field (directed along the  $z$ -axis in Fig. 1.7) increase their energy. Hence an *acceleration* of particles crossing the neutral plane is possible.

Therefore the electric field induces the particle drift toward the neutral plane. On reaching the neutral plane,

the particles become unmagnetized, since the magnetic field is zero there, and are accelerated in the electric field:

ions to the right along the electric field and electrons to the left in Fig. 1.8.

### 1.2.3 Acceleration in a Neutral Current Layer

As we have seen above, on the basis of the gradient drift consideration, one might think that the neutral current layer is perhaps not the best place for a particle acceleration. However this is not true. First, in an isotropic velocity distribution,

this must be a majority of the particles, resulting in a net rightward current, along the electric field, as required for acceleration. Second, as the particle approaches the neutral plane, the Larmor radius  $r_L = cp_\perp/eB$  increases indefinitely. Hence the drift formalism is not applicable here. We have to solve the exact equation of particle motion. In the non-relativistic case, it is of the form

$$m \dot{\mathbf{v}} = e \mathbf{E} + \frac{e}{c} \mathbf{v} \times \mathbf{B}. \quad (1.17)$$

With the electric and magnetic fields given by (1.14) we have the following three equations in the coordinates  $x$ ,  $y$ , and  $z$ :

$$\ddot{x} = 0, \quad \ddot{y} = -\frac{eh}{mc} y \dot{z}, \quad \ddot{z} = \frac{e}{m} \left( E + \frac{h}{c} y \dot{y} \right).$$

Let us rewrite these equations as follows:

$$\ddot{x} = 0, \quad \ddot{y} + \frac{eh}{mc} \dot{z} y = 0, \quad \ddot{z} = \frac{eE}{m} + \frac{eh}{mc} y \dot{y}. \quad (1.18)$$

The last equation is integrated to give

$$\dot{z} = \frac{eE}{m} t + \frac{eh}{2mc} y^2 + \text{const.} \quad (1.19)$$

The motion along the  $y$  axis is *finite*. This is a result of the above analysis of the character of motion in the drift approximation which applies when the particle is far enough from the neutral plane  $y = 0$ . That is the reason why, for large  $t$  (the ratio  $y^2/t \rightarrow 0$ ), the first term on the right of Eq. (1.19) plays a leading role. So we put asymptotically

$$\dot{z} = \frac{eE}{m} t.$$

(1.20)

As we shall see below, (1.20) is the *main* formula which describes the effect of **acceleration by the electric field inside the neutral layer**.

After substituting (1.20) into the second equation of (1.18) we obtain

$$\ddot{y} + \frac{e^2 h E}{m^2 c} t y = 0.$$

Introducing the designation

$$\frac{e^2 h E}{m^2 c} = a^2,$$

we have the oscillator equation

$$\ddot{y} + \omega^2(t) y = 0,$$

(1.21)

where  $\omega^2(t) = a^2 t$ .

Let us try to find the solution of Eq. (1.21) in the form

$$y(t) = f(t) \cos \varphi(t), \quad (1.22)$$

where  $f(t)$  is a slowly changing function of the time  $t$ . Substituting (1.22) in Eq. (1.21) results in

$$\ddot{f} \cos \varphi - 2 \dot{f} \dot{\varphi} \sin \varphi - f \ddot{\varphi} \sin \varphi - f (\dot{\varphi})^2 \cos \varphi + a^2 t f \cos \varphi = 0.$$

Since  $f$  is a slow function, the first term, containing the second derivative of  $f$  with respect to time, can be ignored. The remaining terms are regrouped in the following way:

$$f [ -(\dot{\varphi})^2 + a^2 t ] \cos \varphi - (2 \dot{f} \dot{\varphi} + f \ddot{\varphi}) \sin \varphi = 0.$$

By the orthogonality of the functions  $\sin \varphi$  and  $\cos \varphi$ , we have a set of two independent equations:

$$(\dot{\varphi})^2 = a^2 t, \quad (1.23)$$

$$2 \dot{f} \dot{\varphi} + f \ddot{\varphi} = 0. \quad (1.24)$$

The first equation is integrated, resulting in

$$\varphi = \frac{2}{3} a t^{3/2} + \varphi_0, \quad (1.25)$$

where  $\varphi_0$  is a constant. Substitute this solution in Eq. (1.24):

$$\frac{\dot{f}}{f} = -\frac{1}{2} \frac{\ddot{\varphi}}{\dot{\varphi}} = -\frac{1}{4} t^{-1}.$$

From this it follows that

$$f = C t^{-1/4}, \quad (1.26)$$

where  $C$  is a constant of integration.

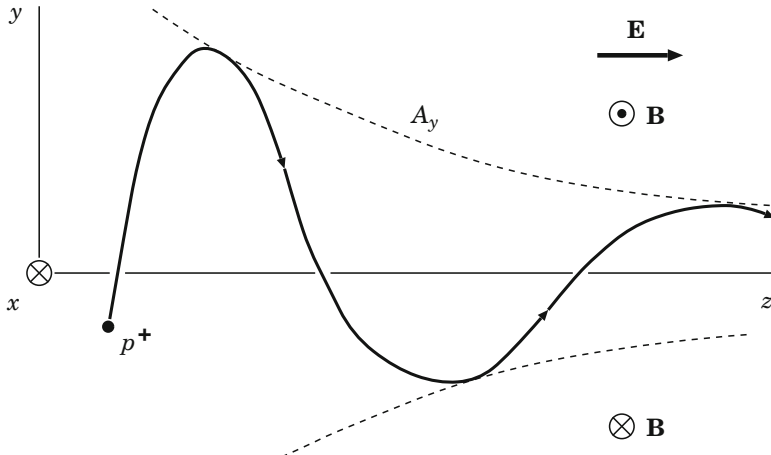


**Fig. 1.9** The trajectory of a positively charged particle accelerated by the electric field  $\mathbf{E}$  in the neighbourhood of the neutral plane inside a neutral current layer

On substituting (1.25) and (1.26) in (1.22), we obtain the sought-after description of the particle trajectory in a current layer:

$$y(t) = C t^{-1/4} \cos\left(\frac{2}{3} a t^{3/2} + \varphi_0\right), \quad (1.27)$$

$$z(t) = \frac{eE}{m} \frac{t^2}{2} + z_0. \quad (1.28)$$

Eliminate the variable  $t$  between formulae (1.27) and (1.28). We have

$$y(z) = C \left[ \frac{2m}{eE} (z - z_0) \right]^{-1/8} \cos \left\{ \frac{2}{3} a \left[ \frac{2m}{eE} (z - z_0) \right]^{3/4} + \varphi_0 \right\}. \quad (1.29)$$

The amplitude of this function

$$A_y \sim z^{-1/8} \sim t^{-1/4} \quad (1.30)$$

slowly decreases as  $z$  increases.

Let us find the ‘period’ of the function (1.29):  $\varphi \sim z^{3/4}$ , hence  $\delta\varphi \sim z^{-1/4} \delta z$ . If  $\delta \simeq 2\pi$ , then

$$\delta z \Big|_{2\pi} \sim z^{1/4}. \quad (1.31)$$

Thus the period of the function (1.29) is enhanced as shown in Fig. 1.9.

Note that the transversal velocity

$$\dot{y} \sim t^{-1/4} \dot{\varphi} \sim t^{1/4} \quad (1.32)$$

grows with time, but slower than the velocity component parallel to the electric field. From the main formula (1.20) it follows that

$$\dot{z} \sim t . \quad (1.33)$$

As a result, the particle is predominantly accelerated in the electric field direction along the current layer.

An exact analytical solution to Eq.(1.21) can be expressed as a linear combination of Bessel functions (Speiser 1965). It has the same properties as (it asymptotically coincides with) the approximate solution. Equation (1.21) corresponds to the equation of a linear oscillator, with the spring constant becoming larger with time. In the neutral current layer, the magnetic force returns the particle to the neutral plane: the larger the force, the higher the particle velocity.

**|** The electric field provides particle acceleration along the reconnecting current layer. This is the main effect.

Needless to say, the picture of acceleration in real current layers is more complicated and interesting. In particular, acceleration efficiency depends strongly upon the small *transversal* component of the magnetic field which penetrates into the reconnecting current layer (RCL) and makes the accelerated particles be ejected from the layer (Speiser 1965). This effect, as well as the role of the *longitudinal* (along the  $z$  axis) component of a magnetic field inside the current layer, will be considered in Chaps. 11 and 13. Magnetical non-neutrality of the current layer is of great significance for acceleration of electrons, for example, in the solar atmosphere.

In fact, real current layers are *non-neutral* not only in the sense of the magnetic field. They are also *electrically* non-neutral; they have an additional electric field directed towards the layer plane from both sides. This electric field is necessary for ion acceleration and will be considered in Chap. 11.

## 1.3 Practice: Exercises and Answers

**Exercise 1.1 (Sect. 1.1.2).** Consider the Lorentz force acting between two parallel electric currents in vacuum.

**Answer.** One of the currents, for example the upper current  $\mathbf{I} = -I\mathbf{e}_z$  in the place  $y = l$  in Fig. 1.3, generates the magnetic field

$$\mathbf{B} = -\frac{2}{c} \frac{I}{R} \mathbf{e}_\varphi . \quad (1.34)$$

This field circulates around the upper current as shown in Fig. 1.10.

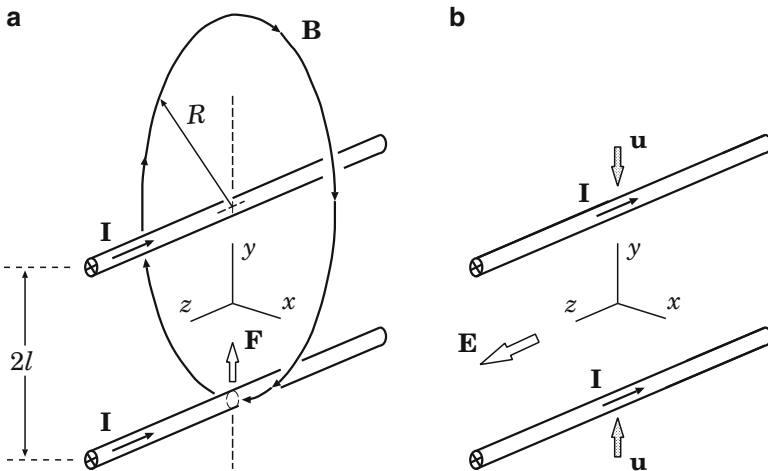


**Fig. 1.10** Two parallel currents: (a)  $2l$  is a distance between the currents; (b) the currents are drawn nearer with velocity  $\mathbf{u}$  and induce the electric field  $\mathbf{E}$ . Note that here the electric currents are antiparallel to the axis  $z$  of the Cartesian coordinates  $x, y, z$

In the place of the second current ( $y = -l$ ), the magnetic field is

$$\mathbf{B} = -\frac{1}{c} \frac{I}{l} \mathbf{e}_x. \quad (1.35)$$

The Lorentz force acting on the second current, on its unit length, is equal to

$$\mathbf{F} = \frac{1}{c} \mathbf{I} \times \mathbf{B} = \frac{1}{c^2} \frac{I^2}{l} \mathbf{e}_y. \quad (1.36)$$

The sign ‘+’ in this formula means that the force  $\mathbf{F}$  is directed from the second current to the first one. Therefore two parallel currents *attract* each other.

**Exercise 1.2 (Sect. 1.1.2).** Under conditions of the previous problem discuss how the potential of interaction  $U$  between two parallel currents depends on the distance  $a = 2l$  between them.

**Answer.** According to formula (1.36), the force between the interacting current is proportional to  $1/a$ . Hence the potential of interaction is proportional to  $\ln a$  with the sign (+) for the parallel currents but with the sign (−) for the anti-parallel electric currents. Integrating (1.36) gives

$$U = \frac{2I^2}{c^2} \ln a + \text{const.} \quad (1.37)$$

The force acting on unit length of one electric current from another one is

$$F = -\frac{dU}{da} = -\frac{2I^2}{c^2} \frac{1}{a}. \quad (1.38)$$

Note that if the current is measured in Ampere then the value of force

$$F \left[ \frac{\text{dyne}}{\text{cm}} \right] \approx -2 \left( \frac{I[\text{Ampere}]}{10} \right)^2 \frac{1}{a[\text{cm}]} . \quad (1.39)$$

The factor ‘10’ is resulted from dividing the value of the light velocity  $c$  by  $3 \times 10^9$  CGSE units.

**Exercise 1.3 (Sect. 1.1.2).** Show that the electric field (1.13) between two parallel electric currents is proportional to the rate of reconnection of magnetic field lines.

**Hint** The term  $A(t)$ , defined by formula (1.11), represents the reconnected magnetic flux as a function of time.

**Exercise 1.4 (Sect. 1.1.2).** What happens if we move the parallel currents in opposite directions?

# Chapter 2

## Reconnection in a Strong Magnetic Field

**Abstract** When two oppositely directed magnetic fields are pressed together, the conductive plasma is squeezed out from between them, causing the field gradient to steepen until a *reconnecting current layer* (RCL) appears and becomes so thin that the collisional or collisionless dissipation determines the magnetic reconnection rate and dynamics of this layer. In this Chapter, the basic magnetohydrodynamic (MHD) properties of the process of a current layer formation are considered in the approximation of a strong magnetic field.

### 2.1 Small Perturbations Near a Neutral Line

#### 2.1.1 Historical Comments

The notion of *reconnection* of magnetic field lines, magnetic reconnection, came into existence in the context of the interpretation of solar flare observations. The review of early works in the field is contained, for example in the eminent paper by [Sweet \(1969\)](#). From the viewpoint of reconnection, **the points and lines where the magnetic field is zero are peculiarities**. This special feature, which is of a topological nature, has already been mentioned in Sect. 1.1 (see Fig. 1.2).

[Giovanelli \(1947\)](#) pointed out that a *highly concentrated* electric current appears readily at an X-type zeroth point in a highly conducting plasma. This is true and important. [Dungey \(1958\)](#) put forward the idea that

unusual *electrodynamic* properties of a plasma emerge in the vicinity of a neutral (or zeroth) point of type X.

Since there was no clear view of the physical essence of reconnection, the notion has been accepted uncritically. It was assumed, for instance, that the mere existence of a zeroth point inevitably leads to spontaneous compression of a magneto-plasma configuration and rapid dissipation of the magnetic field, i.e. a flare ([Dungey 1958](#); [Severny 1962](#)).

However, as was shown by Syrovatskii (1962), given magnetostatic equilibrium near a zeroth point, the plasma is stable with respect to spontaneous compression. The situation changes once the plasma near the zeroth point is subject to an outside action due to an electric field as shown in Fig. 1.4 or due to a MHD wave which is created, for instance, by changes of the magnetic field sources at the photosphere (Fig. 1.1).

This action gives rise to an original *cumulative effect* (Syrovatskii 1966a). We attempted to understand this fundamental property at the qualitative level in Sect. 1.1. Let us illustrate it by the example of the behaviour of *small* MHD perturbations near the zeroth line. Bearing the solar flare case in mind, we consider the reconnection process in the approximation of a strong magnetic field at first.

### 2.1.2 Basic Equation of the 2D Ideal MHD

Let us start from the set of the *ideal* MHD equations (see Part I, Sect. 12.3.2):

$$\frac{\partial \mathbf{v}}{\partial t} + (\mathbf{v} \cdot \nabla) \mathbf{v} = -\frac{\nabla p}{\rho} - \frac{1}{4\pi\rho} \mathbf{B} \times \text{rot } \mathbf{B}, \quad (2.1)$$

$$\frac{\partial \mathbf{B}}{\partial t} = \text{rot}(\mathbf{v} \times \mathbf{B}), \quad (2.2)$$

$$\frac{\partial \rho}{\partial t} + \text{div } \rho \mathbf{v} = 0, \quad (2.3)$$

$$\frac{\partial s}{\partial t} + (\mathbf{v} \cdot \nabla) s = 0, \quad (2.4)$$

$$\text{div } \mathbf{B} = 0, \quad (2.5)$$

$$p = p(\rho, s). \quad (2.6)$$

Here  $\mathbf{v}$  is the macroscopic velocity of plasma considered as a continuous medium,  $s$  is the entropy per unit mass, other notations are also conventional.

We shall consider a two-dimensional (2D) problem of the second type (see Part I, Sect. 14.2.2). The problems of this type treat the plane plasma flows with the velocity field of the form

$$\mathbf{v} = \{ v_x(x, y, t), v_y(x, y, t), 0 \} \quad (2.7)$$

associated with the plane magnetic field

$$\mathbf{B} = \{ B_x(x, y, t), B_y(x, y, t), 0 \}. \quad (2.8)$$

The electric currents corresponding to this field are parallel to the  $z$  axis

$$\mathbf{j} = \{0, 0, j(x, y, t)\}. \quad (2.9)$$

The vector-potential  $\mathbf{A}$  of such a field has as its only non-zero component:

$$\mathbf{A} = \{0, 0, A(x, y, t)\}.$$

The magnetic field  $\mathbf{B}$  is defined by the  $z$ -component of the vector-potential:

$$\mathbf{B} = \text{rot } \mathbf{A} = \left\{ \frac{\partial A}{\partial y}, -\frac{\partial A}{\partial x}, 0 \right\}. \quad (2.10)$$

The scalar function  $A(x, y, t)$  is termed the *vector potential*. This function is quite useful, owing to its properties (for more detail see Part I, Sect. 14.2.2).

### 2.1.3 The Strong Magnetic Field Approximation

In the strong-field-cold-plasma approximation (see Part I, Sect. 13.1.3), the MHD equations for a plane (two-dimensional) flow of ideally conducting plasma (for the second-type problems) are reduced, in the zeroth order in the small parameter

$$\varepsilon^2 = \frac{v^2}{V_A^2}, \quad (2.11)$$

to the following set of equations (Part I, Sect. 14.3):

$$\Delta A = 0, \quad (2.12)$$

$$\frac{d\mathbf{v}}{dt} \times \nabla A = 0, \quad (2.13)$$

$$\frac{dA}{dt} = 0, \quad (2.14)$$

$$\frac{\partial \rho}{\partial t} + \text{div } \rho \mathbf{v} = 0. \quad (2.15)$$

A solution of this set is completely defined inside some region  $G$  on the plane  $(x, y)$ , once the boundary condition is given at the boundary  $S$

$$A(x, y, t)|_S = f_1(x, y, t) \quad (2.16)$$

together with the initial conditions inside the region  $G$

$$\mathbf{v}_{\parallel}(x, y, 0)|_G = \mathbf{f}_2(x, y), \quad (2.17)$$

$$\rho(x, y, 0)|_G = f_3(x, y). \quad (2.18)$$

Here  $\mathbf{v}_{\parallel}$  is the velocity component along field lines. Once the potential  $A(x, y, t)$  is known, the transversal velocity component is uniquely determined by the freezing-in Eq. (2.14) and is equal, at any moment including the initial one, to

$$\mathbf{v}_{\perp}(x, y, t) = (\mathbf{v} \cdot \nabla A) \frac{\nabla A}{|\nabla A|^2} = -\frac{\partial A}{\partial t} \frac{\nabla A}{|\nabla A|^2}. \quad (2.19)$$

From Eq. (2.12) and boundary condition (2.16) we find the vector potential  $A(x, y, t)$  at any moment of time. Next, from Eqs. (2.13) and (2.14) and the initial condition (2.17), the velocity  $\mathbf{v}(x, y, t)$  is determined; the density  $\rho(x, y, t)$  is found from the continuity equation (2.15) and the initial density distribution (2.18).

### 2.1.4 Formation of a Current Layer

The procedure described above is not always possible (see Somov and Syrovatskii 1972). This means that

continuous solutions to the set of Equations (2.12)–(2.15) do not necessarily exist.

Let the boundary and initial conditions be given. The vector potential  $A(x, y, t)$  is uniquely determined by Eq. (2.12) and the boundary condition (2.16). The latter can be chosen in such a way that the field  $\mathbf{B}$  will contain *zeroth* points:

$$\mathbf{B} = \left\{ \frac{\partial A}{\partial y}, -\frac{\partial A}{\partial x}, 0 \right\} = 0. \quad (2.20)$$

Among them, there can exist ones in which the electric field is distinct from zero

$$\mathbf{E} = -\frac{1}{c} \frac{\partial \mathbf{A}}{\partial t} \neq 0. \quad (2.21)$$

Such points contradict the freezing-in Eq. (2.14). We shall call them the *peculiar* points.

The freezing-in condition allows continuous deformation of the strong magnetic field and the corresponding continuous motion of plasma everywhere except at peculiar zeroth points,

i.e. the lines parallel to the  $z$  axis of the Cartesian system of coordinates, where the magnetic field is zero while the electric field is nonzero.

Note that simultaneous vanishing of both fields is quite unlikely. This is the reason why the peculiar points occur rather frequently. They will receive much attention in what follows because they represent the places where a *reconnecting current layer* (RCL) is formed as will be shown below. Here we only stress that

**|** if there is not a zeroth point inside the region  $G$  at the initial time, it does not mean that such a point will never appear there.

An initial field can even be an homogeneous one (Parker 1972). Following the continuous evolution of the boundary condition (2.16), a zeroth point may appear on the boundary  $S$  and, if the electric field at this point does not equal zero, it will create a magnetic field discontinuity which prevents a change of magnetic field topology in the approximation of an ideal plasma. This discontinuity is a *neutral* layer of infinitesimal thickness. In a plasma of finite conductivity, the RCL of finite thickness is formed at a peculiar zeroth point.

The creation of a current layer at the zeroth point which appears on the boundary  $S$  was used at first in the model of *coronal streamers* driven by the *solar wind* (Somov and Syrovatskii 1972); see Exercise 2.1. Just the same, of course, occurs in the 2D model for interacting magnetic fluxes in the corona, compressed by a converging motion of magnetic footpoints in the photosphere (Low 1987; Low and Wolfson 1988).

Another case is an appearance of a couple of neutral points inside the region  $G$ . Anyway, and in all cases,

**|** interaction of magnetic fluxes in the peculiar zeroth point changes the field topology and creates the reconnecting current layer.

This kind of MHD discontinuous flows is of great importance for plasma astrophysics.

### 2.1.5 Classical Formulation of a Problem

Let two equal currents  $I$  flow parallel to the axis  $z$  on lines  $x = 0$ ,  $y = \pm l$  as shown in Fig. 1.3. The magnetic field of these currents is expressed with the aid of the vector-potential  $\mathbf{A}_0$  having only the  $z$  component:

$$\mathbf{A}_0 = \{0, 0, A_0(x, y)\},$$

where

$$A_0(x, y) = \frac{I}{c} \left\{ \ln [x^2 + (y - l)^2] + \ln [x^2 + (y + l)^2] \right\}. \quad (2.22)$$

Near the zeroth line situated on the  $z$  axis, formula (2.22) may be expanded in a Taylor series, the square terms of the expansion being sufficient for our purposes:

$$A_0(x, y) = \frac{2I}{c} (x^2 - y^2)$$

or

$$A_0(x, y) = \frac{h_0}{2} (x^2 - y^2). \quad (2.23)$$

Here  $h_0 = 4I/c$  is the magnetic field gradient in the vicinity of the zeroth line. The gradient of the field is an important characteristic of a reconnection region (see Sect. 8.3). In fact,

$$\mathbf{B}_0 = \text{rot } \mathbf{A}_0 = \left\{ \frac{\partial A_0}{\partial y}, -\frac{\partial A_0}{\partial x}, 0 \right\} = \{-h_0 y, -h_0 x, 0\}. \quad (2.24)$$

The field lines of the hyperbolic field (2.24) are shown in Fig. 1.2.

Let us assume the field  $\mathbf{B}_0$  to be sufficiently strong, so that the Alfvén speed  $V_A$  should be much greater than that of sound  $V_s$  everywhere, the exception being a small region near the zeroth line. On the strength of formula (2.24),

$$V_A^2 = \frac{h_0^2 r^2}{4\pi\rho_0},$$

where  $r = (x^2 + y^2)^{1/2}$  is the radius in the cylindrical frame of reference, i.e. in the plane  $(x, y)$ . Hence the condition

$$V_A^2 \gg V_s^2$$

can be rewritten in the form:

$$r \gg r_s. \quad (2.25)$$

Here

$$r_s = \left( \frac{4\pi n_0 k_B T_0}{h_0^2} \right)^{1/2}, \quad (2.26)$$

$n_0$  and  $T_0$  being the number density and temperature of the plasma at the initial stage of the process,  $k_B$  is Boltzmann's constant.

Let  $l = 1$  in formula (2.22). Then the assumed condition (2.25), together with the condition for applicability of the approximate expression (2.23) for the potential  $\mathbf{A}_0$ , means that the domain of admissible values is

$$r_s \ll r \ll 1. \quad (2.27)$$

We shall consider the MHD processes in this domain, related to magnetic reconnection at the X-type zeroth point.

### 2.1.6 A Linearized Problem for Small Perturbations

Of concern to us at first are *small perturbations* in the region (2.27) relative to the initial equilibrium state

$$\mathbf{v}_0 = 0, \quad \rho_0 = \text{const}, \quad p_0 = \text{const}, \quad \Delta A_0 = 0.$$

Let us consider the plane flows of a plasma with a frozen magnetic field in the plane  $(x, y)$ :

$$\mathbf{v} = \{v_x(x, y, t), v_y(x, y, t), 0\}, \quad \mathbf{B} = \mathbf{B}_0 + \mathbf{b},$$

the small perturbation of magnetic field being

$$\mathbf{b} = \{b_x(x, y, t), b_y(x, y, t), 0\}.$$

Thus, from the mathematical standpoint, the problem at hand belongs to the two-dimensional problems of the *second* type (see Part I, Sect. 14.2.2).

For small perturbations  $\mathbf{v}$ ,  $p$ ,  $\rho$ , and  $A$  (instead of  $\mathbf{b}$ ), the linearized equations of the ideal MHD can be written in the form

$$\begin{aligned} \frac{\partial A}{\partial t} &= -\mathbf{v} \cdot \nabla A_0, \\ \frac{\partial \mathbf{v}}{\partial t} &= -\frac{\nabla p}{\rho_0} - \frac{1}{4\pi\rho_0} \nabla A_0 \Delta A, \\ \frac{\partial \rho}{\partial t} &= -\rho_0 \operatorname{div} \mathbf{v}. \end{aligned} \tag{2.28}$$

The gas pressure gradient in the region (2.27) can be ignored. If we did not ignore the term  $\nabla p$ , the set of Eqs. (2.28), on differentiating with respect to  $t$ , could be transformed to give us

$$\begin{aligned} \frac{\partial^2 A}{\partial t^2} &= \frac{(\nabla A_0)^2}{4\pi\rho_0} \Delta A + \frac{V_s^2}{\rho_0} \nabla A_0 \cdot \nabla \rho, \\ \frac{\partial^2 \mathbf{v}}{\partial t^2} &= \frac{\nabla A_0}{4\pi\rho_0} \Delta (\mathbf{v} \cdot \nabla A_0) + V_s^2 \nabla \operatorname{div} \mathbf{v}, \\ \frac{\partial^2 \rho}{\partial t^2} &= \frac{1}{4\pi} \nabla A_0 \cdot \nabla \Delta A + V_s^2 \Delta \rho. \end{aligned} \tag{2.29}$$

So perturbations in the region (2.27) are seen (see the underlined terms in the first equation) to propagate with the *local* Alfvén velocity  $V_A$ :

$$V_{A0}^2 = V_{A0}^2(r) = \frac{(\nabla A_0(r))^2}{4\pi\rho_0}, \tag{2.30}$$

the result being accurate to small corrections of the order of  $V_s^2/V_{A0}^2$ . This is the case of astrophysical plasma with a strong magnetic field; see the mostly *isotropic* wave  $V_+$  in Part I, Fig. 15.3.

The displacement of the plasma under the action of the perturbation,  $\xi$ , is convenient to introduce instead of the velocity perturbation  $v$ :

$$\mathbf{v} = \frac{\partial \xi}{\partial t}. \quad (2.31)$$

Dropping the terms depending on the pressure gradient, the initial set of Eqs. (2.29) is recast as follows ([Syrovatskii 1966b](#)):

$$\frac{\partial^2 A}{\partial t^2} = V_{A0}^2(r) \Delta A, \quad (2.32)$$

$$\frac{\partial^2 \xi}{\partial t^2} = \frac{V_{A0}^2(r)}{\sqrt{4\pi\rho_0}} \Delta (\xi \cdot \nabla A_0), \quad (2.33)$$

$$\rho = -\rho_0 \operatorname{div} \xi, \quad (2.34)$$

$$A = -(\xi \cdot \nabla) A_0. \quad (2.35)$$

Let us rewrite Eq. (2.32) in the cylindrical frame of reference

$$\frac{\partial^2 A}{\partial t^2} = \frac{h_0^2}{4\pi\rho_0} \left[ r \frac{\partial}{\partial r} \left( r \frac{\partial A}{\partial r} \right) + \frac{\partial^2 A}{\partial \varphi^2} \right].$$

On substituting  $x = \ln r$ , this equation is reduced to the usual wave equation in the variables  $(x, \varphi)$

$$\frac{\partial^2 A}{\partial t^2} = V_a^2 \left( \frac{\partial^2 A}{\partial x^2} + \frac{\partial^2 A}{\partial \varphi^2} \right), \quad (2.36)$$

where

$$V_a = h_0 / \sqrt{4\pi\rho_0}$$

is a constant playing the role of the wave velocity.

### 2.1.7 Converging Waves and the Cumulative Effect

Let us consider an initial perturbation of the potential, which is independent of the cylindrical-frame angle  $\varphi$ :

$$A(r, \varphi, 0) = \Phi(r),$$

where  $\Phi(r)$  is an arbitrary function of  $r$ . In this case the general solution of Eq. (2.36) is

$$A(r, t) = \Phi(\ln r + V_a t). \quad (2.37)$$

The sign  $+$ , which we have chosen, by  $V_a t$  corresponds to the *converging* cylindrical wave, its velocity being

$$V(r) = \frac{dr}{dt} = -r V_a = -V_{A0}(r),$$

i.e. the wave propagates with the Alfvén velocity (see definition (2.30)). The following properties of the wave are of interest ([Syrovatskii 1966b](#)).

(a) **The magnetic field intensity** in such a wave is

$$B_r = \frac{1}{r} \frac{\partial A}{\partial \varphi} = 0, \quad B_\varphi = -\frac{\partial A}{\partial r} = -\frac{\Phi}{r}.$$

As the wave approaches the zeroth line, the field intensity grows

$$B(r) = B(R) \times \frac{R}{r}.$$

Here  $B(R)$  is the field intensity in the wave when its front is at a distance  $R$  from the zeroth line.

(b) **The magnetic field gradient** increases as well

$$\frac{\partial B}{\partial r}(r) = \frac{\partial B}{\partial r}(R) \times \left(\frac{R}{r}\right)^2.$$

Thus

as the cylindrical wave converges to zero it gives rise to a *cumulative* effect in regard to the magnetic field and its gradient.

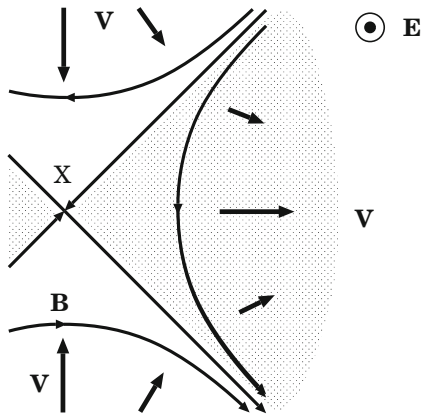
(c) The character of the plasma displacement  $\xi$  in such a wave can be judged from the motion Eq. (2.33). It contains the scalar product  $\xi \cdot \nabla A_0$ . Hence the displacements directed along the field lines are absent in the wave under consideration. The perpendicular displacements

$$\xi = -\frac{A}{(\nabla A_0)^2} \nabla A_0, \quad (2.38)$$

whence, in view of (2.37), it follows that  $|\xi| \sim r^{-1}$ . So

the quantity of the displacement also grows, as the wave approaches the zeroth line of the magnetic field.

**Fig. 2.1** Plasma flows and the density change in small perturbations in the vicinity of a hyperbolic zeroth point X. *Shadow* shows two regions of converging flows; here the plasma density increases



- (d) As for the change in plasma density, we find from Eq. (2.34), using formulae (2.38) and (2.37), that

$$\rho = -\rho_0 \operatorname{div} \xi \sim \frac{1}{r^2} \cos 2\varphi. \quad (2.39)$$

The plasma density increases in a pair of opposite quadrants while decreasing in the other pair (Fig. 2.1). The first pair of quadrants ( $-\pi/4 \leq \varphi \leq \pi/4$  and  $3\pi/4 \leq \varphi \leq 5\pi/4$ ) corresponds to the regions where the plasma flows are convergent. In the second pair ( $\pi/4 < \varphi < 3\pi/4$  and  $5\pi/4 < \varphi < 7\pi/4$ ) of quadrants, the trajectories of the fluid particles diverge, resulting in a decrease of the plasma density.

Therefore, even in a linear approximation,

small perturbations grow in the vicinity of the magnetic field zeroth line. As this takes place, regions appear in which the field and its gradients increase, whereas the plasma density decreases.

The so-called *linear-reconnection* theory takes into account the dissipative processes in the linear approximation (see Sects. 15.1 and 15.2.3).

## 2.2 Large Perturbations Near a Neutral Line

Let us relax the assumption concerning the smallness of the perturbations in the vicinity of a zeroth line. Then, instead of linearized MHD equations, we shall deal with the exact set of two-dimensional equations in the approximation of *strong field* and *cold plasma*, taken in a zeroth order with respect to the small parameter  $\varepsilon^2 = v^2/V_A^2$ , i.e. Eqs. (2.12)–(2.15):

$$\Delta A = 0, \quad (2.40)$$

$$\frac{d\mathbf{v}}{dt} \times \nabla A = 0, \quad (2.41)$$

$$\frac{dA}{dt} = 0, \quad (2.42)$$

$$\frac{\partial \rho}{\partial t} + \operatorname{div} \rho \mathbf{v} = 0. \quad (2.43)$$

Here it is implied that the region in the vicinity of the zeroth line is to be restricted by the condition (2.25).

### 2.2.1 Magnetic Field Line Deformations

As was shown in Part I, Sect. 14.2.2, Eqs. (2.42) and (2.43) are integrated on passing to Lagrangian coordinates

$$\mathbf{r}(\mathbf{r}_0, t) = \mathbf{r}_0 + \boldsymbol{\xi}(\mathbf{r}_0, t). \quad (2.44)$$

Here  $\mathbf{r}_0$  is the coordinate of a fluid particle before displacement, i.e. at the initial moment,  $\mathbf{r}$  is its coordinate at a moment of time  $t$ ,  $\boldsymbol{\xi}(\mathbf{r}_0, t)$  is the *displacement vector* (cf. definition (2.31)). Let us rewrite Eq. (2.44) as the inverse transformation

$$\mathbf{r}_0(\mathbf{r}, t) = \mathbf{r} - \boldsymbol{\xi}(\mathbf{r}, t).$$

Then the continuity equation (2.43) can be written in its Lagrangian form:

$$\rho(\mathbf{r}, t) = \rho_0(\mathbf{r} - \boldsymbol{\xi}(\mathbf{r}, t)) \frac{\mathcal{D}(\mathbf{r} - \boldsymbol{\xi}(\mathbf{r}, t))}{\mathcal{D}(\mathbf{r})}, \quad (2.45)$$

where  $\mathcal{D}(\mathbf{r}_0)/\mathcal{D}(\mathbf{r})$  is the Jacobian transformation from  $\mathbf{r}_0$  coordinates to  $\mathbf{r}$  coordinates.

The integral of the freezing-in Eq. (2.42) is

$$A(\mathbf{r}, t) = A_0(\mathbf{r} - \boldsymbol{\xi}(\mathbf{r}, t)), \quad (2.46)$$

where  $A_0(\mathbf{r}_0)$  is an initial value of the vector-potential.

Had the displacement  $\boldsymbol{\xi}(\mathbf{r}, t)$  been known, formulae (2.46) and (2.45) would have allowed us to uniquely determine the field line deformation and plasma density change in the vicinity of the zeroth line, given the displacement  $\delta l$  of the currents  $I$ . However, to find  $\boldsymbol{\xi}(\mathbf{r}, t)$  generally, we must simultaneously solve Eqs. (2.40) and (2.41), i.e. the set of equations

$$\Delta A = 0, \quad (2.47)$$

$$\frac{\partial^2 \boldsymbol{\xi}}{\partial t^2} \times \nabla A = 0. \quad (2.48)$$

As a rule, to integrate Eq. (2.48), we must have recourse to numerical methods (Somov and Syrovatskii 1976b). Let us try to circumvent the difficulty.

Let us suppose the displacement of the currents occurs sufficiently fast as compared with the speed of sound but sufficiently slow as compared with the Alfvén speed. With these assumptions, the boundary conditions of the problem (see (2.16)) change slowly in comparison with the speed of fast magnetoacoustic waves, which allows us to **consider the field as being in equilibrium at each stage** of the process (see Eq. (2.47)).

The latter assumption actually means that the total displacement  $\xi$  can be held to be a sum of successive small perturbations  $\delta\xi$  of the type (2.38), each of them transferring the system to a close equilibrium state. Since the small displacement  $\delta\xi$  is directed across the magnetic field lines, the total displacement  $\xi$  is also orthogonal to the picture of field lines. To put it another way, the lines of the plasma flow constitute a family of curves orthogonal to the magnetic field lines, i.e. the family of hyperbolae

$$xy = x_0 y_0. \quad (2.49)$$

A numerical solution of the problem (Somov and Syrovatskii 1976b) shows that such a flow is actually realized for comparably small  $t$  or sufficiently far from the zeroth line.

Let us make use of the freezing-in Eq. (2.46) to find another equation relating the coordinates of a fluid particle  $(x, y)$  with their initial values  $(x_0, y_0)$ . In view of formula (2.22) for the initial vector-potential  $A_0(x, y)$ , the magnetic field potential of displaced currents is

$$A(x, y) = \frac{h_0}{4} \left\{ \ln [x^2 + (y - 1 + \delta)^2] + \ln [x^2 + (y + 1 - \delta)^2] \right\}. \quad (2.50)$$

Relative to formula (2.22),  $I/c = h_0/4$ ,  $l = 1$ , and  $\delta l = \delta$ .

Near the zeroth line, with the accuracy of the terms of order  $\delta$ , we find

$$A(x, y) = \frac{h_0}{2} (x^2 - y^2 - 2\delta). \quad (2.51)$$

Substitution of (2.51) in (2.46) gives

$$y^2 - x^2 + 2\delta = y_0^2 - x_0^2. \quad (2.52)$$

Equations (2.49) and (2.52) allow us to express the initial coordinates of a fluid particle  $(x_0, y_0)$  in terms of its coordinates  $(x, y)$  at the moment of time  $t$  (Syrovatskii 1966a):

$$\begin{aligned} x_0^2 &= \frac{1}{2} \left\{ \left[ (x^2 - y^2 - 2\delta)^2 + 4x^2 y^2 \right]^{1/2} + (x^2 - y^2 - 2\delta) \right\}, \\ y_0^2 &= \frac{1}{2} \left\{ \left[ (x^2 - y^2 - 2\delta)^2 + 4x^2 y^2 \right]^{1/2} - (x^2 - y^2 - 2\delta) \right\}. \end{aligned} \quad (2.53)$$

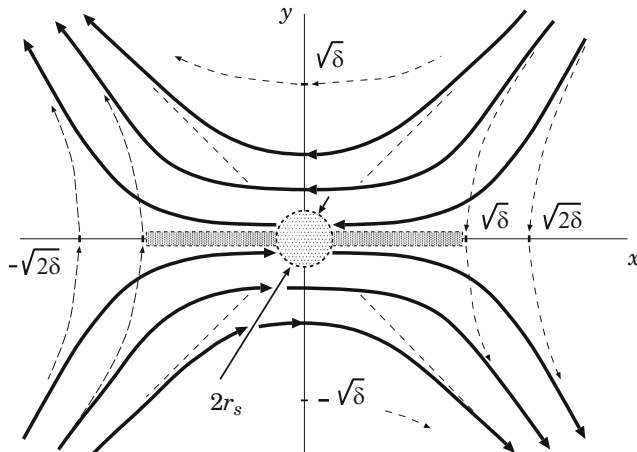


**Fig. 2.2** The deformation of the magnetic field lines in the neighbourhood of a zeroth line

The displacements determined by these expressions are such that the field lines which crossed the  $y$  axis at points  $0, \sqrt{\delta}, \sqrt{2\delta}$ , would take the place of the field lines which crossed the  $x$  axis at points  $\sqrt{2\delta}, \sqrt{\delta}, 0$ , respectively (see Fig. 2.2 in the region  $r \gg r_s$ ).

The plasma displacements and frozen-in field line deformations obtained pertain only to the region  $r \gg r_s$ . The approximation of a strong field and a cold plasma is inapplicable outside this region, i.e.  $r \leq r_s$ . It must also be considered that a region of *strong plasma compression* can arise in the course of the displacement. The conditions for applicability of the strong-field-cold-plasma approximation can be broken down in such regions, thus making it necessary to solve a more general problem. In particular, field deformations can be distinctly different here, owing to *strong electric currents* flowing in these regions. They will be discussed in the next Section.

The main effect demonstrated above is the deformation of the field lines which is schematically shown as two long dashed areas along the  $x$  axis. Here

| a current layer formation is confirmed in the MHD approximation by the presence of oppositely directed magnetic field lines

near the origin of the coordinates in Fig. 2.3. The current inside the current layer is parallel to the  $z$  axis, i.e. parallel to the electric field  $\mathbf{E}$  related to the magnetic field line motion (cf. Fig. 1.4). However, at the edges of the layer, the currents are sometimes opposite in direction (the so-called *reverse currents*) to the one inside the main current layer which is formed at the zeroth line as shown above.

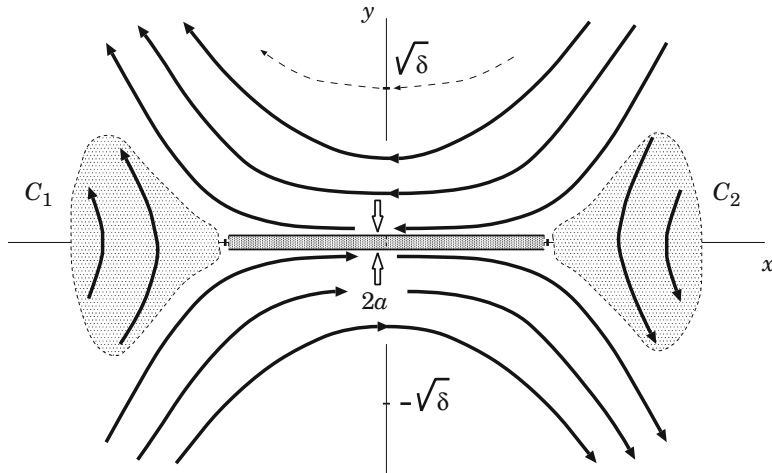


**Fig. 2.3** The plasma distribution near a forming current layer.  $2a$  is the thickness of the current layer

### 2.2.2 Plasma Density Variations

Let us find the density distribution (2.45) by calculating the Jacobian of the reverse transformation of the Lagrangian variables, with the aid of the formulae (2.53). Assuming an homogeneous initial distribution of plasma, we have

$$\frac{\rho(x, y)}{\rho_0} = \frac{x^2 + y^2}{\left[ (x^2 + y^2)^2 + 4\delta(y^2 - x^2) + 4\delta^2 \right]^{1/2}}. \quad (2.54)$$

The formula obtained shows that in the region

$$x^2 < y^2 + \delta \quad (2.55)$$

the displacement of the currents leads to plasma rarefaction. As this takes place, the largest rarefaction occurs for small  $r$  ( $r^2 \ll \delta$ ):

$$\frac{\rho(x, y)}{\rho_0} \sim \frac{r^2}{2\delta}. \quad (2.56)$$

By contrast, in the region  $x^2 > y^2 + \delta$  the plasma is compressed, its density tending to infinity at the points (Fig. 2.3):

$$y = 0, \quad x = \pm \sqrt{2\delta}. \quad (2.57)$$

The approximation of a strong field and a cold plasma is inapplicable in the vicinity of these points, and the actual deformation of the field lines can differ significantly from that found above.

Figure 2.3 illustrates a characteristic distribution of plasma near a current layer ( $-\sqrt{\delta} \leq x \leq \sqrt{\delta}$ ), dissipation of magnetic field being neglected. The regions of strong plasma compression near the points (2.57) are shown by the shadowed regions  $C_1$  and  $C_2$  outside of the layer.

## 2.3 Dynamic Dissipation of Magnetic Field

### 2.3.1 Conditions of Appearance

In the region between the points (2.57), at those the plasma density formally tends to infinity, the character of the displacements can be determined by using the freezing-in condition for the magnetic field lines and taking into account that, as was mentioned in the previous section, plasma spread along the field lines during the rapid displacement of the currents may be neglected. Under these assumptions, the magnetic field deformation is of the form shown in Figs. 2.2 and 2.3. Definition of the current displacement  $\delta$  is given in formula (2.50).

It is important for the following discussion that the whole magnetic flux which crossed the axis  $y$  in the region

$$0 < y < \sqrt{2\delta},$$

namely

$$\Phi = A_0(0, \sqrt{2\delta}) - A_0(0, 0) = h_0 \delta, \quad (2.58)$$

is now confined to the strip  $y \leq r_s$ . The thickness of this strip  $r_s \approx a$  in Fig. 2.3. The field lines of this flux ‘spread’ along the  $x$  axis in the negative direction. The same flux of field lines, but oppositely directed, is situated along the  $x$  axis in the lower half-plane.

Therefore, in the region

$$|x| \leq \sqrt{\delta}, \quad |y| \leq r_s,$$

the magnetic field lines of opposite directions are compressed to form a thin *reconnecting current layer* (RCL). The region of the magnetic field compression is shown in Figs. 2.2 and 2.3 as the long dashed area along the  $x$  axis. The magnetic field gradient in this region is evaluated as

$$h \approx \frac{B}{r_s} \approx \frac{\Phi}{r_s^2} \approx \frac{h_0}{r_s^2} \delta. \quad (2.59)$$

The field gradient  $h$  in the region of the magnetic compression is  $\delta/r_s^2$  times its initial value  $h_0$ . In other words,

the magnetic field gradient inside the current layer is proportional to the value of the external currents displacement  $\delta$ ,

with the proportionality coefficient, by virtue of definition (2.26), being larger, the smaller is the gas pressure as compared with the magnetic one in the reconnecting plasma.

At the same time, according to (2.56) the plasma density in the region  $r^2 < \delta$  decreases by a factor of  $r^2/2\delta$ . This conclusion applies for  $r \gg r_s$  and is of a qualitative character. Nonetheless it is of fundamental importance that we can make an order-of-magnitude evaluation of the ratio of the field gradient to the plasma concentration in the region of the magnetic compression ( $r \approx r_s$ )

$$\frac{h}{n} \approx \frac{h_0}{n_0} \frac{\delta^2}{r_s^4}. \quad (2.60)$$

Recall that in the MHD approximation (see Part I, Sect. 12.2.1) we usually neglect the *displacement current*  $(1/c) \partial \mathbf{E} / \partial t$  as compared with the conductive one

$$\mathbf{j} = ne \mathbf{u}.$$

Here  $e$  is the charge on a particle,  $\mathbf{u}$  is the current velocity, i.e. the velocity of current carriers. Subject to this condition, we may use the ‘truncated’ Maxwell equation

$$\text{rot } \mathbf{B} = \frac{4\pi}{c} \mathbf{j}, \quad (2.61)$$

whence, on setting  $|\text{rot } \mathbf{B}| \approx h$ , the following estimate is obtained

$$\frac{h}{n} \approx 4\pi e \left( \frac{u}{c} \right).$$

**Since the particle velocity  $u$  cannot exceed the speed of light  $c$ , the current density is limited by the value  $j = nec$  and, therefore, the ratio**

$$\frac{h}{n} < 4\pi e. \quad (2.62)$$

On the other hand, from (2.60) this ratio is determined by the value of the displacement  $\delta$  and by the parameters  $r_s$  and  $h_0/n_0$ . Once the condition (2.62) breaks down, by virtue of (2.60), i.e.

$$\frac{h_0}{n_0} \frac{\delta^2}{r_s^4} \geq 4\pi e, \quad (2.63)$$

the displacement current  $(1/c) \partial \mathbf{E} / \partial t$  must be accounted for in Eq. (2.61). It means that, under condition (2.63),

| a strong electric field of an inductive nature arises in the region where magnetic fluxes interact.

A quantitative description of the physical processes in the region involved is difficult and is the subject of the theory of reconnection in current layers. The qualitative effects are as follows.

### 2.3.2 *The Physical Meaning of Dynamic Dissipation*

The appearance of the inductive electric field, independent of the plasma motion, signifies the violation of the freezing-in condition. Thus the motion of the field lines relative to the plasma, which is necessary for their reconnection in the region of interaction of the magnetic fluxes, is allowed. The important aspect of the situation under discussion is that these processes are *independent* of Joule dissipation and can take place in a collisionless plasma. This is the reason why this phenomenon may be termed *dynamic dissipation* (Syrovatskii 1966a) or, in fact, *collisionless reconnection* (see Sect. 2.4.3).

An essential peculiarity of the dynamic dissipation of a magnetic field is that the inductive electric field is directed along the main current  $\mathbf{j}$  in the reconnection region. Hence the electric field does positive work on charged particles, thus increasing their energy. It is this process that provides the transformation of the magnetic energy into the kinetic one, i.e. dynamic dissipation.

As opposed to Joule dissipation, there is no direct proportionality of the current density  $\mathbf{j}$  to the electric field intensity  $\mathbf{E}$  in the case of dynamic dissipation. Given the condition (2.63),

| the current density is saturated at the value  $j \approx nec$ , the field energy going to increase the total energy of a particle,

$$\mathcal{E} = \frac{mc^2}{\sqrt{1 - v^2/c^2}}, \quad (2.64)$$

i.e. the acceleration by the electric field. Thus, under the conditions considered, the field energy converts directly to that of the accelerated particles.

Acceleration occurs along zeroth lines (parallel to the  $z$  axis) which are formed in the current layer region. Recall that the particle motion along a neutral plane (see Sect. 1.2) is stable: the magnetic field returns deviating particles to the neutral plane, as is clear from immediate consideration of the Lorentz force  $(e/c) \mathbf{v} \times \mathbf{B}$ . More realistic analysis of the acceleration problem will be given in Chap. 11.

The condition (2.63) is, in fact, an extreme. This implies the regular acceleration of particles to relativistic energies. In fact, acceleration may take place under much

more modest conditions, when the dynamic dissipation of a magnetic field is, in essence, related to the known phenomenon of the *electric runaway* of particles (primarily electrons; see Part I, Sect. 8.4.2). The condition which in this case replaces the extreme condition (2.63) was derived by Syrovatskii (1966b).

Needless to say, relativistic energies are not always reached in the acceleration process. Some instabilities are, as a rule, excited in the plasma-beam system in the acceleration region. As this takes place, particle scattering and acceleration with the created wave turbulence must be accounted for. However it is important that the general inference as to the possibility of **particle acceleration by an electric field in the magnetic reconnection region** (i.e. dynamic dissipation of the magnetic field) remains valid, in particular, when applied to the solar flare problem (see Sect. 4.1, Chaps. 8 and 11).

## 2.4 Nonstationary Analytical Models of RCL

### 2.4.1 Self-similar 2D MHD Solutions

In connection with the 2D problem of the equilibrium state of a plasma near the X-type zeroth point of magnetic field, Chapman and Kendall (1963) had obtained the exact particular solution of the ideal MHD equations for an *incompressible* fluid. This *self-similar* analytical solution has a perfectly defined character. A fixed mass of a plasma near the zeroth point receives energy from the outside in the form of an electromagnetic-field energy flux. Finally, a *cumulative effect* is developed and arbitrarily large energy densities are attained. The solution demonstrates the tendency to form a current layer near the zeroth point.

Imshennik and Syrovatskii (1967) had found a self-similar solution for an ideal *compressible* fluid. Let us also start from the set of the ideal MHD Eqs. (2.1)–(2.6). Consider the 2D MHD problem of the second type (see Part I, Sect. 14.2.2). Substitute definition (2.10) of the vector potential  $\mathbf{A}$  in the first three equations, we have the following set:

$$\rho \frac{d\mathbf{v}}{dt} = -\nabla p - \frac{1}{4\pi} \Delta A \nabla A, \quad (2.65)$$

$$\text{rot} \frac{d\mathbf{A}}{dt} = 0, \quad (2.66)$$

$$\frac{d\rho}{dt} + \rho \text{ div } \mathbf{v} = 0. \quad (2.67)$$

We assume that the pressure  $p$  is a function of the density  $\rho$  only. This condition is satisfied by any polytropic equation of state. Moreover, as it was shown by Imshennik and Syrovatskii, for the class of solutions of interest to us, the plasma density  $\rho$  depends only on time. Hence, by virtue of the foregoing assumption,

the pressure  $p$  depends only on time too. Therefore the pressure gradient  $\nabla p$  in Eq. (2.65) vanishes. So we have equations:

$$\rho \frac{d\mathbf{v}}{dt} = -\frac{1}{4\pi} \Delta A \nabla A, \quad (2.68)$$

$$\text{rot} \frac{dA}{dt} = 0, \quad (2.69)$$

$$\frac{d\rho}{dt} + \rho \operatorname{div} \mathbf{v} = 0. \quad (2.70)$$

Let us seek a solution of the set of Eq. (2.68)–(2.70) under the following initial conditions.

- (a) The plasma density is constant:

$$\rho(x, y, 0) = \rho_0, \quad (2.71)$$

- (b) The magnetic field is a hyperbolic one (see formula (2.23) where put the field gradient  $h_0 = 2a_0$ ):

$$A(x, y, 0) = a_0(x^2 - y^2), \quad (2.72)$$

- (c) The initial velocity depends linearly on the coordinates, so that there is no flow of plasma across the coordinate axes:

$$v_x(x, y, 0) = Ux, \quad v_y(x, y, 0) = Vy. \quad (2.73)$$

Thus the initial conditions are defined by the four independent quantities  $\rho_0$ ,  $a_0$ ,  $U$ , and  $V$ . We can construct from them three independent combinations with the dimension of time:

$$t_x = \frac{1}{U}, \quad t_y = \frac{1}{V}, \quad t_0 = \frac{(\pi\rho_0)^{1/2}}{|a_0|} \quad (2.74)$$

and not even one combination with the dimension of length. We introduce new variables with dimensions equal to a certain power of the length:

$$\tau = \frac{t}{t_0}, \quad u_x = t_0 v_x, \quad u_y = t_0 v_y, \quad a = \frac{A}{a_0}, \quad g = \frac{\rho}{\rho_0}. \quad (2.75)$$

In terms of these variables, Eqs. (2.68)–(2.70) take the form

$$\frac{\partial}{\partial x} \frac{da}{d\tau} = 0, \quad \frac{\partial}{\partial y} \frac{da}{d\tau} = 0, \quad (2.76)$$

$$g \frac{du_x}{d\tau} = -\frac{1}{4} \frac{\partial a}{\partial x} \Delta a, \quad g \frac{du_y}{d\tau} = -\frac{1}{4} \frac{\partial a}{\partial y} \Delta a, \quad (2.77)$$

$$\frac{dg}{d\tau} + \left( \frac{\partial u_x}{\partial x} + \frac{\partial u_y}{\partial y} \right) g = 0. \quad (2.78)$$

The initial conditions (2.71)–(2.73) then become

$$\begin{aligned} g(x, y, 0) &= 1, & a(x, y, 0) &= x^2 - y^2, \\ u_x(x, y, 0) &= \varepsilon_x x, & u_y(x, y, 0) &= \varepsilon_y y, \end{aligned} \quad (2.79)$$

where

$$\varepsilon_x = U \frac{(\pi \rho_0)^{1/2}}{|a_0|}, \quad \varepsilon_y = V \frac{(\pi \rho_0)^{1/2}}{|a_0|}. \quad (2.80)$$

Thus the problem is completely determined by the two dimensionless parameters (2.80) which are similar to the parameter  $\varepsilon$  in formula (2.11). As to the choice of the unit of length, Eqs. (2.76)–(2.78) impose no limitations whatever. So **the length unit can be chosen arbitrarily**; and both the coordinates  $x$  and  $y$ , together with all the variables in definition (2.75), can be chosen dimensionless.

Therefore

**we consider the problem as a *self-similar* one, more exactly, as the self-similar problem of the *first type***

(Zel'dovich et al. 1966, 2002, Chap. 12). It means that the set of equations in partial derivatives, (2.76)–(2.78), can be reduced to the set of *ordinary* differential equations. Let us do it. Substitute in Eqs. (2.76)–(2.78) the following forms of solution:

$$a(x, y, \tau) = a_x(\tau) x^2 - a_y(\tau) y^2, \quad (2.81)$$

$$g(x, y, \tau) = g(\tau), \quad (2.82)$$

$$u_y(x, y, \tau) = f_y(\tau) y. \quad (2.83)$$

We obtain the following set of five ordinary differential equations for the five unknown functions  $a_x(\tau)$ ,  $a_y(\tau)$ ,  $g(\tau)$ ,  $f_x(\tau)$  and  $f_y(\tau)$ :

$$\dot{a}_x + 2a_x f_x = 0, \quad \dot{a}_y + 2a_y f_y = 0,$$

$$\dot{g} + (f_x + f_y) g = 0,$$

$$\left( \dot{f}_x + f_x^2 \right) g = a_x (a_y - a_x), \quad \left( \dot{f}_y + f_y^2 \right) g = a_y (a_x - a_y). \quad (2.84)$$

The dot denotes differentiation with respect to the dimensionless time  $\tau$ . The initial conditions (2.79) give us the following initial conditions:

$$\begin{aligned} a_x(0) &= 1, & a_y(0) &= 1, & g(0) &= 1, \\ f_x(0) &= \varepsilon_x, & f_y(0) &= \varepsilon_y. \end{aligned} \quad (2.85)$$

Let us eliminate the functions  $f_x$  and  $f_y$  from the first two and last equations of the set (2.84). As a result we get the equation

$$\frac{\dot{a}_x}{a_x} + \frac{\dot{a}_y}{a_y} - 2 \frac{\dot{g}}{g} = 0. \quad (2.86)$$

From this, assuming that the functions  $a_x$ ,  $a_y$  and  $g$  are not equal to zero and using the initial conditions (2.85), we obtain an integral of the set of ordinary equations (2.84):

$$g = (a_x a_y)^{1/2}. \quad (2.87)$$

Since the initial values of these three functions are positive, the subsequent results will pertain to a time interval  $\tau$  for which these quantities remain positive.

#### 2.4.2 Magnetic Collapse at the Zeroth Point

To illustrate the behavior of the solutions (2.81)–(2.83), it is convenient to introduce two functions  $\zeta_x(\tau)$  and  $\zeta_y(\tau)$  such that

$$a_x = \frac{1}{\zeta_x^2}, \quad a_y = \frac{1}{\zeta_y^2}. \quad (2.88)$$

Without loss of generality, we assume that these new functions are positive.

From the first two equations of the set (2.84) and from the integral (2.87) we obtain formulae for the other three unknown functions:

$$f_x = \frac{\dot{\zeta}_x}{\zeta_x}, \quad f_y = \frac{\dot{\zeta}_y}{\zeta_y}, \quad g = \frac{1}{\zeta_x \zeta_y}. \quad (2.89)$$

The set of five Eqs. (2.84) then reduces to two second-order ordinary differential equations for  $\zeta_x(\tau)$  and  $\zeta_y(\tau)$ :

$$\ddot{\zeta}_x = -\zeta_y \left( \frac{1}{\zeta_x^2} - \frac{1}{\zeta_y^2} \right), \quad \ddot{\zeta}_y = \zeta_x \left( \frac{1}{\zeta_x^2} - \frac{1}{\zeta_y^2} \right), \quad (2.90)$$

with the initial conditions

$$\begin{aligned} \zeta_x(0) &= 1, & \zeta_y(0) &= 1, \\ \dot{\zeta}_x(0) &= \varepsilon_x, & \dot{\zeta}_y(0) &= \varepsilon_y. \end{aligned} \quad (2.91)$$

For definiteness, let  $\varepsilon_x > \varepsilon_y$ . Then a solution of the problem has a singular point which is reached after a finite time  $\tau_0$ . When  $\tau \rightarrow \tau_0$  the quantity  $\zeta_x$  tends to a finite value  $\zeta_x(\tau_0)$ , and  $\zeta_y(\tau) \rightarrow 0$ . So we retain in Eqs. (2.90) only the principal terms:

$$\ddot{\zeta}_x = \frac{1}{\zeta_y}, \quad \ddot{\zeta}_y = -\frac{\zeta_x}{\zeta_y^2}. \quad (2.92)$$

In the region  $\tau < \tau_0$  of interest to us, the solution of these equation is

$$\begin{aligned} \zeta_x(\tau) &= \zeta_x(\tau_0) + \dots, \\ \zeta_y(\tau) &= \left(\frac{9}{2}\zeta_x(\tau_0)\right)^{1/3} (\tau_0 - \tau)^{2/3} + \dots \end{aligned} \quad (2.93)$$

Here the terms of higher order of smallness in  $(\tau_0 - \tau)$  have been omitted.

Returning to the variables (2.88) and (2.89), we obtain the asymptotic behavior of the unknown functions near the singularity as  $\tau \rightarrow \tau_0$ :

$$\begin{aligned} a_x &\rightarrow a_x(\tau_0), \quad a_y \rightarrow \left(\frac{2}{9}\right)^{2/3} (a_x(\tau_0))^{1/3} \frac{1}{(\tau_0 - \tau)^{4/3}}, \\ f_x &\rightarrow \varepsilon_x(\tau_0), \quad f_y \rightarrow -\frac{2}{3(\tau_0 - \tau)}, \\ g &\rightarrow \left(\frac{2}{9}\right)^{1/3} (a_x(\tau_0))^{2/3} \frac{1}{(\tau_0 - \tau)^{2/3}}. \end{aligned} \quad (2.94)$$

Here the quantities  $\tau_0$ ,  $a_x(\tau_0)$ , and  $\varepsilon_x(\tau_0)$  depend on the initial conditions (2.79) and can be determined by numerical integrating (Imshennik and Syrovatskii 1967) the complete set of Eqs. (2.76)–(2.78).

Let us consider the fraction of the plasma that is located within a circle of radius equal to unity (Fig. 2.4) at the initial instant  $\tau = 0$ . The corresponding Lagrange line is the circle

$$a_x(0)x^2 + a_y(0)y^2 = 1.$$

Therefore, at any subsequent instant of time, this plasma will be located inside the ellipse

$$a_x(\tau)x^2 + a_y(\tau)y^2 = \frac{x^2}{\zeta_x^2(\tau)} + \frac{y^2}{\zeta_y^2(\tau)} = 1. \quad (2.95)$$

Here functions  $\zeta_x(\tau)$  and  $\zeta_y(\tau)$  introduced above have the simple meaning of semi-axes of this deforming ellipse.

As follows from the obtained solution, the semi-axis whose direction corresponds to a smaller initial velocity vanishes at the instant  $\tau_0$ . At the same time, the second semi-axis remains different from zero and bounded. Thus any initial circle is transformed at the instant  $\tau_0$  into a segment of the  $x$  axis with the ends  $x = \pm \zeta_x(\tau_0)$  as shown in Fig. 2.4.

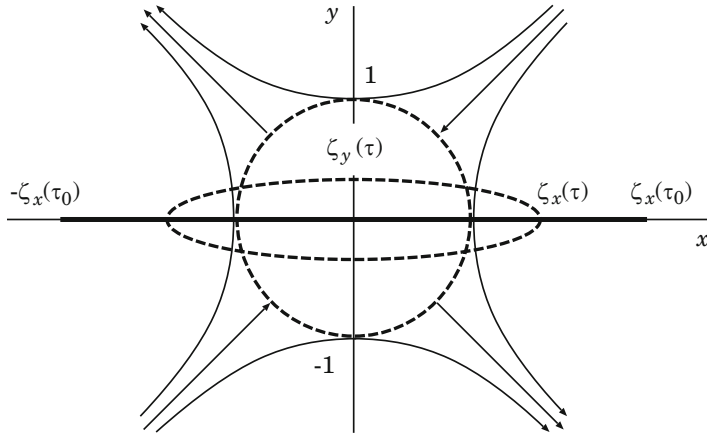


**Fig. 2.4** Magnetic collapse in the vicinity of a hyperbolic zeroth point

Let us consider the behavior of the magnetic field (see definitions (2.72) and (2.81)):

$$\mathbf{B} = h_0 \{ -a_y(\tau) y, -a_x(\tau) x, 0 \}, \quad (2.96)$$

where  $h_0 = 2a_0$  is the gradient of the initial field near the zeroth point. In the limit  $\tau \rightarrow \tau_0$  the field is equal to

$$\mathbf{B} = h_0 \left\{ \mp \frac{1}{\xi_y(\tau)}, -\frac{x}{\xi_x(\tau)}, 0 \right\}, \quad (2.97)$$

where the minus and plus signs correspond to the regions  $y > 0$  and  $y < 0$  respectively. Therefore, when  $\tau \rightarrow \tau_0$ , the magnetic field is always tangent to the  $x$  axis segment into which the ellipse (2.95) degenerates, increases in magnitude without limit, and experiences a discontinuity on the  $x$  axis:

$$B_x(y = +0) - B_x(y = -0) = -\frac{2h_0}{\xi_y(\tau)} \rightarrow \infty. \quad (2.98)$$

The appearance of the discontinuity in the magnetic field corresponds to an unbounded increase in the density of the electric current:

$$j_z = \frac{c}{4\pi} (\operatorname{rot} \mathbf{B})_z = -\frac{c}{4\pi} \Delta A. \quad (2.99)$$

Substituting (2.81) and (2.88) into (2.99), we calculate the current density

$$j_z(\tau) = \frac{ch_0}{4\pi} \left( \frac{1}{\xi_y^2(\tau)} - \frac{1}{\xi_x^2(\tau)} \right). \quad (2.100)$$

From this and from the solution (2.93) it follows that when  $\tau \rightarrow \tau_0$  the current density increases like

$$j_z(\tau) \sim \frac{1}{(\tau_0 - \tau)^{4/3}}. \quad (2.101)$$

So, when  $\tau \rightarrow \tau_0$ , a kind of *magnetic collapse* occurs. The  $x$  component of the field and the  $z$  component of the current density become infinite. The magnetic field is tangential to the  $x$  axis everywhere and changes its sign when passing the plane  $y = 0$ . Therefore

**|** the magnetic collapse results in the generation of a *neutral* current layer after a finite amount of time.

As we mentioned above, a similar solution for incompressible plasma was obtained by [Chapman and Kendall \(1963\)](#). In that solution the quantities  $\xi_x$  and  $\xi_y$  depend exponentially on time  $\tau$ . Thus the magnetic collapse in an *incompressible* fluid requires an *infinite* amount of time.

In general, it is difficult to determine the exact conditions under which the derived plasma motion can occur. The most difficult question is that of the realization of the assumed initial linear distribution of velocity (2.73). In practice, such a distribution could be realized as a small perturbation of an stationary initial state. One might therefore assume, as was done by Chapman and Kendall, that the entire process has the same character as an ordinary instability. However [Imshennik and Syrovatskii \(1967\)](#) showed that

**|** the plasma flow under consideration, the so-called *magnetic collapse*, is caused by external forces and has a cumulative nature

as we saw in Sect. 2.1.7.

[Syrovatskii \(1968\)](#) showed that the ideal MHD self-similar solutions obtained in both [Chapman and Kendall \(1963\)](#) and [Imshennik and Syrovatskii \(1967\)](#) can be set in correspondence with exact boundary conditions that have a physical meaning. These conditions are a particular case of the conditions considered in Sects. 2.1 and 2.2. They correspond to a change of the potential of the external currents producing the hyperbolic magnetic field in accordance with a fully defined law ([Syrovatskii 1968](#)).

### 2.4.3 From Collisional to Collisionless Reconnection

An essential circumstance in magnetic collapse is that the electric current density (2.101) increases more rapidly than the plasma density, and accordingly the particle density

$$n(\tau) \sim g(\tau) \sim \frac{1}{(\tau_0 - \tau)^{2/3}}. \quad (2.102)$$

The specific (per one particle) current density is

$$\frac{j_z}{n} = \frac{ch_0}{4\pi n_0} \left( \frac{\zeta_x}{\zeta_y} - \frac{\zeta_y}{\zeta_x} \right), \quad (2.103)$$

where  $n_0$  is the initial plasma density. In the limit as  $\tau \rightarrow \tau_0$

$$\frac{j_z}{n} = \frac{ch_0}{4\pi n_0} \left( \frac{2}{9a_x(\tau_0)} \right)^{1/3} \left( \frac{1}{\tau_0 - \tau} \right)^{2/3}. \quad (2.104)$$

So the ratio  $j_z/n$  tends to infinity when  $\tau \rightarrow \tau_0$  within the frame of the solution described above. Of course, the solution has no physical meaning near the singularity where a number of quantities increase infinitely.

**|** When a sufficiently high current density is attained, new effects arise, not accounted from by magnetohydrodynamics (MHD).

Here these kinetic effects are. First, when the current density

$$j_z \gtrsim \sigma E_{\text{Dr}}, \quad (2.105)$$

where  $E_{\text{Dr}}$  is the Dreicer field (see Part I, Sect. 8.4.2), an intense *electric runaway* of electrons begins and causes *current instabilities* inside the *reconnecting current layer*. These processes lead to a decrease in an effective conductivity of the plasma inside the current layer (Sect. 8.3), but still does not impose essential limitations on the applicability of MHD to the description of the macroscopic plasma flows.

If, however,

$$j_z \gg \sigma E_{\text{Dr}}, \quad (2.106)$$

direct acceleration of the particles by the strong electric field can set in. This is the case of **dynamic dissipation** of the magnetic field, for example, in solar flares (see the estimations in Sect. 8.1.1). The particle inertia (usually combined with anomalous resistivity due to wave-particle interactions) replaces the classical resistivity in allowing the magnetic reconnection to occur very quickly and practically without any Coulomb collisions.

**Fast collisionless reconnection** seems to be often observed in a high-temperature, rarefied astrophysical plasma in the presence of a strong magnetic field, for example, in solar flares. At a first sight, to describe the collisionless reconnection process, one may try to use an ordinary resistive MHD with a *generalized Ohm's law* (see Part I, Chap. 11) by simply including the electron inertia:

$$E_z = \sigma_{\text{ef}}^{-1} j_z + \frac{4\pi}{(\omega_{pl}^{(e)})^2} \frac{d}{dt} j_z. \quad (2.107)$$

Here  $\sigma_{\text{ef}}$  is an *anomalous* conductivity originated from the wave-particle interaction or the *stochasticity* of the particle orbits.

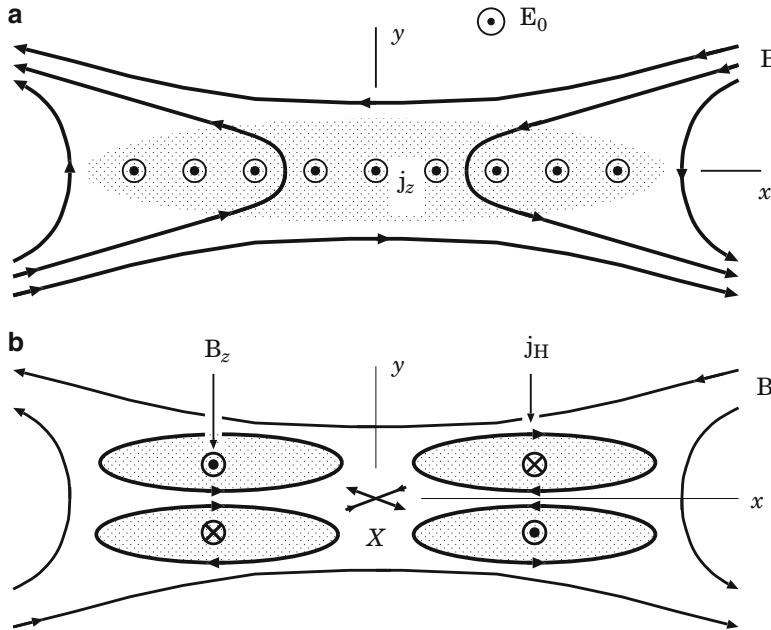


**Fig. 2.5** Structure of magnetic fields and electric currents formed in the vicinity of a hyperbolic zeroth line under action of electric field  $E_0$ . (a) Plane magnetic field  $\mathbf{B}$  of a reconnecting current layer (RCL) in a collisional plasma with isotropic conductivity. (b) Scheme of the out-of-plane magnetic field  $B_z$  at the current-layer cross-section by the plane  $(x, y)$ . Four closed current circuits show the Hall currents  $\mathbf{j}_H$  in the plane of cross-section

The problem will appear soon, however, in such an over-simplified approach because inside actual reconnecting current layers the magnetic field is not equal to zero. This internal (transversal and longitudinal) magnetic field has a strong influence on the particle acceleration by the strong electric field  $E_z$  related to the fast collisionless reconnection. This problem will be discussed in Chap. 11.

#### 2.4.4 Hall Currents in a Reconnecting Current Layer

Considering the initial 2D hyperbolic magnetic field with vector-potential (2.72), one might think that there exists always only the 2D time-dependent magnetic field (Fig. 2.5a):

$$\mathbf{B} = \{ B_x(x, y, t), B_y(x, y, t), 0 \},$$

producing by the basic currents  $j_z$  inside a reconnecting current layer (RCL). These currents are parallel to the  $z$  axis:

$$\mathbf{j} = \{ 0, 0, j_z(x, y, t) \},$$

whereas the third component  $B_z$  should be absent. Thus, the two ‘in-plane’ components  $j_x$  and  $j_y$  of electric current should be also absent. This is not true, of course, in a fully-ionized rarely-collisional plasma, when the electrons *spiral freely* between rare collisions of electrons with ions:

$$\omega_B^{(e)} \tau_{ei} \gg 1. \quad (2.108)$$

Here  $\omega_B^{(e)} = eB/m_e c$  is the electron gyro-frequency,  $\tau_{ei}$  is the electron-ion collisional time. Condition (2.108) corresponds to the *strong* magnetic field and hot rarefied plasma.

Such plasma is described by the generalized Ohm law (see Part I, Sect. 11.3) with the Hall current

$$\mathbf{j}_H = \sigma_H \mathbf{n} \times \mathbf{E}_0, \quad (2.109)$$

where the unit vector  $\mathbf{n} = \mathbf{B}/B$ , and the Hall conductivity

$$\sigma_H = \sigma \frac{\omega_B^{(e)} \tau_{ei}}{1 + (\omega_B^{(e)} \tau_{ei})^2} \approx \sigma (\omega_B^{(e)} \tau_{ei})^{-1} \quad (2.110)$$

with the conductivity  $\sigma = e^2 n / m_e v_{ei} = \sigma_{\parallel}$  which is parallel to magnetic field.

It is clear from formula (2.109) that the Hall currents  $j_x$  along the axis  $x$  are generated since there is the normal component  $B_y$  related to the reconnection process in the RCL (Fig. 2.5a). Thus the Hall currents  $j_x$  are directed from the RCL edges toward its center, toward the zeroth line  $X$  (coinciding with the axis  $z$  in Fig. 2.5b) of magnetic field  $\mathbf{B}$ . In the vicinity of this line, the Hall currents flow in the opposite directions from the midplane  $y = 0$ . They form four closed current circuits in the plane  $(x, y)$ . Therefore

the Hall currents generate the *out-of-plane* magnetic field  $\mathbf{B}_z$  of a quadrupole type:  $\mathbf{B}_z$  is directed oppositely on the opposite sides of the RCL symmetry planes

as shown in Fig. 2.5b.

Such pattern is a typical signature of the Hall MHD reconnection as predicted by theory (e.g., Bhattacharjee 2004; Uzdensky and Kulsrud 2006), observed in numerical simulations and well confirmed in the magnetic reconnection experiment at first by Ren et al. (2005) in the presence of a longitudinal (guide) magnetic field aligned with the X-line. The laboratory experiments by Frank et al. (2008) demonstrate generation of Hall’s currents in the RCLs producing in the 2D magnetic fields with the zeroth line of the X-type, in plasmas with heavy ions.

# Chapter 3

## Generalized Analytical Models of Reconnection

**Abstract** Following the results of numerical experiments on magnetic reconnection, we consider in this Chapter two-dimensional stationary reconnection models that include a thin Syrovatskii-type current layer and four discontinuous magnetohydrodynamic (MHD) flows of finite length attached to its endpoints. The flow pattern is not specified but is determined from a self-consistent solution of the problem in the approximation of a strong magnetic field. This solution allows to study the global structure of the magnetic field and its local properties near the reconnecting current layer and attached discontinuities.

### 3.1 Two Classical Models of Reconnection

In the approximation of a strong magnetic field, [Syrovatskii \(1971\)](#) constructed a simple analytical model of *reconnecting current layer* (RCL) in the form of a plane discontinuity surface that separates the oppositely directed magnetic fields as shown in Fig. 3.1a. The internal structure of this discontinuity implies two-dimensional reconnection in a *neutral* current layer ([Syrovatskii 1966a](#)). In such a RCL the magnetic field component normal to the layer is absent. The transition to a current layer of zero thickness stems from the fact that the thickness of the layer in a highly conductive plasma is much smaller than its width  $2b$ . The points  $x_*$  and  $-x_*$  are the boundary points between a region of *direct* current (DC) and the attached regions of *reverse* current (RC).

An analytical solution was obtained by conformal mapping ([Syrovatskii 1971](#)) for the simple case that the neutral current layer is arising from a lowest-order zeroth point (Fig. 1.2). Let  $h_0$  be the gradient of the external magnetic field in a vicinity of the zeroth point, see (2.24). The solution is expressed in terms of the complex potential (for more detail see Part I, Sect. 14.2.2)

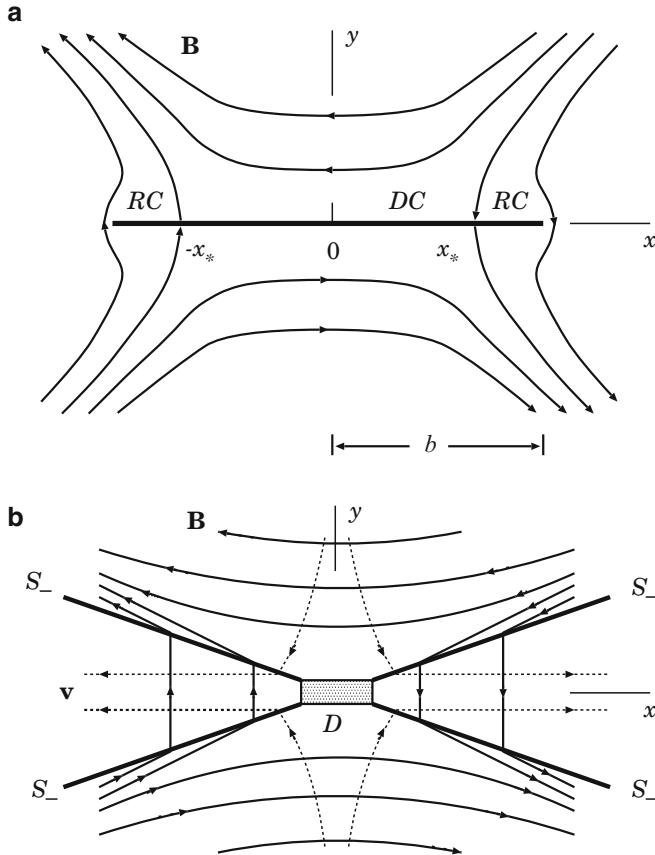


**Fig. 3.1** Two classical two-dimensional models of magnetic reconnection: (a) Syrovatskii's current layer contains a region of direct current ( $DC$ ) and two attached regions of reverse current ( $RC$ ),  $2b$  is the width of a RCL. (b) Petschek's flow consists of a small diffusion region  $D$  and four attached slow MHD shocks  $S_-$

$$\begin{aligned} F(z, t) &= A(x, y, t) + iA^+(x, y, t) \\ &= \frac{h_0}{2} z \sqrt{z^2 - b^2} - \frac{2I}{c} \ln \frac{z + \sqrt{z^2 - b^2}}{b} + A_0(t). \end{aligned} \quad (3.1)$$

This potential has a singularity in the form of a cut on the complex plane  $z = x + iy$  with ends at the points  $x = b$  and  $x = -b$ . In this cut, the surface density of electric current

$$j(x) = \frac{ch_0}{2\pi} (b^2 - x^2)^{1/2},$$

if we assume a quasi-steady regime of reconnection in which there are no reverse currents in the RCL; so  $j(x) = 0$  when  $x = b$  or  $x = -b$ . In this particular case, the total current in the RCL

$$I = \frac{1}{4} ch_0 b^2. \quad (3.2)$$

The function  $A_0(t)$  is the magnetic flux dissipated in the RCL by time  $t$ .

General solutions (3.1) with an arbitrary value of the total current  $I$  in the RCL lead to infinite values of magnetic field on the ends of the RCL. Velocity field and plasma density in the vicinity of the RCL was found in the strong-field-cold-plasma approximation (Sect. 2.1.3) by solving Eqs. (2.13)–(2.15), see [Somov and Syrovatskii \(1976b\)](#), Chap. 3.

**|** The features of plasma flows and density behavior near the RCL explain an origin of the reverse currents.

Moreover they are important in relation to the problem of RCL stability. If the total current is given, the current velocity of electrons increases as the plasma density inside RCL decreases. So, various instabilities can become possible, see Sect. 8.4.

Another classical model of reconnection is called Petschek's flow ([Petschek 1964](#)) and is usually considered as an alternative to Syrovatskii's current layer. In this famous model, the reconnection of magnetic field lines takes place in a small diffusion region  $D$  (Fig. 3.1b) which differs significantly in its physical properties from a neutral RCL ([Syrovatskii 1976a](#)). First, the current density is at a minimum at the center of the region  $D$  but at a maximum at the center of the RCL. Second, as the plasma conductivity increases, the width of the region  $D$  decreases, while the width of the neutral RCL grows. This follows from formula (20) in [Petschek \(1964\)](#) for given values of the Alfvén speed  $V_A$  and Alfvén-Mach number  $M_0$ .

**|** According to Petschek's model, the main conversion of magnetic energy into thermal and kinetic energy of plasma takes place at four attached slow MHD shocks  $S_-$  of infinite length.

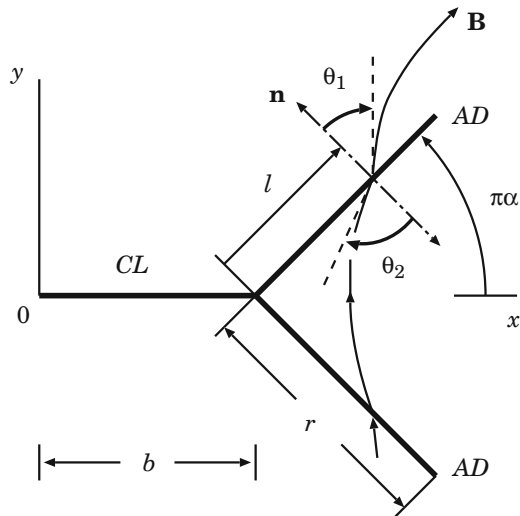
The principal effect of the including the shock waves is to reduce the width over which the magnetic diffusion mechanism must operate, i.e. the width of the diffusion region  $D$ .

In the context of the ‘external-flow’ pattern (see Fig. 50.3 in [Petschek 1964](#)), the shock waves have no thickness in the approximation of ideal MHD and are replaced by discontinuities. The magnetic field outside the region  $D$  and shocks is assumed to be potential, as in Syrovatskii's model. In Fig. 3.1 both models are presented in their canonical form; more recent numerous modifications of these models in collisional and collisionless plasmas are discussed, for example, in books by [Priest \(1982\)](#), [Somov \(1992\)](#), [Biskamp \(1997\)](#) and [Priest and Forbes \(2000\)](#).

## 3.2 Generalized Models of Syrovatskii's Current Layer

Based on the results of numerical experiments on magnetic reconnection ([Brushlinskii et al. 1980](#); [Biskamp 1986](#)), [Markovskii and Somov \(1989\)](#) suggested a two-dimensional model that generalizes the models by Syrovatskii and Petschek.

**Fig. 3.2** The right half of the configuration of electric currents (thick straight segments) consists of a current layer (*CL*) and attached discontinuities (*AD*) of finite length  $r$ ;  $b$  is the current layer half-width



The magnetic field in this model is assumed to be potential in the exterior of the current configuration that includes an infinitely thin neutral current layer shown in Fig. 3.2 in the form of a horizontal cut and four discontinuities *AD* attached to its edges at an angle  $\pi\alpha$ .

The normal component  $\beta$  of a magnetic field **B** and the linear growth coefficient  $h_0$  of the field at infinity are also fixed in the model. The type of discontinuity is not specified but should be found from a self-consistent solution of the problem. Such a solution has been found in an analytical form that admits of effective numerical realization and allows to analyze in detail the structure of magnetic field and its variation with model parameters (Bezrodnykh et al. 2007, 2011).

Another generalization of Syrovatskii's model is needed because the RCL can be disrupted into parallel current filaments or ribbons. This disruption of a thin RCL can emerge from a *tearing instability* (Furth et al. 1963) or when a region of higher electrical resistivity, for example, anomalous resistivity due to the excitation of plasma turbulence, appears (Sect. 8.4). Somov and Syrovatskii (1975) suggested a simple analytical model of a *disrupting current layer* with an infinite width. They showed that

the force of magnetic tensions is proportional to the size of the gap and is tending to increase it acting on the edges of the gap in the RCL.

A strong electric field capable of accelerating charged particles to high energies under astrophysical conditions, e.g., in solar flares, is induced inside this growing gap (Somov and Syrovatskii 1975).

### 3.3 Approach to Finding the Magnetic Field

First of all, we rewrite formula (3.1) for the complex potential of magnetic field in the following form

$$F(z) = \frac{h_0}{2} \left[ z\sqrt{z^2 - b^2} + (b^2 - 2x_*^2) \ln(z + \sqrt{z^2 - b^2}) \right] + \text{const.} \quad (3.3)$$

Here  $x_*$  is the distance from the origin point  $z = x + iy = 0$  to the points where the magnetic field vanishes at the surface of reconnecting current layer (RCL) as shown in Fig. 3.1. So we shall use the geometrical parameter  $x_*$  instead of the total current  $I$ . Then the magnetic field in the vicinity of the Syrovatskii RCL is given by formula

$$B_x - iB_y = -i h_0 \frac{z^2 - x_*^2}{\sqrt{z^2 - b^2}}. \quad (3.4)$$

Now we consider the generalized current configuration shown in Fig. 3.2. Let  $g$  be the exterior of this configuration. Then a plane magnetic field (2.8) at a moment  $t$  can be written in complex form

$$B(z) = B_x(x, y) + iB_y(x, y) \quad (3.5)$$

in the complex plane  $z = x + iy$ .

Let the line  $\Gamma$  depict the system of cuts in the plane  $z$  describing the current configuration mentioned above or any other similar configuration, for example, the same but disrupted (Sect. 3.6). Then we assume that the field component  $B_n$  normal to the line  $\Gamma$  is equal to zero at the *neutral* current layer  $CL$  and is equal to a constant  $\beta$  at the attached cuts corresponding to the attached discontinuities. It is easy to verify that  $B_n$  can be expressed in terms of  $B$  according to the formula

$$B_n = \text{Re} [\nu(z) \bar{B}(z)]. \quad (3.6)$$

Here  $\nu(z)$  is a complex unit normal,  $\text{Re}$  denotes the real part of the quantity in square brackets, and the overbar denotes complex conjugation.

The linear growth condition is set for the function  $B(z)$  at infinity; this condition is reflected by the following asymptotic formula

$$B(x, y) \sim ih_0 \bar{z}, \quad z \rightarrow \infty. \quad (3.7)$$

Here  $h_0$  is a fixed real constant, the magnetic field gradient near the initial zeroth point. This behavior of the field corresponds to the pattern of the lines observed far from the hyperbolic zeroth line (2.23).

To find the magnetic field  $B$ , it is convenient to use a complex conjugate function

$$\mathcal{F}(z) = u(x, y) + iv(x, y) = \bar{B}(z), \quad z \in g, \quad (3.8)$$

because it follows from the field potentiality that the function  $\mathcal{F}(z)$  defined in this way is an analytic function of the complex variable  $z$  in the domain  $g$ .

Substituting  $\mathcal{F}$  for  $B$  in (3.6) and taking into account the above remark about the magnetic field component  $B_n$  normal to  $\Gamma$ , we arrive at the Riemann–Hilbert problem (see [Lavrent'ev and Shabat 1973](#), Chap. 3, Sect. 55) for the analytic function  $\mathcal{F}$ :

$$\operatorname{Re} [v(z)\mathcal{F}(z)] = c(z) \quad \text{on } \Gamma, \quad (3.9)$$

where  $c(z)$  is a known function. The equality  $c(z) = 0$  holds at the current layer points, i.e. the boundary condition is homogeneous. If the model includes the attached discontinuities, then the equality  $c(z) = \beta$ , where  $\beta$  is a fixed constant value.

It follows from (3.7) and (3.8) that

$$\mathcal{F}(z) \sim -ih_0 z, \quad z \rightarrow \infty. \quad (3.10)$$

We assume that the field  $B$  is symmetric, with its component  $B_x$  being even relative to the  $y$  axis and odd relative to the  $x$  axis and with the parity properties of its component  $B_y$  being opposite. So

$$B(z) = \overline{B}(-\bar{z}), \quad B(z) = -\overline{B}(\bar{z}). \quad (3.11)$$

In this case, the original problem (3.9) is reduced to a similar Riemann–Hilbert problem in the complex domain  $G$ , a quarter of the plane  $z$  with a cut (Fig. 3.3a).

Therefore, in order to find the solution  $\mathcal{F}(z)$ , we have to apply a conformal mapping  $\xi = \Phi(z)$  of the domain  $G$  (Fig. 3.3a) onto the upper half-plane  $\mathbb{H}^+$  in Fig. 3.3b and pass to a similar problem in  $\mathbb{H}^+$ . We shall obtain the solution  $\mathcal{P}(\xi)$  of the latter and then find the function  $\mathcal{F}$  by substituting  $\xi = \Phi(z)$  into  $\mathcal{P}(\xi)$ , i.e. we shall write  $\mathcal{F}$  as a superposition

$$\mathcal{F}(z) = \mathcal{P}[\Phi(z)]. \quad (3.12)$$

Since the domain  $G$  is an (infinite) pentagon, the mapping  $\Phi^{-1}(\xi)$  inverse to  $\Phi(z)$  can be written as the Christoffel–Schwarz integral (see [Koppenfels and Stallmann 1959; Lavrent'ev and Shabat 1973](#)):

$$\Phi^{-1}(\xi) = \mathcal{K} \int_0^\xi t^{-1/2} (t - \lambda)^{-\alpha} (t - 1) (t - \tau)^{\alpha-1} dt. \quad (3.13)$$

Here  $\alpha$  is the inclination angle of the cut CDE divided by  $\pi$  (see Fig. 3.3a).

The points  $\xi = \infty$ ,  $\xi = 0$  and  $\xi = 1$  in Fig. 3.3b were chosen to be the preimages of vertices  $A$ ,  $B$  and  $D$ , respectively. The preimages  $\lambda$  and  $\tau$  of vertices  $C$  and  $E$ , along with the integrand factor  $\mathcal{K}$ , are to be found. These unknown quantities satisfy a set of nonlinear transcendental equations ([Koppenfels and Stallmann 1959](#)).

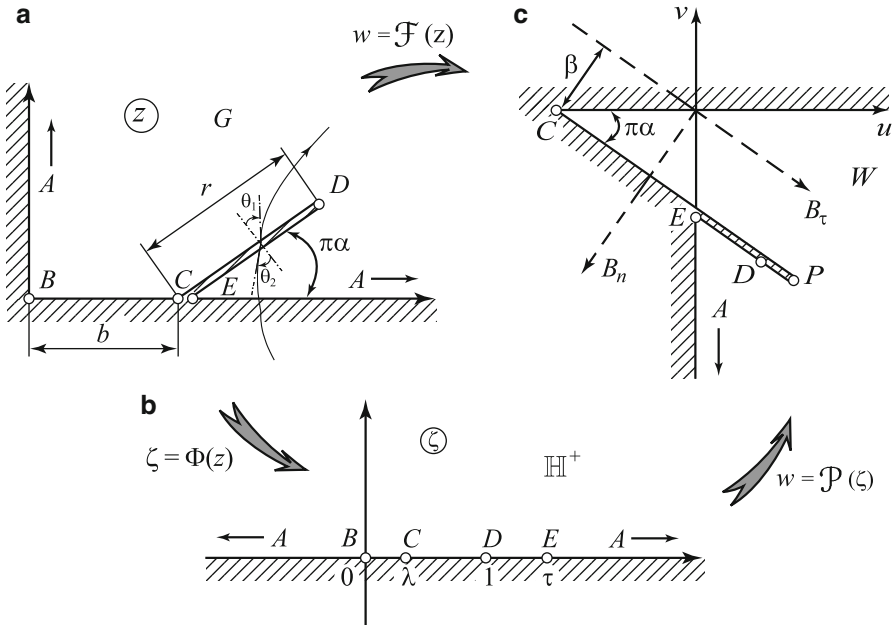


**Fig. 3.3** Scheme for solving the Riemann–Hilbert boundary-value problem: (a) initial domain  $G$  (the first quadrant of the reconnection region) in the complex  $z$  plane, (b) upper half-plane, and (c) magnetic field hodograph domain (From Bezrodnykh et al. 2007; reproduced with permission © Pleiades Publishing, Ltd.)

No analytical solution of such sets was known. So the complex relation between the sought-for parameters and the geometrical parameters of the domain  $G$  can be established only numerically, using Newton's method.

In Fig. 3.3c, the segment  $CPE$  of the boundary of the domain  $\mathcal{W}$  corresponds to the attached discontinuity, the cut  $CDE$  in Fig. 3.3a. The dashed lines indicate the axes on which the normal,  $B_n$ , and tangential,  $B_\tau$ , (with respect to the attached discontinuity plane) magnetic field components are plotted.

## 3.4 Current Layer with Attached Discontinuities

### 3.4.1 Magnetic Field Pattern

As we saw above, finding the magnetic field in the model of a reconnecting current layer (RCL) with attached discontinuities is reduced to the Riemann–Hilbert problem for the analytic function  $\mathcal{F} = \overline{B}$ . Since the field is symmetric relative to the  $x$  and  $y$  axes, it will suffice to consider the problem for  $\mathcal{F}$  in one quarter of the

initial domain, i.e. in the first quadrant with an inclined cut (Fig. 3.3a). The sought-for function  $\mathcal{F}$  can be found from Eq. (3.12), where  $\Phi$  is an auxiliary conformal mapping of the domain  $G$  on to the half-plane  $\mathbb{H}^+$ , and  $\mathcal{P}$  is the solution of the corresponding boundary-value problem in  $\mathbb{H}^+$  (Bezrodnykh et al. 2007):

$$\mathcal{P}(\zeta) = -ih_0\mathcal{K} \int_{\lambda}^{\zeta} \frac{(t-\lambda)^{\alpha-1}}{(t-\tau)^{\alpha+1/2}} (t-p) dt - \frac{\beta}{\sin \pi\alpha}. \quad (3.14)$$

Here

$$p = \frac{\beta}{h_0} \frac{\sqrt{\tau-\lambda}}{\pi^{3/2} \mathcal{K}} \Gamma(1-\alpha) \Gamma\left(\alpha + \frac{1}{2}\right) + 2\alpha(\tau-\lambda) + \lambda, \quad (3.15)$$

$\Gamma(s)$  is the gamma function (e.g., Bateman and Erdelyi 1953), other notation is the same as above.

The analytic function  $w = \mathcal{F}(z)$  makes a conformal mapping of the domain  $G$  onto some domain  $\mathcal{W}$  that is an infinite tetragon (Fig. 3.3c) as follows from representation (3.14) for  $\mathcal{P}$  as the Christoffel–Schwarz integral. Following Lavrent'ev and Shabat (1973) we call  $\mathcal{W}$  the field *hodograph* domain.

In general, the magnetic field pattern qualitatively changes only slightly when the geometrical parameters of domain  $g$  are varied but changes greatly depending on parameter  $\beta$ . The critical values of  $\beta$  are  $\beta = 0$  and  $\beta = \beta_{\max}$ . We can catch an idea of the dependence of the field pattern on the parameter  $\beta$  by comparing Figs. 3.4 and 3.5 which correspond to  $\beta = 0$  and  $\beta = 1 < \beta_{\max}$ ; the remaining parameters are identical for both figures:  $\pi\alpha = \pi/4$  and  $b = r = 1$ .

At  $\beta = 0$ , the magnetic field lines (Fig. 3.4) cross neither the current layer  $CL$  nor the discontinuities  $AD$ . There are no closed field lines and zeroth points inside the domain  $g$  as well as there is no reverse currents. This field configuration coincides with the limiting case of the absence of reverse currents in the analytical solution by Markovskii and Somov (1989), that corresponds to a small length  $r$ .

If  $\beta \in (0, \beta_{\max})$ , then two symmetrically located field lines ‘intersect’ the current layer  $CL$  (Fig. 3.5). The ‘intersection zeroth points’ (for more detail, see Somov and Syrovatskii 1972) separate the current layer segments on which the current flows in opposite directions. As before, there are no closed field lines and zeroth points inside the domain  $g$ . So the formal solution of the mathematical problem may have a real physical meaning. More precisely, in this case, the mathematical formulation of the problem does not require redetermination, i.e. the introduction of additional cuts of the complex plane that correspond to the secondary current layers (see Syrovatskii 1971).

In the limiting case  $\beta = \beta_{\max}$ , the points of intersection of the current layer with the field lines merge together at the coordinate origin, the point  $z = 0$ . This case precisely corresponds to the appearance of a secondary higher-order zeroth point in the current layer:  $B(0) = 0$  (see Fig. 3.6). There are no closed field lines and zeroth field points in the domain  $g$ , however, at  $\beta = \beta_{\max}$ , zeroth points appear outside the current layer and attached shocks.

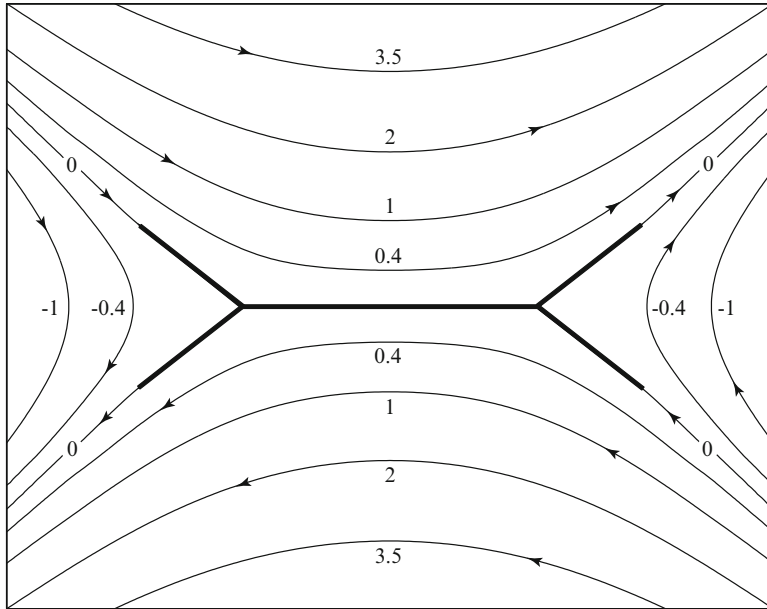


**Fig. 3.4** Magnetic field lines at  $\beta = 0$  are shown by *thin curves* with the field directions indicated by the arrows. The numbers near the curves indicate the values of the vector potential  $A(x, y)$ . The magnetic field lines do not cross the attached discontinuities (From Bezrodnykh et al. 2007; reproduced with permission © Pleiades Publishing, Ltd.)

### 3.4.2 Character of Shock Waves

Let us now consider the angles  $\theta_1$  and  $\theta_2$  (Fig. 3.2) of deflection of the magnetic field vector from the normal to an attached discontinuity, to a shock wave. To reach some qualitative conclusions about the influence of model parameters on the relation between  $\theta_1$  and  $\theta_2$ , it is convenient to turn to the magnetic field hodograph domain  $\mathcal{W}$ , whose example is shown in Fig. 3.3c. The segment  $CPE$  of the boundary of the domain  $\mathcal{W}$  corresponds to the shock. The dashed lines indicate the axes on which the normal,  $B_n$ , and tangential,  $B_\tau$ , (with respect to the shock) magnetic field components are plotted.

Suppose that  $\operatorname{tg} \theta = B_\tau / B_n$ , where  $B_\tau$  and  $B_n$  are calculated at the point  $w$  of the segment  $CPE$  of the boundary of  $\mathcal{W}$ . If the preimage  $z = \mathcal{F}^{-1}(w)$  of the point  $w$  lies in the segments  $CD$  and  $DE$  in Fig. 3.3a, then  $\theta = \theta_1$  and  $\theta = \theta_2$ , respectively.

Analyzing Fig. 3.3c, we see that  $B_n$  is constant and equal to  $\beta$  in the entire segment  $CPE$ . This clearly demonstrates the initial assumption of the model. We also see from Fig. 3.3a, c that there exists a segment of the boundary near the point  $C$  of the boundary of the hodograph domain  $\mathcal{W}$  (and, hence, near the point  $C$  of the boundary of the initial domain  $G$ ) where  $B_\tau < 0$ . Meanwhile, there exists a segment of the boundary near the point  $E$  where  $B_\tau > 0$ . Hence it follows that there exists

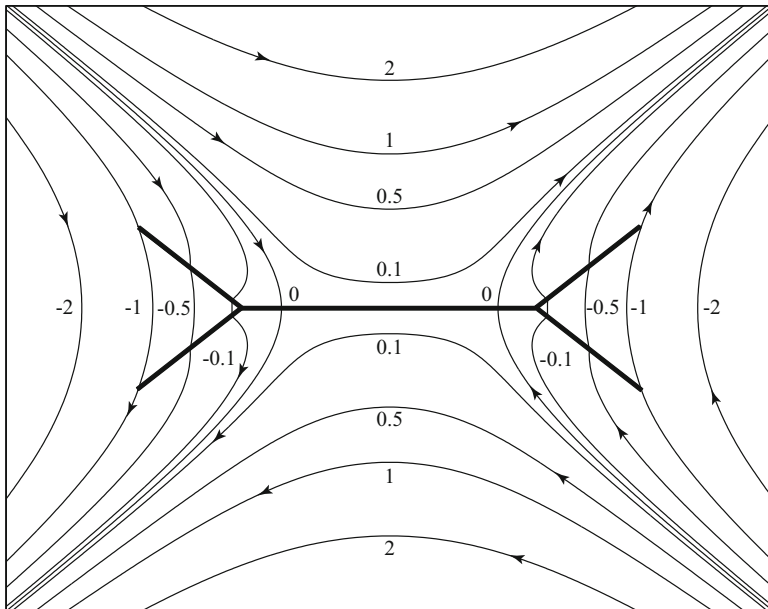


**Fig. 3.5** Current structure (thick straight-line segments) and magnetic field lines (thin curves with the field directions indicated by the arrows) at  $\alpha = 1/4$ ,  $\beta = 1$ , and  $h = 1$ . The field pattern is typical of the general case of physically significant solutions for the problem in the magnetic reconnection regime where reverse currents are present inside the current layer near its endpoints (From Bezrodnykh et al. 2007; reproduced with permission © Pleiades Publishing, Ltd.)

a shock-wave segment  $\gamma_{\text{TA}}$  near the shock base (i.e., near the point of its attachment to the current layer) where the angle  $\theta_1$  is negative and the angle  $\theta_2$  is positive. As has already been noted above, this situation corresponds to a trans-Alfvénic MHD shock wave.

If the inequality  $0 < p < 1$  holds for the parameter  $p$  in representation (3.14), then  $\theta_1 > \theta_2$  near the point  $D$  that is the external endpoint of the shock, which corresponds to a slow MHD shock wave. Since  $\theta_1$  increases continuously from negative values to positive ones, there must exist a segment  $\gamma_{\text{fast}}$  of the arc  $CDE$  at  $0 < p < 1$  where  $\theta_2 > \theta_1$ , which corresponds to a fast shock wave. The hodograph domain  $\mathcal{W}$  shown in Fig. 3.3c corresponds to the described situation.

If  $p > \tau$ , then the hodograph domain differs from that shown in Fig. 3.3c. In this case,  $B_\tau$  at the arc  $CD$  is always greater than this value at the arc  $DE$  of the boundary of the domain  $\mathcal{W}$  and, hence, of the domain  $G$ . This means that the relation  $\theta_2 > \theta_1$  holds at the entire arc  $CDE$ , i.e., the segment of a trans-Alfvénic shock is replaced by the segment of a fast shock wave, while the subsequent transition to a slow MHD shock is absent.

Using Eq. (3.15) for  $p$ , let us rewrite the condition  $p < 1$ , which is sufficient for the simultaneous existence of the segments of the corresponding fast and slow

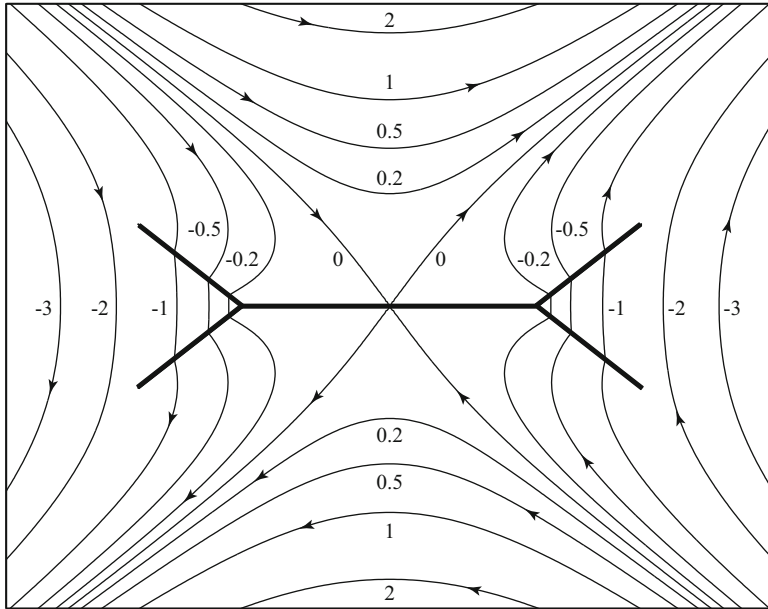


**Fig. 3.6** Magnetic field lines in the limiting case  $\beta = \beta_{\max}$  (From Bezrodnykh et al. 2007; reproduced with permission © Pleiades Publishing, Ltd.)

shocks at the arc  $CDE$  of the boundary of the domain  $G$ , in terms of the model parameters:

$$\frac{\beta}{h_0} < \pi^{3/2} \mathcal{K} \frac{1 - 2\alpha(\tau - \lambda) - \lambda}{\sqrt{\tau - \lambda} \Gamma(1 - \alpha) \Gamma(\alpha + 1/2)}. \quad (3.16)$$

Now let us rewrite the condition  $p > \tau$  under which there is no fast-to-slow shock transition in a similar way:

$$\frac{\beta}{h_0} > \pi^{3/2} \mathcal{K} \frac{\tau - 2\alpha(\tau - \lambda) - \lambda}{\sqrt{\tau - \lambda} \Gamma(1 - \alpha) \Gamma(\alpha + 1/2)}. \quad (3.17)$$

These inequalities are sufficient but not necessary for the existence or nonexistence of this shock transition and both these shock structures are possible under the condition  $1 < p < \tau$ .

### 3.4.3 Changes of a Shock-Wave Type

Now let us come back to consideration of the angles  $\theta_1$  and  $\theta_2$  (Fig. 3.2) of deflection of the magnetic field vector from the normal  $\mathbf{n}$  to the attached discontinuity  $AD$ . Figure 3.7 shows the plots  $\theta_1$  and  $\theta_2$  as the functions of distance  $l$  (measured

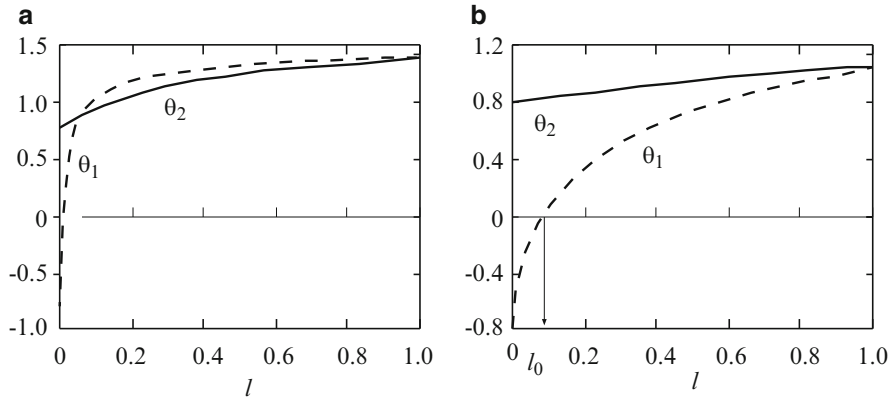


**Fig. 3.7** Distribution of the angles  $\theta_1$  and  $\theta_2$  over the distance  $l$  at the attached discontinuity. (a) The fast-to-slow shock transition is present. (b) No fast-to-slow shock transition arises

from the current layer  $CL$  endpoint along the discontinuity surface) according to calculations in two cases: (a)  $\beta = 0.3$ ,  $h = 1$ , and (b)  $\beta = 1$ ,  $h = 1$ . The inequalities  $1 < p < \tau$  hold in both cases.

We see a gradual changes in the angles of the magnetic field vector relative to the normal to the attached discontinuity surface at displacement  $l$  along this surface from the point  $l = 0$  of attachment to the current layer and to its ‘free edge’  $l = r$ ,  $r = 1$  where the angles  $\theta_1$  and  $\theta_2$  are equal.  $l_0$  corresponds to the point at which the angle  $\theta_1$  changes its sign. Near the point of attachment, in both cases, the angles  $\theta_1$  and  $\theta_2$  are not equal and have opposite signs, with  $\theta_2 > -\theta_1$ . So the shock wave is a trans-Alfvénic shock here. The situation changes when the angle  $\theta_1$  becomes zero at  $l = l_0$ . At this point, the trans-Alfvénic shock wave turns into a *switch-on shock wave* since  $\theta_2 \neq 0$  (see Part I, Sect. 16.2.6). Subsequently, the discontinuous flow passes into the regime of fast shock wave.

Figure 3.7a, which corresponds to the case (a), implies that the attached discontinuity  $AD$  in Fig. 3.2 is divided into three zones corresponding to trans-Alfvénic, fast, and slow shock waves. In Fig. 3.7b, the zones of trans-Alfvénic and fast shock waves are present while the zone of a slow shock wave is absent. So, in this regime of reconnection, there is no transition from the fast shock (through a parallel shock) to a slow MHD shock wave. The presence of the latter is characteristic of *Petschek’s flow* (Petschek 1964).

Recall however that Petschek’s flow corresponds to the model problem on the reconnection of oppositely directed magnetic fields that are uniform at great distances from a reconnection region, formally at infinity. In the generalized models under consideration, the asymptotic magnetic field at great distances is different: the field becomes hyperbolic (2.23). Such a reconnection regime is probably typical of the case where a reconnection region (a magnetic field separator in the corona) is located not very high, at a comparatively small distance from the

‘magnetic obstacle’, i.e., the arcade of flare loops in the corona (Sect. 9.2.2, Fig. 9.6). A similar situation arises in the non-stationary MHD models where the point of fast reconnection inside an infinite current layer lies near a massive, slowly moving ‘magnetic island’.

Trans-Alfvénic shock waves are known to be *non-evolutionary* in both ideal and dissipative MHD (Roikhvarger and Syrovatskii 1974; Markovskii and Skorokhodov 2000); see also Part I, Sect. 17.4.2. Moreover they probably also remain non-evolutionary in a weakly collisional magnetized plasma in the vicinity of *super-hot turbulent-current layers* in solar flares. Therefore we assume that the structure of the discontinuous flows near the endpoints of such a layer is complex. It may resemble the quasi-stationary pattern observed in numerical experiments within dissipative MHD (e.g., Ugai 2008, 2009). However an essentially non-stationary pattern of discontinuous flows attributable to oscillatory disintegration of trans-Alfvénic shocks (Markovskii and Skorokhodov 2000) is also possible. Although the latter possibility seems most likely, in general, this question requires further studies.

Thus we have identified different zones on the MHD discontinuity surfaces attached to a reconnecting current layer with different types of MHD shock waves. In particular, we have found the zones of trans-Alfvénic and and switch-on shock waves, that are known to be non-evolutionary, near the endpoints of a current layer with reverse currents (Bezrodnykh et al. 2011; Ledentsov and Somov 2011). So the question on the real pattern of discontinuous flows in the zones of non-evolutionary near reconnecting current layers requires further investigations.

On the other hand, in many numerical experiments related to dissipative MHD (Brushlinskii et al. 1980; Biskamp 1986, 1997; Chen et al. 1999a,b; Ugai 2008, 2009) and in the experiments on three-dimensional *collisionless* reconnection (e.g., Zeiler et al. 2002) the central reconnection region, i.e., the thin Syrovatskii-type current layer remains surprisingly laminar as discussed in the next Section.

### 3.5 Current Layers in Collisionless Plasma

In order to investigate the structure and stability of a reconnecting current layer (RCL), which develops during reconnection of antiparallel magnetic fields in *collisionless plasma*, many numerical experiments have been done. The presence of two-scales structure is characteristic of collisionless reconnection: an inner *electron current layer* and a more extended region of ion motions (see also Sect. 11.3.2). The dynamics of the electron current layer can be explored, for example, in the three-dimensional (3D) electron MHD approximation (Drake et al. 1997). In this case, it emerges that the electron current layer becomes increasingly thin during its evolution, down to the electron *skin thickness*  $c/\omega_{pl}^{(e)}$ , where  $\omega_{pl}^{(e)}$  is the electron plasma frequency. Subsequently, the electron current layer disrupts into completely turbulent vortex structures.

However the numerical simulation of collisionless reconnection in the 2.5D hybrid approximation ([Shay et al. 1998](#)) shows that

the decoupling of electron and ion motions has important implications for the reconnection rate.

The ions are not constrained to flow through the very thin region (the electron current layer) where the frozen-in constraint is broken. So the ion flux into the dissipation region (say the RCL) can be large. Therefore the reconnection rate is controlled not by electrons but by ions on the ion collisionless skin length scale  $c/\omega_{pl}^{(i)}$ . Thus the resulting reconnection rate accounts for a significant fraction of the Alfvén velocity.

The 3D particle-in-cell simulations performed by [Zeiler et al. \(2002\)](#) show that a strong RCL develops near the X-type zeroth line. However there is no evidence of turbulence that could emerge as a result of anomalous resistivity or viscosity. Moreover there are no electron shear flow and kink instability of the RCL observed in early numerical experiments (e.g., [Drake et al. 1997](#)). The sharp boundary layer between the plasma inflow and outflow regions exhibits the *lower hybrid drift instability* (LHDI). However the fluctuations associated with it do not affect strongly the reconnection rate. As a consequence, the thin RCL remains almost two-dimensional and surprisingly laminar.

A simulation with exactly antiparallel magnetic field ([Scholer et al. 2003](#)) demonstrates that the inductive field of the waves excited by the LHDI leads to fast acceleration of electrons in the center of the RCL and subsequently to a RCL thinning. In the thin current layer, *fast reconnection* sets in which self-organizes in a 2D structure with a single X-type neutral line.

Another simulation is performed by [Scholer et al. \(2003\)](#) for collisionless reconnection in the RCL with a constant *longitudinal* (guide) magnetic field of the same magnitude as the antiparallel field. In this case, the growth rate of the LHDI is reduced but leads nevertheless to electron acceleration in the RCL center and to a thinning of the RCL, followed by reconnection in the single X-type neutral line. Such behavior seems to be reasonable in the physical context discusses in Sect. 8.2.2.

The listed properties of thin RCLs in collisionless plasma provide evidence for Syrovatskii's current layer model.

### 3.6 Disrupting Current Layers

As was mentioned in Sect. 3.2, a reconnecting current layer (RCL) can be disrupted into parallel current filaments or current ribbons. We often see this effect in 2D dissipative MHD numerical experiments (e.g., [Yokoyama and Shibata 1997](#); [Shimizu and Ugai 2003](#)). A force of magnetic tensions acts on the edges of the gap in such a *disrupting current layer* (DCL). This force is proportional to the size

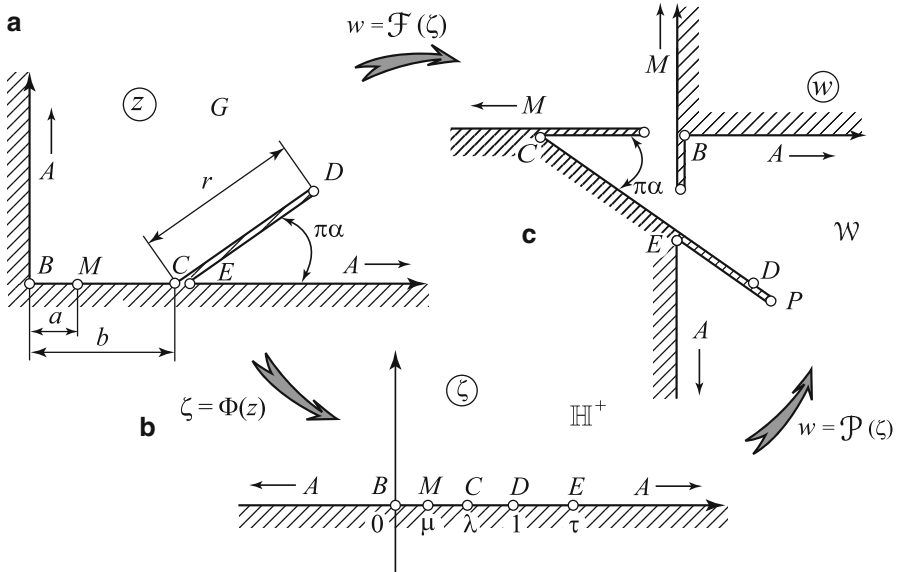


**Fig. 3.8** Scheme for solving the Riemann–Hilbert boundary-value problem in the case of disrupting current layer: (a) an initial domain  $G$  in the first quadrant of the reconnection region in the complex  $z$  plane, (b) the upper half-plane, and (c) the magnetic-field hodograph domain

of the gap and is tending to increase it. A strong electric field capable of accelerating charged particles to high energies under astrophysical conditions, e.g., in solar flares, can be induced inside this growing gap (Somov and Syrovatskii 1975).

According to what was said in Sect. 3.3, to find the magnetic field, it is convenient to introduce the analytic function  $\mathcal{F}$ , complex conjugate to the magnetic field (3.8), for which the Riemann–Hilbert problem (see Lavrent'ev and Shabat 1973, Chap. 3, Sect. 55) in the domain  $G$  in Fig. 3.8a is supplemented by some additional condition in the gap  $BM$ .

The corresponding formulation of the problem is the following:

$$\operatorname{Re}[\mathcal{H}(z)\mathcal{F}(z)] = c(z) \text{ in } G, \quad (3.18)$$

$$\mathcal{H} = \begin{cases} e^{-i\pi/2} & \text{at } AB \text{ and } MC, \\ 1 & \text{at } BM \text{ and } EA, \\ e^{i\pi(1/2+\alpha)} & \text{at } CDE, \end{cases} \quad c = \begin{cases} 0 & \text{at } ABC \text{ and } EA, \\ \beta & \text{at } CDE; \end{cases}$$

the sought-for function satisfies the condition (3.10) of linear growth at infinity and the condition of a square-root growth near the current layer endpoints, that are free from the attached shock waves, i.e. the condition  $|\mathcal{F}(z)| < C |z - a|^{-1/2}, z \rightarrow a$ .

Following the general approach described in Sect. 3.3, we shall first apply the conformal mapping  $\zeta = \Phi(z)$  of the domain  $G$  onto the upper half-plane  $\mathbb{H}^+$ . Denote by  $\mathcal{P}(\zeta)$  the function, into which function  $f(\mathcal{K}, \theta)(z)$  transforms after the

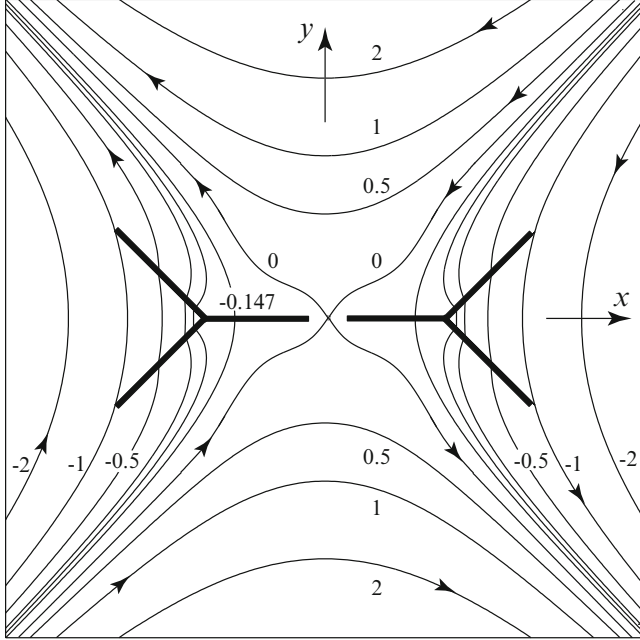


**Fig. 3.9** A disrupting current layer with attached discontinuous flows. Magnetic field lines are shown by *thin curves* with the field directions indicated by *the arrows*. The numbers near the curves indicate the values of the vector potential  $A(x, y)$  (From Bezrodnykh et al. 2011; reproduced with permission © Pleiades Publishing, Ltd.)

conformal mapping, i.e.  $\mathcal{P}(\xi) = f(\mathcal{K}, \theta)[\Phi^{-1}(\xi)]$ . This function satisfies the conditions of the Riemann–Hilbert problem in the half-plane, whose solution can be obtained in terms of a Cauchy-type integral:

$$\mathcal{P}(\xi) = \mathcal{X}(\xi) \left[ h_0 \mathcal{K} + \frac{\beta}{\pi} \int_{\lambda}^{\tau} \frac{t^{-1/2} (t - \mu)^{1/2} (t - \lambda)^{-\alpha} (\tau - t)^{\alpha-1/2}}{t - \xi} dt \right], \quad (3.19)$$

$$\mathcal{X}(\xi) = i \xi^{1/2} (\xi - \mu)^{-1/2} (\xi - \lambda)^{\alpha} (\xi - \tau)^{1/2-\alpha} \quad (3.20)$$

Here  $\alpha$  is the inclination angle of the cut  $CDE$  divided by  $\pi$ , see Fig. 3.8a,  $\mu = \Phi(a)$  is the coordinate of the point  $M$  in the plane  $\xi$  as shown in Fig. 3.8b; for more detail see [Bezrodnykh et al. \(2011\)](#).

Figure 3.9 presents the magnetic field pattern for the model with a disrupting current layer in the presence of attached discontinuous flows. The regions of direct and reverse currents are clearly seen. The refraction of magnetic field lines at the attached discontinuities is similar to that one demonstrated in Sect. 3.4. Therefore, in both cases,

contrary to the expectations following from Petschek's model, the considered MHD discontinuities attached to Syrovatskii's current layer are not slow but trans-Alfvénic shocks,

i.e. the shock waves for which the normal plasma inflow velocity is higher than the upstream Alfvén velocity, while the normal outflow velocity is lower than the downstream Alfvén velocity. So, in both cases, two types of transitions from non-evolutionary shock waves in the vicinity of the RCL to evolutionary ones along discontinuous flows are possible, depending on the RCL model parameters.

### 3.7 Practice: Exercises and Answers

**Exercise 3.1.** The solar corona, consisting mainly of ionized plasma, becomes visible to the naked eye during a total eclipse. The shape of the corona reveals the structure of the solar magnetic field with open field lines at the poles of the Sun and closed field lines above which the distribution of plasma takes the form of *coronal rays* or *coronal streamers* shaped like medieval helmets (see Fig. 3.10). These formations are connected with the large-scale magnetic fields on the surface of the Sun.

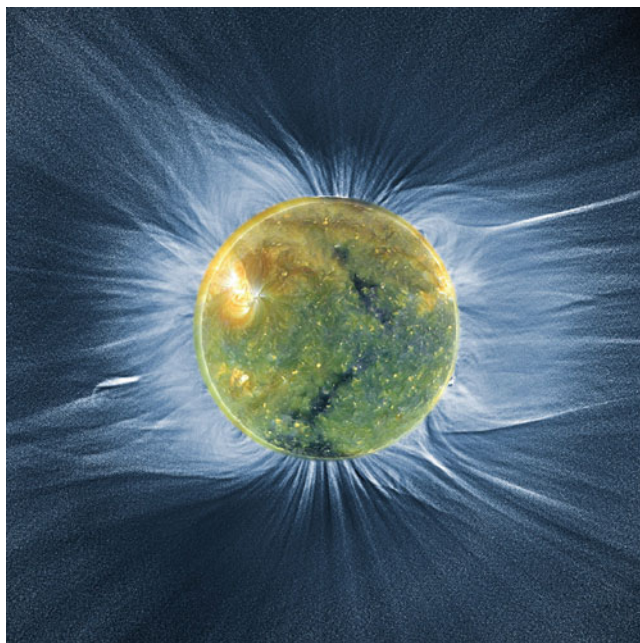


**Fig. 3.10** Composite using the White-Light total eclipse image of 11 July 2010 taken in French Polynesia and the simultaneous AIA (SDO) image of the disk put inside (Courtesy of Jean Mouette and Serge Koutchmy, CNRS France and AIA (SDO) from NASA)

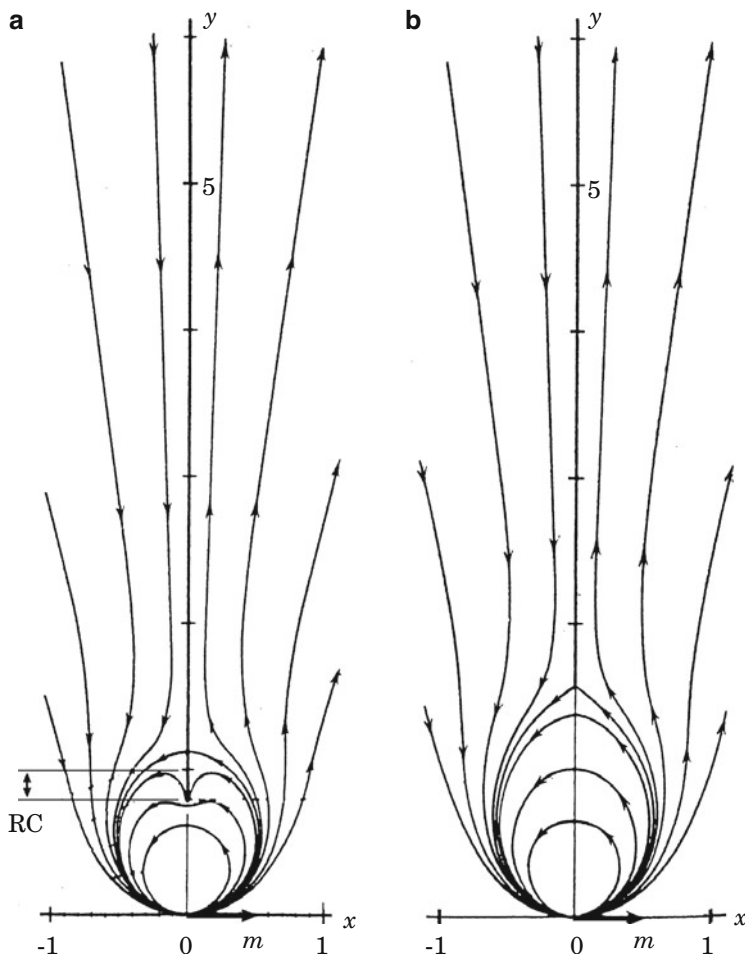


**Fig. 3.11** Magnetic field lines corresponding to the first analytical 2D model for coronal streamer: (a) the general solution with a reverse current in the region  $RC$ ; (b) the particular (stationary) solution without a reverse current

Parker (1958) suggested that outer parts of the corona must be expanding in the form of a *solar wind*. The first calculations of the magnetic field in the corona (see Newkirk and Altschuler 1970) were based on two main premises: the magnetic field over the photosphere is potential up to a certain height in the corona, at which the magnetic field becomes purely radial owing to drawing-out by the solar wind. The magnetic fields calculated under these simplified assumptions exhibited a reasonable correlation with the optical structure of the chromosphere and corona, as well as with the radio- and soft X-ray pictures of the Sun.

It is easy to verify that the coronal magnetic field constructed by this method should contain neutral points where in the presence of plasma the current layers appear. They change geometry of magnetic field. A current layer with quasi-radial magnetic fields of opposite direction on either side of it should appear inside a coronal streamer similar to the current layer in the magnetosphere tail. In both cases the dipole magnetic field is drawn out by the stream of the solar wind plasma: in the corona it is the dipole magnetic field of an extended active region, and in the magnetosphere it is the Earth magnetic field.

Try to formulate the simplest 2D problem of stretching out of a dipole magnetic field by a plasma flow ([Somov and Syrovatskii 1972](#)). Assume that the field is initially frozen in the plasma flow which is accelerated similar to the solar wind. So the approximation of a strong magnetic field is valid near the magnetic dipole. The capture of the field by the solar wind occurs from the interior of the field itself. The plasma slowly flows along the field lines in the strong-field region. However,

as the magnetic field becomes weaker, the plasma flow is smoothly transformed into a radial solar wind that carries an external part of the field away.

As a result, a quasi-stationary picture of magnetic field can be established for a long-lived active region as illustrated by Fig. 3.11b.

# Chapter 4

## Evidence of Reconnection in Solar Flares

**Abstract** The physics of flares on the Sun is now ‘an étalon’ for contemporary astrophysics, in particular for gamma and X-ray astronomy. In contrast to the flares on other stars and to many analogous phenomena in the Universe, solar flares are accessible to a broad variety of observational methods to see and investigate the *magnetic reconnection* effect in high-temperature strongly-magnetized plasma of the corona as well as in low-temperature weakly-ionized plasma in the photosphere.

### 4.1 The Role of Magnetic Fields

#### 4.1.1 Basic Questions

The flares on the Sun were first reported in white light observations by [Carrington \(1859\)](#) and [Hodgson \(1859\)](#). Historically such *white light flares* were considered as the exceptionally powerful impulsive events of *solar activity*. In fact, the frequency of occurrence as well as intensity of solar flares do follow the 11-year sunspot cycle. After more than 150 years, our knowledge of solar flares, especially the white-light flares (see, e.g., Sect. 17.4.2), is still incomplete.

Understanding solar flares has been a major goal of astrophysics since frequent observations of solar flares became available in the 1920s. Early studies showed that flares were preferentially associated with strong complicated magnetic fields (see [Smith and Smith 1963](#)). Estimates of the energy required to power large flares, together with their association with magnetic fields, led to the conclusion that flares must be electromagnetic in origin. Step by step it became more and more clear that a flare is the result of the reconnection of magnetic field lines in the corona.

However there were some objections to the hypothesis that the energy of a solar flare can be stored in the form of a magnetic field of one or several *reconnecting current layers* (RCLs).

1. First, it was claimed that measurements of photospheric magnetic fields do not demonstrate an unambiguous relation between flares and the changes of the magnetic fields. More exactly, the changes in question are those that occur *immediately before* a flare to create it. These changes were supposed to be the cause but not the consequence of the flare.
2. The second objection was related to the time of dissipation of the magnetic field in a volume that would contain the energy necessary for a flare. If this time is estimated in a usual way as the diffusion time in a solar plasma of a finite conductivity, then it is too long compared with the observed duration of the flare.
3. The third objection was the most crucial one: the observers had never seen real RCLs in solar flares.

For more than four decades, starting from [Severny \(1964\)](#), solar observers have been studying flare-related changes in photospheric magnetic fields, which would provide crucial information as to how an active region stores and releases its energy (see also [Lin et al. 1993; Wang 1999](#)). However the role of photospheric fields is still far from being fully understood and is an area of ongoing research (e.g., [Liu et al. 2005; Sudol and Harvey 2005; Wang et al. 2005](#)). What are the answers of the reconnection theory to the objections mentioned above?

### 4.1.2 Concept of Magnetic Reconnection

According to contemporary views, the principal flare process is contingent on the accumulation of the *free magnetic energy* in the corona and chromosphere. At least, this is one of basic concepts (see Chap. 16). By ‘free’ we mean the **surplus energy above that of a potential magnetic field**

$$B_\alpha(\mathbf{r}) = \frac{\partial \psi}{\partial r_\alpha}. \quad (4.1)$$

Here  $\psi(\mathbf{r})$  is the potential of the field, the index  $\alpha = 1, 2, 3$ . The potential field has the same sources (sunspots, background fields) in the photosphere.

In other words, the free magnetic energy is related to the electric currents in the solar atmosphere above the photosphere. A solar flare corresponds to rapid changes of these currents. So we distinguish between two processes: (1) the slow accumulation of flare energy and (2) its fast release, a flare.

Let us see these distinctions in the following classical example – the evolution of the quadrupole configuration of sunspots shown in the two-dimensional (2D) Fig. 4.1. Four sunspots of pairwise opposite polarity are shown:  $N$  and  $S$  represent a bipolar group of sunspots in an active region,  $n$  and  $s$  model a new emerging flux. All four sunspots are placed along the axis  $x$  placed in the photospheric plane  $Ph$  at the bottom of the chromosphere  $Ch$ .

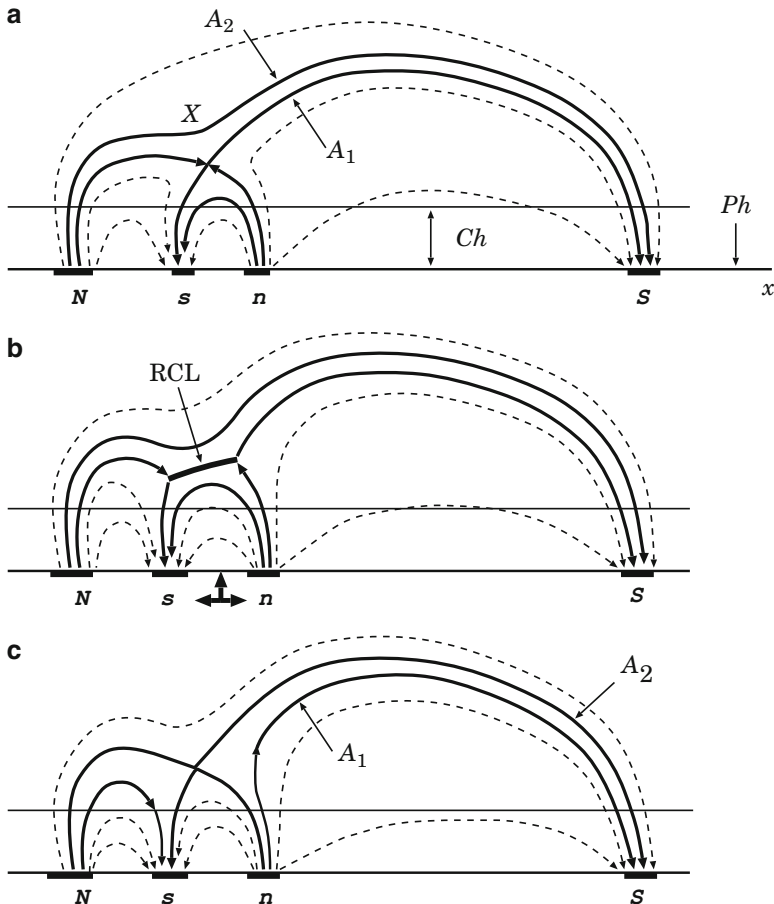


**Fig. 4.1** The classical 2D cartoon of magnetic reconnection in a solar flare. Three states of the potential field: (a) the initial state, (b) the *pre-reconnection* state, (c) the final state after reconnection

As in Fig. 1.6, three consequent states of the potential field are shown. In Fig. 4.1a the field line  $A_1$  is the separatrix line of the initial state (a). This field line will reconnect first.  $X$  is the neutral point (line along the  $z$  axis) of the potential field at the initial state, here the RCL is created at the state (b). The magnetic field line  $A_2$  is the separatrix of the final state (c) or the last reconnected field line. Therefore  $\delta A = A_2 - A_1$  is the reconnected magnetic flux.

In Fig. 4.1b three solid arrows under the photosphere show a slow emergence of new magnetic flux (the sunspots  $n$  and  $s$ ). The sunspots have been emerged but the field lines do not start to reconnect. More exactly, they reconnect *too slowly* because of very high electric conductivity of plasma in the solar corona. In the first approximation, we can neglect this *slow* reconnection.

In general, the redistribution of fluxes appears as a result of the **slow motions and changes of magnetic field sources** in the photosphere. These changes can be either the emergence of a new flux tube from below the photosphere (Fig. 4.1) or many other flows of photospheric plasma, in particular the *shear flows* – inhomogeneous horizontal flows along the neutral line of the photospheric magnetic field. For this reason,

| an actual (*slow* and *fast*) reconnection of magnetic fields in the solar atmosphere is always a three-dimensional phenomenon

(see Sect. 4.2). Sometimes, however, the 2D problems still give a simple illustration of an effect, for example, the formation and dissipation of the RCL at the  $X$  point under action of the photospheric shear (Kusano and Nishikawa 1996; Karpen et al. 1998), see also Sects. 16.3 and 16.4. The term ‘2.5-dimensional’ frequently refers to such 2D MHD problems (in two spatial variables  $x$  and  $y$ ) to point out the presence of the longitudinal field  $B_z$  related to the shear flow.

#### 4.1.3 Some Results of Observations

Let us come back to the first objection (1) in Sect. 4.1.1 to the reconnection theory of solar flares. According to the theory, the free magnetic energy is related to the electric current  $J$  inside the RCL. The flare corresponds to rapid changes of this current. It is clear, however, that the magnetic flux through the photospheric plane  $Ph$  (Fig. 4.1) can change only little over the whole area of a flare during this process, except in some particular places, for example, between close sunspots  $N$  and  $s$ .

It means that sunspots and other magnetic features in the photosphere are weakly affected by the occurrence of a flare because the plasma in the photosphere is almost  $10^9$  times denser than the plasma in the corona where the flare originates. Therefore it is difficult (but still possible) for disturbances in the tenuous corona and upper chromosphere to affect the extremely massive plasma in the photosphere. Only small MHD perturbations penetrate into the photosphere.

The same is true in particular for the vertical component of the magnetic field, which is usually measured. Therefore

| in the first approximation, the photospheric magnetic field changes a little during the solar flare over its whole area.

As a consequence, it is not surprising that after a flare the large-scale structure in the corona can remain free of noticeable changes, because it is determined essentially by the potential part of the magnetic field above the photospheric sources. More exactly, even being disrupted, the large-scale structure will come to the potential field configuration corresponding to the post-flare position of the photospheric sources (see discussion in Sect. 16.5.1).

On the other hand, in the *Bastille day flare* on 2000 July 14 (see Chaps. 6 and 7) as well as in some other large solar flares, it was possible to detect the real changes in the sunspot structure just after a flare.

The outer penumbra fields became more vertical due to magnetic reconnection in the corona during a flare

(Liu et al. 2005; Wang et al. 2005). One can easily imagine such changes by considering, for example, Fig. 4.1 between sunspots *N* and *s*.

Sudoh and Harvey (2005) have used the *Global Oscillation Network Group* (GONG) magnetograms to characterize the changes in the photospheric vertical component of magnetic field during 15 large solar flares. An abrupt, significant, and persistent change in the magnetic field occurred in at least one location within the flaring active region during each event after its start. Among several possible interpretations for these observations, Sudoh and Harvey favor one in which

the magnetic field changes result from the penumbra field relaxing upward by reconnecting magnetic field above the photosphere.

This interpretation is very similar to than one given by Liu et al. (2005) and Wang et al. (2005).

The topological model (Somov et al. 2008) self-consistently explains the following observational effects in the photosphere during and after the large flare on 2000 July 14 (see Chap. 6): (a) the enhancement of the horizontal and vertical magnetic fields at the center of an active region (AR) and the weakening of the horizontal field on the AR periphery; (b) the decrease in the AR magnetic flux as a whole; and (c) the convergence of the center-of-mass positions of opposite magnetic polarities. Therefore the entire set of these observations can be interpreted as the result of a magnetic-field restructuring in the corona caused by magnetic reconnection.

As for the second objection (2) to the hypothesis of accumulation of energy in the form of magnetic field of *slowly-reconnecting* current layers in the solar atmosphere, the rapid dissipation of the field necessary for the flare is naturally explained by the theory of current layers presented in what follows, especially in Chaps. 8 and 9).

## 4.2 The Simple Topological Model of an Active Region

### 4.2.1 The Potential Magnetic Field Approximation

Gorbachev and Somov (1989, 1990) have developed a three-dimensional (3D) model for a *potential* magnetic field in the active region AR 2776 with an extended solar flare on 1980 November 5. Before discussing the active region and the flare (see Sect. 4.3.1), let us consider, at first, the general properties of this class of models called *topological*.

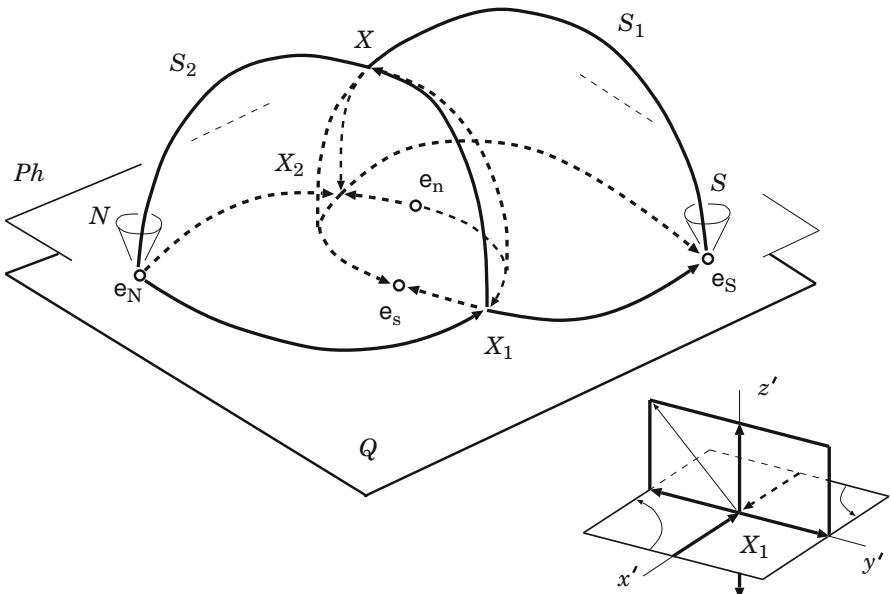


**Fig. 4.2** The model for the magnetic field of four sunspots of pairwise opposite polarity. The sunspots *N* and *S* in the photospheric plane *Ph*. The separatrices *S*<sub>1</sub> and *S*<sub>2</sub> cross at the separator *X*<sub>1</sub>*XX*<sub>2</sub> above the plane *Q* of the effective magnetic ‘charges’ *e*<sub>*N*</sub>, *e*<sub>*S*</sub>, etc

In the simplest variant of the model (Gorbachev and Somov 1988), four magnetic field sources – the magnetic ‘charges’ *e*<sub>*N*</sub> and *e*<sub>*S*</sub>, *e*<sub>*n*</sub> and *e*<sub>*s*</sub>, located in the plane *Q* under the photosphere *Ph* (Fig. 4.2) – are used to reproduce the main features of the observed field in the photosphere related to the four most important sunspots: *N*, *S*, *n* and *s*. As a consequence, the *quadrupole* model reproduces only the large-scale features of the actual field in the corona related to these sunspots. As a minimum, the four sources are necessarily to describe two interacting magnetic fluxes having the two sources per each. The larger number of sources are not necessarily much better.

The main features are two magnetic surfaces, the boundary surfaces called the *separatrices* *S*<sub>1</sub> and *S*<sub>2</sub> (Fig. 4.2). They divide the whole space above the under-photospheric plane *Q* into four regions and, correspondingly, the whole magnetic field into four magnetic fluxes having different linkages. The field lines are grouped into four regions according to their termini. The separatrices of the potential magnetic field are formed from field lines beginning or ending at magnetic zeroth points *X*<sub>1</sub> and *X*<sub>2</sub>. For example, the field lines originating at the point *X*<sub>1</sub> form a separatrix surface *S*<sub>1</sub> (for more detail see Gorbachev et al. 1988).

There is a topologically singular field line *X*<sub>1</sub>*XX*<sub>2</sub> lying at the intersection of the two separatrices, it belongs to all four fluxes (two reconnecting and two reconnected fluxes) that interact at this line – the 3D magnetic *separator*. So

the separator separates the interacting magnetic fluxes by the separatrices above the plane of magnetic sources

(cf. Fig. 1.4a; see also Sweet 1969; Lau 1993). Detection of a separator, as a field line that connects two zeroth points in the Earth magnetotail, by the four *Cluster* spacecraft (Xiao et al. 2007) provides an important step towards establishing an observational framework of 3D reconnection.

#### 4.2.2 Classification of Zeroth Points

Let us clarify the basic properties of the zeroth points of the magnetic field discussed above. In the vicinity of a zeroth point  $X_i$  located at  $\mathbf{r} = \mathbf{r}_i$  in the plane  $Q$ , the vector of magnetic field can be represented in the form

$$B_\alpha(\mathbf{r}) = \frac{\partial \psi}{\partial r_\alpha} = M_{\alpha\beta}(\mathbf{r}_i) \xi_\beta . \quad (4.2)$$

Here  $\psi(\mathbf{r})$  is the potential of the field, the vector  $\xi = \mathbf{r} - \mathbf{r}_i$ , the index  $i = 1, 2$ ; the Greek indices  $\alpha, \beta = 1, 2, 3$  or  $x, y, z$ . The symmetric matrix

$$M_{\alpha\beta}(\mathbf{r}_i) = \frac{\partial^2 \psi(\mathbf{r}_i)}{\partial r_\alpha \partial r_\beta} = \begin{vmatrix} \lambda_1 & 0 & 0 \\ 0 & \lambda_2 & 0 \\ 0 & 0 & \lambda_3 \end{vmatrix} \quad (4.3)$$

in the frame of coordinates  $r'_\alpha$  related to the eigenvectors  $\mathbf{e}'_\alpha$ ,  $\lambda_\alpha$  are the eigenvalues of the matrix. Because the magnetic field is potential, all the  $\lambda_\alpha$  are real numbers (e.g., Dubrovin et al. 1986). Positive eigenvalues  $\lambda_\alpha$  correspond to the magnetic-field lines emerging from a zeroth point and negative  $\lambda_\alpha$  correspond to the field lines arriving at a point  $\mathbf{r}_i$ .

If the determinant

$$\det M_{\alpha\beta}(\mathbf{r}_i) = \lambda_1 \lambda_2 \lambda_3 \neq 0 , \quad (4.4)$$

then the zeroth point is called *non-degenerate*. Such a point is *isolated*, i.e., the magnetic field in its vicinity does not vanish.

Since  $\operatorname{div} \mathbf{B} = 0$ , we obtain a condition

$$\lambda_1 + \lambda_2 + \lambda_3 = 0 . \quad (4.5)$$

Therefore there exist only three following classes of zeroth points of magnetic field (see Gorbachev et al. 1988).

**Type A.** All eigenvalues  $\lambda_\alpha \neq 0$ . This corresponds to two zeroth points shown in Fig. 4.2. At the first point  $X_1$

$$\lambda_1 < 0 , \quad \lambda_2 > 0 , \quad \lambda_3 > 0 . \quad (4.6)$$

Using the analogy with fluid flow, we say that field lines “flow in” along the  $x'$  axis and “flow out” along the separatrix plane ( $y', z'$ ) as shown in the left bottom insert in Fig. 4.2. We shall call this subclass of non-degenerate zeroth point as the Type A— since  $\lambda_1 < 0$ .

On the contrary, at the point  $X_2$

$$\lambda_1 > 0, \quad \lambda_2 < 0, \quad \lambda_3 < 0. \quad (4.7)$$

This will be the Type A+ since  $\lambda_1 > 0$ .

**Type B.** This is a degenerate case

$$\lambda_1 = -\lambda_2 \neq 0, \quad \lambda_3 = 0. \quad (4.8)$$

It can occur, for example, if the investigated zeroth point belongs to a *neutral line* as illustrated by Fig. 1.2.

**Type C.** This is another degenerate case

$$\lambda_1 = \lambda_2 = \lambda_3 = 0. \quad (4.9)$$

It means that three neutral lines intersect at the point  $\mathbf{r}_i$ .

### 4.2.3 The Number of Zeroth Points

In order to use a general theorem of differential geometry on the number of singular points of a 3D vector field (Dubrovin et al. 1986), we have to “smooth” the point “charges” of magnetic field. The smoothed potential  $\psi$  of a positive magnetic source has a local maximum at the point where a positive charge was located. Hence at this point all eigenvalues  $\lambda_\alpha > 0$ . At a singular point with a negative charge, all  $\lambda_\alpha < 0$ , and the potential has a local minimum.

In order to establish a relation between the number of nondegenerate points, we introduce the so-called *topological index*

$$I_{top}(\mathbf{r}_i) = \text{sign} [\det M_{\alpha\beta}(\mathbf{r}_i)] = \text{sign} (\lambda_1 \lambda_2 \lambda_3). \quad (4.10)$$

Here the function  $\text{sign}(x) = +1$  if  $x > 0$  and  $\text{sign}(x) = -1$  if  $x < 0$ . Thus the possible types of nondegenerate points have the indices presented in Table 4.1.

According to Dubrovin et al. (1986, Part II, Chap. 3, Sect. 14), with some essential difference in notations that are standard in physics, we can formulate the following statement (Somov, 2008a,b).

**Table 4.1** The topological indices of singular and zeroth points

Type of a point	$I_{top}$
Maximum of potential $\psi$	+1
Minimum of potential $\psi$	-1
Zeroth point of Type A+	+1
Zeroth point of Type A-	-1

### Theorem 4.1.

For a three-dimensional potential magnetic field, in general three-dimensional case,

$$\sum_i I_{top}(\mathbf{r}_i) = \frac{1}{4\pi} \int \mathbf{B} \left[ \frac{\partial \mathbf{B}}{\partial \theta} \times \frac{\partial \mathbf{B}}{\partial \varphi} \right] \frac{d\theta d\varphi}{B^3} \equiv J, \quad (4.11)$$

where the integral is taken over the sphere of infinite radius.

For example, if the total magnetic charge

$$e_{tot} = \sum_i e_i > 0, \quad (4.12)$$

then the integral  $J = +1$ . Let  $N_{max}$  ( $N_{min}$ ) is the number of maxima (minima) of the potential  $\psi$  of magnetic field  $\mathbf{B}$ ,  $N_{A+}$  ( $N_{A-}$ ) is the number of zeroth points of Type A+ (A-), then according to (4.11) we have

$$N_{max} - N_{min} + N_{A+} - N_{A-} = +1. \quad (4.13)$$

If  $e_{tot} < 0$  then  $J = -1$ , and we write -1 on the right-hand side of Eq. (4.13). If the total magnetic charge

$$e_{tot} = 0, \quad (4.14)$$

the following relation is valid:

$$N_{max} - N_{min} + N_{A+} - N_{A-} = 0. \quad (4.15)$$

For the magnetic field shown in Fig. 4.2,  $N_{max} = N_{min} = 2$ . Hence formula (4.15) gives us an equation

$$N_{A+} = N_{A-} \quad (4.16)$$

but not the total number of zeroth points, that we need.

However, if all the charges are located in the plane Q (the plane  $z = 0$  in what follows), as illustrated by Fig. 4.2, then we can obtain an additional information about the number of zeroth points, another equation. Let us determine the topological index for the two-dimensional (2D) vector field in the same plane

$$\mathbf{B}^{(2)}(x, y) = \{B_x, B_y\} \quad (4.17)$$

**Table 4.2** Topological indices of singular and zeroth points of the 2D field in the plane  $Q$

Type of a point	$I_{top}^{(2)}$
Maximum of potential $\psi$	+1
Minimum of potential $\psi$	+1
Zeroth point (a saddle)	-1

following general definition from (Dubrovin et al. 1986)

$$I_{top}^{(2)}(\mathbf{r}_i) = \text{sign} [\det M_{\alpha\beta}(\mathbf{r}_i)] = \text{sign} (\lambda_1 \lambda_2). \quad (4.18)$$

Here again the function  $\text{sign}(x) = +1$  if  $x > 0$  and  $\text{sign}(x) = -1$  if  $x < 0$ . Hence the possible types of nondegenerate points have the indices presented in Table 4.2.

In this case of a plane arrangement of magnetic charges, we have to rewrite Theorem 4.1 as follows (Somov 2008a).

### Theorem 4.2.

*For a potential magnetic field in the plane  $z = 0$ , in which the magnetic charges are located,*

$$\sum_i I_{top}^{(2)}(\mathbf{r}_i) = \frac{1}{2\pi} \int [\mathbf{B}^{(2)}(x, y)]^{-2} (B_x dB_y - B_y dB_x) \equiv \equiv J^{(2)}, \quad (4.19)$$

*where the integral is taken over the circle of infinite radius in the positive direction of circulation.*

For a plane magnetic field (4.17) of the dipole type (i.e.,  $e_{tot} = 0$  and an effective dipole moment  $\mathbf{m} \neq 0$  in the plane  $z = 0$ ) the integral  $J^{(2)} = 2$ . Thus we have

$$N_{max}^{(2)} + N_{min}^{(2)} - N_A^{(2)} = 2, \quad (4.20)$$

where  $N_{max}^{(2)}$  ( $N_{min}^{(2)}$ ) is the number of maxima (minima) of the potential  $\psi = \psi(x, y, 0)$  in the plane  $z = 0$ ,  $N_A^{(2)}$  is the number of zeroth points, the saddles (e.g., Petrovskii 1964, Chap. 3, Sect. 22). Because of the symmetry relative to the plane  $z = 0$ , everywhere in the plane (outside of the charges)  $B_z = 0$ . Therefore the saddles of the plane field are zeroth points of the 3D magnetic field.

For the magnetic field shown in Fig. 4.2,  $N_{max}^{(2)} = 2$  and  $N_{min}^{(2)} = 2$ . Hence, according to formula (4.20), the number of zeroth points  $N_A^{(2)} = 2$ . By using Eq. (4.16), we conclude that, in the simple case under consideration,

$$N_{A+} = N_{A-} = 1. \quad (4.21)$$

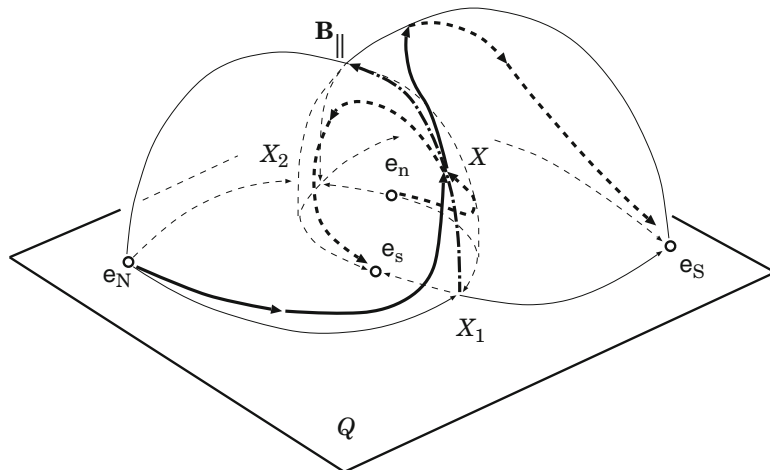


**Fig. 4.3** A schematic view of the same model for magnetic field. The field lines located at the separatrices and connected to the separator due to the 3D reconnection process at the point  $X$ , the vector  $\mathbf{B}_{\parallel}$  is the longitudinal component of a magnetic field

#### 4.2.4 The Electric Currents Needed

The potential magnetic field model does not include any currents and therefore it cannot model the energy stored in the fields and released in solar flares. Thus here we introduce some currents and energetics to a flare model. The *linkage* of real field lines connected to the separator is shown in Fig. 4.3. This Figure does not mean, of course, that we assume the existence of real magnetic charges under the photosphere as well as the real  $X$ -type zeroth points  $X_1$  and  $X_2$  in the plane  $Q$  which does not exist either. We only assume that above the photospheric plane the large-scale magnetic field can be described in terms of such a simple model. We also assume that the actual conditions for reconnection are better at some point  $X$  of the separator rather than at its other points. If the magnetic sources move or/and change, the field also changes.

It is across the separator that the magnetic fluxes are redistributed and reconnected so that the magnetic field could remain potential, if there were no plasma.

In the presence of the solar plasma of low resistivity, the separator plays the same role as the hyperbolic neutral line of magnetic field, familiar from 2D MHD problems (see Syrovatskii 1966a; Sweet 1969; Brushlinskii et al. 1980; Biskamp 1986, 1997); see review of a current state of numerical simulations and laboratory experiments in Yamada et al. (2007). In particular, as soon as the separator appears, the electric field  $\mathbf{E}_0$  induced by the varying magnetic field produces an electric current  $\mathbf{J}$  along the separator. The current interacts with the potential magnetic field

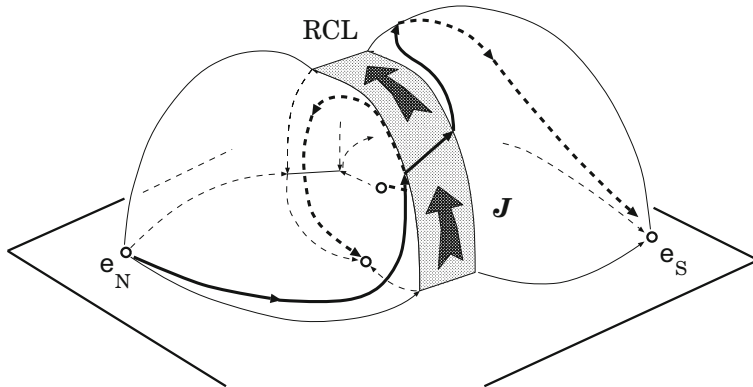


**Fig. 4.4** A schematic view of the *reconnecting current layer* (*RCL*) with a total current  $J$  at the separator

in such a way (Sect. 1.1.3) that the current assumes the shape of a **thin wide current layer** (see RCL in Fig. 4.4).

In the high-conductivity plasma the current layer hinders the redistribution of the magnetic fluxes, their reconnection.

This very *slow* reconnection process results in an energy being stored in the form of magnetic energy of a current layer – the *free* magnetic energy.

Therefore the model assumes that the *slowly-reconnecting* current layer appears at the separator (Syrovatskii 1981; Gorbachev and Somov 1989; Longcope and Cowley 1996) in the solar atmosphere in a pre-flare stage. If for some reason (see (Somov 1992; Cassak et al. 2007; Uzdensky 2007a) the reconnection process becomes fast, then the free magnetic energy is rapidly converted into kinetic energy of particles. This is a *flare*. The rapidly-reconnecting current layer, being in a high-temperature turbulent-current state (Sect. 8.3), provides the flare energy fluxes along the reconnected field lines.

#### 4.2.5 The Longitudinal Magnetic Field

Magnetic reconnection for the 3D models without zeroth points in and above the photosphere, as we assumed in Fig. 4.3 with the plane  $Q$  under the photosphere  $P_h$  in Fig. 4.2, is, in fact, qualitatively the same as the two-dimensional reconnection in the models with a non-zero longitudinal magnetic field. The inductive electric field along the separator is the driving force of the reconnection process. The field lines going into reconnection are forced to become one line and the field lines coming out of reconnection are pulled by the longitudinal electric field. Thus magnetic reconnection in 3D should be taken to mean effects associated with the reconnecting current layer (RCL), as in 2D (Greene 1988; Lau and Finn 1990).

It is important for what follows in Chaps. 11, 13, and 16 that

an actual 3D reconnection at the separator proceeds in the presence of an increasing (or decreasing) *longitudinal* magnetic field  $\mathbf{B}_{\parallel}$

(see Fig. 4.3), which is parallel to the electric current  $\mathbf{J}$  inside the RCL as shown in Fig. 4.4. What factors do determine the increase (or decrease) of the longitudinal field? – The first of them is the global field configuration, i.e. the relative position of the magnetic field sources in an active region. It determines the position of the separator and the value of the longitudinal field at the separator and in its vicinity. This field is not uniform, of course, near the separator.

The second factor is the evolution of the global magnetic configuration, more exactly, the electric field  $\mathbf{E}_0$  related to the evolution and responsible for driven reconnection at the separator. The direction of reconnection – with an increase (or decrease) of the longitudinal magnetic field – depends on the sign of the electric field projection on the separator, i.e. on the sign of the scalar product  $(\mathbf{E}_0 \cdot \mathbf{B}_{\parallel})$ . In general, this sign can be plus or minus with equal probabilities, if there are no preferential configurations of the global field or no preferential directions of the active region evolution. This statement as well as the whole model must be examined by future observations and their analysis.

## 4.3 The Solar Flare on 1980 November 5

### 4.3.1 Observed and Model Magnetograms

As a well studied example, let us consider the extended 1B/M4 flare at 22:33 UT on 1980 November 5 (Duijveman et al. 1983; Rust and Somov 1984). This two-ribbon flare was observed by the satellite *SMM* (Solar Maximum Mission) in soft and hard X-rays (Fig. 4.5).

Three bright *hard* X-ray (HXR) kernels A, B and C are well distinguished in Fig. 4.5b. The *soft* X-ray (SXR) elements of the flare, as seen in Fig. 4.5a, consist presumably of two overlapping coronal loops, AB and BC with their footpoints A, B, and C in the chromosphere have been identified as the compact sources of HXR and H $\alpha$  emission.

Figure 4.6 shows the longitudinal (line-of-sight component) magnetogram of the active region AR 2776 where the flare occurred. Numbers shows a magnitude of magnetic field measured in  $10^2$  G. Two narrow flare ribbons are shown on either side of the photospheric neutral line (PNL). Let us identify the four largest regions in which magnetic field of a single polarity is concentrated in the magnetogram: two of northern polarity and two of souther polarity. Since the active region is comparatively close to the center of the solar disk, the magnetogram represents the vertical component  $B_z$  at the photospheric level fairly well.

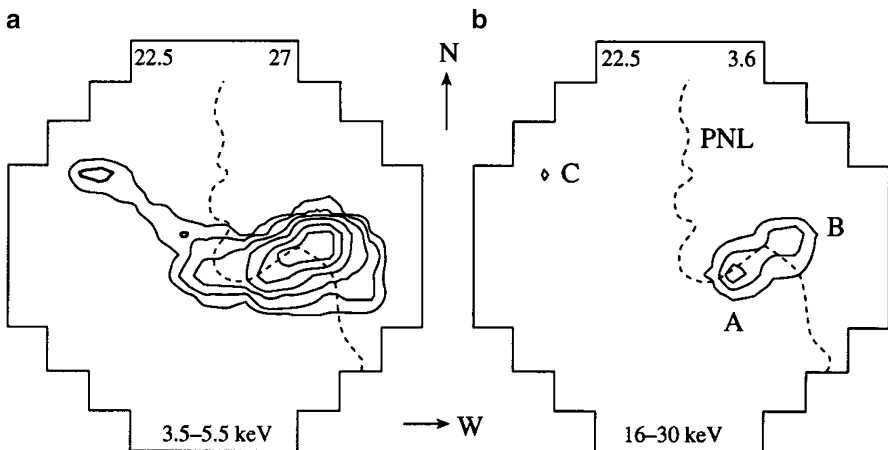


**Fig. 4.5** The solar flare on 1980 November 5 as observed by the Hard X-ray Imaging Spectrometer (HXIS) on board *SMM* satellite in soft (a) and hard (b) X-rays (From Somov 2008a; reproduced with permission © Pleiades Publishing, Ltd.)

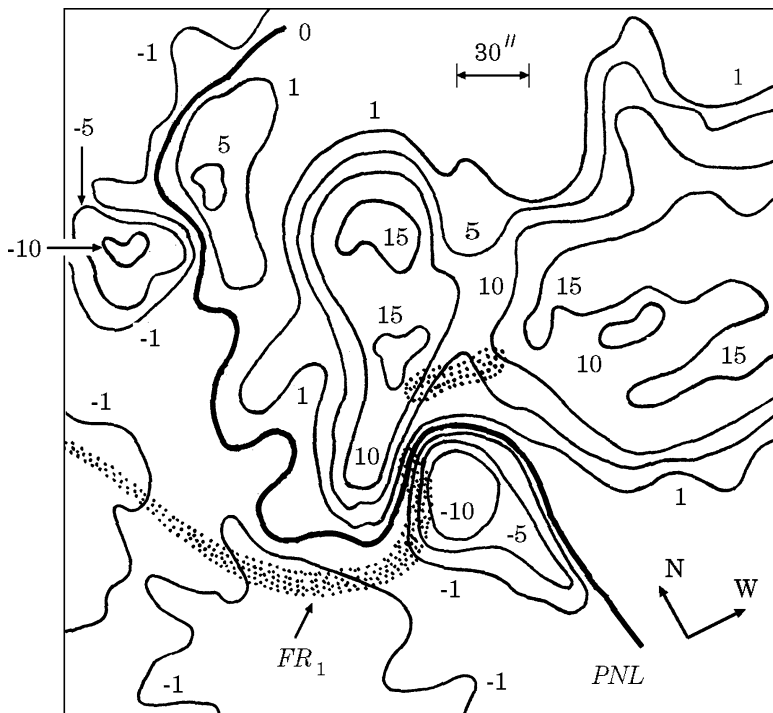


**Fig. 4.6** The line-of-sight component of magnetic field in the active region AR 2776. The flare ribbons are schematically shown as *shadow* areas;  $FR_1$  is the longer one of two (From Somov 2008a; reproduced with permission © Pleiades Publishing, Ltd.)

First, let us try to make a model of the magnetogram shown in Fig. 4.6. With this aim, we calculate the vertical component  $B_z$  of the field in the photospheric plane in the potential approximation, i.e., using for the magnetic-field vector the simple formula

$$\mathbf{B}(x, y, z) = \sum_{i=1}^4 \frac{e_i}{|\mathbf{r} - \mathbf{r}_i|^2} \times \frac{\mathbf{r} - \mathbf{r}_i}{|\mathbf{r} - \mathbf{r}_i|}. \quad (4.22)$$

Here  $e_i$  are the effective charges of magnetic field, and  $\mathbf{r}_i$  are their radius vectors:

$$\begin{aligned} e_1 &= -2.5, \quad \mathbf{r}_1 = \{-0.8, 0, -0.1\}; \\ e_2 &= -1.0, \quad \mathbf{r}_2 = \{0.1, -0.4, -0.1\}; \\ e_3 &= +3.0, \quad \mathbf{r}_3 = \{-0.25, 0.15, -0.1\}; \\ e_4 &= +4.5, \quad \mathbf{r}_4 = \{0.5, 0.16, -0.1\}. \end{aligned}$$

Note that the total magnetic charge

$$e_{tot} = \sum_i e_i = 4 > 0, \quad (4.23)$$

Thus, in order to determine a relation between the number of zeroth points and the numbers of magnetic field sources, we have to use formula (4.13). It gives us an equation

$$N_{A+} = N_{A-} + 1. \quad (4.24)$$

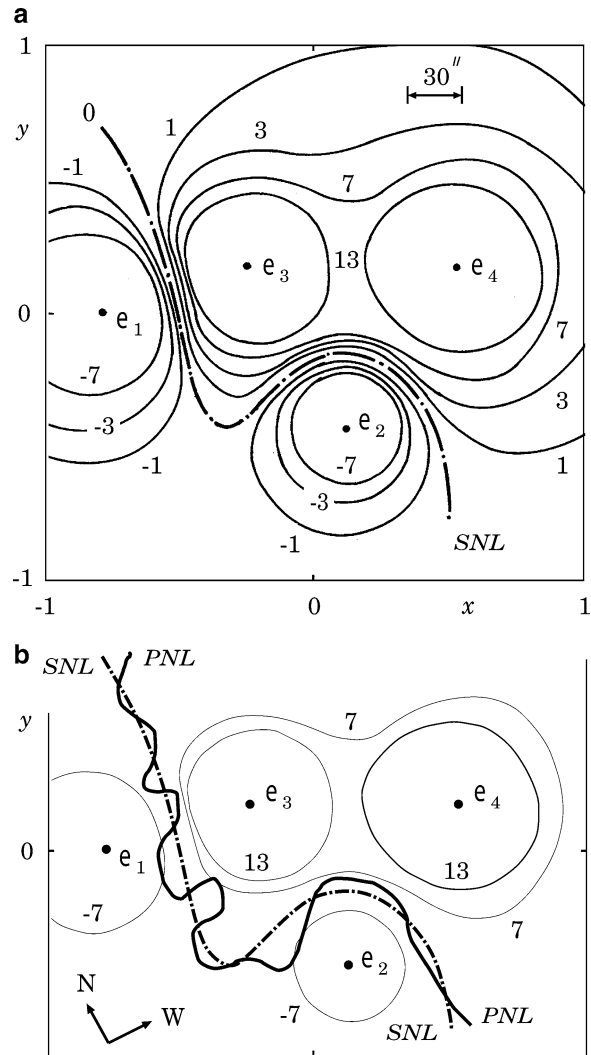
We shall come back to this equation later on, considering the topological portrait of the active region.

The length unit equals  $150'' \approx 1.1 \times 10^{10}$  cm, the strength of magnetic field is measured in  $10^2$  G. The parameters  $e_i$  and  $\mathbf{r}_i$  have been selected in order to reproduce in an optimal way the magnetic fluxes of individual polarities in the photospheric plane  $z = 0$  (see Fig. 4.7a) as well the shape of the photospheric neutral line (*PNL* in Fig. 4.7b). The calculated *simplified* neutral line (*SNL*) smoothes the curve *PNL* well in small scales but conserves its *S*-type shape in a large scale, in the linear scale of the active region.

Because the simplest topological model uses a minimal number of magnetic sources – four, which is necessary to describe the minimal number of interacting magnetic fluxes – two, we call it the *quadrupole-type* model and present it in Fig. 4.7. This label is not an exact definition (because in general and in the case under consideration  $e_N \neq -e_S$  and  $e_n \neq -e_s$ ) but it is convenient for people who know well the *exact-quadrupole* model by Sweet (1969). In fact, as we shall see below, the difference – the presence of another separator in the model by Gorbachev and Somov – is not small and can be significant for actual active regions on the Sun.

The second separator may be important to give accelerated particles a way to escape out of an active region in the interplanetary space.

**Fig. 4.7** The model magnetogram. (a) The numbers near the curves show the constant values of the vertical component of magnetic field in the photospheric plane. Positions and magnitudes of the effective sources of magnetic field, located below this plane, are adjusted to fit the main features of the photospheric magnetogram. (b) The calculated simplified neutral line (*SNL*) approximates the *observed* photospheric neutral line (*PNL*) (From Somov 2008a; reproduced with permission © Pleiades Publishing, Ltd.)



Second, we calculate the magnetic-field lines via numerical integration of the ordinary differential equations

$$\frac{dx}{B_x} = \frac{dy}{B_y} = \frac{dz}{B_z}. \quad (4.25)$$

Here  $(dx, dy, dz)$  is an arch element directed along the field line. The vector  $\mathbf{B}$  is determined at each point by formula (4.22).

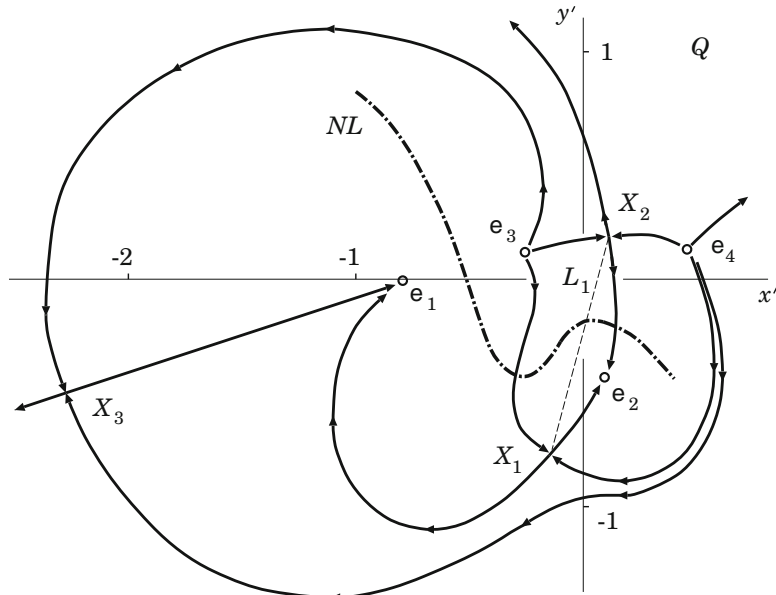


**Fig. 4.8** The topological portrait of the active region

### 4.3.2 Topological Portrait of the Active Region

The topological properties of magnetic field are determined by the number and locations of zeroth points of the field. In the case under consideration, there are three zeroth points in the plane ( $z = -0.1$ ) of the effective magnetic sources, shown in Fig. 4.8. The coordinates of these points are:

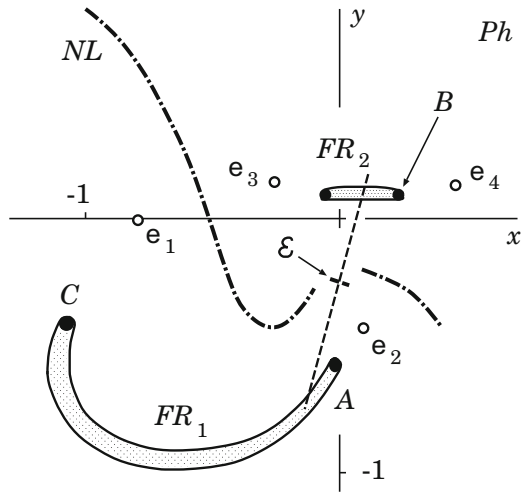
$$\begin{aligned} X_1 &= \{-0.133, -0.739, -0.1\}, \\ X_2 &= \{0.076, 0.179, -0.1\}, \\ X_3 &= \{-2.26, -0.439, -0.1\}. \end{aligned}$$

Figure 4.8 shows the topologically important magnetic-field lines in the plane  $(x', y')$  which is the plane  $Q$  of the effective sources  $e_1, e_2, e_3$ , and  $e_4$ . They reproduce the large-scale features of the observed magnetic field in the photosphere related to the four largest sunspots in the active region. Positions and magnitudes of the sources are adjusted to fit the main topological features of magnetic field (Gorbachev and Somov 1989).

Since the total magnetic charge  $e_{tot} > 0$ , instead of Eq. (4.20) for the number of zeroth points of two-dimensional magnetic field (4.17), we have another equation

$$N_{max}^{(2)} + N_{min}^{(2)} - N_A^{(2)} = 1, \quad (4.26)$$

**Fig. 4.9** The flare ribbons at both sides of the photospheric neutral line  $NL$  in the flare of 1980 November 5



because according to formula (4.19) we find the value  $J^{(2)} = 1$ . It follows from (4.26) that the total number of zeroth points

$$N_A^{(2)} = 3. \quad (4.27)$$

On the other hand,

$$N_A^{(2)} = N_{A+} + N_{A-}. \quad (4.28)$$

With account of Eq. (4.24) taken, we conclude that  $N_{A+} = 2$  and  $N_{A-} = 1$ .

The field lines shown in Fig. 4.8 play the role of separatrices (cf. Fig. 4.2) and show the **presence of two separators** in the active region. Two zeroth points  $X_1$  (the Type  $A_+$ ) and  $X_2$  (the Type  $A_-$ ) are located in the vicinity of the magnetic sources and are connected by the first separator shown by its projection, the thin dashed line  $L_1$ . Near this separator, the field and its gradient are strong and determine the flare activity of the region.

Another separator starts from the zeroth point  $X_3$  (the Type  $A_+$ ) far away from the magnetic sources and goes much higher above the active region to infinity. The second separator can be responsible for flares in weaker magnetic fields and smaller gradients high in the corona. The second separator is also a good place for the particles accelerated along the first separator to escape from the active region in the interplanetary space.

Let us suppose that a part of the flare energy is initially released in some compact region  $\epsilon$  near the apex of the main separator  $X_1X_2$ . Then energy fluxes  $F_\epsilon$  will propagate *along* the field lines connecting the energy source with the photosphere. Projections of the energy source  $\epsilon$  on the photospheric plane  $Ph$  along the field lines are shown as two ‘flare ribbons’  $FR_1$  and  $FR_2$  in Fig. 4.9. Therefore the topological model of a solar flare allows us to identify the flare brightenings, in the

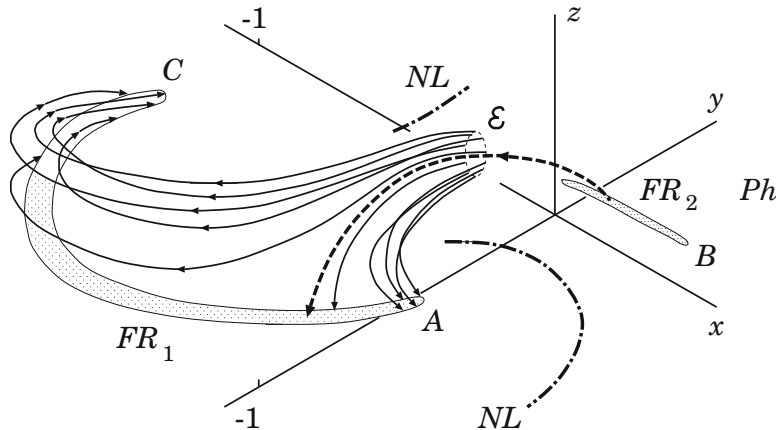


**Fig. 4.10** A picture of potential field lines crossing the region of primary energy release  $\mathcal{E}$ , which is situated at the apex of the main separator (boldface dashed curve). The flare ribbons are formed where these field lines cross the photosphere (plane  $z = 0$ )

hydrogen  $H\alpha$  line as well as in EUV and hard X-rays, with the ribbons located at the intersection of the separatrices with the chromosphere which is placed slightly above the photospheric plane ( $x, y$ ).

The characteristic *saddle* structure of the field in the vicinity of the reconnecting point  $X$  at the separator (cf. Part I, Fig. 14.1) leads to a spatial redistribution of the energy flux  $F_\varepsilon$  of heat and accelerated particles. This flux is efficiently split apart in such a way that it creates the observed long-narrow  $H\alpha$  ribbons in the chromosphere (see  $FR_1$  and  $FR_2$  in Fig. 4.10).

For the first time, the model by [Gorbachev and Somov \(1989\)](#) had reproduced the observed features of the M4/1B flare of 1980 November 5. In particular, the model predicts the simultaneous flaring of the two chromospheric ribbons. Moreover it predicts that a concentration of the field lines that bring energy into the ribbons in the chromosphere is higher at the edges of the ribbons, i.e. at relatively compact regions indicated as  $A$ ,  $B$ , and  $C$ . Here the  $H\alpha$  brightenings must be especially bright. This is consistent with observations of  $H\alpha$  ‘kernels’ in this flare.

### 4.3.3 Features of the Flare Topological Model

The topological model also predicts another signature of flares. Since in the  $H\alpha$  kernels the flare energy fluxes are more concentrated, the impulsive heating of the chromosphere must create a fast expansion of high-temperature plasma upwards into the corona (see [Somov 1992](#)). This effect is known as the chromospheric ‘evaporation’ observed in the EUV and soft X-ray (SXR) emission of solar flares. Evaporation lights up the SXR coronal loops in flares.

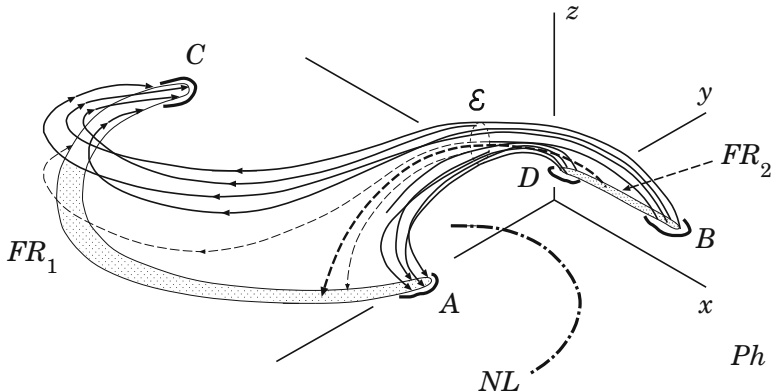


**Fig. 4.11** Field lines that connect the H $\alpha$  kernels A, B, C, and D. Chromospheric evaporation creates a picture of the crossing SXR loops predicted by the topological model for a flare in an active region with the quadrupole-type configuration of magnetic sources under the photosphere

The topological model also shows that the two flare ribbons as well as the four of their edges with H $\alpha$  kernels are magnetically connected to the common region of energy release at the separator (see  $\mathcal{E}$  in Fig. 4.10). Note that Fig. 4.10 demonstrates only the field lines connected to one of the ribbons. Through the same region all four H $\alpha$  kernels are magnetically connected to one another. Therefore

the SXR loops look like they are crossing or touching each other somewhere in the region of energy release

as shown in Fig. 4.11 from Somov et al. (2001, 2002b).

So the model predicts that the reconnecting magnetic fluxes are distributed in the corona in such a way that the **two SXR loops** may look like that they **interact with each other**. That is why the SXR observations demonstrating such structures are usually considered as direct evidence in favor of the model of two *interacting loops* (Sakai and de Jager 1996). The difference, however, exists in the primary source of energy. High concentrations of electric currents and twisted magnetic fields are created inside the interacting loops by some under-photospheric dynamo mechanism. If these currents are mostly parallel they attract each other giving an energy to a flare (Gold and Hoyle 1960). On the contrary,

according to the topological model, the flare energy comes from an interaction of magnetic fluxes that can be mostly potential.

Note that the **S-shaped structures**, when they are observed in SXRs (e.g., Fig. 2 in Pevtsov et al. 1996) or in hydrogen H $\alpha$ -line, are usually interpreted in favor of non-potential fields. In general, the shapes of coronal loops are signature of the *helicity* (Sect. 14.1) of their magnetic fields. The S-shaped loops match flux tubes of *positive helicity*, and inverse S-shaped loops match flux tubes of *negative helicity* (Pevtsov et al. 1996). As we see in Fig. 4.11, the S-shaped structure  $C\mathcal{E}B$

connecting the bright points  $C$  and  $B$  results from the computation of the potential field in the frame of the simple topological model.

Not surprisingly, the potential field produced by four sources may be even more complicated and may look as a strongly non-potential field. Severely **kinked  $\Omega$ -type loops**, sometimes connecting two active regions, might be understood in terms of a simple topological model, see Fig. 8 in [Pevtsov and Longcope \(1998\)](#).

In the active region AR 2776 where the flare on 1980 November 5 was observed, [Den and Somov \(1989\)](#) had found a considerable **shear of a potential field** above the photospheric neutral line near the region of the brightest flare loop  $AB$ . Many authors concluded that an initial energy of flares is stored in magnetic fields with large shear. However, such flares presumably were not the case of potential field having a minimum energy. This means that the presence of observed magnetic shear is not a sufficient condition for generation of a large flare in an active region.

#### 4.3.4 Complexity of a Topological Model

The topological model by [Gorbachev and Somov \(1990\)](#) postulated a global topology for an active region consisting of four main fluxes. Reconnection between, for example, the upper and lower fluxes transfers a part of the magnetic flux to the two side systems. [Antiochos \(1998\)](#) addressed the following question: ‘What is the minimum complexity needed in the magnetic field of an active region so that a similar process can occur in a fully three-dimensional geometry?’ He started with a highly sheared field near the photospheric neutral line held down by an overlying unsheared field. Antiochos concluded that a real active region can have much more complexity than very simple configurations.

The topology of potential magnetic field containing only a small number of photospheric sources can be easily classified. As the numbers of sources increase, a pair of connected sources can have more than one distinct flux domain linking them [Parnell \(2007\)](#). We call these the multiply connected *source pairs*. Pairs of nulls connected by more than one separator are called the multiply connected *null pairs*.

Multiply connected source and null pairs go hand-in-hand such that two separators connecting the same pair of nulls immediately implies multiple flux domains linking the same source pair and vice versa. Since magnetic energy release is significant around separators, the fields with multiply connected source pairs, which have more separators, (a) have more sites for intense energy release and (b) are likely to release energy more quickly than other magnetic fields [Parnell \(2007\)](#). In general, we expect that

the global topology of four-flux systems meeting along a coronal separator is **the basis** underlying eruptive activity of the Sun.

It is unlikely that more than four fluxes would share a common boundary, the same separator. This four-flux topology is precisely what is needed for a flare to occur.

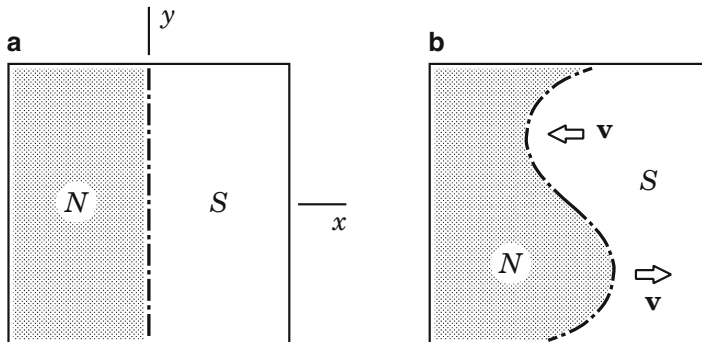


**Fig. 4.12** Model distribution of the vertical component of magnetic field in the photosphere. A vortex flow distorts the photospheric neutral line so that it takes the shape of a letter S

On the other hand, it is clear that the magnetic configurations with more separators have more opportunity to reconnect and would thus more likely to produce flares. Such complicated configuration would presumably produce many small flares to release a large excess of magnetic energy in an active region rather than one large flare.

It is also clear that, in order to accomplish different aims of topological modeling, different methods have to be used. In general, it is not a simple task to implement one or another topological model for a time series of vector magnetograms, paying particular attention to distinguishing real evolution of the photospheric magnetic fluxes from changes due to variations in Earth's atmospheric seeing, as well as uncorrelated noise. Barnes et al. (2005) investigated the reliability of one of such methods and have estimated the uncertainties in its results.

### 4.3.5 The S-Like Morphology and Eruptive Activity

The appearance of separators in the solar atmosphere was initially attributed to the emergence of a new magnetic flux from the photosphere in the region where a magnetic flux already exists as illustrated by Fig. 4.1. In fact, the presence of separators must be viewed as a much more general phenomenon. Figure 4.12a taken from Somov (1985) exhibits the simplest model of the uniform distribution of the vertical component  $B_z$  of the magnetic field in the photosphere. The neutral line  $NL$  divides the region of the field source along the  $y$  axis. In accordance with the fact that it is often visible in solar magnetograms, this region is deformed by photospheric flows with velocity  $v$  in such a way that the neutral line gradually acquires the S-shape as shown in Fig. 4.12b.

At first glance it seems that the magnetic field with such simple sources cannot in principle have any topological peculiarities. However this is not so. Beginning

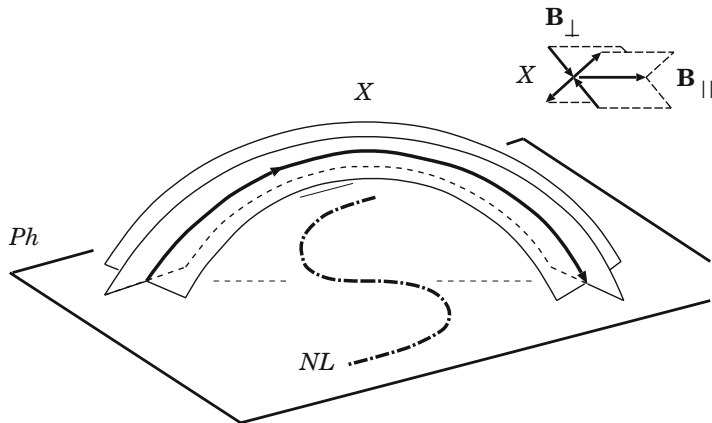


**Fig. 4.13** The ‘rainbow reconnection’ model: the separator  $X$  above the S-shaped bend of the photospheric neutral line  $NL$ . The inset in the *upper right-hand* corner shows the structure of the magnetic field near the top of the separator

with some critical bending of the neutral line, the field calculated in the potential approximation contains a separator as shown in Fig. 4.13 (Somov 1985, 1986). In this figure, the separator  $X$  is located above the photospheric  $NL$  like a *rainbow* above a river which makes a bend. The separator is nearly parallel to the  $NL$  in its central part. The potential field lines just above the  $NL$  are orthogonal to it. This is important to make the simplest 2D models.

By using the topological model, Gorbachev and Somov (1988) demonstrated the appearance and growth of the separator as a result of photospheric vortex flows in the locality of the photospheric neutral line. They showed that the vortex flows or any other photospheric magnetic field changes, creating the S-shape of the neutral line, produce a special topological structure in the field above the photosphere. The peculiarity of this structure is the separator.

The topological ‘rainbow reconnection’ model explains some reliably established properties of two-ribbon flares.

First,

the rainbow reconnection model reveals a connection of large solar flares with the S-shaped bend of photospheric neutral line.

It shows that the neutral line bend must be greater than some critical value. Then it leads to appearance of the separator above the photosphere. So that a necessary condition for magnetic reconnection in the solar atmosphere is satisfied.

Second, the model explains the bipolar picture of a flare: its development simultaneously in regions of different photospheric magnetic field polarities. Moreover it naturally explains the arrangement and shape of the flare ribbons in the chromosphere, the structure observed in X-ray bands like two intersecting loops, and the early appearance of bright flare kernels on the flare ribbon ends.

As viewed in SXRs, the coronal part of active regions consists of discrete bright loops. These loops often collectively form **sinuous S shapes** similar to that one which we saw in Sect. 4.3.3 (see also [Acton et al. 1992](#)). This shape has been named ‘sigmoidal’ by [Rust and Kumar \(1996\)](#) who studied the characteristic of such brightenings in SXRs and found that they are typically evolve from a bright, sharp-edges *sigmoidal features* into either an arcade of loops or a diffuse cloud. Such transient arcades of loops (loop prominence systems) and *long-duration events* (LDEs) are often related to *coronal transients* and *coronal mass ejections* (CMEs).

Using the *Yohkoh* SXR images, [Hudson et al. \(1998\)](#) considered the implications of this scenario in the context of ‘halo’ CMEs. These may correspond to events near the solar disk center. Incorporating data from the *SOHO* Large Angle Spectroscopic Coronagraph (LASCO), this survey found the ‘sigmoid-to-arcade’ development a common feature of active regions associated with the onset of a halo CME.

[Canfield et al. \(1999\)](#) and [Glover et al. \(2000\)](#) performed a similar study incorporating a much wider range of data and observations over an increased range in wavelength. A high proportion of active regions were reviewed with the intention of clarifying which SXR features possess the highest probability of eruption. The results suggest a strong relationship between an overall S-like morphology and the potential of an active region to erupt.

We assume that

the S-like SXR morphology results from the reconnection effect in a high-temperature current layer located at the separator of a quadrupole-type magnetic field of an active region

as was illustrated in Fig. 4.11. Since a pre-event sigmoid disappears leaving a SXR arcade and two ‘transient coronal holes’ ([Sterling and Hudson 1997](#)), opening a closed configuration (see [Syrovatskii and Somov; Syrovatskii 1982](#)) seems to be an important element of the CME onset, which drives reconnection at the separator.

# Chapter 5

## Reconnection in Action

**Abstract** Energy of a solar flare, how can it be estimated in a frame of magnetic reconnection theory? We would like to know also the characteristic time of energy accumulation before a flare as well as the characteristic time of energy release during a flare. Another important question is how to relate the dynamical characteristics of a flare with observed changes of magnetic field in the photosphere. These and some other fundamental properties of solar flares, including the particle acceleration process, are considered in this chapter on the basis of the reconnection theory without invoking many detail assumptions.

### 5.1 A Current Layer as the Source of Energy

#### 5.1.1 Pre-flare Accumulation of Energy

Potential magnetic field has no free energy. Given common and obvious assumptions, the free magnetic energy in the quadrupole-type model described in Chap. 4 is simply the magnetic energy of the total electric current  $J$  in the *reconnecting current layer* (RCL) in the solar atmosphere (as was illustrated by Fig. 4.4):

$$\mathcal{E}_f = \frac{1}{2c^2} LJ^2. \quad (5.1)$$

Here

$$L \approx 2l \ln \frac{2l}{b} \quad (5.2)$$

is the *self-inductance* of the current layer,  $l$  is the distance taken along the separator from the zeroth point  $X_1$  to the point  $X_2$  in Fig. 4.3, and  $b$  is the half-width of the layer.

Since we know the basic physical properties of a pre-flare current layer (see Sect. 8.1.2), we estimate the total current inside the layer as well as its *free magnetic energy* (Syrovatskii 1976b, 1981), the energy of a flare.

If we did not know the properties of the pre-flare reconnection process, we should have considered as an open question the following one. Why can the considerable excess energy be accumulated in the coronal magnetic field during the pre-flare stage without contradicting the natural tendency that lower energy states are more favorable? – We should look for an answer to this question, for example, in a *bifurcation* structure of force-free fields in the corona (Kusano and Nishikawa 1996). However we may continue our consideration of the pre-flare stage as the creation and existence of the slowly-reconnecting current layer. In this way, we see that

slowly-reconnecting current layers in the solar atmosphere can store the magnetic energy  $\mathcal{E}_f$  necessary for flares.

Moreover in a quasi-stationary case (e.g., in the pre-flare state) their output can account for the energetics of the whole active region (Somov and Syrovatskii 1977; Den and Somov 1989). We may nicely call such a state the **minimum current corona** (Longcope and Cowley 1996).

Note that from (5.1) a simple formula follows for the total electric current  $J$  necessary for a solar flare to release the energy  $\mathcal{E}_f$ :

$$J = c \left( \frac{2\mathcal{E}_f}{L} \right)^{1/2} \approx (1-6) \times 10^{11} \text{ Ampere.} \quad (5.3)$$

In this estimate the length  $l$  is set equal to the characteristic size of a large active region,  $l \approx 10^{10}$  cm, and the flare energy to  $\mathcal{E}_f \approx (1-3) \times 10^{32}$  erg. The result agrees with the estimates of the total electric current based on measurements of the magnetic field components in the photospheric plane (Moreton and Severny 1968).

The vector magnetographs determine the transversal field at lower atmospheric levels; the rotor of this field,  $\text{rot } \mathbf{B}$ , yields the vertical current density  $j_z$  (Gopasyuk 1990; Zhang 1995; Wang et al. 1996). Distributions of the intensity of the vertical current inferred from the horizontal magnetic field evolve only gradually and demonstrate mainly two possibilities. One is the emergence of a new electric current from the sub-photosphere. The other is the rearrangement of the current systems in the solar atmosphere.

### 5.1.2 Flare Energy Release

The reconnecting current layers (RCLs) in the pre-flare state can suffer many instabilities: *thermal* instability caused by radiative energy losses (Field 1965), *resistive (overheating)* instability caused by temperature dependence of plasma

conductivity (see [Kadomtsev 1966](#), Sect. 12) *two-stream* instabilities of various types, *structural* instability (Chap. 12), *tearing* instability (Chap. 13) etc. In general it is assumed that

| as a result of one of these instabilities, the magnetic energy of the RCL is rapidly released, and a solar flare starts.

For example, a flare occurs when the current carried on a separator exceeds some threshold. Another possibility is that the temperature of a slowly-reconnecting current layer increases to a critical value. The so-called *topological trigger* (Sect. 6.3) changes the global topology of active regions quickly and can, therefore, dictate the *fast* magnetic reconnection of collisional or collisionless nature in the RCL, say the flare.

At present there are several open questions related to these instabilities: what is the relative importance of each of them, which of them can develop first, and whether an external action upon the RCL is necessary or whether the RCL gradually evolves towards an unstable equilibrium or a non-equilibrium state by itself? – Some attempts to answer these questions using relatively simple models will be demonstrated in what follows. In general, however, answers to these questions depend on the internal structure of the RCL. In its turn this structure depends on the initial and boundary conditions, and on the current layer evolution during previous stages.

Therefore the investigation of RCL dynamics is important for plasma astrophysics. This investigation must include the formation stage, the pre-flare evolution, and the rapid realignment (rupture of the current layer) with transition to a new state characterized by high temperatures and high resistivity (Chap. 8).

In the process of solving this problem many numerical ([Brushlinskii et al. 1980](#); [Antiochos et al. 1997](#)) and laboratory ([Altyntsev et al. 1977](#); [Stenzel and Gekelman 1984](#); [Bogdanov et al. 1986, 2000](#)) experiments have been performed. The hydrodynamic stage of the rise and evolution of pre-flare current layers has been studied in detail. Experiments have shown that a thin, extended RCL can be formed, even in laboratory conditions. To some approximation it has been possible to study the structures of the magnetic field inside the layer and in the ambient plasma, to find the spatial distributions of current and plasma density, the electron and ion temperatures, some other plasma parameters (e.g., [Voronov et al. 2008](#)).

| The laboratory experiments have demonstrated the possibility of a substantial accumulation of free magnetic energy and the explosive disruption of the *thin* wide RCL.

The cause of such disruption, which is accompanied by *fast* reconnection, may be a local resistivity increase related to the development of plasma turbulence.

Future experiments will probably, more than hitherto, concentrate on the study of the conditions for current layer disruption, of nonlinear interactions in the fast reconnection region, and of particle acceleration (see Chap. 11). This would help us to solve the most difficult problem in the reconnection theory and, in particular, give us information necessary to investigate experimentally the characteristics of RCLs as the source of flare energy during the impulsive phase of solar flares.

The disruptive stage of the evolution cannot be described in hydrodynamic terms only: it requires a kinetic description in the disruption region. The *impulsive* electric field induced there efficiently accelerates charged particles (Somov and Syrovatskii 1975). During this process, plasma turbulence is generated. Its intensity depends on the fast particle flux and governs plasma resistivity, reconnection rate, and, as a consequence, the electric field intensity. There is thus a *nonlinear feedback*. Of course, to solve such a self-consistent problem is not easy. We shall, however, bear two limiting cases in mind.

First, low-energy particles interact effectively with the plasma, and most of their energy is rapidly lost by heating the plasma to very high temperatures, the so-called ‘super-hot’ plasma. Second, in the high-energy region, a part of the accelerated particles enters into the *electric runaway* regime (see Part I, Sect. 8.4.2), i.e. it virtually ceases to interact with the plasma in a RCL or its disruption region.

### 5.1.3 The RCL as a Part of an Electric Circuit

We have not discussed yet another problem of the theory of reconnecting current layers as a source of energy for solar flares. This problem has been nicely called *global electrodynamic coupling* (Spicer 1982; Kan et al. 1983). It essentially consists in the question about the role of inductance and resistance in an equivalent electric circuit one of whose components is a current layer in the solar atmosphere. In its simplest form (Baum et al. 1978), the corresponding task can be illustrated by the elementary equation

$$L \frac{d}{dt} J(t) + J(t)R_0 = V(t). \quad (5.4)$$

Here  $V = V(t)$  is the external *electromotive force* (emf) due to variations of photospheric magnetic fields, or simply the potential difference between the points  $X_1$  and  $X_2$  at the ends of the separator in Fig. 4.2. The unknown quantity  $V$  depends on the strength of the photospheric sources and in the simplest approach it is treated as a given function of time.

Let us assume that at the initial moment  $t = 0$ , the current  $J(0)$  along the separator was zero. At this point the external emf  $V(0)$  was completely used up by acting against the self-induction emf:

$$L \frac{dJ}{dt} + 0 = V(0). \quad (5.5)$$

So the current  $J(t)$  will appear.

As soon as a nonzero current  $J(t)$  appears, the voltage drop on the total separator resistance  $R_0$ , according to Eq. (5.4), makes the rate of current increase  $dJ/dt$  in the circuit smaller, which amounts to decreasing the rate of magnetic energy accu-

mulation prior to a flare. The final steady current  $J_s$  depends on the resistance  $R_0$  and the external emf  $V$ :

$$J_s = \frac{V}{R_0}. \quad (5.6)$$

The characteristic time of the process is proportional to the self-inductance  $L$ :

$$\tau_a = \frac{L}{R_0}. \quad (5.7)$$

Note that  $L \sim l$  and  $R_0 \sim \sigma^{-1}l$ . Therefore  $\tau_a \sim \sigma$  does not depend of the length scale  $l$ .

The maximum accumulated energy (5.1) is also proportional to the inductance  $L$  of the equivalent circuit comprising the separator current layer:

$$\mathcal{E}_f = \frac{1}{2c^2} \frac{LV^2}{R_0^2}. \quad (5.8)$$

It is important that the free magnetic energy  $\mathcal{E}_f$  and the energy accumulation time  $\tau_a$  depend also on the total resistance  $R_0$ . In the pre-flare state, the RCL with low Coulomb resistivity has low resistance. For this reason, the accumulated energy can be sufficiently large. The accumulation time is long enough:  $\tau_a \sim 3 \times 10^4$  s (Syrovatskii 1976b).

Schrijver et al. (2005) compared TRACE EUV images of 95 active regions and potential-field source-surface extrapolations based on SOHO MDI magnetograms. It appears that the electric currents associated with coronal non-potentiality have a characteristic timescale  $\tau_{obs} \sim 10\text{--}30$  h. Thus the flare-energy accumulation time  $\tau_a \sim \tau_{obs}$ .

TRACE observations of an emerging active region in the vicinity of an existing active region have been used by Longcope et al. (2005) in order to quantify magnetic reconnection between two active regions. Comparison of the observed EUV loops with the magnetic field lines computed in a topological model (for more detail see Sect. 5.3.3) revealed that the interconnecting EUV loops are consistent with those produced by reconnection at a separator overlying the volume between the active regions. The net energy released is consistent with the amount that could be stored magnetically during the 24 h delay between emergence and reconnection.

From what we have seen it is evident that

to release the accumulated energy in a time  $\tau_f \approx 10^2\text{--}10^3$  s corresponding to the solar flare duration, the total current layer resistance must be increased by 2 to 3 orders of magnitude.

Such an effect can be well the result of the appearance of plasma turbulence (Sect. 8.3). An alternative possibility is an appearance of one or many local current disruptions which have large enough resistance, *electric double layers* (see Chap. 16).

The possibility of formation of the double layers was, for some reason, treated earlier as being alternative or even more in conflict with the concept of reconnection. However, after the laboratory experiment by [Stenzel and Gekelman \(1984\)](#), it became clear that double layers may form inside the RCL. The hypothesis of the formation of electric double layers inside the separator-related RCL can prove useful, in principle, for the explanation of the extremely rapid energy release observed sometimes during solar flares. However, the concept of collisionless reconnection seems to be a more natural and more realistic alternative.

## 5.2 Solar Flares of the Syrovatskii Type

### 5.2.1 General Definitions

Much of the activity in the solar corona is related to the *emergence* of magnetic flux from the solar interior. Flux emergence episodes are continually injecting magnetic fields into the solar atmosphere over a wide range of length- and timescales, from small magnetic elements on a granular size all the way up to the emergence of large active regions.

Emerging active regions interact with preexisting magnetic systems by establishing magnetic links to them, well visible in image series taken, for example, by the *TRACE* satellite. They also cause the ejection of fast, high-temperature flows often seen, for example, with the soft X-ray telescope (SXT) on board the *Yohkoh* satellite.

Observed changes of connectivity and high-temperature jet emission clearly point to reconnection of magnetic field lines

as being effective whenever an upcoming and a preexisting magnetic flux system meet in the corona in spite of the low resistivity of the coronal plasma.

It is essential to understand how the magnetic field emerged from the solar interior interacts with the overlying coronal field. The simplest two-dimensional (2D) model suggested by [Syrovatskii \(1972\)](#) had provided a first glimpse at the physics of a solar flare as a result of emergence of a bipolar magnetic region from under the photosphere into a model corona containing a large-scale *quasi-uniform horizontal* magnetic field (Fig. 5.1a). A *horizontal* reconnecting current layer (RCL) was shown to be formed at the interface between the rising magnetic flux and the ambient coronal field which is antiparallel to the topmost field lines of the upcoming magnetic flux.

The magnetic field lines of the initial coronal field reconnect to those of the rising magnetic flux, so that the corona and the photosphere become magnetically connected.

This process is repeatedly observed in modern space missions like *SOHO*, *TRACE* and *Hinode*.

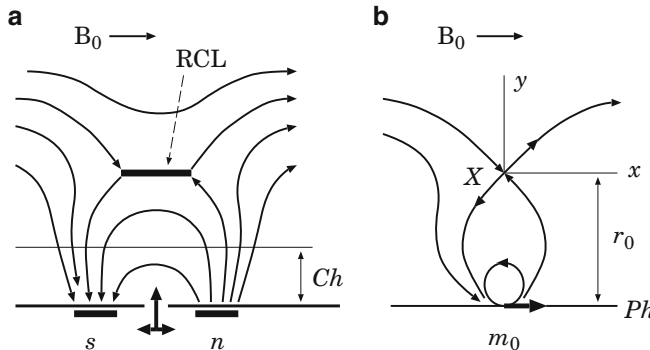


**Fig. 5.1** The Syrovatskii model of a solar flare. (a)  $n$  and  $s$  represent a bipolar source of a new emerging flux in the chromosphere  $Ch$ . The quasi-uniform field  $\mathbf{B}_0$  models locally a large-scale magnetic field in the corona.  $RCL$  is a reconnecting current layer between the interacting magnetic fluxes. (b) The external uniform magnetic field  $\mathbf{B}_0$  is parallel to the magnetic dipole moment  $m_0$

Syrovatskii (1972) considered the simplest model when a neutral line  $X$  is produced by a bipolar group with equivalent magnetic moment  $m_0$  in the photosphere  $Ph$  and superimposed uniform magnetic field  $\mathbf{B}_0$  in the corona (Fig. 5.1b). This field may be produced by neighboring sunspots or a preceding active region. Anyway, the field topology in this case is fully equivalent to the usually considered case of a neutral line  $X$  between two bipolar spot groups (Fig. 1.1). The neutral line  $X$  is a semicircle of radius  $r_0 = (m_0/B_0)^{1/3}$  with its ends on the photosphere  $Ph$ .

### 5.2.2 Accumulation of Flare Energy

Let  $\delta m(t) = m(t) - m_0 \ll m_0$  is a change of magnetic moment of the bipolar group in the flare model by Syrovatskii (1972). In a small vicinity, the neutral line  $X$  can be considered as a straight one directed along the  $z$ -axis of local coordinates. Thus we can express the electromagnetic field through the vector-potential

$$A(x, y, t) = \frac{h_0}{2} (x^2 - y^2 - \delta(t)), \quad (5.9)$$

where

$$h_0 = \frac{3B_0}{r_0} \quad \text{and} \quad \delta(t) = r_0^2 \frac{\delta m(t)}{3m_0}.$$

Recall that the expression (5.9) is valid in a region (see Sect. 2.1.5):

$$r \gg r_s = \left( \frac{4\pi n_0 k_B T_0}{h_0^2} \right)^{1/2}.$$

Here  $n_0$  and  $T_0$  are the number density and temperature of the plasma at the initial stage of the process,  $k_B$  is Boltzmann's constant.

It follows from formula (5.9) that in the vicinity of the neutral line there is a uniform electric field along this line:

$$E = E_z = -\frac{h_0}{2c} \frac{\partial \delta}{\partial t} = -\frac{h_0}{2c} \dot{\delta}. \quad (5.10)$$

This is the field which produces a drift motion of plasma outside the neutral line and a strong electric current near this line (see Sect. 1.1.3).

As was shown in Sect. 2.2, the half-width  $b$  of the current layer is of the order of the radius of the nonlinear region of cumulation, and is approximately given by the expression

$$b \approx \sqrt{\delta} \quad (5.11)$$

(see Figs. 2.2 and 2.3). In a region of this radius near the neutral line, the magnetic field is nearly uniform, with the strength

$$B \approx h_0 \sqrt{\delta}, \quad (5.12)$$

and its sign changes abruptly inside the current layer. Hence the surplus of magnetic energy over the energy of the initial potential field equals

$$\delta W_\delta = W_\delta(t) - W_\delta(0) \approx W_\delta(0) \approx \frac{\pi}{16} h_0^2 \delta^2 r_0, \quad (5.13)$$

which is the initial potential field energy in the non-linear region of radius  $\sqrt{\delta}$ .

Formula (5.13) answers the first two main questions of flare theory: where and in what form does the flare energy accumulate?

### 5.2.3 Stationary Heating of a Current Layer

Now let us consider the physical processes inside a current layer. If the plasma inflow velocity  $v_0$  is small compared to Alfvén velocity  $V_A$ , then the current layer can be considered quasi-stationary in the sense that

$$\frac{B_0^2}{8\pi} \approx \frac{h_0^2 \delta}{8\pi} = n_c k_B (T_e + T_i) \approx n_c k_B T_e, \quad (5.14)$$

where  $T_e$  and  $T_i$  are the electron and ion temperatures. Here we have taken  $T_e \gg T_i$  because the electron energy acquired from the electric field in the current layer is much greater than the proton energy (look, however, at some other possibilities in Fig. 8.5).

Denoting the half-thickness of the layer by  $a$  (see Fig. 2.3), we have for the current density and the current velocity the following formulae:

$$j_c = \frac{c}{4\pi} \frac{h_0 \sqrt{\delta}}{a} \quad \text{and} \quad v_c = \frac{c}{4\pi n_e e} \frac{h_0 \sqrt{\delta}}{a}. \quad (5.15)$$

In general, the half-thickness  $a$  is determined by finite conductivity  $\sigma$  of a plasma:

$$a = \frac{c^2}{4\pi\sigma} \frac{\sqrt{\delta}}{\dot{\delta}}. \quad (5.16)$$

Here we have used the expression  $v_0 \approx \dot{\delta}/2\sqrt{\delta}$  for the plasma inflow velocity (see Syrovatskii 1969). From Eqs. (5.10), (5.15), and (5.16), it follows that Ohm's law  $j = \sigma E$  is valid and that power delivered in a current layer of length  $\pi r_0$  is given by

$$P = \pi r_0 a \sqrt{\delta} \frac{j_c^2}{\sigma} = \pi r_0 \frac{h_0^2}{8\pi} \delta \dot{\delta}. \quad (5.17)$$

Thus final formula (5.17) does not contain the conductivity. This means simply that, in the current-layer formation process (called the cumulative effect; see Sects. 2.1.7 and 2.2) under consideration,

**|** the current-layer half-thickness  $a$  automatically takes the value which gives the needed rate of magnetic energy dissipation.

The latter is determined, as we see from (5.17), by the value of  $\delta \dot{\delta}$  and eventually by the rate of change of magnetic source configuration. Depending on the value of  $\delta \dot{\delta}$ , the dissipation rate may vary from very slow heating of plasma in some regions of the solar atmosphere to very powerful flares.

Let us assume that the current layer becomes so thin that its half-thickness equals the ion gyro-radius:

$$a = \frac{cp_i}{eB} \approx \frac{c(2m_i k_B T_i)^{1/2}}{eh_0 \sqrt{\delta}}, \quad (5.18)$$

where  $p_i$ ,  $m_i$  and  $T_i$  are the momentum, mass and temperature of ions. Since we assume that the temperature of electrons  $T_e \gg T_i$ , the current velocity (5.15) will be greater than the ion-acoustic wave velocity:

$$v_e \approx \left( \frac{2k_B T_e}{m_i} \frac{T_e}{T_i} \right)^{1/2} > \left( \frac{2k_B T_e}{m_i} \right)^{1/2}. \quad (5.19)$$

This is the condition of excitation of ion-acoustic turbulence (for more detail see Sect. 8.4.1), which reduces the conductivity to some finite value  $\sigma$ , even if initially it was formally infinite.

Development of plasma turbulence may serve as one of mechanisms, giving rise to the effective resistivity of a *reconnecting current layer* (RCL) and turbulent heating of the plasma to very high (super-hot) temperatures, corresponding to hard X-ray emission (see Sect. 8.3).

### 5.2.4 Particle Acceleration

Following Syrovatskii (1972), we have considered the ‘*gradual*’ phase of a solar flare with quasi-stationary current layer where a plasma turbulence appears and heats electrons to very high temperatures. However, at least in large flares, the existence of ‘*impulsive*’ phase with large amount of energy in accelerated particles remained unaccounted for. According to Syrovatskii this phase corresponds to the transition from the quasi-stationary reconnection considered above to a highly non-stationary picture due to the rupture of some part of the current layer and interruption of the local current.

As the result of such an interruption there appears a strong electric field of electrostatic Alfvén and Carlqvist (1967) or electromagnetic (Syrovatskii 1969, 1972) origin. In the case of current layer break-off,

the *impulsive* electric field has an electromagnetic origin and can greatly exceed the *quasi-stationary* field

described by formula (5.10). This strong electric field quickly accelerates charged particles.

We can estimate the maximum energy of accelerated particles in the following way. In 2D geometry under consideration a *generalized condition of freezing-in* is valid:

$$\frac{d}{dt} \left( p_z + \frac{Ze}{c} A \right) = 0, \quad (5.20)$$

where  $\mathbf{p}$  is the particle momentum,  $Ze$  is its charge, and  $d/dt = \partial/\partial t + \mathbf{v}\nabla$  is a full derivative on the particle trajectory. Condition (5.20) is a consequence of *Hamilton equations* (see Landau and Lifshitz, *Mechanics*, 1976, Chap. 7, Sect. 40) for the generalized particle momentum  $\mathbf{P} = \mathbf{p} + (Ze/c)\mathbf{A}$  with the vector potential  $\mathbf{A}$  constant in the  $z$ -direction.

When reconnection takes place at some point of the current layer, the vector-potential changes by the value  $\delta A = A_0 - A$ . At this point the particle reaches a momentum

$$p \approx |p_z| = |p_{z,0} - \frac{Ze}{c} \delta A|. \quad (5.21)$$

Neglecting the initial momentum  $p_{z,0}$ , we obtain

$$p = \frac{Ze}{c} |\delta A|. \quad (5.21)$$

In the case of magnetic cumulation considered in Sects. 2.2 and 5.2.2, the maximum value  $\delta A \approx h_0 r_0^2 \delta$ . Hence the maximum *rigidity* (see Part I, Sect. 5.1.3)

$$\mathcal{R} = \frac{pc}{Ze} \approx h_0 r_0^2 \delta \quad (5.22)$$

is the same for all kinds of charged particles. Therefore

the spectra of the accelerated particles of different kinds must be the same in the scale of rigidity.

It is clear, of course, that only a small number of particles can reach such a maximum rigidity.

### 5.2.5 3D Models of the Syrovatskii Type

Following Syrovatskii, we estimated the magnetic energy which can be accumulated by the RCL before a solar flare as well as the characteristic time and other basic parameters of the 2D reconnection process in the flare. However, even in the simplest configuration, the accumulation and release of magnetic energy are highly time dependent, have an intrinsically complex three-dimensional geometry, and contain a wide range of length- and timescales. Hence numerical simulations are necessary to provide better insight.

The three-dimensional (3D) time-dependent resistive MHD equations have been integrated numerically by [Archontis et al. \(2005\)](#) in order to model the process of reconnection between an emerging bipolar region and a preexisting horizontal uniform field in the corona. In the initial stages of contact of the two systems, the magnetic configuration across a forming current layer is similar to the classical X-point type, with mutually antiparallel field lines on both sides of the current layer being joined and ejected sideways.

The RCL is formed with the shape of a narrow arch distributed all around a rising ‘dome’ of the massive emergence from the photosphere of magnetic flux and plasma. The numerical experiment shows the structure and evolution of the RCL. It changes from a structure resembling the simple *tangential* discontinuity to another structure resembling the simple *rotational* discontinuity.

Most of the original subphotospheric flux becomes connected to the coronal field lines.

The ejection of plasma from the RCL gives rise to high-speed and high-temperature *jets*. The acceleration mechanism for those jets is akin to that found in the Syrovatskii 2D model, but the geometry of the jets bears a clear 3D imprint, having a curved-layer appearance with a sharp interface to the overlying coronal field system. Temperatures and velocities of the jets in the numerical experiment are commensurate with those observed by the *Yohkoh* SXT.

## 5.3 Different Types of Solar Flares

### 5.3.1 The Sakao-Type Flares

Sakao et al. (1998) studied the spatial evolution of 14 impulsive flares that clearly show the simple double-source structure (Fig. 5.2) at the peak of the M2 band (33–53 keV) emission in the hard X-ray (HXR) images obtained by the Hard X-ray Telescope (HXT) onboard *Yohkoh*. The distance  $l$  between the sources has been analyzed as a function of time. As a result, two subclasses of flares – *more impulsive* (MI) and *less impulsive* (LI) – have been discovered. We assume that in both subclasses, the three-dimensional reconnection process occurs in the corona at the separator with a *longitudinal* magnetic field.

The difference between the LI and MI flares presumably appears because in the LI flares the reconnection process accompanies an increase of the longitudinal field at the separator (Somov et al. 1998). In contrast, in the MI flares the reconnection proceeds with a decrease of the longitudinal field. Hence the reconnection rate is higher in the MI flares.

To illustrate that the observed variations of the footpoint separation depend on the longitudinal field  $\mathbf{B}_{\parallel}$ , this field is shown near the separator  $X$  in Fig. 5.3. The arrows  $v_0$  and  $v_1$  indicate the reconnection velocity pattern (the inflows and outflows) during the impulsive phase of a flare. Two reconnecting field lines  $f_1$

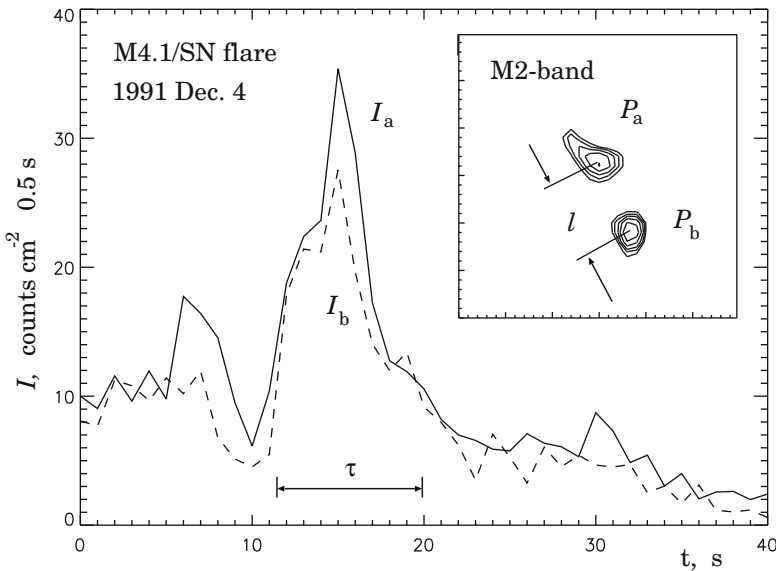


**Fig. 5.2** Typical HXR structure of a selected impulsive flare is shown in the right top corner:  $P_a$  and  $P_b$  are the footpoint sources,  $l$  is a distance between them.  $I_a$  and  $I_b$  are the HXR flux from the footpoint sources as a function of time,  $\tau$  is a total duration of the impulsive phase

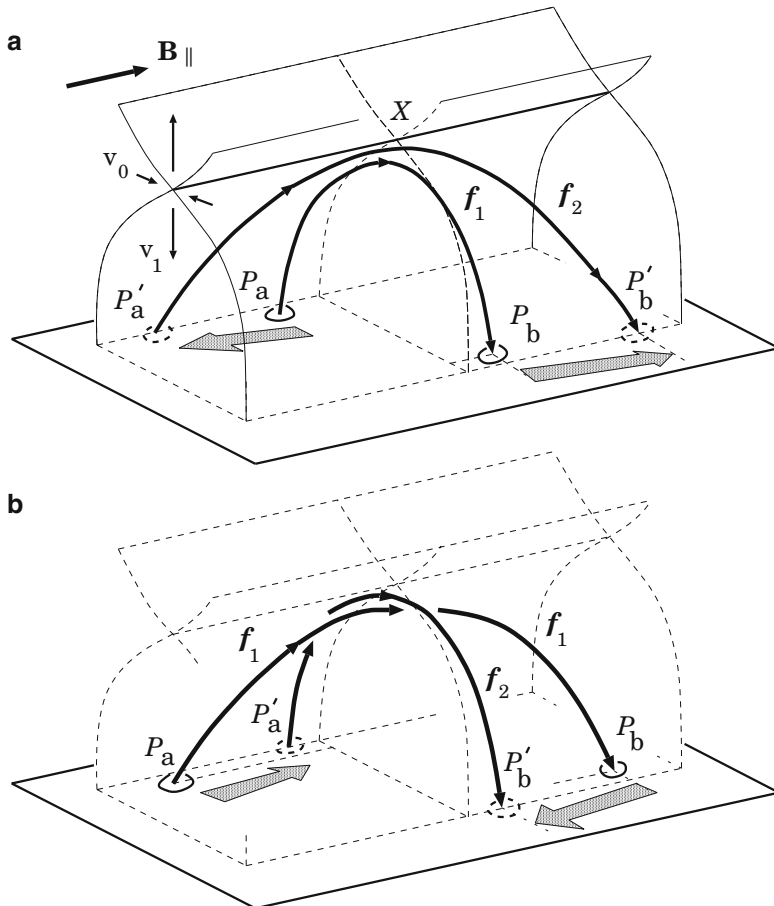


**Fig. 5.3** An apparent motion of the HXR footpoints during the fast reconnection: (a) the footpoint separation rapidly increases in the LI flares, (b) a decreasing footpoint separation in the MI flares

and  $f_2$  arrive at the separator  $X$  and pass through it, the second one after the first. They bring different values of the longitudinal field  $\mathbf{B}_{\parallel}$ . If the second field line  $f_2$  arrives with a stronger longitudinal field than the first one, i.e.  $B_{\parallel 2} > B_{\parallel 1}$ , then the length of the line  $f_2$  after reconnection is obviously larger than the length of the line  $f_1$  as shown in Fig. 5.3a.

Figure 5.3a also shows positions of the footpoints in the chromospheric plane for the same field lines. The footpoints  $P_a$  and  $P_b$ , being impulsively heated by accelerated particles, became bright in HXRs earlier than the footpoints  $P'_a$  and  $P'_b$ . Figure 5.3a demonstrates that,

| if the longitudinal field becomes stronger at the separator, then the footpoint separation will increase during the fast reconnection.

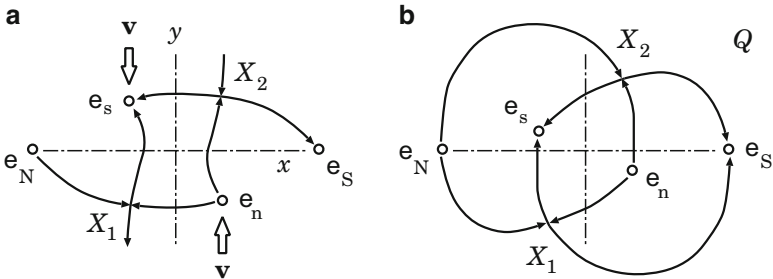


**Fig. 5.4** Two configurations of magnetic sources in the plane  $Q$ , the plane of topological portrait

If, on the contrary, the line  $f_2$  brings a weaker longitudinal field, i.e.  $B_{\parallel 2} < B_{\parallel 1}$ , then the distance between footpoints rapidly becomes shorter as shown in Fig. 5.3b.

The simplest topological model with one separator makes intelligible the observed decrease (increase) of the separation between the HXR sources in the MI (LI) flares (Somov and Merenкова 1999). Let us consider two configurations (a) and (b) in Fig. 5.4 for the four magnetic sources in the source plane  $Q$ . To a different extent they differ from the ideal configuration when all the four sources are placed along the symmetry axis  $x$ . The longitudinal magnetic field at the separator is equal to zero in the ideal symmetrical case.

In general, the pre-reconnection state differs from the ideal configuration, of course. So the longitudinal field already exists at the separator. This field always presents under condition of actual 3D reconnection in the solar atmosphere, and it will increase (or decrease) depending on the direction of evolution of the magnetic field in an active region. For example, the configuration evolves from the *less-ideal* initial state (a) to a *more-ideal* one (b) as shown in Fig. 5.4. Under this direction of evolution, indicated by vector  $v$  in Fig. 5.4, the reconnection process decreases the longitudinal field at the separator.

Following Gorbachev and Somov (1988, 1990), let us suppose that a part of the flare energy is initially released in some compact region  $\mathcal{E}$  near the apex of the separator. Then the energy fluxes will quickly propagate *along* the magnetic-field lines connecting the energy source with the photosphere. Projections of the energy source  $\mathcal{E}$  on the photospheric plane  $Ph$  along the field lines are shown as the two ‘flare ribbons’  $FR$  in Fig. 5.5. Therefore we identify flare brightenings, in the hydrogen  $H\alpha$  line etc., with the ribbons located at the intersection of the separatrices with the chromosphere which is placed slightly above the photospheric plane.

As in the model of the 1B/M4 flare on 1980 November 5, shown in Fig. 4.11,

the *saddle* structure of the magnetic field near the separator splits the flux of heat and accelerated particles in such a way that it creates two long-narrow  $H\alpha$  ribbons in the chromosphere

(see  $FR$  in Fig. 5.5). Moreover the model predicts that a concentration of the field lines that bring energy into the flare ribbons in the chromosphere is higher at the

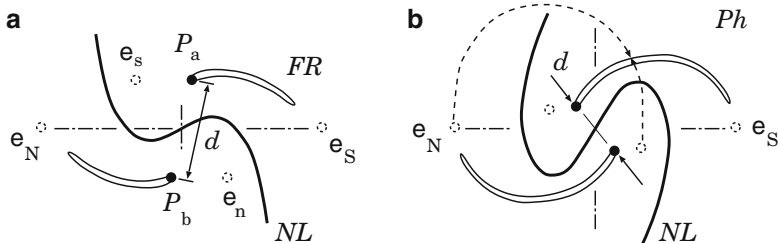


**Fig. 5.5** The long-narrow H $\alpha$  ribbons  $FR$  and H $\alpha$  kernels  $P_a$  and  $P_b$  projected in the photospheric plane  $Q$  both sides of the photospheric neutral line  $NL$

edges of the ribbons, i.e. at relatively compact regions shown by dark points  $P_a$  and  $P_b$ . Here the H $\alpha$  brightenings must be especially bright. This prediction of the model is consistent with observations of H $\alpha$  kernels in some flares.

Figure 5.5 shows that the footpoint separation, which is the distance  $d$  between the points  $P_a$  and  $P_b$ , decreases if the magnetic configuration evolves from the state (a) to state (b), i.e. when the longitudinal magnetic field decreases during the reconnection process at the separator. So the reconnection rate is higher in the MI flares of the Sakao type. In contrast, in the LI flares the magnetic configuration evolves from (b) to (a). This means that the reconnection proceeds with an increase of the longitudinal field, more slowly, and with an increase of the footpoint separation. Therefore we assume that

| if the evolution of the sunspot configuration in an active region goes to a *more ideal* state with a smaller displacement from the symmetry axis, then the *more impulsive* (MI) flares should occur.

This statement must, however, be examined by future observations and their analysis.

### 5.3.2 New Topological Models

When the photospheric magnetic field of active regions was extrapolated into the corona, it was found in many cases (e.g., Aulanier et al. 2000; Bentley et al. 2000) that the large-scale magnetic field of active regions was close to being *potential* indeed. The basic ingredients for reconnection to occur were present. Moreover

| the observed evolution of photospheric field is expected to drive magnetic reconnection and to produce flares

in such active regions.

After Gorbachev and Somov (1988, 1989, 1990), similar investigations have sought observational evidence for reconnection in many solar flares (Mandrini et al. 1991, 1993; Mandrini and Machado 1993; Démoulin et al. 1993; Bagalá et al.

1995; Longcope 1996; Antiochos 1998; Longcope and Silva 1998). The results of these investigations were summarized as follows. Flare brightenings are located at the intersection of the separatrices with the chromosphere and are magnetically connected to one another as well as to a common region close to the separator (cf. Fig. 4.11). In particular, Longcope (1996) and Longcope and Silva (1998) demonstrated clearly how

motions of the photospheric sources (magnetic charges) lead to the build-up of ‘ribbon-like’ current layers parallel to the separator

or two separators (Sect. 4.3.1), as it was, for example, in the case of the solar flare on 1992 January 7.

The magnitude of the current  $J$  at the separator (see formula (5.2)) is related through the self-inductance  $L$  to the magnetic flux change which would have occurred in a potential field in the corona (Syrovatskii 1966a, 1981). By calculating approximate self-inductances of the separator, the topological model, called now the *minimum current corona*, provides an estimate of the current and the associated free energy from a given displacement of the magnetic sources.

The model developed by Longcope and Silva (1998) applies a topological approach to the magnetic field configuration for 7 January 1992. A new bipole ( $\sim 10^{21}$  Mx) emerges amidst a pre-existing active region flux. This emergence gives rise to two current layers along the separators separating the distinct, new and old, magnetic flux systems. Sudden reconnection across the separators transfers  $\sim 10^{20}$  Mx of flux from the bipole into the surrounding flux. The locations of current layers in the model correspond with observed soft X-ray loops. In addition the footpoints and apexes of the current layers correspond with observed sources of microwave and hard X-ray emission. The magnitude of the magnetic energy stored by the current layers compares favorably to the inferred energy content of accelerated electrons.

The occurrence of flares in a quadrupolar magnetic configuration is a well studied topic. Ranns et al. (2000) present multi-wavelength observations of two homologous flares observed by *SOHO* and *Yohkoh*. The preflare conditions are reformed after the first flare by emerging flux. With the continual advancements in image resolution, at all wavelengths, we will learn progressively more about the reconnection process in flares.

### 5.3.3 Reconnection Between Active Regions

An active region is generally assumed to be produced by the buoyant emergence of one or more magnetic flux tubes from below the photosphere. Under this assumption, any coronal field interconnecting two distinct regions must have been produced through magnetic reconnection after emergence. Thus the coronal loops connecting between two active regions offer some of the most compelling evidence of large-scale reconnection in the solar corona (Sheeley et al. 1975; Pevtsov 2000).

The *TRACE* observations in the 171 Å passband show numerous loops interconnecting two active regions and thereby provide a good opportunity to quantify magnetic reconnection. [Longcope et al. \(2005\)](#) have analyzed data from the period 2001 August 10–11, during which active region 9574 emerged in the vicinity of existing active region 9570. They have identified each extreme-ultraviolet (EUV) loop connecting the emerging polarity to a nearby existing active region over the 41 h period beginning at emergence onset.

The topology of the coronal field was modeled as a *potential* field anchored in 36 point sources (i.e., the topological model similar to that one introduced in Sect. 4.2 but with *many* magnetic charges located in the photospheric plane) representing each of the magnetic field concentrations. Geometrical resemblance of the identified EUV loops to post-reconnection (see Fig. 4.1c) field lines from the topological model of the active region pair implicates separator reconnection in their production. More exactly,

comparison of the observed EUV loops with computed field lines reveals that the interconnecting loops are consistent with those produced by reconnection at a separator

overlying the volume between the active regions ([Longcope et al. 2005](#)).

The computed field included a domain of magnetic flux interconnecting one specific charge from the emerging region to another charge of opposite polarity in the pre-existing region. The magnetic flux in this domain increases steadily, in contrast to the EUV loop observations showing that during the first 24 h of emergence, reconnection between the active regions proceeded slowly.

The lack of reconnection caused magnetic stress to accumulate as current layer along the separator (see Fig. 19 in [Longcope et al. 2005](#)). When the accumulated current had reached  $J \approx 1.2 \times 10^{11}$  A, a brief reconnection process was triggered, leading to the transfer of  $\approx 10^{21}$  Mx across the separator current layer. The stressed field had accumulated at least  $\approx 1.4 \times 10^{31}$  ergs, which was then released by the reconnection. Longcope et al. believe that only a small fraction of this energy was dissipated directly at the separator. Presumably the released energy was converted instead into small-scale fluctuations such as a turbulence of Alfvén waves etc.

The reconnection rate was relatively small for the first  $\sim 24$  h of emergence and then rapidly increased to a peak as high as  $10^{17}$  Mx s $^{-1}$  ( $10^9$  V). Thus the most intense period of reconnection occurred after a 1 day delay. The net energy released, and ultimately dissipated, is consistent with the amount that could be stored magnetically during this delay between emergence and reconnection. This seems to be well consistent with the Syrovatskii scenario of *slow* and *fast* reconnection in the solar corona (Sect. 5.1.3).

# Chapter 6

## The Bastille Day Flare and Similar Solar Flares

**Abstract** The famous ‘Bastille day 2000’ flare is still one of the best examples of a solar flare which was well observed by several space- and ground-based observatories and studied in detail extensively by many researchers. The modern observations of the Sun in multiple wavelengths demonstrate, in fact, that the Bastille day flare has the same behavior as many large solar flares. In this chapter, the flare is considered from observational and topological points of view in terms of three-dimensional magnetic reconnection.

### 6.1 Observational Properties of the Bastille Day Flare

#### 6.1.1 General Characteristics of the Flare

On 14 July 2000 near 10:10 UT, a large solar flare with the X-ray importance of X5.7 launched near disk center in the active region NOAA 9077. The event comprised a 3B optical flare as revealed by bright emission throughout the electromagnetic spectrum, the eruption of a giant twisted filament, an extended Earth-directed *coronal mass ejection* (CME), and a large enhancement of accelerated particle flux in interplanetary space. This well-observed flare was called the ‘Bastille day 2000’ flare.

The *Yohkoh* satellite [Ogawara et al. 1991](#); [Acton et al. 1992](#) observed an early phase ( $\sim$ 10:11–10:13 UT) and some of the impulsive phase (from  $\sim$ 10:19 UT) of this famous flare classified as a *long duration event* (LDE). The Soft X-ray Telescope (SXT; [Tsuneta et al. 1991](#)) observed a large arcade in the corona. The width and length of the arcade were  $\sim$ 30,000 km and  $\sim$ 120,000 km, respectively. The Hard X-ray Telescope (HXT; [Kosugi et al. 1991](#)) clearly showed a two-ribbon structure in the energy ranges 33–53 and 53–93 keV. This structure corresponds to a series of footpoints of the SXR arcade (Fig. 6.1).

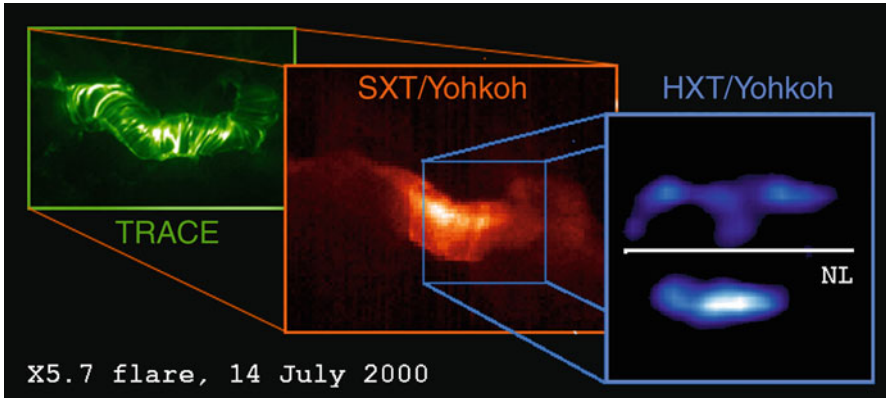


**Fig. 6.1** *Yohkoh* and *TRACE* observations of the Bastille day flare. The right panel shows HXR (53–93 keV) sources aligned along the flare ribbons, which lie at the feet of the arcade loops in the center of the left panels

Solar flares often exhibit a *two-ribbon structure* in the chromosphere, observed for example in H $\alpha$  (Svestka 1976; Zirin 1988; Strong et al. 1999), and this pattern becomes especially pronounced for LDEs of the type often associated with CMEs. The *Skylab* observations in soft X-rays (SXRs) at first established two morphologically distinct classes of flares: confined and eruptive (Pallavicini et al. 1977). The first-type flares were initially believed to be modeled as a simple single-magnetic-loop flare. However the eruptive flare were at once observed as the LDEs accompanied by CMEs and associated with complex coronal arcades of SXR loops and the chromospheric two-ribbon structures.

In the Bastille day flare, the two ribbons were well seen in H $\alpha$  and H $\beta$  (Yan et al. 2001; Liu and Zhang 2001). Fletcher and Hudson (2001) describe the morphology of the EUV ribbons of this flare, as seen in *SOHO*, *TRACE*, and *Yohkoh* data. The two-ribbon structure, however, had never before the Bastille day flare been observed so clearly in HXR as presented in Masuda et al. (2001).

Masuda et al. analyzed the motions of bright HXR kernels (compact intense sources) in the two ribbons of the Bastille day flare during the first and second bursts (S1 and S2) of emission in the HXT bands M1, M2, and H; they cover the energy range of 23–33, 33–53, and 53–93 keV, respectively. Even without an overlay of the HXR images of the flare on the photospheric magnetograms, Masuda et al. speculated that “these bright kernels are footpoints of newly reconnected loops” and that “lower loops, reconnecting early, are highly sheared; the higher loops, reconnecting later, are less sheared”.

This key supposition well supports the idea of three-dimensional reconnection in the corona at a separator with a longitudinal magnetic field. Being introduced to explain the so-called Sakao-type impulsive flares (Sakao et al. 1998), which have double footpoint sources observed in HXRs (see Fig. 5.2), the idea consists in the following. It is easy to imagine that two reconnecting field lines  $f_1$  and  $f_2$  pass

through the separator, the second after the first; see Fig. 5.3. If the first line  $f_1$  has the stronger longitudinal field than the second one, then the length of the line  $f_2$  in the corona after reconnection becomes shorter than the length of the line  $f_1$ . Therefore the distance between bright HXR footpoints in the chromosphere also becomes shorter as shown in Fig. 5.2b.

In general, such a scenario (Sect. 5.2) is consistent with the observed motions of the HXR kernels in the Bastille day flare. However, to make a better judgement about it we need to investigate possible relationships between the HXR kernels (their appearance positions and further dynamics) and the photospheric magnetic field (its structure and evolution).

With the aim of finding such relations, let us adopt the following procedure. First, we overlay the HXR images of the flare on the full-disk magnetograms by the Michelson Doppler Imager (MDI; Scherrer et al. 1995) on board the Solar and Heliospheric Observatory (*SOHO*; Domingo et al. 1995). Second, we overlay the obtained results of the first step on the vector magnetograms of high quality (Liu and Zhang 2001; Zhang et al. 2001) obtained with the Solar Magnetic Field Telescope (SMFT) at Huairou Solar Observing Station (HSOS).

The coalignment of the HXT images with the MDI and SMFT data allows us (Somov et al. 2002a): (a) to identify the most important MDI sunspots with the SMFT spots, whose properties, morphology and evolution have been carefully studied; and (b) to examine the relationships between the HXR kernel behavior during the impulsive phase of the Bastille day flare and the large-scale displacements of the most important sunspots during the two days before the flare, based on precise measurements of the proper motions (Liu and Zhang 2001). The most important findings will be described below; their interpretation will be given in Chap. 7.

### 6.1.2 Overlay HXR Images on Magnetograms

If we wish to study the relationship between the HXR kernels and the underlying magnetic field, we must accurately coalign the *Yohkoh* data (mentioned in the previous section) with simultaneous magnetic field data, for example, the magnetograms from the MDI instrument on the *SOHO*. In principle, such coalignment is possible using the pointing information of the two instruments. In practice, however, there are always quantified and unquantified errors in the pointing of different satellites and even different instruments on the same satellite.

Concerning the Bastille day flare, as observed by *SOHO* and *TRACE*, Fletcher and Hudson (2001) have determined the coalignment of data from the two instruments via cross-correlation of an image made in the white-light channel of *TRACE* and the MDI continuum image of the active region NOAA 9077. This has allowed the authors to locate the EUV ribbon positions on the photospheric magnetic field. Then the HXT and MDI images have been coaligned. When this has been done, the strongest HXR M2 sources occur at the same locations as the strongest EUV sources. This result is reasonable from the physical point of view (see Chap. 2 in Somov 1992).

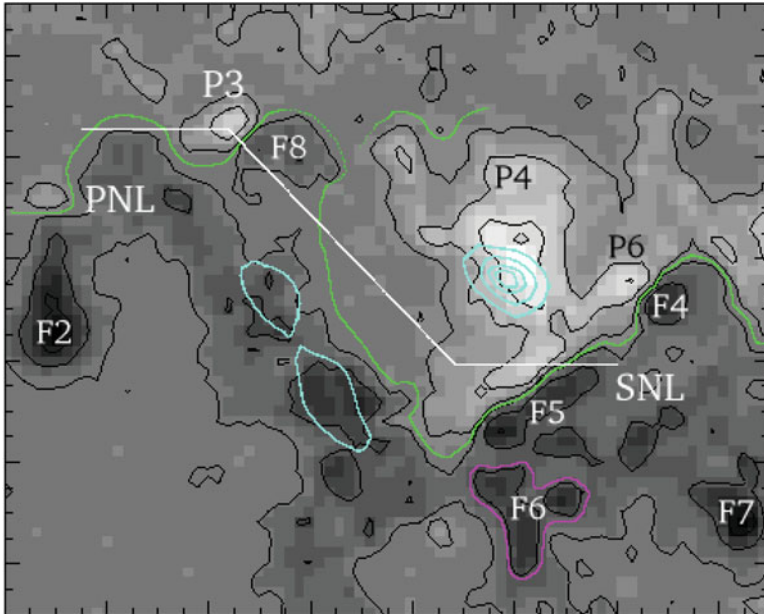


**Fig. 6.2** The HXR source contours (blue curves) at the HXR maximum of the Bastille day flare overlaid on the MDI magnetogram. The green curve PNL represents the photospheric neutral line. SNL is the simplified neutral line

Figure 6.2 shows the HXR source image synthesized during the peak of the flare at 10:27:00–10:27:20 UT; the blue contours are at 25%, 50%, 75% and 90% of the maximum HXR intensity. The sources are superimposed by Fletcher and Hudson (2001) on the MDI magnetic field. The magnetogram is taken at 11:12 UT. White indicates positive line-of-sight field, and black negative; the contours are at  $\pm 100$ , 500 and 1,000 G. The broken straight line SNL indicates the so-called “*simplified neutral line*” of the photospheric magnetic field, as introduced by Masuda et al. (2001). This effective line does not coincide with an actual photospheric neutral line PNL (or the polarity inversion line) but it is used to describe dynamic behavior of the HXR sources during the flare. The physical meaning of the SNL will be given in Sect. 7.1 where we discuss a model of the flare in terms of electric currents related to magnetic reconnection.

We have added to this overlay the notations of some sunspots in the field according to Liu and Zhang (2001). They describe the spots on the photospheric magnetograms obtained with the SMFT by the polarities with “P” and “F” representing the preceding (positive) and following (negative) magnetic polarities respectively. There is a good spatial correspondence between the spots as seen in the MDI magnetogram and the spots in the ground-based magnetogram obtained with the SMFT on July 14 at 08:43:19 UT. This allows us to identify the MDI spots with corresponding spots in the SMFT magnetograms. In this way, we use

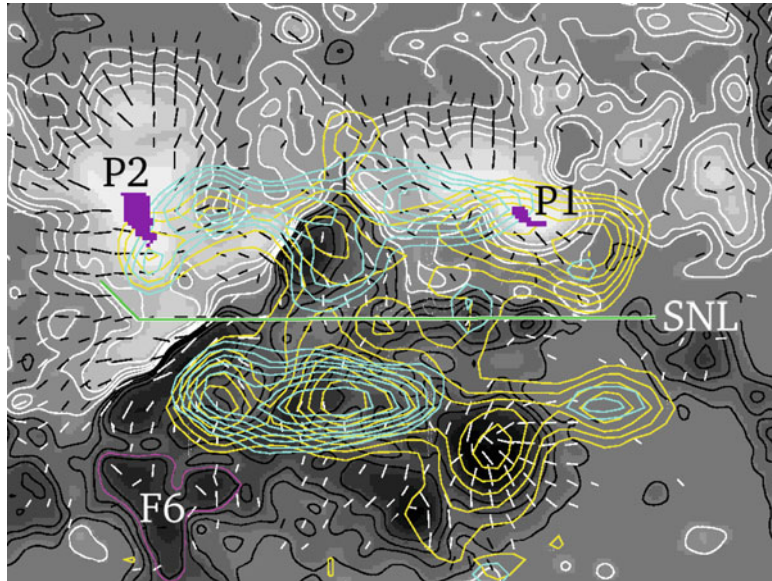


**Fig. 6.3** The HXR source positions in the beginning of the first HXR spike S1 (yellow contours) and near its end (blue contours)

the sunspot notations taken from Fig. 8 in Liu and Zhang (2001) and from Fig. 3 in Liu and Zhang (2002). For example, the “triangular” negative spot F6 in the MDI magnetogram at 11:12 UT in Fig. 6.2 is the same spot F6 in the SMFT magnetogram at 08:43:19 UT shown in Fig. 6.3.

The underlying magnetic field in Fig. 6.3 is the SMFT vector magnetogram at 08:43:19 UT on July 14, taken from Fig. 8d in Liu and Zhang (2001). The contour levels of the line-of-sight field are 160, 424, 677 and 1,071 G. White contours represent positive polarity and black represent negative. The bars are transverse components with their length proportional to intensity. P1 and P2 are the most important positive sunspots.

To overlay the HXT data on the SMFT magnetogram we have used the pointing information for the same satellite and the same instrument, HXT. This procedure gave us the relative position of the HXR images taken in the same energy band during the different HXR spikes: S2 and S1, that is with a small difference in time. Since we already have the coalignment of the HXT data during the spike S2 at 10:27 UT and the magnetogram shown in Fig. 6.2, we simply find the HXR source positions during the spike S1 at 10:19–10:24 UT according to Masuda et al. (2001) on the SMFT magnetogram.

The two overlays in Fig. 6.3 are the HXT H-band images during the first HXR spike S1 in its rising and decay phases. The contour levels are 70.7%, 50.0%, 35.4%, 25.0%, 17.7%, 12.5% and 8.8% of the peak intensity for each of two images.

The first one, shown by yellow contours, is reconstructed in the beginning of the spike S1 at 10:19:37–10:20:27 UT. The second, shown by blue contours, is synthesized just after a peak (at about 10:22 UT) of the spike, at 10:22:17–10:22:45 UT. In this way, Fig. 6.3 allows us to study the evolution of the HXR sources during the first spike. This will be done in the next section in relation with the magnetic field evolution before the flare on the basis of the SMFT data.

### 6.1.3 Questions of Interpretation

Several comments should be made here. First, as mentioned before, the two-ribbon structure is really well seen during the first spike. Two ribbons are most clearly observed in the rising phase and the decay phase of S1. Moreover the bright compact kernels in HXR are observed along the ribbons separated by the simplified magnetic neutral line SNL which is almost exactly aligned in the E-W direction in Figs. 6.3 and 6.1. The appearance of the HXR kernels is not a surprisingly unexpectable result. The chromospheric H $\alpha$ -ribbons typically demonstrate several bright patches, called kernels. However the intensity dynamical range of the *Yohkoh* HXT was not high enough to observe the HXR ribbons in many flares as a typical phenomenon.

Second, if the whole structure, the HXR ribbons and kernels together with the ridge of the huge arcade as it seen in Figs. 2 and 5 in Masuda et al. (2001), is illuminated by fast electrons, then they seem to be accelerated (or, at least, trapped) in a large-scale system of magnetic loops. If we accept the *standard* two-dimensional MHD model of the two-ribbon flares, which was well known as successful in interpretation of the *Yohkoh* SXT observations (Forbes and Acton 1996; Tsuneta 1996; Tsuneta et al. 1997), then this result seems to be consistent with the hypothesis of a *large-scale reconnection* process in the corona, involved in the flare energy release. Moreover, because of a large scale and large energetics of the system of interacting magnetic fluxes, the reconnected parts of magnetic fluxes should be also large. This is clear even if we do not know the exact links of the magnetic field lines before and after reconnection. Therefore the problem of identification and measurement of the reconnected fluxes becomes essential (Fletcher and Hudson 2001).

Third, the brightest HXR kernels do not coincide with the regions of highest line-of-sight field strength, with umbrae of sunspots. The question where the HXR kernels appear and disappear requires a special investigation. Since the HXR kernels are produced as a result of direct bombardment by powerful beams of fast electrons, nonthermal and presumably quasi-thermal, we expect the fast hydrodynamic and radiative response of the transition zone and chromosphere to an impulsive heating by these electrons and secondary XUV emission as discussed in Chap. 2 in Somov (1992).

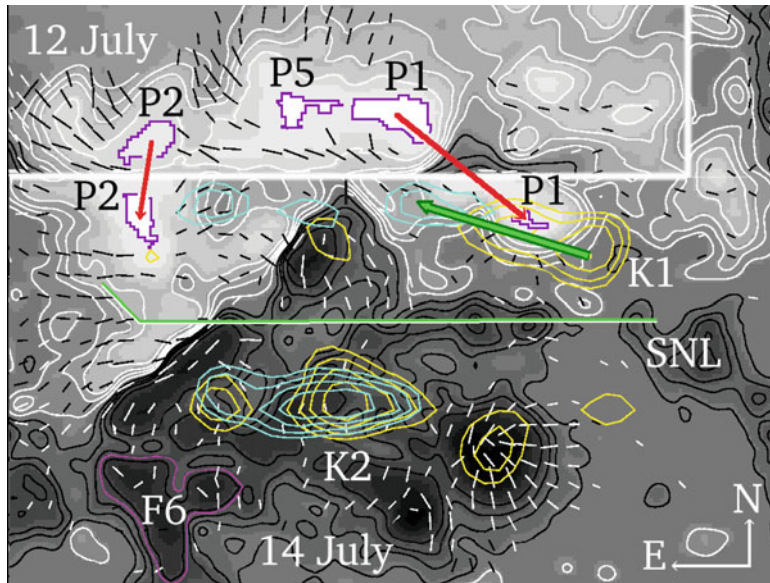


**Fig. 6.4** The position and motion of the strongest HXR sources  $K1$  and  $K2$  relative to the SMFT magnetogram on 14 July

### 6.1.4 Motion of the HXR Kernels

To see the strongest sources of HXR during the first spike S1, we show in Fig. 6.4 only the contours with levels 70.7%, 50.0%, 35.4% and 25.0% of the peak intensity. For this reason, the lower HXR background disappears. However, two HXR ribbons are still well distinguished as two chains of the HXR kernels on either side of the SNL. We shall consider the apparent displacements of the brightest sources.

The most intense kernel  $K2$  in the southern ribbon reappears to the east. However this displacement is much slower in comparison with that of the brightest kernel  $K1$  in the northern ribbon. The displacement of the kernel  $K1$  is shown by the large green arrow. The source  $K1$  moves to the north, that is outward from the simplified neutral line SNL, and to a larger extent it moves to the east, parallel to the SNL. An exact description of the motion of the centroid of the most intensive HXR source in the northern and southern ribbons is presented in Fig. 4 in [Masuda et al. \(2001\)](#). However, what is important for the following discussion is shown above in our Fig. 6.4.

We shall show that the observed displacement of the brightest HXR kernel  $K1$  during the first spike S1 can be related to the magnetic field evolution before the Bastille day flare. It was reasonable to assume that some relationships between the kernel motion and magnetic field structure and evolution do exist ([Somov et al. 1998](#)). However it has not been known how these relations manifest themselves in actual flares or at least in the models which are more realistic than the ideal ‘standard model’ of the two-ribbon flare (see discussion in [Fletcher and Hudson 2001](#)).

### 6.1.5 Magnetic Field Evolution

The active region (AR) NOAA 9077 had one of the most complex magnetic field structures; it was in a typical  $\beta\gamma\delta$  class ([Liu and Zhang 2001, 2002](#)). It produced nearly 130 flares, including 3 flares of the X-class, the largest of those being the X5.7 flare on July 14. The next one in terms of X-ray importance was the X1.9 flare on July 12. We assume that after this very large flare the AR had a minimum of magnetic energy and that 2 days were necessary for the AR to accumulate an energy sufficient for the Bastille day flare.

The motions of the sunspots cause the footpoints of magnetic fluxes to move and interact between themselves in the chromosphere and corona. In the absence of reconnection this process increases the non-potential part of the magnetic energy, the excess available for the next flare or flares. When the original (say on July 12) magnetic configuration is deformed, magnetic gradients and stresses (including the magnetic shear) become enhanced. Moreover, slowly *reconnecting current layers* (RCL) are created at the surfaces that divide different magnetic flux systems, and fast reconnection would be able to release the free magnetic energy as a flare (Sects. 4.1 and 5.1).

[Liu and Zhang \(2001, 2002\)](#) have described the morphology of AR 9077, the proper motions of many spots, and the evolution of the magnetic fields. They have found many interesting peculiarities of the sunspot motions, including a suggested trigger of the flare etc. However we shall restrict ourselves to large scales related to the HXR structure of the Bastille day flare. Let us compare two magnetograms from a time sequence of magnetograms presented in Fig. 8 in [Liu and Zhang \(2001\)](#). We overlay the magnetogram on July 12 in the top panel in Fig. 6.4 on the magnetogram on July 14 in the bottom panel in the same figure. We see that the largest positive spot P1 rapidly moves southwest as shown by the large red arrow. Other big umbrae seem more stable or, at least, do not move so quickly as P1. This is well seen from comparison with the displacement of the second positive spot P2 shown by the small red arrow.

Detail descriptions of the proper motions with precise measurements and results are given by [Liu and Zhang \(2001, 2002\)](#). For example, a small part P5 (shown in our Fig. 6.4) of the umbra P1 moved away from the east end of P1 on July 12, but P5 still followed P1 on July 13 and 14. P1 became smaller but tiny satellite spots formed around it. Figure 5 in [Liu and Zhang \(2001\)](#) shows a variety of spot proper motion velocities. The small spots P5, A1, B2 and B3 were short-lived relative to spot P1 but all of them moved in the same direction as one group.

So the southwest motion of the large spot P1 together with its group 1 is certainly one of the dominant motions in the AR. The other motions and changes of the magnetic field are presented in [Liu and Zhang \(2001\)](#) but they are presumably more important for the second spike S2 and many other manifestations of the Bastille day flare. In this chapter, we shall discuss only the first spike S1. More exactly, we shall consider its position and dynamics with relation to the spot P1 displacement shown above.

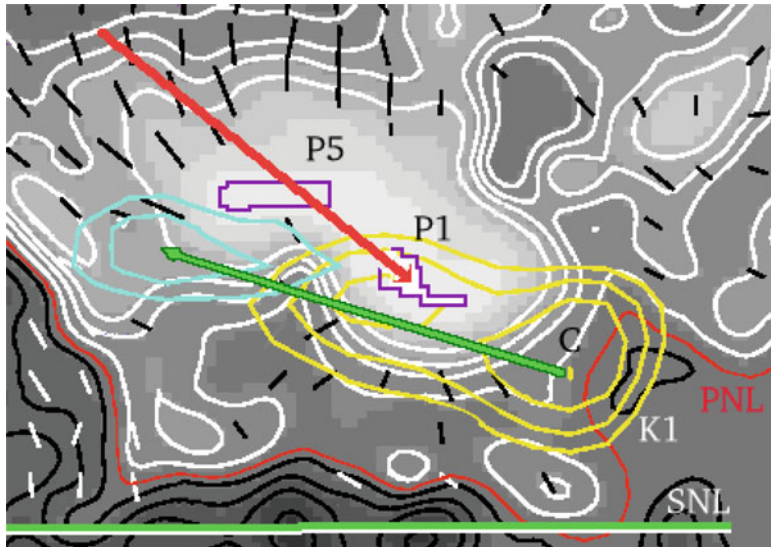


**Fig. 6.5** H-band images of the brightest kernel K1 in the rise and decay of the first HXR spike S1 overlaid on the SMFT magnetogram on July 14

### 6.1.6 The HXR Kernels and Field Evolution

The observed displacement of the brightest kernel K1 during the first spike S1 (as shown by the large green arrow in Fig. 6.4) is directed nearly anti-parallel to the displacement of the strongest positive spot P1 during the 2 days between two largest flares. An interpretation of this fact will be given in the next section. First, let us consider the fact in more detail, as shown in Fig. 6.5.

As in Fig. 6.4, the HXR kernel is shown with four contour levels: 70.7%, 50.0%, 35.4% and 25.0% of the peak intensity. In the rising phase of the spike, the kernel K1 appears in front of the moving spot P1, in its vicinity but not in the umbra. The brightest part of the kernel, indicated as the yellow ‘point’ C in the beginning of the green arrow, locates in a region of weak line-of-sight field: between the contour of the 160 G and the actual photospheric neutral line (the red curve PNL in Fig. 6.5). This is consistent with observations of several flares at H $\alpha$  by a fast CCD camera system installed at Big Bear Solar Observatory (BBSO). Wang and Qiu (2002) compared the initial brightening of flare kernels at H $\alpha$ -1.3 Å with photospheric magnetograms and found that initial brightenings avoided the regions of a strong line-of-sight magnetic field. The observed H $\alpha$  flare morphology and evolution suggest that emission near a magnetic neutral line may come from footpoints of flare loops of small height, where the first accelerated electrons precipitate.

Figure 6.5 also shows that, later on,

the centroid C of the most intense HXR source K1 moves ahead, mostly anti-parallel to the sunspot P1 displacement arrow,

but avoids the strongest field area. In the decay phase of the spike, the centroid arrives at the end of the green arrow in the vicinity of the spot P5 but still remains outside of the line-of-sight field level 1,071 G. One of the possible reasons of such behavior may be in the magnetic-mirror interpretation (Somov and Kosugi 1997). Further investigation is necessary to understand the actual conditions of propagation, trapping, and precipitation of accelerated electrons from the corona into the chromosphere.

However the main problem in the flare physics still remains the primary release of energy. This is the transformation of the excess magnetic energy into kinetic and thermal energy of particles. Such transformation can be done by the reconnection process which occurs at the separator (one or several) with a longitudinal magnetic field. On the basis of the simultaneous multi-wavelength observations, we are interested to understand how such a mechanism can work in the Bastille day flare.

## 6.2 Simplified Topological Model

### 6.2.1 Photospheric Field Model. Topological Portrait

Following Sect. 4.2.1, let us model the photospheric field by using several magnetic “charges”  $q_i$  located in a horizontal plane  $Q$  beneath the photosphere. For example, in order to study the large-scale structure and dynamics of the Bastille day flare, Somov et al. (2005c) replace the five most important regions, in which the magnetic field of a single polarity is concentrated in the *SOHO* MDI magnetogram (Fig. 6.6a), by two sources of northern polarity ( $n_1$  and  $n_2$ ) and three of southern polarity ( $s_1$ ,  $s_2$ , and  $s_3$ ) as shown in Fig. 6.6b. One characteristic feature of the observed and model magnetograms is the  $\omega$ -shaped structure of the photospheric neutral line  $NL$ , shown by the thick curve.

Figure 6.6b also shows contours of the vertical component  $B_z$  of the field in the photospheric plane  $Ph$ ,  $z = 0$ , calculated in the potential field approximation.  $B_z = 0$  at the calculated neutral line  $NL$ . The magnetic charges are located in the source plane  $Q$  at  $z = -0.1$ .

Figure 6.7 represents the same magnetic charges in the source plane  $Q$  and the structure of the magnetic field in this plane. The small arrows show the directions of the magnetic-field vectors in  $Q$ . The points  $X_1$ ,  $X_2$ ,  $X_3$ , and  $X_4$  are the zero-field points (or neutral points), where  $B = 0$ . They are important topological features of the field. The magnetic-field separatrix lines (separatrices), shown by solid curves, pass through these points and the magnetic charges. Thus the separatrices separate the magnetic fluxes connecting different magnetic charges. At the same time,

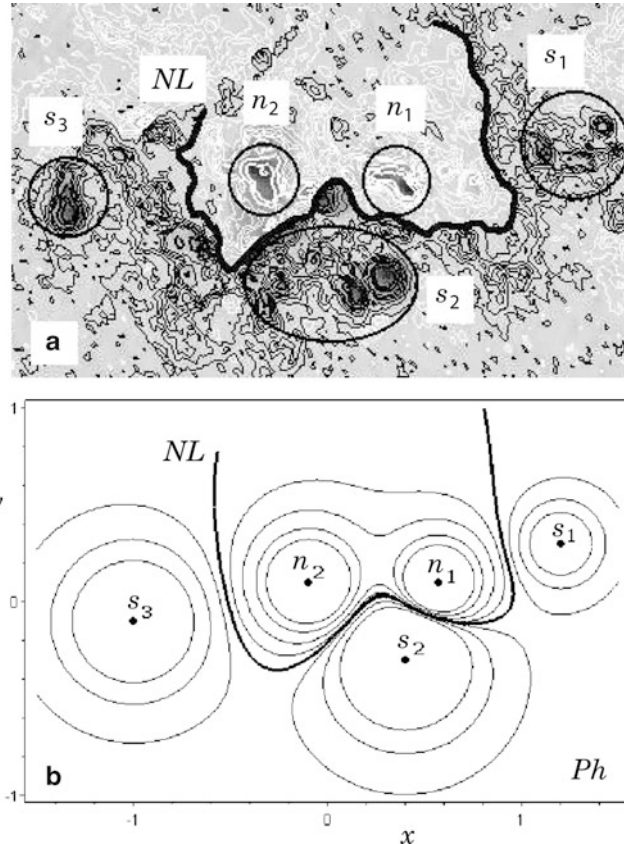


**Fig. 6.6** (a) The *SOHO* MDI magnetogram of the active region NOAA 9077 on July 14, 2000. The most important large-scale sources of the photospheric magnetic field are indicated as  $n_1$ ,  $n_2$ ,  $s_1$ ,  $s_2$ , and  $s_3$ .  $NL$  is the photospheric neutral line. (b) The model magnetogram of the same active region

they are the bases of the separatrix surfaces in the half-space above the plane  $Q$ . Therefore Fig. 6.7 contains all the information about the topology of the large-scale magnetic field of the active region. So we refer to this figure as the *topological portrait* of the active region.

### 6.2.2 Coronal Field Model: Separators

Figure 6.8 demonstrates the three-dimensional structure of magnetic field above the plane of topological portrait. The field lines are shown at different separatrix surfaces that have the forms of “domes” of various size, with their basis being located on separatrix lines in the plane  $Q$ .

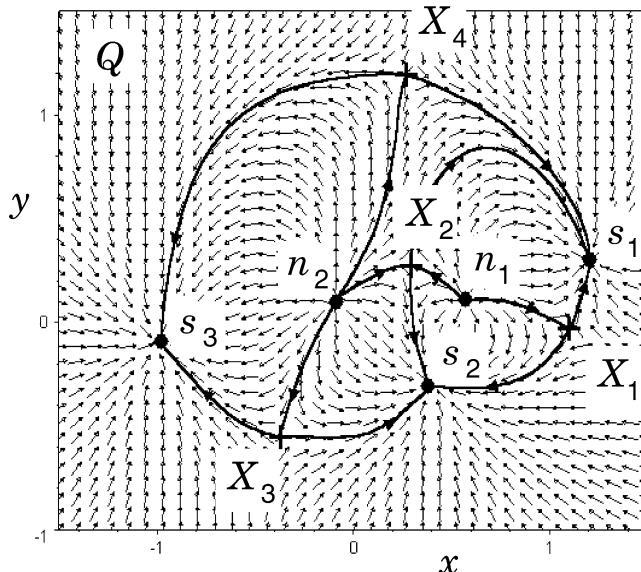


**Fig. 6.7** Topological portrait of the active region NOAA 9077 on July 14, 2000. The magnetic field directions are shown by small arrows in the source plane  $Q$  at the height  $z = -0.1$  beneath the photospheric plane  $Ph$ . The solid curves with arrows are the separatrices that separate the magnetic fluxes connecting different magnetic sources

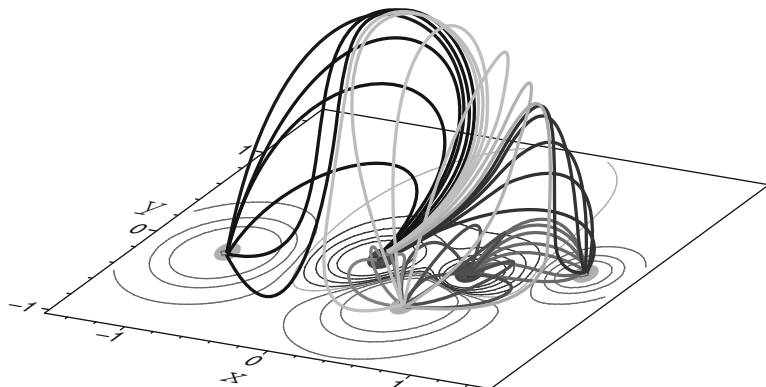
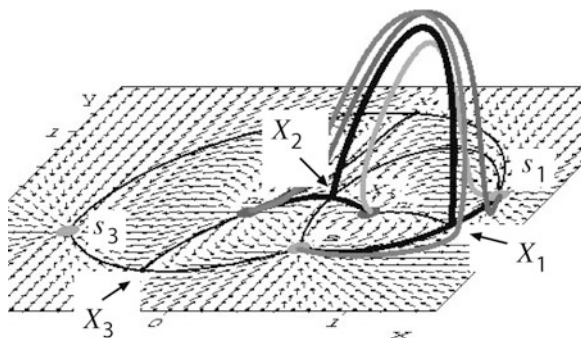


**Fig. 6.8** The magnetic-field lines forming the separatrix surfaces that are the domes bounding the magnetic fluxes of different pairs of sources

The separatrix surfaces intersect along the field lines connecting the neutral points. Each of these critical lines belongs simultaneously to four magnetic fluxes with different connectivity; thus it is called *separator*. During the flare, there is a redistribution of magnetic fluxes – magnetic reconnection at the separators.

**Fig. 6.9** The magnetic-field lines in the vicinity of the separator (the solid dark curve) connecting the neutral points  $X_1$  and  $X_2$



For example, one of the separators connects the points  $X_1$  and  $X_2$  (see Fig. 6.9). Here, at the separator ( $X_1X_2$ ), reconnection occurs during the first stage S1 in the impulsive phase of the Bastille-day flare.

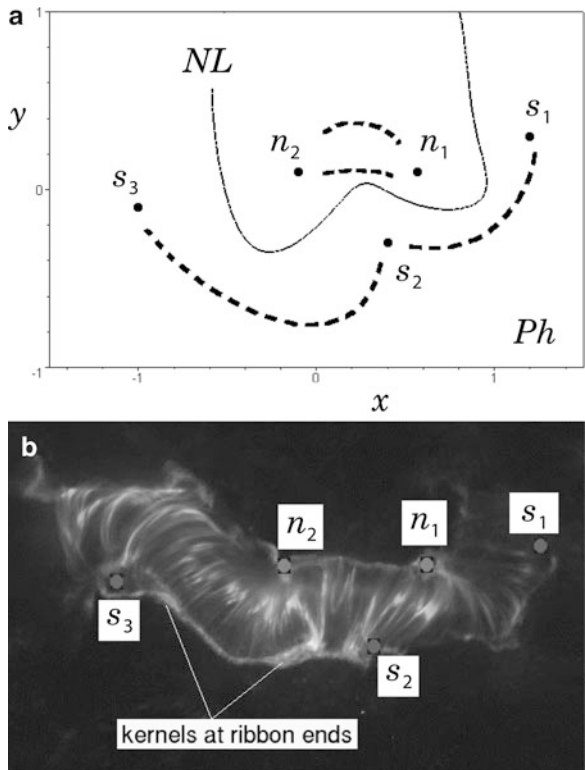
### 6.2.3 Chromospheric Ribbons and Kernels

Reconnection at the separators transforms the accumulated magnetic energy of coronal currents into the thermal and kinetic energy of plasma and accelerated particles. Propagating along the field lines and reaching the chromosphere, these energy fluxes give rise to a complex hydrodynamic and radiative response (see Part I, Sect. 8.3.2). Secondary processes in the chromospheric plasma result in the basic flare behavior observed in the optical, UV, EUV, soft and hard X-rays, and gamma-rays.

Following [Gorbachev and Somov \(1990\)](#), let us assume that the most powerful release of energy and particle acceleration take place near the tops of the two separators. We calculate the magnetic-field lines passing through such sources of energy until their intersection with the photospheric plane  $Ph$ . These field lines form narrow flare ribbons in the chromosphere.

It is natural that different parts of the complex active region NOAA 9077 were important during different stages of the Bastille-day flare in progress. In fact, the two pairs of field sources ( $n_1, n_2$ ) and ( $s_1, s_2$ ) played the domineering role during the first stage S1 of the impulsive phase of the flare as illustrated by Fig. 6.9, while the large-scale structure of the flare during the second stage S2 was mainly determined by the pairs ( $n_1, n_2$ ) and ( $s_2, s_3$ ). In other words, the region of the most powerful release of energy and acceleration of electrons was initially located in the western part of the active region without any significant influence of the spot  $s_3$ , then moves to the eastern part, closer to  $s_3$ . This is clearly visible in the hard and soft X-ray *Yohkoh* images and the *TRACE* EUV images ([Aschwanden and Alexander 2001](#); [Fletcher and Hudson 2001](#); [Masuda et al. 2001](#)).

**Fig. 6.10** (a) Calculated chromospheric ribbons are shown by the dashed curves. (b) TRACE image of the Bastille-day flare at 171 Å



During the second stage S2, the spot  $s_1$  has not its primary influence anymore. Instead, the sources ( $n_1, n_2$ ) and ( $s_2, s_3$ ) are efficiently involved in the flare in a way similar to that one shown in Fig. 6.9. Figure 6.10a, presents similar calculations for chromospheric ribbons during the stages S1 and S2. The calculated ribbons are shown by the dashed curves. The ribbon between sources  $s_1$  and  $s_2$  corresponds to the first stage, and the ribbon between sources  $s_2$  and  $s_3$  to the second. However two calculated ribbons are located between the field sources  $n_1$  and  $n_2$ . The lower ribbon corresponds to the stage S1, and the upper one to the second stage.

Figure 6.10b presents a TRACE image of the flare at 171 Å obtained during the second stage S2. The eastern part (the left site of the image) of the flare is somewhat brighter than the western part. A chromospheric ribbon is clearly visible between the field sources  $s_2$  and  $s_3$ . Bright kernels at the ends of the ribbon are also visible. The observed ribbons are arc-shaped and are in a reasonable agreement with the locations and shapes of the calculated ribbons. However the calculated ribbons are not reproducing some portions of the observed ribbons. This is especially clear when we consider the calculated ribbons in the northern polarity. Two small parallel ribbons between the sources  $n_1$  and  $n_2$  are given by the model while the TRACE observations show one very elongated ribbon.

This discrepancy presumably has the following origins. First, in order to illustrate the effect of a primary energy source at a separator, we have taken a small circle encompassing the separator near its top in a plane perpendicular to the separator. Such a simplistic approach seems to be good for relatively simple active regions with one dominating separator (see Sect. 4.3.1), which is not the case of the active region NOAA 9077. It is no easy task to investigate how the rate of magnetic reconnection (and the related dissipation rate) is distributed along the separators in the active region with a complex topology. Second, the topological model based on the potential field approximation completely neglects the nonpotential components of magnetic field in the active region. This approximation is not justified in places where strong electric currents flow (see Sect. 16.5.2). And finally, we use only five charges while the observed photospheric field is much more complex.

In principle, one could try to achieve a better agreement between the observed chromospheric ribbons and the calculated ones, for example, by introducing an additional magnetic charge  $n_3$  in the most eastern part of the active region (see the spot  $p_3$  in Figs. 1, 3 and 7 in Liu and Zhang 2001). This would allow to reproduce the eastern wing of the northern chromospheric ribbon between sources  $n_2$  and  $n_3$ . One could add more charges  $q_i$  or replace them with more precise distributions of the magnetic-field sources, thereby increasing the number of separators. However, in this way, the model becomes too complicated.

Moreover there is another principal restriction. The real magnetic field and real velocity field in the photosphere always contain at least two components: regular, large-scale and chaotic, small-scale. The topological model should take into account only the first component, with the aim of describing the global reconnection mechanism behind a large flare. The small number of the charges in the model under consideration, five, allows us to reproduce only the most important large-scale features of the *SOHO* MDI magnetogram and keeps the model being simple and clear.

Using the nonpotential, for example, force-free methods to extrapolate the surface field would also be likely to improve the agreement between the topological model and the observations. The most logical next approximation would be to take into account the current layers along the separators. The magnetic field containing the current layer is in force-free equilibrium. An expression can be found for the net current induced in the layer in response to displacement of the photospheric sources (Longcope and Cowley 1996; Longcope 1996).

#### **6.2.4 Reconnected Magnetic Flux**

As we made it above, the topology of the active region was defined by partitioning of the observed photospheric field into a set of discrete sources and determining which pairs were interlinked by magnetic field lines in the corona. The level of topological activity then can be quantified through the transfer of magnetic flux between domains of differing field line connectivity.

The magnetic fields in the active region NOAA 9077 were observed during several days before and after the Bastille-day flare ([Liu and Zhang 2001](#); [Zhang 2002](#)). There were many flares in this active region over this period. The largest one (X5.7) was on July 14 and the next largest in the magnitude (X1.9) was on July 12. It was suggested by [Somov et al. \(2002a\)](#) that the magnetic energy of the active region reached its minimum after this flare and that the energy necessary for the Bastille-day flare was accumulated over the following 2 days (July 12–14).

We have made the model of the photospheric and coronal magnetic fields in the active region NOAA 9077 on July 12 just in the same way as presented above for July 14. It appears that the topological portrait of the active region and the structure of its coronal field did not change significantly during 2 days. For example, in the western part of the active region on July 12, there was also the separator ( $X_1 X_2$ ) connecting in the corona the neutral points  $X_1$  and  $X_2$  in the plane  $Q$  of five magnetic sources. We have calculated the magnetic flux beneath this separator and above the source plane  $Q$ ,  $\Psi_{12}$  on July 12 and  $\Psi_{14}$  on July 14. The difference of these fluxes is  $\delta\Psi = \Psi_{14} - \Psi_{12} \sim 6 \times 10^{21}$  Mx.

What is the physical meaning of  $\delta\Psi$ ? – If there were a vacuum without plasma above the plane  $Q$ , then the flux  $\delta\Psi$  would reconnect at the separator ( $X_1 X_2$ ) over the 2 day evolution of the photospheric field sources, and the magnetic field would remain potential without any excess of magnetic energy. In the low-resistivity plasma, changes in the photospheric sources induce an electric current at the separator in the corona. This current in the coronal plasma forms a current layer which will prevent the reconnection of the flux  $\delta\Psi$  before a flare. Thus, the energy will be accumulated in the magnetic field of the current layer.

There are several important questions related to this scenario.

First, why reconnection cannot destroy the current layer during the long pre-flare state? – In principle, the current layer in this state can suffer many instabilities (see Sect. 5.1.2). Fortunately, many of them can be well stabilized or have a high threshold in many cases of interest. For example, the *tearing instability* is an integral part of magnetic reconnection. The theory of resistive MHD instabilities developed at first for the case of the *neutral* current layers predicts very low threshold ([Furth et al. 1963](#)). However laboratory and numerical experiments, as well as some astrophysical observations, show that the *reconnecting current layers* can be stable for a long time because the tearing mode is suppressed by a small transversal magnetic field, i.e. by a small component of magnetic field which is perpendicular to the current layer (see Sect. 13.4).

The second question is why reconnection is sufficiently slow to permit the current layer build-up during the slow evolution before flaring and fast enough during the flare? – In the pre-flare state, the current layer with the classical Coulomb conductivity has very low resistance  $R_0$ . For this reason, the characteristic time of the energy accumulation process at the separator in the corona,  $\tau_a = L/R_0$  (with the self-inductance  $L$  which is proportional to the separator length  $l_s$ ), can be long enough (say  $3 \times 10^4$  s) in order to accumulate the sufficiently large energy for a large flare (see discussion in Sect. 5.1.3).

It is assumed that, as a result of one of the instabilities mentioned above, the magnetic energy related to the current layer is rapidly released and a flare starts. It is clear that, in order to release the accumulated energy in a time  $\tau_f \sim 10^2\text{--}10^3$  s, the total resistance of the current layer must be increased by two or three orders of magnitude. Such an effect can be well the result of the appearance of *plasma turbulence* or local current disruptions that have large enough resistance, electric *double layers*.

Note that the highly-concentrated currents are necessary to generate plasma turbulence or double layers. This fact justifies the pre-flare storage of magnetic energy in current layers rather than distributed currents in the full volume. The smoothly-distributed currents can be easily generated in a plasma of low resistivity but they dissipate too slowly. On the contrary, the current density inside the pre-flare current layers usually grows with time and reaches one or another limit. For example, wave excitation begins and wave-particle interaction becomes efficient to produce high resistance, or the collisionless *dynamic dissipation* allows the fast process of *collisionless reconnection* (Sect. 8.3.1).

The energy released during the first stage S1 of the Bastille-day flare was estimated to be  $\varepsilon_f \sim (1 - 3) \times 10^{31}$  erg (e.g., Aschwanden and Alexander 2001). If this energy was accumulated as the magnetic energy of the current layer at the separator, then it corresponds to the total current  $J_f \sim (1 - 2) \times 10^{11}$  A along the separator in the corona (Somov et al. 2002a). This value does not contradict to the high level of nonpotentiality of the active region NOAA 9077, which was estimated from measurements of the three components of the photospheric magnetic field (see Fig. 5 in Deng et al. 2001). More exactly, the estimated total vertical current in the photosphere,  $J_z \sim (1 - 2) \times 10^{13}$  A, is significantly larger than the coronal current  $J_f$  at the separator. Note, however, that the nonpotential components of the field in this active region are presumably (see Sect. 16.5.2) related to the following currents: (a) the pre-flare slowly-reconnecting current layers which are highly-concentrated currents flowing along the separators, (b) the smoothly distributed currents which are responsible for magnetic tension generated by the photospheric shear flows, (c) the concentrated currents at the separatrices, also generated by the shear flows.

Anyway, the flare energy  $\varepsilon_f$  is much smaller than the energy of potential field, which Somov et al. (2005c) calculated by using the topological model:  $\varepsilon_{ar} \sim (3 - 6) \times 10^{33}$  erg on July 12 and  $\varepsilon_{ar} \sim (1 - 2) \times 10^{34}$  erg on July 14. Thus we see that

the potential field really dominates the global energetics of the active region and, therefore, determines the large-scale structure of its magnetic field in the corona.

However, in smaller scales, especially in the vicinity of the main neutral line of the photospheric magnetic field, the energy of nonpotential field has to be taken into account in modeling of the Bastille-day flare (Deng et al. 2001; Tian et al. 2002; Zhang 2002). A two-step reconnection scenario for the flare energy process was suggested by Wang and Shi (1993). The first step takes place in the photosphere and manifests as *flux cancellation* observed in the photospheric magnetograms. The second-step reconnection is explosive in nature and directly responsible for the coronal energy release in solar flares.

### 6.2.5 Electric Field

The most rapid reconnection of the magnetic flux  $\delta\Psi$  in the corona occurs during the impulsive phase of the Bastille-day flare. Taking the duration of the first impulsive stage of electron acceleration (during the burst S1 of the hard X-rays with energies exceeding 33 keV) to be  $\delta t \sim 3$  min (Masuda et al. 2001), we can estimate the electric field related to magnetic reconnection:

$$\mathbf{E} = -\frac{1}{c} \frac{\partial \mathbf{A}}{\partial t}. \quad (6.1)$$

Here  $\mathbf{A}$  is the vector potential, i.e.  $\mathbf{B} = \text{rot } \mathbf{A}$ ,  $c$  is the speed of light. The magnetic flux  $\Psi$  is written as a function of  $\mathbf{A}$  as follows:

$$\Psi = \oint_L \mathbf{A} \cdot d\mathbf{l}, \quad (6.2)$$

where  $L$  is the closed contour: the separator plus the line connecting its feet, the neutral points in the source plane  $Q$ .

First, Somov et al. (2005c) have calculated directly the magnetic flux beneath the separator and above the plane  $Q$ ,  $\Psi_{12}$  on July 12 and  $\Psi_{14}$  on July 14. The flux of magnetic field across a surface bounded by the contour  $L$  was just integrated.

Second, in order to be sure in the final results, we can make numerical integration over a “separator loop” as defined by Longcope (1996): (a) from one neutral point along the separator above the plane  $Q$  and parallel to the magnetic field  $\mathbf{B}$  at the separator to another neutral point and then (b) back from the second neutral point to the first one along the separator below the plane  $Q$  and anti-parallel to the magnetic field  $\mathbf{B}$ .

In this way, Somov et al. (2005c) have found the magnetic fluxes on July 12 and 14, and estimated the value of electric field  $E \sim 30$  V/cm. This value is presumably an upper limit but it does not contradict to the electric-field estimates obtained for impulsive flares using the theory of reconnecting *super-hot turbulent-current layer*, SHTCL (Sect. 8.3).

The reconnected magnetic flux can be also estimated in another way. Since the energy fluxes from the separator reconnection region result in the formation of chromospheric ribbons, these ribbons correspond to newly reconnected field lines. In a two-dimensional MHD model for a two-ribbon flare with a vertical current layer (the standard model, see Forbes and Acton 1996), the ascending region of reconnection gives rise to chromospheric ribbons moving in opposite directions from the photospheric neutral lines. In general,

a ribbon’s motion with respect to the photospheric neutral line can be used to estimate the reconnected magnetic flux.

In the Bastille-day flare, [Fletcher and Hudson \(2001\)](#) analyzed the motions of the northern and southern EUV ribbons observed by *TRACE* at the maximum of the HXR burst S2. They estimated the value of the reconnected flux as the total magnetic flux traversed by the ribbons in the north and the south in the eastern part of the active region. During the time interval from 10:26:15 UT to 10:28:58 UT, which is a part of the stage S2,  $\delta\Psi \approx -(14.5 \pm 0.5) \times 10^{20}$  Mx for the southern ribbon and  $\delta\Psi \approx (8.6 \pm 1.4) \times 10^{20}$  Mx for the northern ribbon with the inclusion of the mixed-polarity fields to the north from the photospheric neutral line. Therefore the magnetic flux reconnected during the stage S2 and estimated by Fletcher and Hudson at the level of the photosphere is of the same order of magnitude as the magnetic flux which [Somov et al. \(2005c\)](#) have found for the stage S1 and which is the flux reconnected at the separator ( $X_1 X_2$ ) in the corona.

[Li et al. \(2007\)](#) estimated the magnetic reconnection rate in the term of the reconnection electric field in a two-dimensional MHD approximation:

$$E = \frac{1}{c} V \times B. \quad (6.3)$$

Here  $V$  is the separation velocity of flare ribbons and  $B$  is the magnetic field that the ribbons sweep through. Since the flare occurred near the disk center,  $B$  can be approximately taken as the longitudinal component of the magnetic field obtained from the MDI on the *SOHO* at 09:36 UT before the flare. The mean electric field  $E_{av}$  induced by reconnection is obtained by averaging the electric field inferred in each of the two ribbons.

Comparing the electric field with the nonthermal hard X-rays, [Li et al. \(2007\)](#) found good temporal correlation between them. The first HXR burst S1 at 10:22 UT corresponds to the magnetic reconnection in the western part of the flare ribbons and the maximum  $E_{av} \sim 9.5$  V/cm and the second one S2 at 10:27 UT is due to reconnection in the eastern part with the maximum  $E_{av} \sim 13$  V/cm. Two  $\gamma$ -ray emission peaks were also reported at 10:22 UT and 10:27 UT ([Share et al. 2001](#)).

### 6.2.6 Discussion of Topological Model

The use of the topological model requires that the relevant magnetic polarities are well taken into account. So, at least, they should be spatially well resolved. It is also obvious that the topological model can be relevant for large flares, since it neglects fine temporal behavior and small-scale processes. The model is relatively simple if it concentrates on general evolution of the global structure of large flares. The topological model for large-scale magnetic fields remains simple and clear for such a complex active region as the NOAA 9077 with the complex *sunspot structure*, the

so-called  $\beta\gamma\delta$  configuration, according to [Liu and Zhang 2001](#)), which gave rise to the Bastille-day flare. At the same time, the topological model explains the main features of this well-studied flare.

First, the simplified topological model approximately predicts the location of the flare energy source in the corona and, with a reasonable accuracy, reproduces the locations and shapes of chromospheric ribbons and bright kernels on the ribbons. More accurate models should be constructed, with account of nonpotential components of magnetic field in the active region, in order to reach a better agreement between the model and observations.

Second, the topological model explains the observed large-scale dynamics of the Bastille-day flare as the result of fast reconnection in the reconnecting current layers at separators. It allows us to estimate roughly the reconnection rate and the strength of the large-scale electric fields that presumably accelerate charged particles along the separators. All these effects can be carefully investigated in many flares by using the *Ramaty High Energy Solar Spectroscopic Imager (RHESSI)* high-resolution HXR and gamma- imaging data ([Krucker et al. 2003](#); [Lin et al. 2003a](#); [Krucker et al. 2011](#)).

In order to interpret the temporal and spectral evolution and spatial distribution of HXRs in flares, a *two-step acceleration* was proposed by [Somov and Kosugi \(1997\)](#) with the second-step acceleration via the collapsing magnetic-field lines, the *collapsing magnetic traps* (see Chap. 9). The *Yohkoh* HXT observations of the Bastille-day flare ([Masuda et al. 2001](#)) clearly show that, with increasing energy, the HXR emitting region gradually changes from a *large diffuse source*, which is located presumably above the ridge of soft X-ray arcade, to a two-ribbon structure at the loop footpoints. This result suggests that electrons are in fact accelerated in the large system of the coronal loops, not merely in a particular one. This seems to be consistent with the *RHESSI* observations of large coronal HXR sources; see, for example, the X4.8 flare on 2002 July 23 (see Fig. 2 in [Lin et al. 2003a](#)).

Efficient trapping and continuous acceleration also produce the large flux and time lags of microwaves that are likely emitted by electrons with higher energies, several 100 keV ([Kosugi et al. 1988](#)). [Somov et al. \(2005c\)](#) believe that the lose-cone instabilities ([Benz 2002](#)) of trapped mildly-relativistic electrons in the system of many collapsing field lines (each line with its proper time-dependent lose cone) can provide excitation of radio-waves with a very wide continuum spectrum as observed.

[Qiu et al. \(2004\)](#) presented a comprehensive study of the X5.6 flare on 2001 April 6. Evolution of HXRs and microwaves during the gradual phase in this flare exhibits a separation motion between two footpoints, which reflects the progressive reconnection. The gradual HXRs have a harder and hardening spectrum compared with the impulsive component. The gradual component is also a microwave-rich event lagging the HXRs by tens of seconds. The authors propose that the collapsing-trap effect is a viable mechanism that continuously accelerates electrons in a low-density trap before they precipitate into the footpoints (see Sect. 9.2).

## 6.3 Topological Trigger for Solar Flares

### 6.3.1 What Is That?

The effect of *topological trigger* was suggested too early by [Gorbachev et al. \(1988\)](#). It was also difficult to accept this new idea because a great language barrier between its mathematical background ([Dubrovin et al. 1986](#), Part II, Chap. 3, Sect. 14) and the physical terms used by topological models of solar active regions (Sects. 4.2.1 and 4.3.1). Many people simply understood the simple *topological model* (see references in Sect. 5.3.2) but, unfortunately, not the topological trigger.

Fortunately, [Barnes \(2007\)](#) investigated a relationship between solar eruptive events and the existence of the coronal zeroth points of field, using a collection of over 1,800 vector magnetograms. Each of them was subjected to the charge topology analysis, including determining the presence of coronal zeroth points. It appears that the majority of events originate in ARs above which no zeroth point (a magnetic null) was found. However a much larger fraction of ARs, for which a coronal zeroth point was found, were the source of an eruption than ARs for which no zeroth point was found. Clearly

the presence of a coronal zeroth point is an indication that an active region is more likely to produce an eruption,

as 35% of the ARs for which such a point was found produced eruptions, compared with only 13% of ARs for which no zeroth point was found. We consider this fact as indication that the topological trigger can play a significant role in the origin of eruptive flares. This is also consistent with the study of [Ugarte-Urra et al. \(2007\)](#).

The possibility of a topological approach to the question of the trigger for flares was not often discussed in the literature. [Syrovatskii and Somov \(1980\)](#) considered a slow evolution of coronal fields and showed that, during such an evolution, some critical state can be reached, and fast dynamical phase of evolution begins and is accompanied by a rapid change of magnetic topology. For example, it is possible a rapid ‘break-out’ of a ‘new’ magnetic flux through the ‘old’ coronal field of an AR (Fig. 6.11). When an effective magnetic moment of the internal growing group of sunspots becomes nearly equal an effective moment of the AR ([Syrovatskii 1982](#)), the closed configuration *quickly turns* into the open one.

In this chapter we discuss another possibility. Near a separator the longitudinal component  $B_{\parallel}$  dominates because the orthogonal field  $\mathbf{B}_{\perp}$  vanishes at the separator. Reconnection in the RCL at the separator just conserves the flux of the longitudinal field (see Sect. 8.2.2). At the separator, the orthogonal components are reconnected. Therefore they actively participate in the connectivity change, but the longitudinal field does not.

Thus it seems that the longitudinal field plays a passive role in the topological aspect of the process but it influences the physical properties of the RCL, in particular the reconnection rate. The longitudinal field decreases compressibility of plasma flowing into the RCL.

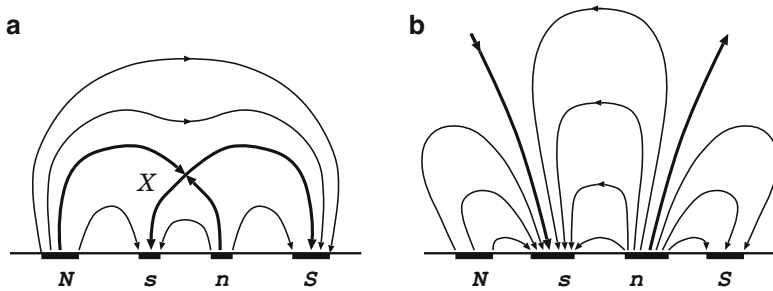


**Fig. 6.11** Topological change of a potential field created by four magnetic sources. (a) The closed configuration with the zeroth point  $X$ . (b) The critical instant when the magnetic field opens (From Somov 2008a; reproduced with permission © Pleiades Publishing, Ltd.)

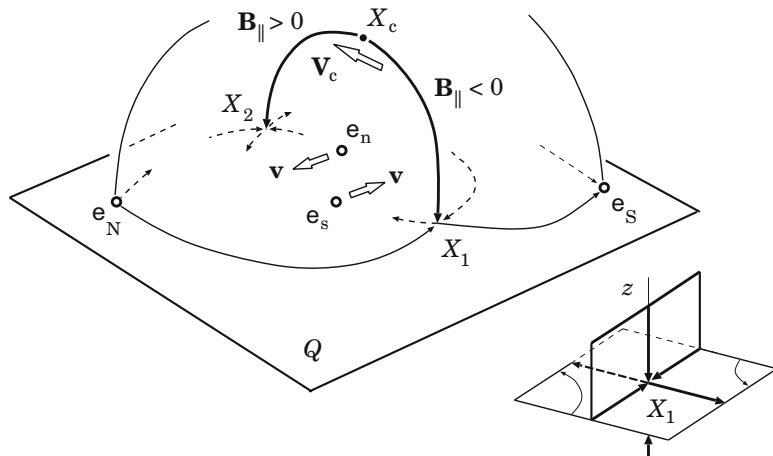


**Fig. 6.12** The zeroth point  $X_1$  rapidly moves along the separator and switches back the longitudinal component  $\mathbf{B}_{\parallel}$  of magnetic field (From Somov 2008a; reproduced with permission © Pleiades Publishing, Ltd.)

When the longitudinal field vanishes, the plasma becomes “strongly compressible”, and the RCL collapses,

i.e. its thickness decreases substantially (see Sect. 2.4.2). As a result, the reconnection rate increases quickly. However this is not the whole story.

The important exception constitutes a zeroth point which can appear on the separator above the photosphere. Gorbatsev et al. (1988) showed that, in this case, even very slow changes in the configuration of field sources in the photosphere can lead to a rapid migration of such a point along the separator (Fig. 6.12) and to a topological trigger of a flare. This essentially 3D effect will be considered below in more detail.

Note that the topological trigger effect is *not* any resistive instability which leads to a change of the topology of the field configuration from pre- to post reconnection state. On the contrary, the topological trigger is a quick change of the global topology, which dictates the fast reconnection of collisional or collisionless origin. Thus

the term “topological trigger” is the most appropriate nomenclature to emphasize the basic nature of the topological effect involved in solar flares,

and it is a welcome usage ([Somov 2008a,b](#)).

### 6.3.2 How Does the Topological Trigger Work?

Let us trace how a rapid rearrangement of the field topology occurs under conditions of slow evolution of photospheric sources with the total charge equals zero. We shall arbitrary fix the positions of three charges, while we move the fourth one along an arbitrary trajectory in the source plane  $Q$ .

Recall that, according to definitions (4.2) and (4.3), the eigenvalue  $\lambda_z$  corresponds to the vertical value of the gradient of magnetic field along a separator at its endpoint, the zeroth point of magnetic field in the plane  $Q$  of magnetic sources, for example, the point  $X_1$  in Fig. 4.2.

Let an initial position of the moving charge corresponds to the values of the topological indices  $I_{top} = -1$  and  $+1$  for the zeroth points  $X_1$  (Type A – with  $\lambda_z > 0$ ) and  $X_2$  (Type A+ with  $\lambda_z < 0$ ) respectively (Fig. 4.2). Thus two points in the plane  $Q$  initially have different indices. Therefore, Eq. (4.15) is satisfied. The separator is the field line connecting these points without a coronal null. This field line emerges from the point  $X_1$  and is directed along the separator to the point  $X_2$ . The value and sign of the magnetic-potential difference between the zeroth points are determined from the relation

$$\Psi_2 - \Psi_1 = \int_1^2 \mathbf{B} d\mathbf{l}, \quad (6.4)$$

where the integral is taken along the separator.  $\Psi_2 - \Psi_1 > 0$  for the field shown in Fig. 4.2.

According to [Gorbachev et al. \(1988\)](#), the moving charge can arrive in a narrow region (let us call it the region  $TT$ ) such that both points in the plane  $Q$  will have the same indices (Fig. 6.12). It follows from the general 3D equation (4.15) that in this case there must also exist two zeroth points outside the plane. They are arranged symmetrically relative to the plane  $Q$  (the plane  $z = 0$  in this section). Figure 6.13 illustrates how these additional points appear.

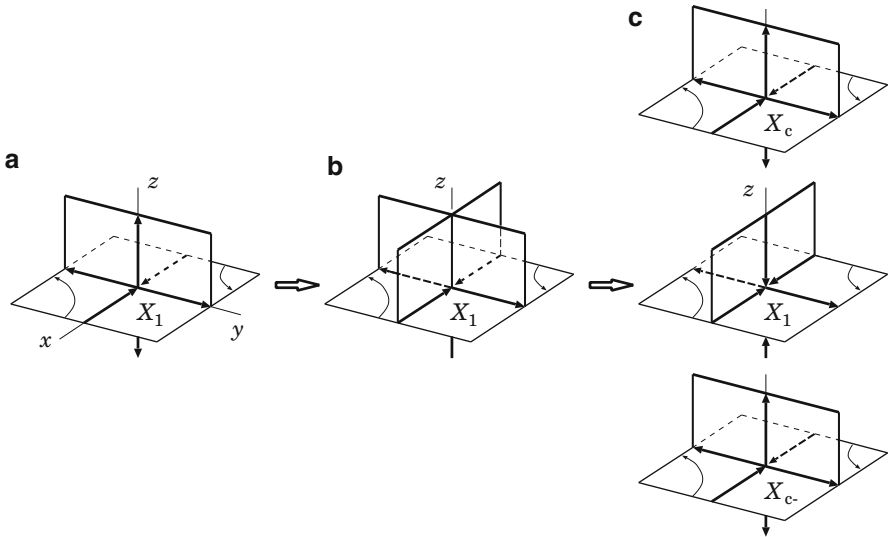


**Fig. 6.13** Changes of the field pattern at the zeroth point  $X_1$  according to Somov (2008a,b). (a) An initial state is the non-degenerate point of the Type A— with  $\lambda_z > 0$ . (b) A degenerate hyperbolic point (line) with  $\lambda_z = 0$  at the beginning of trigger. (c) After the beginning of trigger, the pattern of field is the non-degenerate point of the Type A+ with  $\lambda_z < 0$  and two zeroth points outside the plane  $z = 0$  (From Somov 2008a; reproduced with permission © Pleiades Publishing, Ltd.)

Before the start of trigger, the moving charge is outside of the region  $TT$ , the index  $I_{top} = -1$  and the eigenvalue  $\lambda_z > 0$  at the non-degenerate zeroth point  $X_1$  (Fig. 6.13a). When the moving charge crosses the boundary of the region  $TT$ , the eigenvalue  $\lambda_z$  at the point  $X_1$  vanishes (Fig. 6.13b):

$$\lambda_z(X_1) = 0. \quad (6.5)$$

The point becomes degenerate. At this instant, another pair of zeroth points is born from the point  $X_1$  (Fig. 6.13c). We shall consider only one of them, the point  $X_c$  in the upper half-space  $z > 0$ . This non-degenerate point travels along the separator and merges with the point  $X_2$  in the plane  $z = 0$  when the moving charge emerges from the region  $TT$ . At this instant, the eigenvalue  $\lambda_z$  vanishes:

$$\lambda_z(X_2) = 0. \quad (6.6)$$

As a result of the process described, the direction of the field at the separator has been reversed with the point  $X_2$  of the Type A— with  $\lambda_z > 0$ . After that, the moving charge is located outside the region  $TT$ , there are no zeroth points outside the plane  $z = 0$ . Thus Eqs. (6.5) and (6.6) determine the boundaries of the topological trigger region  $TT$ .

**Fig. 6.14** The topological trigger ( $TT$ ) narrow dashed region is restricted by two boundaries: curves  $C_1$  and  $C_2$  corresponding to Eqs. (6.5) and (6.6), respectively (From Somov 2008a; reproduced with permission © Pleiades Publishing, Ltd.)

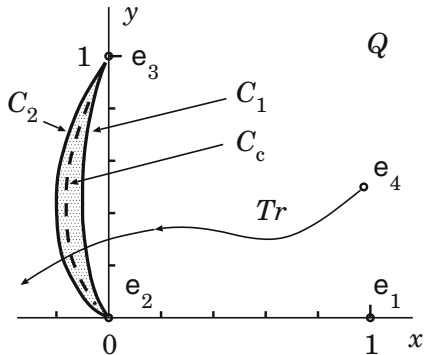


Figure 6.14 presents an illustrative sample of charge configuration. The fixed charges  $e_1 = -e_2 = -e_3 = 1$  are located in the plane  $Q$  at the points  $(1; 0)$ ,  $(0; 1)$  and  $(0; 0)$ , respectively; for more general case see Gorbatchev et al. (1988). The charge  $e_4 = 1$  moves along a trajectory shown by a thin curve  $Tr$ . In the beginning of trigger, it crosses the boundary curve  $C_1$ . Between the boundaries  $C_1$  and  $C_2$  there exists a curve  $C_c$  at which  $\Psi_2 - \Psi_1 = 0$ . The field at the separator changes sign at the point  $X_c$ . Hence the sections  $X_1 X_c$  and  $X_c X_2$  of the separator make contributions of opposite signs to the integral (6.4). These contributions exactly compensate each other for a position of the point  $X_c$  when the trajectory  $Tr$  crosses the curve  $C_c$ .

Typically the region  $TT$  is narrow. That is why small shifts of the moving charge within this region lead to large shifts of the zeroth point  $X_c$  along the separator above the plane  $z = 0$  just creating a *global bifurcation*. Using the analogy with ordinary hydrodynamics (Oreshina and Somov 2009b), we see that the separatrix plane  $(y, z)$  in Fig. 6.13a, which plays the role of a “hard wall” for “flowing in” magnetic flux, is quickly replaced by the orthogonal “hard wall”, the separatrix plane  $(x, z)$  in Fig. 6.13c. Thus the topological trigger drastically changes directions of magnetic fluxes in an AR as illustrated by Fig. 6.15.

In particular, Fig. 6.15b shows that a loop  $e_1 X_c$  quickly grows up. If it reaches a height in the corona, where the solar wind becomes important and pools the magnetic field lines in the interplanetary space (Somov and Syrovatskii 1972), then a fast motion appears as an upward collimated jet along a coronal streamer structure or as a Coronal Mass Ejection (CME).

Another specific sample is a charge arrangement along a straight line, e.g., the axis  $x$  in Fig. 4.1. In this case, owing to the axial symmetry, the entire separator consists of zeroth points. Thus we have a zeroth line. By using an inversion transformation (e.g., Landau et al. 1984):

$$\mathbf{r}' = \frac{R^2}{r^2} \mathbf{r}, \quad (6.7)$$

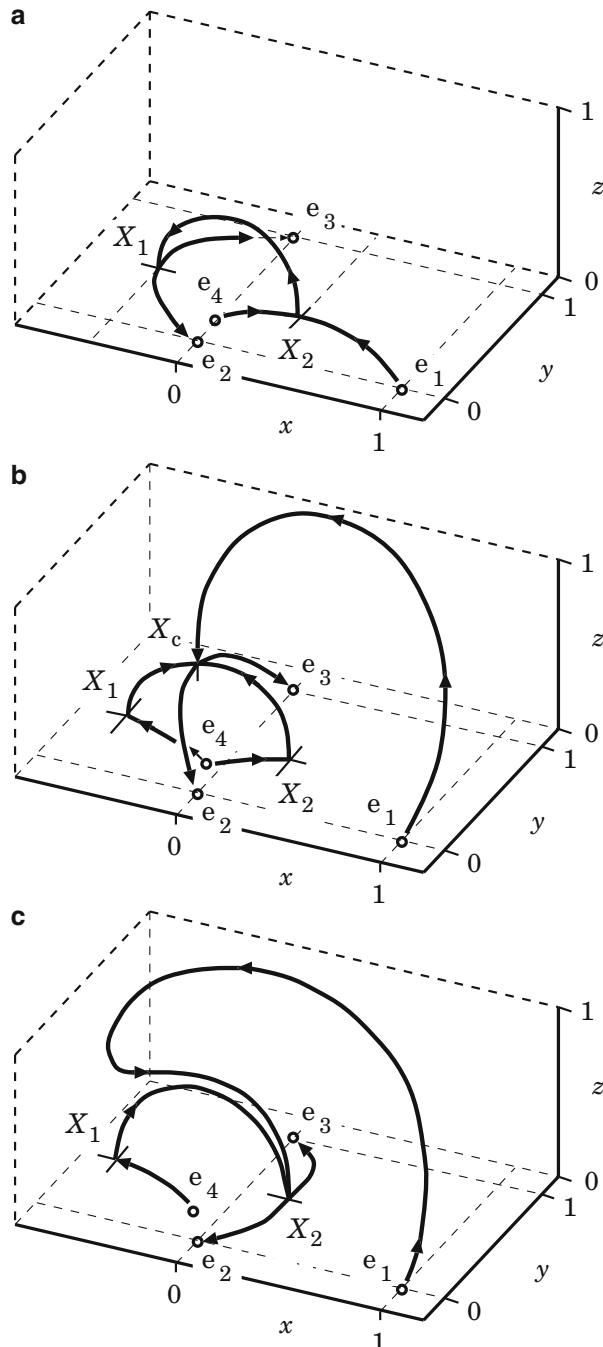


**Fig. 6.15** Global changes of the magnetic field configuration related to the topological trigger effect in the model of an active region as illustrated by Fig. 6.14. (a) An initial state without a coronal null of magnetic field. (b) The coronal null  $X_c$  runs along the separator during the topological trigger process. (c) After the end of the trigger process (From Oreshina and Somov 2009b); reproduced with permission © Pleiades Publishing, Ltd.)

where  $R$  is the inversion radius, it is easy to show that the axial symmetry is not a necessary condition for the appearance of zeroth line. Moreover, the new zeroth line also represents a circle centered in the plane  $z = 0$ . Thus the 3D zeroth lines of the magnetic field can exist if the sunspots do not lie in a straight line.

Up to now, we have considered the travel of one charge while the coordinates and magnitudes of the other three charges were fixed. It is obvious, however, that all the foregoing remains in force in the more general case of variation of the charge configuration. It follows from the results that

a slow evolution of the configuration of magnetic field sources in the photosphere can lead to a rapid rearrangement of the global topology in ARs in the solar corona.

For this reason the phenomenon of topological trigger is necessary to model the large eruptive flares.

## 6.4 The Topological Trigger Does Work

### 6.4.1 The Geoeffective Flares on 2003 November 18

If the topological trigger is a quick change in the global topology of magnetic field that dictates the fast reconnection in large eruptive flares Somov (2008a,b), then the question of precisely how the topological trigger materializes under actual conditions in solar active regions (ARs) remains very important. As a well studied example, we shall consider the AR NOAA 10501 which was located near the centre of the solar disc (N03, E08) on 2003 November 18. Figure 6.16 shows the temporal evolution of the solar X-ray flux observed by *Geostationary Operational Environmental Satellite* (GOES). Five flares occurred on that day. Three of them were observed to originate in this AR: C3.8 at 05:25 UT, M3.2 at 07:52 UT, and M3.9 at 08:30 UT. The second and the third flares were associated with two coronal

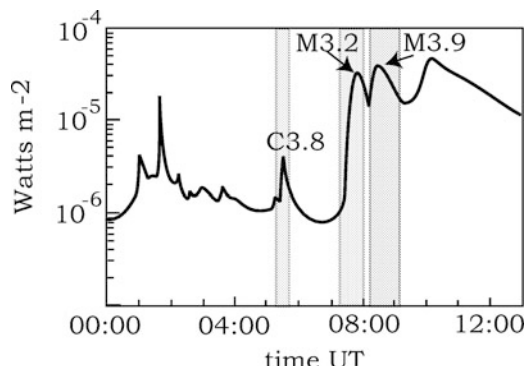
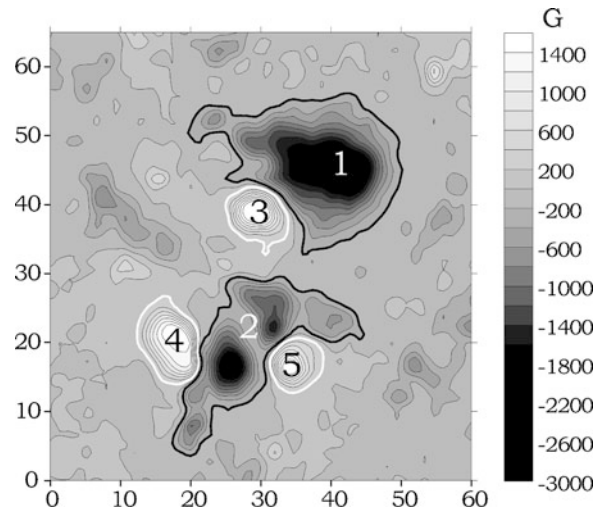


**Fig. 6.16** Temporal evolution of the solar X-ray flux observed by GOES 12 in 1.0–8.0 Å bandwidth on 2003 November 18. The flares occurred in AR 10501 are marked in grey (From Oreshina et al. 2012; reproduce with permission © ESO)

**Fig. 6.17** Magnetogram obtain by MDI/SOHO on 2003 November 18 at 00:00 UT. The white (black) thick lines are 200 G ( $-200$  G) levels. A length unit corresponds to one MDI pixel ( $1.45 \times 10^8$  cm) (From Oreshina et al. 2012; reproduced with permission © ESO)



mass ejections (CMEs), detected by *Large Angle and Spectrometric Coronagraph* (LASCO) on board *SOHO*. The first CME was detected in the C2 field-of-view at 08:06 UT and the second one was observed at 08:50 UT. Two days later, these CMEs produced the most powerful *geomagnetic storm* in the 23rd solar cycle Ermolaev et al. 2005; Srivastava et al. 2009; Chandra et al. 2010).

Figure 6.17 presents the line-of-sight magnetogram obtained by the *Michelson Doppler Imager* (MDI) on-board *SOHO* at 00:00 UT. Five areas are shown where magnetic field was the most intense: two areas of southern (negative) polarity and three areas of northern (positive) polarity. The maximal absolute value of the field for both polarities was about 3,000 G. The value of 200 G has been chosen as a low-boundary intensity level for these areas since the aim of investigation was to study the large-scale magnetic-flux evolution. This threshold also allows to neglect the small-scale changes due to variations in atmospheric seeing and uncorrelated noise. Small areas covering just a few MDI pixels were also neglected because very small fluxes seem unlikely to contribute much to the global topology. So the evolution of these five areas, which include a significant part of the whole AR magnetic flux, was studied (Oreshina et al. 2012).

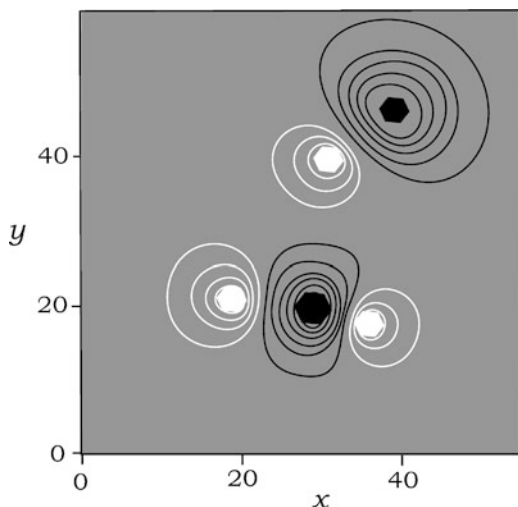
#### 6.4.2 Modeling the Photospheric Magnetograms

Now we wish to construct a topological model of magnetic field in the active region (AR) NOAA 10501 on 2003 November 18 just in the same way as in Sects. 4.3 and 6.2. So, we have to start from the modeling the photospheric magnetograms. An automatic algorithm for choosing the magnetic sources (effective magnetic charges) located beneath the photosphere on one horizontal plane has been developed by

**Table 6.1** Intensities and coordinates of the magnetic-field charges for modeling the magnetogram at 00:00 UT

$i$	$e_i$	$x_i$	$y_i$	$z_0$
1	-98,317	39.5	46.9	-4
2	-79,537	29.2	19.5	-4
3	30,834	30.4	39.6	-4
4	36,272	18.3	21.0	-4
5	35,496	35.7	17.8	-4

**Fig. 6.18** Model magnetogram of the AR NOAA 10501 on 2003 November 18 at 00:00 UT. A length unit is the same one as in Fig. 6.17 (From Oreshina et al. 2012; reproduced with permission © ESO)



Oreshina et al. (2012). The five areas  $R_i$  of the real magnetogram presented in Fig. 6.17 are replaced by five magnetic charges  $e_i$  which coordinates  $x_i$  and  $y_i$  in the plane  $z = z_0$  are calculated as positions of the “center of mass” of every area. The charge intensities  $e_i$  reproduce the values of the observed magnetic fluxes  $\Psi_i$  for each area  $R_i$ . The results are presented in Table 6.1.

The corresponding model magnetogram is shown in Fig. 6.18.

The output of the model provides the global magnetic flux in agreement with the observational values at 92% for positive magnetic flux and 88% for negative flux. The magnetograms of the AR at the subsequent time moments are processed keeping the same depth  $z_0$  of the magnetic-charge plane.

### 6.4.3 Separators and Separatrix Surfaces

The topological portrait of the AR NOAA 10501 on 2003 November 18 at 00:00 UT is shown in Fig. 6.19.

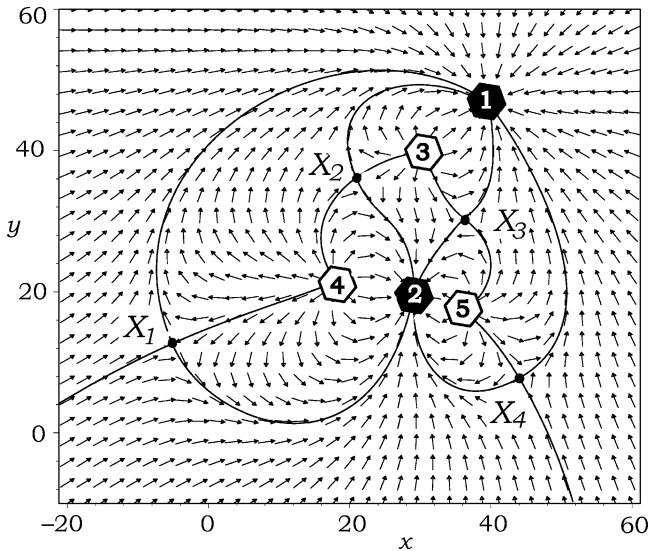


**Fig. 6.19** Vector field created by charges in the magnetic-source plane, the plane of topological portrait. Solid curves are the intersections of the separatrices with this plane.  $X_1$ ,  $X_2$ ,  $X_3$ , and  $X_4$  are the zeroth points of magnetic field (From Oreshina et al. 2012; reproduced with permission © ESO)

Similar to the case of the Bastille-day flare (Sect. 6.2.1), there are four zeroth points in the plane of topological portrait. There are two separators in this AR. The first one connects the points  $X_2$  and  $X_3$  as illustrated by Fig. 6.20. We see that these two points are connecting indeed by a thick curve in the vertical plane which contains the straight segment ( $X_2$ ,  $X_3$ ) and which is perpendicular to the plane of topological portrait (Fig. 6.20, left). This curve represents a magnetic field line, namely the separator going from the zeroth point  $X_2$  to the point  $X_3$ . Note that the eigenvalue  $\lambda_z > 0$  at the point  $X_2$  but  $\lambda_z < 0$  at the point  $X_3$  (cf. Sect. 6.3.2).

The vector field in the vertical plane perpendicular to the straight segment ( $X_2$ ,  $X_3$ ) at the top of the separator contains an  $X$ -type zeroth point (Fig. 6.20, right). This is the  $X$ -type zeroth point of the transverse magnetic field in the vicinity of the separator, i.e. the typical structure that enables magnetic reconnection.

#### 6.4.4 Evolution of Magnetic Field Topology

In order to answer the question of why one magnetic configuration is more likely to reproduce a flare than another one, we have to consider the conditions on separators in an AR. As demonstrated in Sect. 8.2.2, a strong longitudinal (along a separator) component of magnetic field can considerably limit reconnection rate and energy release in a *reconnecting current layer* (RCL). The reason is simple. Decreasing the

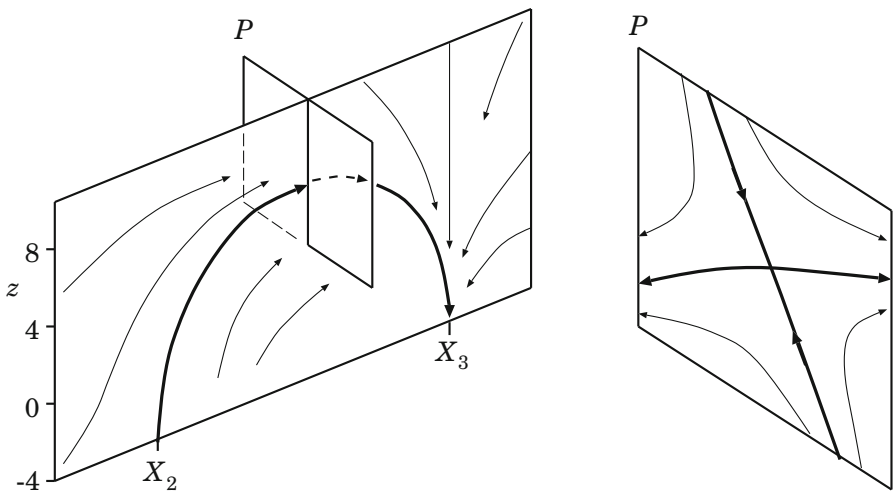


**Fig. 6.20** *Left:* Vector field in the vertical plane containing points  $X_2$  and  $X_3$ ; there is a magnetic field line, the separator connecting these points. *Right:* Vector field in the vertical plane which is located at the top of the separator and is perpendicular to the straight segment  $(X_2, X_3)$ ; there is an  $X$ -type zeroth point of the transverse magnetic field (From Oreshina et al. 2012; reproduced with permission © ESO)

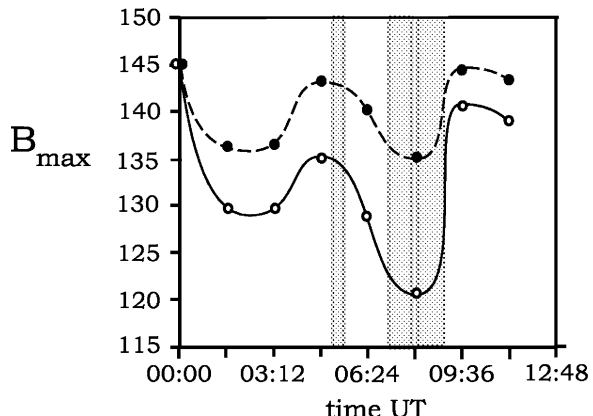
longitudinal magnetic field increases the effective compressibility of plasma, with the frozen-in magnetic field, flowing into the RCL at the separator. As a result, the thickness of the current layer decreases, which leads to increasing the reconnection rate. Recall that the transverse magnetic field at the separator is equal to zero. Therefore

the lower the value of magnetic field at the separator, the better the conditions for magnetic reconnection, for a flare.

This effect was demonstrated by using the topological model of AR NOAA 9077 on 2000 July 12 and 14, i.e. 2 days before the Bastille-day flare and the flare day (Oreshina and Somov 2009b). It was shown that, in this AR, there were also two separators and that the coronal conditions for reconnection on both of them improved significantly before the Bastille-day flare. Now we consider the evolution of the values of magnetic field at the separators in the AR NOAA 10501 on 2003 November 18 on the time scale of several hours before and after the main flares and CMEs.

Oreshina et al. (2012) studied a set of eight magnetograms of this AR, obtained by MDI/SOHO on 2003 November 18 between 00:00 UT and 11:12 UT with 96 min intervals. Figure 6.21 presents the maximum values of magnetic field at both separators for each of the eight time moments. The points are connected by two curves to separate better the processes on two separators. In fact, these processes look similar; moreover,

**Fig. 6.21** Maximum values of magnetic field (in Gauss) at both separators for each of the eight time moments. Black circles correspond to the separator  $X_2X_3$  described above, white circles correspond to the second separator (From Oreshina et al. (2012); reproduce with permission © ESO)



the two largest flares occurred in the vicinity of the deepest minimum of magnetic field at the both separators

(Oreshina et al. 2012).

According to definitions (4.2) and (4.3), the eigenvalue  $\lambda_z$  corresponds to the vertical value of the gradient of magnetic field along a separator at its endpoint, the zeroth point of magnetic field in the plane  $Q$  of magnetic sources, for example, the point  $X_2$  in Fig. 6.20. Thus, the lower the absolute value of the eigenvalue  $\lambda_z$  at a separator endpoint, the lower the absolute value of the magnetic field at this separator, the better the conditions for reconnection.

Such proportionality can not give a perfect correlation because the values of  $\lambda_z$  at two endpoints of a separator can change differently. However it is clear that one should pay special attention to the separators for which the values  $\lambda_z$  decrease significantly. This result seems to be useful to develop a reliable and physically justified method for predicting large solar flares.

#### 6.4.5 Topologically Critical State

Oreshina et al. (2012) studied the magnetic-field structure on both separators at 08:00 UT, i.e. just between the two largest flares (cf. Figs. 6.16 and 6.21). The locations of the effective magnetic charges and their intensities corresponding to this time moment are presented in Table 6.2. The comparison with the initial moment (00:00 UT, Table 6.1) shows that the charges slowly moved within only two MDI/SOHO pixels. The intensities of the first four charges slightly increased, while that of the fifth charge decreased slightly too. However, the magnetic-field configuration became critical so that

even minor changes in the effective-charge characteristics could lead to drastic changes in the large-scale magnetic field in the corona.

**Table 6.2** Intensities and coordinates of the magnetic-field charges for modeling the magnetogram obtained at 08:00 UT

$i$	$e_i$	$x_i$	$y_i$	$z_0$
1	-101,031	39.5	46.9	-4
2	-84,850	27.7	18.6	-4
3	32,098	29.3	39.2	-4
4	40,712	17.2	20.7	-4
5	32,987	35.5	17.9	-4

For example, if the charge  $e_3$  moves along the  $x$ -axis just a little bit, from the point  $x_3 = 29.3$  to the point  $x_3 = 29.4$ , keeping the coordinates and intensities of other charges, then the sign of the eigenvalue  $\lambda_z(X_3)$  would be changed from negative to positive. It means, according to Sect. 6.3.2, that the *topological trigger* should start at the zeroth point  $X_3$ . The magnetic-field direction at the endpoint  $X_3$  is changing along the separator as illustrated by Figs. 6.12 and 6.15; and, therefore, the magnetic structure is quickly changing in the vicinity of the separator.

This example does not mean of course that the movement of exactly the charge  $e_3$  causes the topological trigger in this AR. However it just demonstrates that some *topologically critical state* could be easily reached and trigger drastic changes in the large-scale magnetic-field structure in the vicinity of the separator, thus creating the *coronal mass ejections* (CMEs) related to large solar flares.

# Chapter 7

## Electric Currents Related to Reconnection

**Abstract** The topological model of a flare, with a reasonable accuracy, predicts the location of a flare energy source in the corona. In order to clarify an origin of this energy, we have to consider the non-potential part of magnetic field in an active region. In this Chapter, we discuss the main electric currents related to magnetic reconnection in a large solar flare. More specifically, we continue a study of the Bastille day 2000 flare which topological model was considered in a previous Chapter.

### 7.1 Plane Reconnection as a Starting Point

The two-dimensional (2D) reconnection models for solar flares, including the standard model, are definitely an over-simplification that cannot explain all features of actual flares. However they have to be considered to find a missing element of the flare modeling and to demonstrate how this element should be introduced into the flare interpretation. Moreover some features and predictions of the 2D models still have to be studied and clarified.

#### 7.1.1 Pre-flare Evolution and Energy Accumulation

As in Sect. 5.3.1, we shall consider a *three*-component reconnection in *two* dimensions, at first. With this simplification, which will be discussed in Sect. 7.2.3, the separator is a straight line  $X$  in the corona as shown in Fig. 7.1a by dashed vectors  $X$  above a “simplified neutral line” (see Sect. 6.1.2) in the photospheric plane  $Ph$ .

In the case of the Bastille day 2000 flare, this configuration of magnetic field corresponds to a *central part* of the two-dimensional cartoon picture with two magnetic dipoles (Wang et al. 2005). More exactly, in order to demonstrate possible magnetic connectivity before and after the flare, Wang et al. compared two *TRACE*

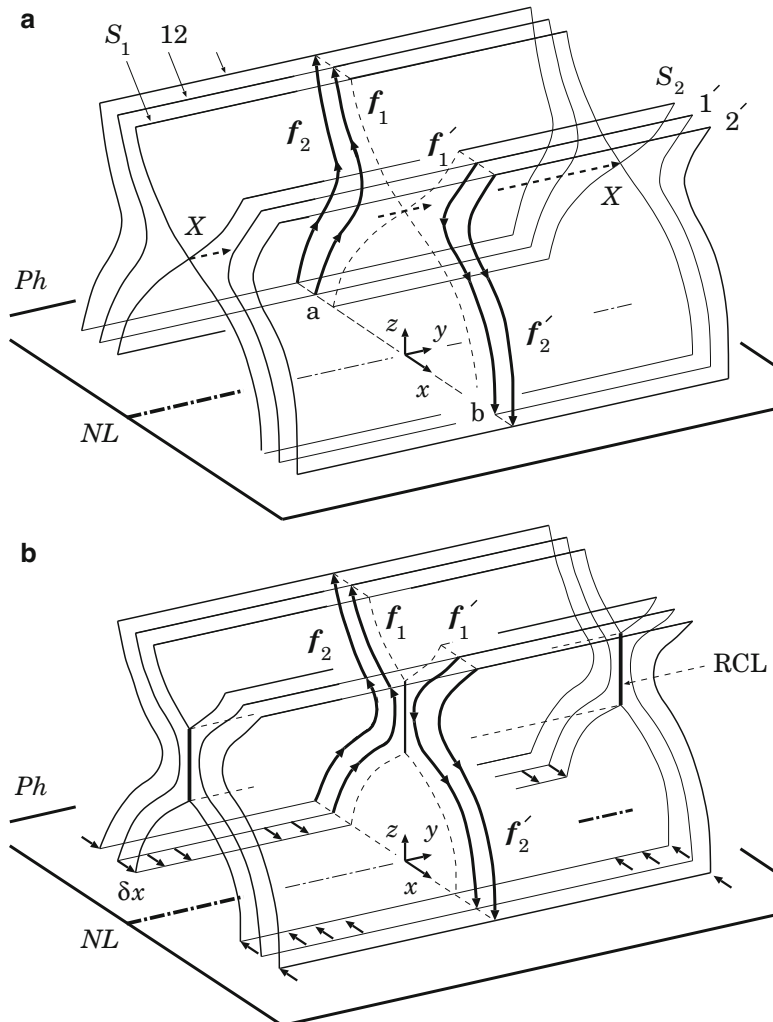


**Fig. 7.1** (a) An initial state of magnetic field. The separatrices  $S_1$  and  $S_2$  cross at the separator  $X$ . (b) The converging flows in the photosphere induce a reconnecting current layer (RCL) in the corona

195 Å images and marked magnetic field line connections based on *TRACE* flux loop structures (see Fig. 8 in Wang et al. 2005). It appears that, before the flare, magnetic fields connect outward in the outer border of the active region; after the flare, connectivity is most obvious between fields inside the active region and close to the photospheric neutral line. Wang et al. were not able to identify the two far footpoints with where the preflare fields connect, even when they studied full disk *SOHO EIT* and *Yohkoh SXT* images. This can be done however.

The active region NOAA 9077 presumably represents the most important *part* of much more extended complex of activity, an *active complex*. We can easily imagine such a complex by considering the multi-wavelength images obtained from the Nançay Radioheliograph, see Figs. 2 and 3 in [Manoharan et al. \(2001\)](#). These figures give us the idea about the active region NOAA 9077 as the center of the complex of activity involved in the CME eruption.

To clarify notation in Fig. 7.1a, we start here from the classical example of ‘reconnection in the plane’, in the plane  $(x, z)$ . A 2D model means, as usual, that all the unknown functions do not depend of the coordinate  $y$ . In addition we assume here that there is no the magnetic field component  $B_y$  which is perpendicular to the plane  $(x, z)$ .

In this case illustrated by Fig. 7.1a, the straight line  $NL$  is the neutral line in the photospheric plane  $(x, y)$ . Above this plane, six magnetic surfaces are shown to discuss the reconnection model. In the scheme, that is usual and sufficient to describe the plane reconnection (e.g., Fig. 4.1), we do not introduce the magnetic surfaces because we simply consider reconnection of magnetic field lines just in one plane, the reconnection plane  $(x, z)$ , that is  $y = 0$ . And we ‘remember’ that, in all other planes with  $y \neq 0$ , we have the same process. This is not necessarily true in general and never true in reality, in three-dimensional configurations of the magnetic fields in solar active regions.

So it is instructive to introduce the magnetic surfaces even in the simplest situation considered here. The magnetic surface 1 in Fig. 7.1a consists of the field lines which are similar to the line  $f_1$  starting at the point  $a$  with coordinates  $x = x_a$ ,  $y = 0$ ,  $z = 0$ . The surface 2 consists of the field lines similar to  $f_2$ . The magnetic field lines  $f_1$  and  $f_2$  illustrate the magnetic flux which goes somewhere upwards ( $z > 0$ ) and left ( $x < 0$ ) in order to connect the central part (which is shown in figure) with an external part (which is not shown) of the activity complex.

For the sake of simplicity, we consider in this Chapter a symmetrical case with the symmetry plane  $x = 0$  for the magnetic surfaces. Hence the field lines  $f'_1$ ,  $f'_2$  etc have the vertical component  $B_z$  of the opposite sign with respect to the similar field lines on the opposite side of  $NL$ . Moreover we have put  $B_y = 0$  to see the ordinary 2D magnetic field configuration in the simplest approach to the reconnection problem.

Among the magnetic surfaces shown in Figure, the two are topologically important: separatrices  $S_1$  and  $S_2$  cross at the separator straight line  $X$  which is parallel to  $NL$ . The separator separates the interacting magnetic fluxes by the separatrices. In addition, it is across the separator that the interacting fluxes are redistributed (more exactly, reconnected) so that the field would tend to keep a minimum energy, to remain potential, if there were no plasma.

Let Fig. 7.1a describe an ‘initial state’ of the magnetic configuration in evolution. Starting from this state, let us introduce the *converging flow* of the photospheric footpoints (for example, two magnetic dipoles join as proposed by [Wang et al. 2005](#)). In the active region NOAA 9077, in its western part, the motions of the sunspot P1 and P2 shown in Fig. 6.4 caused the footpoints of magnetic fluxes to move and interact between themselves before the Bastille day flare.

Such converging flow is illustrated by Fig. 7.1b by the displacement vector  $\delta x$  related to the photospheric velocity component  $v_\perp$

$$\delta x = v_\perp \times \tau, \quad (7.1)$$

where  $\tau$  is the duration of a pre-reconnection stage in the active region evolution. Some part of the magnetic fluxes,  $\delta A$ , would reconnect across the separator  $X$ . Here  $A$  is the  $y$ -component of the vector potential  $\mathbf{A}$  defined by relation  $\mathbf{B} = \text{rot } \mathbf{A}$ .

In a plasma of low resistivity, like coronal plasma, the separator plays the same role as the hyperbolic neutral line (Sect. 4.2.1). The slowly-reconnecting current layer (see RCL in Fig. 7.1b) is developing and growing (we may call this process a ‘pile-up reconnection’) to hinder the redistribution of interacting magnetic fluxes. This results in an excess energy being stored in the form of magnetic energy of a RCL. If  $J$  is the total electric current in the RCL,  $b$  is the half-width of the current layer, then the surplus energy above that of a potential field, having the same sources in the photosphere (see Sect. 5.1), is equal to

$$\mathcal{E}_f = \frac{1}{2c^2} \times L J^2. \quad (7.2)$$

Here

$$L \approx 2l \ln \frac{2l}{b} \quad (7.3)$$

is the self-inductance of the RCL,  $l$  being its length along the separator.

In the case of the Bastille day 2000 flare, the length of the SXR arcade was  $\sim 120,000$  km. So  $l \sim 10^{10}$  cm. With a typical RCL width  $b \sim 10^9$  cm (see Sect. 8.5), we have  $\ln(2l/b) \approx 3$  and

$$\mathcal{E}_f \approx \frac{3}{c^2} \times l J^2 \sim \frac{J^2}{3 \times 10^{10}} \quad (7.4)$$

or

$$\mathcal{E}_f \sim 3 \times 10^8 J(\text{Ampere})^2, \text{ erg}. \quad (7.5)$$

Hence the total current  $J \sim 3 \times 10^{11}\text{--}10^{12}$  Ampere is necessary for a large flare, like the *Bastille day flare*, to release the energy

$$\mathcal{E}_f \sim 3 \times 10^{31}\text{--}3 \times 10^{32} \text{ erg}.$$

These estimates do not contradict to the estimates of the electric current based on measurements of the magnetic field components in the photosphere in the active region NOAA 9077 (Deng et al. 2001; Zhang 2002). More exactly, a level of magnetic non-potentiality in AR NOAA 9077 seemed to be even higher before 14 July than that after the Bastille day flare and that predicted by formula (7.5). This presumably means that some part of free energy is accumulated in surplus

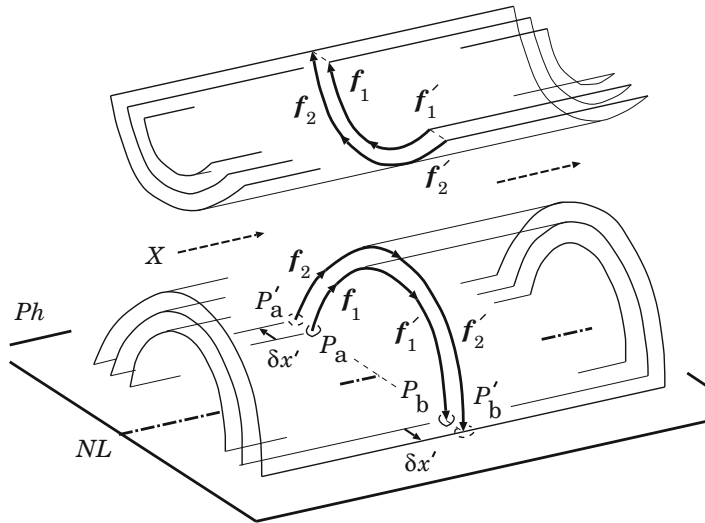


**Fig. 7.2** Apparent motion of footpoints during the fast reconnection process considered in the model of plane reconnection. The footpoint separation in a flare increases with time

to the magnetic energy of the current layer, as an additional energy related to the photospheric shear and photospheric reconnection (Sects. 7.2 and 7.3).

On the other hand, during the Bastille day flare, the total integrated thermal energy was  $\lesssim 3 \times 10^{31}$  erg (Aschwanden and Alexander 2001) which is smaller than the total energy of the flare predicted by formula (7.5). This means that significant part of the flare energy goes to the kinetic energy of the fast plasma motions (i.e. CME) and accelerated particles (Share et al. 2001).

### 7.1.2 Flare Energy Release

What could be expected as a result of fast reconnection in the RCL during a flare? – Fig. 7.2 illustrates such expectations. Being in a *super-hot turbulent-current* state (Sect. 8.3) the *rapidly-reconnecting* current layer provides the powerful fluxes of energy along the reconnected field lines. These fluxes, when they arrive in the upper chromosphere, create impulsive heating of the chromospheric plasma to high temperatures. Fast electrons (accelerated and super-hot) lose their energy by Coulomb collisions with the thermal electrons of plasma (see Chap. 17). This creates a quick hydrodynamic and radiative response of the chromosphere (see Part I, Sect. 8.3.2) observed in SXR, EUV, and optical emission. Inelastic collisions of the fast electrons with thermal protons and other ions generate the HXR bremsstrahlung radiation. For this reason, the footpoints of the reconnected field lines also become bright in HXR.

The EUV and HXR flare ribbons observed by *TRACE* and *Yohkoh* in the Bastille day flare map out the chromospheric footpoints of magnetic field lines newly linked by reconnection in the corona (Fletcher and Hudson 2001; Masuda et al. 2001). So

the bright kernels in the flare ribbons allow us to find the places in the corona where the magnetic reconnection process has the highest rate and produces the most powerful fluxes of energy.

Since the magnetic field lines  $f_1$  and  $f'_1$  reconnect first, they create the *first reconnected line*  $f_1 f'_1$  and the first pair of the chromospheric bright footpoints  $P_a$  and  $P_b$  related to this line as shown in Fig. 7.2. In fact, two field lines being reconnected create two other field lines of different magnetic linkage. In Fig. 7.2, there are two field lines  $f_1 f'_1$ : one goes down (to the chromosphere), the second moves upwards (to the interplanetary space). In order not to obscure the simplest situation, we do not discuss in this Section the upward-moving field lines. Depending on conditions, they have complicated structure and behavior in the upper corona and interplanetary space.

The field lines  $f_2$  and  $f'_2$  will reconnect later on, for example at the end of the first HXR spike S1 described in Sect. 6.1. So they will create a new pair of footpoints  $P'_a$  and  $P'_b$  in different locations. Obviously

the distance between the footpoints of the reconnected field lines will become larger.

This is the well-known prediction of the *standard model* of two-ribbon flares, which is also the well-observed effect of the increasing distance between flare ribbons (Svestka 1976; Zirin 1988).

Wang et al. (2005) compared two *TRACE* images of the active region NOAA AR 9077 before and after the Bastille day flare. They marked the magnetic field line connections based on the *TRACE* flux loop structures. Figure 8 in Wang et al. (2005) clearly shows that, before the flare, magnetic fields connect outward in the outer border of the active region. After the flare, connectivity is most obvious between fields inside the active region and close to the photospheric neutral line. Naturally, the simple 2D model does not allow the authors to identify the two far footpoints with where the preflare fields were connected. These footpoints should be somewhere outside of the active region but, of course, inside the complex of activity. Presumably we see them on the multi-wavelength images obtained from the Nancay Radioheliograph (see Fig. 2 in Manoharan et al. 2001).

From the physical point of view, the predicted and observed displacement  $\delta x'$ , as illustrated in Fig. 7.2, represents the effect of fast relaxation of the non-potential component of the magnetic field related to the RCL which has been generated by the photospheric converging motion. Note that, in general,

$$\delta x' \neq \delta x . \quad (7.6)$$

In the simplest example under consideration, the reason is obvious. Let the field lines  $f_1$  and  $f'_1$  coincide with the separatrices  $S_1$  and  $S_2$  of the initial state shown in

Fig. 7.1a. Then  $\delta x$  represents a photospheric displacement of the initial separatrices. For this reason, the first pair of the bright footpoints  $P_a$  and  $P_b$  shows us the real displacement of the footpoints of the initial separatrices. This is important for interpretation of the flare onset, the beginning of the first HXR spike S1.

On the other hand, the apparent footpoint displacement  $\delta x'$  is directed to the new positions of the bright kernels  $P'_a$  and  $P'_b$ . These are related to the footpoints of the separatrices in a final state of the magnetic field after reconnection. And the final state, in general, does not coincide with the initial one for many reasons. The main one is that presumably the magnetic field can change during a flare (Anwar et al. 1993; Kosovichev and Zharkova 2001). It is natural to assume that

$$\delta x' \lesssim \delta x \quad (7.7)$$

since dissipation of the electric currents in solar flares is presumably never complete.

Therefore the plane reconnection model with a vertical RCL, considered here, predicts that

the flare bright kernels, as they are seen in EUV, HXR or  $H\alpha$ , should separate in opposite directions from the photospheric neutral line, if the photospheric magnetic fields converge to this line before a flare.

Note that the plane-reconnection models of solar flares with a new emerging flux and with a horizontal RCL (Syrovatskii 1972) predict a decreasing footpoint separation (see Sect. 5.2.1).

From the observational point of view, however, actual solar flares are not so simple. Initially, on the basis of *Yohkoh* SXT observations, the flares with the so-called ‘cusped arcade’ (e.g., the well-known 21 February 1992 flare) were often considered as a clear evidence in favor of the standard 2D MHD model; see Shibata et al. (1995), Tsuneta (1996) and references there. In a deeper examination of the SXT data, Uchida et al. (1998), Morita (2001) noted that there are some essential features inexplicable by the *standard model*. Morita et al. showed that the magnetic structure responsible for these flares, including the homologous flares, turned out to be a structure with 3D quadrupole-type magnetic fields (Sect. 4.2.1).

### 7.1.3 Three-Component 2D and 3D Reconnection

In the above we neglected the component of the magnetic field parallel to the separator in order to discuss the classical example of 2D plane reconnection. However, under actual conditions in the solar atmosphere, reconnection always occurs in the presence of a longitudinal component. Moreover the longitudinal component of magnetic field in the vicinity of a separator has several important physical consequences for the reconnection process in solar flares (Sect. 8.2.2). Only those of them will be discussed below that are important for understanding the apparent motions of chromospheric ribbons and bright kernels during a large two-ribbon flare.

As in the previous example, illustrated by Figs. 7.1 and 7.2, we assume that all the geometrical properties of the magnetic field are uniform in the  $y$ -direction. Now we allow the  $y$ -components of the unknown vector functions, for example the magnetic field vector  $\mathbf{B}$ . So the problem under consideration still remains a two-dimensional one, at least in the initial and pre-reconnection stages, until we shall make new assumption that something depends on the coordinate  $y$ . For example, we shall assume in the following Sections that the conditions for field dissipation depend on  $y$ . In this case, the problem becomes essentially three-dimensional when dissipation acts quickly at a certain region determined by a given value of  $y$ . Before we make such an assumption, the problem remains two-dimensional because there is no need and no reason to assume that the longitudinal (parallel to the separator  $X$ ) magnetic field component  $B_{\parallel} = B_y$  is uniform in the plane, i.e. in variables  $(x, z)$ . On the contrary, Somov et al. (1998) assumed that each field line arrives to the separator with its own value of  $B_{\parallel}$ . The only restriction up to now is that the component  $B_{\parallel}$  does not depend on  $y$ .

Near the separator  $X$  the longitudinal component  $B_{\parallel}$  naturally dominates because the orthogonal (perpendicular to the separator) field  $\mathbf{B}_{\perp}$  vanishes at the separator. For this obvious reason,

| the magnetic field lines passing very close to the separator become elongated in the separator direction;

the separator by itself is a unique field line. This and other properties of the separator are well known since the classical work by Gorbachev et al. (1988); they will not be discussed here except one of them which is essential. The reconnection process in the RCL at the separator will just conserve the flux of the longitudinal component  $B_{\parallel}$  (Sect. 8.2.2).

In other words, at the separator, the orthogonal components (i.e. the magnetic field  $\mathbf{B}_{\perp}$ ) are reconnected. Therefore the orthogonal components of the magnetic field actively participate in the connectivity change, but the longitudinal one does not. Hence the longitudinal component plays a relatively passive role in the topological aspect of the process but it influences the physical properties of the RCL, in particular the reconnection rate (see Sect. 8.2.2). However this is usually not the whole story.

The important exception constitutes a neutral point of magnetic field, which can appear on the separator above the photospheric plane. Gorbachev et al. (1988) showed that, in this case,

| even very small changes in the configuration of magnetic field sources in the photosphere can lead to a rapid migration of such a neutral point along the separator in the corona

and to a *topological trigger* of a solar flare (see Sect. 6.3).

So, in the 2D approximation of illustrative value, a three-component reconnection, i.e. the reconnection process inside a RCL which has three components of magnetic field, at the separator can proceed with an increase (or decrease) of the longitudinal component of magnetic field and, as a consequence, with an increase

(or decrease) of the length of the reconnected field lines. According to Somov et al. (1998), in the *more impulsive* (MI) flares, the reconnection process proceeds with a decrease of the longitudinal component and hence with a decrease of the footpoint separation. The physical origin of this kind of flare is discussed in the next Section.

As for the topological trigger, this is essentially the 3D reconnection phenomenon (Sect. 6.3). The relationship between the existence of coronal zeroth points (magnetic nulls) and solar eruptive events was investigated by Barnes (2007) using a collection of over 1,800 vector magnetograms. Each magnetogram was subjected to the topology analysis. It was concluded that the majority of events (74%) originate in the active regions above which no zeroth point was found. However a much larger fraction of the regions for which a coronal zeroth point was found were the source of an eruption (35%) than the active regions without the coronal zeroth point (13%). Thus

the presence of a coronal magnetic zeroth point seems to be a good indication that an active region is more likely to produce an eruptive event.

This is also consistent with the study of Ugarte-Urra et al. (2007).

## 7.2 Photospheric Shear and Coronal Reconnection

### 7.2.1 Accumulation of Magnetic Energy

Figure 7.3 demonstrates the action of a specified photospheric velocity field on different field lines  $f_1$ ,  $f_2$  etc placed at different magnetic surfaces 1, 2 etc. As in the previous Section, a converging flow is present in opposite sides of the neutral line  $NL$  in the photosphere  $Ph$  and creates the reconnecting current layer (RCL) along the separator  $X$  in the corona as shown in Fig. 7.3b. In addition, now a shear flow is superposed on the converging flow in the photosphere. So the separatrices  $S_1$  and  $S_2$  are involved in the large-scale shear flow together with nearby surfaces 1, 2 and  $1'$ ,  $2'$ . When a field line, for example the line  $f_1$ , moves in direction to  $NL$ , it becomes longer along the  $NL$  under action of the shear flow.

Figure 7.3b shows the field lines which were initially in the plane  $(x, z)$  as indicated in Fig. 7.3a. Under action of the shear flow, these lines move out of the plane  $(x, z)$ , except for an upper corona boundary, which is assumed, for the sake of simplicity of illustration, to be unaffected by the photospheric shear.

We assume again that reconnection is too slow to be important yet. We call this stage of the magnetic field evolution the ‘pre-reconnection state’. At this stage, coming between the initial and final one, the magnetic field sources in the photosphere have been displaced to their final pre-flare positions, but the magnetic-field lines have not started to reconnect yet because the plasma conductivity still can be considered as infinite. Therefore the RCL prevents the interacting fluxes from reconnection. The energy of this interaction is just the energy of the magnetic field of the current layer, as in Sect. 1.1.4.

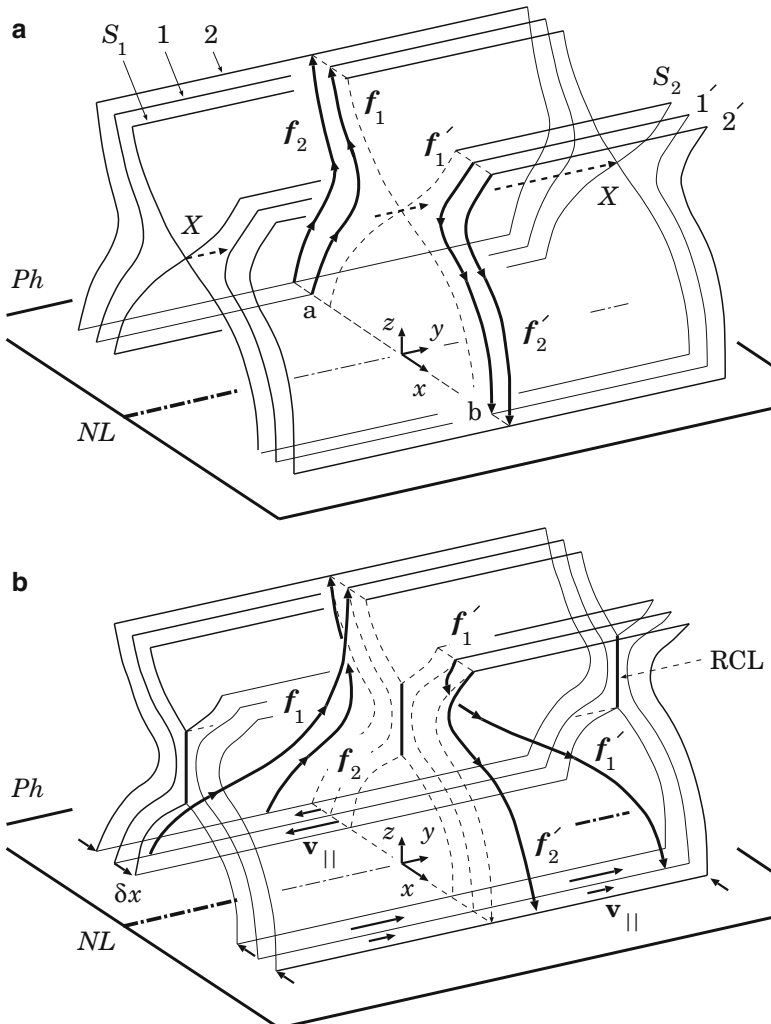


**Fig. 7.3** (a) The initial configuration of the magnetic field is the same as in Fig. 7.1. (b) The converging photospheric flow creates the RCL at the separator  $X$ . In addition, the shear flow with velocity  $\mathbf{v}_{||}$  in the photosphere makes the field lines longer, thus increasing the energy in the magnetic field

Photospheric shear flows add to the energy of the pre-reconnection state an additional energy. This is the energy of magnetic tension generated by the shear because of the ‘freezing-in’ property of the solar plasma. The flow works on the field-plasma system, making the field lines longer. This is always true, even if there are not a separator. In addition, if the pre-flare magnetic-field configuration contains the separator, and

if the bases of the field separatrices are involved in the large-scale photospheric shear flows, then the shear flows induce current layers extending along the separatrices, with the concentrated current flowing parallel to the orthogonal field  $\mathbf{B}_\perp$

(see Sects. 16.3 and 16.4). The origin of this current lies in the discontinuity of the longitudinal component  $B_\parallel$  on the separatrices, created by the photospheric shear flows in the presence of the separator in the corona. Dissipation of the current during a solar flare leads to a decrease of the discontinuity. We call such a process the ‘*shear relaxation*’.

From a mathematical point of view, if the magnetic force dominates all the others, the potential or force-free field is a solution of the MHD equations for an ideal medium in the approximation of a strong field (see Part I, Sect. 13.3.1). Such a field, changing in time according to the boundary conditions in the photosphere, sets the chromospheric and coronal plasma in motion. The magnetic field remains mainly potential but accumulates non-potential components related to electric currents: (a) slowly-reconnecting current layers which are highly-concentrated currents, flowing parallel to the separator, (b) the smoothly distributed currents which are responsible for magnetic tension generated by the photospheric shear flows, (c) the concentrated currents at the separatrices, generated by the shear flows too.

As for the fast reconnection process which tends to release these excesses of magnetic energy during a flare, the main difference is that now a longitudinal magnetic field is present inside and outside the RCL. Hence we shall have a three-component reconnection as mentioned in Sect. 7.1.3.

### 7.2.2 Flare Energy Release and CMEs

The fast reconnection stage of a solar flare, that is the flare impulsive phase, is illustrated by Fig. 7.4. As in the case of plane reconnection demonstrated by Fig. 7.2, in Fig. 7.4b only two pairs of the reconnected field lines are shown. How were they selected among the continuum of the field lines at each magnetic surface before reconnection, as they are shown in Fig. 7.4a?

Note that Fig. 7.4a differs from Fig. 7.3b in one important respect. These figures show the same magnetic surfaces but different field lines. An additional assumption used here is that the physical conditions along the  $y$ -direction are not uniform any longer. More exactly it is assumed that the fastest reconnection place is located in vicinity of the point  $y = 0$  in the reconnecting current layer (RCL) at the separator. For this reason, those field lines are selected which have the nearest distance to the RCL under condition  $y = 0$ . So just these field lines will reconnect first and quickly.

Usually, in three-dimensional topological models, the place of fast reconnection is chosen at the top of the separator. This is assumed, for example, in the model for

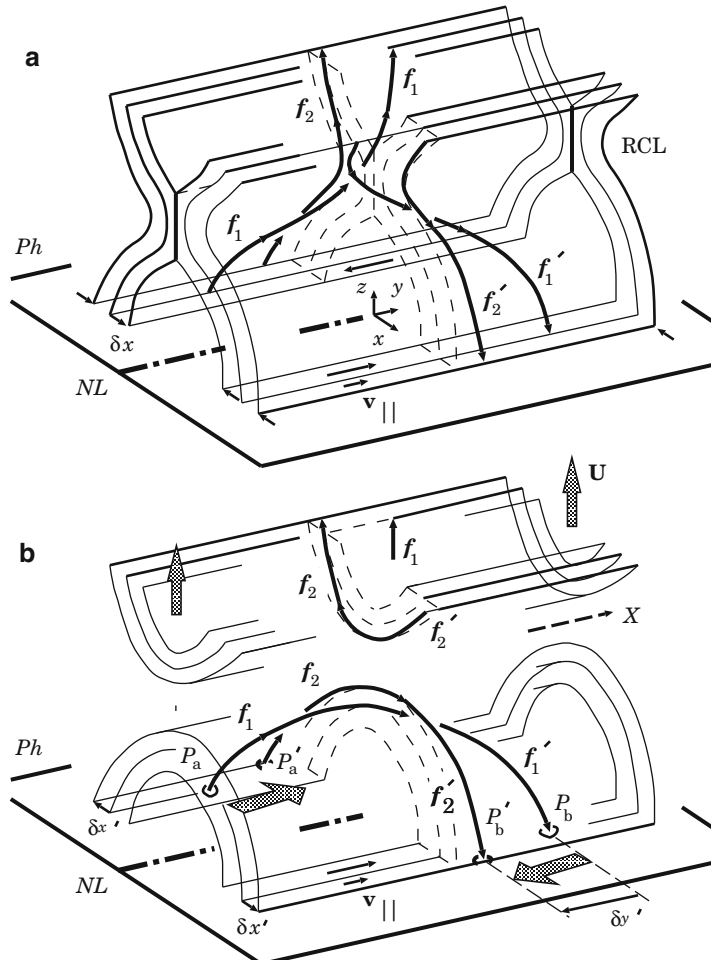


**Fig. 7.4** (a) A pre-reconnection state of the magnetic field in an active region with the converging and shear flows in the photosphere. The field lines are shown which are nearest to the fastest reconnection place ( $y = 0$ ) in the RCL. (b) Rapidly decreasing footpoint separation during the ‘more impulsive’ Sakao-type flares as a consequence of magnetic shear relaxation

the well-studied flare of 1980 November 5 (see sections from 4.3.1 to 4.3.3). In this Section we shall not consider the upward-moving reconnected field lines in detail. They are just indicated in Fig. 7.4b by a velocity vector  $\mathbf{U}$ . As a consequence of the three-component reconnection at the separator, the upward-moving lines may take a twisted-flux-tube shape, which may correspond to a central helical part of a *coronal mass ejection*, CME (see Hirose et al. 2001). This seems to be consistent with

observations of a rapid halo-type CME generated by the Bastille day flare (Klein et al. 2001; Manoharan et al. 2001; Zhang et al. 2001).

In general, the upward disconnection pictured in Fig. 7.4b plays a central role in observed expansion of arcade loops into the upper corona and interplanetary space by creating helical fields which may still be partially connected to the Sun (Gosling et al. 1995; Crooker et al. 2002). It is now commonly used to interpret white-light signatures of CMEs.

In soft and hard X-rays, the coronal structure of a flare can be well seen if a flare has its footpoints occulted by the solar limb. Liu et al. (2008) presented the *RHESSI* data analysis and interpretation of the M1.4 flare on 2002 April 30 at 08:19 UT. The two coronal sources, observed over the 6–30 keV range, appear at different altitudes and show energy-dependent structures with the higher energy emission being closer together. The emission at higher energies in the inner region between the two sources is mainly non-thermal, while the emission at lower energies in the outer region is primarily thermal. The two sources are both visible for about 12 min and have similar light curves and power-law spectra above about 20 keV. These observations suggest that the magnetic reconnection site lies between the two sources.

It is natural that the low-lying SXR-arcade events associated with CMEs are generally interpreted as the consequent brightening of the newly formed arcade (see, e.g., Fig. 2 in Crooker et al. 2002). In terms of the model under consideration, the reconnected field lines below the separator shrink to form magnetic arcade loops. This part will be discussed in the next Section. Here we note only that, in many flares, a pair of conjugate H $\alpha$  kernels and footprint HXR sources shows the converging motion during the rising and impulsive phase clearly demonstrating the relaxation of a sheared magnetic field (e.g., Ji et al. 2006, 2007; Zhou et al. 2008).

### 7.2.3 Flare and HXR Footpoints

The quickest release of energy at the top of the separator creates, at first, the pair of the chromospheric bright points  $P_a$  and  $P_b$  related to the *first* reconnected line  $f_1 f'_1$ . Later on the field lines  $f_2$  and  $f'_2$ , being reconnected at the point  $y = 0$  in the RCL, create the field line  $f_2 f'_2$  with the pair of the bright footpoints  $P'_a$  and  $P'_b$ . Figure 7.4a shows only two pairs of the field lines that reconnect in the plane  $y = 0$ . Being reconnected, they create two pairs of the bright footpoints shown in Fig. 7.4b.

The apparent displacement of the footpoints, from  $P_a$  to  $P'_a$  and from  $P_b$  to  $P'_b$ , now consists of two parts:  $\delta x'$  and  $\delta y'$ . The first one has the same meaning as in the classical 2D reconnection process (Sect. 7.1). The second apparent displacement  $\delta y'$  equals a distance along the  $y$  axis between footpoints of the reconnected field lines  $f_1 f'_1$  and  $f_2 f'_2$ . This value is related to an increase of the length of the field lines on two different magnetic surfaces, generated by the photospheric shear flow along these surfaces. Therefore the displacement  $\delta y'$  during a flare (or a part of its energy release as the first HXR spike S1 in the Bastille day flare) represents the

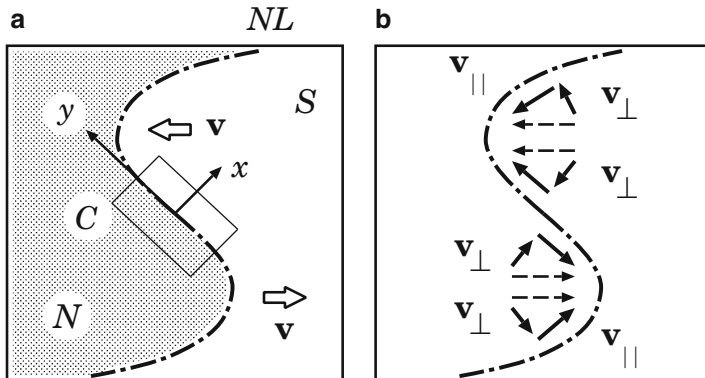


**Fig. 7.5** (a) A photospheric vortex flow distorts the neutral line  $NL$ . (b) A schematic decomposition of the velocity field  $\mathbf{v}$  into the components parallel and perpendicular to the neutral line

effect of relaxation of the non-potential component of the magnetic field related to the photospheric shear flow.

In fact, the ‘rainbow reconnection’ model (Sect. 4.3.5) or the *topological model* with photospheric vortex flows (Gorbachev and Somov 1988), which is mainly the same, predicts the existence of the converging and shear flows in the central region under the top of the separator.

Figure 7.5 illustrates a character of the photospheric velocity field which deforms the neutral line  $NL$  of the vertical component of photospheric magnetic field. The vortex-type flow generates two components of the velocity field: parallel to  $NL$  and directed to  $NL$ . The velocity components  $v_{\parallel}$  and  $v_{\perp}$  are parallel and perpendicular to the photospheric neutral line  $NL$ . The first component of the velocity field provides a shear of magnetic field lines above the photospheric neutral line. The second one tends to compress the photospheric plasma near the  $NL$  and in such a way it can drive magnetic reconnection in the corona and in the photosphere (Sect. 7.3).

To demonstrate the basic physics in the simplest way, we considered only a central region  $C$  in the vicinity of the  $S$ -shaped neutral line  $NL$  in Fig. 7.5b. Here we put the  $y$ -direction along the  $NL$ ; the separator is nearly parallel to  $NL$  as was shown in Fig. 7.1. In actual flares this ‘central part’ can be long enough to be considered in this way. The Bastille-day flare seems to be a good example of such flares because of its extremely regular appearance as a beautifully ‘cylindrical arcade’ in EUV and SXR (Fig. 6.1), which extends more than  $10^{10}$  cm.

In the region  $C$ , the converging flow generates the RCL in the corona above the photospheric neutral line. The shear flow creates the longer magnetic loops which must be reconnected by the RCL. Such loops, being reconnected first, provide the bright footpoints, flare kernels, with a large footprint separation. Later on, the bright footpoints with shorter separation appear. In this way, the *more impulsive* (MI) Sakao-type flares (see definitions and properties of two sub-classes, *more*

*impulsive* (MI) and *less impulsive* (LI) flares, in Sect. 5.3.1) with a decreasing footpoint separation can appear in active regions. This is consistent with the model by Somov et al. (1998).

Why does the footpoint separation increase in the LI flares? – This may be the case when the velocity of the photospheric shear flow decreases near  $NL$ . Hence the second field line  $f_2$  arrives to the separator with a stronger longitudinal field than the first, i.e.  $B_{\parallel 2} > B_{\parallel 1}$ . This can make the reconnection process slower, because the longitudinal field makes the solar plasma less compressible, and the flare less impulsive. However the longitudinal field does not have an overwhelming effect on the parameters of the current layer and the reconnection rate (Sect. 8.2.2). This might be especially true if the compression of the plasma inside the current layer can not be high since its temperature is very high. For example, the effective electron temperature inside a super-hot turbulent-current layer (SHTCL) can be as high as 100–200 MK (see Sect. 8.5.3).

What seems to be more efficient is the following. In the LI flares, after reconnection, the reconnected field line  $f_2$  will be longer than the line  $f_1$  as illustrated by Fig. 5.3a. (It means that reconnection proceeds in the direction of a stronger shear in the LI flares.) So the energy of a longitudinal component of magnetic field becomes larger after reconnection of the shear-related currents (Sect. 16.4). On the contrary, in the MI flares, the reconnection process tends to decrease both excesses of energy: (a) the magnetic energy which comes from the converging flows in the photosphere, i.e. the magnetic energy of RCL, and (b) the energy taken by coronal magnetic fields from the photospheric shear flows. Presumably this circumstance makes the MI flares more impulsive.

We have proposed above that, before the large two-ribbon flares with observed decrease of footpoint separation,

the separatrices are involved in a large-scale shear photospheric flow in the presence of an RCL generated by a converging flow.

This seems to be consistent with conclusion by Schrijver et al. (2005) that shear flows do not by themselves drive enhanced flaring or coronal non-potentiality. These properties related to coronal free energy require appropriately complex and dynamic flux emergence within the preceding  $\sim 10$ – $30$  h. The magnetic and velocity field distributions in the photosphere, more complicated than the simple shear, are necessary to create large solar flares.

For example, Hénoux and Somov (1987) considered an *active complex* with four magnetic sources of interchanging polarities in the photosphere and vortex-type flows in the photosphere around each source. Two systems of large-scale coronal currents are distributed inside two different magnetic cells. These currents are interacting and reconnecting at the separator together with reconnecting magnetic-field lines (see Sect. 16.2.1). Such a process may play a significant role in the dynamics of large solar flares because of a topological interruption of the electric currents.

Even the scenario with the converging and shear flows considered above (Somov et al. 2002a) is still incomplete unless it does not take into account the presence

and eruption of a long twisted filament along the photospheric neutral line before the flare (Liu and Zhang 2001; Yan et al. 2001; Zhang et al. 2001). Bearing this morphological fact in mind, we are going to consider some physical processes in the close vicinity of the polarity reversal line  $NL$  in the photosphere.

### 7.3 Shear Flows and Photospheric Reconnection

Let us return to Fig. 7.3 and consider only the nearest vicinity of the photospheric neutral line  $NL$ . So, on the one hand, the separatrices are outside of the region under consideration but, on the contrary, the effects related directly with  $NL$  become dominant. In the case of the Bastille day flare, the typical distance between the separatrices is  $\sim 3 \times 10^9$  cm. The width of the region which we are going to consider  $\lesssim 3 \times 10^8$  cm.

The *converging flow* toward the polarity reversal line can cause the opposite-polarity magnetic fields to collide in the photosphere and subsequently drive magnetic reconnection there. Converging flows in the photosphere have been reported from many observations (Martin 1998; Kosovichev and Zharkova 2001). Moreover the *flux cancellation* – defined by the mutual disappearance of positive magnetic flux and negative one – has been frequently observed in association with the formation of a quiet pre-flare filament prominence (Martin et al. 1985; Martin 1986; Chae et al. 2001; Zhang et al. 2001).

Figure 7.6 illustrates the possibility of a *photospheric reconnection* process in the presence of the photospheric shear flow. We assume that the initial magnetic field is mainly a potential one sufficiently high above the photosphere, so that the field lines pass above the photospheric neutral line  $NL$  more or less at right angles. However, due to a shear flow, the footpoints on either side of the  $NL$  are displaced along it in opposite directions. This process produces a non-potential magnetic structure, shown in Fig. 7.6a, in which the projections of the field lines onto the photospheric plane  $Ph$  are more closely aligned with the  $NL$ . A motion toward the  $NL$  brings the footpoints closer together and further enhances the magnetic shear. Moreover the converging flow makes the opposite-polarity magnetic fluxes interact and subsequently drives their reconnection in the photosphere as shown in Fig. 7.6b.

The reconnection changes the topology of the field lines arriving at the neutral line  $NL$ . They become disconnected from the photospheric plane inside the *prominence* body. Since the reconnection conserves the flux of the longitudinal magnetic field (see Sect. 8.2.2) generated by the shear flow, the photospheric reconnection leads to the formation of helical field lines which are capable, in principle, of supporting the prominence plasma (van Ballegooijen and Martens 1989).

Filament eruptions in active regions are sometimes an integral part of the phenomena associated with a large two-ribbon flare. Let us assume that, at the beginning of a flare, the prominence erupts and disrupts the magnetic field configuration shown in Fig. 7.6b. In this case, because of fast energy transport along the field lines, the first field line  $f_1$  will be energized first and will creates the bright

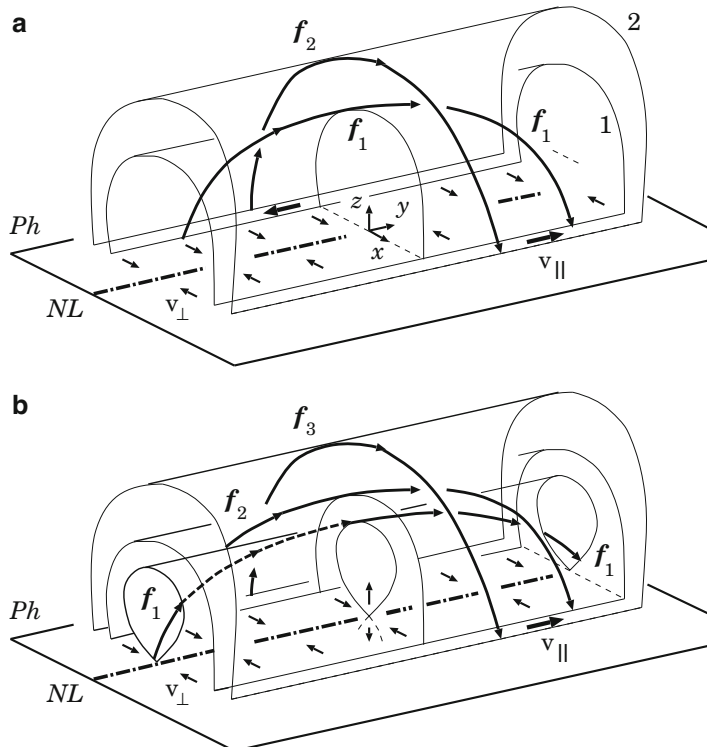


**Fig. 7.6** (a) The converging and shear flows in the photosphere act on the magnetic field lines near the neutral line *NL*. (b) Photospheric reconnection and filament (prominence) formation

footpoints  $P_a$  and  $P_{\perp}$  as shown in Fig. 7.4b. More exactly, the upward-directed reconnection outflow produces a long low loop with the footpoints  $P_a$  and  $P_{\perp}$ . However the downward-directed reconnection outflow creates a short loop (cf. Fig. 1 in [van Ballegooijen and Martens 1989](#)), which submerges, remaining under the photospheric RCL. Next the field line  $f_2$  will become bright and will create the bright footpoints  $P'_a$  and  $P'_{\perp}$ .

Hence a general tendency in the kernel behavior should be similar to that one as for the coronal collisionless reconnection, but

such kinetic phenomena as acceleration of charged particles, their trapping and precipitation are questionable because of high density and low ionization of the photospheric plasma.

An essential aspect of photospheric reconnection is that the atoms have no trouble flowing across the magnetic field lines, the ions are not entirely constrained to follow the field lines as this should be in ordinary MHD.

The remarkable thing about photospheric reconnection is predicted by the model suggested by [Litvinenko and Somov \(1994b\)](#): reconnection effectively occurs only

near the temperature minimum. Here the resistivity is especially high, and a reconnecting current layer (RCL) forms where reconnection proceeds at a rate imposed by the horizontal converging flows of the photospheric plasma.

Magnetic energy is transformed into the thermal and kinetic energy of the resulting vertical motions of cold weakly-ionized plasma

as shown in the central part of Fig. 7.6b. The upward flux of matter through the photospheric RCL into corona is capable of supplying  $10^{17}$  g of cold plasma in a time of  $10^5$  s (see Sect. 15.2.3). This is amply sufficient for the formation of a huge filament prominence.

However, in the pre-flare stage, when the height  $h$  of such a filament is presumably comparable with its width, so  $h \lesssim 10^9$  cm, see Fig. 2 in Liu and Zhang (2001) or Fig. 1 in Zhang et al. (2001), the gravitational energy of the filament

$$\mathcal{E}_{grav} = mgh \lesssim 10^{17} \text{ g} \times 3 \times 10^4 \text{ cm s}^{-2} \times 10^9 \text{ cm} \sim 3 \times 10^{30} \text{ erg} \quad (7.8)$$

is large but still much smaller than the total energy of a large two-ribbon flare  $\mathcal{E}_{fl} \sim (1 - 3) \times 10^{32}$  erg. Moreover this mass requires an additional energy to accelerate it outwards, as typically observed. Therefore the flare energy has to be accumulated in other forms to push plasma upwards (Litvinenko and Somov 1994a; 2001).

In the Bastille day flare on 14 July 2000 (see Chap. 6), the observations of *TRACE* in 171 and 195 Å together with the synchronous ground-based H $\beta$  observations at Huairou Solar Observing Station (HSOS) showed that the filament rupture at some point at 09:48 UT activated the south-west part of the active region NOAA 9077. At 10:10 UT a surge erupted, and a two-ribbon flare started to develop rapidly along the photospheric neutral line (Liu and Zhang 2001). For this reason,

we can believe that the photospheric reconnection and filament eruption played a triggering role in the Bastille day flare.

## 7.4 Motions of the HXR Footpoints in Flares

### 7.4.1 The Footpoint Motions in Some Flares

It is well known that the standard model of a flare (see Kopp and Pneuman 1976; Forbes and Acton 1996) predicts an increasing separation motion of the footpoint (FP) sources as new field lines reconnect at higher and higher altitudes. First results of *RHESSI* observations (Fletcher and Hudson 2002; Krucker et al. 2003) confirm regular but more complex FP motions than that the standard model predicts. Krucker et al. (2003) studied the HXR source motions in the 2002 July 23 flare. Above 30 keV, at least three sources were observed during the impulsive phase. One FP source moved along the photospheric neutral line (*NL*) at a speed of about 50 km/s.

[Asai et al. \(2003\)](#) examined the fine structure inside H $\alpha$ -ribbons during the X2.3 flare on 2001 April 10. They identified the conjugate H $\alpha$ -kernels in both ribbons and found that the pairs of the kernels were related to the FPs of the postflare loops seen in the *TRACE* 171 Å images. As the flare progresses, the loops and pairs of H $\alpha$  kernels moved from the strongly-sheared to the less-sheared configuration. For the X5.7 two-ribbon “Bastille-day” flare on 2000 July 14, the motions of bright HXR kernels from strong-to-weak sheared structure were also observed in the HXR ribbons ([Masuda et al. 2001; Somov et al. 2002a](#)). This fact is consistent with the FP motions predicted by the [Somov et al. \(1998\)](#) model for the MI flares.

[Somov et al. \(2002a\)](#) suggested that, during 2 days before the Bastille-day flare, the bases of magnetic separatrices were slowly moved by the large-scale photospheric flows of two types. First, the shear flows, which are parallel to the *NL*, increase the length of field lines in the corona and produce an excess of energy related to magnetic shear. Second, the converging flows, i.e. the flows directed to the *NL*, create preflare current layers in the corona and provide an excess of energy as a magnetic energy of these layers. During the flare, both excesses of energy are quickly released. Thus, the structure of magnetic field (its topology) and its slow evolution during the days before a flare determine the nature of the flare, more exactly the way of magnetic energy accumulation in an active region and energy release during the flare.

#### 7.4.2 Statistics of the Footpoint Motions

From 1991 September to 2001 December, the *Yohkoh* Hard X-Ray Telescope (HXT) observed about 2000 flares in an energy range above 30 keV. According to the results of analysis of 28 flares, [Sakao \(1994\)](#) inferred that a double source structure (Fig. 5.2) is the most frequent type in an energy range above 30 keV. [Sakao et al. \(1998\)](#) studied the spatial evolution of 14 flares around the peaking time of the M2-band (33–53 keV) emission. For all the flares selected, the separation between the sources was analyzed as a function of time. In seven flares, the FPs moved from each other (the separation velocity  $v_{sep} > 0$ ). The rest of the flares showed decreasing FP separation ( $v_{sep} < 0$ ) or did not show either increasing or decreasing separation of the FPs ( $v_{sep} \sim 0$ ).

These two types of the FP motions were related to the two subclasses of impulsive flares ([Sakao et al. 1998](#)). The flares with  $v_{sep} > 0$  are *less impulsive* (LI): they have a longer duration in the impulsive phase. The flares with a decreasing FP separation are *more impulsive* (MI). However the electron acceleration proceeds with the same high efficiency in the both subclasses of flares; that seemed to be a little bit strange.

[Somov et al. \(2005a\)](#) selected 72 flares according to the following criteria: (a) the integral photon count of HXRs in the M2-band is greater than 1,000 counts per subcollimator, (b) an active region is within 45° of the center of the solar disk.

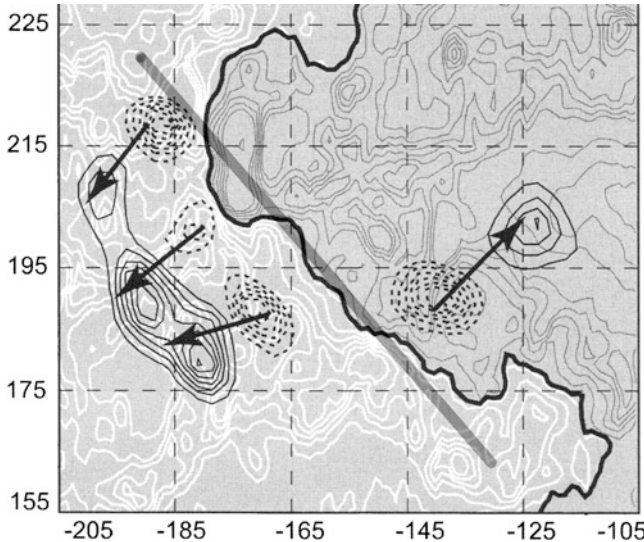


**Fig. 7.7** Position and motion of the HXR sources in the flare on 1998 September 23. The field of view is  $100'' \times 83''$ . The beginnings of arrows correspond to the time 06:56:09 UT, the ends are at 07:08:54 UT. The straight semi-transparent line represents the simplified neutral line (SNL)

The important result is that about 80% of the sources studied have  $V > 3\sigma$ . Here the average velocity  $V$  and the velocity dispersion  $\sigma$  were determined by a linear regression for each of the 198 intense sources that are presumably the chromospheric footpoints (FPs) of flare loops. This fact strongly suggests that: (a) the *moving* sources are usually observed rather than stationary ones, and (b) the *regular* motion of HXR sources during the impulsive phase of flares is rather a general rule than an exception.

In order to reveal the observable types of the FP motions, a significant part of the HXT images (for 43 of 72 flares) were overlayed on the *SOHO* MDI photospheric magnetograms. To relate the source motions to magnetic fields, the fields were characterized by a photospheric neutral line (*NL*) or a *smoothed, simplified* neutral line (SNL; [Gorbachev and Somov 1989](#)). By so doing, the following types of FP motions relative to the SNL can be conditionally distinguished.

#### 7.4.3 The FP Motions Orthogonal to the SNL

In the type I, the HXR sources move mainly away and nearly perpendicular to the SNL. A fraction of such flares appears to be very small: only 2 out of 43 flares. One of them, the M7.1 flare on 1998 September 23 at 06:56 UT, is shown in Fig. 7.7.

The maximal value of velocity in this flare,  $V \approx 20 \text{ km s}^{-1}$ , does not contradict to the typical velocities of the H $\alpha$ -ribbon separation in solar flares (e.g., [Svestka 1976](#)).

However, even in this flare, the question appears how to draw a simplified NL. Presumably the flare does not represent a clear example of the type I flares. The second flare, the X1.0 flare on 2001 November 4 at 16:09 UT, is not free from the same question either. The simple (arithmetical) mean value of the HXR source motion velocity equals  $15 \text{ km s}^{-1}$  in two flares of the type I.

In general, the direction of HXR source motions in a flare depends mainly on the magnetic field configuration. During a flare, reconnection provides powerful fluxes of energy along the reconnected field lines. As the flare progresses,

**|** the footpoints of newly reconnected lines move away from the SNL with a velocity which is proportional to the rate of reconnection.

This is the well-known prediction of the *standard model*, explaining the effect of the increasing separation between flare ribbons. However we see that actual flares are usually not so simple as the standard model predicts. Under actual conditions in the solar atmosphere, reconnection always occurs in a more complicated configuration of field: at least, in the presence of the field component which is parallel to the SNL. As a consequence, the other types of FP motions dominate in flares.

#### 7.4.4 *The FP Motions Along the SNL*

In many flares, the apparent displacements of FPs are directed mainly along the SNL. There are two types of such motions: the FP sources move in anti-parallel directions (type II) or they move in the same direction (type III).

##### 7.4.4 (a) *The Type II of FP Motions*

The type II motions were found in 11 out of the 43 flares. Figure 7.8 shows the M4.4 flare on 2000 October 29 at 01:46 UT as a clear example of the type II. In this flare, the maximal value of the FP motion velocity,  $V \approx 65 \text{ km s}^{-1}$ , is significantly larger than that for the flare H $\alpha$  ribbons. This implies that the FPs mainly move along the ribbons, i.e. along the SNL, similar to the 2000 July 14 flare.

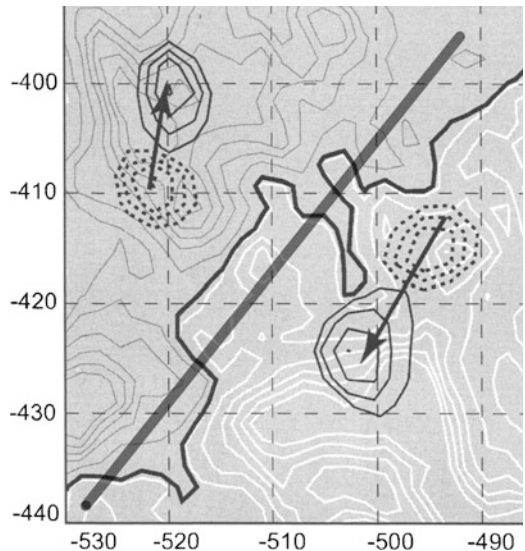
Note that, in general, it may be not simple to distinguish a flare with an increasing FP separation from a flare with a decreasing separation. Both kinds of separations can be present in the same flare of the type II.

**|** In the onset of a flare, the HXR sources move one to another and the distance between them decreases.

Then they pass through a ‘critical point’. At this moment, the line connecting the sources is nearly perpendicular to the SNL.

**|** After that moment, the sources move one from other with increasing separation between them.

**Fig. 7.8** Position and motion of the HXR sources in the flare on 1998 September 23. The field of view is  $100'' \times 83''$ . The beginnings of arrows correspond to the time 06:56:09 UT, the ends are at 07:08:54 UT. The straight semi-transparent line represents the simplified neutral line (SNL)



All these stages are seen in Fig. 7.8. Such a motion pattern seems to be close to that one predicted by the rainbow reconnection model (a sheared vortex flow in the photosphere) assumed by Somov et al. (2002a) for the Bastille day flare.

Liu et al. (2009) presented a detailed imaging and spectroscopic study of the conjugate HXR footpoints observed with *RHESSI* in the X10 flare on 2003 October 29. The double FPs first move toward and then away from each other, mainly parallel and perpendicular to the PNL, respectively. The transition of these two phases of FP unshearing motions coincides with the direction reversal of the motion of the loop-top HXR source (cf. Fig. 7.12) and with the minima of the estimated loop length and LT source.

In some flares analyzed by Somov et al. (2002a), e.g., the flare on 1991 November 15 at 22:37 UT, the separation between the FP sources does not increase monotonically but rather shows *repeated episodes* of small increase and small decrease, while the overall separation increasing. Presumably, as a consequence of this effect, the upward motion of coronal HXR source consists of downward and upward motions, while the overall upward motion dominates; see the decreases ( $D_1$ ,  $D_2$ , and  $D_3$  in Fig. 6a in Liu et al. 2008) of the altitude of the lower HXR loop-top source in the M1.4 flare on 2002 April 30.

As for *Yohkoh* data, a simple code made such deviations in the FP motions smooth and provided only the average velocity,  $V \approx 58 \text{ km s}^{-1}$  in the flare on 1991 November 15. Anyway it is not possible to give a physical classification of flares by dividing them into two wide categories (with converging or diverging FP motions) without considering how these motions are orientated relative to the SNL.

As for the physical interpretation of the type II motions,

the antiparallel motions of the HXR sources represent the effect of relaxation of the non-potential shear component of magnetic field

(Somov et al. 2003b). In contrast to the standard model, such configurations accumulate a sufficient amount of energy for a large flare in the form of magnetic energy of a sheared field.

How are such sheared 3D structures formed? – Large-scale photospheric flows of vortex type presumably play a leading role in this process. They deform the SNL in such way that it acquires the shape of the letter S, as shown in Fig. 7.5, proved that such distortion of the *NL* leads to the separator appearance in the corona above the *NL* (see Fig. 4.13). Developing this idea, we assume that a causal connection exists between the type I and type II flares and the S-shaped bend of the SNL. The vortex flow generates two components of the velocity. The first one is directed to the *NL* and tends to compress the photospheric plasma near the *NL*. In such a way, it can drive magnetic reconnection in the corona and photosphere (Sect. 7.1). The second component is parallel to the *NL* and provides a shear of coronal magnetic-field lines above the photospheric *NL* (Sect. 7.2).

#### 7.4.4 (b) The Type III of FP Motions

Contrary to the type II, in the type III flares, the HXR sources move along the SNL in the same direction as shown in Fig. 7.9. We can see here the X1.2 flare on 2000 June 7 at 15:44 UT, in which both FP sources move with velocity of about  $60 \text{ km s}^{-1}$  parallel to the SNL. This fact suggests that a particle acceleration region in the corona also moves in the same direction during the flare. In terms of the *rainbow reconnection* model, it means that the fastest reconnection place located at the separator moves along the separator. This pattern of motions was found in 13 flares.

In addition, there were eight flares in which the motions away from the SNL were mixed with the other type motions. For example, in the X2.0 flare on 2001 April 12 at 10:15 UT, shown in Fig. 7.10, the projections of the motion vectors on the SNL are not small. This flare represents a superposition of the types I and II. The maximal value of velocity is not large:  $V \approx 21 \text{ km s}^{-1}$ . In the absence of information about the photospheric magnetic field, this flare would be classified as a typical LI flare.

#### 7.4.5 Discussion of Statistical Results

Following the rainbow reconnection model of a two-ribbon flare, we consider the HXR source motions during the impulsive phase of a flare as the chromospheric signature of the progressive reconnection in the corona. Since the FPs of newly

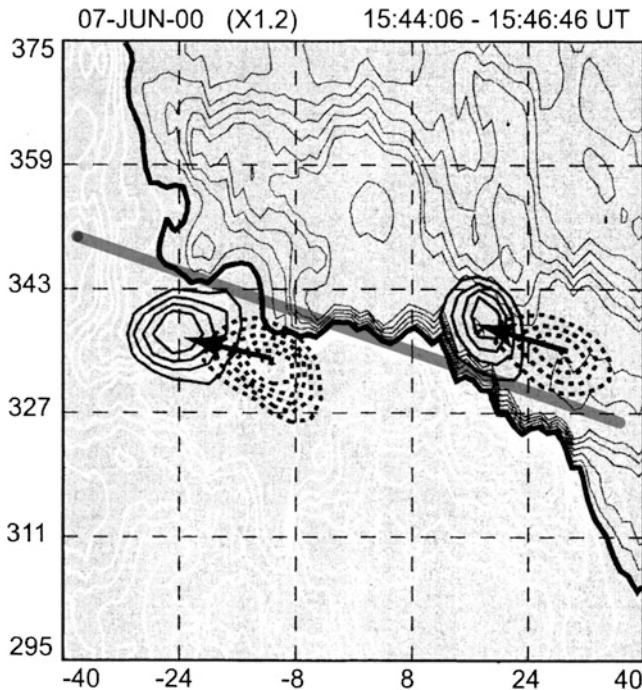


**Fig. 7.9** The type III motions of the HXR sources in the X1.2 flare on 2000 June 7 at 15:44:06–15:46:46 UT. The field of view is  $80'' \times 66''$

reconnected field lines move from those of previously reconnected lines, the places of electron precipitation into the chromosphere change their position during the flare. In order to study the relationship between the direction of motions and the configuration of magnetic field in an active region, we have coaligned the HXT images in 43 flares with MDI magnetograms. In this way, we have inferred that there are *three main types* of the FP motions ([Somov et al. 2005a](#); for more detail and better statistics see [Bogachev et al. 2005](#)).

**The type I** represents the motions of FP sources away from and nearly perpendicular to the SNL, predicted by the standard model of a flare. However only less than 5% of flares show this pattern of motions. The standard model is a strong oversimplification that cannot explain even the main features of actual flares. The evolution of the HXR emitting sources is so complex that it is hardly explained with a simplified model such as the standard model.

In **the type II** flares, the HXR sources on the both sides of the SNL move along the SNL in the opposite directions. Such motions were found in 26% of the flares. This type of motions indicates that the reconnected field lines are highly sheared and the shear angle changes as the flare evolves.

We assume that, before a flare, the shear flows in the photosphere add to the energy of the pre-flare state of an active region an additional energy. It is the energy

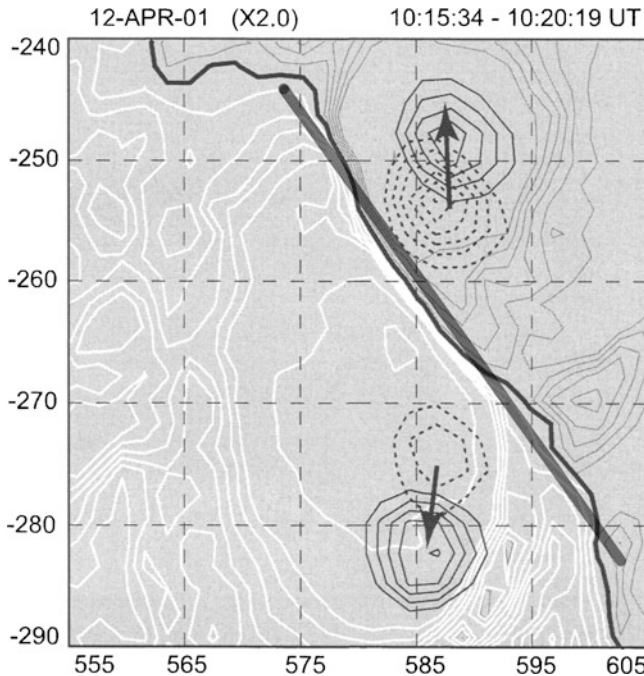


**Fig. 7.10** The motions of HXR sources representing a combination of the type I and type II in the X2.0 flare on 2001 April 12 at 10:15:34–10:20:19 UT. The field of view is  $50'' \times 48''$

of magnetic tension generated by the shear because of the freezing-in property of the solar plasma. The photospheric flows work on the field-plasma system, making the field lines longer. This is always true, even if there are neither a separator nor separatrices of the magnetic field above the photosphere. In such a case, the electric currents responsible for tension are smoothly distributed in a coronal volume above a region of photospheric shear.

If the pre-flare configuration of magnetic field contains separatrices, then the shear flows induce the layers of concentrated currents extending along the separatrices. The origin of these currents lies in the discontinuity of magnetic field on the separatrices (see Sect. 16.3.3). During a flare, reconnection and dissipation of the concentrated current leads to a decrease of the discontinuity. We call such a process the ‘shear relaxation’ (e.g., Somov et al. 2003b). At the same time, the observed evolution from ‘sheared-’ to ‘less-sheared-’ and ‘relaxed-’ HXR pairs also demonstrates the evolution of the flare and post-flare loops.

The mean value of the FP source velocity in the type II flares is of about  $35\text{--}40 \text{ km s}^{-1}$  is significantly larger than the mean velocity in the type I flares,  $\approx 15 \text{ km s}^{-1}$ . Statistics is not sufficiently high to say whether or not the HXR sources are distributed over velocities by the Gaussian law, however, the maximum of

distribution is well located near the mean velocity. The difference which we have found between numbers of flares of the type I and type II means that

the highly-sheared magnetic structures are much more favorable for flare production than simple 2D configurations without the shear flows in the photosphere.

**The type III** is similar to the type II except the HXR sources move in the same direction along the SNL. This happens in about 30% of flares. The parallel motions of the FPs is presumably the chromospheric signature of a ‘horizontal’ displacement of the particle acceleration region in the corona during a flare. The mean velocity is also of about  $35\text{--}40 \text{ km s}^{-1}$ . The  $\text{H}\alpha$  observations by Wang et al. (2003) indicate that an electric field in the corona is not uniform along the RCL at the separator. The peak point of the electric field (related to a region of the most powerful energy release and particle acceleration) can change its position during the flare, moving along the separator. Corollary, all three HXR sources (the loop-top source and two FP sources) move in the same direction along the SNL.

Any flare has not found in that both HXR sources move towards the SNL. Thus all the other motion patterns could be described in the first approximation as a combination of these three basic types. In fact, 19% of flares show the FP motions away from the SNL mixed with other two type motions. Only about 20% of flares seem to be more complicated in the motion scale under consideration. This is not surprising since we know that large and well resolved flares involve multiple loops with complex structure. For such flares, the loop top and associated FP sources are not readily identified and separated.

A dominant part ( $\approx 80\%$ ) of the 43 flares shows a clear or mixed pattern of the HXR source motions, leading us to the idea that

the types I to III are really the three fundamental components of the FP motions in solar flares.

This seems to be reasonable because of the following three relationships. The type I represents the reconnection in the corona. The type II motion indicates the shear relaxations. And the type III is presumably related with a motion of the fastest reconnection place along the arcade, along the separator.

What are the reasons of the apparent prevalence of one or two components over the other in different flares? – We hope to find an explanation in different topological and physical conditions, we expect that this will help reveal the underlying physics. We have studied the relationship between the HXR sources in a flare and the configuration of magnetic field in an active region. However, it is clear that not only the structure of magnetic field (more exactly, its topology) but also its slow evolution before a flare determines the nature of the flare, at least the way of magnetic energy accumulation in an active region and energy release during the flare. Therefore, in a future research, we have to analyze not only distribution of photospheric magnetic fields (in order to reconstruct topology of coronal fields) but also their evolution during sufficiently long time before a flare.

## 7.5 Motions of the Coronal HXR Sources

### 7.5.1 Observational Background

It is well known and is easily understood, even in the frame of the standard model of solar flares, that the observed *upward motion* of coronal hard X-ray (HXR; see Sect. 9.1) sources in flares result from magnetic reconnection in the corona (Sect. 9.2). However *RHESSI* observations have well established a new phenomenon of the apparent *downward motion* of the loop-top (LT) source of HXR emission in an early rising phase of solar flares, which was first reported by [Sui and Holman \(2003\)](#), [Sui et al. \(2004\)](#) in the M1.2 flare on 15th April 2002.

Several authors have reported a contracting motion for solar flaring loops. That is, during the rising phase of solar flares, the LT HXR sources or radio and EUV flaring loops have a descending motion and, at the same time, H $\alpha$  kernels or HXR footpoints (FPs) are converging ([Li and Gan 2005](#); [Ji et al. 2006](#); [Zhou et al. 2008](#)). These observational results support the models proposed that the converging FP motions and contracting motions of flaring loops are the signature of the relaxation of sheared magnetic fields ([Somov et al. 2002a](#); [Ji et al. 2006](#)).

In the few events, it has been found that

- █ during the period of descending motion of the LT HXR source, the distance between the conjugate HXR foot points decreases

([Ji et al. 2007](#); [Liu et al. 2009](#)). The *RHESSI* observations of the M7.6 class flare on 24th October 2003 provide us an excellent opportunity to study various aspects of the flare evolution with imaging and spectroscopic analyses. The *TRACE* images of flaring region in 195 Å and 1,600 Å channels and H $\alpha$  filtergrams well supplemented *RHESSI* data for this study ([Joshi et al. 2009](#)).

The explanation of the rising phase of a flare is beyond the scope of the standard model of two-ribbon flares. Recent observations suggest that the classical picture of such flares described by the standard model is valid after the impulsive phase when we observe the upward motion of LT source and increasing separation of HXR footpoints (FPs). The flare event of 24th October 2003 is one of the clearest examples of this scenario ([Joshi et al. 2009](#)). In the next Section, we discuss the *RHESSI* perception of the rising phase of the flare in terms of the ‘rainbow reconnection’ model (see Sects. 4.3.5 and 7.2.3).

### 7.5.2 Theoretical Interpretation

The rainbow reconnection model takes into account the two kinds of large-scale photospheric flows before a large flare (see Fig. 7.5). First, the shear flows, which are parallel to the photospheric neutral line (*PNL*), increase the length of magnetic-field lines in the corona and, therefore, produce an excess of magnetic energy.

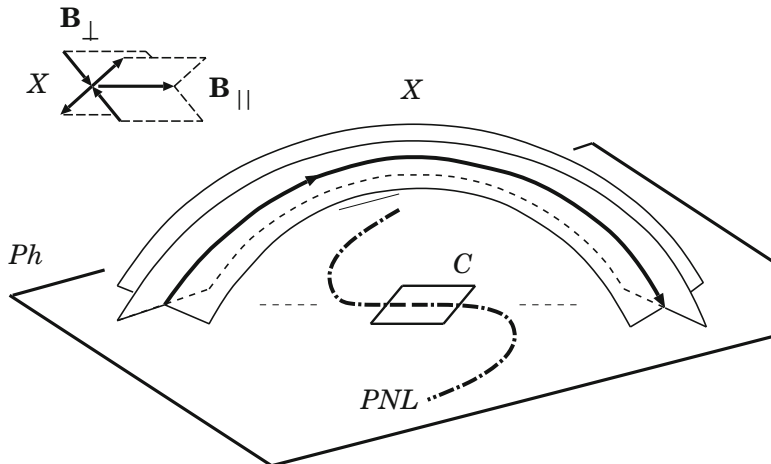


**Fig. 7.11** The ‘rainbow reconnection’ model: the separator  $X$  above the  $S$ -shaped bend of the photospheric neutral line  $PNL$ . The inset in the *upper left-hand* corner shows the structure of magnetic field near the top of the separator with a longitudinal component  $\mathbf{B}_{\parallel}$  (From Somov 2010; reproduced with permission © Pleiades Publishing, Ltd.)

Second, the converging flows, i.e., the flows directed to the  $PNL$ , create the pre-flare current layers in the corona and provide a larger excess of magnetic energy sufficient to produce a large flare.

Recall that, according to the rainbow reconnection model, the separator  $X$  is located above the  $PNL$  like a rainbow above a river which makes a bend as illustrated by Fig. 7.11. The separator is the place where a reconnecting current layer (RCL) can be created, and therefore a preflare energy accumulation can begin. To demonstrate the basic features related to the reconnection process at the separator in the simplest way, we consider only a central region  $C$  in the vicinity of the  $S$ -shaped neutral line  $PNL$ . Here the separator is nearly parallel to  $PNL$ . We put the  $y$ -direction along the  $PNL$  in Fig. 7.12 considered later on.

Being reconnected at the separator, each magnetic field line as well as each thin tube of magnetic flux  $f$  is initially accelerated to high velocity ( $v_1 \gtrsim 1000$  km/s; Sect. 8.5.3) inside a *super-hot turbulent-current layer* (SHTCL). Each tube of reconnected field lines, being frozen into super-hot ( $T_e \gtrsim 10^8$  K; Sect. 8.5.3) plasma, moves out of the SHTCL; in the downflow it forms a magnetic loop with properties of a collapsing magnetic trap (Somov and Kosugi 1997). The longitudinal and transverse sizes of the trap decrease, causing the trapped particles to acquire an additional energy under Fermi and betatron acceleration respectively (Sect. 9.3). The energy distribution of trapped electrons and their HXR emission can be calculated as a function of the trap length and its thickness (Sect. 9.5).

If the electrons injected into the trap from the SHTCL have a power-law energy distribution, then their spectrum remains a power-law one throughout the acceleration process for both the Fermi and betatron mechanisms. For electrons with

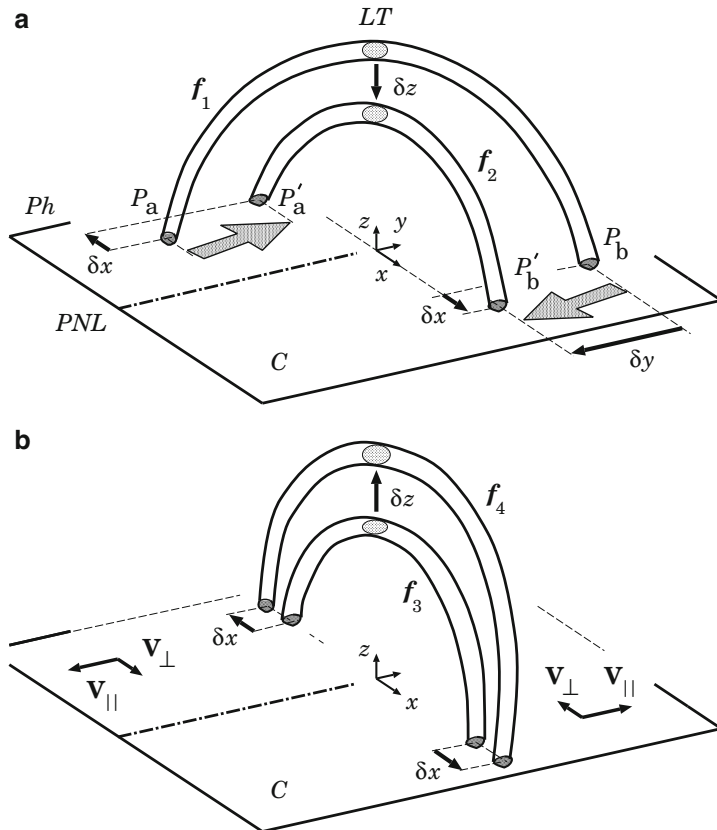


**Fig. 7.12** Schematic representation of the two-phase evolution of a solar flare in terms of the rainbow reconnection model. (a) The first (rising) phase: the rapid decrease of footpoint separation,  $\delta y$ , dominates an increase of distance between flare ribbons,  $\delta x$ . The looptop HXR source *LT* goes down. (b) The second (main) phase: the bright HXR kernels separate in opposite directions from the photospheric neutral line *PNL* and from each other. The looptop source moves upward (From Somov 2010; reproduced with permission © Pleiades Publishing, Ltd.)

a thermal injection spectrum, the model predicts two types of HXR coronal sources. (a) Thermal sources are formed in traps dominated by the betatron mechanism. (b) Nonthermal sources with a power-law spectrum appear when electrons are accelerated by the Fermi mechanism. With account of rare Coulomb collisions inside the trap, a double-power-low spectrum of trapped electrons is formed from a power-law spectrum of electron injection from SHTCL (Sect. 9.6).

It is important that the emission measure of fast electrons, trapped and accelerated inside the collapsing loop, is initially growing slowly with decrease of the loop length  $L(t)$  if we consider Fermi acceleration. As shown in Fig. 9.18a, the emission measure reaches its maximal value only when the loop length becomes as small as of about 0.2–0.1 of its initial length  $L(0)$ . With further shrinkage of the loop,

the emission measure decreases quickly to zero. As a consequence, the flux of HXR emission from the collapsing trap has a maximum at approximately the same values of remaining length of the loop (see  $l(t) = L(t)/L(0) \sim 0.2$  in Fig. 9.19a).

On the other hand, when the loop is just created by reconnection process at the X-point inside a thin reconnecting current layer, it is strongly stressed by magnetic tensions along magnetic field lines in direction from the X-point to the edge of the current layer. That is why the loop shrinks and becomes less stressed. Moreover, under the separator in the corona, the loop top goes down less quickly with the progress of time because the magnetic stress is decreasing continuously. In other words, the loop becomes less non-equilibrium, more close to a state with minimal energy, i.e. the potential state. In such a state, the height of the loop in the corona is naturally proportional to the distance between its feet in the photosphere. Therefore, it is reasonable to assume that, at the time when the collapsing loop has the maximal HXR brightness,

**|** the height of the LT HXR source in the corona is proportional to the distance between the FP HXR sources in the chromosphere.

Now we shall consider the consequences of this assumption coming back to the rainbow reconnection model. Figure 7.12a shows different flux tubes  $f_1$ ,  $f_2$  etc reconnected at different times  $t_1$ ,  $t_2$  etc; here  $t_2 > t_1$  etc. The first flux tube, the loop  $f_1$  manifests two FPs  $P_a$  and  $P_b$  and a LT HXR source  $LT$ . Figure 7.12a illustrates two effects.

The first one is the well-known classical effect, an increase of a distance between the flare ribbons because of reconnection in the coronal SHTCL. The displacements  $\delta x$  of FPs are antiparallel to the converging components  $\mathbf{V}_\perp$  of the velocity field in the photospheres (cf. Sect. 7.1.2). This means that two flare ribbons move out from the  $PNL$  as predicted, for example, by a standard model of two-ribbon flare.

The second effect is less trivial. The displacement  $\delta y$  of the FPs are parallel to the  $PNL$  because of relaxation of the nonpotential component of the field created by the photospheric shear flows before a flare. So this is the magnetic shear relaxation as discussed in Sect. 7.2. The displacements  $\delta y$  of FPs are antiparallel to the photospheric shear velocity  $V_\parallel$ . Since the photospheric shear mainly dominates in the vicinity of the  $PNL$ , during the first phase of a flare  $\delta y \gg \delta x$ .

In order to interpret the observational results related to the first phase, note that the magnetic loop  $f_1$  created earlier than the loop  $f_2$  has a larger altitude of a LT HXR source  $LT$  because the distance between its FPs  $P_a$  and  $P_b$  is larger than the distance between FPs  $P'_a$  and  $P'_b$ . That is why the source  $LT$  in the loop  $f_1$  is located higher in the corona than the  $LT$  source in the tube  $f_2$ . As a result, an apparent motion of the coronal HXR source is directed downwards:  $\delta z < 0$ . The descending motion of the coronal source is typical for the first phase in the flare on October 24, 2003 (Joshi et al. 2009), as well as presumably in many other flares (e.g., Liu et al. 2009).

The second phase of a flare involves in reconnection the magnetic field lines (and flux tubes) whose FPs are located at larger distance from the  $PNL$  and, therefore,

have a smaller shear or practically none as schematically illustrated by Fig. 7.12b. If so, the apparent displacements  $\delta x$  of FPs are directed from each other and from the *PNL*. The distance between FPs becomes larger with time, and the LT HXR source moves upward in agreement with the standard model. This seems to be fairly true for eruptive flares in the later stage when the primary energy source (i.e. reconnection site) is located high enough in the corona. It looks like that the standard model of the two-ribbon flares seems to be ‘asymptotically’ true at later stages. However this is not necessarily a charitable trust. Otherwise the shear effect may continue to work but in the opposite direction. It will increase the FP separation and, as a consequence, the height of the LT HXR sources. This additional magnetic shear must be accumulated before a flare of course.

In several flares of 72 events analyzed by [Somov et al. 2005a](#) on the basis of the *Yohkoh HXT* data, it was not simple to distinguish a flare with a decreasing FP separation parallel to the *PNL* as discussed above from a flare with increasing separation also parallel to the *PNL*, because both kinds of separation were present in the same flare. In the onset of such a flare, the FP sources move one to another and the distance between them decreases. Then they pass through a ‘critical point’. At this particular moment, the line connecting the FP sources is nearly perpendicular to the straight *PNL* (like shown in Fig. 7.12b). In general, we should characterize the photospheric magnetic field by a *smoothed, simplified neutral line (SNL)*, see Sect. 4.3.1) which is not a straight line. After that moment, the FP sources move one from other with increasing separation between them (for example, the M4.4 flare on 2000 October 29 at 01:46 UT; see Fig. 2 in [Somov et al. 2005a](#)).

Such a motion pattern seems to be similar to that one predicted by the rainbow reconnection model after the critical moment shown in Fig. 7.12b. Starting that moment, the shear relaxation must continue ( $\delta y > 0$ ) if the excess of coronal magnetic tensions has been released during the first phase not completely. Otherwise the ordinary reconnection process ( $\delta y = 0$ ) dominates during the second phase describing the ordinary energy release in terms of the classical standard model. Note that in both cases  $\delta x > 0$  and therefore during the second phase the FP separation increases and, as a consequence, the height of the LT HXR sources increases too.

In modeling large two-ribbon flares, like the Bastille Day flare on 2000 July 14, more complicated (in comparison with the illustrative rainbow reconnection model used above) topological models give much better approximation and explain more detail (see Sect. 6.2). However exactly the same physical ideas ([Somov et al. 2002a](#)) concerning the role of photospheric motions before a flare are hold and well supported by modern multi-wavelength investigations of two-ribbon flares. For example, the HXR observations by *RHESSI* show that the conjugated FPs first do move toward and than away from each other, mainly parallel and perpendicular to the *PNL* respectively. Moreover the transition from the first to the second type of these apparent motions coincides with the direction reversal of the motion of the looptop HXR source, i.e. with the transition from the first (rising) to the second (main) phase in flare evolution ([Liu et al. 2009](#)).

## 7.6 Open Issues and Some Conclusions

On the basis of what we saw above, we assume that the energy of a large solar flare (like the Bastille day 2000 flare) is accumulated in the following main forms.

- (a) Magnetic energy of a *slowly-reconnecting current layer* (RCL) at a separator in the corona. This excess energy in the amount sufficient to produce a large two-ribbon flare, like the Bastille day flare, can be accumulated in the pre-flare active region and can be quickly transformed into observed forms of the flare energy if the RCL becomes a *super-hot turbulent-current layer* (SHTCL, see Sect. 8.3).
- (b) The magnetic energy of the *current layers at the separatrices* and the distributed currents generated in the pre-flare active region by the photospheric *shear flows*, seems to be sufficiently high to influence the main reconnection process at the separator (or separators) in a large solar flare. In general, the energy of a large-scale ( $\gtrsim 10^9$  cm) sheared component of magnetic field participates in energetics of the main reconnection process in the corona presumably with a positive (negative) contribution in more (less) impulsive Sakao-type flares.
- (c) In the vicinity of the photospheric neutral line, some part of energy is also accumulated as the energy of the sheared magnetic field and twisted filament. It is not clear, however, if we could consider this to be a part of the pre-flare configuration in the *force-free approximation* which would be the simplest model for a magnetic field configuration to compute and analyze its surplus energy. However the *non-magnetic forces*, including the gas pressure gradient in a high- $\beta$  (high-density and high-temperature) plasma, the inertia-type (proportional to  $\partial \mathbf{v} / \partial t + (\mathbf{v} \cdot \nabla) \mathbf{v}$ ) term, in particular the centrifugal force (Shibasaki 2001), can make the non-force-free part locally significant in the pre-flare structure of an active region. Unfortunately we do not know the value of the related energy excess either observationally or theoretically.

The *non-force-free* component of magnetic field participates in the flare development process, but we do not know from observations whether it plays the primary role in a flare triggering or it is initiated somehow by reconnection at the separator (e.g., Uchida et al. 1998). For example, Antiochos et al. (1999), Aulanier et al. (2000) proposed that reconnection in the corona, above a sheared neutral line, removes a magnetic flux that tends to hold down the sheared low-lying field and thereby allows the sheared field to erupt explosively outward. *Yohkoh*, *SOHO* and *TRACE* data do not seem to be capable of providing the necessary information to make a choice between these two possibilities. We hope this problem will be well investigated with the *Hinode* mission (see Sect. 16.6).

Reconnection at two levels (in the corona and in the photosphere) plays different roles in solar flares. *Photospheric reconnection* seems to be mainly responsible for supply of a cold dense plasma upward, into pre-flare filament *prominences*. Wang and Shi (1993) suggested however that the photospheric reconnection transports the magnetic energy and ‘complexity’ into the rather large-scale structure higher in the

corona. According to [Deng et al. \(2001\)](#), the effect of photospheric reconnection was manifested by the change of non-potentiality at least 9 h before the Bastille day flare. The energy was gradually input into the higher solar levels. Therefore

the slow magnetic reconnection in the photosphere, observed as magnetic flux cancellation, seems to play a key role in the energy build-up process before a solar flare.

Two level reconnection in solar flares has been modeled by [Kusano \(2005\)](#) by numerical integration of the 3D dissipative MHD equations, in those the pressure gradient force and the density variation are neglected. The simulation is initiated by adding a small 3D perturbation to a quasi-static 2D equilibrium, in which the magnetic shear is reversed near the magnetic neutral line in the photosphere. This initial state is given by the solution of the *linear* force-free field equation.

The simulation results indicate that reconnection driven by the resistive tearing mode instability (see Chap. 13) growing on the magnetic shear inversion layer (cf. Fig. 7.6) can cause the spontaneous formation of *sigmoidal structure*. The reconnection of the tearing instability works to eliminate the reversed-shear magnetic field in the lower corona. Furthermore, it is also numerically demonstrated that the formation of the sigmoids can be followed by the explosive energy liberation, if the sigmoids contain sufficient magnetic flux.

**Coronal reconnection**, being slow before a flare, allows to accumulate a sufficient amount of magnetic energy. During a flare, the *fast* reconnection process in the corona, converts this excess of energy into kinetic and thermal energies of fast particles and super-hot plasma. As for the physical mechanism of large solar flares, like the Bastille day flare, we assume that it is the *collisionless three-component reconnection* at the separator in the corona ([Somov et al. 1998](#)).

More specifically, we assume that before the large-scale two-ribbon flares with an observed significant decrease of the footpoint separation, like the Bastille day flare, two conditions are satisfied ([Somov et al. 2002a](#)). First, the separatrices are involved in the large-scale *shear photospheric flow*, which can be traced, for example, by proper motions of main sunspots. The second condition is the presence of an RCL generated by large-scale *converging motion* of the same spots.

These two conditions seem to be sufficient ones for an active region to produce a huge two-ribbon flare similar to the Bastille day flare. Other realizations of large solar flares are possible, of course, but this one seems to be the most favorable situation. At least, in addition to the flare HXR ribbons and kernels, it explains formation of the twisted filament prominences along the photospheric neutral line before and after the Bastille day flare.

# Chapter 8

## Models of Reconnecting Current Layers

**Abstract** Reconnection in astrophysical plasma serves as a highly efficient engine to convert magnetic energy into thermal and kinetic energies of plasma flows and accelerated particles. Stationary models of the reconnection in current layers are considered in this Chapter. Properties of a stationary current layer strongly depends on a state of plasma turbulence inside it. The *super-hot turbulent-current layer* (SHTCL) model fits well for solar flares with different properties: impulsive and gradual, compact and large-scale, thermal and non-thermal.

### 8.1 Magnetically Neutral Current Layers

#### 8.1.1 *The Simplest MHD Model*

Let us consider two consequent approximations used to study the reconnection process in current layers. The first of them was the *neutral* current layer model (Sweet 1969; Parker 1979; Syrovatskii 1981). This was initially the simplest two-dimensional (2D) configuration of steady reconnection. Two oppositely directed magnetic fields are pushed together into the neutral layer as shown in Fig. 8.1. The uniform field  $\mathbf{B}_0$  immediately outside the layer is frozen into the uniform plasma inflow with a velocity  $\mathbf{v}_0$  perpendicular to the field. The plasma flows out of the neutral layer through its edges with a large velocity  $\mathbf{v}_1$  perpendicular to the velocity  $\mathbf{v}_0$ .

The strength of the magnetic field,  $B_0$ , on the inflow sides of the neutral layer can be found out, for example, from the analytical solution of the problem for the vertical current layer in the solar corona above a dipole source of the field in the photosphere (Somov and Syrovatskii 1972). This would be just the case of the so-called ‘standard model’ for solar flares with the *two-ribbon structure* (see Tsuneta 1996, and references there). The strength of the electric field,  $E_0$ , near the

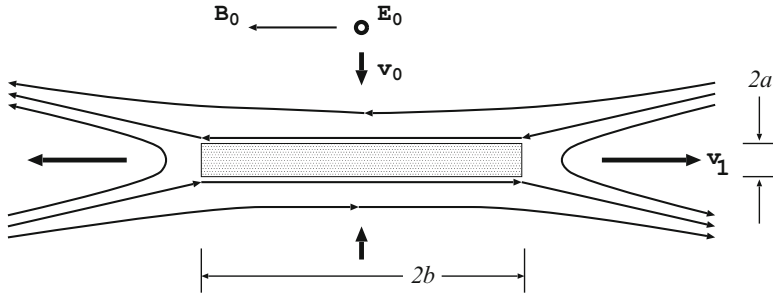


**Fig. 8.1** A schematic drawing of the field lines undergoing reconnection across the neutral current layer according to Sweet-Parker model

current layer can be estimated for a given value of the velocity  $v_0$  for the coronal plasma inflow (Yokoyama et al. 2001) into the *reconnecting current layer* (RCL) and for a given value of the magnetic field  $B_0$ .

By definition, there is no magnetic field inside the neutral layer; that is why it is called a *neutral* or, more exactly, a *magnetically neutral* RCL. This oversimplified approximation seems to be good, however, only for a low-temperature RCL, for example, for *cold dense* pre-flare current layers because heat conduction does not play any role in the energy balance for such RCL (Sect. 8.1.2). Although it is a strong idealization, the approximation of a neutral layer is still useful for several reasons.

First, the neutral layer approximation demonstrates the existence of two linear scales corresponding to two different physical processes. (a) The layer half-thickness

$$a \approx \frac{v_m}{v_0} \quad (8.1)$$

is the dissipative scale responsible for the rate of reconnection; here  $v_m = c^2 (4\pi\sigma)^{-1}$  is the *magnetic diffusivity*. (b) The layer width  $2b$  is responsible for the accumulation of magnetic energy (Syrovatskii 1976a). The wider the reconnecting layer, the larger is the energy accumulated in the region of the reconnecting magnetic fluxes interaction.

Second, the neutral layer approximation indicates that very efficient acceleration of particles can work in the RCL (Sect. 1.2). Let us take as the low limits for the magnetic field  $B_0 \approx 50$  G and for the inflow velocity  $v_0 \approx 20$  km s<sup>-1</sup>. These values are smaller than those estimated from the *Yohkoh* SXT and HXT observations of the well studied impulsive flare on 1992 January 13 – the magnetic field strength in the supposed Petschek-type (Exercise 12.1) upstream plasma 50 G and the inflow speed range 40–140 km s<sup>-1</sup>, respectively (Tsuneta et al. 1997). So the lower limit for the electric field can be estimated as

$$E_0 = \frac{1}{c} v_0 B_0 \approx 1 \text{ V cm}^{-1}. \quad (8.2)$$

This field is much stronger than the Dreicer's field – the electric field strength for which the critical runaway speed is equal to the electron thermal velocity (see Appendix 3):

$$E_{\text{Dr}} = \frac{4\pi e^3}{k_B} (\ln \Lambda) \frac{n}{T} \approx 10^{-4} \text{ V cm}^{-1}. \quad (8.3)$$

Here we have assumed that the density and temperature of the plasma near the RCL  $n_0 \approx 4 \times 10^8 \text{ cm}^{-3}$  and  $T_0 \approx 3 \times 10^6 \text{ K}$ . In fact, near the RCL in solar flares, the magnetic field  $B_0$  can be as high as 100–300 G. So the electric field  $E_0$  can be even stronger by one order of magnitude (Somov et al. 1981).

Since  $E_0 \gg E_{\text{Dr}}$ , we neglect collisional energy losses (Dreicer 1959; Gurevich 1961) as well as wave-particle interaction of fast particles (Gurevich and Zhivlyuk 1966). So

the neutral layer model predicts very impulsive acceleration of charged particles by the direct strong electric field  $\mathbf{E}_0$ .

This advantage of the RCL will be discussed in Chap. 11 with account of the fact that real reconnecting layers are always magnetically non-neutral: they always have an internal magnetic field. The influence of this three-component field inside the RCL on the particle acceleration is considered in Chap. 11. The main disadvantage of the neutral layer model is that it does not explain the high power of the energy release in solar flares. The reason will be explained in Sect. 8.2 by using a less idealized model of the RCL.

### 8.1.2 The Current Layer by Syrovatskii

To establish relations between the parameters of a neutral layer in *compressible* plasma let us use the equations of continuity and momentum. Under conditions of the strong magnetic field (see Part I, Sect. 13.1.3) these equations are rewritten as the following *order-of-magnitude* relations:

$$n_0 v_0 b = n_s v_1 a, \quad (8.4)$$

$$\frac{B_0^2}{8\pi} = 2n_s k_B T, \quad (8.5)$$

$$2n_s k_B T = \frac{1}{2} M n_s v_1^2. \quad (8.6)$$

Here  $n_0$  and  $n_s$  is plasma density outside and inside the layer, respectively.  $T$  is temperature of the plasma inside the layer.

It follows from Eqs. (8.5) and (8.6) that the velocity of outflow from the current layer

$$v_1 = V_{A,S} = \frac{B_0}{\sqrt{4\pi M n_s}} . \quad (8.7)$$

Note that the value of the magnetic field  $B_0$  is taken outside the layer, but for plasma density it is taken *inside* the neutral layer. So the outflow velocity (8.7) *differs* from the Alfvén speed outside the layer

$$V_{A,0} = \frac{B_0}{\sqrt{4\pi M n_0}} . \quad (8.8)$$

The downstream flow velocity  $v_1$  of a compressed plasma is *not* equal to the upstream Alfvén speed outside the layer  $V_{A,0}$ .

Depending on the compression ratio  $n_s/n_0$  the outflow velocity

$$v_1 = V_{A,0} \left( \frac{n_0}{n_s} \right)^{1/2} \quad (8.9)$$

can be much smaller than the Alfvén speed outside the current layer  $V_{A,0}$  (Syrovatskii 1976b).

The inflow velocity equals the velocity of the plasma drift to the neutral layer

$$v_0 = V_d = c \frac{E_0}{B_0} . \quad (8.10)$$

Hence we have to add an equation which relates the electric field  $E_0$  with the current layer parameters. From the Maxwell equation for  $\text{rot } \mathbf{B}$

$$\frac{c B_0}{4\pi a} = \sigma E_0 . \quad (8.11)$$

Here

$$\sigma = \sigma_0 T^{3/2} \quad (8.12)$$

is the *classical* Coulomb conductivity.

Following Syrovatskii (1976b), from Eqs. (8.4)–(8.6) and (8.11) the layer half-thickness  $a$ , its half-width  $b$ , and the plasma density inside the layer  $n_s$  can be expressed in terms of three ‘external’ (assumed known) parameters  $n_0$ ,  $h_0 = B_0/b$ ,  $E_0$  and the unknown equilibrium temperature  $T$  of the plasma inside the current layer:

$$a = b \frac{c}{4\pi\sigma_0} \left( \frac{h_0}{E_0} \right) \frac{1}{T^{3/2}} , \quad (8.13)$$

$$b = 4\pi \left( \frac{k_B \sigma_0^2 M}{4\pi^2} \right)^{1/6} \left( \frac{n_0 E_0^2}{h_0^4} \right)^{1/3} T^{2/3}, \quad (8.14)$$

$$n_s = \left( \frac{\pi \sigma_0^2 M}{4k_B^2} \right)^{1/3} \left( \frac{n_0 E_0^2}{h_0} \right)^{2/3} T^{1/3}. \quad (8.15)$$

To determine the temperature  $T$  let us add the energy equation in the following form:

$$\frac{B_0^2}{4\pi} V_d b = L(T) n_s^2 ab. \quad (8.16)$$

It is assumed here that the temperature of the neutral layer is not high; so the energy transfer from the layer by plasma outflow and by heat conduction play a secondary role. The principal factors are the influx of magnetic energy into the current layer and radiative cooling. The radiative loss function  $L(T)$  can be taken, for example, from Cox and Tucker (1969). More justifications for simple Eq. (8.16) follow from the more detailed numerical model by Oreshina and Somov (1998); see also a comparison between different models in Somov and Oreshina (2000).

Substituting the solution (8.13)–(8.15) in Eq. (8.16) we obtain the following equation for the temperature of the plasma inside the current layer:

$$T = \sigma_0^{2/5} \left( \frac{\pi M}{4k_B^2} \right)^{4/5} \Gamma_s^{4/5} L^{6/5}(T). \quad (8.17)$$

Here

$$\Gamma_s = \frac{n_0^2 E_0}{h_0^2} \quad (8.18)$$

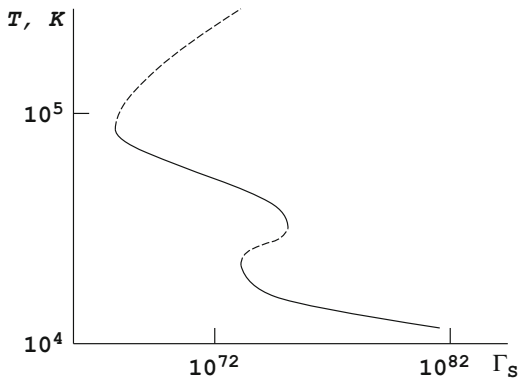
is the dimensional parameter which characterizes the reconnection conditions. Therefore the values  $n_0$ ,  $h_0$ , and  $E_0$  must be specified in advance. The other quantities can be determined from the solution (Exercise 8.1).

Figure 8.2 shows a solution of Eq. (8.17) with two unstable branches indicated by dashed curves. On these branches a small deviation of the temperature from equilibrium will cause the deviation to increase with time. It means that the *thermal instability* of the current layer occurs.

The first appearance of the thermal instability, at  $T \approx 2 \times 10^4$  K, is caused by emission in the  $\text{Ly}\alpha$  line of hydrogen. It can hardly be considered significant since the function  $L(T)$  was taken from Cox and Tucker (1969) without allowance for the absorption of radiation, which may be important for the hydrogen lines in the solar chromosphere. On the contrary, the second break, at

$$T \approx 8 \times 10^4 \text{ K}, \quad \Gamma_s \approx 3.8 \times 10^{26}, \quad (8.19)$$

**Fig. 8.2** The equilibrium temperature of a neutral current layer as a function of Syrovatskii's parameter  $\Gamma_s$ . Two unstable branches are dashed



will necessarily occur because of the maximum in the radiative cooling function  $L(T)$ . Near this maximum, in the region where  $L(T) \propto T^\alpha$  with  $\alpha < 1$ , the *condensation mode* of the thermal instability (Field 1965) occurs (see also Somov and Syrovatskii 1976a, 1982).

Syrovatskii (1976b) assumed that the temperature  $T$  of a *cold dense* current layer in the solar atmosphere gradually increases in the pre-flare stage until the critical values (8.19) are reached. Then the current layer can no longer stay in equilibrium; the radiative losses of energy (i.e., *radiative cooling*) cannot balance the *Joule heating*, and the temperature of the layer rapidly rises. This leads to a flare. In this way, Syrovatskii suggested to identify the thermal instability of a cold dense current layer with the onset of the eruptive phase of a solar flare.

Whether such a *thermal trigger* for solar flares occurs or not is unclear yet (Somov and Syrovatskii 1982). It is clear only that heating of the reconnecting current layer (RCL) leads to the powerful heat-conductive cooling of the plasma electron component. This effect is important for energy balance of a '*super-hot*' ( $T \gtrsim 3 \times 10^7$  K) turbulent-current layer (SHTCL) discussed in Sect. 8.3.

### 8.1.3 Simple Scaling Laws

In order to determine the parameters of a stationary driven reconnection configuration, the stationary *resistive* MHD equations (see Part I, Sect. 12.2.2) must be solved for given boundary conditions. Unfortunately it appears that the problem is too complicated to permit analytical solutions without severe approximations. The severest of them are called the *scaling 'laws'*.

Let us come back to **the Sweet-Parker model** of reconnection in *incompressible* plasma (Sect. 8.1.1). The *order-of-magnitude* relations introduced above (in Sect. 8.1.2) become simpler:

$$v_0 b = v_1 a , \quad (8.20)$$

$$v_0 = \frac{v_m}{a} , \quad (8.21)$$

$$v_1 = V_{A,0} . \quad (8.22)$$

These equations follow from (8.4)–(8.15) and give us the ratio of the inflow (upstream) velocity of the incompressible plasma to the upstream Alfvén speed:

$$\frac{v_0}{V_{A,0}} = \left( \frac{v_m}{V_{A,0} b} \right)^{1/2} . \quad (8.23)$$

The left-hand side of the relation (8.23) is called the Alfvén-Mach number  $M_A$  and is conventionally used as a dimensionless measure of the reconnection rate. The right-hand side is simply related to the magnetic Reynolds number (see Appendix 3), more exactly

$$\text{Re}_m(V_{A,0}, b) = \frac{V_{A,0} b}{v_m} \equiv N_L . \quad (8.24)$$

Here  $N_L$  is called the Lundquist number. Therefore the Sweet-Parker reconnection rate

$$M_A = N_L^{-1/2} .$$

(8.25)

Order-of-magnitude relations similar to (8.25) are often called scaling ‘laws’. They certainly do not have a status of any law but are useful since they simply characterize the *scaling properties* of stationary reconnecting configurations as a proper dimensionless parameter.

Since in formula (8.24) the linear scale  $L$  is taken to be equal to the large half-width  $b$  of the Sweet-Parker neutral layer, the Lundquist number (8.25) is rather a *global* parameter of the reconnection problem. In the most cases of practical interest the Lundquist number is too large, typically  $10^{14}$ – $10^{15}$  in the solar corona (Exercise 8.1), such that the Sweet-Parker rate would lead to reconnection times many orders of magnitude longer than observed in flares. This means that

slowly-reconnecting current layers can exist in the solar corona for a long time.

In general, scaling relations are useful to summarize and classify different regimes and configurations of magnetic reconnection as they are observed, for example, in numerical simulations (see Chap. 6 in Biskamp 1997; Horiuchi and Sato 1994).

## 8.2 Magnetically Non-neutral RCL

Magnetic neutrality of the reconnecting current layer (RCL), as assumed in the previous Section, means that there is no penetration of magnetic field lines through the layer (the *transversal* field  $\mathbf{B}_\perp = 0$ ) as well as no *longitudinal* magnetic field which is parallel to the electric current inside the RCL (the longitudinal field  $\mathbf{B}_\parallel = 0$ ). In general, both assumptions are incorrect (see Somov 1992). The first of them is the most important for what follows in this Chapter.

### 8.2.1 Transversal Magnetic Fields

As it reconnects, every field line penetrates through the current layer as shown in Fig. 8.3. So the reconnecting layer is magnetically non-neutral by definition because of physical meaning of the reconnection process. In many real cases (for example, the magnetospheric tail or interplanetary sectorial current layers) a small transversal component of the magnetic field is well observed. This is also the case of laboratory and numerical experiments (Hesse et al. 1996; Ono et al. 1996; Horiuchi and Sato 1997; Horiuchi et al. 2001).

We characterize the penetration of the magnetic field into the current layer by the parameter

$$\xi_\perp = B_\perp / B_0 \quad (8.26)$$

which is the relative value of the transversal component  $\mathbf{B}_\perp$ ;  $B_0$  is the strength of magnetic field on the inflow sides of the RCL. As distinguished from the neutral-layer approximation, we assume that  $\xi_\perp \neq 0$  and satisfies the inequality

$$a/b \ll \xi_\perp \ll 1. \quad (8.27)$$

What are the consequences of such a penetration?

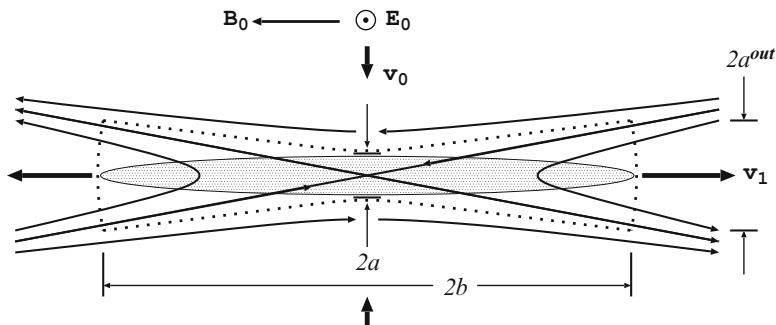


**Fig. 8.3** A magnetically non-neutral reconnecting layer: the electric current distribution is schematically shown by the *shadow*, the *dotted boundary* indicates the field lines going through the current layer

The penetration of even a very small transversal field into the high-temperature layer essentially increases the outflows of energy and mass from the layer along the field lines. The effective cross-section for the outflows of energy and mass is proportional to the outflow scale

$$a^{out} \approx \xi_{\perp} b \gg a. \quad (8.28)$$

Hence, corresponding to three different physical processes,

the magnetically non-neutral current layer is characterized by three different linear scales:

$2a$  is a small dissipative thickness of the layer,  $2b$  is the scale responsible for the energy accumulation process, and  $2a^{out}$  is the linear scale which determines the outflow of energy and mass along the field lines into the surrounding plasma.

As we shall see in Sect. 8.3, even a very small (like  $\xi_{\perp} \approx 10^{-3}$ ) transversal field **B**<sub>⊥</sub> **significantly increases the plasma outflows** as well as the heat-conductive cooling of the non-neutral *super-hot turbulent-current layer* (SHTCL). As a result, its energy output is much larger than that in the neutral layer model for SHTCL. (In the neutral-layer approximation  $a^{out} = a$ .) The last reason will enable us to consider the SHTCL with a small transversal component of the magnetic field as the source of energy in solar flares.

### 8.2.2 *The Longitudinal Magnetic Field*

As we saw in Chaps. 4 and 6, the reconnection process under the actual conditions in the solar atmosphere is released at the separator which differs from the X-type neutral line in that the separator has a *longitudinal* field **B**<sub>||</sub>. In this context, it is necessary to understand the physical effects that are created by the longitudinal field, often called the *guide* field (parallel to the X-line or separator), inside the RCL and its vicinity.

It is intuitively clear that the longitudinal field at the separator decreases the reconnection rate

$$\mathbf{v}_0 = c \frac{\mathbf{E}_0 \times (\mathbf{B}_0 + \mathbf{B}_{\parallel 0})}{B_0^2 + B_{\parallel 0}^2} = c \frac{\mathbf{E}_0 \times \mathbf{B}_0}{B_0^2 [1 + (B_{\parallel 0}/B_0)^2]} . \quad (8.29)$$

Here **B**<sub>0</sub> and **B**<sub>||0</sub> are the strengths of the reconnecting component and of the longitudinal component of the magnetic field on the inflow sides of the layer, respectively. They are not *free* parameters, they have to be determined from a self-consistent solution of the problem on the RCL properties.

The appearance of the longitudinal field changes, first of all, the balance of forces across the layer. The pressures of the plasma and the magnetic field outside the RCL

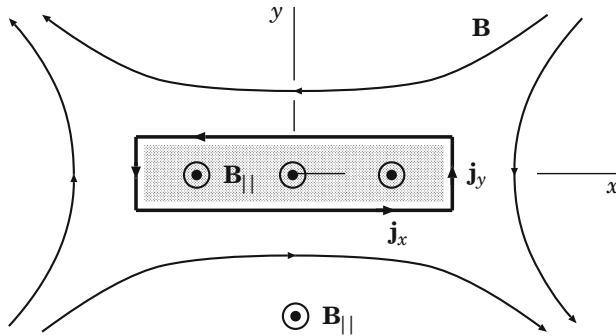


**Fig. 8.4** A model of a reconnecting current layer with a longitudinal component  $\mathbf{B}_{\parallel}$  of a magnetic field

should balance not only the plasma pressure but also the magnetic pressure of the longitudinal field inside it:

$$2n_0k_B T_0 + \frac{B_0^2}{8\pi} + \frac{B_{\parallel 0}^2}{8\pi} = 2n_s k_B T + \frac{B_{\parallel s}^2}{8\pi}. \quad (8.30)$$

Here  $n_0$  and  $n_s$  are the plasma densities outside and inside the current layer.  $T_0$  is the temperature of inflowing plasma outside the layer,  $T$  is the temperature of plasma inside the layer. In the right-hand side of Eq. (8.33)  $B_{\parallel s}$  is the strength of the longitudinal field inside the current layer.

If the longitudinal field could be effectively accumulated inside the current layer, its pressure would impose strong limitations on the layer compression and, hence, on the rate of reconnection. In terms of the *ideal* MHD approximation, the longitudinal field must increase proportionally to the plasma density  $n_s$  inside the layer because the field is frozen in the plasma:

$$B_{\parallel s} = B_{\parallel 0} \frac{n_s}{n_0}. \quad (8.31)$$

On the contrary, in a real finite-conductivity plasma, the increase of the longitudinal field is accompanied by dissipative effects. As soon as the longitudinal field inside the layer becomes stronger than that outside the layer, a gradient of the longitudinal field  $\mathbf{B}_{\parallel}$  will appear and give rise to an electric current circulating in the transversal (relative to the main current  $j_z$  in the layer) plane ( $x, y$ ). This current circulation is represented schematically in Fig. 8.4. Direct evidence of the enhancement of the guide field inside the current layer during its formation was obtained on the basis of magnetic measurements in the laboratory experiments by Frank et al. (2009). It was shown that the total value of  $\mathbf{j}_x$ -current is comparable with the main current  $\mathbf{J}_z$  that produces the current layer itself. Thus, the dissipation was not essential during the stage of current layer formation.

In its turn, the dissipation of circulating current produced by the field compression affects the  $\mathbf{B}_{\parallel}$  field value (Somov and Titov 1985a). Thus the compression of the longitudinal field seems to facilitate its dissipation. In reality, however, this problem proves to be more delicate; see Somov and Titov (1985b), Somov (1992).

The essence of the effect is that any compression of the longitudinal field  $\mathbf{B}_{\parallel}$  within a current layer does create a gradient of the longitudinal field,  $\nabla \mathbf{B}_{\parallel}$ . By so doing, compression generates an associated electric current  $\mathbf{J}_{\perp}$  which circulates in the transversal (relative to the main current  $\mathbf{J}$  in the layer) plane. The ohmic dissipation of the current  $\mathbf{J}_{\perp}$ , circulating around the layer, gives rise to an outward diffusion of the longitudinal field from the current layer and to the Joule heating of the plasma. More exactly, because of ohmic dissipation of the circulating current, plasma moves into the RCL relatively free with respect to the longitudinal component of magnetic field.

It is of importance that

**the total flux of the longitudinal field is conserved**, while the Joule heating due to the  $\mathbf{B}_{\parallel}$  field compression is produced by the dissipation of the reconnecting magnetic field  $\mathbf{B}_0$ .

This effect should be considered quantitatively in the approximation *dissipative* MHD but it is certainly valid also for *collisionless* reconnection in the RCL.

On the one hand, the magnetic field compression decreases the velocity  $v_0$  of plasma inflows. On the other hand, due to the large magnetic diffusion in the small scale of the current layer thickness  $2b$ , the longitudinal field  $\mathbf{B}_{\parallel}$  perhaps does not have an overwhelming effect on the parameters of the current layer and the reconnection rate. For this reason, we regard as likely that

**the longitudinal field  $\mathbf{B}_{\parallel}$  at the separator changes the reconnection rate in the current layer not too strongly in comparison with the transversal magnetic field  $\mathbf{B}_{\perp}$ .**

This is especially true if the compression of the plasma inside the RCL,  $n_s/n_0$ , is not high, for example, in *super-hot turbulent-current layers* (SHTCL) of solar flares (see Sect. 8.4.2). Therefore, in the first approximation, we can neglect the longitudinal magnetic field in the next Section.

## 8.3 Basic Physics of the SHTCL

### 8.3.1 A General Formulation of the Problem

Coulomb collisions do not play any role in the *super-hot turbulent-current layers* (SHTCL). So the plasma inside the SHTCL has to be considered as essentially *collisionless* (Somov 1992). The concept of an anomalous resistivity, which originates from wave-particle interactions, is then useful to describe the fast conversion from

field energy to particle energy. Some of the general properties of such a **collisionless reconnection** can be examined in a frame of a self-consistent model which makes it possible to estimate the main parameters of the SHTCL. Basing on the mass, momentum and energy *conservation laws*, we write the following relations that are valid for a quarter of the current layer and a unit length along the electric current (Somov and Titov 1985b):

$$n_0 v_0 b = n_s v_1 a^{out}, \quad (8.32)$$

$$2n_0 k_B T_0 + \frac{B_0^2}{8\pi} = n_s k_B T \left(1 + \frac{1}{\theta}\right), \quad (8.33)$$

$$n_s k_B T \left(1 + \frac{1}{\theta}\right) = \frac{1}{2} M n_s v_1^2 + 2n_0 k_B T_0, \quad (8.34)$$

$$\chi_{ef} \mathcal{E}_{mag}^{in} + \mathcal{E}_{th,e}^{in} = \mathcal{E}_{th,e}^{out} + \mathcal{C}_{\parallel}^{an}, \quad (8.35)$$

$$(1 - \chi_{ef}) \mathcal{E}_{mag}^{in} + \mathcal{E}_{th,i}^{in} = \mathcal{E}_{th,i}^{out} + \mathcal{K}_i^{out}. \quad (8.36)$$

Here  $n_0$  and  $n_s$  are the plasma densities outside and inside the current layer.  $T_0$  is the temperature of inflowing plasma outside the layer,  $T = T_e$  is an effective electron temperature (the mean kinetic energy of chaotic motion per single electron) inside the SHTCL, the ratio  $\theta = T_e/T_i$ ,  $T_i$  is an effective temperature of ions.

$$v_0 = V_d = c \frac{E_0}{B_0} \quad (8.37)$$

is the velocity of the *electric drift* of plasma in direction to the current layer, and

$$v_1 = V_{A,S} = \frac{B_0}{\sqrt{4\pi M n_s}} \quad (8.38)$$

is the velocity of the plasma outflow from the layer. Compare this approximate formula with (8.7).

The continuity Eq. (8.32) as well as the energy Eqs. (8.35) and (8.36) are of integral form for a quarter of the current layer assumed to be symmetrical and for a unit length along the electric current.

The left-hand sides of the energy equations for electrons (8.35) and ions (8.36) contain the magnetic energy flux (see Part I, formula (12.74))

$$\mathcal{E}_{mag}^{in} = \frac{B_0^2}{4\pi} v_0 b, \quad (8.39)$$

which coincides with the direct heating of the ions and electrons due to their interactions with waves. A relative fraction  $\chi_{ef}$  of the heating is consumed by electrons, while the remaining fraction  $(1 - \chi_{ef})$  goes to the ions.

The electron and ion temperatures of the plasma inflowing to the layer are the same. Hence, the fluxes of the electron and ion thermal energies are also the same:

$$\mathcal{E}_{th,e}^{in} = \mathcal{E}_{th,i}^{in} = \frac{5}{2} n_0 k_B T_0 \cdot v_0 b . \quad (8.40)$$

Because of the difference between the effective temperatures of electrons and ions in the outflowing plasma, the electron and ion thermal energy outflows also differ:

$$\mathcal{E}_{th,e}^{out} = \frac{5}{2} n_s k_B T \cdot v_1 a^{out} , \quad \mathcal{E}_{th,i}^{out} = \frac{5}{2} n_s k_B \frac{T}{\theta} \cdot v_1 a^{out} . \quad (8.41)$$

The ion kinetic energy flux from the layer

$$\mathcal{K}_i^{out} = \frac{1}{2} M n_s v_1^2 \cdot v_1 a^{out} \quad (8.42)$$

is important in the energy balance (8.36). As to the electron kinetic energy, it is negligible and disregarded in (8.35). However, electrons play the dominant role in the *heat conductive* cooling of the SHTCL:

$$\mathcal{C}_{\parallel}^{an} = f_M(\theta) \frac{n_s (k_B T)^{3/2}}{M^{1/2}} a^{out} . \quad (8.43)$$

Here

$$f_M(\theta) = \begin{cases} \frac{1}{4} \left( \frac{M}{m} \right)^{1/2} & \text{at } 1 \leq \theta \leq 8.1 , \\ \left( \frac{M}{m} \right)^{1/2} \theta^{3/2} \left[ \left( 1 + \frac{3}{\theta} \right)^{1/2} - \frac{1}{\theta^{1/2}} \right] \times \\ \times \exp \left[ -\frac{2(\theta+3)}{5} \right] + \left( 1 + \frac{3}{\theta} \right)^{1/2} & \text{for } \theta > 8.1 \\ & \text{or } \theta < 1 . \end{cases} \quad (8.44)$$

is the Manheimer function which allows us to consider the magnetic-field-aligned *anomalous* thermal flux depending on the effective temperature ratio  $\theta$ .

Under the coronal conditions derived from the *Yohkoh* and *RHESSI* data, especially in flares, contributions to the energy balance are not made either by the energy exchange between the electrons and the ions due to collisions, the thermal flux across the magnetic field, and the energy losses for radiation. For example, the radiative cooling time of plasma inside a SHTCL is much longer than the characteristic time  $b/V_{A,S}$ ; see estimates in Uzdensky (2007b). The magnetic-field-aligned thermal flux becomes anomalous and plays the dominant role in the cooling of electron component inside the current layer. All these properties are typical for collisionless ‘super-hot’ ( $T_e \gtrsim 30$  MK) plasma in the solar corona.

Under the same conditions, the effective *anomalous conductivity*  $\sigma_{ef}$  in the Ohm’s law

$$\frac{c B_0}{4\pi a} = \sigma_{ef} E_0 , \quad (8.45)$$

as well as the relative fraction  $\chi_{\text{ef}}$  of the direct heating consumed by electrons, are determined by the wave-particle interaction inside the SHTCL and depend on a type of plasma turbulence and its regime (Chap. 3 in Somov 1992).

Once the current-driven *anomalous resistivity*  $\sigma_{\text{ef}}^{-1}$  build up in the SHTCL, both the reconnection rate and the anomalous resistivity simultaneously grow to enhance each other, eventually giving rise to fast powerful reconnection. Thus we shall assume that the electromagnetic fluctuations in plasma turbulence furnish enough resistivity and enough scattering to convert the acceleration of thermal electrons and ions due to the direct electric field  $E_0$  into thermal energy of particles.

For example, if the resistivity was caused by Coulomb collisions, then it would depend on the electron temperature only. However, when the plasma is in a **collisionless turbulent state**, the electrons carrying the electric current and the ions interact with the electromagnetic-field fluctuations in the waves, which change the resistivity and other transport coefficients of the plasma in a way that depends on the type of waves that grow and level of turbulence (see Sect. 8.4). In this way, the SHTCL can produce significant amount of super-hot plasma.

### 8.3.2 Problem in the Strong Field Approximation

Let the conditions of a strong magnetic field (see Part I, Sect. 13.1.3) be satisfied. Then, the set of Eqs. (8.32)–(8.36) takes the following simpler form:

$$n_0 V_d = n_s V_{\text{A,S}} \xi_{\perp}, \quad (8.46)$$

$$\frac{B_0^2}{8\pi} = n_s k_{\text{B}} T \left( 1 + \frac{1}{\theta} \right), \quad (8.47)$$

$$n_s k_{\text{B}} T \left( 1 + \frac{1}{\theta} \right) = \frac{1}{2} M n_s V_{\text{A,S}}^2, \quad (8.48)$$

$$\chi_{\text{ef}} \frac{B_0^2}{4\pi} V_d = \frac{5}{2} n_s k_{\text{B}} T \cdot V_{\text{A,S}} \xi_{\perp} + f_{\text{M}}(\theta) \frac{n_s (k_{\text{B}} T)^{3/2}}{M^{1/2}} \xi_{\perp}, \quad (8.49)$$

$$(1 - \chi_{\text{ef}}) \frac{B_0^2}{4\pi} V_d = \left( \frac{5}{2} n_s k_{\text{B}} \frac{T}{\theta} + \frac{1}{2} M n_s V_{\text{A,S}}^2 \right) V_{\text{A,S}} \xi_{\perp}. \quad (8.50)$$

In Ohm's law (8.45) it is convenient to replace the effective conductivity  $\sigma_{\text{ef}}$  by effective anomalous resistivity  $\eta_{\text{ef}}$ :

$$\frac{c B_0}{4\pi a} = \frac{E_0}{\eta_{\text{ef}}}. \quad (8.51)$$

In general, the partial contributions to the effective resistivity may be made simultaneously by several processes of electron scattering by different sorts of

waves, so that the resistivity proves to be merely a sum of the contributions:

$$\eta_{\text{ef}} = \sum_k \eta_k . \quad (8.52)$$

The relative share of the electron heating  $\chi_{\text{ef}}$  is also presented as a sum of the respective shares  $\chi_k$  of the feasible processes taken, of course, with the weight factors  $\eta_k / \eta_{\text{ef}}$  which defines the relative contribution from one or another process to the total heating of electrons inside the SHTCL:

$$\chi_{\text{ef}} = \sum_k \frac{\eta_k}{\eta_{\text{ef}}} \chi_k . \quad (8.53)$$

In usual practice (e.g., [Somov, 1992](#)), the sums (8.52) and (8.53) consist of no more than two terms, either of which corresponds to one of the turbulent types or states. Note also that more detailed numerical results ([Somov and Oreshina 2000](#)) confirm validity of the assumptions made above.

### 8.3.3 Basic Local Parameters of the SHTCL

We shall assume that the magnetic field gradient  $h_0$  locally characterizes the potential field in the vicinity of the separator or X-type neutral line (see Fig. 1.2). It means that we consider a less specific configuration of reconnecting magnetic fluxes in comparison with the 2D MHD ‘standard model’ of a solar flare, mentioned in Sect. 8.1.1. We shall also assume that, at distances larger than the current-layer width  $2b$ , the magnetic field structure becomes, as it should be, the same as the structure of the potential field of ‘external sources’, for example, of sunspots in the solar photosphere. So the gradient  $h_0$  is the local parameter which ‘remembers’ the global structure of the potential field.

Under the assumptions made, the field  $B_0$  on the inflow sides of the current layer may be estimated as

$$B_0 \approx h_0 b . \quad (8.54)$$

The second local parameter of the reconnection region is the inflow velocity  $v_0$  or, alternatively, the electric field  $E_0$  determined by formula (8.2). We shall use  $E_0$  in what follows.

In the approximation of a strong magnetic field, the pressure  $p_0$  (or temperature  $T_0$ ) of inflowing plasma is negligible, but its density  $n_0$  certainly has to be prescribed as a local parameter of the reconnection region. In fact, as we shall see below, all characteristics of the SHTCL depend on  $n_0$ .

The dimensionless parameter  $\xi_\perp$  could be, in principle, obtained as a result of the solution of the more self-consistent problem on the current layer structure (Sect. 3.4

in Somov 1992). However in order to keep the problem under consideration as simple as possible, here we shall consider the small (see Inequalities (8.27)) parameter  $\xi_{\perp}$  as the specified one.

Summarizing the formulation of the problem, we see that the set of Eqs. (8.46)–(8.51) becomes closed if the particular expressions (8.52) and (8.53) are added to this set. This allows us to find the following parameters of the SHTCL:  $a$ ,  $b$ ,  $n_s$ ,  $T$ , and  $\theta$ .

### 8.3.4 The General Solution of the Problem

The input set of Eqs. (8.46)–(8.50) exhibits a remarkable property which facilitates the solution of the problem as a whole. The property consists of the fact that the first three Eqs. (8.46)–(8.48) allow us to transform the last two Eqs. (8.49) and (8.50) into a simpler form:

$$2 \chi_{\text{ef}} \frac{n_s}{n_0} = \frac{2.5}{1 + \theta^{-1}} + \frac{f_M(\theta)}{\sqrt{2(1 + \theta^{-1})^{3/2}}} , \quad (8.55)$$

$$2(1 - \chi_{\text{ef}}) \frac{n_s}{n_0} = 1 + \frac{2.5}{1 + \theta} . \quad (8.56)$$

From these two Equations we find the plasma compression and the relative share of the total heating of the electrons in the current layer:

$$\frac{n_s}{n_0} = N(\theta) = 1.75 + \frac{f_M(\theta)}{\sqrt{8(1 + \theta^{-1})^{3/2}}} , \quad (8.57)$$

$$\chi_{\text{ef}} = f_{\chi}(\theta) = 1 - \frac{3.5 + \theta}{2N(\theta)(1 + \theta)} . \quad (8.58)$$

Now we use Eqs. (8.46)–(8.48) together with Ohm's law (8.51) to find the general solution of the problem, which determines the following parameters of the SHTCL: the layer half-thickness

$$a = \frac{c m^{1/2}}{e (2\pi)^{1/2}} \left[ \left( \frac{1 + \theta^{-1}}{N(\theta)} \right)^{1/2} \frac{1}{U_k(\theta)} \right] \times \frac{1}{n_0^{1/2}} , \quad (8.59)$$

its half-width

$$b = (2c)^{1/2} (\pi M)^{1/4} \left[ \frac{1}{N(\theta)} \right]^{1/4} \times n_0^{1/4} \frac{1}{h_0} \left( \frac{E_0}{\xi_{\perp}} \right)^{1/2} , \quad (8.60)$$

the effective temperature of electrons

$$T = \frac{c M^{1/2}}{4k_B \pi^{1/2}} \left[ \frac{1}{(1 + \theta^{-1}) N^{3/2}(\theta)} \right] \times \frac{1}{n_0^{1/2}} \left( \frac{E_0}{\xi_\perp} \right), \quad (8.61)$$

the effective anomalous resistivity

$$\eta_{\text{ef}} = \frac{2m^{1/2}\pi^{1/4}}{e c^{1/2} M^{1/4}} \left[ \frac{(1 + \theta^{-1})^{1/2}}{N^{1/4}(\theta) U_k(\theta)} \right] \times \frac{1}{n_0^{3/4}} (\xi_\perp E_0)^{1/2}. \quad (8.62)$$

Thus to complete the solving this problem, we have to find a form of the function  $U_k(\theta)$  which depends on the regime of the plasma turbulence. This will be done in Sect. 8.4.1.

In addition, from definitions (8.54), (8.37), (8.38), and (8.39), by using the obtained solutions (8.59)–(8.62), we have the following formulae: the magnetic field near the current layer

$$B_0 = (2c)^{1/2} (\pi M)^{1/4} \left[ \frac{1}{N(\theta)} \right]^{1/4} \times n_0^{1/4} \left( \frac{E_0}{\xi_\perp} \right)^{1/2}, \quad (8.63)$$

the reconnection inflow velocity

$$v_0 = \frac{c^{1/2}}{2^{1/2} \pi^{1/4} M^{1/4}} [N(\theta)]^{1/4} \times \frac{1}{n_0^{1/4}} (\xi_\perp E_0)^{1/2}, \quad (8.64)$$

the outflow velocity

$$v_1 = \frac{c^{1/2}}{2^{1/2} \pi^{1/4} M^{1/4}} \left[ \frac{1}{N(\theta)} \right]^{3/4} \times \frac{1}{n_0^{1/4}} \left( \frac{E_0}{\xi_\perp} \right)^{1/2}, \quad (8.65)$$

the power of energy release per unit length along the current layer length  $l_j$

$$\frac{P_s}{l_j} = \frac{B_0^2}{4\pi} v_0 4b = \frac{2c^2 M^{1/2}}{\pi^{1/2}} \left[ \frac{1}{N(\theta)} \right]^{1/2} \times n_0^{1/2} \frac{1}{h_0} \left( \frac{E_0^2}{\xi_\perp} \right), \quad (8.66)$$

the rate of high-temperature plasma production by the SHTCL per unit length along the current layer length  $l_j$

$$\frac{\dot{N}}{l_j} = n_s v_1 4a^{out} = n_0 v_0 4b = 4c \times n_0 \frac{1}{h_0} E_0. \quad (8.67)$$

Formula (8.67) demonstrates a high level of self-consistency for the SHTCL model under consideration. It shows that

the total flux of plasma through the current layer depends only on the plasma density  $n_0$  on the inflow sides of the layer, the driving electric field  $E_0$ , and the gradient  $h_0$  of potential magnetic field

in the vicinity of the X-type neutral point. It is remarkable that other parameters, like the dimensionless parameter  $\xi_\perp$ , as well as the assumptions on the plasma turbulence inside the SHTCL, discussed in the next Section, do not influence the total flux of plasma passing through the current layer.

## 8.4 Plasma Turbulence Inside the SHTCL

### 8.4.1 Marginal and Saturation Regimes

When the electron current velocity  $u = j/n_s$  in plasma exceeds a critical value (see, e.g., [Mikhailovskii 1975](#)), the instabilities due to current flow of electrons appear. A rapid decrease in the plasma electric conductivity occurs and anomalous resistivity arises ([Kadomtsev 1976](#); [Artsimovich and Sagdeev 1979](#)). The condition needed for current instability in a reconnecting current layer (RCL) is that the current layer thickness is of the order of the ion gyroradius ([Syrovatskii 1981](#)). Thus the turbulent current layers must be sufficiently thin. According to [Syrovatskii \(1972\)](#),

the development of the *thin current layers* (TCL) in the solar atmosphere leads to plasma turbulence

and correspondingly to a fast rate of magnetic field dissipation in solar flares with the heating of plasma to high temperatures, the high-velocity plasma ejections, and the acceleration of particles to high energies.

Let us consider the turbulence which is due only to the *ion-cyclotron (ic)* and *ion-acoustic (ia)* instabilities. The Coulomb collisions between particles are assumed to be negligible. So the sums (8.52) and (8.53) consist of no more than two terms; either of which corresponds to one of the said turbulence types. In reality, the *ion-cyclotron* waves prove to be excited earlier than the *ion-acoustic* waves at all values of the temperature ratio  $\theta \lesssim 8$  as it is seen in Fig. 8.5.

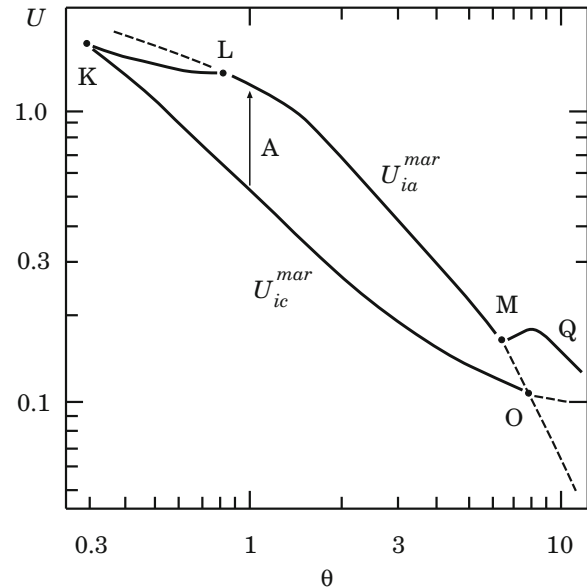
In the case of the *marginal* regime of turbulence (e.g., [Duijveman et al. 1981](#)), the current velocity of electrons inside the SHTCL

$$u = \frac{E_0}{en_s\eta_{\text{ef}}} \quad (8.68)$$

coincides with the critical velocity  $u_k$  of the  $k$ -type wave excitation. Hence, in formulae (8.59) and (8.62), the unknown function

$$U_k(\theta) = U_k^{\text{mar}}(\theta) = \frac{u_k}{V_{\text{Te}}} . \quad (8.69)$$

**Fig. 8.5** The relative current velocity of electrons,  $U = u/V_{Te}$  as a function of the temperature ratio  $\theta = T_e/T_i$  inside the SHTCL. The individual ‘arcs’ of the curves correspond to four different regimes of plasma turbulence. The dashed continuations of the ‘arcs’ are the critical velocities of excitation of corresponding waves. The arrow A shows that, in equilibrium plasma with  $\theta = 1$ , the ion-cyclotron waves (the curved section KO) are excited earlier than the ion-acoustic waves (the arc LO)



For example, the ion-cyclotron instability becomes enhanced when the electron current velocity  $u$  is not lower than the critical value  $u_{ic}$  of the ion-cyclotron ( $ic$ ) waves. In the marginal regime of the ion-cyclotron turbulence

$$U_{ic}^{mar}(\theta) = \frac{u_{ic}}{V_{Te}}. \quad (8.70)$$

This function is shown as the curved section KO in Fig. 8.5.

As long as the ion-cyclotron waves are not saturated, the electron current velocity  $u$  remains approximately equal to  $u_{ic}$  and thus it is possible to calculate the effective anomalous resistivity  $\eta_{ef}$  from Eq. (8.68). Therefore, if the current velocity of electrons  $u$  in the SHTCL does not exceed the ion-acoustic wave excitation threshold  $u_{ia}$ , only the ion-cyclotron waves will contribute to anomalous resistivity  $\eta_{ef}$  and the factor  $\chi_{ef}$ .

In the marginal regime of turbulence, the wave-particle interaction is *quasilinear*. However, in the case of sufficiently strong electric field  $E_0$ , the *nonlinear* interactions become important, thereby giving rise to another state of ion-cyclotron turbulence. In this regime, Ohm’s law can no longer define the resistivity (contrary to the marginal regime), but determines the electron current velocity. Regarding the resistivity, this is inferred from the turbulence saturation level.

In the *saturated* regime of turbulence,  $U_k(\theta)$  must be replaced by certain functions  $U_{ic}^{sat}(\theta)$ , shown by the curved section KL in Fig. 8.5, and  $U_{ia}^{sat}(\theta)$ , shown by the arcs MQ in the same Figure, for the ion-cyclotron and ion-acoustic turbulence, respectively (see Sect. 3.3 in Somov 1992).

### 8.4.2 Formulae for the Basic Parameters of the SHTCL

Let us rewrite the general solution (8.59)–(8.62) of the problem on the current-layer basic parameters as follows: the SHTCL half-thickness

$$a = 7.5 \times 10^5 f_a(\theta) \times \frac{1}{n_0^{1/2}}, \text{ cm}; \quad (8.71)$$

the half-width of the layer

$$b = 3.7 \times 10^{-1} f_b(\theta) \times n_0^{1/4} \frac{1}{h_0} \left( \frac{E_0}{\xi_\perp} \right)^{1/2}, \text{ cm}; \quad (8.72)$$

the effective temperature of electrons inside the current layer

$$T = 4.0 \times 10^{13} f_T(\theta) \times \frac{1}{n_0^{1/2}} \left( \frac{E_0}{\xi_\perp} \right), \text{ K}; \quad (8.73)$$

the effective anomalous resistivity

$$\eta_{\text{ef}} = 8.5 \times 10^{-4} f_\eta(\theta) \times \frac{1}{n_0^{3/4}} (\xi_\perp E_0)^{1/2}, \text{ s}. \quad (8.74)$$

Here we write separately the functions which are determined by the plasma turbulence inside the current layer:

$$f_a(\theta) = \left( \frac{1 + \theta^{-1}}{N(\theta)} \right)^{1/2} \frac{1}{U_k(\theta)} \approx 2.9, \quad (8.75)$$

$$f_b(\theta) = \frac{1}{N^{1/4}(\theta)} \approx 6.8 \times 10^{-1}, \quad (8.76)$$

$$f_T(\theta) = \frac{1}{(1 + \theta^{-1}) N^{3/2}(\theta)} \approx 8.2 \times 10^{-2}, \quad (8.77)$$

$$f_\eta(\theta) = \frac{(1 + \theta^{-1})^{1/2}}{N^{1/4}(\theta) U_k(\theta)} \approx 4.3. \quad (8.78)$$

Bearing in mind the discussion of solar flares in Sect. 8.5, we calculate the right-hand sides of functions (8.75)–(8.78) in the marginal regime of the ion-acoustic turbulence:

$$\theta \approx 6.5, \quad N \approx 4.8, \quad U_k = U_{ia}^{mar} \approx 0.17, \quad (8.79)$$

see Sect. 3.3 in [Somov \(1992\)](#).

The magnetic field on the inflow sides of the current layer can be found from formula (8.63):

$$B_0 = 3.7 \times 10^{-1} f_b(\theta) \times n_0^{1/4} \left( \frac{E_0}{\xi_{\perp}} \right)^{1/2}, \text{ G.} \quad (8.80)$$

From (8.64) it follows that the reconnection inflow velocity

$$v_0 = 8.1 \times 10^5 N^{1/4}(\theta) \times \frac{1}{n_0^{1/4}} (\xi_{\perp} E_0)^{1/2}, \text{ km s}^{-1}. \quad (8.81)$$

From (8.65) and (8.66) we obtain the outflow velocity of super-hot plasma

$$v_1 = 8.1 \times 10^5 N^{-3/4}(\theta) \times \frac{1}{n_0^{1/4}} \left( \frac{E_0}{\xi_{\perp}} \right)^{1/2}, \text{ km s}^{-1}, \quad (8.82)$$

and the power of energy release per unit length along the current layer length  $l_j$

$$\frac{P_s}{l_j} = 6.0 \times 10^8 N^{-1/2}(\theta) \times n_0^{1/2} \frac{1}{h_0} \left( \frac{E_0^2}{\xi_{\perp}} \right), \text{ erg s}^{-1} \text{ cm}^{-1}. \quad (8.83)$$

The rate of super-hot plasma production by the SHTCL is found from (8.67):

$$\frac{\dot{N}}{l_j} = 1.2 \times 10^{11} \times n_0 \frac{1}{h_0} E_0, \text{ s}^{-1} \text{ cm}^{-1}. \quad (8.84)$$

Recall that in all these formulae the electric field  $E_0$  is measured in the CGSE units.

The main advantage of the analytical solution in comparison with numerical solutions is that the formulae given here clearly show the dependence of the SHTCL basic parameters on the *external* parameters of a reconnection region (i.e. the magnetic-field gradient  $h_0$  in the vicinity of a separator, the strength of the inductive electric field  $E_0$  and the plasma density  $n_0$ ) as well as on the *internal* parameter of the model,  $\xi_{\perp}$ . The last parameter should be studied in a more self-consistent manner (see Sect. 3.4.3 in [Somov 1992](#)).

### 8.4.3 The Applicability of the Model

The applicability scope of the SHTCL model was considered in [Somov \(1992\)](#) with account of the *ion-acoustic* and *ion-cyclotron* instabilities in marginal and saturated regimes. It follows from this consideration that

the best agreement between the average quantities predicted by the SHTCL model and those observed in solar flares can be achieved in the marginal regime of ion-acoustic turbulence.

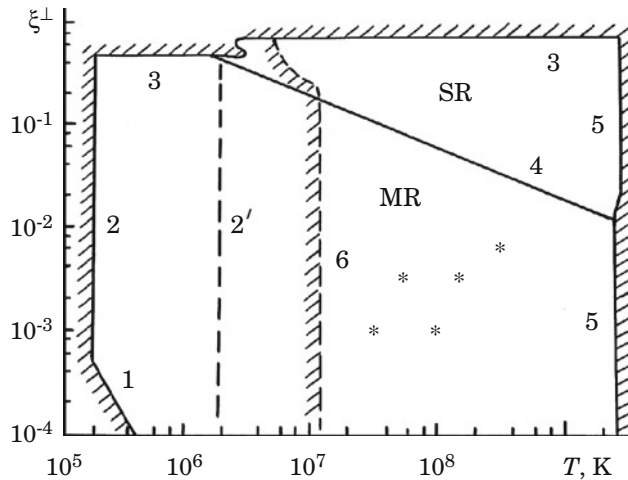


**Fig. 8.6** The applicability domain of the SHTCL model with ion-acoustic turbulence. Boundary 1 corresponds to the condition (8.85) that the Coulomb collisions can be neglected. Boundaries 2, 2' and 3 are determined by conditions (8.86) and (8.87) of the strong magnetic field approximation. Straight line 4 separates the marginal (MR) and saturated (SR) regimes of ion-acoustic turbulence. Boundary 5 means that, according to (8.88), the magnetic field  $B_0$  does not affect the plasma turbulence. Boundary 7 corresponds to the condition (8.89) of a small role of the longitudinal magnetic field in the force balance

Thus we shall consider in this Section only the case of the ‘pure’ ion-acoustic turbulence, when the contribution of ion-cyclotron turbulence to the total resistivity is negligible. This case is shown in Fig. 8.6 in terms of the effective temperature  $T$  of electrons inside the current layer and the parameter  $\xi_\perp = B_\perp/B_0$  which is the relative value of the transversal component  $\mathbf{B}_\perp$  of magnetic field.

First of all, let us recall that, in Sect. 8.3.1, the problem on collisionless reconnection in SHTCL was formulated under the assumption that the Coulomb collisions between particles can be neglected, i.e.

$$\eta_{\text{ef}} \gg \eta_{\text{cl}}. \quad (8.85)$$

Here the effective *anomalous* resistivity  $\eta_{\text{ef}}$  is determined by formula (8.62),  $\eta_{\text{cl}}$  is the inverse to the *classical* Coulomb conductivity (8.12) with the temperature  $T$  given by formula (8.61). Thus we rewrite inequality (8.85) in terms  $T$  and  $\xi_\perp$  and show it as the straight shaded boundary 1 in Fig. 8.6, for which the value of the plasma density  $n_0$  near the SHTCL is taken to be  $10^{11} \text{ cm}^{-3}$ . We see that

the condition of negligible Coulomb collisions has very little effect on the applicability scope of the SHTCL model.

Second, in Sect. 8.3.2, we took the conditions of the strong magnetic field approximations:

$$\frac{B_0^2}{8\pi} \gg 2n_0k_B T_0 \quad (8.86)$$

and

$$\frac{B_0^2}{8\pi} \gg \frac{\rho_0 v_0^2}{2}. \quad (8.87)$$

Here  $n_0$  and  $T_0$  are the density and temperature of plasma outside the current layer.  $B_0$  is the strength of magnetic field on the inflow sides of the layer, which is calculated by using formula (8.63). The reconnection inflow velocity  $v_0$  is determined by formula (8.64).

Both inequalities can be transformed to the coordinates  $T$  and  $\xi_\perp$ . In the marginal regime of ion-acoustic turbulence, inequality (8.86) takes the simple form  $T \gg 0.09 T_0$ . This inequality is represented in Fig. 8.6 by the straight shaded boundary 2 for  $T_0 = 2 \times 10^6$  K and the dashed line 2' for  $T_0 = 2 \times 10^7$  K. Inequality (8.87) is shown by the curved dashed boundary 3. It is clear that

| the approximation of strong magnetic field does not strongly restrict the applicability domain of the SHTCL model.

The condition of *magnetic non-neutrality* (8.27) of current layer imposes certain limitations on the admissible values of  $\xi_\perp$ . However the limitation from below ( $\xi_\perp b \gg a$ ) is realized at very small values of  $\xi_\perp$  beyond the parametric domain which may prove to be of interest to applications. Therefore it is not presented in Fig. 8.6.

Until now, we tacitly assumed that the magnetic field does not directly affect the plasma turbulence. In the case of ion-acoustic turbulence, this assumption only valid if the electron Larmor frequency  $\omega_B^{(e)}$  (see Appendix 3) is much below the electron plasma frequency  $\omega_{pl}^{(e)}$ , i.e.

$$\omega_B^{(e)} \ll \omega_{pl}^{(e)}. \quad (8.88)$$

This inequality gives us boundary 5 in Fig. 8.6 for the magnetic field  $B_0$  given by formula (8.63). We see that

| the effect of the main component  $B_0$  of magnetic field on the plasma turbulence inside the SHTCL becomes perceptible only at relativistic values of the electron temperature.

The next limitation arises from the assumed small contribution of the *longitudinal* magnetic field to the force balance (8.47) in the SHTCL and is characterized by the inequality

$$B_{\parallel s} \ll B_0. \quad (8.89)$$

Here  $B_{\parallel s}$  is the longitudinal field assumed to be frozen in plasma inside the SHTCL (8.31). Inequality (8.89) for the marginal regime of ion-acoustic turbulence is shown as boundary 6 in Fig. 8.6 under condition that outside the current layer  $B_{\parallel 0} = 10$  G and  $n_0 = 10^{10}$  cm<sup>-3</sup>.

The energy release power (8.66) and the reconnection rate (8.64), which are necessary for solar flares to be accounted for, can be obtained in the marginal

regime (domain MR) of ion-acoustic turbulence if  $\xi_{\perp} \gtrsim 10^{-3}$ , see five stars (\*) in Fig. 8.6. Thus a small parameter of the SHTCL model,  $\xi_{\perp}$ , is really small; on average  $\xi_{\perp} \sim 3 \times 10^{-3}$ .

#### 8.4.4 The SHTCL with a Small Transverse Field

With the average value of the small parameter of the SHTCL model,

$$\xi_{\perp} = B_{\perp}/B_0 \sim 3 \times 10^{-3}, \quad (8.90)$$

we finally have the following approximate formulae: the current-layer half-thickness

$$a = 2.2 \times 10^6 \times \frac{1}{n_0^{1/2}}, \text{ cm}; \quad (8.91)$$

the half-width of the current layer

$$b = 4.6 \times n_0^{1/4} \frac{1}{h_0} E_0^{1/2}, \text{ cm}; \quad (8.92)$$

the effective temperature of electrons

$$T = 1.1 \times 10^{15} \times \frac{1}{n_0^{1/2}} E_0, \text{ K}; \quad (8.93)$$

the effective anomalous resistivity

$$\eta_{\text{ef}} = 2.0 \times 10^{-4} \times \frac{1}{n_0^{3/4}} E_0^{1/2}, \text{ s}; \quad (8.94)$$

the magnetic field on the inflow sides of the current layer

$$B_0 = 4.6 \times n_0^{1/4} E_0^{1/2}, \text{ G}; \quad (8.95)$$

the reconnection inflow velocity

$$v_0 = 6.6 \times 10^4 \times \frac{1}{n_0^{1/4}} E_0^{1/2}, \text{ km s}^{-1}; \quad (8.96)$$

the outflow velocity of super-hot plasma

$$v_1 = 4.6 \times 10^6 \times \frac{1}{n_0^{1/4}} E_0^{1/2}, \text{ km s}^{-1}; \quad (8.97)$$

the power of energy release per unit length along the current layer length  $l_j$

$$\frac{P_s}{l_j} = 2.0 \times 10^{11} \times n_0^{1/2} \frac{1}{h_0} E_0^2, \text{ erg s}^{-1} \text{ cm}^{-1}; \quad (8.98)$$

and the rate of high-temperature plasma production by the SHTCL

$$\frac{\dot{N}}{l_j} = 1.2 \times 10^{11} \times n_0 \frac{1}{h_0} E_0, \text{ s}^{-1} \text{ cm}^{-1}. \quad (8.99)$$

Formulae (8.91)–(8.99) depend on **three principal parameters of the reconnection region**: the gradient of the magnetic field  $h_0$  in the vicinity of separator, the value of the inductive electric field  $E_0$  and the plasma density  $n_0$ .

For applications to the solar flares in the next Chapter we also introduce the *heating time*  $t_h$  which is the time for a given magnetic-field line to be connected to the SHTCL. In other words, during the time  $t_h$ , the thermal flux from the SHTCL along the field line heats the super-hot plasma flowing out of the current layer along this field line. Let us take by definition

$$\begin{aligned} t_h &= \frac{2b}{v_1} = 4(\pi M)^{1/2} [N(\theta)]^{1/2} \times n_0^{1/2} \frac{1}{h_0} \\ &= 2.0 \times 10^{-11} \times n_0^{1/2} \frac{1}{h_0}, \text{ s}. \end{aligned} \quad (8.100)$$

In all these formulae all the quantities, except the temperature, are measured in CGS units; the temperature is given in degrees Kelvin.

## 8.5 SHTCL in Solar Flares

### 8.5.1 Why Are Flares So Different But Similar?

Even if one considers the flares driven by reconnection in the SHTCL with the same kind of plasma turbulence, then one can see from the solution described above that very different physical processes will dominate in a flare depending on physical conditions. The advantage which this analytical solution gives us is that we can estimate the most important parameters which determine the physical difference in solar flares.

Let us consider, first, the reconnection inflow velocity  $v_0$  of plasma in the vicinity of the SHTCL. According to formula (8.96),  $v_0$  does not depend on the magnetic-field gradient  $h_0$ . For given values of the plasma density  $n_0$  and the electric field  $E_0$ , the inflow velocity is shown in Fig. 8.7. On average, the characteristic value of the reconnection velocity is  $v_0 \sim 10 \text{ km s}^{-1}$ .

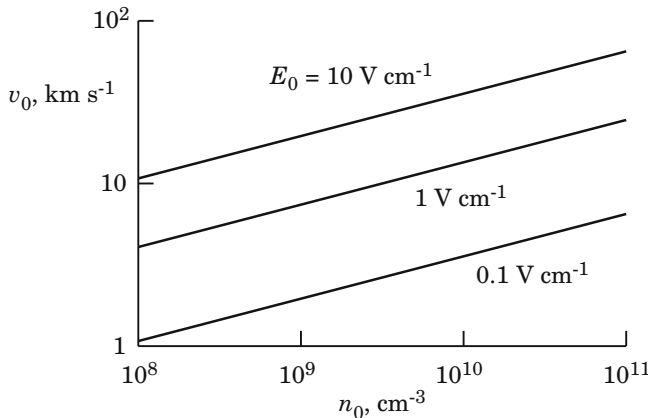


**Fig. 8.7** The reconnection inflow velocity  $v_0$  in the vicinity of the SHTCL as a function of the plasma density  $n_0$  and the electric field  $E_0$

So the reconnection inflow velocity during the ‘main’ or ‘hot’ phase of solar flares is much higher than that one in the pre-flare state (cf. Exercise 8.1).

Second, if the characteristic value of the upstream Alfvén speed in the undisturbed solar corona  $V_{A,0} \approx 3 \times 10^4 \text{ km s}^{-1}$  (see (8.107)), then the parameter  $\varepsilon \approx 3 \times 10^{-4}$ . Hence the parameter  $\varepsilon^2 \approx 10^{-7}$  is really very small. Therefore the approximation of a strong magnetic field (see Part I, Sect. 13.1.3) is well applicable to the SHTCL in solar flares. Except, the parameter  $\gamma^2$  is small but not so small as  $\varepsilon^2$ :

$$\gamma^2 \approx \frac{V_s^2}{V_{A,0}^2} \sim 10^{-4} \gg \varepsilon^2 \sim 10^{-7}. \quad (8.101)$$

So the condition (13.20) in Part I would be well satisfied in the undisturbed corona near the SHTCL.

This means that, in a first approximation, the small parameter  $\gamma^2$  is more important than the small parameter  $\varepsilon^2$  (see Part I, Eq. (13.22)). Hence we cannot neglect the gas-pressure-gradient effects in the vicinity of the SHTCL.

We have to take into account a compression of the plasma by a magnetic field frozen in the plasma near the SHTCL.

That is why, in the SHTCL model, we use the plasma density  $n_0 \sim 10^9 - 10^{11} \text{ cm}^{-3}$  which is different from the plasma density in the undisturbed corona. In other words, the thin SHTCL, being in equilibrium considered here, is presumably embedded into a thicker plasma layer.

### 8.5.2 Magnetic-Field Gradient Effects

Let us conventionally distinguish *impulsive* and *gradual* flares in the following way. If the difference in the time scale of a flare  $t_f$  would be mainly determined by the difference in its linear size  $l_f$ , then the impulsive flares should have the stronger gradient  $h_0$  near the separator of the potential field in an active region (see Sect. 4.2.1). By thinking so, we would believe that

the impulsive solar flares are the compact flares in strong magnetic fields,

for example, flares in the low corona not far from sunspots. On the contrary, the gradual flares or the so-called *long duration events* (LDEs; Pallavicini et al. 1977) may occur in a large-scale region placed high in the corona at a significant distance above the strong sunspots.

The theory of magnetic reconnection in super-hot turbulent-current layers (Sects. 8.3 and 8.4) allow us to unify the both types of solar flares. For definiteness, let us put  $l_f \approx 3 \times 10^9$  cm as a typical value at an imaginary boundary between compact (impulsive) and large-scale (long-duration or gradual) flares; see Sect. 17.4.1 in Somov (2000). In that case, the typical value of the field gradient  $h_f = B_f/l_f$ , where  $B_f$  is a typical value of the external (with respect to the reconnecting current layer) magnetic field in the photosphere. Since in sunspots  $B_f \approx 10^3$  G, we take

$$h_f = \frac{B_f}{l_f} \approx 3 \times 10^{-7} \text{ G cm}^{-1} \quad (8.102)$$

as a boundary value of the field gradient. Therefore, by our conventional definition, which is not always true, in impulsive flares  $h_0 > h_f$  but in gradual flares  $h_0 < h_f$ .

Note that the half-thickness  $a$  of the current layer, its temperature  $T$  and effective anomalous resistivity  $\eta_{\text{ef}}$ , the magnetic field  $B_0$  on the inflow sides of the current layer, the inflow and outflow velocities  $v_0$  and  $v_1$  do *not* depend on the gradient  $h_0$ . This remarkable feature follows from formulae (8.91), (8.93)–(8.97), respectively. Perhaps, that is why

there still exists some similarity between solar flares, in spite of the great difference in their observed scales and shapes.

On the contrary, the current-layer half-width  $b$  and, as a consequence, the power of energy release per unit length along the current  $P_s/l_j$  and the rate of high-temperature plasma production by the SHTCL  $\dot{N}/l_j$  are inverse proportional to the field gradient  $h_0$ , see formulae (8.92), (8.98) and (8.99). The plasma production rate is proportional to the electric field  $E_0$ , which is typical for driven reconnection.

Numerical simulations performed by Chen et al. (1999b) for two *standard* models (one with the X-type reconnection point at a high altitude and another one with the reconnection point at a low altitude) seem to confirm that both type of solar flares can be unified in the way suggested above.

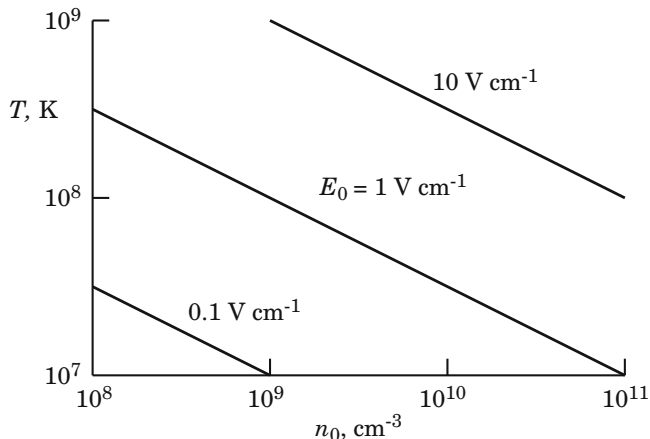


**Fig. 8.8** The effective temperature of electrons inside the SHTCL as a function of the plasma density  $n_0$  and the driving electric field  $E_0$

### 8.5.3 The Role of the Plasma Density

Also conventionally, we shall distinguish *thermal* and *non-thermal* flares. Plasma heating is an unavoidable phenomenon in all flares. The relative role of the thermal part of a flare certainly depends on collisional relaxation processes (see Part I, Sect. 8.3) mainly in the secondary (Somov 1992) transformations of the flare energy. It is natural to assume that

| the plasma density  $n_0$  determines the importance of collisions in flares:  
the higher the density, the faster is the thermalization.

The thermal flares, having the high plasma density, have to produce very efficient heating but inefficient acceleration. The opposite seems to be true for the non-thermal flares.

The solutions (8.59)–(8.66) show that all parameters of the SHTCL depend on the density  $n_0$ . Generally, this dependence is not strong ( $n_0^{1/2}$ ,  $n_0^{1/4}$  etc.), but the difference in density can be large. This is important for what follows. For example, Fig. 8.8 shows the effective temperature  $T$  of electrons (see formula (8.93)) as a function of the plasma density  $n_0$  and electric field  $E_0$ . As we see,

| the effective electron temperatures greater than  $10^8 \text{ K}$  can be easily reached in solar flares.

Moreover the effective temperature of electrons does not depend on the field gradient  $h_0$ . So the SHTCL may well exist in both impulsive and gradual flares.

In the conditions of the ‘main’ or ‘hot’ phase of solar flares the characteristic parameters of such collisionless current layers, computed in the frame of the model described above (see also Table 3.3.3 in Somov 1992), are the followings.

- (a) The effective electron temperature inside the super-hot turbulent-current layer  $T_e \approx 100 - 200$  MK, the temperature ratio  $\theta = T_e/T_p \approx 6.5$ . The plasma compression  $n_s/n_0 \approx 4.8$  is not high.
- (b) The effective dissipative thickness of the current layer  $2a \approx 20$  cm is very small but its width  $2b \approx (1-2) \times 10^9$  cm is large, for this reason the linear scale (8.28) for the outflows of energy and mass  $2a^{out} \approx (3-6) \times 10^6$  cm is not small. This scale should be considered as *actual* thickness of the SHTCL.
- (c) The anomalously high resistivity  $\eta \approx (3-10) \times 10^{-13}$  s is induced by the ion-acoustic turbulence in a marginal regime inside the SHTCL. Under this condition, the energy release power per unit layer length  $l_j$  (along the direction of current inside the layer) is

$$P_s/l_j \approx (1-7) \times 10^{19} \text{ erg (s cm)}^{-1}$$

if the plasma inflow velocity  $v_0 \approx 10-30$  km s $^{-1}$ . Hence, if the current layer length  $l_j \approx 3 \times 10^9$  cm, then the power of energy release

$$P_s \approx 3 \times 10^{28} - 2 \times 10^{29} \text{ erg s}^{-1}. \quad (8.103)$$

The outflow velocity equals  $v_1 \approx 1,400-1,800$  km s $^{-1}$ .

#### 8.5.4 Super-Hot Plasma Production

How much super-hot plasma is generated by the SHTCL in a solar flare? – According to formula (8.99), for the impulsive flares with the magnetic-field gradient  $h_0 \approx 5 \times 10^{-7}$  G cm $^{-1}$ , the rate of high-temperature plasma production by the SHTCL (per unit length along the current layer length  $l_j$ ) is

$$\dot{N}/l_j \approx 2 \times 10^{17} n_0 E_0, \text{ s}^{-1} \text{ cm}^{-1}. \quad (8.104)$$

If we take the maximal value of the electric field  $E_0 \approx 10$  V cm $^{-1}$  and plasma density  $n_0 \approx 10^9-10^{10}$  cm $^{-3}$ , then we estimate the rate of plasma production as  $\dot{N}/l_j \approx 10^{25}-10^{26}$  s $^{-1}$  cm $^{-1}$ .

Let us take the characteristic length  $l_j \sim l_f \approx 3 \times 10^9$  cm and the characteristic value of the impulsive phase duration  $\tau \approx 30$  s. Then the amount of super-hot plasma produced by the SHTCL can be estimated as

$$N = \frac{\dot{N}}{l_j} \times l_j \tau \approx (10^{36}-10^{37}) \text{ particles}. \quad (8.105)$$

This amount of high-temperature (super-hot) particles is comparable with the total number of accelerated electrons

having energies larger than  $\approx 10$  keV during the impulsive phase of a typical flare. So, in principle, the SHTCL can produce an observable amount of the super-hot plasma (Sect. 9.2) and pre-accelerated particles: protons and other ions.

Let us estimate the emission measure of the super-hot plasma. The 2D distributions of temperature and pressure, that follow from the *Yohkoh* SXT and HXT observations (Tsuneta et al. 1997), do not allow us to estimate the volume  $V_{sh}$  occupied by super-hot plasma. So we have to start from a rather arbitrary assumption frequently used in this situation as a first approximation. If the plasma would be distributed uniformly over the large volume of a flare  $V_f = l_f^3$ , then the emission measure should be

$$EM_{min} = \frac{N^2}{l_f^3} \approx 3 \times (10^{43}-10^{45}) \text{ cm}^{-3}. \quad (8.106)$$

This is not the case. The emission measure can be much higher because the super-hot plasma is concentrated in a much smaller volume, more exactly, in a compact source above the soft X-ray (SXR) loops (see Figs. 9.6 and 9.7). So the value (8.106) is only a *lower limit* to the emission measure of the super-hot plasma in real flares. A reasonable value of the volume filling factor  $V_{sh}/V_f$ , which we may assume, is of about  $3 \times 10^{-4}-10^{-3}$ . That is why the super-hot plasma was observed in flares by the HXT on board *Yohkoh*.

### 8.5.5 Before and After *Yohkoh*

Before *Yohkoh*, a little indirect evidence of the super-hot plasma was known. First, the high-resolution ( $\approx 1$  keV) spectral measurements (Lin et al. 1981) from 13 to 300 keV of a flare on June 27, 1980 have shown, at energies below  $\approx 35$  keV, an extremely steep spectrum which fits to that from the Maxwellian distribution with an electron temperature  $T_e \approx 34$  MK and an emission measure  $EM \approx 3 \times 10^{48} \text{ cm}^{-3}$ . Second, statistical properties of a large number of solar flares detected with the Hard X-Ray Burst Spectrometer (HXRBS) on the satellite *Solar Maximum Mission* (*SMM*) allowed to confirm the existence of super-hot thermal flares (Type A) with temperatures 30–40 MK (Dennis 1985, 1988).

Third, the 2D distributions of electron temperature and emission measure of the ‘hot’ (say  $10 \leq T_e \leq 30$  MK) and super-hot plasma (Den and Somov 1989) were calculated for the 1B/M4 flare on November 5, 1980 (see also Sect. 4.3.1) on the basis of data obtained with the Hard X-ray Imaging Spectrometer (HXIS) on board *SMM*. It was shown that

the large and small SXR ‘interacting loops’ do not coincide with the location of super-hot plasma in a long structure ( $\approx 1$  arc min) during the long after-impulsive phase of the flare.

The emission measure of the super-hot plasma in this flare was estimated as  $EM \sim 10^{47} \text{ cm}^{-3}$ . In two maxima, the effective electron temperature reaches enormous values,  $T_e \approx 50\text{--}60 \text{ MK}$  (Den and Somov 1989), determined with accuracy better than 20%.

Hard X-ray imaging telescopes on board *Hinotori* observed a super-hot plasma of 30–35 MK with an emission measure of the order of  $10^{49} \text{ cm}^{-3}$  (Tsuneta et al. 1984; Tanaka 1987). The same super-hot plasma was also detected by the Bragg-type spectrometer (Tanaka 1987).

Fast flows of the hot plasma can produce a symmetrical broadening of the optically thin SXR lines observed during solar flares. This broadening is larger than the thermal one. A comparison of the observed profiles of the Fe XXV emission lines with the predictions of the SHTCL model suggests that the presence in the flare region of several small-scale or one (or a few) large-scale curved SHTCL (Antonucci et al. 1996).

\* \* \*

The *Yohkoh* data obtained simultaneously with the HXT, SXT, and BCS offered an opportunity for a detailed analysis which is necessary to distinguish the super-hot plasma components of different origins in different classes of flares as well as at different phases of the flare development.

Fast outflows of super-hot plasma create complicated dynamics of plasma in an external (relative to the current layer) region (see Sect. 9.2.2). If the distance between the SHTCL and the magnetic obstacle is not large, then the outflow becomes wider but does not relax in the coronal plasma before reaching the obstacle. Moreover, if the plasma velocity still exceeds the local fast-magnetoacoustic-wave velocity, a *fast* MHD shock wave appears ahead the obstacle (see Fig. 9.4).

If, on the contrary, the distance is large, the outflow of super-hot plasma relaxes gradually with (or even without) a collisional shock depending on the height and the conditions in an active region where a flare occurs (e.g., Tsuneta 1996). For example, collisional relaxations can be fast just near the SHTCL if the plasma density is relatively high but its temperature inside the reconnecting current layer is relatively low.

We do not discuss in this Chapter an existence of slow or fast MHD shocks (or other MHD discontinuities) which may be attached to external edges of the collisionless SHTCL. It will be reasonable to discuss such structures as a part of the current layer evolutionarity problem in Chap. 12, see also Exercise 12.1.

### 8.5.6 *On the Particle Acceleration in a SHTCL*

The collisionless transformation of the magnetic energy of a current layer into kinetic energy of particles inside the non-steady 2D reconnecting current layer (RCL) was introduced by Syrovatskii (1966a) as a *dynamic dissipation*. An essential peculiarity of the dynamic dissipation is that

the inductive electric field  $\mathbf{E}_0$  is directed along the current in the reconnecting current layer; this field does positive work on charged particles, thus increasing their energy.

Naturally, some instabilities of two-stream or current origin are excited in the plasma-beam system in the RCL. Wave-particle interactions transform a part of this work into direct heating of ions and electrons. This is the case of super-hot turbulent-current layer (SHTCL).

Three-component collisionless reconnection (Ono et al. 1996; Horiuchi and Sato 1997) includes several natural complications. For example, large ion viscosity possibly contributes to the thermalization process of the ion kinetic energy. However the general inference as to the possibility of particle acceleration and heating inside the collisionless RCL (i.e. dynamic dissipation of the magnetic field) remains valid and is used in the SHTCL model. This allows us to consider the SHTCL as the primary source of flare energy and, at least, the first-step acceleration mechanism.

## 8.6 Open Issues of Reconnection in Flares

The existing models of magnetic reconnection in the solar atmosphere can be classified in two wide groups: global and local ones (Fig. 8.9).

The global models are used to describe actual active regions or even complexes of activity on the Sun in different approximations and with different accuracies (Somov 1985, 1986; Gorbachev and Somov 1989, 1990; Demoulin et al. 1993; Bagalá et al. 1995; Tsuneta 1996; Tsuneta et al. 1997; Antiochos 1998; Longcope and Silva 1998; Aschwanden et al. 1999; Somov 2000; Morita 2001; Somov et al. 2002a; Barnes 2007; Longcope and Beveridge 2007; Ugarte-Urra et al. 2007). We make no attempt

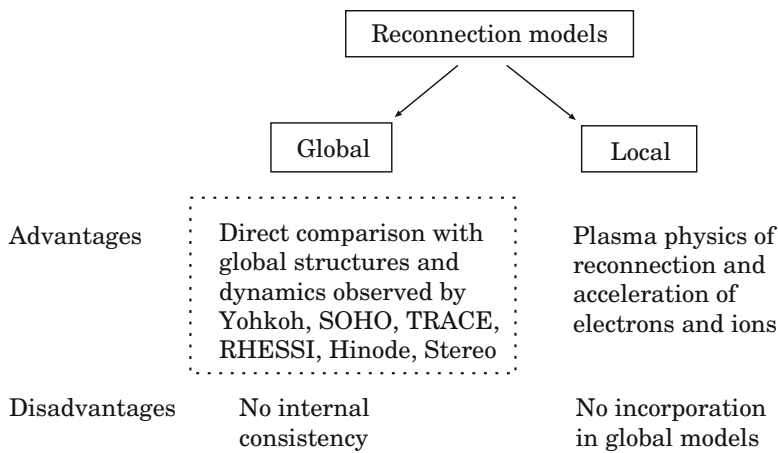


**Fig. 8.9** Models of magnetic reconnection in the solar atmosphere

to review all these models, stationary or non-stationary, 2D or 3D, but just remark that

the main advantage of the global models for magnetic reconnection in solar flares is a direct comparison between the results of computation and the observed large-scale patterns.

For example, the ‘rainbow reconnection’ model (Sect. 4.3.5) is used to reproduce the main features of the observed magnetic and velocity fields in the photosphere related to the large-scale photospheric *vortex* flows. As a consequence, the model reproduces, in the potential approximation, the large-scale features of the actual field in the corona, related to these flows before a solar flare.

The advantage of the local models is that they take kinetic effects into account and allow us to develop the basic physics of magnetic reconnection in solar flares. In general, many analytical, numerical, and combined models of reconnection exist in different approximations and with different levels of self-consistency (e.g., [Biskamp 1994](#); [Priest and Forbes 2000](#); [Somov 2000](#)). It becomes more and more obvious that

*collisionless* reconnection in a ‘super-hot’ rarefied plasma is an important process in considering active phenomena like solar flares.

This process was introduced by [Syrovatskii \(1966a,b\)](#) as a *dynamic dissipation* of magnetic field in a reconnecting current layer (RCL) and leads to fast conversion from field energy to particle energy, as well as a topological change of the magnetic field (e.g., [Horiuchi and Sato 1997](#); [Horiuchi et al. 2001](#)).

General properties and parameters of the collisionless reconnection can be examined in a frame of local models based on the mass, momentum, and energy conservation laws. As discussed in this Chapter, a particular feature of the models is that electrons and ions are heated by wave-particle interactions in a different way; contributions to the energy balance are not made by energy exchange between electrons and ions. The magnetic-field-aligned thermal flux becomes anomalous and plays the role in the cooling of the electrons in the *super-hot turbulent-current layer* (SHTCL). These properties are typical for collisionless plasmas under the coronal conditions derived from the observational data from *Yohkoh* and *RHESSI*, the *SOXS* mission ([Jain et al. 2006](#)). Unfortunately, the local models, like the SHTCL model, are not incorporated yet in the global 3D consideration of the reconnection effect in the corona. Only a few first steps have been made in this direction (e.g., [Somov and Kosugi 1997](#); [Somov et al. 1998](#)).

Future models should join ‘global’ and ‘local’ properties of the magnetic reconnection effect under solar coronal conditions. For example, chains of plasma instabilities, including kinetic instabilities, can be important for our understanding of the types and regimes of plasma turbulence inside the collisionless current layers with a large longitudinal magnetic field. In particular it is necessary to evaluate anomalous resistivity and selective heating of particles in such a SHTCL.

Heat conduction is also anomalous in the high-temperature plasma of solar flares. Self-consistent solutions of the reconnection problem will allow us to explain the energy release in flares, including the open question of the mechanism or

combination of mechanisms which explains the observed acceleration of electrons and ions to high energy (see Chap. 11). One can be tempted to use, however, the MHD approximation to describe solar flares, since this approximation may give a global picture of plasma motions.

To understand the 3D structure of reconnection in flares is one of the most urgent problems. Actual flares are 3D dynamic phenomenon of electromagnetic origin in a highly-conducting plasma with a strong magnetic field. The Sakao-type flares (Sect. 5.3.1) were a clear first example which showed that 3D models of flares should be involved in treatment of *Yohkoh* data. It was not possible to explain these simple flares in the framework of 2D MHD models.

*Yohkoh* observations with HXT, SXT, and BCS had offered us the means to check whether phenomena predicted by solar flare models of a definite type (such as the 2D MHD *standard* model or the quadrupole-type *topological* model described in Sect. 4.2) do occur. There were apparent successes of the standard model, for example, in the morphology of flares with cusp geometries. However some puzzling discrepancies did also exist, and further development of realistic 3D models is required.

## 8.7 Practice: Exercises and Answers

**Exercise 8.1.** Evaluate the characteristic value of the global Lundquist number (8.24) for a current layer with the classical Coulomb conductivity in the solar corona before an impulsive flare. Compare a predicted reconnection rate with the real one.

**Answer.** First, let us formally apply the Sweet-Parker scaling property (8.25) to the Syrovatskii current layer (see Sect. 8.1.2). Consider the main parameters of the neutral layer at the limit point (8.19) of thermal instability. The values  $n_0 \approx 5 \times 10^8 \text{ cm}^{-3}$ ,  $h_0 \approx 5 \times 10^{-7} \text{ Gauss cm}^{-1}$ , and  $E_0 \approx 1.2 \times 10^{-1} \text{ V cm}^{-1}$  have been specified in advance. The other quantities have been determined from the Syrovatskii solution. For example, the half-width of the current layer  $b \approx 7 \times 10^8 \text{ cm}$ , the magnetic field near the layer  $B_0 = h_0 b \approx 340 \text{ Gauss}$ , the plasma density inside the *cold dense* neutral layer  $n_s \approx 2 \times 10^{14} \text{ cm}^{-3}$ .

The upstream Alfvén speed (8.8):

$$V_{A,0} = 2.18 \times 10^{11} \frac{B_0}{\sqrt{n_0}} \approx 3 \times 10^9 \text{ cm s}^{-1} \approx 0.1 c . \quad (8.107)$$

Here  $c$  is the light speed.

The global Lundquist number (8.24):

$$N_L = \frac{V_{A,0} b}{v_m} \approx 2.3 \times (10^{14} - 10^{15}) . \quad (8.108)$$

Therefore the Sweet-Parker reconnection rate (8.25) predicted for the Syrovatskii neutral layer is extremely low:

$$M_A = N_L^{-1/2} \approx (2.1-6.7) \times 10^{-8}. \quad (8.109)$$

Let us compare this rate with the one which directly corresponds to the Syrovatskii model. According to formula (8.10) the inflow velocity

$$v_0 = V_d = c \frac{E_0}{B_0} \approx 3.5 \times 10^4 \text{ cm s}^{-1} = 0.35 \text{ km s}^{-1}. \quad (8.110)$$

Hence an actual reconnection rate in the Syrovatskii neutral layer

$$M_{A,S} = \frac{v_0}{V_{A,0}} \approx 1.1 \times 10^{-5} \gg M_A. \quad (8.111)$$

Obviously a difference in the reconnection rate is related to the compressibility of the plasma in the Syrovatskii model. With account of the plasma compressibility inside the reconnecting current layer, the actual reconnection rate

$$M_{A,S} = \frac{v_0}{V_{A,0}} = \left( \frac{n_s}{n_0} \right)^{1/2} N_L^{-1/2}.$$

(8.112)

In the frame of Syrovatskii's model for the neutral layer

$$\left( \frac{n_s}{n_0} \right)^{1/2} > 10^2. \quad (8.113)$$

So

the astrophysical plasma compressibility is really very important factor in the magnetic reconnection theory.

# Chapter 9

## Collapsing Magnetic Traps in Solar Flares

**Abstract** Reconnection in super-hot turbulent-current layers (SHTCLs) creates *collapsing* magnetic traps in the solar corona. In this Chapter, we discuss the possibility that coronal HXR emission is generated as bremsstrahlung of the fast electrons accelerated in the collapsing traps due to joint action of the Fermi-type first-order mechanism and betatron acceleration.

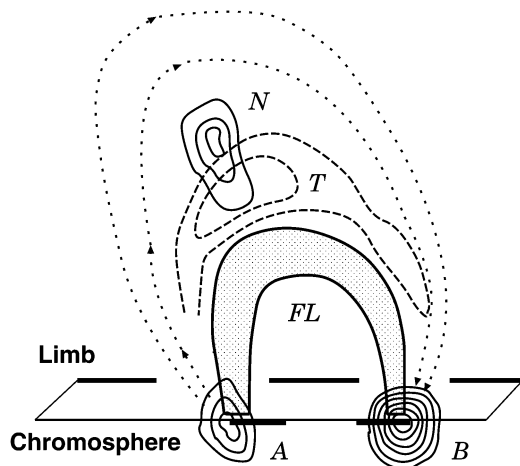
### 9.1 Coronal HXR Sources in Flares

#### 9.1.1 General Properties and Observational Problems

An unexpected feature of solar flares was the presence of a hard X-ray (HXR) source located in the corona (Fig. 9.1). Such emission interpreted as the *bremsstrahlung* of fast electrons was not predicted by theory because of very low density of coronal plasma. Space observations before the *Yohkoh* satellite had not sufficient sensitivity to observe these relatively faint emissions.

At first, a coronal source of HXRs was detected in the impulsive flare which occurred at the limb on 1992 January 13 and is well known as *Masuda's flare* (Masuda et al. 1994). The source was observed in the HXT energy bands M1 (23–33 keV) and M2 (33–53 keV) and had a relatively hard spectrum with index  $\gamma \sim 4$ . It was located above a SXR flare loop. Another source was observed in the L-band (14–23 keV), had a very soft spectrum, and looked similar to the SXR loop. This quasi-thermal emission of a ‘*super-hot*’ (with the effective electron temperature  $T_e \gtrsim 30$  MK) plasma started in the impulsive phase and became dominant in the gradual phase of the flare. In some flares, non-thermal sources seemed to be too weak and only such quasi-thermal component was observed during almost the whole flare period. For example, in the flare of 1992 February 6, the HXR spectrum was fitted by the thermal spectrum with  $T_e \sim 40$  MK (Kosugi et al. 1994).

**Fig. 9.1** A coronal HXR source in a flare: the non-thermal ( $N$ ) and quasi-thermal ( $T$ ) components of the HXR emission above a flare loop  $FL$ .  $A$  and  $B$  are the chromospheric HXR footpoints



Masuda's analysis was extended by Petrosian et al. (2002). Of 18 X-ray-bright limb flares analyzed, 15 flares showed well-detectable loop-top (LT) emission. The absence of LT emission in the remaining cases was most likely due to the finite dynamic range of the HXT. The coronal LT emission is presumably a common feature of all flares. This is one of the important properties of flares, which has to be investigated by using high resolution data of the *Reuven Ramaty High Energy Solar Spectroscopic Imager (RHESSI)* satellite (Lin et al. 2002).

Different types of coronal HXR sources may exist simultaneously even in a single flare (Masuda 2002). Some sources *slowly move upward* during a flare. For example, in the flare on 1992 October 4, a clear upward motion was observed in the impulsive phase as shown in Fig. 2 in Masuda et al. (1998). The flare had a multiple spikes in the HXR time profile. The position of the footpoints (FPs) changed at the time of each HXR spike. This observation suggests that the energy release process proceeds not only in a vertical direction, like reconnection in the '*standard*' model, but also in horizontally-different places.

The number of impulsive flares, in which the presence of the above-the-loop-top (ALT) source was well confirmed, was small. Mainly, these were three flares: 1992 January 13, 1993 February 17, 1994 January 16. Their L-band images had been synthesized by Sato et al. (1999). However these flares did not look intense enough for an analysis of motion of the coronal source.

Due to the work in recalibrating the HXT and improvement of the software, it became possible to study the coronal source in *long duration events* (LDEs). The size of LDEs is generally larger than that of impulsive flares. In a typical LDE, the extended HXR source lies above or slightly overlapping the SXR loops (Sato 1997; Masuda et al. 1998). The source observed in the L-band has two components – thermal and nonthermal. The source is maintained for a much longer time than the compact sources in impulsive flares. The shape of the HXR source is indicative of a high-temperature cusp region tracing an arcade of loops (Sato 1997).

In the X1.2 flare on 1998 April 23, coronal HXR sources showed complex structure unlike any previously observed (Sato 2001). Dominant thermal and nonthermal sources did not come from the same loop-top region. Non-thermal sources included two sources in the low corona ( $\sim 3 \times 10^3$  km) and an extended source in the high corona ( $\sim 5 \times 10^4$  km). The low and high coronal sources had common features such as a hard spectrum and a related evolution of spatial structures. The high coronal source showed a delayed peak. These observations suggest that energetic phenomena occur in the low corona at first, and energized electrons are then injected into a high coronal region (Sato 2001).

### **9.1.2 Upward Motion of Coronal HXR Sources**

Harra et al. (1998) analyzed two LDEs observed by *Yohkoh*. They concluded that the SXR loops were located below the HXR emission of the ALT source. For the LDE of 1992 November 2, the ALT source rose with a velocity of  $\approx 3$  km/s. For the 28 June 1992 event, it was not possible to follow the HXR images for a long time due to the poor count statistics. So the ascent velocity was not estimated. The improved L-band images synthesized with the revised MEM for three LDEs, including the 1992 November 2 event, have been published (see Fig. 13 in Sato et al. 1999) but the ascent velocity was not estimated.

The *RHESSI* mission provides high-resolution imaging from soft X-rays to  $\gamma$ -rays and allows the HXR source motions to be studied in detail. For example, the HXR observations of the 2002 July 23 flare show FP emissions originating from the chromospheric ribbons of a magnetic arcade and a coronal (LT or ALT) source moving with a velocity of  $\sim 50$  km/s (Krucker et al. 2003; Lin et al. 2003a). Some part of this velocity is presumably directed upward, another part along the ribbons. LT and FP sources are also seen in the limb X28 flare on November 4, 2003. The limb flare on 2002 April 15, demonstrates that, after the HXR peak, the coronal HXR source moved upward at velocity  $\sim 300$  km/s, presumably indicating a *fast* upward outflow from reconnecting current layer (RCL) or its upward expansion (Sui and Holman 2003).

Sui et al. (2004) studied the *RHESSI* images of three homologous flares that occurred between April 14 and 16, 2002. The flares share the following common features: (a) The higher energy loops are at higher altitude than those of lower energy loops, indicating the hotter loops are above the cooler ones. (b) Around the start of the HXR impulsive phase, the altitude of the looptop centroid decreases with time. (c) Then the altitude increases with time with velocities up to 40 km/s. (d) A separate coronal source appears above the flare loop around the start time and stays stationary for a few minutes. (e) The looptop centroid moves along a direction which is either away from or toward the coronal source above the loop.

These features are presumably associated with the formation and development of a RCL between the looptop and the coronal source. Physical parameters of such RCL seem to be consistent with the model of super-hot turbulent-current layer

(SHTCL). Moreover [Sui et al. \(2004\)](#) found a correlation between the loop growth rate and the HXR (25–50 keV) flux of the flare.

The faster the magnetic reconnection site moves up in the corona, the faster the reconnection rate in a solar flare.

More energetic electrons are produced and, therefore, more HXR emission is observed.

Different parts of the flare ‘mechanism’ in the corona can be seen in HXR emission, depending on conditions. These parts are the reconnection downflows in a cusp area, the reconnection site itself and with its vicinity, the reconnection upflows with or without ‘plasmoid’. They certainly have different physical properties and demonstrate different observational signatures of the flare mechanism, that should be studied in detail. In the next Section, we shall start such a study from the simplest situation, a slow upward motion of the coronal HXR source above the SXR loop in a limb flare.

### 9.1.3 *Yohkoh Data on Average Upward Velocity*

[Somov et al. \(2005b\)](#) have searched through the *Yohkoh* HXT/SXT Flare Catalogues ([Sato et al. 2003](#)) for appropriate limb flares using Masuda’s two criteria: (a) The heliocentric longitude of an active region must be greater than  $80^\circ$ . This ensures maximum angular separation between the loop top (LT) and footpoint (FP) sources. (b) The peak count rate in the M2-band must be greater than ten counts per second per subcollimator ( $\text{counts s}^{-1} \text{SC}^{-1}$ ). Thus at least one image can be formed at energies 33–53 keV, where thermal contribution is expected to be lower.

[Masuda \(1994\)](#) found 11 such limb flares before 1993 September. After 1993 September up to 1998 August, [Petrosian et al. \(2002\)](#) found additional eight flares. Thus there were 19 flares from 1991 October through 1998 August that satisfy these conditions. Only 15 of these flares show detectable LT emission. [Somov et al. \(2005b\)](#) have added some limb flares after 1998 August, that met Masuda’s criteria. However, for the study of the upward motion of a coronal HXR source, only six flares from this set were selected that have a simple structure: a compact LT source moving upward during sufficiently long time.

Some flares have complex behavior and structure with multiple LT and FP sources (see [Aschwanden et al. 1999](#); [Petrosian et al. 2002](#)). The coronal sources may appear and disappear, change direction of motion, or combine with another source as a flare evolves (e.g., the limb flare of 1993 February 17 at 10:35 UT); this can lead to erroneous interpretations if the spatial and time resolution is not sufficiently high. After all removals, we limited our analysis to the six flares. For 5 of these flares  $V > 3\sigma$ , where the average velocity  $V$  and the velocity dispersion  $\sigma$  were determined by a linear regression. Two of them are presented below.

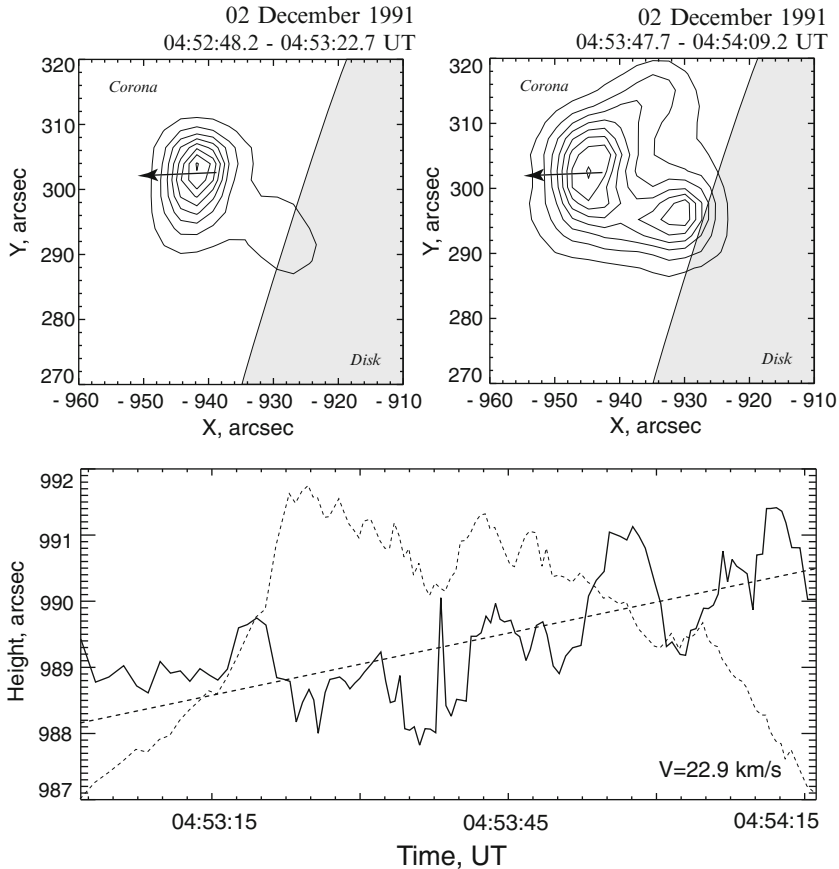


**Fig. 9.2** The HXR sources and their motions during the 1991 December 2 flare. *Upper panels*: HXT images in two different times. *Lower panel*: Height of the upper source as a function of time. The *dashed straight line* shows the averaged upward motion. The *dashed thin curve* is the HXR emission coming from the upper coronal source

1991 December 02. – The M3.6 flare at approximately 04:53 UT with the location coordinates N16° E87° occurred in the active region 6952, which just started to appear from the East limb (Fig. 9.2).

Two upper panels show the HXT images in the M2 band (33–53 keV) integrated from 04:52:48.2 UT to 04:53:22.7 UT (*left*) and from 04:53:47.7 UT to 04:54:09.2 UT (*right*). The eight contour levels are 12 %, 24 %, 36 %, 48 %, 60 %, 70 %, 82 % and 98 % of the peak intensity for each panel. The arrows show the direction of the HXR source motions. The lower panel shows the height of the upper source centroid as a function of time. The dashed straight line represents

the averaged upward motion derived by the method of least squares to estimate the average upward velocity. The dashed thin curve is the HXR emission coming from the selected coronal source area as a function of time.

Presumably, a low part of the flare was partially occulted by the solar limb and, for this reason, it did not show significant chromospheric emission in the M2-band (33–53 keV) at first. Alternatively, the chromospheric emission in the beginning of the flare was weak indeed. The HXT images show two sources (Fig. 9.2) associated with a compact flaring SXR loop. One of them that appears high above the limb was probably an LT source. It was observed rather inside the SXT loop than above it (see Petrosian et al. 2002). The other fainter source was laying at lower altitudes and could be either an LT or an FP source. This source also shifted its position but we were not able to investigate its motion with sufficient accuracy.

In contrast to the Masuda flare, the coronal HXR source here was bright and long lived (see the dashed thin curve which shows the HXR emission coming from the coronal source area as a function of time). During the initial phase, the average height of the source did not change significantly. The motion seems to be downward in the beginning of the flare like the LT centroid motion in the homologous flares observed by RHESSI (Sui et al. 2004).

The height of the LT source begun to increase only after 04:53:20–04:53:30 UT. We tried to make the downward part of a motion track. However an accuracy was not sufficient to study this part. It is enough only to estimate the average velocity during the HXR flare. The average upward velocity of the LT source is  $\approx 23 \pm 7$  km/s. The lower (FP) source showed the most strong emission at the time when the LT source rose.

*1992 January 13.* – Masuda’s flare started at approximately 17:27 UT, it was one the most famous events and had been studied extensively. The flare occurred close to the west limb of the Sun. In Fig. 9.3 we see three bright sources here, one LT-source and the other two at the footprints. The coronal HXR source located well above the apex of the SXR loop. So this is an ALT source. Its emission was weaker than the FP emission. From 17:28:03 to 17:28:07 UT the LT source disappeared, then arose again for several seconds and faded away completely. Its displacement was about 2''. The corresponding upward velocity is  $\approx 16 \pm 2$  km/s.

Slow ascending motions of sources can be seen in several flares. However, only in five flares, it was possible to estimate the velocity of the upward motion with values between 10 and 30 km/s. These results do not mean, of course, that the HXR source moves monotonically upward. We simply calculated just the average upward velocity expected in view of the standard model of flares. On the other hand, the motion seems to be downward, for example, in the beginning of the flare shown in Fig. 9.2. The accuracy of the *Yohkoh* HXT data was not sufficiently high to investigate this actual effect discovered by *RHESSI* (Sui and Holman 2003). Therefore, the motion of the coronal HXR sources in flares should be studied statistically better by using the *RHESSI* high-resolution imaging data.

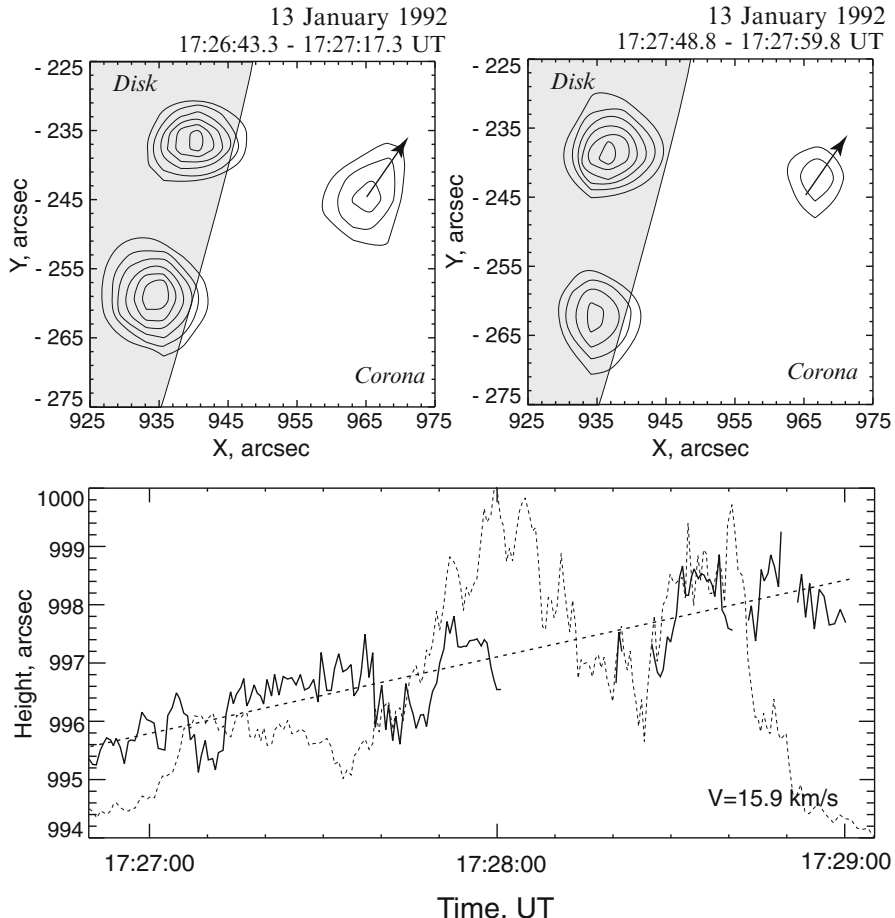


**Fig. 9.3** The same as Fig. 9.2 for the 1992 January 13 flare, Masuda's flare

#### 9.1.4 RHESSI Observation of Coronal X-Ray Sources

Liu et al. (2008) presented data analysis and interpretation of an M1.4-class flare observed with the Ramaty High Energy Solar Spectroscopic Imager (*RHESSI*) on April 30, 2002. This event, with its footpoints occulted by the solar limb, exhibits a rarely observed, but theoretically expected by the SHTCL models for solar flares with a ‘vertical’ RCL, double-source structure in the corona. The two coronal sources, observed over the 6–30 keV range, appear at different altitudes and show energy-dependent structures with the higher-energy emission being closer together.

Spectral analysis implies that the emission at higher energies in the inner region between the two sources is mainly non-thermal, while the emission at lower energies in the outer region is primarily thermal. The two sources are both visible for about

12 min and have similar light curves and power-law spectra above about 20 keV. These observations suggest that the magnetic reconnection site lies between the two sources. Bi-directional outflows of the released energy in the form of super-hot plasma and accelerated particles from a SHTCL can be the source of the observed radiation.

The spatially resolved thermal emission below about 15 keV indicates that the lower source has a larger emission measure but a lower temperature than the upper source. This is likely the result of the differences in the magnetic field and plasma density of the two sources because they move upward and downward in the corona under different initial and boundary conditions.

## 9.2 The Collapsing Trap Effect in Solar Flares

### 9.2.1 Fast Electrons in Coronal HXR Sources

[Fletcher \(1995\)](#) proposed that the coronal HXR sources as well as the footpoint (FP) sources are *non-thermal* in origin and are generated by the same population of fast electrons, with enhanced emission near the top of loops due to initially high pitch-angle distribution of accelerated electrons orbiting the magnetic field near their site of injection before being scattered into the loss-cone. [Hudson and Ryan \(1995\)](#) argued that the impulsive part of the coronal HXR source cannot be thermal, because the thermalization timescale for the *super-hot* plasma with the inferred temperature and density is longer than the observed timescale of variations of emission.

According to [Kosugi \(1996\)](#), the trapped fast electrons create the coronal above-the-loop-top (ALT) source of HXR. Meanwhile, the electrons precipitating from the trap generate the *thick-target* bremsstrahlung (see Sect. 17.2.4) in the chromosphere, observed as the FP sources of HXR near the feet of a flare loop. The *collapsing trap* model, where mirroring particles become energized by the first-order Fermi-type acceleration mechanism in the cusp region between the super-hot turbulent-current layer (SHTCL) and the fast oblique *collisionless* shock (FOCS) front, explains several observed properties of the coronal HXR source ([Somov and Kosugi 1997](#)).

One of the questions in the context of this Section is whether or not the observed upward motion of the coronal HXR source in limb flares can be related to the upward motion of the FOCS. An answer to this question depends on two factors: (a) physical properties of the FOCS, and (b) physical and geometrical properties of a magnetic obstacle (MO), the region of strong magnetic field, which stops the fast downflow of super-hot plasma and which is observed in SXR as a coronal loop or an arcade of loops.

### 9.2.2 Fast Plasma Outflows and Shocks

Reconnection serves as a highly efficient engine to convert magnetic energy into thermal and kinetic energies of plasma flows and accelerated particles (Sect. 4.1). The collisionless reconnection theory (more exactly, the model of a super-hot turbulent-current layer (SHTCL, Sect. 8.3) under the coronal conditions derived from the *Yohkoh* data) shows that the SHTCL can be considered as the source of flare energy and, at least, the first-step mechanism in a *two-step acceleration* of electrons and ions to high energies (Somov and Kosugi 1997).

Fast outflows of super-hot collisionless plasma create complicated dynamics in an external (relative to the SHTCL) region; this dynamics should be a topic of special research. From the physical point of view, it is difficult to find a proper approximation which takes into account both collisionless and collisional effects (see, however, Bogachev and Somov 2009). From the mathematical point of view, it is not simple to construct a self-consistent model of the *collapsing trap* even in a simple kinematic 2D MHD approximation (Giuliani et al. 2005).

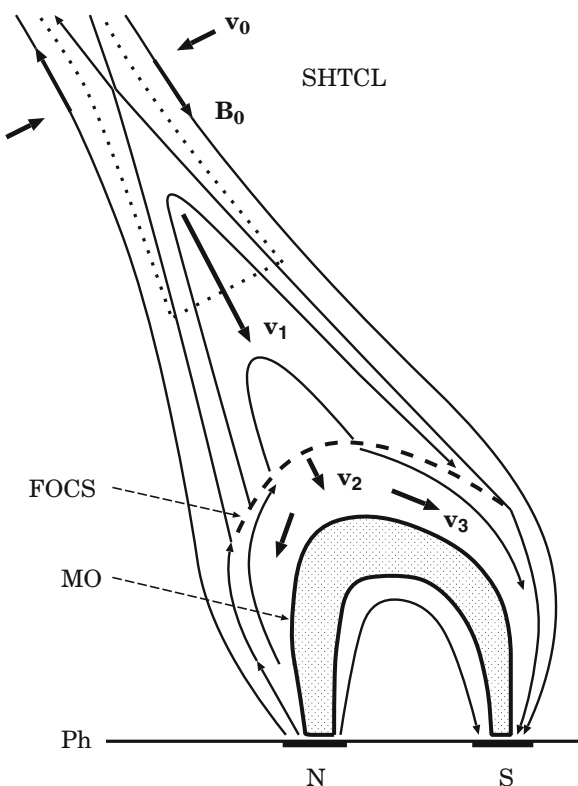
It is clear, however, that the interaction of the fast flow of super-hot plasma with an external plasma and magnetic field strongly depends on the initial and boundary conditions, especially on the relative position of the outflow source (the SHTCL) and the magnetic ‘*obstacle*’ – the region of the strong external field. Near the boundary of this region the energy density of the outflow becomes equal to the energy density of the field which tries to stop the flow. In Fig. 9.4 the magnetic obstacle is shown as a shadowed loop placed schematically above two sunspots *N* and *S* in the photosphere *Ph*.

Something similar was observed by the SXT on the *Yohkoh* during the limb flare in 1999 January 20. Images from the SXT show the formation of a large arcade of loops as well as high-speed flows in the region immediately above the flare loops (McKenzie and Hudson 1999). Downward-traveling dark voids appear in the SXR images. They presumably represent the cross-section of flux tubes; their downward motion would be interpretable as shrinkage of the field lines due to magnetic tension. Some of the voids slow down and stop as they approach the top of the arcade.

The coronal imaging instruments on *SOHO* study fast ( $>1,000$  km/s) coronal mass ejections (CMEs) which may be responsible for accelerating some of the energetic particles very high in the corona. The LASCO coronagraphs identify motion of plasma in both directions along a radius vector. Simnett (2000) has suggested that such bi-directional flows seen by LASCO are evidence for reconnection in *coronal streamers* (Somov 1991). Therefore the *SOHO* observations have identified the sites of reconnecting magnetic fields in the high corona.

Let us assume that the distance  $l_1$  between the source of a fast outflow (an edge of the HTTCS) and the stagnation point 2 at the magnetic obstacle is not too large (Fig. 9.5). This means that the outflow becomes *wider* but does not relax in the coronal plasma before reaching the obstacle. Moreover, if the flow velocity still exceeds the local velocity of a fast magnetoacoustic wave, a fast MHD shock appears ahead the obstacle, which is similar to the terrestrial bow shock ahead the magnetosphere (see Sect. 10.2.2).

**Fig. 9.4** A SHTCL as the source of the super-hot plasma outflow with velocity  $v_1$ . Magnetic obstacle (MO) is the SXR loop shown by shadow.  $v_2$  is the postshock velocity,  $v_3$  is the velocity of expansion of the compressed plasma along the field lines toward the feet of the loop



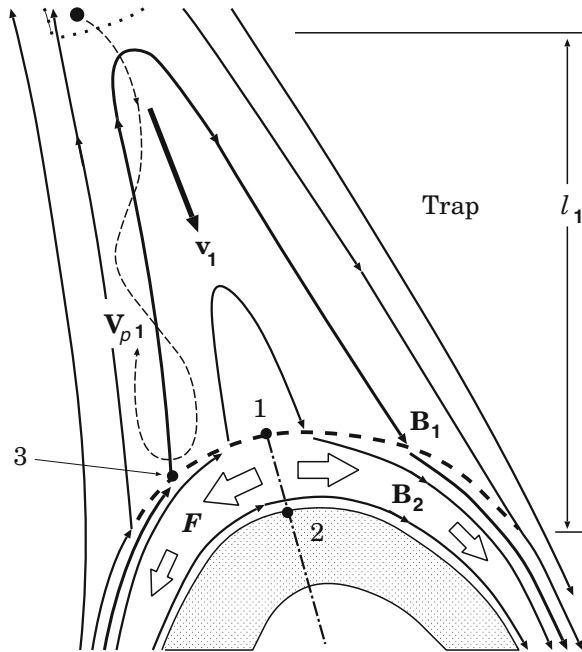
By analogy with the ordinary hydrodynamics of supersonic flows, we assume that the shock front reproduces the shape of the obstacle smoothly and on a larger scale (Fig. 9.5), more exactly, the shape of the upper part of the obstacle facing the incoming flow. This is true if the incoming flow is uniform or quasi-uniform. Generally, the incoming flow may significantly differ from a quasi-uniform one. Hence the shock may have a more complicated shape. This is, however, not crucial to the effect of the collapsing magnetic trap discussed below. For simplicity, in Fig. 9.5, all the field lines ejected by the SHTCL penetrate through the shock. Therefore all super-hot plasma and all particles pre-accelerated by the SHTCL, being frozen into the reconnected field lines, interact with the shock.

For what follows the most important point is that, with respect to the particles pre-accelerated and to super-hot particles energized by the SHTCL, the shock should be considered as a *fast oblique collisionless shock* (FOCS).

### 9.2.3 Particle Acceleration in Collapsing Trap

Being frozen into super-hot plasma, the reconnected field lines move out of the SHTCL and form magnetic loops at the height  $l_1$  above the magnetic obstacle.

**Fig. 9.5** A magnetic trap between the SHTCL and the shock front; an accelerated particle moves with velocity  $v_{p1}$  along the field lines. Big arrows  $F$  show heat fluxes, directed along the field lines



The top of each loop moves with a high velocity  $v_1 \approx 1,400\text{--}2,000 \text{ km s}^{-1}$ . The local fast magne-toacoustic wave speed  $\approx 1,000 \text{ km s}^{-1}$ . Therefore a fast shock may appear between the SHTCL and the obstacle. Let us assume that both feet of a loop penetrate through the shock front ahead the obstacle.

Depending on the velocity and pitch-angle, some of the particles pre-accelerated by the SHTCL may pass directly through the magnetic field jump related to the shock. Others may either be simply reflected by the shock or interact with it in a more complicated way.

For the particles reflected by the shock the magnetic loop represents a trap whose length decreases from the initial length  $L_0 \approx 2l_1$  to zero (*collapses*) with the velocity  $v_m \approx 2v_1$ . Therefore the lifetime of each magnetic field line – of each collapsing trap – is equal to

$$t_1 \approx l_1/v_1 \sim 10 \text{ s}, \quad (9.1)$$

if  $l_1 \approx 10^4 \text{ km}$  and  $v_1 \approx 10^3 \text{ km s}^{-1}$  are taken as the characteristic values for the length and velocity.

During the trap lifetime  $t_1$  the reflected fast particles move between two magnetic corks – the reflecting points where the field line crosses the shock front. Since these corks (or magnetic mirrors) move to each other with the velocity  $v_m$ , the particles trapped inside the trap are ‘heated’ quickly by the first-order Fermi-type mechanism.

For the electrons pre-accelerated by the SHTCL we estimate the characteristic value of the velocity as  $V_{e,1} \approx 10^{10} \text{ cm s}^{-1}$ . Hence the characteristic time between two subsequent reflections of a particle is estimated as

$$\tau_1 \approx 2l_1/V_{e,1} \sim 0.1 \text{ s.} \quad (9.2)$$

Since  $\tau_1 \ll t_1$ , the conditions of the periodic longitudinal motions change *adiabatically* slowly (see Part I, Sect. 6.1). Then the *longitudinal* adiabatic invariant is conserved (Part I, Sect. 6.2):

$$I = \oint p_{\parallel} dl \approx p_{\parallel}(t) \cdot 4l(t) = \text{const.} \quad (9.3)$$

Here  $p_{\parallel} = p \cos \theta$  is the particle longitudinal momentum,  $\theta$  is its pitch angle. From (9.3) it follows that

$$p_{\parallel}(t) = p_{\parallel}(0) \frac{l_1}{l(t)} \approx p_{\parallel}(0) \frac{1}{1 - (t/t_1)}. \quad (9.4)$$

When the magnetic trap collapses, the longitudinal momentum of a particle grows *infinitely* within the *finite* lifetime  $t_1$ .

Neglecting an unknown change of the transversal momentum, we see that the particle kinetic energy of longitudinal motion increases within the time scale  $t_1$ :

$$\mathcal{K}_{\parallel}(t) = \frac{1}{2m} p_{\parallel}^2 = \mathcal{K}_{\parallel}(0) \frac{1}{[1 - (t/t_1)]^2}. \quad (9.5)$$

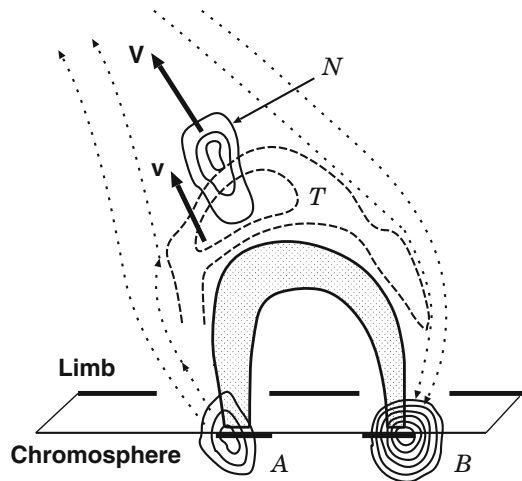
That is why we can assume, for example, that just the trap lifetime  $t_1$  is responsible for the observed few-second delay in the higher energies of the hard X-ray (HXR) and gamma-ray emission (Bai et al. 1983).

The main objection usually raised against Fermi acceleration is that the Fermi mechanism is ‘neither efficient nor selective’. A magnetic mirror reflects particles on a non-selective basis: thermal particles may be reflected as well as supra-thermal ones. Hence most of the primary energy – the kinetic energy of the fast flow of super-hot plasma – goes into bulk heating of the plasma rather than the selective acceleration of only a small minority of the fast particles. This ‘disadvantage’ appears to be the main *advantage* of the Fermi mechanism when applied to solar flares in the frame of the collapsing trap model (Somov and Kosugi 1997).

First, the collapsing trap heats and compresses the super-hot plasma. Thus it becomes visible in HXR emission. Second, the same mechanism lifts some electrons from a quasi-thermal distribution and accelerates them to higher energies; even better, it can further accelerate the electrons pre-accelerated by the SHTCL. The trap of the accelerated electrons is seen as the non-thermal component of the coronal HXR source in flares. Third,

being non-selective, the collapsing magnetic trap can accelerate not only electrons but also protons and other ions to high energies.

**Fig. 9.6** The non-thermal ( $N$ ) and quasi-thermal ( $T$ ) components of the coronal HXR emission and their apparent motion.  $A$  and  $B$  are the chromospheric footpoints



This is a big problem for many other acceleration mechanisms.

Super-hot plasma trapped inside the collapsing loops certainly also contributes to the HXR and radio emission above the SXR loop. The total coronal HXR emission consists of two parts: non-thermal and quasi-thermal. The model predicts, however, a significant difference between them. Being more collisional, the super-hot plasma is less confined inside the trap. For this reason the non-thermal emission dominates at higher energies and occupies a more compact ‘vertical’ (Fig. 9.6) HXR source in comparison with more extended ‘horizontal’ distribution of a quasi-thermal emission at lower energies. This seems to be well consistent with the *Yohkoh* results (Tsuneta et al. 1997).

Electron acceleration in the collapsing trap seems to be consistent with the results of the wavelet analysis of the solar flare HXR (Aschwanden et al. 1998). This analysis yields a dynamic decomposition of the power at different timescales  $\tau$ . The lifetime  $t_1$  may correspond to the dominant peak time  $\tau_{\text{peak}}$  detected in the wavelet scalograms. The collapsing trap scenario is also consistent with the observed correlations, because the acceleration time is proportional to the spatial size of the collapsing trap ( $\tau_{\min} \sim l_1$ ).

#### 9.2.4 The Upward Motion of Coronal HXR Sources

Further development required for the collapsing trap model is a quantitative consideration of the upward motion of the coronal X-ray sources predicted by the model (Somov et al. 1999). It is clear that the super-hot plasma heated and compressed inside the trap will unavoidably relax in the downstream flow behind the shock. This relaxation is strongly influenced by thermal conductive cooling,

hydrodynamic expansion as well as by radiative energy losses. The dynamics of relaxation may not be simple and will depend on the initial and boundary conditions.

The behavior of the magnetic field behind the shock seems to be more determined – the incoming field lines simply accumulate between the obstacle and the shock. Hence the shock must move upward together with the HXR source in the upstream side (Fig. 9.6) and the SXR source in the downstream side.

In the adiabatic approximation, the post-shock pressure would reach extremely high values. As a result, the shock should be accelerated to speeds of order 1,000 km/s. This value exceeds by two orders of magnitude the upward speed of the coronal HXR source observed in flares, which usually does not exceed 10–20 km/s.

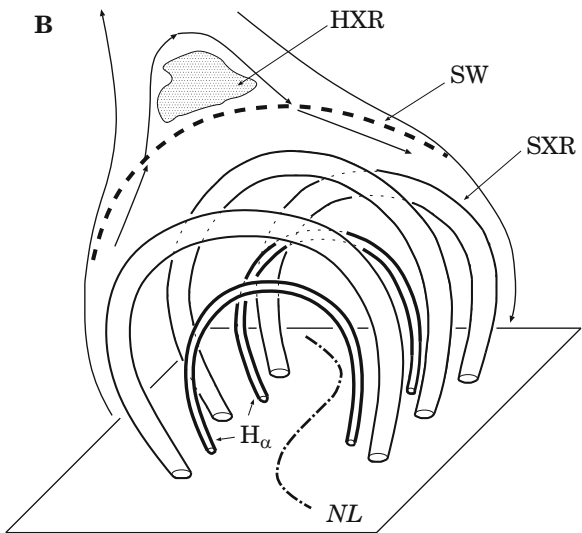
Post-shock energy losses considerably change shock parameters. [Bogachev et al. \(1998\)](#) have considered three mechanisms of energy losses from the shock-compressed super-hot plasma: anomalous heat conduction, hydrodynamic expansion, and radiation. According to estimates, timescales of the first two processes do not exceed a few seconds, whereas radiative losses are much slower and can be initially neglected.

A fast removal of heat from the post-shock super-hot plasma and its expansion lead to a considerable decrease of the temperature and, as a consequence, of the gas pressure. As a result, the shock speed  $v_2$  noticeably decreases. For large flow speeds  $v_1$ , the shock speed  $v_2$  is proportional to the Alfvén speed upstream, i.e. directly proportional to the field  $B_1$ , frozen into the plasma, and inversely proportional to the square root of electron number density  $n_1$ . In particular, if we adopt  $n_1 \approx 2 \times 10^9 \text{ cm}^{-3}$  and  $B_1 \approx 0.5 \text{ G}$ , then the shock is moving at a speed of order 10 km/s, which coincides with the observed upward speed. Of course, this combination of  $n_1$  and  $B_1$  is not unique; we give it here just as the most plausible one on the basis of the *Yohkoh* observations.

However, if we assume higher densities of the flow, we have to assume stronger fields frozen into super-hot plasma. This is acceptable. On the other hand, the shock speed only very weakly depends on the temperature and on the upstream speed. For this reason, a considerable uncertainty in these quantities (especially in the latter one) practically does not affect the results. Moreover, taking into account that the magnetic obstacle is not ideal ([Somov et al. 1999](#)) and hence some of plasma with the frozen-in field can ‘filter through’ it (Fig. 9.7) with speeds  $v_4 \approx v_2$ . This allows us to obtain better agreement of the upward shock speed  $v_2$  with observations for stronger magnetic fields in the corona above the shock.

To conclude, a fast MHD or collisionless shock wave with heat-conductive cooling of the post-shock plasma may play an important role in the dynamics of a coronal source of HXR during a solar flare. The upward speed of the shock is determined by two processes: accumulation of magnetic flux behind the shock and ‘filtering’ of cold dense filaments (together with the frozen-in field) through the magnetic obstacle. This scenario agrees with the observed hierarchy of hot (SXR) and cool (H $\alpha$ ) loops. For a more detailed comparison of the observed distributions of temperature and emission measure of the source, a more accurate model is required: it must take into account the actual structure of interaction of the super-Alfvén flow of super-hot magnetized plasma with a magnetic obstacle.

**Fig. 9.7** The two level structure of the SXR and H $\alpha$  loops in the solar corona, created as a result of an instability of the magnetic obstacle.  $NL$  is the photospheric neutral line,  $B$  represents the magnetic field lines in the corona



### 9.2.5 Trap Without a Shock Wave

If, on the contrary to the assumption made above, the distance  $l_1$  between the SHTCL and the stagnation point is large enough, then the fast flow of ‘super-hot’ plasma relaxes gradually with (or without) collisional shock depending on the height of the reconnection site and other conditions in an active region where the flare occurs. For example, collisional relaxation can be very fast near the SHTCL if the plasma density is relatively high but the temperature inside the RCL is relatively low.

Let us consider the configuration of a magnetic trap with field lines rapidly moving down but without any shock (Fig. 9.8).

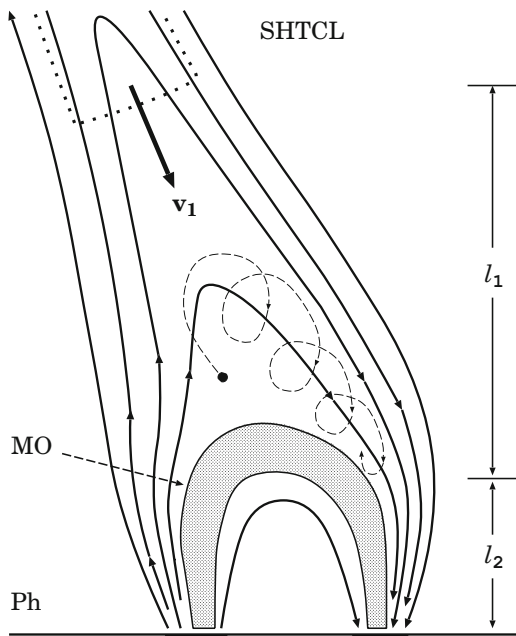
The strongly decreasing length of the field lines leads to a decrease of the distance between the mirror points and a consequent Fermi-type acceleration of charged particles, while the general increase of the magnetic field strength gives rise to the betatron acceleration. Both effects are considered in Sect. 9.3 in the adiabatic approximation by using two adiabatic invariants. For the sake of simplicity, let us consider the first effect as a starting point.

In this case, instead of formula (9.4), we have for the collapsing trap without a shock wave another simple formula:

$$\begin{aligned} p_{\parallel}(t) &\approx p_{\parallel}(0) \frac{(l_1 + l_2)}{l_2 + (l_1 - v_1 t)} \\ &\Rightarrow p_{\parallel}(0) \frac{(l_1 + l_2)}{l_2}, \quad \text{when } t \rightarrow t_1. \end{aligned} \quad (9.6)$$

So the trap does not collapse.

**Fig. 9.8** Trap without a shock. A SHTCL provides the plasma outflow. Magnetic obstacle (*MO*) is the SXR loop shown by shadow. The stretched field lines are carried away from the SHTCL by reconnection outflow and relax to a lower energy state. Since the magnetic field strength increases with decreasing coronal height, particles can be trapped within this configuration



If the height  $l_2$  of the magnetic obstacle is not small, the adiabatic heating of fast particles inside the trap is less efficient than in the collapsing trap with the shock. The small height  $l_2$  is probably the case of the so-called ‘shrinkage’ of X-ray loops, as observed at first by the *Yohkoh* SXT (McKenzie and Hudson 1999). Such situation is expected when magnetic reconnection takes place high in the corona, far from photospheric magnetic-field sources, as follows, for example, from the *SOHO* observations made with LASCO (e.g., Wang and Sheeley 2002; see also discussion in Sect. 9.2.2).

In the physics of the Earth magnetosphere, the similar process of recovering the dipole-type geometry of magnetic field lines is called *dipolarization*. It follows the transient reconnection in the magnetotail. Dipolarizations are often observed and well investigated in the near-Earth and in the mid-tail plasma layer (see Sergeev et al. 2008; Runov et al. 2009).

## 9.3 Acceleration Mechanisms in Traps

### 9.3.1 Fast and Slow Reconnection

Collapsing magnetic traps are formed by the process of collisionless reconnection in the solar atmosphere. Figure 9.9 illustrates two possibilities. Fast (Fig. 9.9a) and

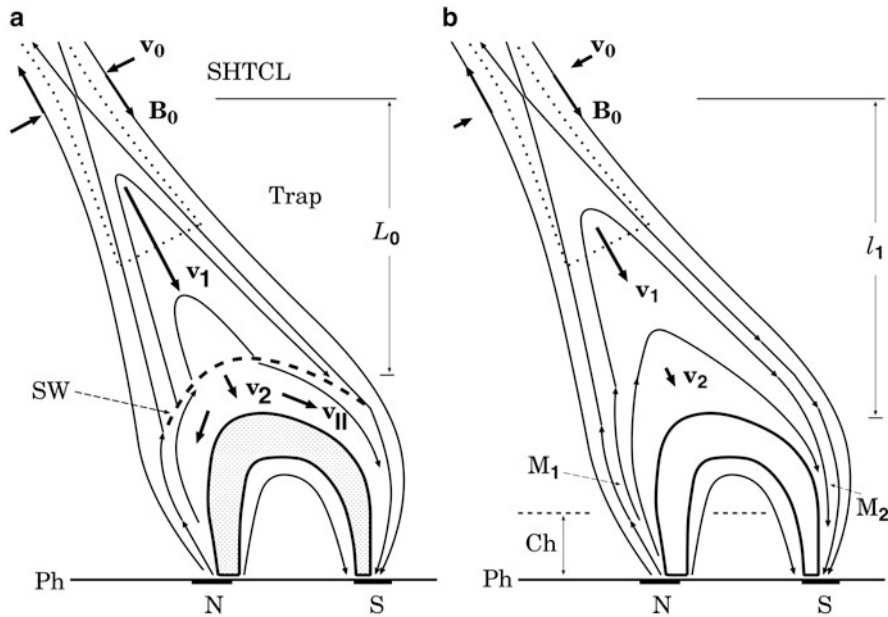


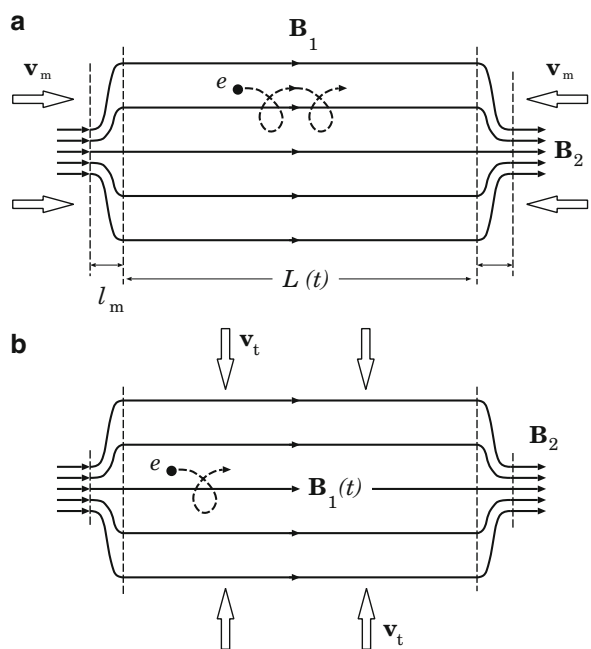
**Fig. 9.9** Plasma flows related to a super-hot turbulent-current layer (SHTCL): the inflows with a relatively low velocity  $v_0$ , the downward outflow with a super-Alfvén velocity  $v_1$ . (a) SW is the shock wave above the magnetic obstacle.  $v_2$  is the post-shock velocity,  $v_{||}$  is the velocity of spreading of the compressed plasma along the field lines toward the feet of the loop. (b) The supra-arcade downflow and collapsing trap without a shock.  $M_1$  and  $M_2$  are the mirroring points where the field becomes sufficiently strong to reflect fast particles above the chromosphere ( $Ch$ )

slow (Fig. 9.9b) modes of reconnection are sketchy shown in the corona above the magnetic obstacle, the region of a strong magnetic field, which is observed in SXRs as a flare loop (shaded).

In the first case, let us assume that both feet of a reconnected field loop path through the shock front (SW in Fig. 9.9a) ahead the obstacle. Depending on the velocity and pitch-angle, some of the particles preaccelerated by the SHTCL may penetrate through the magnetic-field jump related to the shock or may be reflected. For the particles reflected by the shock, the magnetic loop represents a trap whose length  $L(t)$ , the distance between two mirroring points at the shock front, measured along a magnetic-field line, decreases from its initial value  $L(0) \approx 2L_0$  to zero (the top of the loop goes through the shock front) with the velocity  $\approx 2v_1$ . Therefore, the lifetime of each collapsing trap  $t_1 \approx L_0/v_1$ .

In the case of slow reconnection, there is no a shock wave, and the trap length  $L(t)$  is the distance between two mirroring points ( $M_1$  and  $M_2$  in Fig. 9.9b), measured along a reconnected magnetic-field line. In both cases, the electrons and ions are captured in a trap whose length decreases. So the particles gain energy from the increase in parallel momentum.

**Fig. 9.10** Two main effects in a collapsing trap. (a) Magnetic mirrors move toward each other with velocity  $v_m$ . (b) Compression of the trap with velocity  $v_t$



Note that the opposite effect – a decrease in parallel momentum and the related adiabatic cooling – should occur for particles trapped between two slow shocks in the Petschek-type MHD reconnection model (see Tsuneta and Naito (1998), Fig. 1) because the length of the trap (the distance between the two slow shocks in the reconnection downflow) increases with time. However, Tsuneta and Naito considered acceleration by a fast termination shock; more exactly, they assumed that nonthermal electrons in solar flares can be efficiently accelerated at the fast shock (see the same Figure) by the first-order Fermi-type process if the diffusion length is sufficiently small. The opposite limiting case will be assumed in what follows.

Thus, in the first approximation, we shall neglect collisions of particles ahead of the shock wave (Fig. 9.9a) or in the trap without a shock (Fig. 9.9b). In both cases, the particle acceleration can be demonstrated in a simple model – a long trap with short mirrors (Fig. 9.10). The decreasing length  $L(t)$  of the trap is much larger than the length  $l_m$  of the mirrors; the magnetic field  $\mathbf{B} = \mathbf{B}_1$  is uniform inside the trap but grows from  $\mathbf{B}_1$  to  $\mathbf{B}_2$  in the mirrors. The quantity  $B_2/B_1$  is called the mirror ratio; the larger this ratio, the higher the particle confinement in the trap. The validity conditions for the model are discussed by [Somov and Bogachev \(2003\)](#).

### 9.3.2 *The First-Order Fermi-Type Acceleration*

We consider the traps for those the length scale and timescale are both much larger than the gyroradius and gyroperiod of an accelerated particle. Due to strong separation of length and timescales, the magnetic field inside a trap can be considered as uniform and constant (for more detail see [Somov and Bogachev 2003](#)). If so, then the longitudinal momentum of a particle increases with a decreasing length  $L(t)$ , in the adiabatic approximation, as

$$p_{\parallel}(l) = \frac{p_{\parallel 0}}{l}. \quad (9.7)$$

Here  $l = L(t)/L(0)$  is the dimensionless length of the trap. The transverse momentum is constant inside the trap,

$$p_{\perp} = p_{\perp 0}, \quad (9.8)$$

because the first adiabatic invariant is conserved:

$$\frac{p_{\perp}^2}{B} = \text{const.} \quad (9.9)$$

Thus the kinetic energy of the particle increases as

$$K(l) = \frac{p_{\parallel}^2 + p_{\perp}^2}{2m} = \frac{1}{2m} \left( \frac{p_{\parallel 0}^2}{l^2} + p_{\perp 0}^2 \right). \quad (9.10)$$

The time of particle escape from the trap,  $l = l_{es}$ , depends on the initial pitch-angle  $\theta_0$  of the particle and is determined by the condition

$$\tan \theta_0 = \frac{p_{\perp 0}}{p_{\parallel 0}} \leq \frac{1}{R l_{es}}, \quad (9.11)$$

where

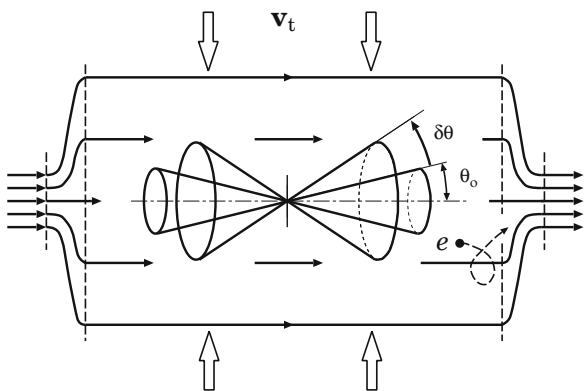
$$R = \left( \frac{B_2}{B_1} - 1 \right)^{1/2}. \quad (9.12)$$

The kinetic energy of the particle at the time of its escape is

$$K_{es} = \frac{p_{\perp 0}^2}{2m} (R^2 + 1) = \frac{p_{\perp 0}^2}{2m} \frac{B_2}{B_1}. \quad (9.13)$$

One can try to obtain the same canonical result by using more complicated approaches. For example, [Giuliani et al. \(2005\)](#) numerically solved the drift equations of motion (see Part I, Sect. 5.2). However it is worthwhile to explore first

**Fig. 9.11** The betatron effect in a collapsing magnetic trap. As the trap is compressed with velocity  $v_t$ , the loss cone becomes larger. A particle escapes from the trap earlier with an additional energy due to betatron acceleration



the simple analytical approach presented in this Chapter to investigate the particle energization processes in collapsing magnetic traps in more detail before starting to use more sophisticated methods and large-scale simulations.

### 9.3.3 The Betatron Acceleration in a Collapsing Trap

If the thickness of the trap also decreases with its decreasing length, then the strength of the field  $\mathbf{B}_1$  inside the trap increases as a function of  $l$ , say  $B_1(l)$ . In this case, according to (9.9), the transverse momentum increases simultaneously with the longitudinal momentum (9.7):

$$p_{\perp}(l) = p_{\perp 0} \left( \frac{B_1(l)}{B_1} \right)^{1/2}. \quad (9.14)$$

Here  $B_1 = B_1(1)$  is the initial (at  $l = 1$ ) value of magnetic field inside the trap.

The kinetic energy of a particle

$$K(l) = \frac{1}{2m} \left( \frac{p_{\parallel 0}^2}{l^2} + p_{\perp 0}^2 \frac{B_1(l)}{B_1} \right) \quad (9.15)$$

increases faster than that in the absence of trap contraction, see (9.10). Therefore it is natural to assume that the acceleration efficiency in a collapsing trap also increases.

However, as the trap is compressed, the loss cone becomes larger (Fig. 9.11),

$$\theta_{es}(l) = \arcsin \left( \frac{B_1(l)}{B_2} \right)^{1/2}. \quad (9.16)$$

Consequently, the particle escapes from the trap earlier.

On the other hand, the momentum of the particle at the time of its escape satisfies the condition

$$p_{\parallel}(l) = R(l) p_{\perp}(l), \quad (9.17)$$

where

$$R(l) = \left( \frac{B_2}{B_1(l)} - 1 \right)^{1/2}. \quad (9.18)$$

Hence, using (9.14), we determine the energy of the particle at the time of its escape from the trap

$$K_{es} = \frac{p_{\perp}(l)^2}{2m} (R(l)^2 + 1) = \frac{p_{\perp 0}^2}{2m} \frac{B_1(l)}{B_1} \frac{B_2}{B_1(l)} = \frac{p_{\perp 0}^2}{2m} \frac{B_2}{B_1}. \quad (9.19)$$

The kinetic energy (9.19), that the particle gains in a collapsing trap with compression, is equal to the energy (9.13) in a collapsing trap without compression, i.e. without the betatron effect.

Thus the compression of a collapsing trap (as well as its expansion or the transverse oscillations) does not affect the final energy that the particle acquires during its acceleration.

**|** The faster gain in energy is *exactly* offset by the earlier escape of the particle from the trap

(Somov and Bogachev 2003).

The acceleration efficiency, which is defined as the ratio of the final ( $l = l_{ls}$ ) and initial ( $l = 1$ ) energies, i.e.

$$\frac{K_{es}}{K(1)} = \frac{p_{\perp 0}^2}{p_{\perp 0}^2 + p_{\parallel 0}^2} \frac{B_2}{B_1} = \left( \frac{p_{\perp 0}}{p_0} \right)^2 \frac{B_2}{B_1}, \quad (9.20)$$

depends only on the initial mirror ratio  $B_2/B_1$  and the initial particle momentum or, to be more precise, on the ratio  $p_{\perp 0}/p_0$ . The acceleration efficiency (9.20) does not depend on the compression of collapsing trap and the pattern of decrease in the trap length either.

It is important that

**|** the acceleration time in a collapsing trap with compression can be much shorter than that in a collapsing trap without compression.

For example, if the cross-section area  $S(l)$  of the trap decreases proportionally to its length  $l$ :

$$S(l) = S(1) l, \quad (9.21)$$

then the magnetic field inside the trap

$$B_1(l) = B_1(1) / l, \quad (9.22)$$

and the effective parameter

$$R(l) = \left( R^2 - \frac{1-l}{l} \right)^{1/2}, \quad (9.23)$$

where  $R$  is defined by formula (9.12). At the critical length

$$l_{cr} = \frac{1}{1+R^2}, \quad (9.24)$$

the magnetic field inside the trap becomes equal to the field in the mirrors, and the magnetic reflection ceases to work. If, for certainty,  $B_2/B_1 = 4$ , then  $l_{cr} = 1/4$ . So contraction of the collapsing trap does not change the energy of the escaping particles but this energy is reached at an earlier stage of the magnetic collapse when the trap length is finite. In this sense, the betatron effect increases the actual efficiency of the main process – the particle acceleration on the converging magnetic mirrors.

### 9.3.4 The Betatron Acceleration in a Shockless Trap

If we ignore the betatron effect in a shockless collapsing trap, shown in Fig. 9.9b, then the longitudinal momentum of a particle is defined by the formula (instead of (9.7))

$$p_{\parallel}(t) \approx p_{\parallel}(0) \frac{(l_1 + l_2)}{l_2 + (l_1 - v_1 t)} \Rightarrow p_{\parallel}(0) \frac{(l_1 + l_2)}{l_2}, \quad \text{when } t \rightarrow t_1. \quad (9.25)$$

The particle acceleration on the magnetic mirrors stops at the time  $t_1 = l_1/v_1$  at a finite longitudinal momentum that corresponds to a residual length ( $l_2$  in Fig. 9.9b) of the trap.

Given the betatron acceleration due to compression of the trap, the particle acquires the same energy (9.13) by this time or earlier if the residual length of the trap is comparable to a critical length  $l_{cr}$  determined by a compression law (see [Somov and Bogachev 2003](#)). Thus the acceleration in shockless collapsing traps with a residual length becomes more plausible. The possible observational manifestations of such traps in the X-ray and optical radiation are discussed by [Somov and Bogachev \(2003\)](#). The most sensitive tool to study behavior of the electron acceleration in the collapsing trap is radio radiation. We assume that wave-particle interactions are important and that two kinds of interactions should be considered in the collapsing trap model.

The first one is resonant scattering of the trapped electrons, including the loss-cone instabilities and related kinetic processes (e.g., [Benz \(2002\)](#)), Chap. 8. Resonant scattering is most likely to enhance the rate of precipitation of the

electrons with energy higher than 100 keV, generating microwave bursts. The loss-cone instabilities of trapped mildly-relativistic electrons (with account taken of the fact that there exist many collapsing field lines at the same time, each line with its proper time-dependent loss cone) would provide excitation of waves with a very wide continuum spectrum. In a flare with a slowly-moving upward coronal HXR source, an ensemble of the collapsing field lines with accelerated electrons would presumably be observed as a slowly moving type IV burst with a very high brightness temperature and with a possibly significant time delay relative to the chromospheric footpoint emission.

The second kind of wave-particle interactions in the collapsing trap-plus-precipitation model is the streaming instabilities (including the current instabilities related to a return current) associated with the precipitating electrons.

## 9.4 Main Properties of Trapped Particles

### 9.4.1 Dominant Mechanism of Acceleration

In this Section, we develop a model of a trap in which both the Fermi and betatron accelerations are in action. This model will allow us to compare the efficiencies of the two mechanisms, as applied to the problem of electron acceleration in solar flares and to the observed HXR sources in the solar corona (see Sect. 9.1).

Let us consider the electrons confined in an axially-symmetric magnetic-flux tube with a field  $B$  that is minimal at the center of the trap,  $B = B_1$ , and increases at its edges to  $B_2$ , as illustrated, for example, in Fig. 9.10.  $B_2$  and  $B_2/B_1$  are commonly called the field in the magnetic mirrors and the mirror ratio, respectively. We shall describe the transverse contraction of the tube by the quantity

$$b(t) = B(t)/B_1, \quad (9.26)$$

which changes from the initial value of  $b(0) = 1$  at which  $B(0) = B_1$  to the maximal value

$$b_m = B_2/B_1, \quad (9.27)$$

at which the field at the center of the trap,  $B(t)$ , becomes equal to the field in the mirrors,  $B_2$ , and, therefore, the trap ceases to confine the particles.

To describe the change in the trap length  $L$  with time, we use the parameter

$$l(t) = L(t)/L_0, \quad (9.28)$$

which decreases from  $l(0) = 1$  to  $l = 0$  or to a certain very low value corresponding to the residual trap length (see Figs. 9.8 and 9.9b).

As discussed above, we assume that the adiabatic invariants are conserved: the longitudinal invariant

$$p_{\parallel} L = p_{\parallel 0} L_0 = \text{const} \quad (9.29)$$

and the transverse invariant

$$p_{\perp}^2 / B = p_{\perp 0}^2 / B_0 = \text{const}. \quad (9.30)$$

Combining (9.26) and (9.28) with (9.29) and (9.30), we find how the particle momentum components change as the length of the trap decreases and as it contracts:

$$p_{\parallel} = \frac{p_{\parallel 0}}{l} \quad (9.31)$$

and

$$p_{\perp} = p_{\perp 0} \sqrt{b}, \quad (9.32)$$

respectively.

In the case of Fermi acceleration, the longitudinal momentum increases according to (9.31), while the transverse momentum remains constant. The betatron acceleration increases the transverse momentum (9.32) and does not change the longitudinal one. As a result, the Fermi and betatron accelerations are always accompanied, respectively, by a decrease and an increase in the pitch angle. When both mechanisms act simultaneously, the pitch angle changes as follows:

$$\operatorname{tg} \theta = \frac{p_{\perp}}{p_{\parallel}} = l \sqrt{b} \left( \frac{p_{\perp 0}}{p_{\parallel 0}} \right) = l \sqrt{b} \operatorname{tg} \theta_0. \quad (9.33)$$

If  $l \sqrt{b} < 1$ , then the pitch angle of the accelerated particles decreases. Although both mechanisms act in such a trap, it is closer in particle behavior to a collapsing trap with Fermi acceleration. If, alternatively,  $l \sqrt{b} > 1$ , then the pitch angle of particles during their acceleration increases. In this case, the trap is closer in properties to a trap with betatron acceleration. The condition

$$l \sqrt{b} = 1 \quad (9.34)$$

separates these two cases.

When condition (9.34) is satisfied, the trapped particles accelerate without any change in their pitch angle:  $\operatorname{tg} \theta = \operatorname{tg} \theta_0$ . If the physical model with a collapsing trap as its element allows the functions  $b(t)$  and  $l(t)$  to be determined observationally or theoretically, then we can determine which type of acceleration dominates throughout the trap contraction process or even at its different stages by comparing these functions.

The kinetic energy of the non-relativistic particles captured into a contracting trap is

$$\mathcal{K} = \frac{p_{\parallel}^2 + p_{\perp}^2}{2m} = \frac{1}{2m} \left( \frac{p_{\parallel 0}^2}{l^2} + b p_{\perp 0}^2 \right) = \mathcal{K}_0 \left( \frac{\cos^2 \theta_0}{l^2} + b \sin^2 \theta_0 \right); \quad (9.35)$$

it can only increase since  $l \leq 1$   $b \geq 1$ . Here  $\mathcal{K}_0 = p_0^2/2m$  is the initial energy of the particle. The energy is transferred mainly to the longitudinal (along the magnetic field lines) and transverse degrees of freedom under the dominant Fermi ( $l\sqrt{b} < 1$ ) and betatron ( $l\sqrt{b} > 1$ ) accelerations, respectively. When  $l\sqrt{b} = 1$ , the energy is distributed uniformly between the degrees of freedom, and its increase does not depend on the pitch angle:  $\mathcal{K} = \mathcal{K}_0/l^2$ . We call this case the isotropic acceleration.

In general, the energy of the particle increases until it falls into the loss cone. The particle pitch angle at this time is defined by the equation

$$\operatorname{tg} \theta_{es} = \frac{1}{\sqrt{B_2/B - 1}} = \frac{1}{\sqrt{b_m/b - 1}}. \quad (9.36)$$

Comparing (9.33) and (9.36), we find that the relation

$$l^2 b \operatorname{tg}^2 \theta_0 = \frac{1}{b_m/b - 1}$$

or

$$\frac{1}{l^2 \operatorname{tg}^2 \theta_0} = b_m - b. \quad (9.37)$$

must hold at the time of particle escape from the trap.

Let us transform formula (9.35) for the particle energy as follows:

$$\mathcal{K} = \mathcal{K}_0 \sin^2 \theta_0 \left( \frac{1}{l^2 \operatorname{tg}^2 \theta_0} + b \right).$$

Substituting in this formula condition (9.37) yields the particle energy at the escape time

$$\mathcal{K}_{es} = \mathcal{K}_0 b_m \sin^2 \theta_0. \quad (9.38)$$

If the trap contracts not only in the longitudinal direction but also in the transverse direction, then the particle in the trap acquires an additional energy through its betatron acceleration. So the acceleration rate increases. However the final energy that the particle acquires does not change. This is because the loss cone (9.36) depends on the mirror ratio. As the magnetic-flux tube contracts, the mirror ratio decreases, while the loss cone grows. This reduces the particle confinement time exactly to the extent needed to compensate for the effect of their faster acceleration as we already saw in Sect. 9.3.3.

For any combination of the Fermi and betatron accelerations, the particle final energy remains constant

and is defined by formula (9.38). This property simplifies the analysis of the problem in which particles with initial energy  $\mathcal{K}_0$  arrive from the coronal reconnecting current layer, while particles with energy  $\mathcal{K}_{esc}$  precipitate from the trap into the chromosphere. The particle acceleration mechanism inside the trap may not be concretized; each of them or both lead to the same final energy at the exit from the trap.

The second conclusion drawn from formula (9.38) is a constraint on the energy that a particle gains in the trap. The maximum energy depends only on the mirror ratio:

$$\mathcal{K}_{max} = \mathcal{K}_0 b_m. \quad (9.39)$$

In solar flare, electrons with initial energy  $\mathcal{K}_{ef} \sim 10 \text{ keV}$  can be accelerated to energies  $\sim 1 \text{ MeV}$  only inside traps with a mirror ratio  $b_m = B_2/B_1 \gtrsim 100$ . For this reason, no efficient particle acceleration is possible inside the trap formed above the front of an adiabatic shock, since the jump in field at its front does not exceed  $B_2/B_1 = 4$ . Bogachev et al. (1998) showed that the mirror ratio could increase by more than an order of magnitude if the adiabatic approximation is inapplicable to the shock, for example, due to rapid cooling of postshock plasma (see also Exercise 9.3).

#### 9.4.2 Anisotropy of Trapped Particles

The distribution of the particles captured into a collapsing trap transforms with time because their energy changes and they escape into the loss cone. Let us consider first the former effect.

The initial distribution of electrons is determined by the energization processes that precede their injection into the trap, i.e., by their heating to anomalously high temperatures and their preacceleration in the super-hot turbulent-current layer (SHTCL). Let the initial electron distribution  $f_0(\mathcal{K}_0)$  be given and normalized in the standard way:

$$dN(\mathcal{K}_0, \theta_0) = N_0 f_0(\mathcal{K}_0) d\mathcal{K}_0 2\pi \sin \theta_0 d\theta_0, \quad (9.40)$$

$$\int_0^\infty f_0(\mathcal{K}_0) d\mathcal{K}_0 \int_0^\pi 2\pi \sin \theta_0 d\theta_0 = 4\pi \int_0^\infty f_0(\mathcal{K}_0) d\mathcal{K}_0 = 1, \quad (9.41)$$

where  $N_0$  is the number of electrons injected into the trap. Here, the initial distribution of electrons is assumed to be independent of the pitch angle. We also assume that the trap is symmetric relative to the magnetic mirrors. Both these assumptions may be abandoned when needed.

The relationship between the initial distribution function  $f_0(\mathcal{K}_0)$  and the distribution function  $f(\mathcal{K}, \theta)$  of the trapped ( $\theta > \theta_{es}$ ) particles is defined by the condition for the conservation of the number of particles

$$2\pi f(\mathcal{K}, \theta) \sin \theta = 2\pi \mathcal{P} f_0(\mathcal{K}_0) \sin \theta_0, \quad (9.42)$$

where the transformation Jacobian

$$\mathcal{P} = \frac{\partial \theta_0}{\partial \theta} \frac{\partial \mathcal{K}_0}{\partial \mathcal{K}} - \frac{\partial \theta_0}{\partial \mathcal{K}} \frac{\partial \mathcal{K}_0}{\partial \theta}.$$

Since, according to (9.33), the change in pitch angle does not depend on energy, the Jacobian  $\mathcal{P}$  is

$$\mathcal{P} = \frac{\partial \theta_0}{\partial \theta} \frac{\partial \mathcal{K}_0}{\partial \mathcal{K}}. \quad (9.43)$$

Substituting (9.43) into (9.42) yields

$$f(\mathcal{K}, \theta) = \frac{\sin \theta_0}{\sin \theta} \frac{\partial \theta_0}{\partial \theta} \frac{\partial \mathcal{K}_0}{\partial \mathcal{K}} f_0(\mathcal{K}_0). \quad (9.44)$$

Let us find first the derivative  $\partial \mathcal{K}_0 / \partial \mathcal{K}$ . The relationship between the initial and final particle energies is defined by formula (9.35). Let us transform it as follows:

$$\mathcal{K} = \frac{\mathcal{K}_0}{l^2} \left( \frac{1 + b l^2 \operatorname{tg}^2 \theta_0}{1 + \operatorname{tg}^2 \theta_0} \right). \quad (9.45)$$

According to (9.33)

$$b l^2 \operatorname{tg}^2 \theta_0 = \operatorname{tg}^2 \theta. \quad (9.46)$$

We substitute (9.46) into (9.45):

$$\mathcal{K}_0 = \left( \frac{\sin^2 \theta}{b} + l^2 \cos^2 \theta \right) \mathcal{K}; \quad (9.47)$$

whence we find the derivative

$$\frac{\partial \mathcal{K}_0}{\partial \mathcal{K}} = \frac{\sin^2 \theta}{b} + l^2 \cos^2 \theta. \quad (9.48)$$

Let us introduce the function

$$A_\theta = \frac{\sin^2 \theta}{b} + l^2 \cos^2 \theta \quad (9.49)$$

and rewrite (9.47) and (9.48) as

$$\mathcal{K}_0 = A_\theta \mathcal{K}, \quad (9.50)$$

$$\frac{\partial \mathcal{K}_0}{\partial \mathcal{K}} = A_\theta. \quad (9.51)$$

Let us now calculate the first two factors in formula (9.44). First, we transform them:

$$\frac{\sin \theta_0}{\sin \theta} \frac{\partial \theta_0}{\partial \theta} = - \frac{1}{\sin \theta} \frac{\partial}{\partial \theta} \cos \theta_0 = - \frac{1}{\sin \theta} \frac{\partial}{\partial \theta} \frac{1}{\sqrt{1 + \operatorname{tg}^2 \theta_0}}.$$

Using (9.46), we substitute  $\operatorname{tg} \theta_0$  for  $\operatorname{tg} \theta$  and obtain after transformation

$$\frac{\sin \theta_0}{\sin \theta} \frac{\partial \theta_0}{\partial \theta} = \frac{l}{b} \frac{1}{((\sin^2 \theta)/b + l^2 \cos^2 \theta)^{3/2}} = \frac{l}{b} \frac{1}{A_\theta \sqrt{A_\theta}}. \quad (9.52)$$

Substituting (9.50)–(9.52) into (9.44) yields the distribution of the trapped electrons in kinetic energy and pitch angle

$$f(\mathcal{K}, \theta) = \frac{l}{b \sqrt{A_\theta}} f_0(\mathcal{K} A_\theta). \quad (9.53)$$

Now integrating (9.53) over the energy yields the particle pitch-angle distribution

$$f(\theta) = \int_0^\infty f(\mathcal{K}, \theta) d\mathcal{K} = \frac{l}{b \sqrt{A_\theta}} \int_0^\infty f_0(\mathcal{K} A_\theta) d\mathcal{K}. \quad (9.54)$$

The function  $A_\theta$  was factored outside the integral sign since it does not depend on energy.

Let us make the substitution  $\mathcal{K}_0 = \mathcal{K} A_\theta$ :

$$f(\theta) = \frac{l}{b A_\theta^{3/2}} \int_0^\infty f_0(\mathcal{K}_0) d\mathcal{K}_0.$$

According to (9.41), the integral on the right-hand side is equal to  $1/4\pi$ . Thus, the function

$$f(\theta) = \frac{1}{4\pi} \frac{l}{b A_\theta^{3/2}} = \frac{1}{4\pi} \frac{l \sqrt{b}}{(\sin^2 \theta + b l^2 \cos^2 \theta)^{3/2}} \quad (9.55)$$

is the sought-for pitch-angle distribution of the trapped electrons (Bogachev and Somov 2005). It is shown in Fig. 9.12a for the Fermi acceleration ( $b \equiv 1$ ) and in Fig. 9.12b for the betatron acceleration ( $l \equiv 1$ ). In both cases, the initial distribution ( $l = 1, b = 1$ ) was assumed to be isotropic. The subsequent evolution depends on which of the acceleration mechanisms dominates. For the Fermi mechanism, the electron pitch angles decrease, and the pitch-angle distribution is elongated along the trap axis, the  $x$  axis. In the trap with the betatron acceleration, the number of electrons with large pitch angle increases, and the pitch-angle distribution grows in the direction perpendicular to the  $x$  axis. In the boundary case ( $l \sqrt{b} = 1$ ), the electrons are accelerated with the isotropic distribution retained.

#### 9.4.3 The Number of Trapped Particles

The intensity of the HXR emission is proportional to the number of electrons  $N$  inside the trap. Let us find this number. Knowing how the particle pitch-angle

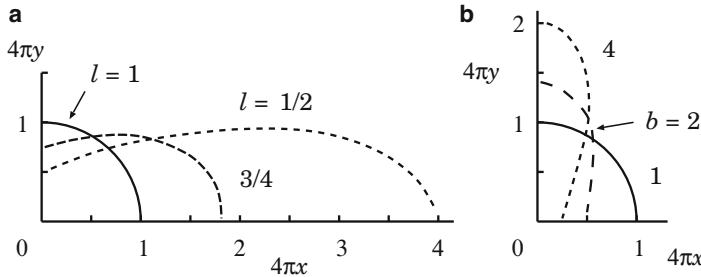


**Fig. 9.12** Change in the pitch-angle distribution of the trapped electrons as the trap contracts. (a) A longitudinally contracting trap; the particles are accelerated by the Fermi mechanism. Distributions corresponding to the decreasing length  $l = L/L_0 = 1, 3/4, 1/2$  are shown. (b) A transversely contracting trap; the particles are accelerated by the betatron mechanism under the magnetic-field contractions  $b = B/B_1 = 1, 2$ , and 4 (From [Bogachev and Somov 2005](#); reproduced with permission © Pleiades Publishing, Ltd.)

distribution (9.55) changes, let us determine how many particles are outside the loss cone, i.e., the total number of particles confined in the trap:

$$N = N_0 \int_{\theta_{es}}^{\pi - \theta_{es}} f(\theta) 2\pi \sin \theta d\theta = N_0 l \sqrt{b} \int_{\theta_{es}}^{\pi/2} \frac{\sin \theta d\theta}{(\sin^2 \theta + b l^2 \cos^2 \theta)^{3/2}}. \quad (9.56)$$

Here  $\theta_{es}$  is the loss cone (9.36), which, as the trap, is assumed to be symmetric relative to the magnetic mirrors.

Transforming the integrand

$$\frac{\sin \theta d\theta}{(\sin^2 \theta + b l^2 \cos^2 \theta)^{3/2}} = \frac{d (\tan^2 \theta)}{2 (\tan^2 \theta + b l^2)^{3/2}},$$

and making the substitution  $t = \tan^2 \theta$  yields

$$N = N_0 l \sqrt{b} \int_{t_0}^{\infty} \frac{dt}{(t + b l^2)^{3/2}}, \quad (9.57)$$

where

$$t_0 = \frac{b}{b_m - b}.$$

Performing the integration, we find the number of electrons in the trap ([Bogachev and Somov 2005](#)):

$$N = N_0 \frac{l \sqrt{b_m - b}}{\sqrt{1 + (b_m - b) l^2}}; \quad (9.58)$$

cf. formula (17) in [Somov and Bogachev \(2003\)](#).

If the trap length decreases, while the parameter  $b$  does not change, then the particles in the trap are accelerated by the Fermi mechanism. In this case, setting  $b = 1$  in (9.58)  $b = 1$ , we obtain

$$N = N_0 \frac{l \sqrt{b_m - 1}}{\sqrt{1 + (b_m - 1) l^2}}, \quad (9.59)$$

where  $l$  decreases from 1 to 0. For a transversely contracting trap corresponding to the betatron acceleration, the parameter  $l = 1$ , while  $b$  increases from 1 to  $b_m$ . The change in the number of particles in such a trap is defined by the formula

$$N = N_0 \frac{\sqrt{b_m - b}}{\sqrt{b_m - b + 1}}. \quad (9.60)$$

The results of the corresponding calculations are shown in Fig. 9.13a, b for traps with different mirror ratios  $b_m$ . In Fig. 9.13b, the parameter  $(b - 1)/(b_m - 1)$ , which changes from 0 to 1 at any  $b_m$ , rather than the parameter  $b$ , which changes from  $b = 1$  to  $b = b_m$ .

The number of electrons confined in the trap, that produce a HXR burst in the coronal source of emission, is always smaller the number  $N_0$  of electrons initially injected into it since some of the electrons (denote their number by  $N_{pr}$ ) immediately precipitate into the loss cone and escape from the trap through the magnetic mirrors. According to (9.58), the fraction of the electrons that directly fall into the chromosphere is

$$\frac{N_{pr}}{N_0} = 1 - \sqrt{1 - 1/b_m}. \quad (9.61)$$

Thus, for example, a trap with the mirror ratio  $b_m = 100$  captures 99.5% of the injected particles.

#### 9.4.4 Density of Trapped Particles

Let us define the mean electron density in the trap as the number of electrons  $N$  divided by the volume  $V$  of the trap:

$$n = N/V. \quad (9.62)$$

$n_0 = N_0/V_0$  is the initial electron density in the trap; therefore

$$n = n_0 \frac{N}{N_0} \frac{V_0}{V}. \quad (9.63)$$

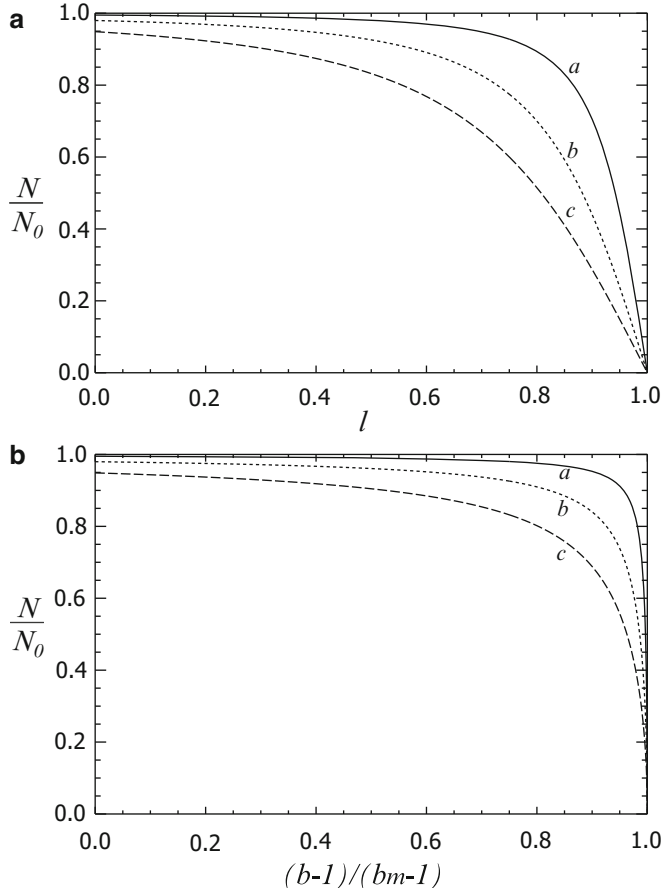


**Fig. 9.13** Change in the number of electrons in collapsing traps of different types. Curves  $a$ ,  $b$ ,  $c$  correspond to the mirror ratios  $b_m = B_2/B_1 = 100, 25, 10$ , respectively; (a) Fermi acceleration and (b) betatron acceleration (From Bogachev and Somov 2005; reproduced with permission © Pleiades Publishing, Ltd.)

In general, the change in the number of particles  $N/N_0$  in a collapsing trap is defined by formula (9.58). Let us find the change in trap volume  $V/V_0$ . If  $L$  is the trap length and  $S$  is its cross-sectional area, then

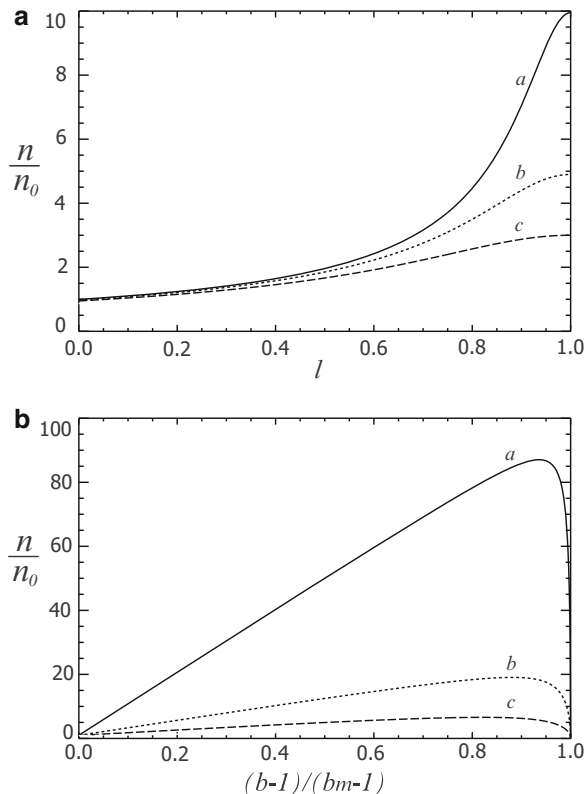
$$\frac{V_0}{V} = \frac{L_0}{L} \frac{S_0}{S} = \frac{L_0}{L} \frac{B}{B_1} = \frac{b}{l}; \quad (9.64)$$

here, we use the conservation of the magnetic flux through the trap cross-section:  $BS = B_1 S_0$ . Comparing (9.58), (9.63) and (9.64), we obtain

$$n = n_0 \frac{b \sqrt{b_m - b}}{\sqrt{1 + (b_m - b)l^2}}; \quad (9.65)$$

cf. formula (19) in Somov and Bogachev (2003).

**Fig. 9.14** Change in the density of electrons captured in collapsing traps of different types. Curves *a*, *b*, *c* correspond to the mirror ratios  $b_m = B_2/B_1 = 100, 25, 10$ , respectively; (a) Fermi acceleration and (b) betatron acceleration (From Bogachev and Somov 2005; reproduced with permission © Pleiades Publishing, Ltd.)



For the Fermi acceleration ( $b = 1$ )

$$n = n_0 \frac{\sqrt{b_m - 1}}{\sqrt{1 + (b_m - 1)l^2}}, \quad (9.66)$$

while for the betatron acceleration ( $l = 1$ )

$$n = n_0 \frac{b \sqrt{b_m - b}}{\sqrt{b_m - b + 1}}. \quad (9.67)$$

The results of calculations using formulae (9.66) and (9.67) are shown in Fig. 9.14a, b (Bogachev and Somov 2005), respectively.

The volume of a collapsing trap approaches zero. In principle, this could lead to an unbounded increase in the density of the trapped particles. Fig. 9.14a, b show that this does not occur. In a trap with the Fermi acceleration, the density of the accelerated electrons in it increases monotonically to

$$n_{max} = n_0 \sqrt{b_m - 1}. \quad (9.68)$$

In traps with the betatron acceleration, the density at  $b \rightarrow b_m$  becomes zero, passing through its maximum (9.68) before this.

Substituting the inequalities  $l \geq 0$  and  $b \leq b_m$  into (9.65), let us estimate the maximum density of electrons in the trap for an arbitrary combination of the Fermi and betatron accelerations:

$$n_{max} \leq 2 n_0 \left( \frac{b_m}{3} \right)^{3/2}. \quad (9.69)$$

Based on the increase in the density of the accelerated electrons inside the coronal HXR source during a solar flare, we can estimate the mirror ratio in a collapsing trap from (9.69):

$$b_m \geq 3 \left( \frac{1}{2} \frac{n_{max}}{n_0} \right)^{2/3}. \quad (9.70)$$

It follows from formulae (9.65)–(9.67) and Fig. 9.14 that

the betatron acceleration of particles is accompanied by the largest increase in their density among all types of traps.

Since the collision frequency between the trapped protons and electrons increases with their density, the betatron acceleration should be accompanied by stronger burst of HXR bremsstrahlung than the Fermi acceleration. This conclusion is confirmed by the results of the next Section.

#### 9.4.5 Total Energy of Trapped Particles

Two main factors determine the total kinetic energy of the trapped particles: the increase in the energy of each particle as it accelerates and the decrease in the number of particles. The combined effect of these processes can result in an increase in the total energy of all particles in the trap whose time profile is similar to the HXR burst intensity during a solar flare. The total kinetic energy of the accelerated electrons can be estimated from observations using the thick- and thin-target models (see Sects. 17.2.3 and 17.2.4).

The distribution of the trapped particles in energy and pitch angle is given by formula (9.53). Let us multiply it by the particle kinetic energy  $\mathcal{K}$  and the total number of injected particles  $N_0$  and integrate:

$$\mathcal{F} = N_0 \int_0^{\infty} \int_{\theta_{es}}^{\pi-\theta_{es}} f(\mathcal{K}, \theta) \mathcal{K} d\mathcal{K} 2\pi \sin \theta d\theta; \quad (9.71)$$

the integration over the pitch angle is performed outside the loss cone  $\theta_{es}$ , see (9.36). Substituting in (9.53) yields

$$\mathcal{F} = 4\pi N_0 \frac{l}{b} \int_{\theta_{es}}^{\pi/2} \frac{\sin \theta}{\sqrt{A_\theta}} d\theta \int_0^\infty f_0(\mathcal{K} A_\theta) \mathcal{K} d\mathcal{K}.$$

Next we make the substitution  $\mathcal{K}_0 = \mathcal{K} A_\theta$ :

$$\mathcal{F} = N_0 \frac{l}{b} \int_{\theta_{es}}^{\pi/2} \frac{\sin \theta}{A_\theta^2 \sqrt{A_\theta}} d\theta \int_0^\infty 4\pi f_0(\mathcal{K}_0) \mathcal{K}_0 d\mathcal{K}_0. \quad (9.72)$$

The second integral in (9.72) is equal to the mean kinetic energy of the electrons at the time of their injection:

$$\mathcal{F}_0 = \int_0^\infty f_0(\mathcal{K}_0) \mathcal{K}_0 d\mathcal{K}_0 \int_0^\pi 2\pi \sin \theta_0 d\theta_0 = 4\pi \int_0^\infty f_0(\mathcal{K}_0) \mathcal{K}_0 d\mathcal{K}_0. \quad (9.73)$$

The mean kinetic energy of the electrons at the time of their injection can be determined from observations or by theoretical analyzing the reconnection process in a current layer. For example, if the temperature  $T_{ef}$  of the super-hot plasma injected from the super-hot turbulent-current layer (SHTCL, see Sect. 8.5) is known, then

$$\mathcal{F}_0 = \frac{3}{2} k_B T_{ef}.$$

In general, combining (9.72) and (9.73), we obtain

$$\mathcal{F} = N_0 \mathcal{F}_0 \frac{l}{b} \int_{\theta_{es}}^{\pi/2} \frac{\sin \theta}{A_\theta^2 \sqrt{A_\theta}} d\theta, \quad (9.74)$$

where the function  $A_\theta$  is defined by formula (9.49). Let us transform the integrand in (9.74):

$$\frac{\sin \theta}{A_\theta^2 \sqrt{A_\theta}} d\theta = \frac{b^2 \sqrt{b} \sin \theta d\theta}{(\sin^2 \theta + b l^2 \cos^2 \theta)^{2.5}} = \frac{b^2 \sqrt{b} \sin \theta d\theta}{\cos^5 \theta (\operatorname{tg}^2 \theta + b l^2)^{5/2}}.$$

Further,

$$\frac{\sin \theta}{A_\theta^2 \sqrt{A_\theta}} d\theta = \frac{b^2 \sqrt{b}}{2} \frac{(\operatorname{tg}^2 \theta + 1)}{(\operatorname{tg}^2 \theta + b l^2)^{5/2}} d(\operatorname{tg}^2 \theta). \quad (9.75)$$

Substituting (9.75) into (9.74) and changing the variables  $t = \operatorname{tg}^2 \theta$  yields

$$\mathcal{F} = N_0 \mathcal{F}_0 \frac{l b \sqrt{b}}{2} \int_{t_0}^{\infty} \frac{t + 1}{(t + b l^2)^{5/2}} dt, \quad (9.76)$$

where

$$t_0 = \frac{b}{b_m - b}.$$

Performing the integration in (9.76), we have

$$\mathcal{F} = \frac{\mathcal{F}_0 N}{3} \left( 2b + \frac{b_m}{l^2 (b_m - b) + 1} \right), \quad (9.77)$$

where  $N$  is the number of particles in the trap defined by formula (9.58). In particular,

$$\mathcal{F} = \frac{\mathcal{F}_0 N}{3} \left( 2 + \frac{b_m}{l^2 (b_m - 1) + 1} \right) \quad (9.78)$$

for traps with the Fermi acceleration ( $b = 1$ ) and

$$\mathcal{F} = \frac{\mathcal{F}_0 N}{3} \left( 2b + \frac{b_m}{b_m - b + 1} \right) \quad (9.79)$$

for traps with betatron acceleration ( $l = 1$ ). The results of calculations are shown in Fig. 9.15a, b.

The change of the total kinetic energy of the electrons has the form of a burst. The burst height has relatively small values  $\mathcal{F}/\mathcal{F}_0 \lesssim 15$  for a trap with the Fermi acceleration ( $b = 1$ ) and maximum values  $\mathcal{F}/\mathcal{F}_0 \lesssim 65$  for a trap with betatron acceleration ( $l = 1$ ). Any other combination  $l$  and  $b$  leads to a result that is limited by these two extreme cases.

Thus we make the following conclusions.

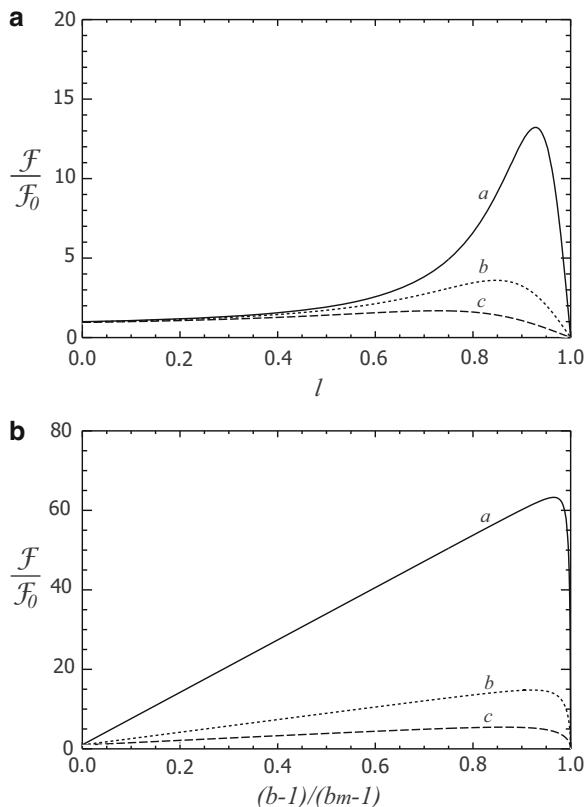
First, the highest energy  $\mathcal{K}_{max}$  that an electron acquires in a collapsing trap does not depend on the acceleration mechanism. It is the same for all types of traps, irrespective of which of the two mechanisms dominates; see formulae (9.38) and (9.39) in Sect. 9.4.1. The maximum energy of an electron depends only on the mirror ratio  $b_m$  of a trap.

Second, a trap with the dominant betatron acceleration confines the particle better. The density  $n$  of the trapped particles (see Sect. 9.4.4) and their total energy  $\mathcal{F}$  reach values that are significantly higher than the maximum possible values of these quantities in a trap with the dominant Fermi acceleration. As a consequence,

the collapsing traps with the dominant betatron acceleration must produce HXR bursts in the solar corona with amplitudes higher than and duration shorter than those in the bursts generated in collapsing traps with the dominant Fermi acceleration,

see Somov and Bogachev (2003) and Bogachev and Somov (2005).

**Fig. 9.15** Change in the total kinetic energy of electrons captured in traps of different types. Curves *a*, *b*, *c* correspond to the mirror ratios  $b_m = B_2/B_1 = 100, 25, 10$ , respectively; (a) Fermi acceleration and (b) betatron acceleration (From Bogachev and Somov 2005; reproduced with permission © Pleiades Publishing, Ltd.)



## 9.5 Diagnostics of Collapsing Traps

### 9.5.1 Spectrum of Trapped Particles

Thus the particles in the solar corona are accelerated during flares in two stages. During the first one, the electrons and ions are heated by the wave-particle interactions and are accelerated mainly by the electric field in super-hot turbulent-current layer (SHTCL). During the second stage, the particles are captured into collapsing magnetic trap, where their kinetic energy additionally increases through the first-order Fermi mechanism and the betatron mechanism. The energy distribution of trapped electrons and their HXR emission can be calculated as a function of the trap length and its thickness (Bogachev and Somov 2007).

Once again we consider a trap with decreasing length and thickness. We are interested in how the energy distribution of the trapped electrons changes with time. If  $N_0$  non-relativistic electrons with a distribution  $f_0(\mathcal{K})$ , where  $\mathcal{K}$  is the particle kinetic energy, fall into the trap at an injection time, then, as the trap contracts to the

sizes corresponding to given  $l$  and  $b$ , the number of electrons in it decrease to (see Sect. 9.4.3):

$$N = N_0 \frac{l \sqrt{b_m - b}}{\sqrt{1 + (b_m - b) l^2}}, \quad (9.80)$$

while their distribution function, normalized as

$$dN = 2\pi N_0 f(\mathcal{K}) \sqrt{\mathcal{K}} d\mathcal{K} \sin \theta d\theta,$$

takes the form

$$f(\mathcal{K}, \theta) = \frac{l}{b} f_0(\mathcal{K} A_\theta). \quad (9.81)$$

Here

$$A_\theta = \frac{1 + (b l^2 - 1) \cos^2 \theta}{b}$$

is a function of the dimensionless parameters  $l$  and  $b$  and the pitch angle  $\theta$ .

Since, according to (9.80), the number of electrons captured into a collapsing trap approaches zero as  $l \rightarrow 0$ , we introduce their energy spectrum  $f(\mathcal{K})$  normalized in a such way that

$$dN = 4\pi N f(\mathcal{K}) \sqrt{\mathcal{K}} d\mathcal{K}, \quad (9.82)$$

where  $N$  is the number of electrons in the trap (9.80).

Let us write the number of electrons (9.82) in the energy range  $d\mathcal{K}$  as an integral of the distribution  $f(\mathcal{K}, \theta)$  over the pitch angle  $\theta$  outside the loss cone:

$$dN = 2\pi N_0 \sqrt{\mathcal{K}} \int_{\theta_{es}}^{\pi - \theta_{es}} f(\mathcal{K}, \theta) \sin \theta d\theta, \quad (9.83)$$

where the loss cone is defined by

$$\cos \theta_{es} = \sqrt{1 - B/B_2} = \sqrt{1 - b/b_m}.$$

Equating (9.82) and (9.83) using (9.81), we obtain

$$f(\mathcal{K}) = \frac{N_0}{N} \frac{l}{b} \int_{\theta_{es}}^{\pi/2} f_0(\mathcal{K} A_\theta) \sin \theta d\theta$$

or, after the change of variable  $x \equiv \cos \theta$ ,

$$f(\mathcal{K}) = \frac{N_0}{N} \frac{l}{b} \int_0^{\sqrt{1-b/b_m}} f_0(\mathcal{K} A_x) dx. \quad (9.84)$$

Here

$$A_x = \frac{1 + x^2(b l^2 - 1)}{b} \quad (9.85)$$

is a function similar to  $A_\theta$ , however it depends not on the pitch angle  $\theta$  but on the integration variable  $x$ .

Formula (9.84) describes the energy distribution of the trapped electrons for any injection spectrum  $f_0(\mathcal{K}_0)$ , for example, a power-law or Maxwellian. In the former case

$$f_0(\mathcal{K}_0) = C_0 \mathcal{K}_0^{-\phi}. \quad (9.86)$$

Substituting (9.86) in (9.84) yields

$$f(\mathcal{K}) = C \mathcal{K}^{-\phi}. \quad (9.87)$$

Thus the power-law spectrum of electrons in a collapsing trap remains a power-law one with a constant spectral index  $\phi$  while the coefficient  $C$  increases as

$$C(b, l) = C_0 \frac{\sqrt{1 + (b_m - b) l^2}}{b \sqrt{b_m - b}} \int_0^{\sqrt{1-b/b_m}} \left[ \frac{1 + x^2(b l^2 - 1)}{b} \right]^{-\phi} dx. \quad (9.88)$$

If the trap contracts in the transverse direction while its length remains constant, then in this special case corresponding to betatron acceleration

$$C = \lim_{b \rightarrow b_m} C(b, l = 1) = C_0 b_m^{\phi-1.5}. \quad (9.89)$$

Let us now analyze the spectrum of the trapped electrons if it was a thermal one with temperature  $T_0$  at the injection time:

$$f_0(\mathcal{K}_0) = \frac{1}{4\pi} \frac{2}{\sqrt{\pi k^3 T_0^3}} \exp\left(-\frac{\mathcal{K}_0}{k T_0}\right). \quad (9.90)$$

Substituting (9.90) in (9.84) yields

$$f(\mathcal{K}) = \frac{N_0}{N} \frac{l}{b} \frac{1}{4\pi} \frac{2}{\sqrt{\pi k^3 T_0^3}} \int_0^{\sqrt{1-b/b_m}} \exp\left(-\frac{\mathcal{K} A_x}{k T_0}\right) dx. \quad (9.91)$$

Let us take into account Eqs. (9.80) and (9.85) for the number of particles  $N$  and the function  $A_x$ . After their substitution in (9.91) we obtain

$$\begin{aligned} f(\mathcal{K}) &= \frac{\sqrt{1 + (b_m - b) l^2}}{b \sqrt{b_m - b}} \frac{1}{4\pi} \frac{2}{\sqrt{\pi k^3 T_0^3}} \exp\left(-\frac{\mathcal{K}}{b k T_0}\right) \times \\ &\times \int_0^{\sqrt{1-b/b_m}} \exp\left(-\frac{\mathcal{K}}{k T_0} \frac{b l^2 - 1}{b} x^2\right) dx. \end{aligned} \quad (9.92)$$

The integral on the right-hand side of formula (9.92) can be reduced to the error integral  $\text{erf } x$  (see Jahnke et al. 1960). Therefore, the sought-for electron distribution function takes the form

$$f(\mathcal{K}) = \frac{1}{b k T_0} \frac{\sqrt{C^2 + 1}}{C} \frac{1}{4\pi\sqrt{\mathcal{K}}} \exp\left(-\frac{\mathcal{K}}{b k T_0}\right) \text{erf}\left(C \sqrt{\frac{\mathcal{K}}{b k T_0}}\right), \quad (9.93)$$

where

$$C = \sqrt{(1 - b/b_m)(bl^2 - 1)}.$$

Formula (9.93) shows that, if the electron energy distribution at the injection time was thermal, then it does not remain Maxwellian but is modified differently for the Fermi and betatron mechanisms during the acceleration in a collapsing trap.

Let us consider the two cases separately.

First, if the trap contracts in the transverse direction then the electrons are accelerated by the betatron mechanism until the field in the trap becomes equal to the field in the magnetic mirrors. Calculating the corresponding limit  $b \rightarrow b_m$  for formula (9.93) under condition  $l = 1$ , we obtain an energy distribution of the trapped electrons in the form

$$\lim_{b \rightarrow b_m} f(\mathcal{K}) = \frac{1}{4\pi} \frac{2}{\sqrt{\pi k^3 (b_m T_0)^3}} \exp\left(-\frac{\mathcal{K}}{k(b_m T_0)}\right). \quad (9.94)$$

Formula (9.94) describes a Maxwell distribution with temperature  $b_m T_0$ . Thus, in a contracting trap with initial mirror ratio  $b_m$ , the spectrum of the trapped electrons (and, hence, their bremsstrahlung spectrum) changes in the following sequence: thermal with the temperature  $T_0 \rightarrow$  nonthermal  $\rightarrow$  thermal with the temperature  $b_m T_0$ .

Note that the kinetic energy of a particle under betatron acceleration is distributed between the degrees of freedom not uniformly but in the following proportions. As the trap contracts, the longitudinal temperature does not change and remains equal to  $(1/3) T_0$ , while the transverse temperature increases from  $(2/3) T_0$  to  $(b_m - 1/3) T_0$ . This leads to the result obtained above for the angle-integrated energy spectrum of accelerated electrons.

Second, if the length of the trap decreases but the trap does not contract transversely, then the particles are accelerated by the Fermi mechanism. Setting  $b = 1$  in formula (9.93), we see that the coefficient  $C$  in (9.93) in this case becomes imaginary. However the distribution  $f(\mathcal{K})$ , of course, remains real. As  $l \rightarrow 0$  this distribution of the trapped electrons tends to

$$\begin{aligned} \lim_{l \rightarrow 0} f(\mathcal{K}) &= \frac{1}{k T_0} \frac{1}{\sqrt{b_m - 1}} \frac{1}{4\pi\sqrt{\mathcal{K}}} \exp\left(-\frac{\mathcal{K}}{k T_0}\right) \\ &\times \text{erfi}\left(\sqrt{\frac{b_m - 1}{b_m}} \sqrt{\frac{\mathcal{K}}{k T_0}}\right). \end{aligned} \quad (9.95)$$

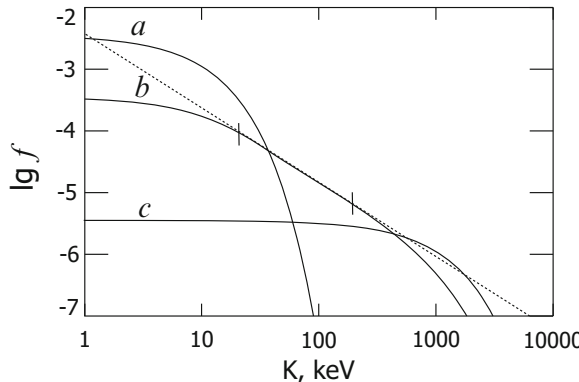


**Fig. 9.16** Energy spectrum of the captured electrons in a collapsing trap with mirror ratio  $b_m = 100$ : (a) the initial Maxwellian distribution with temperature  $T = 10^8$  K. (b) the final particle distribution as the trap length decreases – the Fermi acceleration; the dashed straight line indicates the slope of the power-law segment of the spectrum. (c) the final thermal distribution of electrons as the trap contracts transversely – betatron acceleration (From Bogachev and Somov 2007; reproduced with permission © Pleiades Publishing, Ltd.)

Here  $\text{erfi}(x)$  is an imaginary value of the error function (Jahnke et al. 1960):

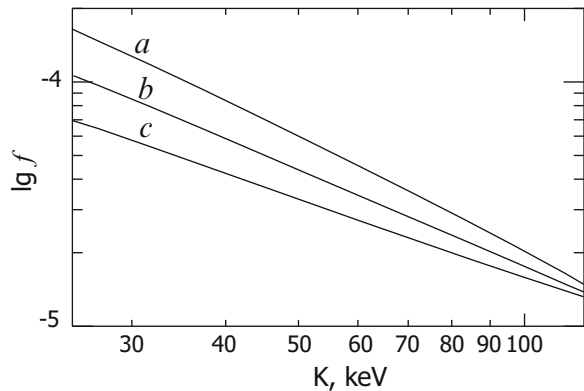
$$\text{erfi}(x) = -i \text{erf}(ix) = \frac{2}{\sqrt{\pi}} \int_0^x \exp(t^2) dt.$$

The results of calculations for traps of both types are presented in Fig. 9.16. Curve *a* indicates the Maxwellian spectrum at the time of electron injection into the trap. Curve *b* shows the spectrum of the accelerated electrons for  $l \rightarrow 0$  calculated using formula (9.95). Curve *c* is the spectrum for  $b \rightarrow b_m$  calculated using formula (9.94).

The distribution formed when thermal electrons are accelerated by the Fermi mechanism differs greatly from the Maxwellian distribution in the energy range from  $\sim 20$  to  $\sim 200$  keV. Here, as the trap length decrease, a rectilinear segment of the spectrum is formed. So, in this segment, the electrons have a power-law distribution in kinetic energy:  $f \sim K^{-\varphi}$ , where  $\varphi$  is the spectral slope that depends on the trap mirror ratio  $b_m$ .

Figure 9.17 shows the electron spectra under Fermi acceleration in traps with various mirror ratios  $b_m$ . In all three cases, the spectrum is a power-low one but with a different slope that depends on the mirror ratio: the spectra are harder in traps with larger  $b_m$ . As  $b_m$  increases, the extent of the region of the power-law spectrum also increases toward the high energies: the spectrum is cut off at energies 130–150 keV for  $b_m = 25$  and extends to 0.5–1.0 MeV for  $b_m = 100$ . The minimum energy starting from which the spectrum becomes a power-law one changes only slightly with  $b_m$  and is approximately equal to 15–20 keV.

**Fig. 9.17** Shape of the power-low segment of the spectrum as a function of the trap mirror ratio  $b_m$ : (a)  $b_m = 25$ , (b)  $b_m = 50$ , and (c)  $b_m = 100$  (From Bogachev and Somov 2007; reproduced with permission © Pleiades Publishing, Ltd.)



### 9.5.2 The Emission Measure of HXR Bremsstrahlung

The hard X-ray (HXR) emissivity of a collapsing magnetic trap is characterized by the so-called emission measure

$$ME = \int_0^V n_1 n_2 dV,$$

which depends on the densities of the interacting particles responsible for observed bremsstrahlung emission:  $n_1$  (electrons) and  $n_2$  (protons), and on the volume  $V$  of the emitting region in the corona. Let us define  $ME$  as a function of the trap length and its diameter. Integration over the trap volume yields

$$ME = N_e n_p, \quad (9.96)$$

where  $N_e$  is the total number of electrons in the trap and  $n_p$  is the proton density. The number of trapped particles is defined by formula (9.80), while the formula for their density was derived in Sect. 9.4.4:

$$n = n_0 \frac{b \sqrt{b_m - b}}{\sqrt{1 + (b_m - b) l^2}}. \quad (9.97)$$

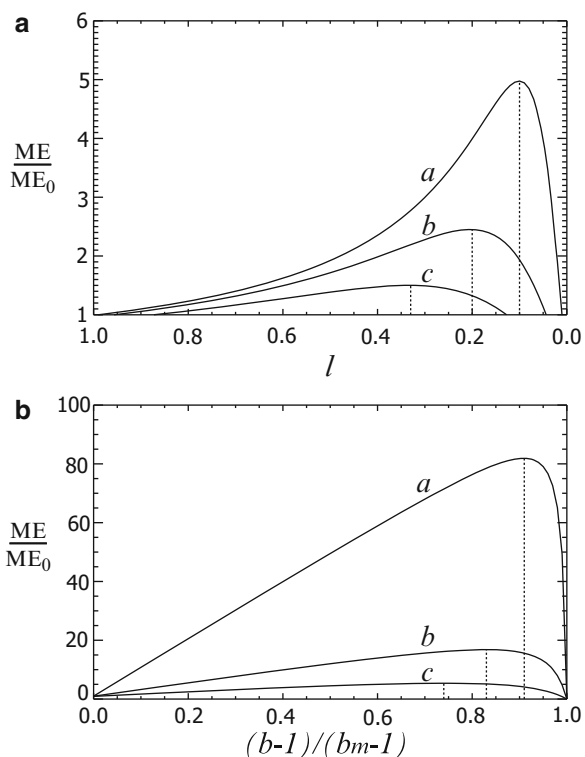
Substituting (9.97) and (9.80) in (9.96), we obtain

$$ME = ME_0 \frac{bl (b_m - b)}{1 + (b_m - b) l^2}, \quad (9.98)$$

where  $ME_0$  is the initial emission measure equal to the product of the proton density and the number of electrons at the injection time:

$$ME_0 = n_{p0} N_{e0}.$$

**Fig. 9.18** Emission measure of radiation from a collapsing trap as a function of its contraction in the longitudinal (**a**) and transverse (**b**) directions. The calculations were performed for three mirror ratios: (a)  $b_m = 100$ , (b)  $b_m = 25$ , and (c)  $b_m = 10$ . The vertical dashed lines indicate the times of the HXR flux reaches its maximum (From Bogachev and Somov 2007; reproduced with permission © Pleiades Publishing, Ltd.)



If the trap contracts only in one direction (in its length), then formula (9.98) is simplified: for the Fermi acceleration

$$ME = ME_0 \frac{l(b_m - 1)}{1 + (b_m - 1)l^2}, \quad (9.99)$$

for the betatron acceleration

$$ME = ME_0 \frac{b(b_m - b)}{1 + (b_m - b)}. \quad (9.100)$$

The results of calculations using formulae (9.99) and (9.100) are presented in Fig. 9.18. The emission measure of fast electrons, trapped and accelerated inside the collapsing loop, is initially growing slowly with decrease of the loop length  $L(t)$  if we consider, at first, Fermi acceleration. As shown in Fig. 9.18a, the emission measure reaches its maximal value only when the loop length becomes as small as of about 0.2–0.1 of its initial length  $L(0)$ . With further shrinkage of the loop, the emission measure decreases quickly to zero. As a consequence,

the flux of HXR emission from the collapsing trap has a maximum at approximately the same values of remaining length of the loop,

see  $l(t) = L(t)/L(0) \sim 0.2$  in Fig. 9.19a.

Similar behavior is demonstrated in the loops with dominant betatron acceleration as shown in Fig. 9.18b. However the increase in the emission measure in traps with betatron acceleration is larger than that in traps with Fermi acceleration.

The electrons inside the betatron traps produce more intense bremsstrahlung than the electrons in Fermi traps.

### 9.5.3 The Spectrum of HXR Bremsstrahlung

In Sect. 9.5.1, we have found the energy spectrum  $f(\mathcal{K})$  of the electrons captured into a collapsing trap. In the energy range  $[\mathcal{E}_X, \mathcal{E}_X + d\mathcal{E}_X]$ ,  $\Phi(\mathcal{E}_X) d\mathcal{E}_X$  photons of energy  $\mathcal{E}_X$  are produced in one second:

$$dN_X = \Phi(\mathcal{E}_X) d\mathcal{E}_X.$$

The total energy emitted from the trap in this energy rang is

$$dI_X = \Phi(\mathcal{E}_X) \mathcal{E}_X d\mathcal{E}_X. \quad (9.101)$$

The number of emitting electrons,  $dN_{\mathcal{K}}$ , is related to the number of photons produced by them,  $dN_X$ , by the formula

$$\frac{dN_X}{d\mathcal{E}_X} = n_p \int_{\mathcal{E}_X}^{\infty} v_e(\mathcal{K}) \sigma(\mathcal{K}, \mathcal{E}_X) dN_{\mathcal{K}}(\mathcal{K}).$$

Here  $n_p$  is the proton density in the emission region,  $v_e$  is the electron velocity, and  $\sigma$  is the differential cross-section of bremsstrahlung. Expressing the number of photons in terms of their emission spectrum  $\Phi(\mathcal{E}_X)$  using (9.101) and the number of electrons in terms of their distribution  $f(\mathcal{K})$  using (9.82), we obtain

$$\Phi(\mathcal{E}_X) = 4\pi n_p N_e \int_{\mathcal{E}_X}^{\infty} v_e(\mathcal{K}) \sigma(\mathcal{K}, \mathcal{E}_X) f(\mathcal{K}) \sqrt{\mathcal{K}} d\mathcal{K}. \quad (9.102)$$

The most intense non-thermal X-ray emission from solar flares is observed in the energy range 20–100 keV and is produced by electrons of the same energies. Therefore, it will suffice to give non-relativistic formulae. Let us express the electron velocity in terms of their kinetic energy:

$$v_e(\mathcal{K}) = \sqrt{2\mathcal{K}/m_e}. \quad (9.103)$$

For the bremsstrahlung cross-section in the non-relativistic approximation, we use the formula (Berestetskii et al. 2001):

$$\sigma(\mathcal{K}, \mathcal{E}_X) = \frac{8\alpha r_0^2}{3} \frac{m_e c^2}{\mathcal{K} \mathcal{E}_X} \ln \frac{1 + \sqrt{1 - \mathcal{E}_X/\mathcal{K}}}{1 - \sqrt{1 - \mathcal{E}_X/\mathcal{K}}}, \quad (9.104)$$

where  $r_0 = 2,82 \times 10^{-13}$  cm is the classical electron radius, and  $\alpha \sim 1/137$  is the fine-structure constant.

Substituting (9.103) and (9.104) in (9.102) yields

$$\Phi(\mathcal{E}_X) = C_X \frac{n_p N_e}{\mathcal{E}_X} \int_{\mathcal{E}_X}^{\infty} f(\mathcal{K}) \ln \frac{1 + \sqrt{1 - \mathcal{E}_X/\mathcal{K}}}{1 - \sqrt{1 - \mathcal{E}_X/\mathcal{K}}} d\mathcal{K}, \quad (9.105)$$

where

$$C_X = 4\pi \frac{8\alpha r_0^2}{3\sqrt{m_e/2}} m_e c^2 = 1.86 \times 10^{-14} \text{ cm}^3 \text{ keV}^{1/2} \text{ c}^{-1}.$$

Formula (9.105) establishes the relationship between the “instantaneous” distribution of the trapped electrons and their bremsstrahlung spectrum. If  $f(\mathcal{K})$  is a power-law distribution with index  $\phi$ , and since the slowly changing logarithmic factor may be considered constant compared to the exponential, the produced bremsstrahlung also has a power-law spectrum with slope  $\phi + 1$ . This is a well-known prediction of the thin-target theory (see Sect. 17.2.3) for the emission of electrons in a tenuous plasma.

Expressing  $N_e$ ,  $f(\mathcal{K})$  and  $n_p$  in terms of their values at the injection time using formulae (9.80), (9.84) and (9.97), we obtain

$$\begin{aligned} \Phi(\mathcal{E}_X, l, b) &= C_X \frac{n_{p0} N_{e0}}{\mathcal{E}_X} \frac{l \sqrt{b_m - b}}{\sqrt{1 + (b_m - b)/l^2}} \\ &\times \int_{\mathcal{E}_X}^{\infty} \int_0^{\sqrt{1-b/b_m}} f_0(\mathcal{K} A_x) \ln \frac{1 + \sqrt{1 - \mathcal{E}_X/\mathcal{K}}}{1 - \sqrt{1 - \mathcal{E}_X/\mathcal{K}}} dx d\mathcal{K}. \end{aligned} \quad (9.106)$$

Thus the problem of calculating the trap emission spectrum from a given injection spectrum has been solved. The solution of the inverse problem, i.e., reconstructing the injection spectrum  $f_0$  from the observed emission spectrum  $\Phi$ , is more complex since Eq. (9.106) for  $f_0(\mathcal{K}_0)$  is a second-order integral equation.

The results of calculations using formula (9.106) are presented in Fig. 9.19. The calculations were performed for a thermal injection spectrum with  $T = 10^8$  K. According to these calculations, if  $10^{36}$  electrons have been injected into the trap, then the trap produces  $10^{28}$ – $10^{29}$  (depending on the acceleration mechanism) photons with energy 25 keV per second at the emission maximum, which corresponds

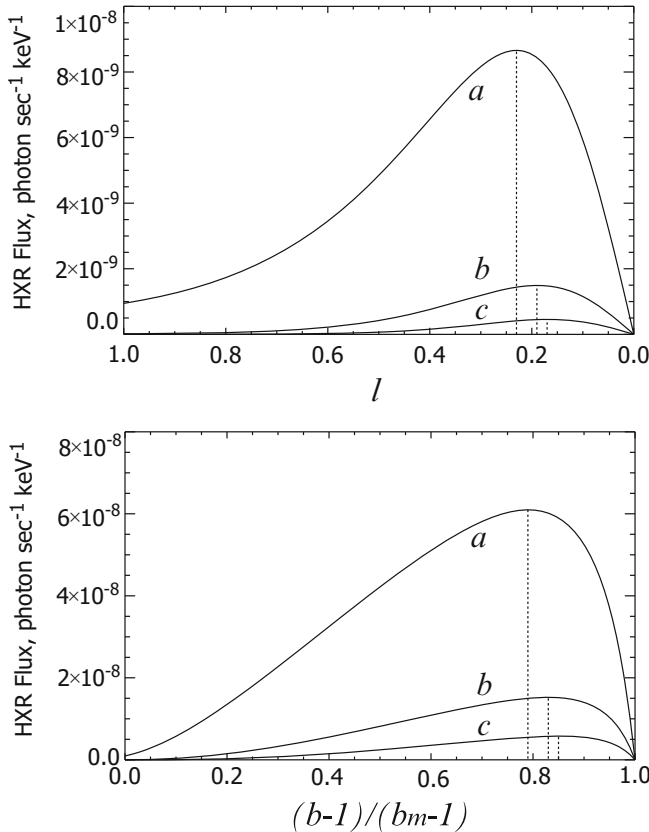


**Fig. 9.19** The HXR flux from a collapsing trap in three energy ranges directions: *a* – 25 keV, *b* – 50 keV, and *c* – 75 keV, as a function of the trap contraction in the longitudinal (**a**) and transverse (**b**) directions (From [Bogachev and Somov 2007](#); reproduced with permission © Pleiades Publishing, Ltd.)

to their flux at the Earth orbit  $10^3$ – $10^4$  photons  $\text{cm}^{-2}$ . This value agrees with the *RHESSI* measurements in this spectral range. At a lower or higher photon flux, the number of trapped electrons would increase or decrease proportionally.

The intensity of the HXR bremsstrahlung from a collapsing trap is also affected by its mirror ratio. Information about the dependence of the flux on the mirror ratio, energy range and acceleration mechanism is given in the Table 9.1. At the same number of injected electrons, the traps with betatron acceleration produce several times more intense HXR bursts than the traps with Fermi acceleration.

The higher-energy emission in a trap can be delayed relative to the lower-energy emission. If the injection spectrum is thermal with  $T = 10^8$  K, then the delay of the emission in the 75-keV range relative to that in the 25-keV range is  $\Delta l \approx 0.05$ , i.e., about 5% of the trap lifetime. For betatron acceleration, the calculations yield similar delay.

**Table 9.1** HXR flux (the number of photons per second) from a collapsing trap at the burst peak normalized to the number of injected electrons

$b_m = 3$	$b_m = 10$			$b_m = 100$		
	25 keV	50 keV	75 keV	25 keV	50 keV	75 keV
Flux from a betatron trap						
$4.9 \times 10^{-9}$	$5.2 \times 10^{-10}$	$8.9 \times 10^{-11}$	$6.1 \times 10^{-8}$	$1.5 \times 10^{-8}$	$5.8 \times 10^{-9}$	$9.0 \times 10^{-7}$
Flux from a Fermi trap						
$1.6 \times 10^{-9}$	$1.0 \times 10^{-10}$	$1.4 \times 10^{-11}$	$8.7 \times 10^{-9}$	$1.5 \times 10^{-9}$	$4.6 \times 10^{-10}$	$5.3 \times 10^{-8}$
Flux ratio (betatron to Fermi)	3.1	5.2	6.4	7.0	10.0	12.6
					17.0	20.6
						24.1

It is of interest to compare the experimental HXR spectrum with the theoretical spectrum calculated in the model of a collapsing trap. For example, Lin et al. (2003b) reported the results of their study of the non-thermal HXR source observed by the *RHESSI* in the solar corona during the July 23, 2002 flare. The HXR spectrum was a power-law one with a knee at 20 keV and slopes of  $\phi \sim 7$  and  $\phi \sim 5$  to the right and to the left of the knee, respectively. Using formula (9.106), we can interpret this spectrum as the spectrum of the bremsstrahlung produced by an ensemble of  $4 \times 10^{29}$  electrons with a power-law injection spectrum and slope  $\phi_e = 7$  captured and accelerated in a collapsing coronal trap with proton density  $n_{p0} = 10^9 \text{ cm}^{-3}$  and initial mirror ratio  $b_{m0} = 20$  (for more detail see Bogachev and Somov 2007).

## 9.6 Coulomb Collisions in Collapsing Traps

### 9.6.1 Qualitative Description of Expected Effects

In the collisionless approximation used above, which is applicable for electrons and ions with velocities much higher than their thermal velocity, only two factors affect the motion of trapped particles: Fermi and betatron acceleration in a collapsing magnetic trap. Let us consider the actual situation more carefully.

The electrons and ions in a trap do not move freely but interact with one another and with a “background” plasma, i.e. the plasma formed by electrons and ions with velocities close to the thermal ones. Although these effects result from the action of Coulomb forces, we shall distinguish them based on the following considerations. Elastic interactions between particles do not change their total energy and momentum but redistribute it between slow and fast particles as well as they change the angular distribution of particles (see Part I, Sect. 4.1). In particular,

Coulomb collisions result in particle scattering which leads to particle diffusion in pitch angle.

This is of fundamental importance for analysis of the efficiency of the acceleration mechanisms given below.

Naturally, it does not follow from the conservation of the total kinetic energy and momentum of two particles as they collide elastically that scattering does not affect the acceleration efficiency in the trap. It was shown in Sect. 9.3.3 in collisionless approximation that, irrespective of the acceleration mechanism (Fermi, betatron, or both; see also Sect. 9.4.1), the ratio of final particle energy  $\mathcal{K}_{es}$  to the initial energy  $\mathcal{K}_0$  is defined by the formula

$$\mathcal{K}_{es}/\mathcal{K}_0 = b_m \sin^2 \theta. \quad (9.107)$$

Here  $\theta$  is the particle pitch angle,  $b_m$  is the initial mirror ratio, i.e. the ratio of the magnetic field in the magnetic mirrors,  $B_2$ , to the initial field at the trap center,  $B_1$ :

$$b_m = B_2/B_1. \quad (9.108)$$

Thus if the particles are scattered in the direction of large pitch angles ( $\theta \rightarrow \pi/2$ ), then their final energy  $\mathcal{K}_{es}$  increases, although the energy  $\mathcal{K}_0$  remains constant. Similarly, diffusion in the direction of small pitch angles ( $\theta \rightarrow 0$ ) reduces the acceleration efficiency. The preferential direction of the pitch-angle diffusion depends on the particle pitch-angle distribution and can be different at different stages of trap collapse and in different segments of the pitch-angle distribution and the energy spectrum.

Generally, when particular acceleration mechanisms in astrophysical plasmas are considered, the role of Coulomb collisions is reduced to the energy losses of the accelerated particles, in particular, to the presence of a “loss barrier” at low velocities (e.g., [Korchak 1980; Bykov et al. 2000](#)). As a result,

Coulomb collisions are believed to reduce the efficiency of any acceleration mechanism.

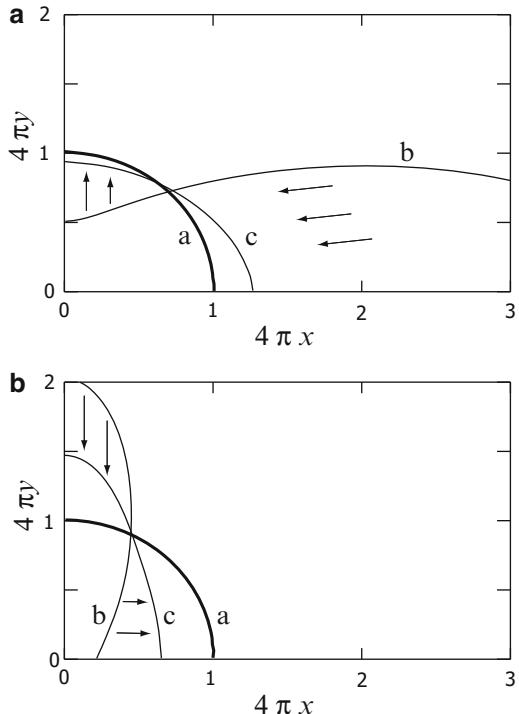
Meanwhile, it follows from general principles (see Sect. 14.3) that weak collisions between the accelerated electrons in collapsing magnetic traps, which cause their isotropization, increase the phase space volume of the particles involved in the acceleration process. Thus, in general, the electron acceleration efficiency in collapsing traps can be increased significantly. In this Section, we are interested in the question of precisely how this effect is realized in collapsing traps of solar flares.

### 9.6.2 Isotropization Effect of Scattering

In order to solve the problem of the effect of Coulomb collisions on the particle acceleration in a collapsing magnetic trap, we use the method of numerical simulations described in detail by [Bogachev and Somov \(2009\)](#). The essence of numerical model consists in the following. We are not interested in the question of precisely where a particle is located inside the trap at each time. We characterize the particle by two parameters: its kinetic energy  $\mathcal{K}$  and pitch angle  $\theta$ , and investigate their variations. The factors changing these parameters include the betatron and Fermi accelerations, the scattering and braking of particles in the background plasma.

Let us denote the numerically calculated distribution function  $f_n(\mathcal{K}, \theta)$ , the subscript  $n$  distinguishes it from the exact function. Our main goal will be to compare the simulation results with the formulae derived in the collisionless approximation. This gives an insight into the extent to which the collisions between particles affect the efficiency of their acceleration in collapsing traps and the shape of their spectrum.

**Fig. 9.20** Change in the pitch-angle distribution of trapped particles. (a) Fermi acceleration:  $a$  – initial distribution which is assumed to be isotropic,  $b$  – distribution at  $l = 0.5$  in the collisionless approximation,  $c$  – the same distribution but with particle scattering. (b) Betatron acceleration:  $a$  – initial distribution,  $b$  – distribution at  $b = 4$  in the collisionless approximation,  $c$  – the same distribution with particle scattering (From Bogachev and Somov 2009; reproduced with permission © Pleiades Publishing, Ltd.)



We begin with an analysis of the pitch-angle distribution

$$f_n(\theta) = \int_0^\infty f_n(\mathcal{K}, \theta) \sqrt{\mathcal{K}} d\mathcal{K}. \quad (9.109)$$

In collapsing trap with lifetimes shorter than 10 s, Coulomb scattering affects only slightly the particle pitch-angle distribution. However, in long-lived traps with lifetimes longer 100 s, the role of scattering is more significant. The results of calculations for this case are shown in Fig. 9.20.

Curve  $a$  in both panels indicates the initial distribution which was assumed to be isotropic. As the trap collapses, this distribution is modified. In collisionless approximation, as was shown in Sect. 9.4.2, it changes as

$$f(\theta) = \frac{1}{4\pi} \frac{l \sqrt{b}}{\left( \sin^2 \theta + b l^2 \cos^2 \theta \right)^{3/2}} \quad (9.110)$$

and takes the shape  $b$ . In the approximation with Coulomb scattering, the pitch-angle distribution of trapped particles takes the shape  $c$ . The difference between curves  $b$  and  $c$  shows that, as would be expected, the collisions of particles causes

isotropization of their pitch-angle distribution. As a result, the later is intermediate between two limits: the collisionless and isotropic ones. The stronger the interaction, the closer the distribution to the isotropic limit.

If we select a sector of pitch angles  $[\theta, \theta + d\theta]$  in the pitch-angle distribution, then the number of particles in the sector can both increase and decrease compared to the collisionless case as a result of their scattering. Let us call this effect the different directions of isotropization as they are indicated by the arrows in Fig. 9.20. These directions differ for Fermi and betatron accelerations. In traps with Fermi acceleration (Fig. 9.20a), scattering increases the number of particles in the region of large pitch angles (see vertical arrows) and tend to fill the region of small  $\theta$  (see mostly horizontal arrows). In contrast, in traps with betatron acceleration, the particles escape from the region of large pitch angles and tend to fill the region of pitch angles close to zero. Thus

the pitch angles of the scattered particles predominantly increase for Fermi acceleration and decrease in traps with betatron acceleration compared to the collisionless case.

### 9.6.3 Particle Confinement

We shall say that Coulomb collisions increase the efficiency of particle confinement if the number of particles inside the trap,

$$N_n = 2N_0 \int_0^{\infty} \int_{\theta_{es}}^{\pi - \theta_{es}} f_n(\mathcal{K}, \theta) \sqrt{\mathcal{K}} d\mathcal{K} \sin \theta d\theta, \quad (9.111)$$

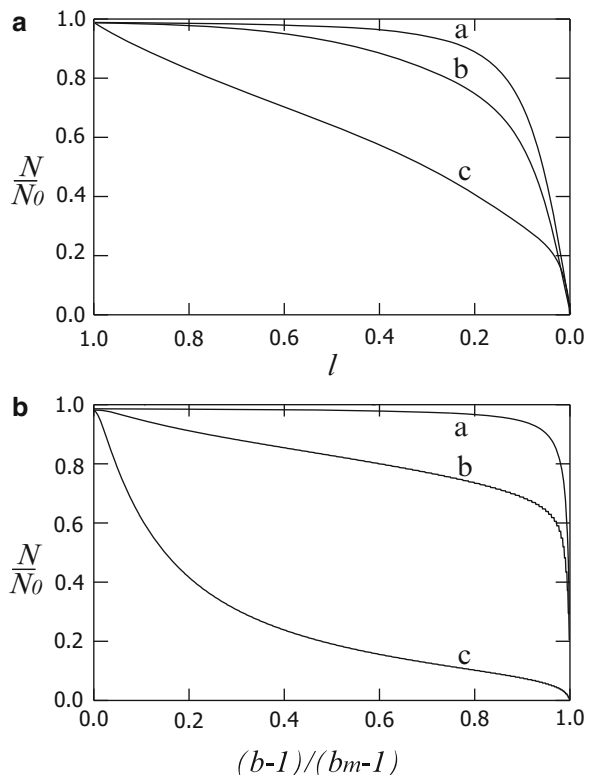
increases compared to that in the collisionless case (see Sect. 9.4.3). If it decreases then collisions reduce the efficiency of confinement. The results of calculations are shown in Fig. 9.21. Curve *a* corresponds to collisionless acceleration in a collapsing trap, while curves *b* and *c* were obtained in the approximation of weak and strong collisions (for more detail see [Bogachev and Somov 2009](#)). Their comparison shows that the trap confines particles most efficiently in the collisionless approximation. Even weak scattering of particles transfers some of them into the loss cone, i.e. reduces the number of particles in the trap. The stronger the scattering, the faster the particle precipitation: in the case of strong collisions (curve *c*) the number of particles is appreciably smaller than that in the case of weak ones (curve *b*).

The particle scattering efficiency depends on the particle acceleration mechanism. At the same scattering times, traps with Fermi acceleration (Fig. 9.21a) confine particles better than those with betatron one. The reason is that in the case of betatron acceleration, the particles are scattered mainly in the direction to the loss cone where they are ejected from the trap. In contrast,

in the collapsing traps with Fermi acceleration, the particle diffusion in pitch angle proceeds in a direction away from the loss cone.

This increases the time of particle confinement in the trap.

**Fig. 9.21** Change in the number of particles in a trap. (a) Fermi acceleration and (b) betatron acceleration. Everywhere:  $a$  – the collisionless approximation,  $b$  – a short-lived trap with a lifetime of 10 s with particle scattering, and  $c$  – a long-lived trap with a lifetime of 1,000 s with particle scattering (From Bogachev and Somov 2009; reproduced with permission © Pleiades Publishing, Ltd.)



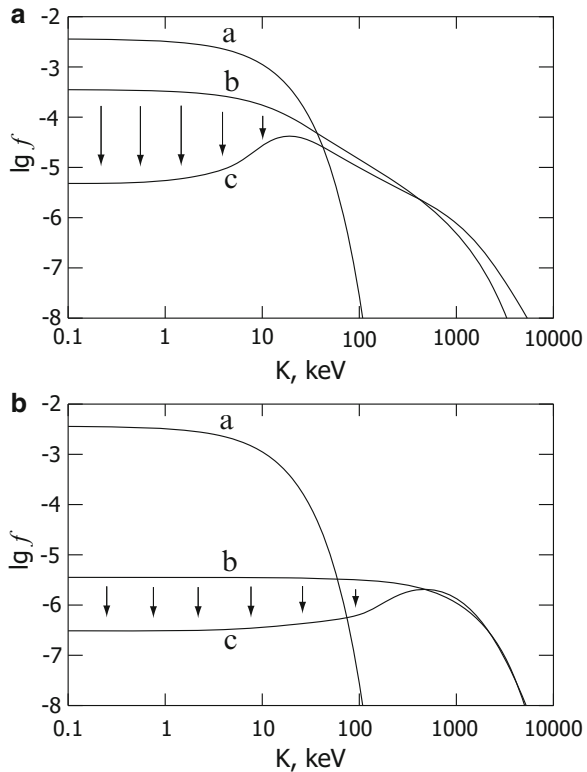
Both these effects are clearly seen in Fig. 9.20 which shows the preferential directions of the particle diffusion in pitch angle. It can be said that the two effects (loss-cone filling and pitch-angle diffusion) collectively reduce the efficiency of particle confinement for betatron acceleration and partially cancel each other out for Fermi acceleration. As a result, a difference in the efficiencies of particle confinement in traps of different type arises.

Note that, in the collisionless approximation, the transversally collapsing betatron traps confine particles better than the longitudinally collapsing Fermi traps. However this is not true for the case of strong scattering: a larger number of particles and their higher density can be reached in the case of Fermi acceleration.

#### 9.6.4 Spectrum of Trapped Particles

The Coulomb collisions of particles also changes significantly their spectrum. Figure 9.22 shows the results of calculation of the particle energy distribution using the formula

**Fig. 9.22** Energy distribution of particles in a trap. **(a)** Fermi acceleration and **(b)** betatron acceleration. Everywhere:  $a$  – an initial particle distribution which is assumed to be thermal with  $T = 10^8$  K,  $b$  – the final distribution in the collisionless approximation, and  $c$  – a final distribution with particle scattering (From Bogachev and Somov 2009; reproduced with permission © Pleiades Publishing, Ltd.)

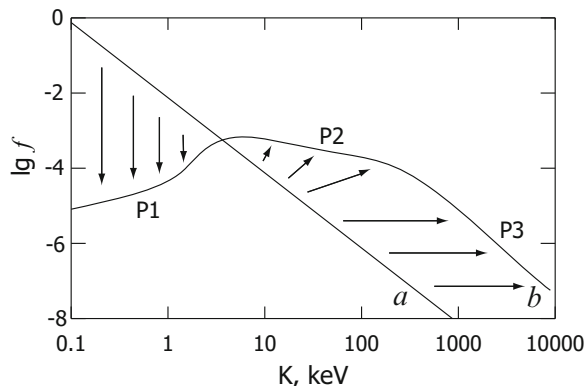


$$f_n(\mathcal{K}) = 2\pi \int_{\theta_{es}}^{\pi - \theta_{es}} f_n(\mathcal{K}, \theta) \sin \theta d\theta \quad (9.112)$$

for a Maxwellian injection spectrum. Compared to the collisionless approximation, the fraction of low-energy particles with  $\mathcal{K} < 10$  keV, which interact with one another most efficiently and are the first to be scattered into the loss cone, decreases sharply in this distribution. In addition, the slope of the power-law segment of the spectrum decreases in traps with Fermi acceleration.

The investigation of power-law injection spectra is also significant practically. In the collisionless approximation, the shape of these spectra does not change during acceleration: the power-law distribution just shifts to the right along the energy axis (see Sect. 9.5.1). However, if the particles interact with one another, then the power-law shape is not retained (Fig. 9.23). A dip  $P_1$  is formed in the region of low energies because of angular diffusion, this part of the distribution escape through the loss cone. A power-law segment  $P_2$  with a smaller slope than that of the injection spectrum is formed in the region of energies from  $\sim 10$  to  $\sim 100$  keV. Finally, in the region of collisionless acceleration, which corresponds to higher energies  $\gtrsim 100$  keV, the spectrum  $P_3$  remains a power law with the initial slope but shifts to the right. As

**Fig. 9.23** Change in the power law distribution of particles in a collapsing trap:  $a$  – an initial particle distribution and  $b$  – the final distribution (From Bogachev and Somov 2009; reproduced with permission © Pleiades Publishing, Ltd.)



a result of these changes, the particle spectrum at energies above 10 keV becomes a double power law. Such spectra were detected during *RHESSI* observations of solar flares (e.g., Lin et al. 2003a).

If apart from the particle scattering and the related pitch-angle diffusion of particles into the loss cone, we take into account the particle braking in a background plasma inside the collapsing trap, then we have to know the plasma density inside the trap as the trap collapses. The plasma density changes due to the decrease in trap volume and the plasma escape through the loss cone. The former effect should lead to an increase in density while the latter effect should decrease it.

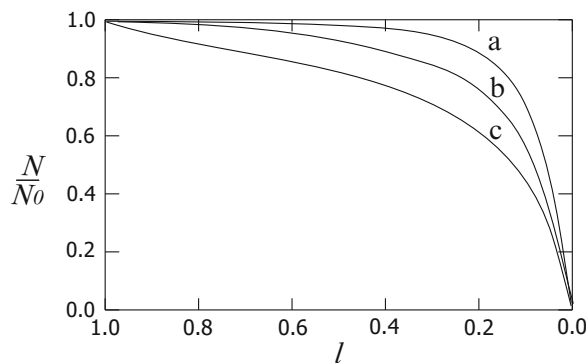
Calculations by Bogachev and Somov (2009) showed that both these effects are roughly balanced, i.e. the plasma density  $n_{pl}$  is kept approximately at the same level throughout the acceleration process. In traps with short lifetimes  $n_{pl} \approx n_0$ , while in long-lived traps, where the scattering into loss cone plays a greater role,  $n_{pl} \approx 0.1 n_0$ , i.e. the mean density is approximately an order of magnitude lower than the initial one. The calculations also showed the presence of plasma with a density up to  $10^{10} \text{ cm}^{-3}$  affects only slightly the particle spectrum. To be more precise, this effect turns out to be negligible compared to main factors: the acceleration of particles and their scattering due to Coulomb interaction with one another. Higher densities of super-hot plasma in coronal HXR sources seem to be contradict to observations by *Yohkoh* (e.g., Tsuneta et al. 1997).

A plasma with density  $n_{pl} \lesssim 3 \times 10^9 \text{ cm}^{-3}$  cannot efficiently influence the electrons with energy 50–100 keV. So their acceleration in a collapsing trap can be considered as virtually collisionless. The spectra of electrons in the corresponding energy range are described with a high accuracy by formulae derived in collisionless approximation (see Sect. 9.5.1).

### 9.6.5 Particle Braking and Confinement

It was shown in Sect. 9.6.3 that even weak scattering of particles transfers some of them into the loss cone and, therefore, reduces the number of particles in a collapsing magnetic trap. The particle braking in a background plasma inside the

**Fig. 9.24** Number of particles in a collapsing trap: *a* – no collisions, *b* – the same trap with particle scattering, *c* – the trap with scattering and braking (From Bogachev and Somov 2009; reproduced with permission © Pleiades Publishing, Ltd.)



trap also affects the efficiency of particle confinement, of course. Figure 9.24 shows the function  $N(l)$ , the change in the number of particles in the trap, for three cases: (*a*) collisionless acceleration, (*b*) acceleration with particle scattering, and (*c*) acceleration with particle scattering and braking in plasma. We see that, in the latter case, the particles are confined least efficiently. Nevertheless, even in the latter case, collapsing traps are capable of confining more than 20 % for a long time (up to half of their lifetime) in long-lived traps. This percentage exceeds 80 % for short-lived traps with Coulomb collisions and 90 % for short-lived traps with collisionless acceleration.

The efficiency of particle confinement also depends on the predominant acceleration mechanism, the Fermi or betatron one. In the collisionless approximation, the particles are better confined with betatron acceleration. This is not true when collisions are taken into account: a larger number of particles and their higher density are reached in the case of Fermi acceleration.

## 9.7 Final Remarks About Collapsing Traps

In order to interpret the temporal and spectral evolution as well as the spatial distribution of hard X-rays (HXR) in solar flares, a two-step acceleration was proposed by Somov and Kosugi (1997) with the second-step acceleration via the collapsing magnetic-field lines. The *Yohkoh* HXT observations of the Bastille-day flare (Masuda et al. 2001) clearly show that, with increasing energy, the HXR emitting region gradually changes from a *large diffuse source*, which is located presumably above the ridge of soft X-ray arcade, to a two-ribbon structure at the loop footpoints. This result suggests that

fast electrons are in fact accelerated in the large system of the coronal loops, not merely in a particular one.

This seems to be well consistent with the *RHESSI* observations of large coronal HXR sources, for example, in the X4.8 flare on 2002 July 23 (see Fig. 3 in Lin et al. 2003a).

Efficient trapping and continuous acceleration also produce the large flux and time lags of microwaves that are likely emitted by electrons with higher energies, several hundred keV (Kosugi et al. 1988). We believe that the lose-cone instabilities (Benz 2002) of trapped mildly-relativistic electrons in the system of many collapsing field lines (each line with its proper time-dependent loss cone) can provide excitation of radio-wave with a very wide continuum spectrum.

Qiu et al. (2004) presented a comprehensive study of the X5.6 flare on 2001 April 6. Evolution of HXRs and microwaves during the gradual phase in this flare exhibits a separation motion between two footpoints, which reflects the progressive reconnection. The gradual HXRs have a harder and hardening spectrum compared with the impulsive component. The gradual component is also a microwave-rich event lagging the HXRs by tens of seconds. The authors propose that

the collapsing-trap effect in solar flares is a viable mechanism that continuously accelerates electrons in a low-density trap before they precipitate into the footpoints.

Imaging radio observations (e.g., Li and Gan 2005) should provide another way to investigate properties of collapsing magnetic traps. It is not simple, however, to understand the observed phenomena relative to the results foreseen by theory. With the incessant progress of magnetic reconnection, the loop system newly formed after reconnection will grow up, while every specific loop will shrink. Just because of such a global growth of flare loops, it is rather difficult to observe the downward motion of newly formed loops. The observations of radio loops by Nobeyama Radioheliograph (NoRH) are not sufficient to resolve specific loops. What is observed is the whole region, i.e., the entire loop or the loop top above it. Anyway, combined microwave and HXR imaging observations are essential in the future.

Recall that if the electrons injected into the trap from the *super-hot turbulent-current layer* (SHTCL) have a power-law energy distribution, then their spectrum remains a power-law one throughout the acceleration process for both the Fermi and betatron mechanisms. For electrons with a thermal injection spectrum, the model predicts two types of HXR coronal sources. (a) Thermal sources are formed in traps dominated by the betatron mechanism. (b) Nonthermal sources with a power-law spectrum appear when electrons are accelerated by the Fermi mechanism. With account of rare Coulomb collisions inside the trap, a double-power-low spectrum can be formed from a power-law spectrum of electron injection from SHTCL (Bogachev and Somov 2009).

As we saw above,

Fermi acceleration has significant advantages in collapsing magnetic traps as compared with the betatron mechanism which mainly heats the low-energy electrons.

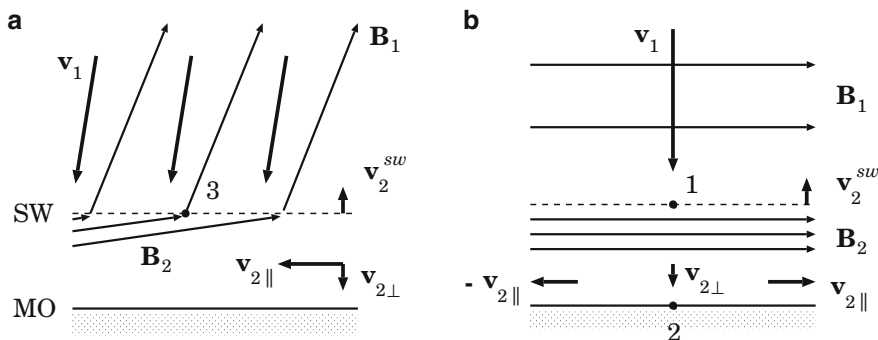


**Fig. 9.25** The velocity and magnetic fields in the vicinity of: (a) an arbitrary point 3 in Fig. 9.5 and (b) point 1 related to the stagnation point 2 at the magnetic obstacle MO

Similar conclusion seems to be well confirmed by the Interball-Tail observations of electron distributions after the so-called *dipolarization* (recovering a dipolar structure of magnetic field) phase of a magnetospheric substorm (Smets et al. 1999). In particular, modeling shows that Fermi acceleration is the leading process, compared to betatron heating (see also Somov and Bogachev 2003).

## 9.8 Practice: Exercises and Answers

**Exercise 9.1.** Consider the velocity and magnetic fields in the vicinity of the shock front locally at two points. One of them is point 1 related to the stagnation point 2 at the surface of the magnetic obstacle (MO) in Fig. 9.5. The other is point 3 located somewhere far from point 1.

**Answer.** Near point 3 the reconnection outflow with velocity  $v_1$  crosses the shock front and continues to move downwards relative to the front with a small perpendicular component  $v_{2\perp}$  and a large velocity component  $v_{2\parallel}$ , which is parallel to the surface of the front (see Fig. 9.25a). In the presence of the obstacle MO, the first component is compensated by a slow upward motion of the shock with velocity  $v_2^{sw} = -v_{2\perp}$ .

Near point 1 the flow crosses the front and diverges in such a way that the velocity  $v_2 = 0$  at the stagnation point 2. So the plasma mainly flows out of the vicinity of this point (Fig. 9.25b). On the contrary, new field lines arrive through the shock but, being unidirectional, they cannot disappear there. They are accumulated between the front (SW) and the magnetic ‘wall’ (MO). Magnetic field  $B_2$  increases. Thus we expect the upward motion of the shock with some velocity  $v_2^{sw}$ .

**Exercise 9.2.** Derive an Equation which relates the parameters of the plasma and magnetic field upstream and downstream the shock in the vicinity of point 1 in Fig. 9.25b.

**Answer.** Let us write the MHD continuity Equations for the fluxes of mass, momentum, and energy across the shock front. Considering a pure-hydrogen plasma, we write its pressure and density in terms of the electron number density  $n$  and temperature  $T$ :

$$p = 2nk_B T, \quad \rho = m_p n, \quad (9.113)$$

$m_p$  is the proton mass,  $k_B$  is the Boltzmann constant. We also assume here, for simplicity, that

$$T_e = T_p = T.$$

With (9.113), the three conservation laws become:

$$n_1 (v_1 + v_2) = n_2 v_2, \quad (9.114)$$

$$2n_1 k_B T_1 + m_p n_1 (v_1 + v_2)^2 + \frac{B_1^2}{8\pi} = 2n_2 k_B T_2 + m_p n_2 v_2^2 + \frac{B_2^2}{8\pi}, \quad (9.115)$$

$$\frac{\gamma}{\gamma - 1} \frac{2k_B T_1}{m_p} + \frac{(v_1 + v_2)^2}{2} + \frac{B_1^2}{4\pi m_p n_1} = \frac{\gamma}{\gamma - 1} \frac{2k_B T_2}{m_p} + \frac{v_2^2}{2} + \frac{B_2^2}{4\pi m_p n_2}. \quad (9.116)$$

Freezing of the magnetic field into the plasma is described by the Equation

$$\frac{B_1}{n_1} = \frac{B_2}{n_2}. \quad (9.117)$$

Here  $v_1$  is the speed of the outflow from the RCL in the immovable reference frame, connected with the ‘immovable’ obstacle (MO). We neglect the slow proper motion of the obstacle because the SXR loops move upwards much slower than the coronal HXR source. In Eqs. (9.114)–(9.116) velocity  $v_2 \equiv v_2^{sw}$  is directed upward and represents the velocity of the shock with respect to the obstacle. Hence,  $v_1 + v_2$  is the velocity of the plasma inflow to the shock;  $n_1$  and  $n_2$ ,  $T_1$  and  $T_2$ ,  $B_1$  and  $B_2$  are electron number density, temperature, and magnetic field upstream and downstream the shock,  $\gamma$  is the adiabatic exponent.

Equations (9.114)–(9.117) yield a relationship, allowing us to determine the front velocity  $v_2$  from the known onflow parameters  $n_1$ ,  $T_1$ ,  $B_1$ , and  $v_1$ :

$$\begin{aligned} 2v_2^3 + (3 - \gamma) v_2^2 v_1 - (\gamma - 1) v_2 v_1^2 \\ - (2 - \gamma) V_A^2 v_1 - 2(V_A^2 + V_s^2) v_2 = 0. \end{aligned} \quad (9.118)$$

Here  $V_A$  and  $V_s$  are the Alfvén and sound speeds in the upstream plasma.

**Exercise 9.3.** The shock-heated plasma inevitably loses energy because of fast heat-conduction cooling. Fast expansion of the compressed super-hot plasma along

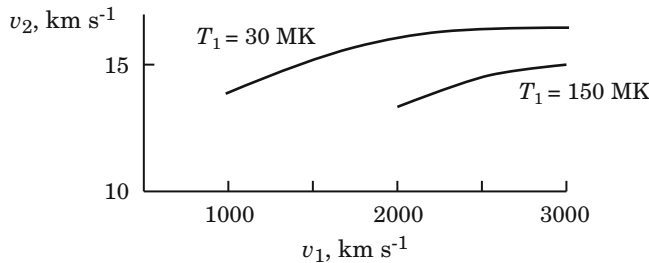


**Fig. 9.26** Shock speed  $v_2$  versus the speed of the onflowing stream  $v_1$  of the super-hot plasma and its temperature  $T_1$

the field lines also reduces its temperature and pressure. Both cooling mechanisms play an important role in the energy balance, leading to a fast decrease of the post-shock temperature. Radiative cooling of the plasma becomes dominating later, at lower temperatures:  $T_2 < 10^7$  K. Suppose a rapid fall of the temperature  $T_2$ , which must inevitably result in a fast decrease of the gas pressure to values negligible in comparison with the high post-shock magnetic pressure:

$$2n_2k_B T_2 \ll \frac{B_2^2}{8\pi}. \quad (9.119)$$

Consider properties of such a shock with fast cooling.

**Answer.** Condition (9.119) allows us to simplify Eq. (9.115):

$$2n_1k_B T_1 + m_p n_1 (v_1 + v_2)^2 + \frac{B_1^2}{8\pi} = m_p n_2 v_2^2 + \frac{B_2^2}{8\pi}. \quad (9.120)$$

Moreover Eq. (9.116) is no more necessary. From (9.120), (9.114) and (9.117) there follows an Equation for the shock speed:

$$\frac{1}{\gamma} V_s^2 v_2^2 + v_2^3 v_1 + v_2^2 v_1^2 - V_A^2 v_2 v_1 - \frac{1}{2} V_A^2 v_1^2 = 0. \quad (9.121)$$

The shock speed  $v_2$  as a function of the super-hot flow speed and its temperature is shown in Fig. 9.26. The dependence of  $v_2$  on the temperature  $T_1$  as well as on the upstream speed  $v_1$  is so weak that in wide ranges of these parameters we see practically the same values of  $v_2$ ,  $10 < v_2 < 20$  km/s.

So

the *fast* shock with fast cooling *slowly* moves upwards. Moreover such shock can provide a significant compression of a magnetic field necessary for particle trapping and acceleration

(Somov et al. 1999).

**Exercise 9.4.** Conditions of the second invariant conservation are well satisfied for electrons trapped in collapsing traps of solar flares (Somov and Kosugi 1997). For ions, however, the acceleration has a more discrete character than for electrons (Somov et al. 2002c). Find how the number of collisions suffered by a trapped ion does depend on the current length of a collapsing trap.

**Answer.** Each reflection of an ion on a moving mirror leads to an increase of the parallel velocity  $\delta V = 2v_m$ . After  $n$  reflections the parallel velocity of the ion becomes equal to

$$V_n = V_0 + 2nv_m \quad \text{or} \quad V_n = V_{n-1} + 2v_m. \quad (9.122)$$

After the reflection number  $n$  the ion moves from one mirror with velocity (9.122) to another mirror moving in an opposite direction with velocity  $v_m$ . If  $L_n$  is the length of the trap at the time of the reflection  $n$ , then the time  $\delta t_n$  between consequent reflections can be found from the simple kinematic condition

$$L_n - v_m \delta t_n = V_n \delta t_n. \quad (9.123)$$

Hence the time of flight of the ion between the reflection  $n$  and the reflection  $n+1$

$$\delta t_n = \frac{L_n}{V_n + v_m}. \quad (9.124)$$

During this time, the length of the trap decreases on  $2v_m \delta t_n$ . Thus the length of the trap at the time of the reflection  $n$  is

$$L_n - L_{n+1} = 2v_m \delta t_n. \quad (9.125)$$

Let us assume that fast ions are injected into the trap in its center at the time  $t_0 = 0$ . Then, before the first reflection at the time  $\delta t_0$ , each ion passes the distance  $L_0/2 - v_m \delta t_0 = V_0 \delta t_0$ . From this condition

$$\delta t_0 = \frac{L_0}{2(V_0 + v_m)}. \quad (9.126)$$

Substituting (9.126) in formula (9.125) with  $n = 0$  gives us the first decrease of the trap length

$$L_0 - L_1 = 2v_m \delta t_0 = v_m \frac{L_0}{V_0 + v_m}. \quad (9.127)$$

Thus

$$L_1 = L_0 - v_m \frac{L_0}{V_0 + v_m} = L_0 \frac{V_0}{V_0 + v_m}. \quad (9.128)$$

Acting similarly for any reflection number  $n$  we find a general formula which relates the trap length  $L_n$  with  $n$ :

$$L_n = L_0 \frac{V_0}{V_0 + v_m} \frac{V_0 + v_m}{V_0 + 2nv_m - v_m} = L_0 \frac{V_0}{V_0 - v_m + 2nv_m}. \quad (9.129)$$

From here, the number of reflections as a function of the discrete lengths  $L_n$  is equal to

$$n = \frac{L_0 V_0 + L_n (v_m - V_0)}{2v_m L_n}. \quad (9.130)$$

For arbitrary value of the trap length  $L$  and for any number  $n$ , we introduce the step-function

$$n = \mathcal{N} \left( \frac{L_0 V_0 + L (v_m - V_0)}{2v_m L} \right), \quad (9.131)$$

where  $\mathcal{N}(x) = 0, 1, 2, \text{etc.}$  is the integer part of the argument  $x$ .

As the trap becomes shorter and shorter, the trapped particle is accelerated, and the number of accelerations per second increases.

**Exercise 9.5.** How does kinetic energy of a trapped ion increase in a collapsing trap?

**Answer.** Substituting (9.131) in formula (9.122) gives us a relationship between the ion velocity  $V$  and the trap length  $L$ :

$$V(L) = V_0 + 2v_m \mathcal{N} \left( \frac{L_0 V_0 + L (v_m - V_0)}{2v_m L} \right). \quad (9.132)$$

By using the dimensionless parameter  $l(t) = L(t)/L_0$ , we rewrite (9.132) as follows

$$V(l) = V_0 + 2v_m \mathcal{N} \left( \frac{V_0 (1-l) + l v_m}{2v_m l} \right). \quad (9.133)$$

Since for a non-relativistic ion, the momentum  $\mathbf{p} = m_i \mathbf{V}$ , the parallel momentum variation as a function of  $l$  is given by

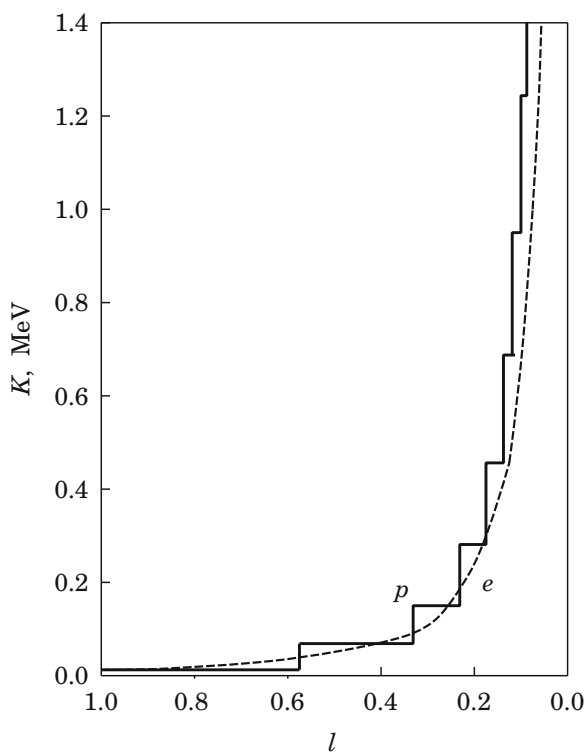
$$p_{\parallel i}(l) = m_i V_{\parallel i}(l) = p_{\parallel i 0} + 2m_i v_m \mathcal{N} \left( \frac{p_{\parallel i 0} (1-l) + m_i v_m l}{2m_i v_m l} \right), \quad (9.134)$$

instead of formula (9.4). Here, as above,  $\mathcal{N}$  is the step function of its argument or simply the number of mirroring reflections of a given particle. The parallel motion energy of an ion is growing as

$$\mathcal{K}_{\parallel i}(l) = \frac{m_i}{2} V_{\parallel i}(l)^2 \quad (9.135)$$

$$= \frac{m_i}{2} \left[ \left( \frac{2\mathcal{K}_{\parallel i 0}}{m_i} \right)^{1/2} + 2v_m \mathcal{N} \left( \frac{(1-l)\sqrt{2\mathcal{K}_{\parallel i 0}/m_i} + v_m l}{2v_m l} \right) \right]^2.$$

**Fig. 9.27** Kinetic energy of electrons and protons in a collapsing magnetic trap as a function of its length



For comparison, we show in Fig. 9.27 the kinetic energy of a proton (the solid steps) and of an electron (the dashed curve) as a function of  $l$ . Initially, the energy steps for the proton are not frequent but follow the second invariant curve of the electron. Later on, when the kinetic energy of the electron becomes close to  $m_e c^2$ , its energy grows more slowly than the one of the proton. For example, a proton with an initial energy  $K_0 \approx k_B T$ , where  $T \approx 10^8$  K is a typical temperature for a *super-hot turbulent-current layer* (see Sects. 8.3 and 8.5), has a kinetic energy twice higher than the one of an electron at  $l \approx 0.1$  with the same initial energy. At the same time, reflections of the proton on magnetic mirrors become more frequent, and the second adiabatic invariant is conserved. So, conservation of the second invariant is not a bad approximation for trapped protons.

After a number of bounces the ion's pitch angle becomes less than the loss-cone pitch angle, and it passes through the mirror, never to return. An accelerated particle escapes from a trap as soon as

$$p_{\parallel} \geq R p_{\perp}, \text{ where } R = \left( \frac{B_2}{B_1} - 1 \right)^{1/2}. \quad (9.136)$$

As soon as the increase of its parallel momentum under the acceleration process is high enough to satisfy this condition, a particle escapes from the trap. Every particle is able to escape the collapsing magnetic trap before the length of the trap shrinks to zero.

**Exercise 9.6.** Discuss how the Liouville theorem can be used together with the first two adiabatic invariants in order to find the spectra of particles accelerated in collapsing magnetic trap ([Smets et al. 1999](#); [Apatenkov et al. 2007](#)).

# Chapter 10

## Solar-Type Flares in Laboratory and Space

**Abstract** The super-hot turbulent-current layer (SHTCL) theory offers an attractive opportunity for laboratory and astrophysical applications of the magnetic reconnection. New data on the mechanism of magnetic energy transformation into kinetic and thermal energies of a super-hot plasma at the Sun require new models of reconnection under conditions of anomalous resistivity, which are similar to that ones investigated in toroidal devices performed to study turbulent heating of a collisionless plasma.

### 10.1 Solar Flares in Laboratory

#### 10.1.1 Turbulent Heating in Toroidal Devices

The electric resistivity of plasma is the important macroscopic parameter that can be assessed relatively straightforwardly in laboratory experiments. In order to clarify the basic physical mechanisms behind the anomalous resistivity, much effort has been spent. Many experiments were done to investigate the feasibility of using *turbulent heating* as a means of injecting a large power into toroidal devices: stellarators and *tokamaks*, the plasma devices constructed in the form of a torus, where a cylinder is made to bend and close on itself. Much progress has been made in understanding the anomalous resistivity and concurrent plasma heating by *current-driven turbulence* (CDT), the turbulence driven by a current parallel to a magnetic field (for a review see [de Kluiver 1991](#)). In general,

the electric conductivity  $\sigma$  of plasma exhibits an anomalous reduction when the electric field  $E$  exceeds a threshold.

The electric conductivities observed in the toroidal devices are highly anomalous, and scales with the electric field as

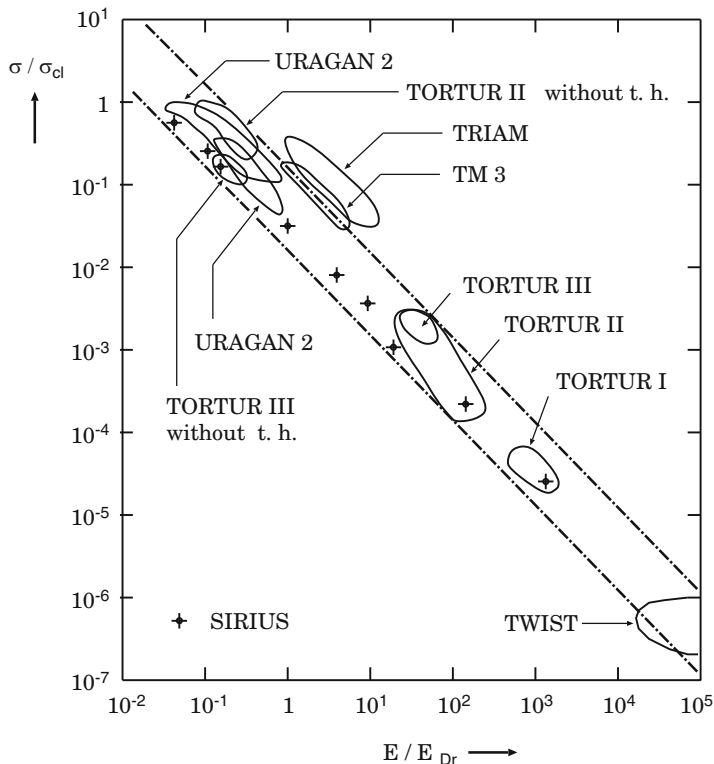


**Fig. 10.1** Normalized conductivity  $\sigma/\sigma_{cl}$  versus the normalized electric field  $E/E_{Dr}$  in various toroidal devices (de Kluiver 1991)

$$\frac{\sigma}{\sigma_{cl}} \approx 0.1 \frac{E_{Dr}}{E}. \quad (10.1)$$

Here  $\sigma_{cl} = \sigma_0 T^{3/2}$  is the classical conductivity,  $\sigma_0 \approx 1.44 \times 10^8 / \ln \Lambda$ ,  $\ln \Lambda$  is the Coulomb logarithm; the Dreicer's field (see Appendix C)

$$E_{Dr} \approx 6.4 \times 10^{-10} \frac{n}{T} \ln \Lambda, \text{ V.} \quad (10.2)$$

The scaling law (10.1) is valid in the range of electric fields

$$10^{-2} \leq E/E_{Dr} \leq 10^5.$$

The corresponding ratio  $\sigma/\sigma_{cl}$  varies from 10 to  $10^{-6}$ . Almost all known nonlinear process (from quasilinear to strong turbulence) are likely to be involved in the experiments. However all data points from considerably different devices fall in a narrow band indicated in Fig. 10.1.

Formulae (10.1) and (10.2) give us

$$\sigma \approx 3.0 \times 10^{-5} \frac{T^{1/2} n}{E}, \quad \text{s}^{-1}. \quad (10.3)$$

So, instead of using complicated methods to find the anomalous conductivity in different regimes of CDT, as it was done in Sect. 8.3, we can apply the simple empirical formula (10.3).

### 10.1.2 Current-Driven Turbulence in Current Layers

Let us assume that the electron temperature exceeds significantly the ion one in the *super-hot turbulent-current layer* (SHTCL):

$$T_e \gg T_i, \quad T = T_e.$$

In the reconnecting current layer (RCL), magnetic field lines inflow together with plasma at a relatively small velocity  $v$ , reconnect inside the layer and then outflow at a large velocity  $V$ . It follows from the set of Eqs. (8.46)–(8.51) that:

$$n_0 v b = n V \xi b, \quad (10.4)$$

$$\frac{B_0^2}{8\pi} = n k_B T, \quad n k_B T = \frac{1}{2} M n V^2, \quad (10.5)$$

$$\frac{c B_0}{4\pi a} = \sigma E_0, \quad (10.6)$$

$$\mathcal{E}_{mag}^{in} = \mathcal{E}_{th}^{out} + K^{out} + C_{||}. \quad (10.7)$$

In the continuity Eq. (10.4)

$$v = c E_0 / B_0$$

is the plasma drift velocity into the layer. It follows from Eq. (10.5) that the velocity of the plasma outflow is

$$V = \frac{B_0}{\sqrt{4\pi M n}}. \quad (10.8)$$

The magnetic field near the RCL is estimated as (8.54).

The energy Eq. (10.7) includes the magnetic enthalpy flux into the layer

$$\mathcal{E}_{mag}^{in} = \frac{B_0^2}{4\pi} v b, \quad (10.9)$$

which coincides with the Joule heating of the RCL, i.e.  $(j^2/\sigma)a b$ . The thermal enthalpy flux from the layer along the magnetic field lines is

$$\mathcal{E}_{th}^{out} = \left( \frac{5}{2} n_e k_B T_e + \frac{5}{2} n_i k_B T_i \right) V \xi b \approx \frac{5}{2} n k_B T \times V \xi b, \quad (10.10)$$

where allowance is made for  $n_i = n_e \equiv n$  and  $T_i \ll T_e = T$ . The kinetic energy flux of the plasma outflowing from the layer is

$$K^{out} = \left( \frac{1}{2} M n V^2 + \frac{1}{2} m n V^2 \right) V \xi b \approx \frac{1}{2} M n V^2 \times V \xi b, \quad (10.11)$$

since the ion mass  $M$  exceeds significantly the electron mass  $m$ .

The heat flux along the field lines can be taken as (8.43). Therefore, in general, the new models presented below are similar to the simple ‘test models’ of a SHTCL, described in Chap. 3 in Somov (1992), or, more exactly to an ‘one-temperature model’ (Somov and Titov 1983; see also Somov 1981). We remind that the heat flux in the test model was considered as saturated at  $1 \leq \theta \leq 8.1$ ; this only approximately satisfies inequality  $T_e \gg T_i$ . We shall keep in the next section the same value of the flux

$$C_{\parallel} = \frac{n (k_B T)^{3/2}}{4 m^{1/2}} \xi b, \quad (10.12)$$

in order to demonstrate clearly the effect of formula (10.3) for estimating the turbulent conductivity:

$$\sigma = \sigma_1 \frac{T^{1/2} n}{E_0}, \text{ s}^{-1}, \quad \text{where} \quad \sigma_1 \approx 2.98 \times 10^{-5}. \quad (10.13)$$

Later on, the anomalous value of the heat flux will be adopted which corresponds to  $\theta \gg 1$ . So a better agreement will be reached between the initial assumptions and designed functions; moreover the question will be solved on a sensitivity of the SHTCL model to the heat flux value.

Equation (10.7) does not include the thermal enthalpy flux into the RCL

$$\mathcal{E}_{th}^{in} = (5 n_0 k_B T_0) v b \ll \mathcal{E}_{th}^{out}, \quad (10.14)$$

as long as the coronal plasma temperature  $T_0 \ll T$ , and the kinetic energy flux of the plasma flowing into the layer

$$K^{in} = \left( \frac{1}{2} M n_0 v^2 + \frac{1}{2} m n_0 v^2 \right) v b \ll K^{out}, \quad (10.15)$$

as  $v^2 \ll V^2$  in the strong field approximation. We neglect also the magnetic enthalpy flux from the current layer

$$\mathcal{E}_{mag}^{out} = \frac{B_y^2}{4\pi} V \xi b \ll \mathcal{E}_{mag}^{in}, \quad (10.16)$$

since  $B_y^2 \ll B_0^2$ . Moreover, as is shown in the test model, the following factors do not influence the energy balance of the SHTCL under the corona conditions: the energy exchange between electrons and ions due to Coulomb collisions, the heat flux across a magnetic field, and the energy losses due to radiation.

### 10.1.3 Parameters of a Current Layer with CDT

Let us find the unknown values  $a$ ,  $b$ ,  $n$ , and  $V$  from Eqs. (10.4)–(10.6) considering the temperature  $T$  as an unknown parameter. We obtain the following formulae:

$$a = 2^{1/6} \pi^{-1/3} k_B^{5/6} M^{-1/6} c^{2/3} \sigma_1^{-1} \left[ n_0^{-1/3} E_0^{-1/3} \xi^{1/3} \right] T^{1/3}, \quad (10.17)$$

$$b = 2^{5/6} \pi^{1/3} k_B^{1/6} M^{1/6} c^{1/3} \left[ n_0^{1/3} E_0^{1/3} h_0^{-1} \xi^{-1/3} \right] T^{1/6}, \quad (10.18)$$

$$n = 2^{-4/3} \pi^{-1/3} k_B^{-2/3} M^{1/3} c^{2/3} \left[ n_0^{2/3} E_0^{2/3} \xi^{-2/3} \right] T^{-2/3}, \quad (10.19)$$

$$V = 2^{1/2} k_B^{1/2} M^{-1/2} T^{1/2}. \quad (10.20)$$

Now from Eq. (10.7), we derive the temperature as a function of the parameters  $n_0$ ,  $h_0$ ,  $E_0$ , and  $\xi$ . On this purpose, let us rewrite (10.7):

$$\frac{B_0^2}{4\pi} v b = \frac{1}{2} (Mn V^2 + 5n k_B T) V \xi b + \frac{n (k_B T)^{3/2}}{4m^{1/2}} \xi b. \quad (10.21)$$

Transform the terms on the right-hand side:

$$\frac{1}{2} (Mn V^2 + 5n k_B T) V \xi b = \frac{7}{4} \frac{n_0}{n} \frac{B_0^2}{4\pi} v b, \quad (10.22)$$

$$\frac{n (k_B T)^{3/2}}{4m^{1/2}} \xi b = \frac{1}{8} \left( \frac{M}{2m} \right)^{1/2} \frac{n_0}{n} \frac{B_0^2}{4\pi} v b. \quad (10.23)$$

Substituting (10.22) and (10.23) in Eq. (10.21) yields

$$\frac{n}{n_0} = \frac{7}{4} + \frac{1}{8} \left( \frac{M}{2m} \right)^{1/2} \approx 5.54. \quad (10.24)$$

From this, with allowance for formula (10.19), we find the temperature

$$T = \frac{2}{\left[ 7 + \sqrt{M/8m} \right]^{3/2}} \pi^{-1/2} k_B^{-1} M^{1/2} c \left[ n_0^{-1/2} E_0 \xi^{-1} \right]. \quad (10.25)$$

Thus formulae (10.24), (10.25), (10.17), (10.18), and (10.20) determine the current layer characteristics  $n$ ,  $T$ ,  $a$ ,  $b$ , and  $V$  via the external parameters  $n_0$ ,  $E_0$ ,  $h_0$ , and the dimensionless parameter  $\xi$ . Apart from the SHTCL parameters mentioned above, the energy release power per unit of the layer length has been calculated:

$$\frac{P}{l} = \frac{B_0^2}{4\pi} v 4b = \frac{1}{\pi} c E_0 h_0 b^2. \quad (10.26)$$

Comparison of the parameters estimated in the framework of the well studied test models with the results of the new models shows that the previous and new results differ only slightly. This indicates an agreement between two different approaches to the estimation of anomalous conductivity: the theoretical one used in the test models, and the empirical one described by de Kluiver (1991). For example, with the electric field  $E_0 \approx 0.1 - 6.9 \text{ V cm}^{-1}$  the test model predicts the conductivity  $\sigma \approx 3 \times 10^{12} - 6 \times 10^{11} \text{ s}^{-1}$ , which is the well suitable range for solar flares and CMEs (Somov 1992). For the same electric field, the new model yields  $\sigma \approx 2 \times 10^{13} - 6 \times 10^{11} \text{ s}^{-1}$ .

### 10.1.4 The SHTCL with Anomalous Heat Conduction

Let now the electric conductivity be determined by formula (10.13) and heat conduction flux by

$$C_{\parallel} = \frac{n (k_B T)^{3/2}}{M^{1/2}} \xi b. \quad (10.27)$$

Here it is taken into account that  $f_M(\theta) = 1$  at  $\theta \gg 1$ , see formulae (8.43) and (8.44). Equation (10.7) in this case has the following form:

$$\frac{B_0^2}{4\pi} v b = \frac{1}{2} (M n V^2 + 5 n k_B T) V \xi b + \frac{n (k_B T)^{3/2}}{M^{1/2}} \xi b. \quad (10.28)$$

Solving procedure of the set of Eqs. (10.4)–(10.6) and (10.28) is similar to that one developed earlier. From Eq. (10.28) we obtain the ratio

$$\frac{n}{n_0} = \frac{7}{4} + 2^{-3/2} \approx 2.1. \quad (10.29)$$

From here, taking into account (10.19), the RCL temperature is found:

$$T = \frac{1}{4 [(7/4) + 2^{-3/2}]^{3/2}} \pi^{-1/2} k_B^{-1} M^{1/2} c \left[ n_0^{-1/2} E_0 \xi^{-1} \right]. \quad (10.30)$$

So, in the framework of the new models of a SHTCL with the anomalous heat conduction, the values describing the RCL ( $n$ ,  $T$ ,  $a$ ,  $b$ , and  $V$ ) are determined by formulae (10.29), (10.30), (10.17), (10.18), and (10.20). Their estimations, obtained for the same initial data as in the test models, show that a replacement of the saturated heat flux by the anomalous one leads to decreasing  $C_{\parallel}$  by a factor of 2–3. This slightly influences the results. The RCL becomes hotter and more rarefied, its thickness and width somewhat increase. A factor of changes does not exceed 4. Therefore a choice of the turbulent heat flux (saturated or anomalous) model generally is not a crucial point when a rough comparison is made of the local models of a RCL. However

the choice of the heat transport regime in a super-hot plasma may be of importance for interpreting the hard X-rays of solar flares

(Somov and Kosugi 1997; Somov et al. 1998).

The energy release power per unit of length of the layer, depending on conditions, varies over a wide range: from  $\sim 10^{15}$  to  $\sim 10^{19}$  erg/(cm s), i.e. for the SHTCL with characteristic length  $L \sim 10^{10}$  cm, the power is high as  $10^{29}$  erg/s which is sufficient to account for the most powerful flares and CMEs (Somov 1992). So

the collisionless 3D reconnection in the solar active phenomena seems to be similar to the magnetic reconnection investigated in laboratory, in the toroidal devices: tokamaks and stellarators.

Classically, most electrons are expected to run away in strong electric fields. However the experiments in the toroidal devices, most of which have been made in well magnetized plasmas, indicate that effective braking mechanisms exist to retard runaway electrons. In this way, a sufficiently strong electric field creates the state of the CDT. This state is macroscopically characterized by a large decrease of conductivity  $\sigma$  from the classical value  $\sigma_{cl}$ .

With the anomalous decrease of conductivity, Joule dissipation is enhanced by a factor  $\sigma_{cl}/\sigma$  and leads to rapid plasma heating to extremely high temperatures. *Yohkoh* and *RHESSI* observations of super-hot plasma in solar flares clearly indicate that

the anomalous conductivity and accompanying turbulent heating are macroscopic manifestations of the CDT in the place of collisionless reconnection (the SHTCL) in solar flares

as well as in the surrounding coronal plasmas heated by anomalous heat fluxes.

## 10.2 Reconnection in the Earth Magnetosphere

### 10.2.1 Magnetospheric Physics Problems

The fundamental importance of magnetic reconnection as a universal process in space plasmas, that provides rapid transformation of energy from magnetic

field to particles, is well recognized. However theoretical studies and numerical simulations prove to be difficult, especially when attempts are made to involve the kinetic phenomena. Laboratory experiments cannot properly reproduce the required physical conditions. Satellite observations are the only way to probe the Earth's magnetospheric plasma and to investigate reconnection in it systematically. This approach however requires the multi-instrumental and multiprobe measurements with significant coverage of the reconnection region, which is difficult to achieve with existing spacecraft owing to the highly dynamical and small-scale nature of related phenomena.

As a consequence, there remain many basic questions in the physics of magnetospheric reconnection. What is the reconnection geometry? What effects control the reconnection rate? Why does reconnection often evolve from a slow gradual stage to short reconnection pulses? How does reconnection proceed in specific conditions, for example, in a *thin current layer* embedded within a relatively thick plasma layer of the magnetotail? What is the role of turbulence?

First, we start from the causes of reconnection in the Earth magnetosphere.

### 10.2.2 Origin of Magnetospheric Reconnection

The interaction between the *solar wind* and Earth's *magnetosphere* is the primary driver of many processes occurring in the magnetosphere and ionosphere. The coupling between the solar wind and the magnetosphere is mediated and controlled by an *interplanetary magnetic field* (more exactly, by its north-south component) in the solar wind through the process of magnetic reconnection with the dipole magnetic field of the Earth as illustrated by Fig. 10.2.

Reconnection occurs on the dayside if the interplanetary magnetic field (*IMF*) is directed southwardly as shown in Fig. 10.2b. The ‘day-side’ reconnection turns closed field lines of the Earth into open field lines: one end is connected to the Earth and the other in the solar wind (*SW*). The reconnected field lines take part in the anti-sun-ward motion of the solar wind and get dragged to the nightside. Here they enhance the tail lobes. Hence reconnection must again occur on the nightside, and the new closed field lines must return to the dayside. Therefore

magnetic reconnection gives rise to convection of solar plasma through the Earth magnetosphere.

As a result of reconnection at two neutral points, magnetic flux is transported from the dayside of the magnetosphere to the nightside.

The plasma dynamics in the magnetosphere is associated with the electric current flows. There are several sources of currents in the magnetosphere (Fig. 10.3). The *magnetopause current* (*MPC*) is essentially due to the interaction between the solar wind (*SW*) and the dipole magnetic field of the Earth. This current flows eastward on the dayside magnetopause (*MP*), around the polar cusps, and westward on the

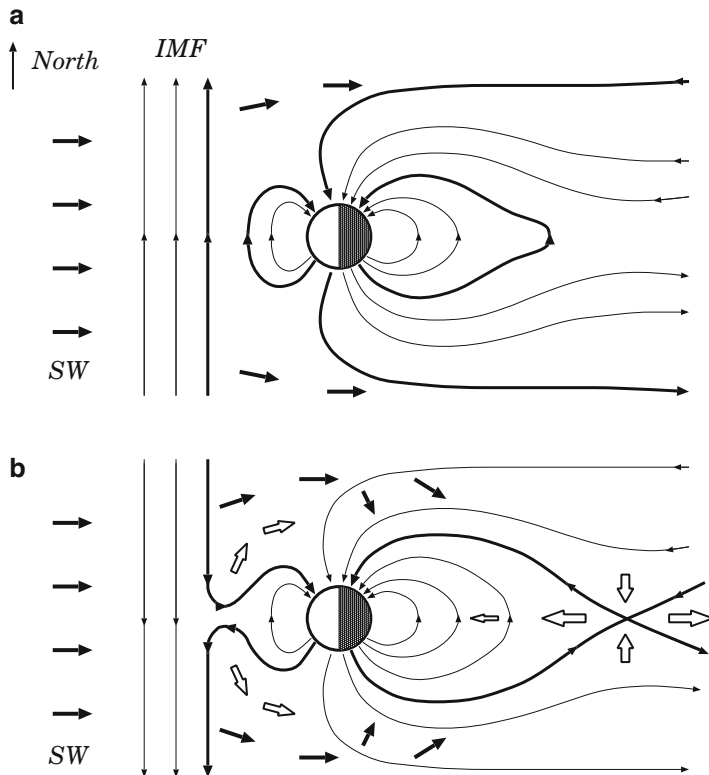
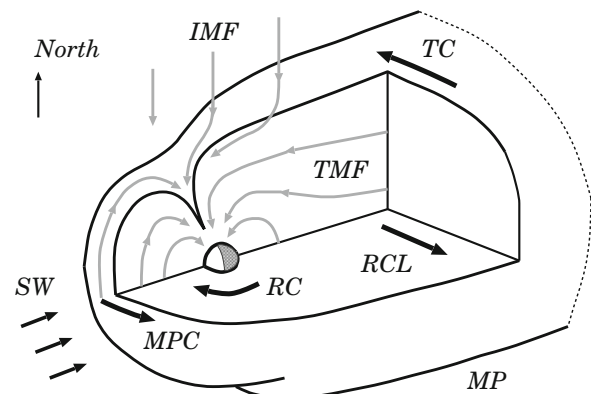


**Fig. 10.2** Schematic of the process of reconnection in the magnetosphere. (a) A northward interplanetary magnetic field. No reconnection and no energy flow into the magnetosphere. Energy flow is indicated by *solid arrows*. (b) Reconnection opens the magnetosphere and allows entry of plasma, momentum, and energy. Magnetospheric convection is indicated by the *open arrows*

**Fig. 10.3** Sketch of the magnetosphere (cf. Fig. 10.2b), representing the main structures of magnetic fields and electric currents



nightside magnetopause where it is called the *tail current* (*TC*). The *cross-tail current*, i.e. reconnecting current layer (*RCL*), flows eastward in the magnetic equatorial plane of the magnetotail (Dungey 1961); see also Russell (1995).

3D magnetospheric configurations that represent pressure balance across the magnetopause were found for a variety of actual conditions (e.g., Sotirelis and Meng 1999) allowing for the cross-tail current and *ring current* (*RC*) in Fig. 10.3. Many different configurations were presented for general reference. The magnetospheric magnetic pressure was calculated by using the current systems of the model by Tsyganenko (1996) together with self-consistently calculated magnetopause shapes and currents.

The dynamics of the Earth's magnetosphere is variable and depends upon: (a) orientation and strength of the IMF, and (b) physical parameters of the solar wind. This complicated interaction was often viewed with considerable success using the implicit assumption of laminar plasma flows and quasi-stationary reconnection. However, new conceptions of the magnetospheric dynamics are being developed, in which turbulence plays a fundamental role (e.g., Antonova and Tverskoi 1998; Borovsky and Funsten 2003a,b).

### 10.2.3 MHD Simulations of Space Weather

As we discussed in introduction, solar flares and coronal mass ejections (CMEs) strongly influence interplanetary and terrestrial space by virtue of shock waves, hard electromagnetic radiation and accelerated particles (e.g., Kivelson and Russell 1995). That is why *space weather* is of growing importance to the scientific community and refers to conditions at a particular place and time on the Sun and in the solar wind, magnetosphere, ionosphere, and thermosphere that can influence the performance and reliability of spaceborne and ground-based technological systems and can affect human life or health (Wright 1997; de Jager 2005; Hanslmeier 2007; Liliensten 2007). These influences have prompted efforts to enhance our understanding of space weather and develop effective tools for space weather prediction.

Global MHD simulations have been used for a long time to model the global magnetospheric configuration and to investigate the response of the magnetosphere-ionosphere system to changing solar wind conditions (see review by Lyon 2000). Variations in the solar wind can lead to disruptions of space- and ground-based systems caused by enhanced electric currents flowing into the ionosphere and increased radiation in the near-Earth environment.

A focus of many MHD investigations was the study of magnetospheric ‘events’. In addition to this study, there have been several applications of MHD models to the study of coronal and solar wind plasma flows. For example, the ideal MHD approximation was efficiently used by Groth et al. (2000) to simulate the initiation, structure, and evolution of a CME and its interaction with the magnetosphere-ionosphere system.

Groth et al. have developed a new parallel adaptive mesh refinement (AMR) finite-volume scheme to predict the ideal MHD flows in a complete fully three-dimensional space weather event. So the simulation spans the initiation of the solar wind disturbance at the surface of the Sun to its interaction with the Earth's magnetosphere-ionosphere system. Starting with generation of a CME at the Sun, the simulation follows the evolution of the solar wind disturbance as it evolves into a magnetic cloud and travels through the interplanetary space and subsequently interacts with the terrestrial magnetosphere-ionosphere system.

## 10.3 Flares in Accretion Disk Coronae

In this section we discuss the possibility of applying the theory of magnetic reconnection in solar flares to astrophysical phenomena accompanied by fast plasma ejection, powerful fluxes of heat and radiation, impulsive acceleration of electrons and ions to high energies. We use the well-tested models of the SHTCL to evaluate an ability to release a free magnetic energy in the *accretion disk* coronae of compact stars, for example, neutron stars.

### 10.3.1 Introductory Comments

The accretion disks presumably have a corona which interacts with a magnetic field generated inside a disk. Drawing on developments in solar flare physics, [Galeev et al. \(1979\)](#) suggested that the corona is heated in magnetic loops which have buoyantly emerged from the disk. Reconnection of buoyant fields in the lower density surface regions may supply the energy source for a hot corona. Another feature related to the disk corona is the possibility of a flare energy release similar to solar flares. They are accompanied by fast directed plasma ejections (jets), coronal mass ejections (CMEs) into interplanetary space, powerful fluxes of hard electromagnetic radiation.

If a plasma in the disk corona is optically thin and has a dominant magnetic pressure, the circumstances are likely to be similar to the solar corona. Therefore it is also possible to imagine some similarity between solar flares and the X-ray flares in the accretion disk coronae. Besides the effect of heating the disk corona, reconnection is able to accelerate electrons and protons to relativistic energies ([Lesch and Pohl 1992; Bednarek and Protheroe 1999](#)). Starting from well-tested models for magnetic reconnection in the solar corona during flares, we examine whether the magnetic reconnection may explain the hard X-ray emission of stars.

## 10.3.2 Models of the Star Magnetosphere

### 10.3.2.1 Global and Local Magnetic Fields

Let us assume that the magnetic fields in the magnetosphere of a star (for example, the *pulsar magnetosphere*; see [Becker 2009](#)) with an accretion disk consist of two components of different origin. The first, *regular* large-scale magnetic component is related to the proper magnetic field of a star and large-scale electric currents flowing in the accretion disk as a whole. This component is similar to the large-scale quasi-stationary magnetic field in the solar corona, including the coronal streamers, or in the Earth magnetosphere, including the magnetotail.

The second component represents the *chaotic* magnetic fields generated by the differential rotation and turbulence in the accretion disk. The MHD turbulence inside the disk gives rise to the dynamo mechanism with a wide spectrum of scales for magnetic fields emerging at the disk's surfaces into its corona. These fields, interacting between themselves and with the large-scale regular field of the magnetosphere, create flares of different scales in the corona of the disk. We believe that they heat the corona and accelerate particles to very high energy via magnetic reconnection in myriads of large and small flares similar to solar flares.

By analogy with the solar corona or the Earth magnetosphere, we shall assume that, in the magnetosphere of a compact star, the magnetic-field energy density greatly exceeds that of the thermal, kinetic and gravitational energy of the accreting plasma:

$$\frac{B^2}{8\pi} \gg 2nk_B T, \quad \frac{B^2}{8\pi} \gg \frac{\rho v^2}{2}, \quad \text{and} \quad \frac{B^2}{8\pi} \gg \rho g. \quad (10.31)$$

So the magnetic field can be considered in the *strong field* approximation. This means, in fact, that the magnetic field is mainly potential in the magnetosphere everywhere outside the field sources: a star, an accretion disk, and the magnetospheric boundaries. At least,

**|** the magnetic field is potential in a large scale, in which the field determines the *global* structure of the magnetosphere.

This 3D structure is illustrated by Fig. 10.4 ([Somov et al. 2003a](#)).

Here  $\mathbf{m}$  is a magnetic dipole moment of a star which rotates with an angular velocity  $\Omega$ . The velocity of plasma flow inside the accretion disk  $D$  is shown by vectors  $\mathbf{V}$ . The large-scale regular magnetic field  $\mathbf{B}$  is presented by two pairs of field lines separated by the accretion disk. Such structure seems to be well supported by results of the fully three-dimensional MHD simulations (see [Romanova et al. 2004](#), Fig. 4).  $S_u$  and  $S_d$  are the upper and bottom boundary surfaces of the magnetosphere.  $C_u$  is a cusp at the upper boundary. The outer surfaces  $S_u$  and  $S_d$  play the role of the magnetopause; their location and configuration are determined primarily by the condition of pressure equilibrium. The interaction between the magnetosphere and the surrounding plasma makes the outer boundaries highly asymmetric.

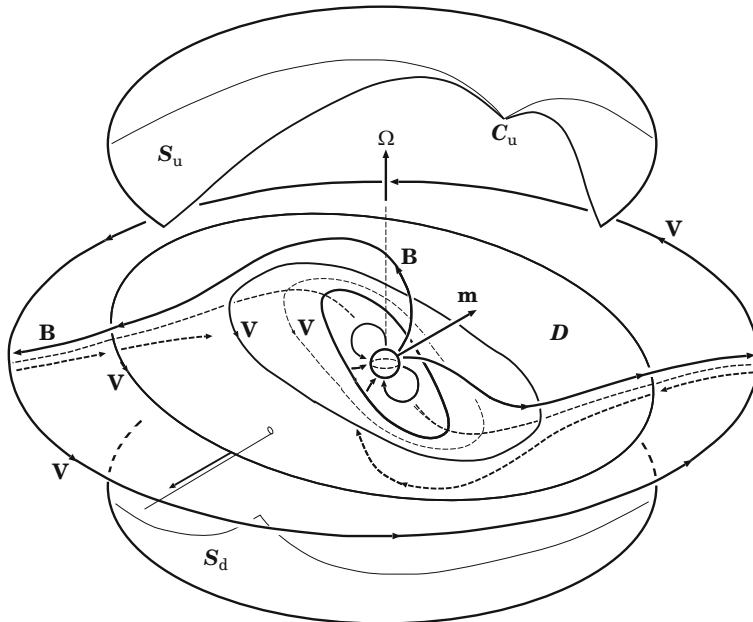


**Fig. 10.4** A three-dimensional picture of the star magnetosphere. The field lines  $\mathbf{B}$  show the transition from the dipolar field of a rotating magnetized star to the tail-like field above and below an accretion disk  $D$ . The solid curves with arrows  $\mathbf{V}$  represent the velocity field of the differentially rotating flows inside the disk

### 10.3.2.2 An Auxiliary Two-Dimensional Problem

To estimate characteristic values of the large-scale magnetic field and its gradient in the corona of an accretion disk, we have to find the structure of the field inside the magnetosphere created by a dipole field of a star and a regular field generated by the disk. Let us consider a simplified two-dimensional problem on the shape of a magnetic cavity and the shape of the accretion disk under assumption that this cavity, i.e. the magnetosphere, is surrounded by a perfectly conducting uniform plasma with a gas pressure  $p_0$ .

Two conditions have to be satisfied at the boundary surface  $S$  which consists of two surfaces: the upper one  $S_u$  and the bottom  $S_d$  (compare Figs. 10.4 and 10.5). These conditions are the equality of magnetic and gas pressure,

$$\left. \frac{B^2}{8\pi} \right|_S = p_0 = \text{const}, \quad (10.32)$$

and tangency of the magnetic field along the boundary  $S$ ,

$$\mathbf{B} \cdot \mathbf{n} \Big|_S = 0. \quad (10.33)$$

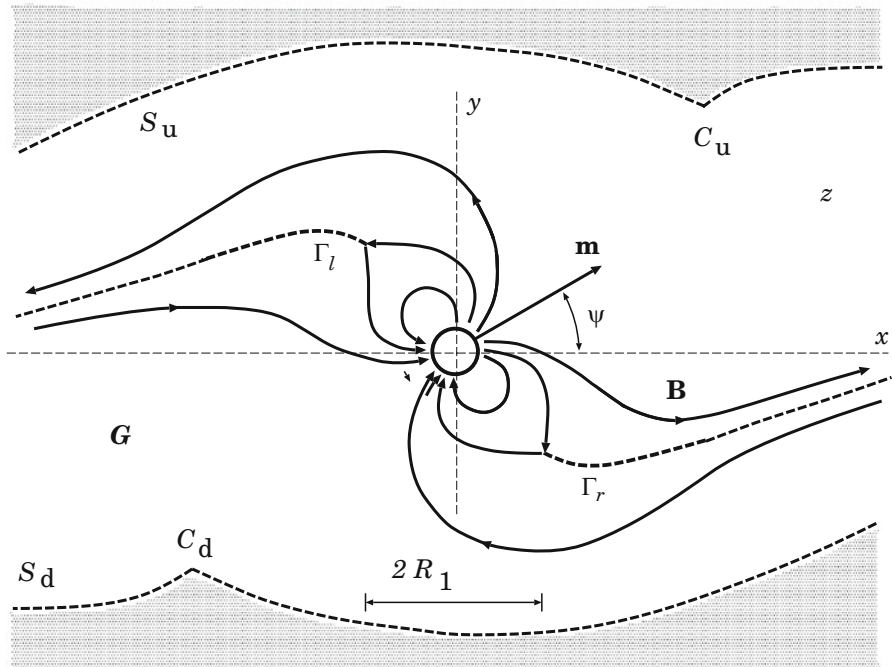


**Fig. 10.5** A two-dimensional model of the star magnetosphere.  $\Gamma_l$  and  $\Gamma_r$  are the cross sections of the accretion disk  $D$  by the plane determined by two vectors: the dipole moment  $\mathbf{m}$  of the star and its angular velocity  $\Omega$  in Fig. 10.4. An auxiliary plane  $z$  corresponds to the complex variable  $z = x + iy$ .  $R_1$  is the inner radius of the disk.  $S_u$  and  $S_d$  together with  $\Gamma_l$  and  $\Gamma_r$  constitute the boundary of the singly connected domain  $G$  in the plane  $z$

Condition (10.33) means that, along the boundary  $S$ ,

$$\operatorname{Re} F(z) = A(x, y) = \text{const.} \quad (10.34)$$

Here a complex potential  $F(z)$  is an analytic function

$$F(z, t) = A(x, y, t) + i A^+(x, y, t), \quad (10.35)$$

within the domain  $G$  in the complex plane  $z$  except at the point  $z = 0$  of the dipole and the current layers  $\Gamma_l$  and  $\Gamma_r$  related to the accretion disk.  $A^+(x, y, t)$  is a conjugate harmonic function connected with  $A(x, y, t)$  by the Cauchy-Riemann condition

$$A^+(x, y, t) = \int \left( -\frac{\partial A}{\partial y} dx + \frac{\partial A}{\partial x} dy \right) + A^+(t), \quad (10.36)$$

where  $A^+(t)$  is a quantity independent of the coordinates  $x$  and  $y$ .

The magnetic field vector, according to definition  $\mathbf{B} = \text{curl } \mathbf{A}$ , is:

$$\mathbf{B} = B_x + i B_y = -i \left( \frac{dF}{dz} \right)^*, \quad (10.37)$$

the asterisk denoting the complex conjugation. After introducing the complex potential, we apply the methods of the complex variable function theory, in particular the method of *conform mapping*, to determine the magnetic field. This has been done, for example, to determine the structure of the magnetic field in solar coronal streamers ([Somov and Syrovatskii 1972](#)).

By analogy with the solar coronal streamers or with the Earth magnetotail, we assume that the large-scale regular magnetic field reverses its direction from one side of the accretion disk to the other:

$$\mathbf{B} \Big|_{\Gamma+} = -\mathbf{B} \Big|_{\Gamma-}. \quad (10.38)$$

So, with respect to the large-scale field of the global magnetosphere, the accretion disk electric current is considered, for simplicity, as the large-scale *neutral* current layer  $\Gamma$ .

We also assume that a conform transformation  $w = w(z)$  maps the domain  $G$  shown in Fig. 10.5 onto the circle  $|w| \leq 1$  in an auxiliary complex plane  $w = u + iv$  so that the point  $z = 0$  goes into the centre of the circle without rotation of the magnetic dipole as shown in Fig. 10.6.

Then the complex potential inside the circle has the following form:

$$F(w) = i Q \left( \ln \frac{w - e^{i\alpha}}{w e^{i\alpha} - 1} + \ln \frac{w - e^{i(\pi-\alpha)}}{-w e^{i(\pi-\alpha)} + 1} \right) + i e^{-i\psi} w + \frac{i e^{i\psi}}{w}. \quad (10.39)$$

Here  $Q$  is a ‘magnetic charge’, the value which is proportional to the flux of the ‘open’ field lines, that go from a star to infinity. An angle  $\alpha$  is a free parameter of the problem, which determines the type of a selected solution (for more mathematical details see [Somov et al. 2003a](#)).

### 10.3.3 Power of Energy Release in the Disk Coronae

Let us consider some consequences of the solution of the auxiliary two-dimensional problem. For parameters  $m \approx 10^{30} \text{ G cm}^3$ ,  $\psi = \pi/4$ ,  $p_0 \approx 1.4 \times 10^6 \text{ dynes cm}^{-2}$ , we obtain that the inner radius  $R_1$  of the accretion disk (Fig. 10.5) is about  $4 \times 10^8 \text{ cm}$ . The half-size of the magnetosphere is about  $6 \times 10^8 \text{ cm}$ . These values seem to be in agreement with those inferred for the 4U1907 + 09 neutron star and similar objects ([Mukerjee et al. 2001](#)). At a distance of  $5 \times 10^8 \text{ cm}$  from the star, the magnetic-field strength is  $(1 - 2) \times 10^4 \text{ G}$  while the magnetic-field gradient is  $h_0 \sim 10^{-6} - 10^{-2} \text{ G cm}^{-1}$ .

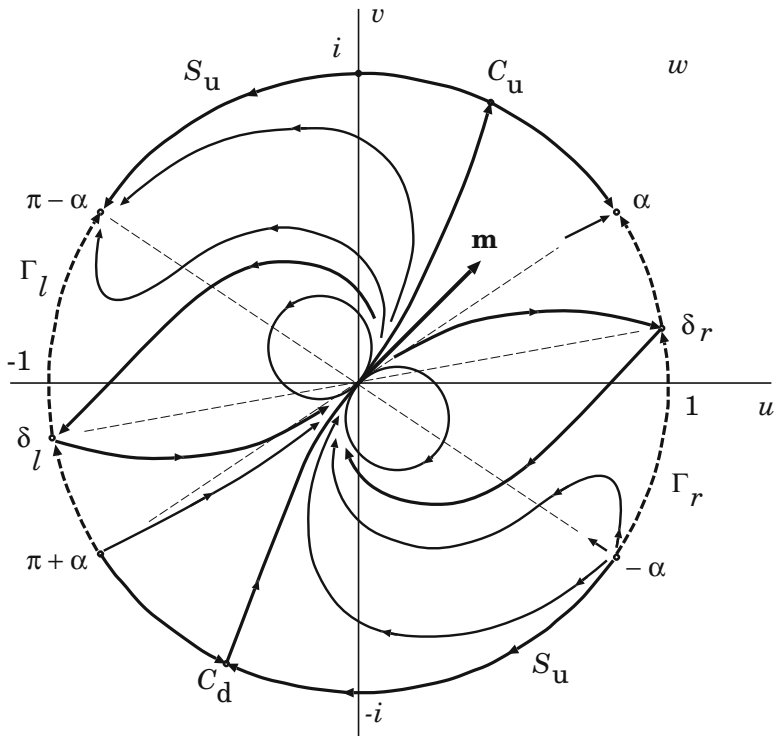


**Fig. 10.6** A solution of the two-dimensional problem inside the unit circle in the complex plane  $w = u + iv$ . The domain  $G$  in the plane  $z$  shown in Fig. 10.5 is mapped onto the unit circle

From the solution of the problem on the SHTCL parameters (see Sect. 10.1.3) we find the power released per one current layer. For example, for the input parameters  $n_0 \approx 10^{13} \text{ cm}^{-3}$ ,  $h_0 \approx 10^{-2} \text{ G cm}^{-1}$ ,  $E_0 \approx 10^3 \text{ CGSE units}$ , and  $\xi \approx 0.1$  (Somov et al. 2003a), we obtain the half-width  $b \approx 5 \times 10^6 \text{ cm}$  and the power released per unit length along the current layer length  $l$ :

$$\frac{P_1}{l} = \frac{B_0^2}{4\pi} v 4b = \frac{1}{\pi} c E_0 h_0 b^2 \approx 3 \times 10^{24} \text{ erg s}^{-1} \text{ cm}^{-1}. \quad (10.40)$$

Let us assume that the SHTCL length  $l$  has the same order of magnitude as its width  $2b$ . Then the power released by a single SHTCL is  $P_1$ . We assume that new layers are continually forming in the disk corona as a result of permanently emerging new magnetic loops. Let us consider an inner part of the ring-shaped accretion disk. Let the inner radius be  $R_1 \sim 4 \times 10^8 \text{ cm}$  while the outer radius is  $R_2 \sim 8 \times 10^8 \text{ cm}$ . Its area is thus  $S_r = \pi(R_2^2 - R_1^2)$ , while the area of a single RCL is  $S_1 = l \times 2b$ .

Thus, in the inner part of the accretion disk, a number  $N \sim 2S_r/S_1$  of current layers exist simultaneously. The total energy release per second is

$$\begin{aligned} P \sim N P_1 &= \frac{2 S_r}{S_1} \times P_1 = \frac{2 \pi (R_2^2 - R_1^2)}{l 2 b} \times \frac{c}{\pi} E_0 h_0 b^2 l = \\ &= (R_2^2 - R_1^2) c E_0 h_0 b \sim 7 \times 10^{35} \text{ erg s}^{-1}. \end{aligned} \quad (10.41)$$

This estimate (which should be, in fact, considered as a lower limit, according to [Somov et al. 2003a](#)) does not contradict to the total power released by some neutron stars such as Aql X – 1, SLX1732 – 304, 4U0614 + 09, 4U1915 – 05, SAX J1808.4 – 3658 ([Barret et al. 2000](#)). So the magnetic reconnection in accretion disk coronae is a powerful mechanism which may explain the observed X-ray emission from neutron stars.

Disk accretion to a rotating star with an inclined dipole magnetic field has been studied by three-dimensional MHD simulations ([Romanova et al. 2004](#)). It was shown that the hot spots arise on the stellar surface because of the impact on the surface of magnetically channelled accretion streams. The results are of interest for understanding the variability of classical T Tauri stars, millisecond pulsars, and cataclysmic variables.

## 10.4 The Giant Flares

The so-called *giant flares* are produced via annihilation of magnetic fields (i.e. magnetic reconnection) of a highly magnetized neutron star, a *magnetar*. This annihilation deposits energy in the form of photons and pairs near the surface of the neutron star. The pair-radiation plasma evolves as an accelerating *fireball*, resulting in a thermal radiation burst carrying the bulk of the initial energy with roughly the original temperature and a fraction of energy in the form of relativistic pairs. The thermal spectrum of giant flares and their temperatures support this scenario.

On 2004 December 27, a giant flare from SGR (soft gamma-ray) 1806-20 was the most powerful flare of gamma rays ever measured on Earth (for a review see [Nakar et al. 2005](#)). Its energy of  $3 \times 10^{46}$  erg was released at a distance of 15 kpc during about 0.2 s. The spectrum of the flare is consistent with that of a cooling blackbody spectrum with an average temperature of  $175 \pm 25$  keV. Like other giant flares, this flare was followed by a pulsed softer X-ray (SXR) emission that lasted more than 380 s. Radio afterglow was detected from Very Large Array (VLA) observations. After 1 week the radio source was extended to a size of  $(0.6 - 0.9) \times 10^{16}$  cm. Therefore a significant amount of energy was emitted in the form of a relativistic ejecta around the same time that the gamma-ray flare was emitted.

# Chapter 11

## Particle Acceleration in Current Layers

**Abstract** The inductive electric field is directed along the current inside a collisionless reconnecting current layer (RCL). This strong field does positive work on charged particles, thus increasing their energy impulsively, for example, in solar flares or flares in the accretion disk coronae of compact astrophysical objects.

### 11.1 Magnetically Non-neutral RCLs

#### 11.1.1 An Introduction in the Problem

Magnetic reconnection determines many phenomena in astrophysical plasma (for a review of pioneering works see [Sweet 1969](#); [Syrovatskii 1981, 1982](#)). The theory of reconnection in a *super-hot turbulent-current layer* (SHTCL, see Sect. 8.3) explains the total amount of energy accumulated before solar flares, the power of energy released during flares and some other parameters of flares (Sect. 8.5). In particular, it has been shown ([Litvinenko and Somov 1991](#)) that acceleration by the electric field induced by reconnection, and scattering of particles by *ion-acoustic turbulence* in an SHTCL lead to the appearance of about  $10^{35} - 10^{36}$  electrons with a power-law spectrum and with energies of the order of tens of keV. Future development of the theory should result in models for the total number of accelerated particles, their maximum energy and the rate of particle acceleration ([Bai and Sturrock 1989](#); [Somov 1992](#); [Hudson and Ryan 1995](#); [Miroshnichenko 2001](#)).

In this section we return to the question of the maximum energy of particles accelerated in a RCL, which has been formulated in Sect. 1.2. Three points are important here.

- (a) The problem of particle motion in a magnetic field which changes the sign of its direction and in the electric field related to reconnection has been considered many times. [Speiser \(1965\)](#) found particle trajectories near the neutral plane

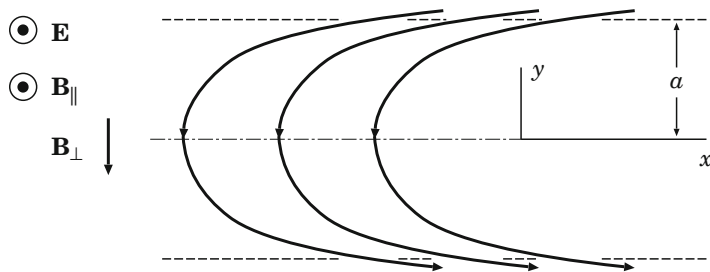


**Fig. 11.1** The projection of field lines inside the RCL to the plane ( $x, y$ );  $\mathbf{B}_{\parallel}$  is the longitudinal magnetic field.  $\mathbf{E}$  is the inductive electric field related to magnetic reconnection

where the magnetic field is zero. The physical meaning of the Speiser solution is in the following. Formally speaking,

a charged particle can spend an *infinite* time near such a neutral plane and can take an infinite energy from the electric field.

However, under real conditions in astrophysical plasma, the probability of such a situation is small; usually the magnetic field in the ‘reconnecting plane’, i.e. the current layer, has non-zero *transversal* and *longitudinal components*. Therefore actual current layers are *magnetically* non-neutral RCLs. This is of importance for their energetics (Chap. 8), stability (Chap. 13), and for the mechanism of acceleration that will be considered in the present chapter.

(b) [Speiser \(1965\)](#) showed also that

even a small transversal field changes the particle motion in such a way that the particle leaves the RCL after a *finite* time,

the particle energy being finite. In what follows we show that this time is small and the energy is not sufficient in the context of solar flares.

(c) Can we increase the time spent by the particle inside the RCL? – In the following it will be shown that ([Somov and Litvinenko 1993](#))

the longitudinal field increases the acceleration time and, in this way, strongly increases the efficiency of particle acceleration

thus allowing us to explain the first step of acceleration of electrons in solar flares. An iterative method will be presented in Sect. 11.1.3, which gives us an approximate general solution of the problem.

### 11.1.2 Dimensionless Parameters and Equations

Let us consider a reconnecting current layer (RCL) placed in the ( $x, z$ ) plane in Fig. 11.1. More exactly, this can be a right-hand-side part of the magnetically

non-neutral RCL as shown in Fig. 8.3 or a part of a more complicated magnetic configuration. The electric field  $\mathbf{E}$  and current density  $\mathbf{j}$  are parallel to the  $z$  axis; so the associated magnetic field components are parallel to the  $x$  axis and change their sign in the plane  $y = 0$ . Therefore we prescribe the electric and magnetic fields inside the current layer as follows (Litvinenko and Somov 1993):

$$\mathbf{E} = \{0, 0, E_0\}, \quad \mathbf{B} = \{-y/a, \xi_{\perp}, \xi_{\parallel}\} B_0. \quad (11.1)$$

Here  $B_0$  is a typical value of the magnetic field in the vicinity of the RCL; the dimensionless parameters  $\xi_{\perp}$  and  $\xi_{\parallel}$  are constants;  $a$  is the half-thickness of the layer.

One may consider the function  $B_x(y) = -y/a$  as a *linear* approximation to the Harris-type magnetic field,  $B_x(y) \sim \tanh(y/a)$ , (see Sect. 13.6.1). However, contrary to the case of *static* magnetic field (Tsalas et al. 2001), we consider the *stationary* magnetic reconnection. Thus the electric field  $E_0 \neq 0$  (see Sect. 1.1). Therefore, in Formula (11.1),  $E_0$  is non-vanishing constant. Note also that we shall deal mainly with particle trajectories (or orbits) lying in the vicinity of the reversal plane  $(x, z)$ , for which  $|y| < a$ , the region of validity of the linear model is sufficient (see Fig. 1 in Tsalas et al.).

The non-relativistic equation of motion for a particle with mass  $m$  and charge  $q = Ze$  is

$$m \frac{\partial \mathbf{v}}{\partial t} = q \left( \mathbf{E} + \frac{1}{c} \mathbf{v} \times \mathbf{B} \right). \quad (11.2)$$

Let us take the half-thickness  $a$  of the layer as a unit of length and the inverse gyro-frequency  $\omega_B^{-1} = mc/qB_0$  as a unit of time. Then Eq. (11.2) can be rewritten in the dimensionless form:

$$\frac{\partial^2 x}{\partial t^2} = \xi_{\parallel} \frac{\partial y}{\partial t} - \xi_{\perp} \frac{\partial z}{\partial t}, \quad (11.3)$$

$$\frac{\partial^2 y}{\partial t^2} = -\xi_{\parallel} \frac{\partial x}{\partial t} - y \frac{\partial z}{\partial t}, \quad (11.4)$$

$$\frac{\partial^2 z}{\partial t^2} = \varepsilon + \xi_{\perp} \frac{\partial x}{\partial t} + y \frac{\partial y}{\partial t}. \quad (11.5)$$

Here the dimensionless electric field

$$\varepsilon = \frac{mc^2 E_0}{aqB_0^2}. \quad (11.6)$$

Two non-linear terms are introduced in Eqs. (11.4) and (11.5) by the dependence of the reconnecting component of the magnetic field,  $B_y$ , on the ordinate  $y$ .

The influence of *plasma turbulence* on particle motions is ignored in Eq. (11.2). This is justified provided the time spent by a particle inside the RCL is less than the inverse frequency of the wave-particle interactions  $\nu(v)$ . For the typical case, like the ion-acoustic turbulence,

$$\nu(v) = \nu_{\text{eff}} \left( \frac{\sqrt{k_B T / m}}{v} \right)^3, \quad (11.7)$$

$T$  being the temperature in the layer. For typical parameters of SHTCL (Chap. 8), the effective collision frequency can be estimated as

$$\nu_{\text{eff}} \approx \xi_{\perp} \omega_B \approx 10^6 \text{ s}^{-1}.$$

Hence the turbulence can be ignored for suprathermal particles, once the time spent by a particle inside the SHTCL does not exceed

$$\tau_{\text{eff}} = (\xi_{\perp} \omega_B)^{-1} \approx 10^{-6} \text{ s}.$$

On integrating linear equation (11.3) and non-linear equation (11.5) and substituting the results in (11.4), the set of Eqs. (11.3)–(11.5) becomes

$$\frac{\partial x}{\partial t} = \xi_{\parallel} y - \xi_{\perp} z + c_1, \quad (11.8)$$

$$\begin{aligned} \frac{\partial^2 y}{\partial t^2} + \xi_{\parallel}^2 y &= - \left( \varepsilon t + \xi_{\perp} x + \frac{1}{2} y^2 + c_2 \right) y \\ &\quad + \xi_{\parallel} (\xi_{\perp} z - c_1), \end{aligned} \quad (11.9)$$

$$\frac{\partial z}{\partial t} = \varepsilon t + \xi_{\perp} x + \frac{1}{2} y^2 + c_2. \quad (11.10)$$

Let  $x_0$ ,  $y_0$ , and  $z_0$  be the initial coordinates of the particle. If its initial velocity is assumed to be negligible then the constants of integration are as follows:

$$c_1 = -\xi_{\parallel} y_0 + \xi_{\perp} z_0, \quad c_2 = -\xi_{\perp} x_0 - \frac{1}{2} y_0^2. \quad (11.11)$$

This assumption does not mean that a particle trajectory does not depend of the particle's initial velocity but it means that, for some type of trajectories and for sufficiently high (but non-relativistic) velocities, we can hope to find an asymptotic solution of the Speiser type (see Sect. 1.2.3) or a similar type.

In principle, the problem can be analytically solved, of course, even without the assumption that the initial velocities of accelerated particles are small. This can be done, for example, in the guiding center approximation. In fact, an actual

non-relativistic solution of the problem is sensitive to a choice of initial velocity ([Oreshina and Somov 2009a](#)). There exists a minimum of initial velocity, below which there are no stable trajectories. Moreover, for a given value of initial velocity, stable trajectories take place only in a certain range of directions. However, in this section, we shall be mainly interested in an approximate approach to the solution which describes an asymptotical behavior of accelerated particles at stable trajectories.

### ***11.1.3 An Iterative Solution of the Problem***

The simple-looking set of ordinary differential equations [\(11.3\)](#)–[\(11.5\)](#) for the single particle motion inside the RCL is still complex, because the equations are not linear in the variables. As surprising as it may seem, we cannot solve these equations exactly, except for very special cases or with some significant simplifications. So, how could we proceed?

At first glance it may seem that the most natural and straightforward way to find a general solution of the problem is a numerical integration of the set of Eqs. [\(11.3\)](#)–[\(11.5\)](#) with the initial conditions: the coordinates and velocity components of a particle at  $t = 0$ . Less trivial and more productive is another approach. We can rewrite the equations of motion in the Hamiltonian form with the *usual* Hamiltonian [\(11.33\)](#) or with the *transformed* Hamiltonian [\(11.40\)](#). This will offer to us two opportunities:

- (a) To investigate how the parameters of the RCL can influence such important property of particle accelerator as its *stochasticity* (see Sects. [11.2.1](#) and [11.2.2](#)); and
- (b) To investigate and distinguish different types of particle orbits depending on the initial conditions (see Sect. [11.2.5](#)).

Until the particle leaves the layer, the value of  $y(t)$  is small, since the layer is supposed to be thin. In the plane  $(x, z)$  the particle's motion is much less restricted. As was mentioned in Sect. [11.1.2](#), we would like to consider the Speiser type of orbits or generalization of this type. With this idea in mind, let us start from assumption that the behavior of the functions  $x(t)$  and  $z(t)$  does not depend strongly on the exact form of the solution  $y(t)$ . For this reason the Eqs. [\(11.8\)](#) and [\(11.10\)](#) can be solved by the following iterative procedure. First, we prescribe some function

$$y(t) = y^{(0)}(t).$$

Second, using this function, we calculate  $x^{(0)}(t)$  and  $z^{(0)}(t)$  from Eqs. [\(11.8\)](#) and [\(11.10\)](#). Third, we use these functions to find a small correction  $y^{(1)}(t)$  from Eq. [\(11.9\)](#).

In zeroth approximation Eq. (11.9) takes the simplest form

$$\frac{\partial^2 y^{(0)}}{\partial t^2} + \xi_{\parallel}^2 (y^{(0)} - y_0) = 0, \quad (11.12)$$

whence  $y^{(0)} = y_0 = \text{const}$ . Now, from Eqs. (11.8) and (11.10), we find the zeroth order functions:

$$\begin{aligned} x^{(0)}(t) &= x_0 + (\sin \xi_{\perp} t - \xi_{\perp} t) \varepsilon / \xi_{\perp}^2, \\ z^{(0)}(t) &= z_0 + (1 - \cos \xi_{\perp} t) \varepsilon / \xi_{\perp}^2. \end{aligned} \quad (11.13)$$

In this approximation the projection of the particle's trajectory on the plane  $(x, z)$  is a cycloid curve whose shape does not depend on the longitudinal field  $B_z = \xi_{\parallel} B_0$ . Physically, formulae (11.13) describe the particle drift in the perpendicular fields  $B_y = \xi_{\perp} B_0$  and  $E_z = E_0$  (see Appendix C), the influence of the  $B_z$  component being neglected.

Now let us write an equation which will allow us to find a correction to  $y^{(0)}(t)$ . Making use of (11.9) and (11.13), we obtain

$$\frac{\partial^2 y}{\partial t^2} + \left( \xi_{\parallel}^2 + \varepsilon \frac{\sin \xi_{\perp} t}{\xi_{\perp}} \right) y = \xi_{\parallel}^2 y^{(0)} + (1 - \cos \xi_{\perp} t) \varepsilon \frac{\xi_{\parallel}}{\xi_{\perp}}. \quad (11.14)$$

So the character of the particle motion is determined by two dimensionless parameters:  $\xi_{\parallel}$  and  $\xi_{\perp}$ . Depending on them, two cases can be considered.

### 11.1.3.1 No Longitudinal Field

The case  $\xi_{\parallel} = 0$  means that there is no longitudinal magnetic field inside the RCL. Equation (11.14) becomes

$$\frac{\partial^2 y}{\partial t^2} + \left( \varepsilon \frac{\sin \xi_{\perp} t}{\xi_{\perp}} \right) y = 0. \quad (11.15)$$

This is the equation of a one-dimensional oscillator with a time-dependent frequency. From (11.15), together with (11.13), Speiser's results follow. In particular, a particle can remain inside the layer only for the time

$$\tau = \frac{\pi}{\xi_{\perp}}. \quad (11.16)$$

When  $t > \tau$ , the particle quickly moves out of the layer, since the frequency formally becomes an imaginary value. At this instant,

$$\frac{\partial x(\tau)}{\partial t} = -\frac{2\varepsilon}{\xi_{\perp}}, \quad \frac{\partial z(\tau)}{\partial t} = 0. \quad (11.17)$$

Note that in the case of a neutral layer  $\xi_{\perp} = 0$  and the particle acceleration along the  $z$  axis is not restricted. According to (11.16),  $\tau \rightarrow \infty$ ; the non-relativistic kinetic energy increases as

$$\mathcal{K} \sim z \sim \tau^2,$$

while the oscillation amplitude decreases as  $A_y \sim \tau^{-1/4}$  (see formula (1.30)).

If  $\xi_{\perp} \neq 0$  and the electric field is small enough,

$$\varepsilon < \frac{1}{2} \xi_{\perp}^3, \quad (11.18)$$

then small oscillations near the plane  $y = 0$  are stable, and particles are not pushed out of the layer. However, in the SHTCL model pertaining to *solar flare* conditions (Sect. 8.5),  $\xi_{\perp} \sim 10^{-3}$  and  $\varepsilon \sim 10^{-5}$ . Therefore the inequality (11.18) cannot be satisfied and particles go out of the RCL without being accelerated.

In modern physics of Earth *magnetospheric tail*, two-component models of the current-layer magnetic field are widely used (e.g., Zelenyi et al. 2007; Zelenyi et al. 2009). The stationary magnetic field of a current layer is typically taken according to Harris model (Harris 1962) with a constant perpendicular magnetic field (Lembege and Pellat 1982). In order to avoid the problem with particle acceleration in such model of current layer, the static or moving magnetic fluctuations are supposed to be superimposed on this stationary background magnetic field.

It appears that the presence of even static magnetic turbulence can substantially increase the particle residence time in the current layer. As a result of longer drift motion in the direction of electric field, particles gain more energy (Veltri et al. 1998; Greco et al. 2002). This mechanism can provide significant heating of particles in a magnetospheric tail current layer. In what follows we focus on another mechanism of particle energization due to electric field in a current layer with a longitudinal (guiding) magnetic field.

### 11.1.3.2 Stabilization by the Longitudinal Field

The case  $\xi_{\parallel} \neq 0$ , the RCL with a longitudinal field. Equation (11.14) describes an oscillator the frequency of which changes with time and which is also subject to the action of an external periodic force. Hence the oscillating system represented by Eq. (11.14) is not closed and may have resonance increases of  $y = y(t)$ . This corresponds to the particle going out of the layer.

It is important, however, that the particle's motion can become *stable* provided  $\xi_{\parallel}$  is large enough. Here we assume that the domains of stability can exist for sufficiently large values of the longitudinal magnetic field. The simple argument is that, if the longitudinal field is strong enough, then the particles tend to follow the

orbits mostly parallel to the direction of the longitudinal field, which is also parallel to the electric field. Such particles stay within the RCL and they are accelerated by the electric field.

In this case a particle remains in the vicinity of the layer plane,  $y = 0$ . For the resonance effects to be absent, the oscillation frequency must always be real:

$$\xi_{\parallel}^2 > \frac{\varepsilon}{\xi_{\perp}}. \quad (11.19)$$

Once the inequality (11.19) is valid, some particles do not leave the RCL due to unstable trajectories. Were it not for the turbulence, these particles would simply drift along the RCL, gaining energy. The ion-acoustic turbulence in SHTCL (cf. formula (11.7)) makes the particle motion more complex.

### 11.1.4 The Maximum Energy of an Accelerated Particle

In general, the kinetic energy gain of escaping particles is a function of the physical parameters of the RCL and of the initial conditions that determine the orbits of particles. An issue of great concern is, however, what is the maximum energy to which a particle can be accelerated by the RCL?

For the case of a strong longitudinal magnetic field, the maximum velocity can be evaluated as

$$v_{\max} \approx \xi_{\parallel}. \quad (11.20)$$

Here a unit of velocity (Sect. 11.1.2) is

$$V_1 = a \omega_L = \frac{aqB_0}{mc}. \quad (11.21)$$

Therefore the longitudinal field qualitatively changes the character of particle motion inside the layer. As an example, let us consider electron acceleration in SHTCL during *solar flares*.

The SHTCL model allows us to express the characteristics of a current layer through the external parameters of a reconnection region: the concentration of plasma  $n_0$  outside the layer, the electric field  $E_0$ , the magnetic field gradient  $h_0$  and the relative value  $\xi_{\perp}$  of a transversal magnetic field (see Chap. 8). In the case  $\xi_{\parallel} = 0$  (no longitudinal field), i.e. (11.17), the maximum electron energy is given by

$$\mathcal{E}_{\max} = 2 mc^2 \left( \frac{E_0}{\xi_{\perp} B_0} \right)^2 \quad (11.22)$$

or, using the SHTCL model,

$$\mathcal{E}_{\max} (\text{keV}) \approx 5 \times 10^{-9} T (\text{K}). \quad (11.23)$$

Formula (11.23) shows that acceleration in the RCL without a longitudinal field is not efficient: for the temperature inside the layer  $T \approx 10^8$  K, the maximum energy of accelerated electrons is only 0.5 keV.

Let us consider now the case of a non-zero longitudinal field. The stabilization condition (11.19) can be rewritten in dimensional units as follows:

$$\left(\frac{B_{\parallel}}{B_0}\right)^2 > \frac{mc^2 E_0}{aq B_{\perp} B_0}. \quad (11.24)$$

In the frame of the SHTCL model the last inequality becomes especially simple:

$$B_{\parallel} > 0.1 B_0. \quad (11.25)$$

Thus the longitudinal component can be one order of magnitude smaller than the reconnecting components related to the electric current in the current layer.

The maximum energy (written in dimensional units) of accelerated electrons in the RCL is

$$\mathcal{E}_{\max} = \frac{1}{2m} \left( \frac{qa B_{\parallel}}{c} \right)^2 \quad (11.26)$$

or, in the SHTCL model,

$$\mathcal{E}_{\max} (\text{keV}) \approx 10^{-5} \xi_{\parallel}^2 T (\text{K}). \quad (11.27)$$

If the current-layer temperature  $T \approx 10^8$  K and  $\xi_{\parallel}^2 \approx 0.1$ , formula (11.27) gives  $\mathcal{E}_{\max} \approx 100$  keV. Therefore

**|** the longitudinal magnetic field increases the acceleration efficiency to such a degree that it becomes possible to interpret the *first stage* or the *first step* of electron acceleration in solar flares

as the particle energization process in a non-neutral SHTCL.

The results obtained are clear. On the one hand, the transversal field turns a particle trajectory in the layer plane (the plane  $(x, z)$  in Fig. 11.1). At some point, where the projection of velocity  $v_z$  on the electric field direction changes its sign, the Lorentz force component associated with the field component  $B_x = (-y/a) B_0$  pushes the particle out of the layer. This process is described by Eq. (11.4) with  $\xi_{\parallel} = 0$ , or by Eq. (11.15). On the other hand, a non-zero longitudinal magnetic field tries to turn the particle back to the layer. This effect is related to the first term on the right-hand side of Eq. (11.4). That is why the maximum velocity of a particle is proportional to the gyro-frequency in the longitudinal field.

### 11.1.5 The Non-adiabatic Thickness of Current Layer

The condition (11.24) is simply understood from the physical point of view. In the absence of a longitudinal magnetic field, there exists a region near the neutral plane ( $x, z$ ), where the adiabatic approximation is not valid (see Sect. 1.2.3). So we had to solve Eq. (11.2) to determine the character of the particle motion. The thickness of this region which is called the *non-adiabatic thickness* of a current layer equals

$$d = (r_L a)^{1/2} = \left( \frac{mc v a}{qB_0} \right)^{1/2}. \quad (11.28)$$

Here the maximum velocity  $v \approx cE_0/\xi_{\perp}B_0$  is substituted in the formula for the Larmor radius  $r_L$  (see Appendix C).

The longitudinal magnetic field tends to keep particles ‘frozen’ and to confine them inside the layer. Obviously such a confinement can become efficient, once

$$r_L(B_{\parallel}) < d, \quad (11.29)$$

where

$$r_L(B_{\parallel}) = \frac{mcv}{qB_{\parallel}} = \frac{r_L}{\xi_{\parallel}}. \quad (11.30)$$

This last expression coincides with condition (11.24).

The condition given by inequality (11.19) or (11.24), which is the same, is not sufficient to ensure stability of all orbits, of course. A detailed study of the solutions of Eq. (11.14) shows that the *instability* domains of considerable width exist for relatively low values of  $B_{\parallel}$  (Efthymiopoulos et al. 2005). For super-Dreicer electric fields, these domains (bands) are very narrow so that the criterion (11.19) is an acceptable approximation in order to consider the electron acceleration in solar flares.

\* \* \*

Let us remind that, in the solar atmosphere, reconnection usually takes place at the separators with the non-zero transversal and longitudinal components of the magnetic field (Sect. 4.1). This effect was already considered in the MHD approximation from the viewpoint of the RCL energetics (Chap. 8). The longitudinal and transversal components of the magnetic field are also important for the current layer stability (Chap. 13). As was shown in this section, the longitudinal field has strong influence on the kinetics of suprathermal particles: the magnetically non-neutral SHTCL does efficient work as an electron accelerator and, at the same time, as a trap for fast electrons in solar flares.

## 11.2 Regular Versus Chaotic Acceleration

Considerable attention is reasonably focused on the phenomenon of *dynamic chaos*. The stochastic behaviour of a dynamic system is due to its intrinsic nonlinear properties rather than some external noise (Lichtenberg and Lieberman 1983). A particular example of such a system is a particle moving in the RCL.

So far both numerical (Chen and Palmadesso 1986) and analytic (Büchner and Zelenyi 1989) treatments of the particle's motion have concentrated on a current layer with a small magnetic field component perpendicular to the layer. This small *transversal* component has been shown to give rise to chaotic particle behaviour. However current layers in the solar atmosphere usually have also *longitudinal* (parallel to the electric field inside the RCL) magnetic field components. The purpose of this section is to illustrate the influence of the longitudinal field on the character of particle motion in non-neutral current layers.

### 11.2.1 Reasons for Chaos

Let us consider the RCL with the electric and magnetic fields (11.1). An approximate solution to Eqs.(11.3)–(11.5) of particle motion in such current layer was discussed above. Now we consider some general properties of this set of equations, starting from the fact that it possesses three exact constants of motion – the *invariants* of particle motion:

$$C_x = \dot{x} - \xi_{\parallel} y + \xi_{\perp} z, \quad (11.31)$$

$$C_z = \dot{z} - \xi_{\perp} x - \frac{1}{2} y^2 - \varepsilon t, \quad (11.32)$$

$$H = \frac{1}{2} (\dot{x}^2 + \dot{y}^2 + \dot{z}^2) - \varepsilon z. \quad (11.33)$$

Here  $H$  is the usual Hamiltonian (see Landau and Lifshitz 1976, Chap. 7, Sect. 40).

Rewrite the set of master Eqs.(11.3)–(11.5) in the Hamiltonian form. The usual way to do this is to introduce the four generalized coordinates

$$Q = \{t, x, y, z\} \quad (11.34)$$

and the generalized momenta

$$P = \left\{ -H, \dot{x} - \xi_{\parallel} y, \dot{y}, \dot{z} - \xi_{\perp} x - \frac{1}{2} y^2 \right\}. \quad (11.35)$$

Then the equations of motion take the form

$$\dot{Q}_i = \frac{\partial \mathcal{H}}{\partial P_i}, \quad \dot{P}_i = -\frac{\partial \mathcal{H}}{\partial Q_i} \quad (i = 0, 1, 2, 3), \quad (11.36)$$

where

$$\mathcal{H} = H(P, Q) + P_0. \quad (11.37)$$

The *transformed* Hamiltonian  $\mathcal{H}$  is formally time-independent since  $t$  is treated as another coordinate variable. The constants of motion are now as follows:

$$C_x = P_x + \xi_{\perp} z, \quad (11.38)$$

$$C_z = P_z - \varepsilon Q_0, \quad (11.39)$$

$$\mathcal{H} = \frac{1}{2} (P_x + \xi_{\parallel} y)^2 + \frac{1}{2} P_y^2 + \frac{1}{2} \left( P_z + \xi_{\perp} x + \frac{1}{2} y^2 \right)^2 - \varepsilon z + P_0. \quad (11.40)$$

The Hamiltonian system (11.36) is integrable if the three constants of motion are in *involution*, i.e. their Poisson brackets are zero

(see [Landau and Lifshitz 1976](#), Chap. 7, Sect. 42). Otherwise the system is likely to demonstrate *chaotic* behaviour, i.e. the particle trajectory inside the current layer is unpredictable.

Straightforward calculation, based on the definition (see Part I, Exercise 1.2) for the Poisson brackets, shows that

$$[\mathcal{H}, C_x] = 0 \quad \text{and} \quad [\mathcal{H}, C_z] = 0.$$

However, for  $C_x$  and  $C_z$  we find

$$[C_x, C_z] = \xi_{\perp},$$

$$(11.41)$$

so that the constants  $C_x$  and  $C_z$  are not in involution.

[Chen and Palmadesso \(1986\)](#) have obtained this result for the case  $\xi_{\parallel} = 0$  and numerically showed the particle trajectory to be chaotic. In what follows our attention will be drawn to the fact that a non-zero longitudinal magnetic field leaves the result (11.41) unchanged. This means that **the chaos is entirely due to the transversal field** which is proportional to  $\xi_{\perp}$  inside the RCL.

Moreover, as will be proved below,

the longitudinal magnetic field tends to make the particle trajectory bounded and integrable inside the RCL.

Therefore an additional constant of motion must be present in the set of equations under consideration for a sufficiently large value of the parameter  $\xi_{\parallel}$  (Litvinenko 1993). Seemingly, this constant cannot be expressed in terms of elementary functions.

### 11.2.2 The Stabilizing Effect of the Longitudinal Field

Because of the presence of three constants of motion, the phase trajectory – the particle trajectory inside a six-dimensional phase space  $X$  – is restricted to a three-dimensional surface. It follows from Eqs. (11.31) to (11.33) that the particle coordinate and velocity components are subject to the relation

$$H = \frac{1}{2} \dot{y}^2 + \frac{1}{2} (\xi_{\parallel} y - \xi_{\perp} z)^2 + \frac{1}{2} \left( \varepsilon t + \xi_{\perp} x + \frac{1}{2} y^2 \right)^2 - \varepsilon z = \text{const}, \quad (11.42)$$

where zero initial conditions are assumed for simplicity.

A useful way to study the character of the particle motion is to calculate the curvature of the *energy surface*  $H = H(P, Q)$ .

The negative curvature  $K$  implies the exponentially fast divergence with time of initially close trajectories.

In its turn, that gives rise to chaos. Analogous inferences can be drawn concerning the particle motion in the usual coordinate space (Anosov 1969). Provided the curvature  $K \leq 0$ , the asymptotic (for large  $t$ ) behaviour of the trajectory is indistinguishable from that of random motion, which corresponds to stochasticity.

As was shown by Speiser (1965, 1968), particle motions in the current layer plane and across it occur almost independently. Thus, while studying the instability in the  $y$  direction, it is justifiable to consider the two-dimensional energy surface  $H = H(y, \dot{y})$ , treating  $x$  and  $z$  as some time-dependent constants. Attention must be centered on the motion along the  $y$  axis, which is known to possess the strongest instability (Speiser 1965). Therefore the quantity to be calculated is

$$K = \frac{H_{\dot{y}\dot{y}} H_{yy} - H_{\dot{y}y}^2}{(1 + H_{\dot{y}}^2 + H_y^2)^2}. \quad (11.43)$$

Assuming that  $\xi_{\parallel}^2 \ll 1$  and that the particle is near the layer plane (i.e.,  $y \ll 1$ ), we show that the denominator of formula (11.43) approximately equals unity. Anyway, being positive, it does not influence the sign of  $K$ . The curvature of the energy surface is calculated to be

$$K(t) \approx \xi_{\parallel}^2 + \varepsilon t + \xi_{\perp} x + \frac{3}{2} y^2, \quad (11.44)$$

or on making use of the invariant (11.32),

$$K(t) \approx \xi_{\parallel}^2 + \dot{z}(t) + y^2(t). \quad (11.45)$$

It is known that  $\dot{z} \geq -\varepsilon/\xi_{\perp}$  (Speiser 1965). Thus **strong chaos is expected** in the vicinity of the neutral plane  $y = 0$ , provided  $\xi_{\parallel} = 0$ . In this case the model of Büchner and Zelenyi (1989) is applicable. On the other hand, inside the RCL and in its vicinity,

**|** a sufficiently strong longitudinal magnetic field tends to suppress chaos and make the particle motion more regular.

The necessary condition for such a suppression is  $K > 0$ , that is

$$\xi_{\parallel} > \left( \frac{\varepsilon}{\xi_{\perp}} \right)^{1/2}. \quad (11.46)$$

So, in another way, we arrive at an inequality which coincides with (11.19). The inequality (11.46) gives  $\xi_{\parallel} > 0.1$  for typical solar flare conditions if the particles under consideration are electrons (Somov 1992; Somov et al. 1998; Somov and Merenкова 1999). Litvinenko and Somov (1993) have been the first to pay attention to this important property of the magnetically non-neutral current layer.

### 11.2.3 Characteristic Times of Processes

It might seem surprising that  $\xi_{\parallel}$  in Inequality (11.46) should tend to infinity for  $\xi_{\perp} \rightarrow 0$ . However it is incorrect to consider such a limiting case. The point is that the time needed for the instability to start developing is of the order of  $\xi_{\perp}^{-1}$  (Speiser 1965). Hence, while being formally unstable, the particle's motion in the limit of small  $\xi_{\perp}$  is regular for all reasonable values of time.

The result (11.46) is easy to understand from the physical viewpoint. A typical time for destabilization of the  $y$ -motion, i.e. the time for divergence of initially close trajectories inside the current layer, is (in dimensional units)

$$t_{\perp} = \left( \frac{am}{F} \right)^{1/2}, \quad (11.47)$$

where the Lorentz force component is evaluated to be

$$F \approx \frac{1}{c} q v B_0 = \frac{1}{c} q \frac{cE}{B_{\perp}} B_0 = \frac{qE}{\xi_{\perp}} \quad (11.48)$$

and some typical value of  $v = cE/B_{\perp}$  is assumed;  $q = Ze$ . The instability creating the chaos becomes suppressed once it has no time for developing, i.e.

$$t_{\perp} > t_{\parallel}, \quad (11.49)$$

$t_{\parallel}$  being the time scale introduced by the longitudinal magnetic field:

$$t_{\parallel} = \frac{mc}{qB_{\parallel}} = \frac{mc}{\xi_{\parallel} qB_0}. \quad (11.50)$$

Once (11.49) is valid, the particle becomes magnetized inside the current layer and its trajectory is no longer chaotic. Clearly the inequality (11.49) is equivalent to condition (11.46).

### 11.2.4 Dynamics of Accelerated Electrons in Solar Flares

A question at this point is: What observational data can be used to verify the above-presented results? To put it another way: What are the observational consequences of chaotic or regular particle dynamics? – Such consequences do exist.

Let us consider electron acceleration in solar flares. The accelerated electrons spiral in the coronal magnetic field and produce flare radio emission. Using the data on radio pulsations, Kurths and Herzel (1986), Kurths et al. (1991), and Isliker (1992) have calculated the dimension of the *pseudo-phase space* related to the electron source. The technique for reconstructing phase space from a one-dimensional data array is described by Schuster (1984), where also the references to original works can be found.

The dimension of the pseudo-phase space serves as a measure of chaos: the larger the dimension, the more chaotic is the system.

Using the data on ms-spikes, Isliker (1992) has found that the degree of chaos varied from flare to flare and during the course of a flare. He conjectured that such behaviour was due to some *exterior* (to the electron source) parameter which could change with time. Based on the above discussion, the role of this parameter may be ascribed to the value of the longitudinal magnetic field.

This conclusion is in agreement with previous findings. From the theoretical viewpoint, the longitudinal field is determined by the photospheric sources and does change in time. It is this change that can be responsible for flare onset, i.e., the longitudinal field can be the ‘*topological trigger*’ of a solar flare (Sect. 4.2.1). As far as observations are concerned, the electron acceleration during flares is likely to occur at the separators with a strong longitudinal field, where magnetically non-neutral current layers are formed (Sect. 4.1). As indicated above, the relative value of this field,  $\xi_{\parallel} = B_{\parallel} / B_0$ , determines whether the acceleration occurs in a regular or stochastic manner. To summarize,

the motion of electrons in magnetically non-neutral current layers of solar flares becomes **regular rather than chaotic**, once the relative value of the longitudinal magnetic field  $\xi_{\parallel} > 0.1$ .

This fact has important implications for the dynamics of the electron acceleration in solar flares. It would be also of interest to perform calculations analogous to those of [Isliker \(1992\)](#), in the context of the geomagnetic tail.

### ***11.2.5 Initial Conditions of Motion***

Many authors have addressed the question of how will distributions of particles with initial conditions in the interior of a RCL evolve under action of electric and other force fields. Most of such studies rely on numerical integrating the equations of motion for large numbers of particles. For example, [Gontikakis et al. \(2006\)](#) calculated the particle orbits by integrating the equations of motion derived by using the Hamiltonian (11.40).

Beside such calculations, [Gontikakis et al. \(2006\)](#) have developed an approximated analytical theory that describes the orbits of particles and allows to determine the boundaries of the domains in the velocity space separating different types of orbits. In the RCL model described in Sect. 11.1.2, three types of orbits are distinguished: (a) chaotic orbits leading to escape by stochastic acceleration, (b) regular orbits leading to escape along the field lines of the reconnecting magnetic components, and (c) mirror-type regular orbits that are trapped in the RCL, making mirror oscillations.

[Gontikakis et al.](#) have also found the “sticky” chaotic orbits, that remain trapped in the current layer for very long times, before they finally escape. Such orbits are important because they enhance the population of particles that supports the self-consistency of the current layer. Therefore the phenomenon of “stickiness” should be taken into account in numerical simulations of collisionless reconnection.

### ***11.2.6 Particle Simulations of Collisionless Reconnection***

A particle simulation study (e.g., [Horiuchi and Sato 1997](#)) has investigated collisionless driven reconnection in a sheared magnetic field by modeling the response of a collisionless plasma to an external driving flow. They specifically studied the effects of the transversal and longitudinal magnetic fields on the rate of reconnection and the acceleration of electrons.

[Litvinenko \(1997\)](#) has used the model for electron acceleration in a magnetically non-neutral current layer, described in Sect. 11.1, to interpret the results of the simulation. He explained the electron energization in both two-dimensional ( $\xi_{\perp} \neq 0$ ,  $\xi_{\parallel} = 0$ ) and three-dimensional ( $\xi_{\perp} \neq 0$ ,  $\xi_{\parallel} \neq 0$ ) magnetic fields. An agreement was obtained between the analytical predictions and the numerical results for the electron energy gain, the acceleration time, the longitudinal field diving rise to adiabatic particle motion, and the scaling with  $B_{\parallel}$  of the collisionless resistivity due to particle escape from the RCL.

The particle simulation, therefore, has substantiated the theoretical modeling presented in Sect. 11.1. This is important both for future more general analytical models of particle acceleration and for the application of the existing models, for example, to the electron acceleration in solar flares (Sects. 11.1.4 and 11.2.4).

Although the particle simulation (Horiuchi and Sato 1997) had not been run for a sufficient time to study the acceleration of protons, it did show that the question of proton acceleration is more complicated. Their motion, as we shall see in the next section, is influenced by the polarization electric field arising due to charge separation. Because it is much more difficult to magnetize a proton than an electron, the protons tend to escape the current layer across its border even when the electrons are well magnetized by the longitudinal field  $B_{\parallel}$ . This leads to the generation of a transversal electric field  $E_{\perp}$  directed towards the plane of the layer. This field may have important consequences for the proton motion as we discuss below.

**Recommended Reading:** Froyland (1992) and Contopoulos (2002).

## 11.3 Ion Acceleration in Current Layers

### 11.3.1 Ions Are Much Heavier Than Electrons

In Sect. 11.1 we considered the particle acceleration in a current layer, taking into account not only the reconnecting field  $\mathbf{B}_0$ , parallel to the  $x$  axis, but also a small transversal field component  $B_{\perp} = \xi_{\perp} B_0$ , parallel to the  $y$  axis as shown in Fig. 11.1. In solar flares, a typical relative value of the transversal field is  $\xi_{\perp} \sim 10^{-3} \div 10^{-2}$  (see Somov 1992, Fig. 3.3.9). In what follows, for definiteness, we adopt the value of  $\xi_{\perp} \approx 3 \times 10^{-3}$  for our estimates. The basic Speiser's (1965) result is that both the energy gain  $\delta\mathcal{E}$  and the time that the particles spend in the magnetically non-neutral RCL,  $\delta t_{\text{in}}$ , are finite.

The transversal magnetic field makes the particle turn in the plane of the layer, and then a component of the Lorentz force expels it from the RCL plane almost along the field lines

(see Fig. 3 in Speiser 1965). The distance that the particle can travel along the layer equals the Larmor diameter determined by the transversal field and a typical speed of the particle.

Litvinenko and Somov (1993) generalized the results of Speiser (1965) by including into consideration the *longitudinal* (parallel to the main electric field  $\mathbf{E}$  in Fig. 11.1) magnetic field  $\mathbf{B}_{\parallel}$  in the layer.

The longitudinal field efficiently magnetizes fast electrons in the RCLs of solar flares, but it cannot significantly influence the motion of the accelerated protons and heavier ions.

The Larmor radius of ions is much larger than the Larmor radius of electrons having the same velocity because ions are much heavier than electrons. As a consequence of this fact, the critical longitudinal field, necessary to magnetize a particle and to accelerate it, is proportional to the square root of the particle mass (see (11.24)). Hence we can use, first, the Speiser's non-relativistic formulae, derived for the case when an ion of mass  $m$  and charge  $q = Ze$  enters the RCL with a negligible velocity:

$$\delta\mathcal{E} = 2mc^2 \left( \frac{E_0}{B_\perp} \right)^2, \quad (11.51)$$

$$\delta t_{\text{in}} = \frac{\pi mc}{q B_\perp}. \quad (11.52)$$

Generalizations of these formulae to particles with nonzero initial velocities are given in Sect. 11.3.3.

Thus, on the one hand, electrons can acquire even relativistic energies in current layers with a nonzero longitudinal field  $B_\parallel$  (Litvinenko and Somov 1993). On the other hand, application of formulae (11.51) and (11.52) to the RCL, formed, for example, behind a rising coronal mass ejection – CME (see Sect. 11.4), shows that a nonzero field  $B_\perp$  radically restricts the energy of heavier particles:  $\delta\mathcal{E}$  for protons cannot exceed 20 MeV if a typical value of  $\xi_\perp = 3 \cdot 10^{-3}$  ( $B_\perp = 0.3$  G) is assumed.

Therefore the relativistic energies cannot be reached after a single ‘interaction’ of a proton with the layer (cf. Martens 1988). To overcome this difficulty, Martens conjectured that the relativistic acceleration could take place in RCL regions where  $B_\perp \rightarrow 0$  (the neutral layer approximation), and the protons are freely accelerated by the electric field. This conjecture, however, does not seem to be adequate for actual RCLs, where reconnection always occurs in the presence of a transversal magnetic field. Though we expect the latter to vary somewhat along the RCL (Somov 1992), the region with a vanishing  $B_\perp$  is so small that a particle will quickly leave the region (and hence the RCL) before being accelerated. Thus we are led to modify the classic Speiser's model significantly.

Let us propose that a proton (or another ion) interacts with the RCL more than once, each time gaining a finite, relatively small amount of energy. The effect could be the required relativistic acceleration. A similar model was considered in the context of acceleration in the geomagnetic tail (see Sect. 2.4 in Schabansky 1971). However, the magnetic structures in the solar atmosphere are quite different from that of the geomagnetic tail; and conditions also differ. Therefore formulae given by Schabansky are inapplicable to the problem at hand. For this reason, we have to consider another model in application to the solar atmosphere.

### 11.3.2 Electrically Non-neutral Current Layers

The factor that makes positively charged particles return to the RCL is the *transversal* electric field  $\mathbf{E}_\perp$ , which is parallel to the  $y$  axis in Fig. 11.2 and directed

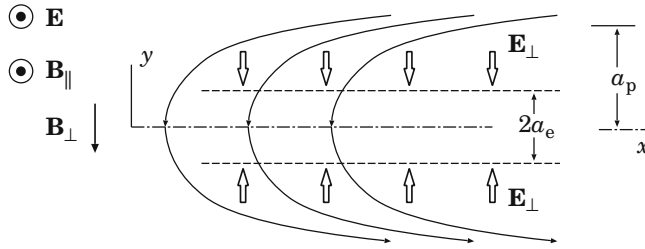


**Fig. 11.2** An electrically non-neutral current layer:  $\mathbf{E}_{\perp}$  is the transversal component of the electric field.  $\mathbf{E}$  is the electric field related to the reconnection process

toward the layer plane from both sides (cf. Fig. 11.1). What is the origin of this electric field?

As we saw in the previous section, protons and other ions, having much larger masses than the electron mass, have significantly larger Larmor radii. Both electrons and protons try to escape from magnetic confinement inside the RCL. They are deflected by the magnetic field when they move out of the layer. However the trajectories of electrons are bent to a much greater degree owing to their smaller mass. As for the much heavier protons and ions, they stream out of the layer almost freely. Hence the charge separation arises, leading to the electric field  $\mathbf{E}_{\perp}$  at both sides of the layer. This field detains the protons and ions in the vicinity of the electron current layer (Harris 1962; see also Chap. 5 in Longmire 1963; Hoh 1966; Dobrowolny 1968).

In an exact self-consistent one-dimensional model of the *electrically* non-neutral current layer due to Harris (1962), this field equals

$$E_{\perp} = 2\pi \sigma^q. \quad (11.53)$$

Here the magnitude of the electric charge density integrated over the layer thickness is

$$\sigma^q = \left( \frac{u}{c} \right)^2 nea, \quad (11.54)$$

$u$  is the current velocity of electrons in the RCL.

Let us estimate the velocity  $u$  from the Maxwell Equation for  $\text{rot } \mathbf{B}$  as

$$u = \frac{c}{4\pi} \frac{B_0}{nea}. \quad (11.55)$$

On substituting (11.55) and (11.54) in (11.53), we obtain

$$E_{\perp} \approx \frac{k_B T}{e a}, \quad (11.56)$$

where the equation  $B_0^2/8\pi \approx nk_B T$  has been used,  $T$  being the plasma temperature in the layer.

It is not obvious a priori that Harris's solution applies to actual RCLs with nonzero  $\xi_\perp$  and finite conductivity  $\sigma$ . It should be valid, however, for small  $\xi_\perp$ , at least as a first approximation. In fact all we need for our calculations is the electric potential

$$\phi = \int E_\perp dy, \quad (11.57)$$

which we take to equal  $k_B T/e$ , the usual value owing to spread of a 'cloud' of charged particles.

The following point is worth emphasizing here. The charge separation that gives rise to the potential  $\phi$  mainly stems from the motion of protons perpendicular to the layer plane. At the same time, some protons are known to leave the layer almost along its plane. This property is a characteristic feature of the Speiser's mechanism of acceleration. It seems obvious that

even a modest transversal electric field will considerably influence the motion of the particles, leaving the layer, because they always move almost perpendicular to this field.

Having made this qualitative remark, we now proceed to calculating the energy gain rate and maximum energy for the protons being accelerated in the RCL, taking into account both the main components of electromagnetic field ( $\mathbf{B}_0$  and  $\mathbf{E}_0$ ) and the transversal ones ( $\mathbf{B}_\perp$  and  $\mathbf{E}_\perp$ ).

### 11.3.3 Maximum Particle Energy and Acceleration Rates

According to the model delineated above, a positively charged particle ejected from the RCL may be quickly reflected and moves back to the layer. The reason for this is the electric field  $\mathbf{E}_\perp$ , directed perpendicular to the current layer, which always exists outside the RCL (Harris 1962). It is of importance for what follows that the accelerated protons and other ions are ejected from the layer almost *along* the field lines (Speiser 1965). The transversal electric field efficiently locks the particles in the RCL because they always move almost in the plane of the layer. On getting into the layer again, the particles are further accelerated and the cycle repeats itself.

In order to find the properties of the acceleration mechanism, we need to dwell at some length on the particle motion outside the RCL. Let us consider a proton leaving the RCL plane with energy  $\mathcal{E}$  and momentum  $\mathbf{p}$ . According to Speiser (1965), the component of the momentum perpendicular to the layer is

$$p_\perp \approx \xi_\perp p \ll p \quad (11.58)$$

for such a proton. The perpendicular component of the equation of motion for the particle outside the electron current layer is

$$\frac{d}{dt} p_{\perp}(t) = -qE_{\perp}. \quad (11.59)$$

Here we neglect the magnetic force, in order not to obscure the essential physical point made in this section. Equation (11.59) allows us to estimate the time spent by the proton between two successive interactions with the RCL,

$$\delta t_{\text{out}} = \frac{2 p_{\perp}}{qE_{\perp}} \approx \frac{2 \xi_{\perp} p}{qE_{\perp}}. \quad (11.60)$$

The largest energy attainable is determined by the condition that the potential (11.57) is just enough to prevent the proton from leaving the RCL. In other words, the field  $\mathbf{E}_{\perp}$  must cancel the perpendicular momentum  $\mathbf{p}_{\perp}$ . The energy conservation gives:

$$\mathcal{E}_{\max} = (\mathcal{E}_{\max}^2 - p_{\perp}^2 c^2)^{1/2} + q\phi, \quad (11.61)$$

where

$$p_{\perp}^2 c^2 = \xi_{\perp}^2 (\mathcal{E}_{\max}^2 - (mc^2)^2). \quad (11.62)$$

Eliminating the unknown  $p_{\perp}$  between (11.61) and (11.62), we get the maximum energy

$$\mathcal{E}_{\max} = q\phi \frac{1}{\xi_{\perp}^2} \left[ 1 + \left( 1 - \xi_{\perp}^2 + \frac{\xi_{\perp}^4 (mc^2)^2}{q^2 \phi^2} \right)^{1/2} \right]. \quad (11.63)$$

According to formulae (11.56) and (11.57), here the electric field potential  $\phi \approx k_B T/e$ . Formula (11.63) shows that

protons can actually be accelerated to GeV energies in the super-hot turbulent-current layers (SHTCLs) in solar flares

(see Chap. 8): for instance  $\mathcal{E}_{\max} \approx 2.4$  GeV provided  $T_e \approx 10^8$  K. Even larger energies can be reached in RCL regions with a smaller transversal magnetic field.

Note in passing that if a particle leaves the layer with the velocity that is perpendicular to the magnetic field lines outside the RCL, the magnetic reflection is very efficient too. In this case it occurs in a time of order the inverse gyrofrequency in the field  $\mathbf{B}_0$ .

The resulting acceleration rate can be estimated as

$$\frac{d\mathcal{E}}{dt} \approx \frac{\langle \delta\mathcal{E} \rangle}{\delta t_{\text{in}} + \delta t_{\text{out}}}. \quad (11.64)$$

Here

$$\langle \delta\mathcal{E} \rangle = 2\mathcal{E} \left( \frac{E_0}{B_{\perp}} \right)^2 \quad (11.65)$$

is the relativistic generalization of the Speiser formula (11.51) for the average energy gain. The averaging needs to be introduced because, in general, a term linear in a component of the particle momentum appears in the expression for  $\delta\mathcal{E}$  (cf. Speiser and Lyons 1984).

In much the same way

$$\delta t_{\text{in}} = \frac{\pi \mathcal{E}}{c q B_{\perp}} \quad (11.66)$$

is the relativistic generalization of the Speiser formula (11.52). The approach using the differential equation (11.64) is quite justified once the inequality  $\langle \delta\mathcal{E} \rangle \ll \mathcal{E}_{\max}$  holds.

Equation (11.64), with account taken of the formulae (11.60), (11.65), and (11.66), can be integrated in elementary functions. To simplify the problem further, we note that

$$\frac{\delta t_{\text{in}}}{\delta t_{\text{out}}} = \frac{\pi E_{\perp}}{2 \xi_{\perp} B_{\perp}} \left( \frac{\mathcal{E}}{pc} \right) \approx 10^3 \frac{\mathcal{E}}{pc} \gg 1. \quad (11.67)$$

Hence it is justifiable to ignore the second term in the denominator of Eq. (11.64). The simplified equation is integrated to give the kinetic particle energy

$$\mathcal{K}(t) \equiv \mathcal{E} - mc^2 = \frac{2}{\pi} c q E_0 \left( \frac{E_0}{B_{\perp}} \right) t, \quad (11.68)$$

whence the time of the particle acceleration is

$$t_{\text{ac}}(\mathcal{K}) \approx 0.03 \left( \frac{\mathcal{K}}{1 \text{ GeV}} \right) \text{ s}. \quad (11.69)$$

This result demonstrates the possibility of very efficient acceleration of protons and other ions by the direct electric field in the RCL (Litvinenko and Somov 1995). At the same time, taking care of the actual magnetic field structure has considerably diminished (by a factor of  $E_0/B_{\perp} = V/(\xi_{\perp} c) \approx 10^{-1}$ ) the magnitude of the energy gain rate, as compared with the case  $B_{\perp} = 0$ .

Alternatively, we could rewrite formula (11.68) to obtain the energy  $\mathcal{E}$  as a function of the number of particle entries to the RCL,  $N_{\text{int}}$ :

$$\mathcal{E}(N_{\text{int}}) = mc^2 \exp \left[ 2 \left( \frac{E_0}{B_{\perp}} \right)^2 N_{\text{int}} \right]. \quad (11.70)$$

Therefore the particle must interact with the RCL

$$N_{\max} \approx \left( \frac{B_{\perp}}{E_0} \right)^2 \approx 10^2 \quad (11.71)$$

times in order to reach a relativistic energy. As was shown above (see Eq. (11.63)), the transversal electric field outside the RCL is actually capable of providing this number of reentries into the current layer.

In principle, the protons and other ions could leave the RCL along its plane rather than across it. This is not likely, however, because of a very short acceleration time  $t_{ac}$ ; the distance a proton can travel along the layer when being accelerated is less than  $c t_{ac} \approx 10^9$  cm, that does not exceed a typical RCL width and length  $10^9 \div 10^{10}$  cm.

Therefore we have estimated the efficiency of the acceleration process in the frame of the simple RCL model which contains several taciturn assumptions. One of them is a modification of the steady two-dimensional model for the SHTCL (Chap. 8) with account of the Harris type equilibrium across the layer. Such a possibility does not seem surprising one a priory but it certainly has to be considered in detail somewhere else.

Another assumption is that the initially assumed conditions of the layer equilibrium are not changed due to the acceleration, more exactly, during the characteristic time of the acceleration of a particle. In fact, we consider the number of particles accelerated to high energies as a small one in comparison with the number of current driving thermal electrons inside the RCL. However, in general, it remains to be seen that this assumption can be well justified without careful numerical modeling of the real plasma processes in the region of reconnection and particle acceleration.

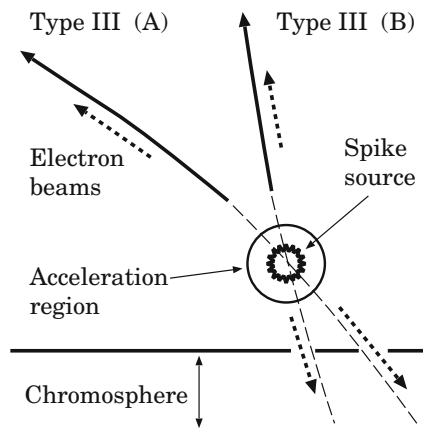
## 11.4 How Are Solar Particles Accelerated?

### 11.4.1 Place of Acceleration

It was widely believed that the most-energetic and longest-lasting *solar energetic particle* events (SEPs) observed in interplanetary space result from acceleration by the bow shocks of coronal mass ejections (CMEs). However, using gamma-ray, X-ray and radio diagnostics of interacting (with the solar plasmas and magnetic fields) particles and spaceborne and ground-based detection of  $\gtrsim 20$  MeV protons at 1 AU during two large events (1989 September 29 and October 19), Klein et al. (1999) demonstrated that time-extended acceleration processes **in the low and middle corona**, far behind the CME, leave their imprints in the proton intensity time profiles in interplanetary space for one or several hours after the onset of the solar flare. So the bow shock is not the main accelerator of the high-energy protons.

Electrons accelerated to  $\sim 1\text{--}100$  keV are frequently observed in interplanetary space. The energy spectrum has a power-law shape, often extending down to  $\gtrsim 2$  keV without clear signatures of collisional losses. Electron events showing enhanced electron fluxes at energies as low as 0.5 keV were observed by Lin et al. (1996). This requires an acceleration in a low-density coronal plasma.

**Fig. 11.3** Location of the acceleration region with respect to a type III burst (labeled A) and an associated spike source. A second type III (labeled B) is displayed in a case of two simultaneous bursts. The upward moving electrons produce type III bursts and the downward moving electrons lose their energy in the chromosphere



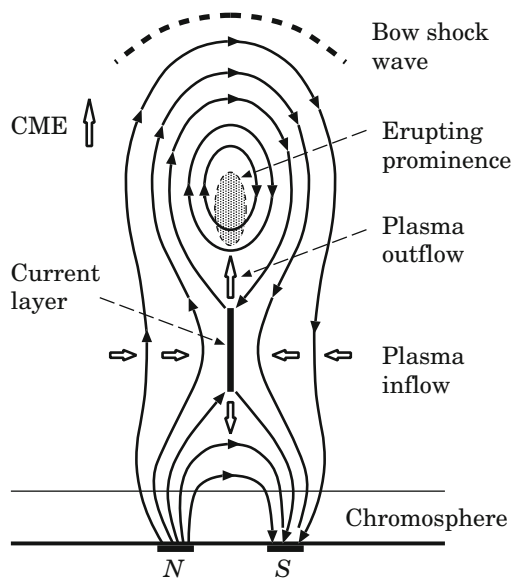
Low-energy (2–19 keV) impulsive electron events observed in interplanetary space have been traced back to the Sun, using their interplanetary type III radiation and metric-decimetric radio-spectrograms (Benz et al. 2001). The highest frequencies and thus the radio signatures closest to an acceleration region have been studied. All the selected events have been found to be associated with the interplanetary type III bursts. This allows to identify the associated coronal radio emission. The start frequency yields a lower limit to the density in the acceleration region of the order of  $3 \times 10^8 \text{ cm}^{-3}$ .

It is obvious that a 3D reconstruction of source locations depends on a chosen model of the coronal density in terms of absolute heights. However the relative positions are not altered by changing the atmospheric models. The trajectories of the type III bursts may be stretched and shifted in height but the topology of the burst remains the same. Figure 11.3 (cf. Paesold et al. 2001) displays a sketch depicting a possible location of acceleration with respect to two simultaneous bursts.

The spatial association of narrow band metric radio spikes with type III bursts has been analyzed by using data provided by the Nancay Radioheliograph (NRH) and the Phoenix-2 spectrometer (ETH Zurich), see Paesold et al. (2001). It has been found that the spike source location, presumably an acceleration region, is consistent with the backward extrapolation of a trajectory of the type III bursts, tracing a magnetic field line. In one of the five analyzed events, type III bursts with two different trajectories originating from the same spike source were identified.

These findings support the hypothesis that narrow metric spikes are closely related to the acceleration region (Krucker et al. 1997). Escaping beams of electrons cause the type III emission. Energetic electrons appear to be injected into different and diverging coronal structures from one single point as illustrated in Fig. 11.3. Such a diverging magnetic field geometry is a standard ingredient of magnetic reconnection in the corona.

**Fig. 11.4** When passing through the corona, a prominence strongly disturbs magnetic field and creates a CME. The disturbed field will relax to its initial state via reconnection. This is assumed to accompany by a prolonged energy release and particle acceleration



### 11.4.2 Time of Acceleration

Litvinenko and Somov (1995) have suggested that the *time-extended* (or late, or second) acceleration of protons and perhaps heavier ions to relativistic energies during the late phase of large-scale solar flares (e.g., Akimov et al. 1996) occurs in a ‘vertical’ *reconnecting current layer* (RCL) as illustrated by Fig. 11.4. Here the field lines are driven together and forced to reconnect below erupting loop prominences. The time of RCL formation corresponds to the delay of the **second phase of acceleration** after the first (or early), impulsive phase. The mechanism invoked (the direct electric field acceleration) is, in fact, quite ordinary in studies of the impulsive phase (Syrovatskii 1981; Chupp 1996). There are good reasons to believe that the same mechanism also can efficiently operate during the second phase of the acceleration in large-scale flares occurring high in the corona.

First, the early radio imaging observations of solar flares by Palmer and Smerd (1972) and Stewart and Labrum (1972) were indicative of particle acceleration at the cusps of helmet magnetic structures in the corona. These are exactly the structures where RCLs are expected to form according to the *Yohkoh* observations in soft and hard X-rays (Kosugi 1996; Kosugi and Somov 1998).

Note that the acceleration by Langmuir turbulence inside the RCL in the helmet structure, invoked at first by Zhang and Chupp (1989) to explain the electron acceleration in the flare of April 27, 1981, is too slow to account for the generation of relativistic protons and requires an unreasonably high turbulence level. Specific models have been designed to explain the particle acceleration in magnetic cusp geometry, in particular the two-step acceleration model with a RCL and *magnetic collapsing trap*, described in Sect. 9.2.

The second argument in favor of particle acceleration by direct electric field is that the gamma-ray emission during large flares consists of separate peaks with a characteristic duration of 0.04–0.3 s (Gal et al. 1994; Akimov et al. 1996). If this behavior is interpreted in terms of a succession of separate acts of the acceleration, then the shock mechanism is also too slow since the acceleration time would be

$$t_{\text{ac}} = 50 \left( \frac{100 \text{ G}}{B_0} \right) \left( \frac{\mathcal{E}}{1 \text{ GeV}} \right) \text{ s} \approx 50 \text{ s} \quad (11.72)$$

(Colgate 1988). By contrast, as we saw above,

the direct electric field inside the RCL provides not only the maximum energy but also the necessary energy gain rate

(see formula (11.69)). High velocities (up to the coronal Alfvén speed) of erupting filaments and other CMEs imply a large direct electric field in the RCL. This is the reason why the acceleration mechanism considered is so efficient in *fast transient phenomena* in the corona (Somov 1981). Strong variability of gamma-emission may reflect the regime of impulsive, bursty reconnection in the RCL.

An interesting feature of the mechanism considered is that neither the maximum energy nor the acceleration rate depend upon the particle mass. Hence the mechanism may play a role in the preferential acceleration of heavy ions during solar flares.

Recall that Martens (1988) applied the Speiser (1965) model when considering relativistic acceleration of protons during the late phase of flares. However it turned out necessary to assume an idealized geometry of the magnetic field in the RCL, viz.  $\mathbf{B}_\perp \rightarrow 0$ , in order to account for the relativistic acceleration. We have seen that the difficulty can be alleviated by allowing for the transversal electric field  $\mathbf{E}_\perp$  outside the layer. This field necessarily arises in the vicinity of the RCL (Harris 1962).

Though MHD shocks are usually thought to be responsible for the relativistic generation of protons during the late phase of extended (gradual) gamma-ray/proton flares (Bai and Sturrock 1989), another mechanism – the direct electric field acceleration in RCL – can explain the proton acceleration to the highest energies observed, at least in flares with strong variability of gamma-emission. Of course, the same sudden mass motions that lead to formation of current layers also give rise to strong shock waves, e.g., attached shock waves considered in generalized analytical model (Sect. 3.4) So the two mechanisms of acceleration can easily coexist in a solar flare.

### 11.4.3 Spectrum of Accelerated Particles

Until 2006 there has been no direct measurements of the protons with energy greater 1 GeV in *solar energetic particles* (SEPs). The spectrum of SEPs covering the energy range from  $\approx \text{MeV/nucleon}$  to at least several GeV/nucleon could not be

measured by a single device; spacecraft, balloon and neutron monitor data were used for this purpose (Ryan et al. 2000; Bazilevskaya 2005). Since the majority of SEP events have a spectrum turnover around 100 MeV/nucleon (Ryan 2000), it is important to measure the whole energy range by a single instrument. Another task is to find the upper limit of acceleration processes at the Sun.

These important problems were solving by the PAMELA experiment housed on board the Russian satellite *Resurs-DK1* (Casolino et al. 2008). The experiment was designed to study with great accuracy the cosmic rays of galactic, solar and trapped (in the Van Allen belts) nature in a wide energy range (protons: 80 MeV–700 GeV, electrons: 50 MeV–400 GeV). The characteristics of PAMELA allowed real time measurements of different particle spectra, important in understanding the acceleration and propagation mechanisms which took place at the Sun and in the heliosphere.

PAMELA measured the solar component of cosmic rays over a very wide energy range where the upper limit was determined by the size and spectral shape of a SEP event. For example, on 2006 December 13 at 02:38 UT, the X3.4/4B solar flare occurred in active region NOAA 10930 with coordinates S06°, W23° (Zhang et al. 2007). The flare produced a full-halo CME with a projected speed in the sky of about 1,800 km/s.

The intensity of the associated SEP event was also quite unusual for the solar minimum conditions of the 23rd cycle. Starting at 02:50 UT on the same day, various neutron monitors with threshold (cut-off) rigidities (see Part I, Sect. 6.4) below about 4.5 GeV recorded a *Ground Level Enhancement* (GLE) with relative increases up to more than 80%. Muon monitors were also able to detect the GLE event. Differential proton spectra were directly measured by GOES, ACE, STEREO and SAMPLEx at energies below 400 MeV. The PAMELA measurements in different periods of the event showed that protons were accelerated up to 3–4 GeV (Casolino et al. 2009).

After the same flare on 2006 December 13, the *IceTop* air shower array at the South Pole detected an unusual GLE (Abbasi et al. 2008). By numerically simulating the response of the *IceTop* tanks, which are *Cherenkov detectors* (see Part I, Sect. 7.4) with multiple thresholds, the particle energy spectrum have been determined in the energy range 0.6–7.6 GeV with a nearly constant spectral index.

## 11.5 Cosmic Rays and Cosmic Gamma-Rays

The cosmic ray energy spectrum extends from 1 GeV to 100 EeV (the prefix “E” is for “exa”, i.e.  $10^{18}$ ). To be accelerated at such high energies, a particle has to be submitted to powerful electromagnetic fields. Such energies hardly can be reached by any one-shot mechanism. In the late forties, the *Fermi mechanism* was introduced as the stochastic and repetitive scattering by ‘magnetic clouds’. However such a process is a very slow one and to reach the highest energies under ‘normal conditions’, the necessary acceleration time often exceeds the age of the Universe.

Many models with extreme parameters or assumptions were proposed in the past. They mostly rely on relativistic shock acceleration such as in hot spots of powerful radio-galaxies. However such galaxies are rare objects. The second type models relate the ultra-high-energy cosmic rays to another long-lasting astrophysical puzzle, the *Gamma Ray Bursts* (GRBs). These are characterized by the emission of huge amounts of energies (a non-negligible fraction of the mass energy of the Sun) over a very short time, minutes.

GRBs are observed as gamma rays but with, in some cases, X-ray and optical counterparts. Their distribution is uniform over the sky; and they happen at a rate of 2–3 per day. Young black holes, neutron stars and magnetars were proposed as putative sources of cosmic rays, because these rapidly rotating *compact objects* possibly are the sources of the most intense magnetic fields in the universe. Among the many hypotheses proposed about the nature of cosmological GRBs ([Cheng and Romero 2004](#); [Becker 2009](#); [Colpi et al. 2009](#)), the capability of such relativistic systems to reach the required energies are investigated in the context of the *magnetic reconnection* concept.

The model of a non-equilibrium magnetosphere of a compact relativistic object ([Somov 2011](#)) demonstrates peculiar properties of fast *relativistic reconnection* and particle acceleration in a magnetosphere produced by the interaction of a large-amplitude shock wave with the magnetic field of a relativistic star. At the first state, the shock strongly compresses and deforms the stellar magnetosphere. The forces of plasma inertia generate a system of direct (as in an ordinary magnetosphere like the Earth magnetosphere) and *reverse currents*.

Grabbing and entraining part of magnetic flux, the shock wave acts as a slingshot that stretches a rubber band, i.e. produces magnetic tensions. The latter determine the strength and direction of a relativistic jet. In this situation, induced fast reconnection in a reconnecting current layer accelerates charged particles to huge energies; and the magnetic field of the narrow magnetospheric tail channels and directs the particles along its axis. Emission of these particles is observed in hard X- and gamma-rays. Unfortunately, the proposed scenario does not answer yet the question of how promising the model is for quantitative interpreting the observations of cosmic bursts of hard electromagnetic radiation.

# Chapter 12

## Structural Instability of Reconnecting Current Layers

**Abstract** The interrelation between the stability and the structure of reconnecting current layers governs their nonlinear evolution and determines a reconnection regime. In this chapter we study the structural instability of the reconnecting current layer, i.e. its evolutionarity.

### 12.1 Some Properties of Current Layers

#### 12.1.1 Current Layer Splitting

The continuous MHD flow of a perfectly conducting medium is impossible in the *zeroth point* of a magnetic field, in which the electric field differs from zero. In the vicinity of this peculiar point the frozen-in condition breaks down (Sect. 2.1.4), and the *reconnecting current layer* (RCL in Fig. 12.1) – the discontinuity dividing magnetic fields of opposite directions – forms there in compliance with the statement of Syrovatskii (1971). Later on Brushlinskii et al. (1980), Podgornii and Syrovatskii (1981), and Biskamp (1986, 1997) observed the splitting of the RCL into other MHD discontinuities in their numerical experiments.

This splitting (or bifurcation) of the RCL is usually discussed in relation to the configuration suggested by Petschek (1964), which appears in particular during the reconnection of uniform magnetic fluxes (see Exercise 12.1). It consists of a system of MHD discontinuities, crossing in the small central diffusion region  $D$ .

As distinct from Petschek's configuration, the thin wide current layer can form in the vicinity of a hyperbolic zeroth point of a strong magnetic field as illustrated by Fig. 12.2. In fact, the structure of attached discontinuities is even more complicated as shown in Sect. 3.4. Just this more complicated case has been realized in the numerical MHD experiments carried out by Brushlinskii et al. (1980), Podgornii and Syrovatskii (1981), Biskamp (1986), Antiochos et al. (1997), and Karpen et al. (1998) and will be considered below.

**Fig. 12.1** Thin current layers: (a) without reverse electric currents, and (b) with two reverse currents ( $RC$ ),  $DC$  is a region of direct current

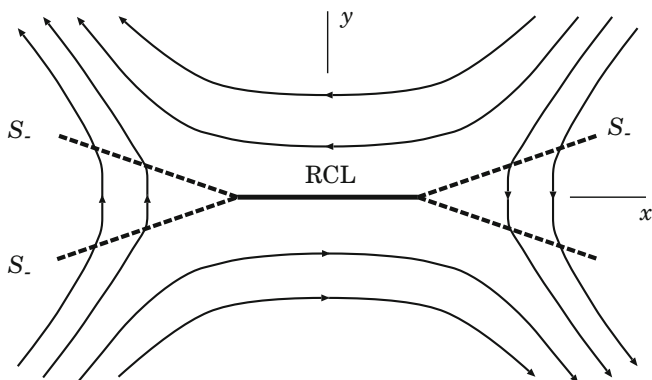
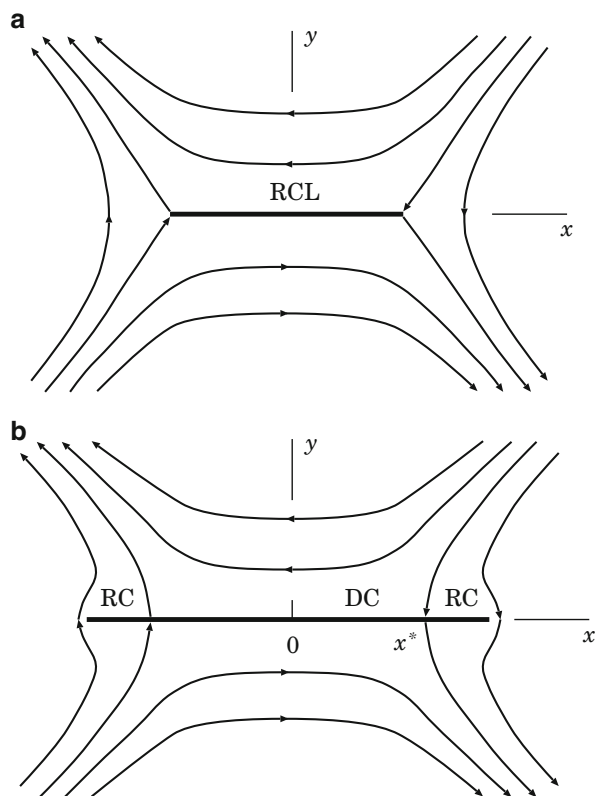


**Fig. 12.2** A splitted current layer ( $RCL$ ) with the attached MHD discontinuities – the four slow shock waves ( $S_-$ )

The process of splitting of the current layer means a change of the regime of magnetic reconnection, since the distribution of electric current becomes two-dimensional. In the present chapter we consider the conditions under which the splitting takes place and point out its possible reason. This reason is the *non-evolutionarity* of the RCL as a discontinuity or its *structural* instability.

### 12.1.2 Evolutionarity of Reconnecting Current Layers

The one-dimensional equations of ideal MHD have discontinuous solutions: fast and slow shock waves, tangential, contact and Alfvén discontinuities, peculiar shocks (Part I, Chap. 16). As was shown, a steady discontinuity may exist in a real plasma only if it is stable with respect to the break up into other discontinuities or the transition to some unsteady flow (Part I, Chap. 17).

Let the MHD quantities be subjected to an infinitesimal perturbation at the initial instant of time. Then a linear passage of waves out from the discontinuity occurs. If the amplitudes of these waves and the displacement of the discontinuity are uniquely determined from the linearized boundary conditions, then the problem of the *time evolution* of the initial perturbation has a single solution. If this problem does not have a single solution, then the supposition that the initial perturbation is small is not valid. In this case

the infinitesimal perturbation results in an instant (in the approximation of an ideal medium) non-linear finite-amplitude change of the original flow.

This is a *non-evolutionary* discontinuity. Note that, as distinct from a non-evolutionary discontinuity, the perturbation of an unstable evolutionary discontinuity remains infinitesimal during a small enough period of time.

The criterion of evolutionarity results from the comparison of two numbers.  $N_w$  is the number of the independent unknown parameters: the amplitudes of outgoing, i.e. reflected and refracted, waves and the displacement of the discontinuity, describing infinitesimal perturbation. And  $N_e$  is the number of independent boundary conditions (equations) which infer the unknown parameters by the amplitudes of the incident waves. If these numbers are equal, then the discontinuity satisfies the requirement of evolutionarity. Otherwise the problem of the time evolution of an initial infinitesimal perturbation does not have a solution, or else it has an infinite amount of solutions. Such a discontinuity cannot exist in a real medium.

As the direction of the propagation of a wave depends on the relationship between its group velocity and the flow velocity,

the requirement of evolutionarity gives the restriction on the unperturbed MHD quantities on both sides of the discontinuity.

In particular, the shock waves turn out to be evolutionary when either the upflow and the downflow velocities are larger than the Alfvén speed (fast shocks) or smaller than it (slow shocks).

The RCL cannot be reduced to a one-dimensional flow, since the inhomogeneity of velocity in it is two-dimensional, and is characterized by two spatial parameters. The thickness of the layer, i.e. the distance  $2a$  between the reconnecting magnetic fluxes (see Fig. 1.5), determines the rate of magnetic field dissipation in it, but the width  $2b$  characterizes the storage of magnetic energy in the domain of the flux interaction.

In what follows we obtain the conditions under which, in a plasma of high conductivity, infinitesimal perturbations interact with the RCL as with a discontinuity, and the problem of its evolutionarity with respect to such perturbations can be solved.

### 12.1.3 Magnetic Field Near the Current Layer

Consider the thin current layer, appearing in the vicinity of the zeroth point of a magnetic field

$$\mathbf{B}_0 = (h_0 y, h_0 x, 0),$$

at which the electric field

$$\mathbf{E} = (0, 0, E)$$

differs from zero. The magnetic field lines, frozen into the plasma, drift along the  $y$  axis into the layer, where the frozen-in condition breaks down, reconnect in it, and flow out along the  $x$  axis. [Syrovatskii \(1971\)](#) represented the coordinate dependence of the field  $\mathbf{B}$  outside the layer in a complex form, supposing that the half-thickness of the current layer  $a$  (size along the  $y$  axis) equals zero (see Fig. 12.1),

$$B_y + i B_x = h_0 (\zeta^2 - (x^*)^2) (\zeta^2 - b^2)^{-1/2} \quad (12.1)$$

(see also Chap. 3 in [Somov and Syrovatskii 1976b](#)). Here the complex variable  $\zeta = x + iy$ ,  $b$  is the half-width of the layer (size along the  $x$  axis),  $c$  is the speed of light, and  $I$  is the total current in the layer. The quantity  $I$  varies through the range  $0 \leq I \leq ch_0 b^2 / 4$ . At the points

$$x^* = \pm \sqrt{\frac{1}{2} b^2 + \frac{2I}{ch_0}} \quad (12.2)$$

the magnetic field changes its sign (see formula (12.1) and Fig. 12.1b).

For  $|x| < |x^*|$  the direction of the current coincides with the direction of the electric field. This is direct (DC) current in Fig. 12.1b. However for  $|x^*| < |x| < b$  it has the opposite direction (*reverse currents RC*). If  $x \sim b$  and  $b - |x^*| \sim b$ , then

the reverse current is comparable with the forward one. Suppose that precisely this configuration appears. In so doing all MHD quantities outside (but near) the RCL may be treated as quasi-homogeneous everywhere, except in some neighborhood of the points  $x = x^*$  and  $x = \pm b$ , which are excluded from the further consideration.

Given the plasma conductivity  $\sigma$  is infinite the quantity  $b$  increases indefinitely with time. If  $\sigma$  is limited, then the finite width  $2b$  settles in finite time ([Syrovatskii 1976a](#)) and  $a/b \neq 0$ , although  $a \ll b$ . In this case, as distinct from (12.1),  $B_y \neq 0$  on the surface of the current layer. However, when  $\sigma$  is large enough,  $B_x \gg B_y$  outside some neighborhood of the points (12.2). Later on  $B_y$  is assumed to be zero. More general formulation of the problem is given in Sect. 3.4 in [Somov \(1992\)](#).

### 12.1.4 Reconnecting Current Layer Flows

Let the flow of the plasma satisfy the MHD approximation. If  $a \ll b$ , all quantities except the velocity  $\mathbf{v}$  are quasi-homogeneous along the  $x$  axis inside the layer. As for the inhomogeneity of the velocity, it is two-dimensional, since it follows from the mass conservation equation that at the point  $x = 0, y = 0$

$$\frac{\partial v_x}{\partial x} = -\frac{\partial v_y}{\partial y}$$

because of the flow symmetry. Therefore the RCL cannot be reduced to a one-dimensional flow. This is obvious because

**|** two reconnecting magnetic fluxes move towards each other and the plasma flow inside the current layer is thus two-dimensional.

If the conductivity is infinite it becomes a tangential discontinuity in the limit  $t \rightarrow \infty$ .

Let us consider a settled RCL. Then the electric field  $\mathbf{E}$  is independent of time. This being so the ratio  $a/b$  was estimated by [Syrovatskii \(1976a\)](#) from the steady-state Ohm's law

$$\frac{a}{b} \sim \frac{\nu_m h_0}{c E}, \quad (12.3)$$

where  $\nu_m$  is the magnetic diffusivity. Besides, in the stationary model, the electric field is independent of the coordinates. Hence

**|** in the region of direct current the plasma flows into the layer, but in the regions of reverse currents it flows out along the  $y$  axis.

Such character of the conductive plasma flows is shown schematically in Fig. 12.3. The velocity component  $v_y$  changes the sign when the plasma flows from the region DC of direct current into two regions RC of reverse current, which are the same regions as in Fig. 12.1b. This is important for counting the number  $N_w$  of the outgoing small-amplitude waves.

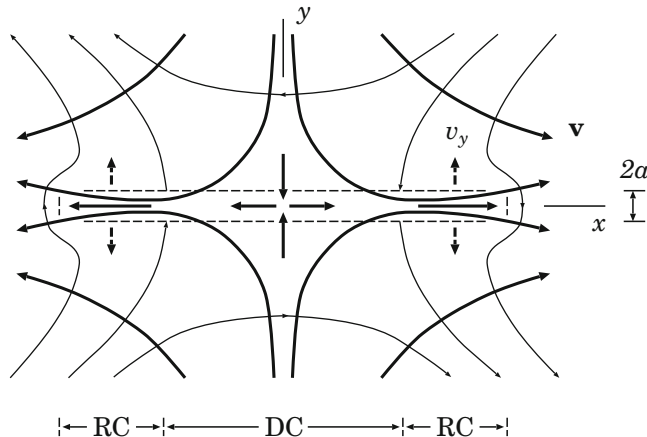


**Fig. 12.3** Plasma flows inside the RCL and in its vicinity

### 12.1.5 Additional Simplifying Assumptions

Let us suppose that all dissipative factors except the magnetic diffusivity  $\nu_m$  equal zero, but  $\nu_m$  is so small that

$$\frac{cE}{h_0 b} \ll \frac{h_0 b}{\sqrt{4\pi\rho}}. \quad (12.4)$$

The left side of this inequality represents the characteristic value of the drift velocity directed to the current layer  $v_y$ , the right side gives the value of the Alfvén speed  $V_A$ .

Consider also that

$$\rho^{in} \sim \rho^{ex}. \quad (12.5)$$

Here the indexes ‘in’ and ‘ex’ denote the quantities inside and outside the layer. Such a distribution was, for example, in the numerical experiment by [Brushlinskii et al. \(1980\)](#).

On the surface of the current layer the magnetic field increases without bound but the drift velocity tends to zero, if the conductivity is infinite. At the same time the quantity of the pressure  $p$  outside the RCL is close to its value for  $\zeta = \infty$  and does not equal zero or infinity for all  $\sigma$ . On this basis it may be thought that, outside the neighborhood of the point (12.2), the sound velocity  $V_s$  satisfies the condition

$$v_y^{ex} \ll V_s^{ex} \ll V_A^{ex},$$

$$(12.6)$$

when the conductivity is large enough. Inequalities (12.6) are well consistent with the magnetostatic approximation (see Part I, Sect. 13.1.3).

Taking the characteristic values of these quantities for an active region in the solar corona:

$$v_y \sim 10 \text{ km/s}, \quad V_s \sim 100 \text{ km/s}, \quad V_A \sim 1,000 \text{ km/s},$$

we see that the approximation (12.6) well holds there.

As far as the component of the velocity  $v_x$  is concerned, its modulus grows from zero for  $x = 0$  to

$$| v_x^{in} | \sim \frac{h_0 b}{\sqrt{4\pi\rho}} \quad (12.7)$$

for  $x = x^*$  (Sirovatskii 1971) and then reduces to zero for  $|x| = b$ . Outside, the component  $v_x$  also does not exceed the characteristic Alfvén speed.

Let us now investigate the infinitesimal perturbation of the RCL using the outlined properties of the plasma flow.

## 12.2 Small Perturbations Outside the RCL

### 12.2.1 Basic Assumptions

Let us assume that the MHD quantities  $Q$  are subjected to an infinitesimal perturbation  $\delta Q$ . For the sake of simplicity, suppose that

$$\delta v_z \equiv 0 \quad \text{and} \quad \delta B_z \equiv 0,$$

and outside the current layer the perturbation satisfies the WKB approximation (see Landau et al. 1984, Chap. 10, Sect. 85, Geometrical optics). Then its wave vector  $\mathbf{k}$ , in the zeroth order in terms of the small parameter  $1/kb$ , is determined from the dispersion equation

$$\omega_0 \left[ i k^2 V_s^2 (\mathbf{k} \mathbf{V}_A)^2 - V_s^2 k^2 \omega_0 (i \omega_0 - v_m k^2) - i k^2 V_A^2 \omega_0^2 + \omega_0^3 (i \omega_0 - v_m k^2) i k^2 V_s^2 (\mathbf{k} \mathbf{V}_A)^2 \right] = 0, \quad (12.8)$$

where  $\omega_0 = \omega - \mathbf{k} \mathbf{v}$ .

Let us impose the following restriction on the frequency  $\omega$ :

$$\frac{v_y}{a} \ll \omega_{\parallel} \ll \frac{V_s}{a},$$

(12.9)

where

$$\omega_{\parallel} = \omega - k_x v_x. \quad (12.10)$$

Besides, also for the sake of simplicity, we put

$$v_y \sim \frac{V_s^3}{V_A^2}. \quad (12.11)$$

We will show in Sect. 12.5.3 that precisely this velocity appears in the criterion of evolutionarity for the RCL.

### 12.2.2 Propagation of Perturbations Normal to a RCL

At first, let us consider the case of the propagation of the perturbations normal to the current layer, i.e. the perturbations with  $k_x = 0$ . In the zeroth order in terms of the small parameters, given by inequality (12.9), the solutions of Eq. (12.8) take the form

$$k_y^d = -i \frac{v_y}{v_m} \frac{V_A^2}{V_s^2}, \quad (12.12)$$

$$k_y^0 = \frac{\omega}{v_y}, \quad (12.13)$$

$$k_y^- = \frac{\omega}{v_y}, \quad (12.14)$$

$$k_y^+ = \pm \frac{\omega}{V_A}. \quad (12.15)$$

Here the root (12.14) is twofold.

The WKB approximation (Landau et al. 1984, Chap. 10) holds for these perturbations if

$$1/k_y^+ b \ll 1$$

since  $|k_y^+|$  is the least wave number. This is equivalent to the following condition for the frequency  $\omega$ :

$$\omega \gg \frac{h_0}{\sqrt{4\pi\rho}}. \quad (12.16)$$

When condition (12.16) is true, the derivatives of the unperturbed quantities over the coordinates in the linear MHD equations are negligible and the dispersion equation (12.8) is valid.

To obtain the criterion of evolutionarity it is necessary to classify the perturbations according to whether they are incoming to the current layer or outgoing

from it. Generally, such a classification has to be made by the sign of the sum of the projections of the velocity  $\mathbf{v}$  of the medium and the *group* velocity on the normal to the layer. However, as it was mentioned by Kontorovich (1959), in the case of normal propagation it is sufficient to determine only the sign of the phase velocity, since in the absence of frequency dispersion the latter coincides with the projection of the group velocity on the direction of the vector  $\mathbf{k}$  in the system of coordinates, where the plasma is at rest.

The perturbation with the wave vector  $k_y^0$  from formula (12.13) corresponds to an *entropy wave* (see Part I, Sect. 15.2.1), but  $k_y^-$  from solution (12.14) corresponds to the *slow magnetoacoustic wave* propagating perpendicularly to the magnetic field. In the system of coordinates, where the moving plasma is at rest, their phase velocities equal zero, but in the laboratory system they coincide with the plasma velocity  $\mathbf{v}$ . This being so,

**|** both perturbations are incoming to the RCL when the plasma flows into it, and are outgoing ones when the plasma flows out.

Besides, by virtue of the left side of inequality (12.9), we have conditions

$$k_y^0 \gg 1/a \quad \text{and} \quad k_y^- \gg 1/a.$$

Hence the RCL is not a discontinuity for the perturbations (12.13) and (12.14).

The perturbation with the wave vector  $k_y^+$  from solution (12.15) represents *fast magnetoacoustic waves*. Their phase velocity  $\omega/k_y^+$  satisfies the condition  $V_{ph}^+ \gg v_y$  (see (12.6) and (12.15)) and is aligned with the normal to the RCL or opposed to it. So one of them is always incoming to the layer and the other is outgoing from it, regardless of the sign of  $v_y$ . As distinct from  $k_y^0$  and  $k_y^-$ , the quantity  $k_y^+ \ll 1/a$ , and the waves (12.15) interact with the RCL as with a discontinuity.

The perturbation  $k_y^d$  from solution (12.12) is a *dissipative wave* and it damps within a distance which is much smaller than the layer half-thickness  $a$ . Consequently, as was pointed out by Roikhvarger and Syrovatskii (1974), its amplitude does not appear in the boundary conditions on the surface of a discontinuity. This being so, the dissipative effects outside the RCL are negligible.

Thus, in the case of normal propagation,

**|** there is one outgoing wave on each side of the current layer when the plasma flows into it (in the region DC of forward current),

and there are four of such waves, when the plasma flows out (in the domains RC of the reverse currents).

### 12.2.3 The Inclined Propagation of Perturbations

Let us now turn to the inclined propagation. To solve the problem of the evolutionarity of the current layer as a discontinuity, it is necessary to obtain the solution of Eq. (12.8) with common  $\omega$  and  $k_x$ . Kontorovich (1959) showed that, for a given flow,

the number of waves incoming to the  $x$  axis and outgoing from it, with common  $\omega$  and  $k_x$ , is independent of  $k_x$ , i.e. of the angle of propagation (see also Chap. 3 in [Anderson 1963](#)). Thus it is sufficient to determine the number of such waves for  $k_x = 0$ . From the preceding it follows that, when the plasma flows into the layer (the region DC of the forward current in Fig. 12.1b), there is one outgoing wave on each side of it. But when the plasma flows out there are four of them.

For the RCL under condition (12.9), however, the number of the perturbations with  $k_y \ll 1/a$  (i.e. those for which the amplitudes are discontinuous across it) depends on  $k_x$ . If  $k_x = 0$ , then there are two of such perturbations, determined by the wave vector  $k_y^+$  from (12.15). As will be shown below, there are three for the inclined propagation. This fact is important in our further considerations.

The wave vector of a slow magnetoacoustic wave is given by the formula

$$|\mathbf{k}^-| = \frac{\omega}{v_y \sin \theta + v_x \cos \theta \pm |V_{ph}^-|}, \quad (12.17)$$

where  $V_{ph}^-$  is the phase velocity, and  $\theta$  is the angle between  $\mathbf{k}^-$  and the  $x$  axis. Here the scalar product  $\mathbf{kv}$  is represented in the form

$$\mathbf{kv} = |\mathbf{k}^-| \times (v_y \sin \theta + v_x \cos \theta).$$

With  $V_s \ll V_A$  the following expression for  $|V_{ph}^-|$  is valid:

$$|V_{ph}^-| = \frac{V_A V_s}{V_\perp} |\cos \theta| \left[ 1 + \frac{1}{2} \frac{V_A^2 V_s^2}{V_\perp^4} \cos^2 \theta + o\left(\frac{V_A^2 V_s^2}{V_\perp^4}\right) \right], \quad (12.18)$$

where  $V_\perp^2 = V_A^2 + V_s^2$ .

Let us choose the angle  $\theta_0$  in such a way that  $|V_{ph}^-| \sim V_s$ , i.e.  $|\cos \theta_0|$  is not small, and find the solutions of Eq. (12.8) for fixed  $\omega$  and

$$k_x = |\mathbf{k}^-| \cos \theta_0. \quad (12.19)$$

For this purpose let us separate out the unknown variable  $k_y$

$$\begin{aligned} (\omega_\parallel - k_y v_y) & \left[ (v_m v_y V_s^2) k_y^5 + \left( i v_y^2 V_\perp^2 - v_m \omega_\parallel V_s^2 \right) k_y^4 \right. \\ & - (2i \omega_\parallel v_y V_\perp^2) k_y^3 + i \left( \omega_\parallel^2 V_\perp^2 - k_x^2 V_A^2 V_s^2 \right) k_y^2 \\ & - \left[ 2i \omega_\parallel v_y \left( V_\perp^2 k_x^2 - 2 \omega_\parallel^2 \right) \right] k_y \\ & \left. + i k_x^2 \left( \omega_\parallel^2 V_\perp^2 - k_x^2 V_A^2 V_s^2 \right) - i \omega_\parallel^4 \right] = 0. \end{aligned} \quad (12.20)$$

Here condition (12.9) is used.

In the zeroth order in terms of the small parameters, given by Inequality (12.9), this equation has the following solutions: (12.12) and

$$k_y^0 = \frac{\omega_{\parallel}}{v_y}, \quad (12.21)$$

$$k_y^{1-} = \frac{2\omega_{\parallel}}{v_y}, \quad (12.22)$$

$$k_y^{2-} = k_x \tan \theta_0, \quad (12.23)$$

$$\begin{aligned} k_y^s = \frac{1}{2} \left[ \frac{\omega_{\parallel} V_s^2 \cos^2 \theta_0}{2v_y V_A^2} \pm \left( -\frac{4\omega_{\parallel}^2}{V_s^2} + \frac{\omega_{\parallel}^2 V_s^4 \cos^4 \theta_0}{4v_y^2 V_A^4} \right. \right. \\ \left. \left. \pm 2 \sin \theta_0 |\cos \theta_0| \sqrt{\frac{\omega_{\parallel}^2 V_s}{v_y V_A^2}} \right)^{1/2} \right]. \end{aligned} \quad (12.24)$$

The sign in the round brackets in (12.24) coincides with the sign in front of  $|V_{ph}^-|$  in formula (12.17), but that in front of the round brackets specifies two different solutions of Eq. (12.20). From inequality (12.9) it follows that for the perturbations (12.21) and (12.22)  $k_y \gg 1/a$ , but for (12.23) and (12.24), on the contrary,  $k_y \ll 1/a$ .

The waves  $k_y^{1-}$  and  $k_y^{2-}$  are slow magnetoacoustic ones, here with the angle between  $\mathbf{k}^{2-}$  and the  $x$  axis equals  $\theta_0$  for  $k_x$  from (12.19). As for the waves  $k_y^s$ , they may be either slow magnetoacoustic or the *surface* ones, depending on the ratio  $v_y V_A^2 / V_s^3$ . Recall that if the perturbations are characterized by a common  $\theta$ , but not  $k_x$ , as in the present case, then there are always two slow waves, but the rest are fast magnetoacoustic waves.

If the expression in the round brackets in formula (12.24) is negative, then  $k_y^s$  has an imaginary part and the corresponding perturbations increase or decrease exponentially with the characteristic length, which is much smaller than  $a$ , while propagating away from the surface.

Investigation of the polynomial of the second degree in  $v_y$  in the round brackets in formula (12.24) shows that it equals zero at the points

$$v_y = \frac{V_s^3}{4V_A^2} |\cos \theta_0| \times (\pm \sin \theta_0 \pm 1). \quad (12.25)$$

Here the sign in front of  $\sin \theta_0$  is given by the sign in formula (12.17). Two signs in front of 1 determine two ends of the length on the axis of  $v_y$ , within which the perturbations (12.24) are slow magnetoacoustic waves. Outside this length they become surface waves. The one of them, which increases, while propagating away from the surface, should be rejected as it does not satisfy the boundary condition at infinity. As was stated by Kontorovich (1959), the decreasing perturbation should be classified as outgoing from the discontinuity surface.

Below we will use the fact that for large enough velocities,  $v_y$ , the waves (12.24) are surface ones, independent of  $\theta_0$ . It may be shown that the function  $v_y(\theta_0)$ , determined by formula (12.24), is restricted by modulus from above by the quantity

$$v_y^{max} = \frac{3\sqrt{3}}{16} \frac{V_s^3}{V_A^2}, \quad (12.26)$$

here the maximum value (12.26) is reached for  $\theta_0 = \pi/6$ . If

$$|v_y| > v_y^{max}, \quad (12.27)$$

the waves (12.24) are surface ones for all  $\theta_0$ .

The surface perturbation, which decreases with distance from the  $x$  axis, does not transfer energy away from the layer surface, because its amplitude equals zero at  $y = \infty$ . However this

surface wave enters into the total perturbation of the RCL and its amplitude must be determined from the boundary conditions. In this sense the wave is classified as an outgoing one.

As for the increasing perturbation, it is formally an incoming wave, but it must be discarded, since it tends to infinity as  $y \rightarrow \infty$ . Note that for this reason in the domain of the plasma outflow, where only one incoming wave is possible, the incoming waves are absent, for a given  $\theta_0$ , when  $|v_y| > v_y^{max}$ .

Note that  $v_y^{max}$  coincides with the maximum value of the projection of the group velocity of a slow magnetoacoustic wave on the  $y$  axis, which in the approximation  $V_s \ll V_A$  has the form

$$(V_{gr}^-)_y = \frac{V_s^3}{V_A^2} \sin \theta \cos^3 \theta. \quad (12.28)$$

Moreover this value is also reached for the angle  $\theta = \pi/6$ . So inequality (12.27) means that

all slow magnetoacoustic waves are either incoming or outgoing, provided the plasma flows into or out of the RCL.

To solve the problem of evolutionarity of the current layer we now have to derive boundary conditions. They relate the amplitudes of the perturbations with  $k_y \ll 1/a$  (that interact with the layer as with a discontinuity) on two sides of the surface.

However, as distinct from a one-dimensional discontinuity, the waves with  $k_y \ll 1/a$  outside the current layer may lead to the perturbations for which the inverse inequality is valid in the interior. Furthermore, since inside the layer the dissipative effects are essential, the wave numbers of these perturbations have imaginary parts that tend to infinity in the limit  $a/b \rightarrow 0$ . This means that the magnitude of the perturbation increases without bound, and therefore

the linearized one-dimensional boundary conditions generally do not hold at the reconnecting current layer (RCL)

(Markovskii and Somov 1996). This fact can be understood in the next section from the analysis of the perturbations inside the current layer.

## 12.3 Perturbations Inside the RCL

### 12.3.1 Linearized Dissipative MHD Equations

Let us deduce the equations for the perturbed MHD quantities  $\delta Q$  inside the current layer. In this case  $y \lesssim a$ . We linearize the dissipative MHD equations (see Part I, Sect. 12.2.2).

For  $Q_z \equiv 0$  and  $\partial \delta Q / \partial z \equiv 0$  the equations for  $\delta v_z$  and  $\delta B_z$ , which we put equal to zero, are separated from the equations for the other small quantities. In the latter we may neglect the derivatives  $\partial p / \partial x$ ,  $\partial \mathbf{B} / \partial x$ , and  $\partial \rho / \partial x$  in the approximation  $a \ll b$ . The left side of inequality (12.9) allows us also to neglect the derivative  $\partial v_x / \partial x$ .

Consider, for example, the linear equation of mass conservation

$$\begin{aligned} \frac{\partial \delta \rho}{\partial t} + \delta \rho \frac{\partial v_x}{\partial x} + \rho \frac{\partial \delta v_x}{\partial x} + \delta v_x \frac{\partial \rho}{\partial x} + v_x \frac{\partial \delta \rho}{\partial x} \\ + v_y \frac{\partial \delta \rho}{\partial y} + \delta \rho \frac{\partial v_y}{\partial y} + \delta v_y \frac{\partial \rho}{\partial y} + \rho \frac{\partial \delta v_y}{\partial y} = 0. \end{aligned} \quad (12.29)$$

Since, inside the RCL, the inhomogeneity of the velocity is two-dimensional then, together with the terms proportional to  $\partial v_x / \partial x$ , we have to neglect the terms with  $\partial v_y / \partial y$ .

Let us choose the sign in formula (12.17) coinciding with the sign of  $v_x$ . Inside the layer  $|v_x|$  is a growing function of  $|y|$ , but  $k_x$  is constant. So from formulae (12.10) and (12.17) it follows that  $|\omega_{\parallel}|$  increases, while  $|y|$  decreases, and satisfies the condition

$$|\omega_{\parallel}| > |\omega_{\parallel}^{ex}|. \quad (12.30)$$

Estimating

$$\frac{\partial \delta \rho}{\partial t} + v_x \frac{\partial \delta \rho}{\partial x} \sim \omega_{\parallel} \delta \rho, \quad \frac{\partial v_y}{\partial y} \sim \frac{v_y^{ex}}{a},$$

we get from (12.30) and the left side of (12.9) that

$$\frac{\partial \delta \rho}{\partial t} + v_x \frac{\partial \delta \rho}{\partial x} \gg \delta \rho \frac{\partial v_y}{\partial y}, \quad \text{q.e.d.}$$

If the other sign in (12.17) is chosen, then a value of  $y$  exists for which  $\omega_{\parallel} = 0$  and this inequality does not hold.

Similar reasoning is valid for the other equations. Hence  $\partial Q/\partial x = 0$  in the zeroth order in terms of the small parameters given by relation (12.9). Besides, we put  $\partial Q/\partial t = 0$  in all equations.

Following Syrovatskii (1956), let us substitute  $\partial \delta Q/\partial t$  by

$$-i\omega \left( \delta Q - \xi \frac{\partial Q}{\partial y} \right) \equiv -i\omega \hat{D}Q, \quad (12.31)$$

and  $\partial \delta Q/\partial x$  by  $i k_x \hat{D}Q$ , where  $\xi$  is the displacement of the layer as a unit. Then we obtain the set of *linear ordinary* differential equations with respect to  $y$

$$i\omega_{\parallel} \hat{D}\rho = ik_x \rho \hat{D}v_x + (\rho \delta v_y)' + v_y \delta \rho', \quad (12.32)$$

$$ik_x \hat{D}B_x + \delta B'_y = 0, \quad (12.33)$$

$$i\omega_{\parallel} \rho \hat{D}v_x = ik_x \hat{D}p + \rho v_y \delta v'_x - \frac{B'_x \delta B_y}{4\pi} + v'_x \rho \delta v_y, \quad (12.34)$$

$$i\omega_{\parallel} \rho \delta v_y = \delta \left( p + \frac{B_x^2}{8\pi} \right)' + \rho v_y \delta v'_y - ik_x \frac{B_x \delta B_y}{4\pi}, \quad (12.35)$$

$$i\omega_{\parallel} \hat{D}p = ik_x \gamma p \hat{D}v_x + \gamma p \delta v'_y + \delta(p' v_y) - \frac{(\gamma - 1)}{2\pi} v_m B'_x \delta B'_x, \quad (12.36)$$

$$i\omega_{\parallel} \hat{D}B_x = (B_x \delta v_y)' + v_y \delta B'_x - v'_x \delta B_y - v_m \delta B''_x, \quad (12.37)$$

where the prime denotes the differentiation with respect to  $y$ . Here we make use of the equality

$$p + \frac{B_x^2}{8\pi} = \text{const}, \quad (12.38)$$

which follows from the  $y$  component of the unperturbed momentum equation.

### 12.3.2 Boundary Conditions

Under certain restrictions on the unperturbed MHD quantities  $Q$  and the frequency  $\omega$ , the *boundary conditions* (the conservation laws), which relate the amplitudes of the small perturbations on both sides of the current layer, may be deduced from the set of linear equations (12.32)–(12.37).

For a one-dimensional discontinuity these conditions are obtained as a result of integrating the linear equations over the thickness of the domain in which the unperturbed quantities change substantially, and allowing this thickness (the thickness  $2a$  of the layer shown in Fig. 12.3) to tend to zero.

Let us integrate, for example, the induction equation (12.37), substituting  $v'_x = -\omega'_{\parallel}/k_x$  (see definition (12.10)) and  $\delta B_y$  from Eq. (12.33)

$$i\omega_{\parallel}^{ex} \int_{-a}^{+a} \delta B_x dy = \{ B_x (\delta v_y + i\omega_{\parallel} \xi) \} + \int_{-a}^{+a} v_y \delta B'_x dy - v_m \{ \delta B'_x \}. \quad (12.39)$$

Here and below, the braces denote the jump of a quantity over a discontinuity. Supposing that  $\delta Q$  varies only slightly inside the discontinuity, if  $k_y^{ex} a \ll 1$  outside it, we can estimate the integral proportional to  $\omega_{\parallel}^{ex}$ :

$$\omega_{\parallel}^{ex} \int_{-a}^{+a} \delta B_x dy \sim \omega_{\parallel}^{ex} \delta B_x^{ex} a.$$

Let us compare this expression with the jump

$$\{ B_x \delta v_y \} \sim B_x^{ex} \delta v_y^{ex}.$$

In the case under study the requirement  $k_y^{ex} a \ll 1$  is satisfied for the waves (12.23) and (12.24). The relationship between the perturbations  $\delta Q$  in such waves, in approximation (12.6) and (12.9), is given by the formulae:

$$\begin{aligned} \delta p &\sim V_s^2 \delta \rho, & \delta v_x &\sim V_s \frac{\delta \rho}{\rho}, & \delta B_x &\sim B_x \left( \frac{V_s}{V_A} \right)^2 \frac{\delta \rho}{\rho}, \\ \delta v_y &\sim V_s \left( \frac{V_s}{V_A} \right)^2 \frac{\delta \rho}{\rho}, & \text{and} && \delta B_y &\sim B_x \left( \frac{V_s}{V_A} \right)^2 \frac{\delta \rho}{\rho}. \end{aligned} \quad (12.40)$$

Taking (12.40) into account, we find that the condition

$$\omega_{\parallel}^{ex} \int_{-a}^{+a} \delta B_x dy \ll \{ B_x \delta v_y \}$$

coincides with the inequality  $k_y^{ex} a \ll 1$ , i.e. with the right side of (12.9).

Similar reasoning for the other terms in Eq. (12.37) leads to the following boundary condition

$$\{ B_x (\delta v_y + i\omega_{\parallel} \xi) \} = 0. \quad (12.41)$$

The application of this approach to Eq. (12.33) gives

$$\{ \delta B_y - i k_x B_x \xi \} = 0. \quad (12.42)$$

As in the magnetoacoustic waves, in approximation (12.9)

$$\delta v_y = -\frac{\omega_{\parallel} \delta B_y}{k_x B_x}, \quad (12.43)$$

Equations (12.41) and (12.42) are satisfied if

$$\delta B_y = i k_x \xi B_x^{ex}, \quad (12.44)$$

and, consequently,

$$\delta v_y = -i \omega_{\parallel}^{ex} \xi. \quad (12.45)$$

As distinct from a one-dimensional discontinuity,  $\delta Q$  changes substantially inside the RCL. We will show that the perturbation with  $k_y^{ex} \ll 1/a$  outside the RCL may lead to perturbations inside it, for which  $k_y^{in} \gg 1/a$  and  $k_y^{in}$  has an imaginary part. These perturbations increase or decrease exponentially on the characteristic length which is much smaller than  $a$ . So the above estimations of the terms in Eq. (12.37) are generally not valid.

### 12.3.3 Dimensionless Equations and Small Parameters

To deduce the boundary conditions on the RCL as on the surface of a discontinuity, let us obtain the solutions of the set (12.32)–(12.37) inside the layer for given  $\omega$  and  $k_x$ . Assume that outside the layer only the amplitudes of the waves with  $k_y^{ex} \ll 1/a$  differ from zero. Let us bring Eqs. (12.32)–(12.37) to a dimensionless form by the following substitution of variable and unknown functions:

$$y = a \tilde{y}, \quad Q = Q^{ex} \tilde{Q}, \quad \delta Q = \delta Q^{ex} \delta \tilde{Q}, \quad (12.46)$$

$$\xi = \frac{\delta v_y^{ex}}{\omega_{\parallel}^{ex}} \tilde{\xi}, \quad k_x = \frac{\omega_{\parallel}^{ex}}{V_s^{ex}} \tilde{k}_x, \quad (12.47)$$

$$\delta v_y = -i \tilde{\xi} \omega_{\parallel} + \frac{a \omega_{\parallel}^{ex}}{V_s^{ex}} \delta v_y^{ex} \tilde{\omega}_{\parallel} \delta \tilde{v}_y, \quad (12.48)$$

$$\delta B_y = i k_x \xi B_x + \frac{a \omega_{\parallel}^{ex}}{V_s^{ex}} \delta B_y^{ex} \delta \tilde{B}_y. \quad (12.49)$$

Here the quantities  $\delta Q^{ex}$  are related by formula (12.40), the tilde denotes the dimensionless functions and the expressions for  $\delta v_y$  and  $\delta B_y$  contain the boundary values (12.44) and (12.45) in an explicit form.

Let us insert expressions (12.46)–(12.49) into Eqs. (12.32)–(12.37) and introduce the following four small parameters in accordance with the basic assumptions (12.9) and (12.11):

$$\varepsilon_0 = \frac{v_y^{ex}}{a \omega_{\parallel}^{ex}}, \quad \varepsilon_1 = \frac{a \omega_{\parallel}^{ex}}{V_s^{ex}}, \quad \varepsilon_2 = \frac{v_y^{ex}}{V_s^{ex}}, \quad \varepsilon_3 = \left( \frac{V_s^{ex}}{V_A^{ex}} \right)^2. \quad (12.50)$$

As a result, we obtain equations describing the dimensionless functions,

$$i \tilde{\omega}_{\parallel} \delta \tilde{\rho} = i \tilde{k}_x \tilde{\rho} \delta \tilde{v}_x + \varepsilon_3 (\tilde{\rho} \tilde{\omega}_{\parallel} \delta \tilde{v}_y)' + \varepsilon_0 \tilde{v}_y \delta \tilde{\rho}', \quad (12.51)$$

$$i \tilde{k}_x \delta \tilde{B}_x + \delta \tilde{B}'_y = 0, \quad (12.52)$$

$$i \tilde{\omega}_{\parallel} \tilde{\rho} \delta \tilde{v}_x = i \tilde{k}_x \delta \tilde{p} - \frac{1}{\tilde{k}_x} \varepsilon_3 \tilde{\omega}_{\parallel} \tilde{\omega}'_{\parallel} \tilde{\rho} \delta \tilde{v}_y - \tilde{B}'_x \delta \tilde{B}_y + \varepsilon_0 \tilde{v}_y \tilde{\rho} \delta \tilde{v}'_x, \quad (12.53)$$

$$( \delta \tilde{p} + \tilde{B}_x \delta \tilde{B}_x )' = \varepsilon_2 \varepsilon_3 \tilde{\rho} \tilde{v}_y \left[ i \tilde{\xi} \tilde{\omega}'_{\parallel} - \varepsilon_1 (\tilde{\omega}_{\parallel} \delta \tilde{v}_y)' \right] \\ + \varepsilon_1 \varepsilon_3 \tilde{\omega}_{\parallel}^2 \tilde{\rho} \left( \tilde{\xi} + i \varepsilon_1 \delta \tilde{v}_y \right) - \varepsilon_1 \tilde{k}_x \tilde{B}_x \left( \tilde{k}_x \tilde{\xi} \tilde{B}_x - i \varepsilon_1 \delta \tilde{B}_y \right), \quad (12.54)$$

$$i y \tilde{\omega}_{\parallel} \delta \tilde{p} = i y \tilde{k}_x \tilde{p} \delta \tilde{v}_x + \varepsilon_3 \left[ \tilde{p} (\tilde{\omega}_{\parallel} \delta \tilde{v}_y)' + \frac{1}{\gamma} \tilde{\omega}_{\parallel} \tilde{p}' \delta \tilde{v}_y \right] \\ + \varepsilon_0 [\tilde{v}_y \delta \tilde{p}' - 2(\gamma - 1) \tilde{B}'_x \delta \tilde{B}'_x], \quad (12.55)$$

$$i \tilde{\omega}_{\parallel} \delta \tilde{B}_x = (\tilde{B}_x \tilde{\omega}_{\parallel} \delta \tilde{v}_y)' + \frac{1}{\tilde{k}_x} \tilde{\omega}'_{\parallel} \delta \tilde{B}_y + \varepsilon_0 (\tilde{v}_y \delta \tilde{B}'_x - \delta \tilde{B}''_x). \quad (12.56)$$

This is the complete set of dimensionless equations valid on the RCL as a discontinuity surface.

### 12.3.4 Solution of the Linearized Equations

Since we are interested in the solutions of the set of Eqs. (12.51)–(12.56) in approximation (12.9), let us allow the small parameters  $\varepsilon_i$  (except the parameter  $\varepsilon_3$ ) to tend to zero. Then the equations reduce to the following simpler ones:

$$i \tilde{\omega}_{\parallel} \delta \tilde{\rho} = i \tilde{\rho} \delta \tilde{v}_x, \quad (12.57)$$

$$i \delta \tilde{B}_x + \delta \tilde{B}'_y = 0, \quad (12.58)$$

$$i \tilde{\omega}_{\parallel} \tilde{\rho} \delta \tilde{v}_x = i \delta \tilde{p} - \varepsilon_3 \tilde{\omega}_{\parallel} \tilde{\omega}'_{\parallel} \tilde{\rho} \delta \tilde{v}_y - \tilde{B}'_x \delta \tilde{B}_y, \quad (12.59)$$

$$(\delta \tilde{p} + \tilde{B}_x \delta \tilde{B}_x)' = 0, \quad (12.60)$$

$$i \tilde{\omega}_{\parallel} \delta \tilde{p} = i \tilde{p} \delta \tilde{v}_x + \varepsilon_3 \left[ \tilde{p} (\tilde{\omega}_{\parallel} \delta \tilde{v}_y)' + \frac{1}{\gamma} \tilde{\omega}_{\parallel} \tilde{p}' \delta \tilde{v}_y \right], \quad (12.61)$$

$$i \tilde{\omega}_{\parallel} \delta \tilde{B}_x = (\tilde{B}_x \tilde{\omega}_{\parallel} \delta \tilde{v}_y)' + \tilde{\omega}'_{\parallel} \delta \tilde{B}_y. \quad (12.62)$$

The terms proportional to  $\varepsilon_3$  are retained in Eqs. (12.59) and (12.61), since inside the current layer the quantities

$$\left( \tilde{\omega}'_{\parallel}, \tilde{\omega}_{\parallel} \right) \lesssim 1/\sqrt{\varepsilon_3}$$

(see (12.7)) and  $(\tilde{p}, \tilde{p}') \sim 1/\varepsilon_3$  (see equality (12.38)). Besides, the expression for  $\tilde{k}_x$ , which follows from (12.18) and (12.19), is used

$$\tilde{k}_x = 1 + O(\varepsilon_2) + O(\varepsilon_3). \quad (12.63)$$

In the set (12.57)–(12.62) the Eqs. (12.57) and (12.59) are not differential, but serve as the algebraic definitions of the functions  $\delta\tilde{v}_x$  and  $\delta\tilde{\rho}$ . After the substitution of  $\delta\tilde{B}_x$  from Eq. (12.58) to (12.62), the latter becomes the full derivative with respect to  $\tilde{y}$  and, by integrating, is brought to the form

$$\delta\tilde{B}_y + \tilde{B}_x \delta\tilde{v}_y = 0. \quad (12.64)$$

The constant of integration in this equation is put equal to zero, as the perturbation outside the layer represents the superposition of magnetoacoustic waves, for which (12.43) holds. The integration of Eq. (12.60) gives

$$\delta\tilde{p} + \tilde{B}_x \delta\tilde{B}_x = C_0. \quad (12.65)$$

The substitution of (12.59), (12.64) and (12.65) in Eq. (12.61) reduces it to

$$\begin{aligned} & \left[ \varepsilon_3 \tilde{p} + \tilde{B}_x^2 \left( 1 - \frac{\tilde{p}}{\tilde{\rho} \tilde{\omega}_{\parallel}^2} \right) \right] \delta\tilde{v}'_y + \left( \frac{1}{\gamma} \varepsilon_3 \tilde{p}' + \tilde{B}_x \tilde{B}'_x \right) \delta\tilde{v}_y \\ &= i C_0 \left( 1 - \frac{\tilde{p}}{\tilde{\rho} \tilde{\omega}_{\parallel}^2} \right). \end{aligned} \quad (12.66)$$

Expressing the dimensionless values in the coefficient in front of  $\delta\tilde{v}_y$  in terms of the dimensional ones, we find that they are equal to

$$\left( p + \frac{B_x^2}{8\pi} \right)' \frac{4\pi a}{(B_x^{ex})^2} = 0. \quad (12.67)$$

(see equality (12.38)).

Hence the solution of the set (12.58), (12.60)–(12.62) is

$$\delta\tilde{v}_y = iC_0 \int \frac{\left(1 - \tilde{p}/\tilde{\rho}\tilde{\omega}_{\parallel}^2\right) d\tilde{y}}{\varepsilon_3 \tilde{p} + \tilde{B}_x^2 \left(1 - \tilde{p}/\tilde{\rho}\tilde{\omega}_{\parallel}^2\right)} + C, \quad (12.68)$$

$$\delta\tilde{B}_y = -\tilde{B}_x \delta\tilde{v}_y, \quad (12.69)$$

$$\delta\tilde{B}_x = -i(\tilde{B}_x \delta\tilde{v}_y)', \quad (12.70)$$

$$\delta\tilde{p} = C_0 - \tilde{B}_x \delta\tilde{B}_x. \quad (12.71)$$

The solution (12.68)–(12.71) has a singularity at the point  $\tilde{y}_0$ , in which

$$\tilde{A} \equiv \varepsilon_3 \tilde{p} + \tilde{B}_x^2 \left(1 - \frac{\tilde{p}}{\tilde{\rho}\tilde{\omega}_{\parallel}^2}\right) = 0, \quad (12.72)$$

and the function in the integral in (12.68) turns to infinity. However it may be shown by expressing  $\delta Q'$  in terms of  $\delta Q$  in the set (12.32)–(12.37) that it has a singularity only for  $y = 0$ , where  $v_y = 0$ . This means that in some neighborhood of  $\tilde{y}_0$  we cannot neglect the small parameters in the set (12.51)–(12.56) and turn to (12.57)–(12.62). The vicinity of the point  $\tilde{y}_0$  will be considered below.

Let us now find the remaining solutions of the set of Eqs. (12.51)–(12.56) in the domain where the formulae (12.68)–(12.71) are valid. We suppose, for the sake of definiteness, that  $v_x^{in} \sim V_s^{ex}$  (see (12.7)), i.e.  $\tilde{\omega}_{\parallel}^2 \sim 1/\varepsilon_3$ . Such a relation holds if  $x$  is not close to 0 and  $\pm b$ . The solution (12.68)–(12.71) is valid when the expression in the integral in (12.68) is of order of unity. Since, inside the current layer  $\tilde{B}_x \lesssim 1$  and  $\tilde{p} \sim 1/\varepsilon_3$ , it follows from (12.68) and (12.72), that in this case

$$\tilde{A} \sim 1. \quad (12.73)$$

Then the remaining solutions of the set (12.51)–(12.56) satisfy the WKB approximation inside the RCL and may be found from the dispersion equation (12.20).

Let us express the dimensionless quantities in  $\tilde{A}$  in terms of the dimensional ones and take into account that

$$k_x = \omega_{\parallel}^{ex} / V_s^{ex}.$$

Then we find that the quantity  $\tilde{A}$  is related with the coefficient in front of  $k_y^2$  in dispersion equation (12.20) in the following way:

$$A = \omega_{\parallel}^2 V_{\perp}^2 - k_x^2 V_A^2 V_s^2 \sim \omega_{\parallel}^2 (V_A^{ex})^2 \tilde{A}. \quad (12.74)$$

Under condition (12.73) in the zeroth order in terms of the small parameters  $\varepsilon_i$  (see definition (12.50)) the solutions of Eq. (12.20) take on the form (12.21) and

$$k_y^d = \frac{\omega_{\parallel}}{v_y}, \quad (12.75)$$

$$k_y^- = \pm \sqrt{\frac{iA}{V_s^2 v_m \omega_{\parallel}}}, \quad (12.76)$$

$$k_y^* = \frac{1}{A} \left[ \omega_{\parallel} v_y F \pm \sqrt{\omega_{\parallel}^2 v_y^2 F^2 - A (k_x^2 A - \omega_{\parallel}^4)} \right], \quad (12.77)$$

where

$$F = V_{\perp}^2 k_x^2 - 2 \omega_{\parallel}^2.$$

From the basic Inequality (12.9) it follows that the wave vectors (12.21), (12.75), and (12.76) satisfy the WKB approximation inside the RCL. The dispersion equation is valid for them, as in the limit  $k_y \gg 1/a$  the terms with the derivatives of unperturbed quantities in Eqs. (12.32)–(12.37) are negligible.

The expressions (12.42), (12.75), and (12.76) give us four solutions of the set of Eqs. (12.32)–(12.37). By contrast, the perturbations (12.77) do not satisfy the WKB approximation, since they have  $1/k_y a \rightarrow 0$ . In this case we cannot neglect the derivatives of unperturbed quantities in the set of Eqs. (12.32)–(12.37), so we cannot use Eq. (12.20). These perturbations are described by formulae (12.68)–(12.71).

Thus we have shown that

there are four perturbations, which satisfy the WKB approximation inside the RCL, regardless of the value of  $k_x$ .

Recall that outside the current layer there are also four of such perturbations in the case of normal propagation, but in the case of oblique propagation there are three. Therefore in the latter case the perturbations with  $k_y \ll 1/a$  and  $k_y \gg 1/a$  transform to each other.

## 12.4 Solution on the Boundary of the RCL

In order to obtain the boundary conditions it is necessary to determine the value of the perturbation on the boundary of the current layer, i.e. for  $Q = Q^{ex}$ . In this case

$$a \ll y \ll 1/k_y^{ex}.$$

If  $Q = Q^{ex}$ , then the solution (12.68)–(12.71) is not valid, since the coefficients in Eq. (12.66) are much smaller than unity (see definitions (12.46)) and the small parameters cannot be neglected in deducing of this equation.

Let us find the solutions of Eqs. (12.51)–(12.56) in the neighborhood of the boundary of the RCL in the domain

$$\tilde{Q} \sim 1. \quad (12.78)$$

Note that as  $p^{in} \gg p^{ex}$  and  $\omega_{\parallel}^{in} \gg \omega_{\parallel}^{ex}$ , the value of  $\tilde{y}$  exists, for which  $\tilde{p} \gg 1$  and  $\tilde{\omega}_{\parallel} \gg 1$ , although for  $\tilde{y} \gg 1$  always  $\tilde{Q}'/\tilde{Q} \ll 1$ .

Substitute Eq. (12.52) in (12.56) and then substitute (12.56) and (12.53) in Eq. (12.54), in the same way as for deduction of (12.66), but hold the terms proportional to the small parameter  $\varepsilon_0$

$$\begin{aligned} i\tilde{\omega}_{\parallel} \left(1 - \frac{\tilde{p}}{\tilde{\rho}\tilde{\omega}_{\parallel}^2}\right) \delta\tilde{p} &= \tilde{\omega}_{\parallel} \varepsilon_3 \left( \tilde{p} \delta\tilde{v}_y' + \frac{1}{\gamma} \tilde{p}' \delta\tilde{v}_y \right) \\ &\quad - \frac{\tilde{p}}{\tilde{\rho}\tilde{\omega}_{\parallel}} \tilde{B}_x' \delta\tilde{B}_y + \varepsilon_0 \tilde{v}_y \left( \frac{\tilde{p}}{\tilde{\omega}_{\parallel}} \delta\tilde{v}_x' + \delta\tilde{p}' \right). \end{aligned} \quad (12.79)$$

Here we use (12.63) and the inequality  $\varepsilon_0 \ll (\varepsilon_2, \varepsilon_3)$ , which follows from condition (12.9).

As the derivatives  $\delta\tilde{v}_x'$  and  $\delta\tilde{p}'$  appear in (12.78) with small parameters, in the first order they may be expressed from Eqs. (12.59) and (12.60), which do not contain small parameters. Let us integrate equation (12.59) and use (12.64) and (12.65). Then, taking into account that  $\tilde{Q}' \ll 1$  and considering (12.67), we find the equation describing the function  $\delta\tilde{v}_y$ ,

$$i\varepsilon_0 \tilde{B}_x^2 \tilde{v}_y \left(1 + \frac{\tilde{p}}{\tilde{\rho}\tilde{\omega}_{\parallel}^2}\right) \delta\tilde{v}_y'' + \tilde{\omega}_{\parallel} \tilde{A} \delta\tilde{v}_y' = iC_0 \tilde{\omega}_{\parallel} \left(1 - \frac{\tilde{p}}{\tilde{\rho}\tilde{\omega}_{\parallel}^2}\right) \quad (12.80)$$

(cf. Eq. (12.66)). Three cases differ.

(a) Let

$$1 - \tilde{p}/\tilde{\rho}\tilde{\omega}_{\parallel}^2 \gg \varepsilon_0,$$

then  $\tilde{A} \gg \varepsilon_0$  (see definition (12.72)), as in the domain (12.78)  $\varepsilon_3 \tilde{p} \ll \varepsilon_0$ , and Eq. (12.66) is valid.

(b) Let

$$1 - \tilde{p}/\tilde{\rho}\tilde{\omega}_{\parallel}^2 \lesssim \varepsilon_0,$$

then  $\tilde{A} \lesssim \varepsilon_0$  and all the terms in Eq. (12.79) are essential. In this case, in the first order, it is sufficient to substitute  $\delta\tilde{p}$  in Eq. (12.79) from (12.65), but not from (12.54). So the small parameter  $\varepsilon_1$  does not enter in Eq. (12.80).

(c) On the boundary of the layer ( $|\tilde{Q}| = 1$ ),

$$1 - \frac{\tilde{p}}{\tilde{\rho}\tilde{\omega}_{\parallel}^2} = 0, \quad \tilde{A} = 0,$$

and Eq. (12.80) transforms to  $\delta\tilde{v}_y'' = 0$ . After integrating, this equality turns to the following one:

$$\delta\tilde{v}_y = C_* \tilde{y} + C. \quad (12.81)$$

Expression (12.81) together with (12.69)–(12.71) defines three solutions of the set of Eqs. (12.51)–(12.56). The remaining three solutions for  $|\tilde{Q}| = 1$  satisfy the WKB approximation with the wave vectors (12.12), (12.21), and (12.22).

\* \* \*

Let us now return to the vicinity of the point  $\tilde{y}_0$ , in which  $\tilde{A} = 0$ . From Eq. (12.38) and condition (12.7) it follows that the point  $\tilde{y}_0$  may generally be situated either in the domain  $\tilde{y} \lesssim 1$  or  $\tilde{y} \gg 1$ . If

$$\tilde{y}_0 \lesssim 1, \quad (12.82)$$

then the terms containing  $\tilde{v}'_y$  appear in the equation for  $\delta\tilde{v}_y$  with  $\tilde{A} = 0$ . As  $\tilde{v}'_y \sim 1$ , they are found to be comparable with the terms proportional to  $\partial v_x / \partial x$ , which we have neglected when deducing the set of Eqs. (12.32)–(12.37). Because of this, to determine  $\delta\tilde{v}_y$  in the vicinity of  $\tilde{y}_0$ , in the present case, it is necessary to solve a partial differential equation.

Let

$$\tilde{y}_0 \gg 1, \quad (12.83)$$

then  $\tilde{v}'_y \ll 1$  and for  $\tilde{y} = \tilde{y}_0$ , in the first order,  $\delta\tilde{v}_y$  is described by an ordinary differential equation. In particular, in the domain (12.78), it is the Eq. (12.80). It does not have a singularity for  $\tilde{A} = 0$  and the solutions of the set of Eqs. (12.51)–(12.56) in the vicinity of  $\tilde{y}_0$  are given by the formulae (12.81), (12.69)–(12.71), (12.12), (12.21), and (12.22).

Finally let us establish the correspondence between the perturbations outside and inside the RCL. Assume that (12.83) holds and, for  $\tilde{y} \lesssim 1$  (12.73) is true.

Solving the set of Eqs. (12.51)–(12.56) in the domain

$$1 \ll (\tilde{p}, \tilde{\omega}_{\parallel}^2) \ll 1/\varepsilon_3,$$

it may be shown that the following correspondence takes place. The perturbations, which are described by the wave vectors  $k_y^d$  from (12.12) and  $k_y^0$  from (12.21) outside the RCL, transform into (12.76) and (12.21) inside it, i.e. represent the same roots of Eq. (12.20) for the different values of  $\tilde{y}$ .

**|** The wave (12.22) transforms into one of the perturbations (12.76), with the sign ‘−’ or ‘+’ depending on the sign of  $v_y$ .

Hence the superposition of (12.23) and (12.24) corresponds to the superposition of (12.68)–(12.71) and the other perturbation (12.76).

Besides, the frequency  $\omega_{\parallel}$  from the interval (12.9) may be chosen in such a way, that the solution proportional to  $C_0$  exists inside the RCL for all  $\tilde{y}$ . In this case the solution proportional to  $C_*$ , in the domain (12.78), transforms, for  $\tilde{y} \lesssim 1$  into the perturbation with the wave vector (12.76). Thus

the three waves with  $\lambda_y^{ex} \gg a$  outside the RCL cause the perturbation inside the RCL, for which  $\lambda_y^{in} \ll a$ .

So now we can formulate the conditions of evolutionarity for the RCL.

## 12.5 The Criterion of Evolutionarity

### 12.5.1 One-Dimensional Boundary Conditions

Let us now turn to the criterion of evolutionarity. With this end in view, we deduce the boundary conditions on the RCL as a surface of a discontinuity. There are two possibilities.

- If the amplitudes of the perturbations (12.21), (12.75), and (12.76) with  $k_y \gg 1/a$  inside the layer differ from zero, then the boundary conditions, similar to those which hold on one-dimensional discontinuities, do not exist on its surface. If this were not so, then the quantity  $\delta v_y$  would remain constant after a transition across the layer, by virtue of condition (12.45). However the magnitude of the perturbations (12.21), (12.75), and (12.76) changes substantially within the distance  $a$  and (12.45) is not valid in a general case.
- We consider below only such perturbations that the amplitudes of the modes (12.21), (12.75), and (12.76) equal zero. This requirement is obeyed by the solution of Eqs. (12.32)–(12.37), if the constant  $C_0$  differs from zero, but the other constants equal zero (see the end of Sect. 12.4).

Let us obtain the boundary conditions which the solution proportional to  $C_0$  satisfies. Due to (12.81), formulae (12.48) and (12.49) give the boundary values (12.44) and (12.45) for  $\delta v_y$  and  $\delta B_y$ . From (12.45) it follows that

$$\{\delta v_y\} = 0. \quad (12.84)$$

As for condition (12.44), it is equivalent to (12.45) and does not result in an additional boundary condition. Expression (12.71) determines the second boundary condition

$$\left\{ \delta p + \frac{B_x \delta B_x}{4\pi} \right\} = 0. \quad (12.85)$$

Finally formula (12.70) means that

$$\delta B_x = 0 \quad (12.86)$$

on both sides of the discontinuity, since  $\delta \tilde{v}'_y = 0$  and  $\tilde{B}'_x = 0$ .

The appearance of the equality (12.86) is caused by the fact that we consider the perturbation, for which only the constant  $C_0$  differs from zero, but not an arbitrary one. Given another perturbation is present inside the RCL, the condition (12.86) is generally not satisfied. As  $\delta B_x$  in magnetoacoustic waves do not equal zero, condition (12.86) together with (12.84) and (12.85) represents four boundary conditions, relating the amplitudes of the waves outside the RCL. Note that equalities (12.57) and (12.58) do not give additional boundary conditions, since they are valid for the perturbations in magnetoacoustic waves.

### 12.5.2 Solutions of the Boundary Equations

Now we write Eqs. (12.84)–(12.86) in an explicit form, i.e. expressing all small quantities in terms of the perturbation of density. As was pointed out at the end of Sect. 12.4, the superposition of the waves (12.23) and (12.24) outside the RCL corresponds to the superposition of the solutions (12.68)–(12.71) and (12.76) inside it.

This being so, the waves (12.23) and (12.24) are present outside the RCL, but the amplitudes of the waves (12.12), (12.21), and (12.22) equal zero, if inside it only the constant  $C_0$  differs from zero. Using the relationship between the perturbations of MHD quantities in magnetoacoustic waves in approximation (12.9) we obtain from the boundary conditions (12.84)–(12.86), respectively

$$\sum_{i=1}^3 \frac{k_{y+}^{(i)}}{(k^{(i)})^2} \left( \delta \rho_+^{(i)} + \delta \rho_-^{(i)} \right) = 0, \quad (12.87)$$

$$\sum_{i=1}^3 \frac{1}{(k^{(i)})^2} \left( \delta \rho_+^{(i)} - \delta \rho_-^{(i)} \right) = 0, \quad (12.88)$$

$$\sum_{i=1}^3 \left( \frac{k_y^{(i)}}{k^{(i)}} \right)^2 \delta \rho_{\pm}^{(i)} = 0. \quad (12.89)$$

Here the indexes + and – denote the quantities outside the RCL for  $y = +\infty$  and  $y = -\infty$ , the index  $i$  specifies three waves (12.23) and (12.24); and it is taken into account that

$$k_{y+}^{(i)} = -k_{y-}^{(i)}$$

due to the plasma flow symmetry.

Let us find the solutions of these equations for the cases of the inflowing and the outflowing of a plasma, i.e. determine the amplitudes of outgoing waves versus the amplitudes of incident ones.

If the plasma flows into the layer, then there are two outgoing waves: one on each side. As there are four equations, set (12.87)–(12.89) has solutions only for a definite relationship between the amplitudes of incident waves. If these amplitudes are arbitrary, then the set of Eqs. (12.87)–(12.89) does not have a solution. It means that for such perturbations condition (12.86) cannot be satisfied. Since equality (12.86) is valid always, when  $C_0$  is the only constant which differs from zero, a violation of this equality results in the fact that the other constants, i.e. the amplitudes of the perturbations with  $k_y^{in} \gg 1/a$ , differ from zero. Hence, in this case, the boundary conditions do not exist on the surface of the layer, i.e. it is not a discontinuity, and the conclusion of its evolutionarity cannot be obeyed.

Let the plasma flow out from the current layer. In this case there are four outgoing waves (two on each side). Denote them by the indexes  $i = 1, 2$ . Then their amplitudes  $\delta\rho_{\pm}^{(1,2)}$  are expressed in terms of the amplitudes  $\delta\rho_{\pm}^{(3)}$  of incident waves in the following way

$$\begin{aligned}\delta\rho_{\pm}^{(1)} &= -\frac{1}{2} \left( \frac{k^{(1)}}{k^{(3)}} \right)^2 \frac{k_y^{(2)} - k_y^{(3)}}{k_y^{(2)} - k_y^{(1)}} \\ &\times \left[ \frac{k_y^{(3)}}{k_y^{(1)}} \left( \delta\rho_{+}^{(3)} + \delta\rho_{-}^{(3)} \right) \pm \frac{k_y^{(2)} + k_y^{(3)}}{k_y^{(2)} + k_y^{(1)}} \left( \delta\rho_{+}^{(3)} - \delta\rho_{-}^{(3)} \right) \right],\end{aligned}\quad (12.90)$$

$$\delta\rho_{\pm}^{(2)} = -\left( \frac{k^{(2)}}{k^{(3)}} \right)^2 \left[ \left( \frac{k_y^{(3)}}{k^{(3)}} \right)^2 \delta\rho_{\pm}^{(3)} + \left( \frac{k_y^{(1)}}{k^{(1)}} \right)^2 \delta\rho_{\pm}^{(1)} \right].\quad (12.91)$$

In formula (12.90) all the quantities  $k_y^{(i)}$  are taken for one side of the discontinuity. From (12.90) it follows that if  $k_y^{(1)} = k_y^{(2)}$  and  $k_y^{(2)} \neq k_y^{(3)}$ , then  $\delta\rho_{\pm}^{(1)}$  turns to infinity, i.e. the coefficients of refraction and reflection are not limited.

Let us find the conditions under which the wave vectors of two outgoing waves coincide. In Sect. 12.2 it was shown that if

$$|\nu_y^{ex}| < \frac{3\sqrt{3}}{16} \frac{V_s^3}{V_A^2},\quad (12.92)$$

then the resonant angle  $\theta_0^*$  exists, for which the expression in the round brackets in formula (12.24) equals zero and two roots (12.24) coincide. This angle is determined by Eq. (12.25).

Provided  $\theta_0 = \theta_0^*$ , both waves (12.24) are outgoing, since if the plasma flows out from the current layer, then there is only one incoming wave. In the present case its wave vector is given by formula (12.23) and  $k_y^{(2)} \neq k_y^{(3)}$ . If condition (12.92) is not valid, then the expression in the round brackets in (12.24) is negative and the

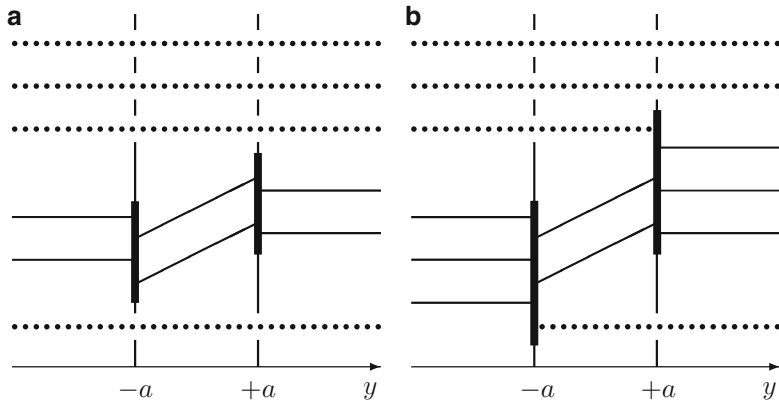


**Fig. 12.4** Schematic representation of solutions of the linear MHD equations in the case of normal (a) and oblique (b) propagation

corresponding waves are surface ones for all  $\theta_0$  (see Sect. 12.2). In this case all wave vectors are different and  $k_y^{(i)} \neq \pm k_y^{(j)}$  for  $i \neq j$ . So the coefficients of refraction and reflection are limited.

For the definite, but rather general, distribution of the unperturbed MHD properties inside the RCL the expressions describing the perturbation (and thus the transition between the perturbations with  $k_y \ll 1/a$  and  $k_y \gg 1/a$ ) can be found in an analytical form (Markovskii and Somov 1996). These solutions are represented schematically in Fig. 12.4.

Horizontal solid and dotted lines represent the solutions with  $k_y \ll 1/a$  and  $k_y \gg 1/a$  respectively. Inclined lines represent the solutions that do not satisfy the WKB approximation. Superposition of perturbations on one side of the bold line  $y = \pm a$  transforms to superposition of perturbations on the other side.

In the case of normal propagation the long waves,  $k_y \ll 1/a$ , do not transform to the short ones,  $k_y \gg 1/a$ , (see Fig. 12.4a). In this case the long waves interact with the RCL as with a tangential discontinuity, i.e. as if  $v_y$  equals zero. The amplitudes of the waves satisfy the linearized boundary conditions for magnetoacoustic waves at a tangential discontinuity with  $v_{x1} = v_{x2}$ :

$$\left\{ \delta p + \frac{B_x \delta B_x}{4\pi} \right\} = 0, \quad \{ \delta v_y \} = 0. \quad (12.93)$$

There are thus two boundary equations and two outgoing waves (see Sect. 12.2.2) regardless of the sign of  $v_y$ . Moreover these equations always have a unique solution, therefore the RCL is evolutionary with respect to normally propagating waves.

Another situation arises in the case of oblique propagation. In this case long waves outside the layer transform inside it to short waves. This imposes two additional boundary conditions on the perturbations that interact with the layer as

with a discontinuity, because for such perturbations the amplitudes of short waves must be equal zero. Therefore

the reconnecting current layer (RCL) behaves like a discontinuity only with respect to a specially selected perturbation.

We emphasize that the conditions (12.93) appear as a result of the properties of the solutions of the linearized MHD equations, while the additional conditions occur due to the fact that we consider the perturbation which is not arbitrary. An otherwise additional condition generally does not hold.

With respect to these perturbations the problem of evolutionarity can be posed. However, the conclusions on non-evolutionarity are different for the domain of direct current, where the plasma flows into the RCL, and for the domains of reverse current, where the plasma flows out.

### 12.5.3 Evolutionarity and Splitting of Current Layers

Thus we have obtained the criterion of evolutionarity for the RCL as a discontinuity.

If the plasma flows into the layer (in the region DC of the direct current in Figs. 12.1b and 12.3) or if inequality (12.92) does not hold, then **the conclusion of non-evolutionarity cannot hold**. In this case the current layer either does not behave like a discontinuity or else the problem of its infinitesimal perturbation has a single solution. The last is the case when we can consider an ordinary problem of linear stability. For example, the question on the linear tearing instability always exists concerning the central part (the region of the direct current) of the RCL (see Chap. 13).

Let the relation (12.92) be valid, provided the plasma flows out from the layer (in the regions RC of the reverse current in Figs. 12.1b and 12.3), and the outflow velocity is less than the projection of the group velocity of a slow magnetoacoustic wave on the normal to the layer (see (12.92)). Then the perturbation exists, for which, firstly, the boundary conditions on the surface of the layer are true, and, secondly, the amplitudes of the outgoing waves are as large as is wished, compared with the amplitudes of the incident ones in the limit  $\varepsilon_i \rightarrow 0$ , i.e. when the conductivity is large enough.

Such a perturbation inside the RCL is the solution of the set of Eqs. (12.32)–(12.37) proportional to  $C_0$ , and is characterized by the resonant angle  $\theta_0^*$  from (12.25) outside it. Thus the perturbation is not described by linear equations and the problem of its time evolution does not have a single solution. Hence the current layer is non-evolutionary, as **the initial perturbation of the MHD flow is not small**. This perturbation may be the splitting of the RCL into shock waves that are observed in the numerical experiments carried out by Brushlinskii et al. (1980), Podgornii and Syrovatskii (1981), and Biskamp (1986, 1997).

Therefore we have found a possible cause of splitting of the RCL into a set of the one-dimensional MHD discontinuities observed in numerical experiments. Moreover we have obtained the condition under which the splitting takes place. This allows us to unify the two regimes of magnetic reconnection in current layers: with attached shocks (see Chap. 3) and without them. Such a unified model can be used to describe unsteady phenomena in astrophysical plasma, which occur as a result of magnetic reconnection.

## 12.6 Practice: Exercises and Answers

**Exercise 12.1.** Discuss basic properties of the Petschek-type reconnecting region with the four slow MHD shocks shown in Fig. 12.5 ([Petschek 1964](#)).

**Answer.** As shown in Fig. 12.5, there is a diffusion region  $D$  which occupies a small central part of the area under consideration. Two pairs of the slow MHD shock waves  $S_-$  propagate away from the diffusion region. These shocks may be regarded loosely as current layers extending from the reconnecting current layer (RCL) in Fig. 12.2.

While plasma flow carries magnetic field through these shock waves, the direction of the magnetic field vector rotates towards the normal, and the strength of the field decreases in this process. When the inflow velocity  $v_0$  is much less than the Alfvén velocity, the angle  $\alpha$  becomes very small, which makes the external flow almost uniform. As the inflow velocity increases, the inclination of the waves increase, which in turn decreases the field strength at the diffusion region.

[Petschek \(1964\)](#) estimated the maximum inflow velocity by assuming that the magnetic field in the inflow regions is potential and uniform at large distances. The reconnection rate turns out to be

$$\frac{v_0}{V_{A,0}} \approx \frac{1}{\log Re_m}. \quad (12.94)$$

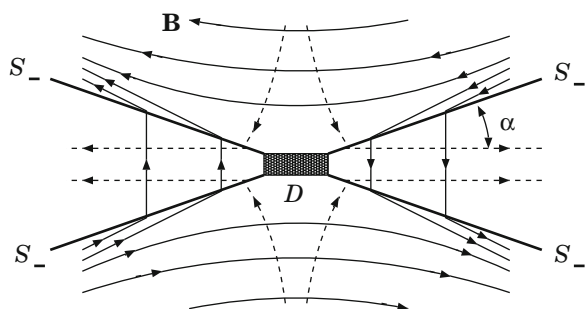


**Fig. 12.5** The Petschek-type reconnecting flow

When the magnetic Reynolds number  $\text{Re}_m$  is sufficiently large, the Petschek reconnection rate would still correspond to a much faster inflow compared to the Sweet-Parker rate given by formula (8.23). In this sense, [Petschek \(1964\)](#) was the first to propose a *fast reconnection* model.

The elegance of this simple model has meant that it has been possible to generalize it in several ways; this has been done by different authors. These further developments cast even more serious doubt on the validity of the Petschek model. Since the reconnection rate may depend sensitively on the boundary conditions, building detailed and realistic models of reconnection is an extremely challenging problem (see [Biskamp 1997](#)).

# Chapter 13

## Tearing Instability of Reconnecting Current Layers

**Abstract** The tearing instability can play a significant role in dynamics of reconnecting current layers, but it is well stabilized in many cases of interest. For this reason, quasi-stationary current layers can exist for a long time in astrophysical plasma, for example in the solar corona, in the Earth magnetospheric tail.

### 13.1 The Origin of the Tearing Instability

#### 13.1.1 Two Necessary Conditions

Among the host of the low-frequency instabilities appearing in thin reconnecting current layers (e.g., Zelenyi et al. 2009), the tearing mode is of fundamental value for processes which transform ‘free’ magnetic energy into other kinds of energy. In a sense,

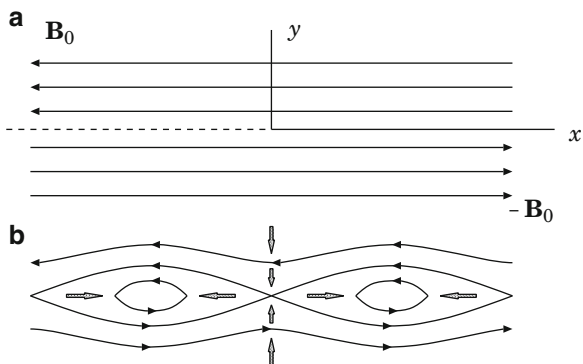
the tearing instability of current layers is an integral part of the magnetic reconnection effect.

It is conceivable that the instability can play the role of a triggering mechanism for many of its essentially geostationary manifestations in astrophysical plasma – flares on the Sun and in magnetospheres of the Earth and other astrophysical bodies.

The tearing instability has a universal character and arises in reconnecting current layers over quite a wide range of their parameter values. In fact, it is seen from the 2D picture of the magnetic field lines shown in Fig. 13.1a, that this state with the neutral current layer at  $y = 0$  is energetically high and hence it must tend to a lower one, depicted in Fig. 13.1b.

Such a transition may be interpreted as a process of coalescence of parallel currents constituting the current layer. However, for ideally conducting plasma, the process is impossible since it implies the displacement of field lines, leading to their tearing and the formation of closed loops – magnetic islands. This transition, i.e. the

**Fig. 13.1** (a) Magnetic field ‘reversal’, a peculiarity of the configuration of field lines in a neutral current layer. (b) Magnetic-field lines in the course of the tearing instability; the arrows show the plasma velocity directions



reconnection of field lines, is known to be forbidden by the condition of magnetic lines freezing into plasma (see Part I, Sect. 12.3.2). Such a restriction is removed given a finite (even if very high) electric conductivity. Thus

for the tearing instability to develop, two conditions are necessary:  
 (1) magnetic field reversal and (2) the availability of a finite electric conductivity.

The instability is called *tearing* because, as we have seen, its growth, once unbounded, causes the current layer to tear into separate filaments.

### 13.1.2 Historical Comments

(a) **The tearing instability.** Before giving an account of the theory of the tearing instability, let us briefly describe the history of the question. [Dungey \(1958\)](#) supposed that the availability of a neutral line in a plasma with finite conductivity leads to the instability giving rise to the current concentration. This hypothesis was based on the consideration of a *non-equilibrium* configuration of the magnetic field with an X-line whose separatrix (forming the letter X) lines intersect at an angle not equal to  $\pi/2$  (see also discussion of the paper by [Zwingmann et al. \(1985\)](#) in Chap. 16).

The presence of the instability was experimentally found in configurations of a pinch type ([Colgate and Furth 1960](#)), for which stability had been predicted by the ideal MHD theory. Using Dungey’s mechanism, [Furth \(1961\)](#) qualitatively explained the current layer tearing instability. [Murty \(1961\)](#) investigated the same process theoretically and found the presence of the tearing mode in a resistive current layer for the low conductivity case. Finally,

the theory of *resistive* MHD instabilities was thoroughly developed for the case of the *neutral* current layer without plasma flows,

in the famous work of [Furth et al. \(1963\)](#).

In the framework of the kinetic approach the first fundamental results on the tearing instability were obtained by [Coppi et al. \(1966\)](#). They showed that the tearing instability arises from coupling between a negative energy wave and a dissipative process. Landau resonance of electrons inside and near the zero magnetic field plane was proposed to provide the appropriate dissipation mechanism (Sect. 13.6).

- (b) Stabilization mechanisms.** In parallel with the investigation of the tearing instability, mechanisms resulting in its stabilization were searched for. Why? – The point is that laboratory and numerical experiments, as well as astrophysical observations, contrary to theoretical predictions, allowed one to conclude that **reconnecting current layers can be stable for a long time**. The appearance of such stable states is of paramount importance, in particular, for the physics of reconnecting current layers (RCLs) in the astrophysical plasma.

[Furth \(1967\)](#) proposed the hypothesis that the tearing mode is suppressed by a small *transversal* magnetic field (i.e., perpendicular to the current layer). As pointed out by [Pneuman \(1974\)](#),

such a *non-neutral* current layer, cannot be topologically affected by an infinitesimal displacement,

as opposed to a neutral current layer that does not contain a transversal field. This suggests that a disturbance of *finite* amplitude is necessary to disturb the RCL, i.e. the configuration could be *metastable* (see Sect. 13.6.3). The stabilizing effect of the transversal field was demonstrated in the frame of the kinetic approach by [Schindler \(1974\)](#), and [Galeev and Zelenyi \(1976\)](#). It was shown by [Pellat et al. \(1991\)](#) that the Harris-type current layer is completely stable against the ion tearing mode in the presence of a finite value of a transversal magnetic component.

On the contrary, [Janicke \(1980, 1982\)](#) considered the same hypothesis in the context of MHD and drew the conclusion that the stabilizing influence was absent. This was the reason why a fundamental indecision as to the role of the transversal field remained for a long time. On the one hand, [Somov and Verneta \(1988, 1989\)](#) demonstrated a considerable stabilizing effect within the limits of the MHD approach. They also explained the reasons for negative results due to Janicke. Incidentally, on the other hand, [Otto \(1991\)](#) and [Birk and Otto \(1991\)](#) once again confirmed the conclusion that, in the context of Janicke's model, the transversal component of the magnetic field does not change the tearing increment. A comparative review of alternative approaches is given in [Somov and Verneta \(1993\)](#). As we shall also see in Sect. 13.4,

the transversal component of the magnetic field does modify the collisional tearing mode in such a way that it results in its stabilization.

Having finished this brief introduction, we come now to an account of the basic theory of the tearing instability.

## 13.2 The Simplest Problem and Its Solution

In Chap. 12, we obtained the criterion of evolutionarity for the RCL with respect to magnetoacoustic waves. We saw that in the region of the direct current, the current layer either does not behave like a discontinuity or else the problem of its small perturbation has a single solution. Therefore, in this region, we are well motivated to consider an ordinary problem of linear stability.

### 13.2.1 The Model and Equations for Small Disturbances

We begin by obtaining an expression for the growth rate of a *pure* tearing instability without additional stabilizing or destabilizing effects. For this purpose, we consider the case when the instability increment is much larger than the inverse time of magnetic diffusion  $\tau_r$ . As will be shown in Sect. 13.5, once these quantities are of the same order, the effect of plasma compressibility becomes decisive. Provided diffusion may be ignored, plasma drift into the reconnecting current layer (RCL) becomes unimportant since its characteristic time is also  $\tau_r$ . For the case  $\omega \gg V/b$  ( $\omega$  is the instability increment,  $V$  is the speed of plasma outflow from the RCL,  $b$  is its half-width, see Fig. 1.5), the plasma flow along the current layer is negligible as well.

Let us consider the instability in a *linear* approximation:

$$f(\mathbf{r}, t) = f_0(\mathbf{r}) + f_1(\mathbf{r}, t).$$

Unperturbed quantities in the frame of the simplest model depend only upon the  $y$  coordinate which is perpendicular to the current layer as shown in Fig. 13.1a:

$$f_0 = f_0(y).$$

Hence small perturbations are of the form

$$f_1(\mathbf{r}, t) = f_1(y) \exp[i(k_x x + k_z z) + \omega t], \quad (13.1)$$

provided  $1/k_x \ll b$ .

The set of the MHD equations for an *incompressible* plasma with a finite conductivity  $\sigma$  is reduced to the following one:

$$\begin{aligned} \text{rot} \left( \rho \frac{d\mathbf{v}}{dt} \right) &= \text{rot} \left( \frac{1}{4\pi} \text{rot} \mathbf{B} \times \mathbf{B} \right), \\ \frac{\partial \mathbf{B}}{\partial t} &= \text{rot}(\mathbf{v} \times \mathbf{B}) - \text{rot} \left( \frac{\eta}{4\pi} \text{rot} \mathbf{B} \right), \\ \frac{\partial \rho}{\partial t} + \mathbf{v} \cdot \nabla \rho &= 0, \quad \frac{\partial \eta}{\partial t} + \mathbf{v} \cdot \nabla \eta = 0, \\ \text{div } \mathbf{v} &= 0, \quad \text{div } \mathbf{B} = 0. \end{aligned}$$

Here  $\eta = c^2/\sigma$  is the value proportional to magnetic diffusivity (see Appendix C); the other symbols are conventional. This set gives the following equations for the perturbations:

$$\begin{aligned} \omega \operatorname{rot}(\rho_0 \mathbf{v}_1) &= \operatorname{rot} \left\{ \frac{1}{4\pi} [(\mathbf{B}_0 \cdot \nabla) \mathbf{B}_1 + (\mathbf{B}_1 \cdot \nabla) \mathbf{B}_0] \right\}, \\ \omega \mathbf{B}_1 &= (\mathbf{B}_0 \cdot \nabla) \mathbf{v}_1 - (\mathbf{v}_1 \cdot \nabla) \mathbf{B}_0 - \frac{1}{4\pi} (\nabla \eta_0 \times \operatorname{rot} \mathbf{B}_1 \\ &\quad - \eta_0 \Delta \mathbf{B}_1 + \nabla \eta_1 \times \operatorname{rot} \mathbf{B}_0 - \eta_1 \Delta \mathbf{B}_0), \\ \omega \rho_1 + \mathbf{v}_1 \cdot \nabla \rho_0 &= 0, \quad \omega \eta_1 + \mathbf{v}_1 \cdot \nabla \eta_0 = 0, \\ \operatorname{div} \mathbf{v}_1 &= 0, \quad \operatorname{div} \mathbf{B}_1 = 0. \end{aligned}$$

These dimensional equations are reduced to two dimensionless equations containing  $y$  components of the velocity and magnetic field perturbations as unknown variables:

$$(\tilde{\rho} W')' = \alpha^2 \tilde{\rho}^2 W - \frac{S^2 \alpha^2}{p} (\alpha^2 F \Psi + F'' \Psi - F \Psi''), \quad (13.2)$$

$$\Psi'' = \left( \alpha^2 + \frac{p}{\tilde{\eta}} \right) \Psi + \left( \frac{F}{\tilde{\eta}} + \frac{\tilde{\eta}' F'}{p \tilde{\eta}} \right) W. \quad (13.3)$$

Here

$$\begin{aligned} \Psi &= \frac{B_{1y}}{B(a)}, \quad W = -i v_{1y} k \tau_r, \quad \mu = \frac{y}{a}, \\ F &= \frac{\mathbf{k} \cdot \mathbf{B}_0}{k B(a)}, \quad k = (\mathbf{k}^2)^{1/2}, \quad \alpha = k a, \quad \tau_r = \frac{4\pi a^2}{\langle \eta \rangle}, \\ \tau_A &= \frac{a (4\pi \langle \rho \rangle)^{1/2}}{B(a)}, \quad S = \frac{\tau_r}{\tau_A}, \quad p = \omega \tau_r, \quad \tilde{\eta} = \frac{\eta_0}{\langle \eta \rangle}, \quad \tilde{\rho} = \frac{\rho_0}{\langle \rho \rangle}. \end{aligned}$$

Thus we intend to solve Eqs. (13.2) and (13.3). As will be seen from the final results, the tearing instability is a *long-wave* mode:

$$\alpha^2 \ll 1. \quad (13.4)$$

Hence this case is considered from the beginning. For definiteness, the following distribution of the unperturbed field is chosen:

$$\mathbf{B}_0 = F(\mu) \mathbf{e}_x,$$

where

$$F(\mu) = \begin{cases} -1, & \mu < -1, \\ \mu, & -1 < \mu < 1, \\ 1, & \mu > 1. \end{cases}$$

Let us examine the instability mode with the *fastest* growth, for which the condition

$$\mathbf{k} \parallel \mathbf{B}_0$$

holds. Assume that

$$S \gg 1, \quad (13.5)$$

i.e., the plasma is highly-conductive (compare definition of  $S$  with definition of the magnetic Reynolds number (Appendix C) where  $v = V_A$ ,  $L = a$ ). What this means is that

**||** dissipative processes in such a regime are not large in magnitude, while they play a principle role in the tearing instability,  
as was mentioned in the previous section.

### 13.2.2 The External Non-dissipative Region

Starting from some distance  $y$  from the neutral plane  $y = 0$  of the current layer, the dissipative processes may be ignored. We shall call this region the *external non-dissipative* one. In the limiting case

$$S = \frac{\tau_r}{\tau_A} = \frac{V_A a}{v_m} \rightarrow \infty,$$

Equation (13.2) is simplified to

$$\Psi'' - \left( \alpha^2 + \frac{F''}{F} \right) \Psi = 0. \quad (13.6)$$

The function  $\Psi$  should be even for reasons of symmetry:

$$\Psi(-\mu) = \Psi(\mu). \quad (13.7)$$

The boundary condition for the sought-after function must be formulated for  $\mu \rightarrow \infty$ :

$$\Psi \rightarrow 0. \quad (13.8)$$

Since  $\mu = y/a \neq 0$ , Eq. (13.6), under conditions (13.7) and (13.8), has the following solution:

$$\Psi = \begin{cases} A \exp [\alpha(\mu + 1)], & \mu < -1, \\ A \{[\cosh \alpha + (1 - \alpha^{-1}) \sinh \alpha] \cosh \alpha \mu + \\ + [\sinh \alpha + (1 - \alpha^{-1}) \cosh \alpha] \sinh \alpha \mu\}, & -1 < \mu < 0, \\ \Psi(-\mu), & \mu > 0. \end{cases} \quad (13.9)$$

Here  $A$  is an arbitrary constant.

The derivative  $\Psi'$  suffers a rupture at the point  $\mu = 0$ , with

$$\Delta' = \left. \frac{\Psi'}{\Psi} \right|_{-0}^{+0} \approx \frac{2}{\alpha} \quad (13.10)$$

for  $\alpha^2 \ll 1$ . This fact signifies that the solution applicable in the external non-dissipative region corresponds to a singular current at the  $\mu = 0$  plane.

The approximation  $S \rightarrow \infty$  is not applicable in a neighbourhood of the point  $\mu = 0$ . This will be called the *internal dissipative* region. Outside this region the solution is described by the function (13.9) which, for  $\mu \rightarrow 0$  (once  $\alpha^2 \ll 1$ ), gives the asymptotic expression

$$\Psi \sim \text{const} \left( 1 + \frac{1}{\alpha} |\mu| \right). \quad (13.11)$$

### 13.2.3 The Internal Dissipative Region

Let us consider now the neighbourhood of the point  $\mu = 0$  where the condition  $S \rightarrow \infty$  does not hold. Since this region is sufficiently small, the quantities  $\tilde{\rho}$  and  $\tilde{\eta}$  may be assumed to vary weakly inside it. On using this assumption and making the change of variables

$$\theta = \left( \frac{\alpha^2 S^2}{p} \right)^{1/4} \mu, \quad (13.12)$$

$$Z = \Psi'', \quad (13.13)$$

the set of Eqs. (13.2) and (13.3) results in the equation for the function  $Z = Z(\theta)$

$$Z''' = (\nu + \theta^2) Z' + 4\theta Z. \quad (13.14)$$

This equation must be supplemented by the conditions

$$\begin{aligned} Z(-\theta) &= Z(\theta), \\ Z \rightarrow 0 &\quad \text{for } \theta \rightarrow \infty. \end{aligned} \tag{13.15}$$

We find from (13.14) to (13.15) that the sought-after function  $Z(\theta)$  has the following asymptotic behaviour for  $\theta \gg 1$  ( $\theta \rightarrow \infty$ ):

$$Z \sim A_1 \exp(-\theta^2/2) + B \theta^{-4}. \tag{13.16}$$

For  $\theta < 1$  the function  $Z(\theta)$  has no singularities and can be expanded in a Taylor series.

In order to obtain the dispersion relation the integrals

$$I_0 = \int_0^{+\infty} \Psi'' d\mu, \quad I_1 = \int_0^{+\infty} \Psi'' \mu d\mu \tag{13.17}$$

have to be evaluated. On normalizing the function  $Z(\theta)$  by the condition

$$Z(0) = 1,$$

we find from (13.16) that

$$\tilde{I}_0 = \int_0^{+\infty} Z(\theta) d\theta \approx 1, \quad \tilde{I}_1 = \int_0^{+\infty} Z(\theta) \theta d\theta \approx 1. \tag{13.18}$$

The integrals (13.17) are expressed through (13.18).

For the function  $\Psi(\theta)$ , we have

$$\Psi(\theta) = \int_0^\theta d\theta_1 \int_0^{\theta_1} Z(\theta_2) d\theta_2,$$

whence

$$\Psi(\mu) \sim \text{const} \left( 1 + \frac{I_0}{(1/p) - I_1} |\mu| \right) \tag{13.19}$$

for  $\theta \rightarrow \infty$ . Here it is taken into account that

$$\Psi''_{\mu\mu}(0) = p \Psi(0).$$

### 13.2.4 Matching of the Solutions and the Dispersion Relation

As is seen from the asymptotic solution (13.16), the approximation  $S \rightarrow \infty$  is valid once  $\mu \gg \varepsilon_0$ , where

$$\varepsilon_0 = \left( \frac{p}{\alpha^2 S^2} \right)^{1/4}. \quad (13.20)$$

Hence the function (13.19) must coincide with (13.12). Equating them results in the dispersion equation

$$\left( 1 - \frac{p^{3/2}}{\alpha S} \right) - p \alpha \left( \frac{p}{\alpha^2 S^2} \right)^{1/4} = 0. \quad (13.21)$$

There is no difficulty in understanding that, given the ratio

$$\frac{p^{3/2}}{\alpha S} \ll 1, \quad (13.22)$$

the equation is reduced to

$$p \approx \left( \frac{S}{\alpha} \right)^{2/5}, \quad (13.23)$$

while given

$$p \alpha \left( \frac{p}{\alpha^2 S^2} \right)^{1/4} \ll 1, \quad (13.24)$$

it reduces to

$$p = (\alpha S)^{2/3}. \quad (13.25)$$

Conditions (13.22) and (13.24) are equivalent to

$$p \alpha^2 \gg 1 \quad (13.26)$$

and

$$p \alpha^2 \ll 1, \quad (13.27)$$

respectively. Region (13.26) may be termed that of ‘short’ waves, whereas region (13.27) is that of ‘long’ waves. In the former the growth rate increases with the increase of the wavelength, while decreasing in the latter.

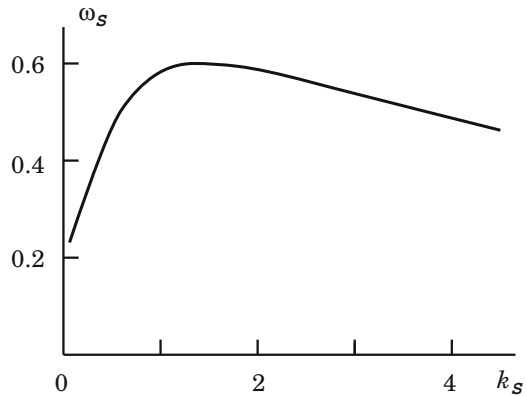
At  $p \alpha^2 \sim 1$ , i.e., when  $\alpha \sim S^{1/4}$ , the growth rate reaches the maximum

$$p_{\max} \sim S^{1/2}. \quad (13.28)$$

Recall that the dimensionless parameters

$$\alpha = ka = \frac{2\pi a}{\lambda}, \quad p = \omega \tau_r.$$

**Fig. 13.2** The dependence of the tearing instability increment  $\omega_s$  on the wave vector  $k_s$



Without using the condition  $\alpha^2 \ll 1$ , Eq. (13.6) shows that  $\Delta' \approx 0$  for  $\alpha \approx 1$ . So the tearing instability completely disappears for  $\alpha \approx 1$  and exists in the region of the wave length

$$\lambda > 2\pi a.$$

(13.29)

That is why it is called a *long-wave* instability.

As  $\alpha \rightarrow S^{-1}$ , the increment tends to  $\tau_r^{-1}$ . As was mentioned earlier, in this case, i.e. in the region  $\alpha < S^{-1}$ , the effect of compressibility becomes dominant. It will be discussed in Sect. 13.5.

Expression (13.23) was obtained analytically by Furth et al. (1963); they also obtained the dependence (13.25) numerically. The results of the numerical solution of the general Eq. (13.21) are given in Fig. 13.2, using the notation

$$\omega_s = \omega \tau_r S^{-1/2}, \quad k_s = ka S^{1/4}. \quad (13.30)$$

Recall that the dimensionless parameter  $S$  is the Lundquist number (8.24) but determined with respect to the current-layer thickness  $a$ .

## 13.3 Physical Interpretation of the Instability

### 13.3.1 Acting Forces of the Tearing Instability

We now present another derivation of the dispersion relations, based on the consideration of the physical mechanism of the tearing instability (Furth et al. 1963). Let us make use of the absolute system of units where the speed of light  $c = 1$ . Besides, every coefficient of order unity will be set equal to unity.

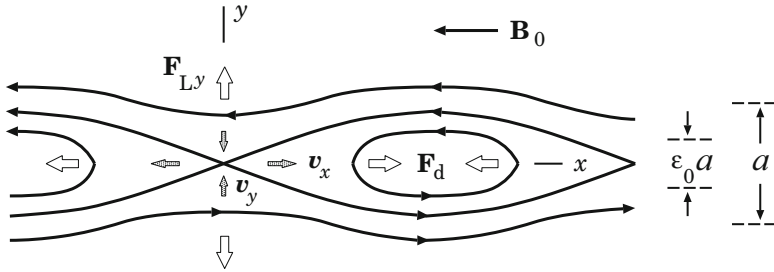


**Fig. 13.3** The magnetic field lines and the velocity in the course of the development of a tearing instability. The small arrows show velocity directions. Forces are shown by thick empty arrows.  $\varepsilon_0 a$  is the internal region thickness. The case  $\varepsilon_0 < \alpha$  is shown

Let a small perturbation appear in the reconnecting current layer (RCL). As a consequence of the magnetic field structure (namely, the antiparallel directions of reconnecting components on either side of the neutral plane), a *driving force*  $F_d$  of the instability arises, accelerating the plasma along the  $x$  axis, i.e. along the width of the layer (see Fig. 13.3). This force corresponds to a simple fact:

the parallel electric currents flowing inside the neutral layer attract each other and tend to coalesce into separate current filaments.

Thus the driving force of the instability generates plasma motions inside the RCL, directed along the  $x$  axis, with a velocity  $v_{1x}$ . As this takes place, the surrounding plasma must, by virtue of the flow continuity, flow into the internal region with a velocity  $v_{1y}$ . As a consequence, the electric current  $j_s$  arises, giving rise to the corresponding Lorentz force  $F_{Ly}$ , hindering the plasma from flowing into the internal region:

$$j_s = \sigma v_{1y} \varepsilon_0 B, \quad F_{Ly} = j_s \varepsilon_0 B = \sigma v_{1y} (\varepsilon_0 B)^2.$$

Here we have taken into account that the reconnecting component of the field at the boundary of the internal region is equal to  $B_x(y) = \varepsilon_0 B$ , where  $\varepsilon_0 a$  is the thickness of the internal region.

The force  $F_{Ly}$  is directed against the plasma motion and is comparable in magnitude with the driving force  $F_d$  of the instability.

Hence the power with which the driving force performs work on a unit volume of the plasma is

$$P = v_{1y} F_{Ly} = \sigma v_{1y}^2 (\varepsilon_0 B)^2. \quad (13.31)$$

This power goes to acceleration of the plasma; that is why

$$P = K, \quad (13.32)$$

where  $K$  is the kinetic energy acquired by the unit plasma volume in unit time:

$$K = \omega\rho v_{1x}^2 = \omega\rho \frac{v_{1y}^2}{(k\epsilon_0 a)^2}. \quad (13.33)$$

Here use is made of the incompressibility condition  $\operatorname{div} \mathbf{v} = 0$ :

$$v_{1x} = \frac{v_{1y}}{k\epsilon_0 a}.$$

On comparing (13.31) and (13.33), an expression for the thickness of the internal dissipative region is found,

$$\epsilon_0 = \left( \frac{\omega\rho}{k^2 a^2 B^2 \sigma} \right)^{1/4}, \quad (13.34)$$

which coincides with expression (13.9), obtained earlier from the analytical solution.

### 13.3.2 Dispersion Equation for Tearing Instability

Let us now find the dispersion relations. In the dissipative region, where the flows of plasma and field lines are relatively independent, the first addendum on the right-hand side of Ohm's law

$$\eta \mathbf{j} = \mathbf{E} + \mathbf{v} \times \mathbf{B}$$

dominates the second one, though these two are of the same order of magnitude. What this means is that  $\epsilon_0 a$  must be taken in such a way that

$$\eta j_1 \sim E_1. \quad (13.35)$$

However the plasma and magnetic field line motions are not completely independent, even in the internal dissipative region. The electric field perturbation  $E_1$  is related with that of the magnetic field perturbation  $B_1$  through

$$E_1 \sim \frac{\omega B_{1y}}{k}.$$

Using the Maxwell's equations

$$\operatorname{rot} \mathbf{B} = \frac{4\pi}{c} \mathbf{j} \quad \text{and} \quad \operatorname{div} \mathbf{B} = 0,$$

we obtain

$$j_1 \sim \frac{B_1''}{4\pi k} \quad (13.36)$$

once  $ka < 1$ . Relations (13.35) and (13.36) give rise to

$$\frac{\omega B_{1y}}{\eta} \sim \frac{B_{1y}''}{4\pi}. \quad (13.37)$$

Now the quantity  $B_{1y}''$  has to be evaluated. As a consequence of a partial freezing-in, magnetic field deviations during the plasma motion along the layer in a region with a thickness

$$a\tilde{\varepsilon} \sim a^2 k,$$

since  $a\tilde{\varepsilon}\lambda \sim a^2$ . For

$$a\tilde{\varepsilon} > a\varepsilon_0 \quad (13.38)$$

this gives the estimate

$$B_{1y}'' \sim \frac{B_{1y}'}{\varepsilon_0 a} \sim \frac{B_{1y}}{\varepsilon_0 a \tilde{\varepsilon} a} \sim \frac{B_{1y}}{\varepsilon_0 k a^3}, \quad (13.39)$$

whereas for

$$a\tilde{\varepsilon} < a\varepsilon_0 \quad (13.40)$$

one has

$$B_{1y}'' \sim \frac{B_{1y}'}{\varepsilon_0 a} \sim \frac{B_{1y}}{(\varepsilon_0 a)^2}. \quad (13.41)$$

It is a simple matter to see that the inequality (13.38) is equivalent to the inequality (13.26) determining the region of short-wave perturbations, while the inequality (13.40) is equivalent to (13.27) which corresponds to the long-wave region. Substituting the relations (13.39) and (13.41) in (13.37), with care taken of (13.34), leads to the dispersion relations:

$$\omega^5 = \frac{\eta^3 B^3}{a^{10} \rho} \frac{1}{k^2} \quad (13.42)$$

for the case (13.38), and

$$\omega^3 = \frac{\eta B^2}{a^2 \rho} k^2 \quad (13.43)$$

for the case (13.40). Equations (13.42) and (13.43) are easily shown to be equivalent, respectively, to Eqs. (13.23) and (13.25), obtained analytically in Sect. 13.2.

## 13.4 The Stabilizing Effect of Transversal Field

While describing the effect of a transversal magnetic field, our attention will be centered on the physical picture of the phenomenon. In this way we are able to understand the stabilization mechanism and easily obtain the dispersion relations for the tearing instability with a transversal field.

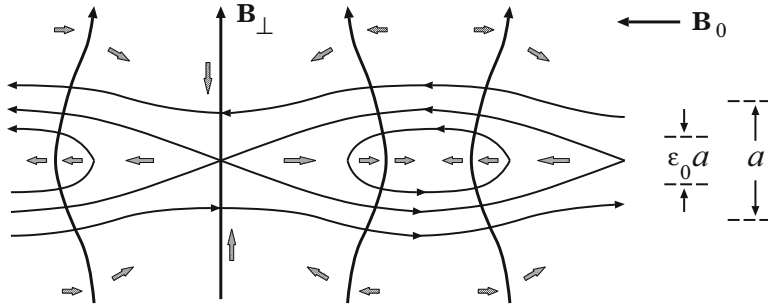


**Fig. 13.4** The magnetic field lines and velocities for the tearing instability in the RCL with a transversal magnetic field

Given the transversal field, the plasma moves along the width of the RCL, overcoming the braking influence of the transversal field as shown in Fig. 13.4. Taking this fact into account, we have instead of (13.32) to write down

$$P = K + \Pi. \quad (13.44)$$

The second term on the right is the work done in a unit of time against the force  $F_{B\perp}$  related to the transversal field  $B_\perp$ , and it is given by

$$\Pi = v_{1x} F_{B\perp}. \quad (13.45)$$

Here

$$F_{B\perp} = j_{B\perp} B_\perp \quad \text{and} \quad j_{B\perp} = \sigma v_{1x} B_\perp. \quad (13.46)$$

Using Eqs. (13.45) and (13.46) and  $\operatorname{div} \mathbf{v} = 0$ , the power  $\Pi$  is evaluated to be

$$\Pi = \sigma B_\perp^2 \frac{v_{1y}^2}{(k \epsilon_0 a)^2}. \quad (13.47)$$

Substituting the relations (13.31), (13.33), and (13.46) in the relation (13.44) gives

$$\sigma v_{1y}^2 (\epsilon_0 B)^2 = \frac{\omega \rho v_{1y}^2}{(k \epsilon_0 a)^2} + \sigma B_\perp^2 \frac{v_{1y}^2}{(k \epsilon_0 a)^2}.$$

From this there immediately follows an estimate for the thickness of the internal dissipative region with the transversal field at hand:

$$\epsilon_0 = \left( \frac{\omega \rho}{k^2 a^2 B^2 \sigma} \right)^{1/4} \left( 1 + \frac{\sigma B_\perp^2}{\omega \rho} \right)^{1/4} \quad (13.48)$$

or

$$\varepsilon_0(\xi_\perp) = \varepsilon_0(0) \left( 1 + \frac{\xi_\perp^2 S^2}{p} \right)^{1/4}.$$

Here  $\xi_\perp = B_\perp/B$  and the internal region thickness for  $B_\perp = 0$  is designated as  $\varepsilon_0(0)$ . Now  $\varepsilon_0(\xi_\perp)$  is implied in the expressions (13.36)–(13.41) by  $\varepsilon_0$ . Substituting (13.48) in (13.36)–(13.41) gives the dispersion relations:

$$\omega^5 = \frac{\eta^3 B^3}{a^{10} \rho} \frac{1}{k^2} - \frac{B_\perp^2}{\rho \eta} \omega^4$$

in the short-wave region

$$\varepsilon_0 < \alpha, \quad (13.49)$$

and

$$\omega^3 = \frac{\eta B^2}{a^2 \rho} k^2 - \frac{B_\perp^2}{\rho \eta} \omega^2$$

in the long-wave region

$$\varepsilon_0 > \alpha. \quad (13.50)$$

Let us rewrite the same dispersion relations in the dimensionless form

$$p^5 = \left( \frac{S}{\alpha} \right)^2 - \xi_\perp^2 S^2 p^4 \quad (13.51)$$

and

$$p^3 = \alpha^2 S^2 - \xi_\perp^2 S^2 p^2 \quad (13.52)$$

for the cases (13.49) and (13.50), respectively. It is easy to comprehend that

the transversal component of magnetic field decreases the tearing mode increment over the whole wave range and also decreases the wavelength at which the increment peaks.

The rigorous analytic solution (Somov and Verneta 1989) gives us the dispersion relation

$$\Delta^{1/4} \left( \frac{\alpha^2 S^2}{p} \right)^{1/4} \left( 1 - \frac{p^{3/2}}{\alpha S} \Delta^{-1/2} \right) - p \alpha \left( \frac{\pi}{2} \right)^{1/2} = 0, \quad (13.53)$$

where

$$\Delta = \left( 1 + \frac{\xi_\perp^2 S^2}{p} \right)^{-1}. \quad (13.54)$$

From Eq. (13.53) the dispersion relations (13.51) and (13.52) follow, given the conditions (13.49) and (13.50), respectively.

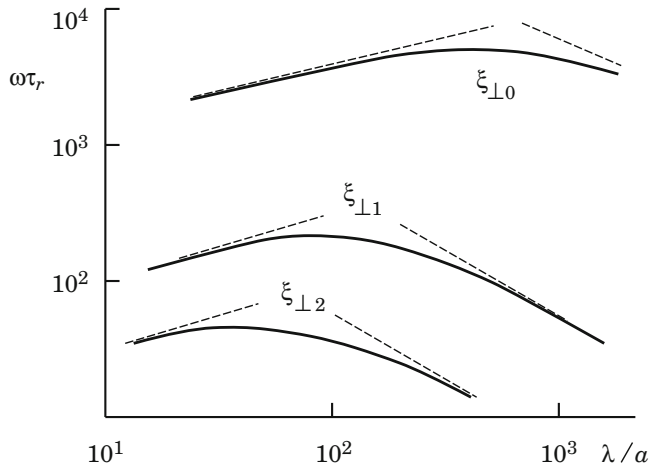


**Fig. 13.5** The dependence of the collisional tearing instability increment on the wavelength and the transversal component of magnetic field

The stabilizing influence of the transversal field is demonstrated by Fig. 13.5 on which the graphs of the instability increment  $\omega\tau_r$  dependence on the wave length  $\lambda/a$  are presented for  $S = 10^8$  and three values of the transversal field:  $\xi_{\perp 0} = 0$ ,  $\xi_{\perp 1} = 10^{-4}$ , and  $\xi_{\perp 2} = 10^{-3}$ . The solutions of the asymptotical Eqs. (13.51) and (13.52) are shown by the straight dotted lines, the solutions of the exact Eq. (13.53) are shown by solid curves. The figure shows that,

as the transversal magnetic field increases, the increment of the tearing instability in the reconnecting current layer (RCL) decreases and its maximum moves to the short-wave region.

Nishikawa and Sakai (1982) have numerically solved a set of eigen-mode equations in a RCL with the transversal magnetic field. The mode associated with magnetic island formation was investigated. It was found that the transversal component strongly modifies this mode and has a significant stabilizing effect on the collisional tearing mode.

## 13.5 Compressibility and a Longitudinal Field

### 13.5.1 Neutral Current Layers

Let us find the conditions under which compressibility of plasma should be taken care of and show the effect of compressibility on the tearing instability of

the reconnecting current layer (RCL). For simplicity's sake, we first restrict our attention to the case  $B_y = B_\perp = 0$  and  $B_z = B_\parallel = 0$ .

During development of the tearing instability, the plasma starts moving along the width of the layer as shown in Fig. 13.3. Given the finite value of the sound velocity,  $V_s$ , the plasma in the neighbourhood  $|\delta x| < V_s / \omega$  of the reconnection point is drawn into the motion in a characteristic time of the instability growth  $\omega^{-1}$ . Provided  $V_s / \omega > \lambda$ , the plasma may be considered incompressible. In the opposite case

$$\frac{V_s}{\omega} < \lambda \quad (13.55)$$

the compressibility of the plasma must be accounted for:  $\operatorname{div} \mathbf{v} \neq 0$ . In this case the estimate

$$\frac{v_{1x}}{(V_s / \omega)} \sim \frac{v_{1y}}{\varepsilon_0 a} \quad (13.56)$$

holds, where  $\varepsilon_0 a$  is the internal region dimension.

Let us compare the work done by the driving instability force (Sect. 13.3) in unit time on unit volume,

$$P \sim \sigma v_{1y}^2 (\varepsilon_0 B)^2,$$

with the kinetic energy acquired in unit time by the unit plasma volume drawn into the motion along the RCL within the neighbourhood  $|\delta x| < V_s / \omega$  of the reconnection point,

$$K \sim \omega \rho_0 v_{1x}^2 \sim \omega \rho_0 \left( \frac{V_s}{\omega} \frac{1}{\varepsilon_0 a} \right)^2 v_{1y}^2.$$

Here relation (13.56) is used. Equating  $P$  and  $K$  gives an estimate for  $\varepsilon_0$ :

$$\varepsilon_0 \sim \left( \frac{\rho_0 V_s^2}{\omega a^2 \sigma B^2} \right)^{1/4} \sim \left( \frac{1}{\omega \tau_r} \frac{V_s^2}{V_{Ax}^2} \right)^{1/4}, \quad (13.57)$$

where  $V_{Ax} = B_x / \sqrt{4\pi\rho}$  is the Alfvén speed.

Now substituting the quantity (13.57) for  $\varepsilon_0$  in formulae (13.37)–(13.41) immediately results in the dispersion relation

$$\omega \approx \frac{1}{\tau_r} \frac{V_{Ax}^2}{V_s^2}.$$

Thus it is seen that

because of compressibility of the plasma, a new branch of the tearing instability arises in the reconnecting current layer

in the long-wave region

$$\lambda > \lambda_0 \approx \frac{V_s}{\omega} \sim 2\pi a S \left( \frac{V_{Ax}}{V_s} \right)^{-3}, \quad (13.58)$$

which was absent for an incompressible plasma ( $\omega \rightarrow 0$  for  $\lambda > \lambda_0$ ). Recall that so far we have treated the case  $B_\perp = 0$ ,  $B_\parallel = 0$ , i.e. the magnetically neutral current layer.

### 13.5.2 Non-neutral Current Layers

In the context of the above treatment, the role of a longitudinal magnetic field  $B_z = B_\parallel \neq 0$  (along the electric current in the RCL) becomes clear. While compressing a plasma with a longitudinal field which is in fact frozen into the plasma, **the work is to be done to compress the longitudinal field** (Somov and Titov 1985b). Thus, given the longitudinal field, the plasma pressure is suppressed by the sum of the plasma pressure and the magnetic one (related to the longitudinal field). This leads to the change

$$V_s \rightarrow \left( V_s^2 + V_{A\parallel}^2 \right)^{1/2}, \quad (13.59)$$

where  $V_{A\parallel} = B_\parallel / \sqrt{4\pi\rho}$ , which describes the stabilizing influence of the longitudinal field. Once

$$B_\parallel > B_x(a), \quad (13.60)$$

**the instability caused by the compressibility becomes suppressed.**

Note that the values obtained for the growth rate of the instability are comparable with the inverse time of magnetic diffusion  $\tau_r^{-1}$ . Magnetic diffusion, however, is neutralized by the plasma drift into the RCL (see Sect. 3.5 in Somov 1992) and the stationary zero configuration persists for a time  $t_s \gg \tau_r$ . If the condition

$$\rho_{\text{out}} \ll \rho_{\text{in}} \quad (13.61)$$

is satisfied, where  $\rho_{\text{out}}$  and  $\rho_{\text{in}}$  are the plasma densities inside and outside the layer, respectively; the plasma drift into the RCL cannot usually suppress the tearing instability (see, however, Pollard and Taylor 1979). Hence the tearing instability of the RCL can play an essential role as a universal dynamic instability (Somov and Verneta 1993).

The rigorous analytic solution of the problem concerning the compressibility effect on the tearing mode development was given by Verneta and Somov (1993).

In actual RCLs, the plasma continuously flows into the layer through its wide surfaces and flows out through the narrow side boundaries (see Fig. 8.3).

| The fast outflow of plasmas from the reconnecting current layer can be of principal importance for its tearing stability

(Syrovatskii 1981). The accelerating outflow along the main ( $B_x$ ) magnetic field, which is present in the configuration with the velocity stagnation point, causes a substantial decrease in the magnitude of the linear growth rate and, for some parameter ranges, stabilization (Ip and Sonnerup 1996).

## 13.6 The Kinetic Approach

### 13.6.1 The Tearing Instability of Neutral Layer

We now describe the tearing instability in the framework of the collisionless plasma model, starting from the Vlasov equation (Part I, Sect. 3.1.2)

$$\frac{\partial f_k}{\partial t} + \mathbf{v} \frac{\partial f_k}{\partial \mathbf{r}} + \frac{\mathbf{F}_k}{m_k} \frac{\partial f_k}{\partial \mathbf{v}} = 0. \quad (13.62)$$

Here

$$\mathbf{F}_k = q_k \left( \mathbf{E} + \frac{1}{c} \mathbf{v} \times \mathbf{B} \right)$$

and symbols  $k = e, i$  denote electrons and ions, respectively.

As equilibrium distribution functions describing the reconnecting current layer (RCL), it is appropriate to choose (Harris 1962)

$$f_k^{(0)}(y) = n_0 \exp \left\{ -\frac{1}{k_B T_k} \left[ \frac{1}{2} m_k v^2 - \vartheta_k \left( m_k v_z + \frac{1}{c} q_k A^{(0)} \right) \right] \right\}. \quad (13.63)$$

The notation is conventional. Here the vector potential  $\mathbf{A} = \mathbf{e}_z A$  for a two-dimensional magnetic field  $\mathbf{B} = \text{curl } \mathbf{A}$  is introduced. The scalar potential is excluded by choosing  $\vartheta_i/T_i = -\vartheta_e/T_e$ .  $\vartheta_e$  and  $\vartheta_i$  are the flow velocities of electrons and ions.

Such distribution functions (as can be shown using Maxwell's equations) specify a current layer with the following characteristics:

(a) The equilibrium magnetic field

$$\mathbf{B} = B_0(y) \mathbf{e}_x,$$

where

$$B_0(y) = B_0 \tanh \frac{y}{a}$$

(13.64)

on choosing

$$A^{(0)}(y) = \text{const} \times \ln \cosh \frac{y}{a};$$

(b) The plasma density in the RCL

$$n^{(0)}(y) = n_0 \cosh^{-2} \frac{y}{a}, \quad (13.65)$$

where

$$n_0 = \frac{1}{k_B(T_e + T_i)} \frac{B_0^2}{8\pi};$$

(c) The RCL half-thickness

$$a = \frac{2ck_B(T_e + T_i)}{eB_0(\vartheta_i - \vartheta_e)}. \quad (13.66)$$

Therefore a magnetically-neutral one-dimensional current layer of the Harris type is considered.

Near the plane  $y = 0$  where  $B_0 = 0$ , particle motion is almost free inside a non-adiabatic region of thickness  $2d_k$  (cf. definition (11.28)). Outside this region the particles are magnetized. The quantity  $d_k$  can be evaluated as follows (see also Sect. 11.1.5). The local Larmor radius of a particle at the boundary of the region is

$$r_L^{(k)}(d_k) = \frac{V_{Tk} m_k c}{q_k B_0(d_k/a)}.$$

Equating it to the internal dissipative region thickness

$$r_L^{(k)}(d_k) \approx d_k,$$

we find

$$d_k \approx \sqrt{a r_L^{(k)}},$$

(13.67)

where  $r_L^{(k)}$  is the Larmor radius in the  $B_0$  field. Thus the motion of particles of kind  $k$  is assumed to be free inside the region  $|y| < d_k$ , whereas they are magnetized once  $|y| > d_k$ .

★ ★ ★

Equations (13.62) will be solved in a *linear* approximation. The Fourier components of the perturbations are of the form

$$f^{(1)}(\mathbf{r}, t) = f^{(1)}(y) \exp(\omega t + ikx). \quad (13.68)$$

Recall that the case  $\mathbf{k} \parallel \mathbf{B}_0$  is considered. The initial Eq.(13.62) give, for perturbations,

$$(\omega + ikv_x) f_k^{(1)} = -\frac{1}{m_k} \mathbf{F}_k^{(1)} \cdot \frac{\partial f_k^{(0)}}{\partial \mathbf{v}}.$$

These equations determine the approximate form of the perturbed distribution function, the connection between  $f_k^{(1)}$ ,  $E^{(1)}$ , and  $A^{(1)}$ :

$$f_k^{(1)} = \frac{q_k f_k^{(0)}}{k_B T_k} \left\{ \vartheta_k A^{(1)} + E^{(1)} \frac{v_z}{\omega + ikv_x} \right\}. \quad (13.69)$$

The first term on the right-hand side represents the influence of the magnetic field perturbation and the second one represents the interaction between the electric field of a wave and particles.

The latter contribution is negligible outside the RCL as the particle motion becomes adiabatic and there is no electric field along the magnetic field lines.

From Maxwell's equations, the perturbation electric field

$$E^{(1)} = -\frac{1}{c} \omega A^{(1)}.$$

(13.70)

Final results show that the instability growth rate complies with the condition

$$\omega < k \mathcal{V}_{Tk}, \quad (13.71)$$

where (different from the mean thermal velocity introduced in Part I, Sect. 8.1.4)

$$\mathcal{V}_{Tk} = \sqrt{\frac{2k T_k}{m_k}}. \quad (13.72)$$

Therefore we consider a low-frequency mode of the instability. This is the reason for assuming that

$$\frac{1}{v_x - i(\omega/k)} \approx i\pi \delta(v_x) + \text{Vp} \left( \frac{1}{v_x} \right) \quad (13.73)$$

(the Sokhotsky formula). Here Vp is the principal value of an integral (see Vladimirov 1971, Chap. 2, Sect. 7).

★ ★ ★

If  $W$  is the total kinetic energy of the particles in the perturbation, then the growth rate

$$\frac{dW}{dt} = \sum_k q_k \int E^{(1)} v_z f_k^{(1)} d^3 \mathbf{v} dy. \quad (13.74)$$

On the other hand, the energy conservation law gives

$$\frac{dW}{dt} = -\frac{1}{8\pi} \frac{d}{dt} \int (B^{(1)})^2 dy. \quad (13.75)$$

Substituting (13.69) and (13.73) in formula (13.74), we get

$$\begin{aligned} \frac{dW}{dt} &= \frac{\pi}{k} \sum_k \frac{q_k}{k_B T_k} \int_{-d_k}^{+d_k} \left[ \int f_k^{(0)} \delta(v_x) (E^{(1)} v_z)^2 d^3 \mathbf{v} \right] dy \\ &\quad - \frac{1}{4\pi} \frac{d}{dt} \int_{-\infty}^{+\infty} \frac{n(y)}{n(0)} \left( \frac{A^{(1)}}{a} \right)^2 dy \stackrel{\text{def}}{=} \sum_k \frac{d}{dt} W_k^r - \frac{d}{dt} W^m. \end{aligned} \quad (13.76)$$

Here  $dW_k^r/dt$  is the growth rate of the kinetic energy of the resonant particles of kind  $k$  in the region  $|y| < d_k$ , whereas  $dW^m/dt$  is the rate of energy decrease of the remaining particles.

The electron resonance term is  $(r_L^{(i)} / r_L^{(e)})^{1/2}$  times greater than the ion one. Taking this fact into account, we find from formulae (13.75) and (13.76) for electrons ( $k = e$ )

$$\begin{aligned} W^r &= \omega \int_{-d_e}^{+d_e} \left[ \int f_e^{(0)} \delta(v_x) \left| (A^{(1)})^2 v_z \right|^2 d^3 \mathbf{v} \right] dy \\ &= \frac{k_B T_e}{8\pi e^2} \int_{-\infty}^{+\infty} \left\{ \left| \frac{\partial A^{(1)}}{\partial y} \right|^2 + |A^{(1)}|^2 \left( k^2 - \frac{2}{a^2 \cosh^2(y/a)} \right) \right\} dy \\ &= W^m - \frac{1}{8\pi} \int (B^{(1)})^2 dy. \end{aligned} \quad (13.77)$$

From this it follows that the *energy transfer to electrons* exists in the region

$$ka < 1 \quad \text{or} \quad \lambda > 2\pi a \quad (13.78)$$

(cf. condition (13.29)). This process constitutes the development of the *electron* mode of the instability.

The electron mode of the tearing instability arises from the coupling of a negative energy perturbation (associated with filamentation of the original magnetically-neutral current layer) to the electron energization due to Landau resonance

(see Part I, Sect. 7.1.2).

Formula (13.77) gives us the following estimate for the growth rate of the electron tearing instability:

$$\omega \approx \left( \frac{a}{r_L^{(e)}} \right)^2 \frac{d_e}{\mathcal{V}_{Te}}. \quad (13.79)$$

Coppi et al. (1966) first proposed the *electron tearing* instability as a mechanism of explosive reconnection in the Earth magnetotail during substorm break-up (Sect. 13.6.3).

### 13.6.2 Stabilization by the Transversal Field

As we mentioned above, the Landau resonance of electrons inside a neutral current layer was proposed to provide the appropriate collisionless dissipation which is necessary for the spontaneous reconnection in the geomagnetic tail during a sub-storm (Coppi et al. 1966). However Schindler (1974) showed that nonzero magnetic field component  $B_\perp$  normal to the current layer *magnetizes* the electrons and restricts them from being resonant. As a result, the required dissipation relies upon the ions that are still unmagnetized. So Schindler proposed the so called *ion tearing* instability, in which the dissipation is due to ion Landau resonance. In this model the electrons act only as a charge neutralizing background.

Galeev and Zelenyi (1976) found, however, that the magnetized electrons can change the basic character of the tearing perturbation, thus making the ion energization invalid as a driver for the instability. Therefore the kinetic tearing instability can be suppressed by the transversal (i.e. perpendicular to the current layer plane) magnetic field. Let us consider this effect in some detail.

- (a) We begin by considering sufficiently small values of the transversal field  $B_\perp$ , for which the inequality

$$\omega_L^{(e)} = \frac{eB_\perp}{m_e c} < \omega \quad (13.80)$$

holds. Here  $\omega_L^{(e)}$  is the electron gyro-frequency in the transversal magnetic field  $\mathbf{B}_\perp$ ; recall that  $\omega$  is the instability increment.

In this case **electrons** in the region  $|y| < d_e$ , where the reconnecting magnetic field components tend to zero, **are in Landau resonance with the electric field perturbation** (13.70). As a consequence, the electron tearing mode develops in the reconnecting current layer (see above).

- (b) As the transversal field increases, the Larmor frequency  $\omega_L^{(e)}$  increases as well. When  $\omega_L^{(e)} > \omega$  the electron resonance with the electric field perturbation breaks down and the electron mode of the instability becomes stabilized (Schindler 1974). This takes place for

$$\frac{B_{\perp}}{B_0} = \xi_{\perp} > \left( \frac{r_{\text{L}}^{(\text{e})}}{a} \right)^{5/2} \left( 1 + \frac{T_i}{T_e} \right). \quad (13.81)$$

If the electron mode of the tearing is stabilized, there remains the possibility for ions to become the resonant particles, gaining energy. However electron gyration also stabilizes the ion mode up to the values ([Galeev and Zelenyi 1976](#)):

$$\frac{B_{\perp}}{B_0} < \left( \frac{r_{\text{L}}^{(\text{e})}}{a} \right)^{1/4} \left( 1 + \frac{T_i}{T_e} \right)^{-1/2}. \quad (13.82)$$

Thus there exists a ‘split’ – a range of values of the magnetic field transversal component

$$\left( \frac{r_{\text{L}}^{(\text{e})}}{a} \right)^{5/2} \left( 1 + \frac{T_i}{T_e} \right) < \frac{B_{\perp}}{B_0} = \xi_{\perp} < \left( \frac{r_{\text{L}}^{(\text{e})}}{a} \right)^{1/4} \left( 1 + \frac{T_i}{T_e} \right)^{-1/2}. \quad (13.83)$$

Here the **linear kinetic tearing instability becomes suppressed** ([Galeev and Zelenyi 1976](#)). By using this result [Somov and Verneta \(1988\)](#) have shown that

**|** the transversal magnetic field effect ensures the tearing **stability** of reconnecting high-temperature (super-hot) turbulent-current layers

during the ‘main’ or ‘hot’ phase of solar flares ([Somov and Verneta 1993](#); see also Sect. 3.5 in [Somov 1992](#)).

### 13.6.3 The Tearing Instability of the Geomagnetic Tail

Although the tearing instability was first proposed as a clue mechanism of magnetospheric substorms many years ago ([Coppi et al. 1966](#)), its prime role among other substorm processes was persistently challenged. The main theoretical reason was the proof by [Lembege and Pellat \(1982\)](#) that

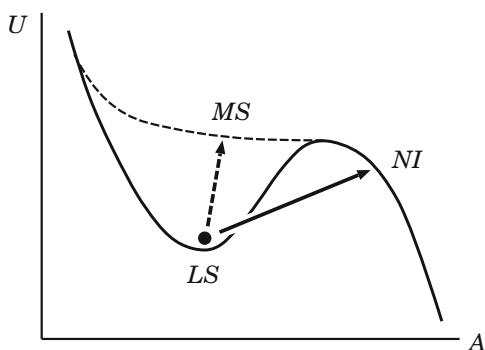
**|** the sign of the energy of the tearing mode perturbations can be changed from negative to positive one due to the drift motion of magnetized electrons inside the reconnecting current layer (RCL).

This conclusion is similar to that one of [Galeev and Zelenyi \(1976\)](#) but Lembege and Pellat showed in particularly that this effect stabilizes the tearing instability under the condition

$$\xi_{\perp} = \frac{B_{\perp}}{B_0} < \frac{\pi}{4} ka \quad (13.84)$$

regardless the temperature ratio  $T_e/T_i$ . Here  $a$  corresponds to the current-layer half-thickness according to the Harris formula (13.64).

**Fig. 13.6** The effective potential  $U$  as a function of the state parameter  $A$



Condition (13.84) shows that in the case of adiabatic electrons the tearing instability can be stabilized only for very short wavelengths

$$\lambda < \lambda_{\min} = \frac{\pi^2}{2} \frac{a}{\xi_\perp}. \quad (13.85)$$

They are too short to be relevant to the underlying spontaneous reconnection process in the geomagnetic tail current layer. In fact, condition (13.85) coincides with that of the WKB approximation in the stability analysis and as a result has made the *linear* tearing instability as the substorm mechanism suspect.

There were many attempts to restore necessarily the linear ion instability as a clue substorm process. All of them look, however, pretty inconsistent with a general representation of the substorm as a relatively fast unloading process in the tail of the magnetosphere. The substorm is usually preceded and prepared by the quasi-static changes in the tail during the growth phase (Nagai et al. 1998; Kokubun and Kamide 1998).

From a consideration of observational constraints on the onset mechanism Sitnov et al. (1997) and Sitnov and Sharma (1998) concluded that

the tearing instability must have a considerable initial stage when the equilibrium magnetic field topology is still conserved.

Moreover the instability is shown to have no linear stage. Instead, either the explicitly nonlinear or pseudolinear instability of negative energy eigenmode can develop. So the unavoidable *nonlinearity* is a key element of the substorm.

Sitnov et al. use the theory of catastrophes (Haken 1978; Guckenheimer and Holmes 1983) to consider a substorm as *backward bifurcation* in an open nonlinear system. In general, the *theory of catastrophes* is widely accepted as an appropriate mathematical tool to describe abrupt changes in a low-dimensional system driven by quasi-stationary evolution of a set of control parameters. The theory can be applied if we treat the tearing instability as a process for the growth of a large-scale one-mode perturbation.

In Fig. 13.6 the effective potential  $U$  of the geomagnetic tail current layer near the marginal state of a tearing instability is shown as a function of the state parameter  $A$ .

A process of quasi-stationary transformation of the potential minimum ( $LS$ ) into the point of inflection ( $MS$ ) is shown by the dashed arrow.

Being located near the bottom of the potential  $U$  well before the catastrophe, the **system is linearly stable** ( $LS$ ) because of positive energy of small perturbations from the minimum. The transition to instability is possible only at the moment of the catastrophe or before the catastrophe under the influence of a *finite* amplitude perturbation (the large solid arrow) necessary to surmount the potential barrier. In both cases the destabilization of the system proves to be nonlinear.

Many difficulties of the substorm theory have arisen presumably not from the incorrect physics involved but rather from irrelevant mathematical treatment of the instability problem. Suitable treatment of the tearing instability as a backward bifurcation can resolve some long-standing problems in the theory including the consistent description of both triggered and spontaneous onsets. Much more can be done due to further elaboration of this promising approach to the magnetospheric substorm mechanism.

# Chapter 14

## Magnetic Reconnection and Turbulence

**Abstract** The open issues focused on in this chapter presumably will determine the nearest future as well as the most interesting perspectives of plasma astrophysics. Magnetic energy release due to reconnection in the very complex systems of magnetic flux tubes (for example, a cosmic MHD turbulent plasma) is one of these issues.

### 14.1 Reconnection and Magnetic Helicity

#### 14.1.1 General Properties of Complex MHD Systems

We are going to consider some important properties of the reconnection process in complex magnetic field configurations containing many places (points or lines) where reconnection occurs. Such a situation frequently appears in astrophysical plasmas, for example in a set of *closely packed* flux tubes suggested by Parker (1972). The tubes tend to form many reconnecting current layers (RCLs) at their interfaces. This may be the case of active regions on the Sun when the field-line footpoint motions are slow enough to consider the evolution of the coronal magnetic field as a series of equilibria, but fast enough to explain *coronal heating* (see Sects. 14.2.1 and 14.4.2).

Another example of a similar complex structure is the ‘*spaghetti*’ model of solar flares suggested by de Jager (1986) or the ‘avalanche’ model of them (Parker 1988; Lu and Hamilton 1991; Zirker and Cleveland 1993). The last assumes that the energy release process in flares can be understood as *avalanches of many small reconnection events*. LaRosa and Moore (1993) propose that the large production rate of energetic electrons in solar flares (Sect. 11.1) is achieved through MHD *turbulent cascade* (see Part I, Sect. 7.2.3) of the bulk kinetic energy of the outflows from many separate reconnecting current layers (see also Antonucci et al. 1996).

How can we estimate the rate of magnetic energy release due to reconnection in such a very complex system of flux tubes? – The inherent complexity of the field configuration which can be used as a model does not allow any optimism in an attempt to solve the dissipative MHD problem numerically.

**|** An alternative approach to that of solving the MHD equations as they stand is to reformulate them in terms of invariant quantities.

As we have seen in Part I, Sect. 9.4, the mass, momentum and energy are conserving quantities and can be used to construct invariants. For example, the total energy of a system before reconnection is equal to the total energy after reconnection plus dissipation. A less familiar invariant in ideal MHD is the *magnetic helicity* or, more exactly, the *global* magnetic helicity (see Exercise 14.1):

$$\mathcal{H} = \int_V \mathbf{A} \cdot \mathbf{B} \, d^3\mathbf{r}. \quad (14.1)$$

Here  $\mathbf{A}$  is a vector potential for field  $\mathbf{B}$ , and  $V$  is the plasma volume bounded by a magnetic surface  $S$ , i.e.

$$\mathbf{B} \cdot \mathbf{n} |_S = 0. \quad (14.2)$$

[Woltjer \(1958\)](#) showed that

**|** in ideal magnetohydrodynamic motions the global magnetic helicity  $\mathcal{H}$  is conserved in any closed magnetic flux tube.

Woltjer's theorem may be extended to open-end flux tubes as well, provided the ends do not suffer any motion. In order to explain the observed toroidal field reversal in reversed-field pinches, [Taylor \(1974\)](#) generalized the ideal MHD result derived by Woltjer to a class of dissipative motions. Woltjer's theorem can also be used to show that the fields which minimize the magnetic energy subject to given initial and boundary conditions are in general *force-free fields* (Exercise 14.2).

The magnetic helicity, defined by definition (14.1), provides a measure of the *linkage* or knottedness of field lines (e.g., [Berger 1988, 1989](#)). **The helicity is a topological property of a magnetic field** (see, for example, Exercise 14.1). In ideal MHD there is no reconnection. For this reason, the magnetic helicity is conserved.

If we do not have ideal MHD there is some reconnection, and helicity is not conserved. However

**|** reconnection at a large magnetic Reynolds number generally conserves the global magnetic helicity to a great extent.

In laboratory ([Taylor 1974, 1986](#)), solar ([Berger 1984](#)) and magnetospheric ([Wright and Berger 1989](#)) plasmas the fraction of helicity dissipated is normally very small.

The approximate conservation of magnetic helicity has been successful in calculating heating rates in the solar corona (Sect. 14.2.1). The main idea here is that

the magnetic field tends to minimize its energy, subject to the constraint that its topological characteristic – helicity – is fixed.

Reconnection gives the fastest way for this relaxation. The magnetic configuration in the region which is subject to reconnection should relax towards a constant- $\alpha$  force-free field. Such a field is also called the *linear* force-free field. Taylor (1974) used this conjecture – Taylor’s hypothesis – to predict the formation of a Lundquist field in actively reconnecting fusion devices.

Interestingly, however, it is observed in some laboratory experiments that the relaxation can take place without the conservation of global magnetic helicity. Presumably such unexpected loss of helicity may be related to a *self-organization* effect in a reversed field plasma (Hirano et al. 1997). Even if the value of  $\mathcal{H}$  is null at the initial stage, the plasma relaxes to a certain field configuration by producing the toroidal magnetic field and  $\mathcal{H}$ .

### 14.1.2 Two Types of MHD Turbulence

Turbulence in ordinary fluids has great consequences: it changes the properties of flow and changes a large-scale flow pattern, even under time averaging. Turbulence introduces the *eddy diffusion* and *eddy viscosity*, and it increases momentum coupling and drag forces by orders of magnitude (see Mathieu and Scott 2000; Pope 2000). It should obviously have a wide variety of consequences in magnetized astrophysical plasmas, even in the MHD approximation.

There are at least two distinct types of the MHD driven turbulence.

First, when the external large-scale **magnetic field is strong**, the resulting turbulence can be described as the nonlinear interactions of Alfvén waves (e.g., Goldreich and Sridhar 1997). Early works by Iroshnikov (1964) and Kraichnan (1965) obtained a  $k^{-3/2}$  spectrum for both magnetic energy and kinetic energy in the presence of a dynamically significant magnetic field.

However these works were based on the assumption of isotropy in wave number space (see Part I, Sect. 7.2.2), which is difficult to justify unless the magnetic field is very weak. Goldreich and Sridhar (1997) assume a critical level of anisotropy, such that magnetic and hydrodynamic forces are comparable, and predict a  $k^{-5/3}$  spectrum for strong external field turbulence. Solar wind observations (see Leamon et al. 1998), which are well within the strong magnetized regime, and numerical studies (Cho and Vishniac 2000a) seem to support the Kolmogorov type scaling law.

Second, when the external **magnetic field is weak**, the MHD turbulence near the scale of the largest energy-containing eddies or vortices will be more or less like ordinary hydrodynamic turbulence with a small magnetic back reaction. In this regime, the turbulent eddy turnover time at the large scale  $L/V$  is less than the

Alfvénic time of the scale  $L/B$ . Here  $V$  and  $B$  are rms velocity and magnetic field strength divided by  $(4\pi\rho)^{1/2}$  respectively, and  $L$  is the scale of energy injection (recall that we consider driven turbulence) or the largest energy-containing eddies.

Various aspects of the weak external field MHD turbulence have been studied both theoretically and numerically. Since large-scale magnetic fields are observed in almost all astrophysical objects, the generation and maintenance of such fields is one of the most important issues in this regime. In the *mean field* dynamo theory ([Moffatt 1978](#); [Parker 1979](#)),

turbulent motions at small scales are biased to create an electromotive force along the direction of the large-scale magnetic field.

This effect, called the  $\alpha$ -effect, works to amplify and maintain large-scale magnetic fields.

Whether or not the  $\alpha$ -effect actually works depends on the structure of the MHD turbulence, especially on the mobility of the field lines. For example, when equipartition between magnetic and kinetic energy densities occurs at any scale larger than the dissipative scale, the mobility of the field lines and the  $\alpha$ -effect may be greatly reduced.

In the case of hydrodynamical turbulence, the energy cascades to smaller scales (see Part I, Fig. 7.3). If we introduce an uniform **weak magnetic field**, turbulent motions will stretch the magnetic field lines and divert energy to the small-scale magnetic field.

As the field lines are stretched, the magnetic energy density increases rapidly, until the generation of small-scale magnetic structures is balanced by the magnetic back reaction

at some scale between  $L$  and the dissipation scale  $l_{\min}$ .

This will happen when the magnetic and kinetic energy densities associated with a scale  $l$  ( $l > l_{\min}$ ) are comparable so the Lorentz forces resist further stretching at or below that scale. However stretching at scales larger than  $l$  is still possible, and the magnetic energy density will continue to grow if  $l$  ( $l < L$ ) can increase. Eventually, a final stationary state will be reached.

What is the scale of energy equipartition? What is the magnetic field structure? – The answer to the later question depends on the nature of diffusive processes acting on the magnetic field.

Suppose that magnetic field lines are unable to smooth the tangled fields at small scales. Then, as a result of the turbulent energy cascade and the subsequent stretching of field lines,

magnetic fields may have thin fibril structures with many polarity reversals within the energy equipartition scale  $l$ .

Consequently, magnetic structures on the equipartition scale are highly elongated along the external magnetic field direction ([Batchelor 1950](#)). This is the kind of picture one obtains by considering passive advection of magnetic fields in a chaotic flow (for a review see [Ott 1998](#)).

On the other hand, if we assume that MHD turbulence is always capable of relaxing tangled field lines at small scales, then we expect eddies at the final equipartition scale to be nearly isotropic ([Cho and Vishniac 2000b](#)).

### 14.1.3 Helical Scaling in MHD Turbulence

The turbulent flows and tangled magnetic fields seem to be observed, for example, in the Earth's magnetosphere, particularly in the plasma sheet (see [Borovsky and Funsten 2003a,b](#)). Here the turbulence appears to be a turbulence of eddies rather than a turbulence of Alfvén or other MHD waves. In this dynamical respect, it is similar to the turbulence observed in the solar wind. As for dissipation, two mechanisms appear to be important. One of them is electric coupling of the turbulent flows to the resistive ionosphere. The second one is a *direct cascade* of energy in the turbulence to small scales (see Part I, Sect. 7.2.2) where internal dissipation should occur at non-MHD scales.

The possibility of the self-similar cascade transfer of the hydrodynamic helicity flux over the spectrum was first introduced by [Brissaud et al. \(1973\)](#). The following two scenarios were analyzed from the standpoint of the dimensionality method: (a) the simultaneous transfer of energy and helicity with constant fluxes over the spectra of both parameters, (b) a constant helicity flux determining the energy distribution.

The influence of the hydrodynamic helicity is obvious from a physical standpoint:

**|** two helical vortices with strong axial motion in one direction have a tendency to merge because of the Bernoulli effect.

In other words, helicity should result in redistribution of the chaotic energy. Moreover a helicity flux that characterizes the variation of the mean helicity should also appear. Above all, helicity has an effect on the spectral features of turbulence. As for the spectra, variations occur in incompressible, compressible, and stratified media, as shown by [Moiseev and Chkhetiani \(1996\)](#). One of the tendencies inherent in helical media is the **energy transfer to the long-wavelength region** due to the tendency of helical vortices to merge.

According to [Moiseev and Chkhetiani \(1996\)](#), the mechanism that generates the mean hydrodynamic helicity leads to a second cascade range in addition to the Kolmogorov range (Part I, Sect. 7.2.2). The constant that does not depend on the scale of the helicity here is its flux. Nevertheless this requirement, like the requirement that the energy flux  $F$  be constant in the Kolmogorov range, is not inflexible. The spectral characteristics undergo significant changes. They are associated, as we understand, with at least a partial **inverse cascade** into the large-scale region.

There is a broad class of effects that generate both hydrodynamic helicity itself and large helicity fluctuations under terrestrial and astrophysical conditions. In particular, the simultaneous presence of such factors as temperature and density gradients, shearing flows, and nonuniform rotation is sufficient.

Like the direct cascade in the Kolmogorov turbulence, the inverse cascade is accomplished by nonlinear interactions, suggesting that *nonlinearity is important*. However a spectral type of inverse cascade is the strongly nonlocal inverse cascade process, which is usually referred to as the  $\alpha$ -effect ([Moffatt 1978](#); [Krause and Rädler 1980](#)). This effect exists already in linear kinematic problems.

A strong indication, that the  $\alpha$ -effect is responsible for large-scale magnetic field generation, comes from detailed analysis of three-dimensional simulations of forced MHD turbulence ([Brandenburg 2001](#)). This may seem rather surprising at the first glance, if one pictures large-scale field generation as the result of an inverse cascade process, that ([Brandenburg and Subramanian 2000](#))

**|** the exact type of nonlinearity in the MHD equations is unessential as far as the nature of large-scale field generation is concerned.

However, magnetic helicity can only change on a resistive timescale. So the time it takes to organize the field into large scales increases with magnetic Reynolds number.

#### 14.1.4 Large-Scale Solar Dynamo

Magnetic activity in the Sun occurs on a wide range of spatial and temporal scales. The small-scale photospheric fields are highly intermittent (see Sect. 14.4). The large-scale magnetic fields display remarkably ordered dynamics, involving cycles of activity with well-defined rules. There is an 11 year period for sunspot activity. At the beginning of a cycle, sunspot first appear in pairs at mid-latitudes. Then subsequently the sites of emergence migrate towards the equator over the course of the cycle.

The magnetic orientation of the sunspot pairs reverses from one cycle to the next. So the full magnetic cycle has a mean period of 22 years. The exact period of magnetic activity varies slightly and is a useful measure of the strength of solar activity, with shorter periods corresponding to a more active Sun. The magnetic cycle is also chaotically modulated on a longer timescales and exhibits intervals of reduced sunspot activity known as grand minima with a characteristic period of about 2,000 years.

Such organized dynamics on time-scales that are short compared to diffusive times requires the systematic regeneration of magnetic fields by the MHD dynamo.

The smaller scale photospheric field is believed to result from local dynamo action in the convective flows at or near the solar surface (e.g., [Cattaneo 1999](#), see also Sect. 15.5). It is likely that the large-scale (global) magnetic field is generated deeper within the Sun, probably at the interface between the solar convective zone and the radiative zone. The sunspot observations are most straightforwardly interpreted as the surface emergence of a large-scale toroidal field. The generation of such a field relies on the presence of differential rotation which stretches out poloidal field lines into strong regular toroidal field (Part I, Sect. 20.1.5).

Helioseismology, which can assess the internal differential rotation by using frequency splitting of acoustic modes, has revealed the existence of a large radial shear below the convective zone (see Part I, Fig. 20.4), now known as the solar *tachocline*. Here the angular velocity profile changes from being largely constant on radial lines in the convective zone to nearly solid body rotation in the radiative interior. This radial shear layer is certainly suitable for generating a strong toroidal field from any poloidal field there.

Parker (1993) postulated that the toroidal field results from the action of the shear on any poloidal component of the field in the tachocline region, while the weaker poloidal field is generated throughout the convection zone by the action of cyclonic (helical) turbulence. The key to this model is that

the transport of magnetic fields in the convective zone is enhanced relative to that in the stable layer as a result of the turbulent convective flows.

The poloidal magnetic flux that is generated in the convective zone is readily transported by the enhanced diffusivity there, and some of it is then expelled into the region below.

However strong toroidal fields produced in the tachocline are not transported away from their region of generation because of the relatively low turbulent diffusivity there. Hence the strong toroidal field may be stored successfully in the radiative region without significantly modifying the convection in the separate layer above. Recent dynamo models have built on this interface concept.

## 14.2 Coronal Heating and Flares

### 14.2.1 Coronal Heating in Solar Active Regions

Heyvaerts and Priest (1984) and Browning (1988) developed the model of current dissipation by magnetic reconnection, adapting Taylor's hypothesis to the conditions in a solar active region. They assumed that at any time the most relaxed accessible magnetic configuration is a **linear force-free field** which can be determined from the evolution of magnetic helicity. By so doing, Heyvaerts and Priest illustrated the role of the velocity  $v$  of photospheric motions in coronal heating. No heating is produced if these motions are very slow, and negligible heating is also produced when they are very fast. So

coronal heating presumably results from photospheric motions which build up magnetic stresses in the corona at a rate comparable to that at which reconnection relaxes them.

The corresponding heating rate can be estimated in order of magnitude by:

$$F \approx \frac{B^2}{4\pi} v \left( \frac{l_b}{l_b + l_v} \right) \left( \frac{\tau_d v}{l_b} \right), \quad (14.3)$$

where  $\tau_d$  is the effective dissipative time,  $l_b$  and  $l_v$  are scale lengths for the magnetic field and velocity at the boundary. (Terms in brackets are limiting factors smaller than 1.) The results showed that a substantial contribution to coronal heating can come from current dissipation by reconnection.

Reconnection with a small magnetic Reynolds number can produce significant dissipation of helicity, of course.

[Wright and Berger \(1991\)](#) proved that helicity dissipation in two-dimensional configurations is associated with the retention of some of the inflowing magnetic flux by the reconnection region  $R_r$ . When the reconnection site is a simple Ohmic conductor, all the field parallel to the reconnection line (the longitudinal component of magnetic field) that is swept into the region  $R_r$  is retained ([Somov and Titov 1985a,b](#)). In contrast, the inflowing magnetic field perpendicular to the line is annihilated. [Wright and Berger \(1991\)](#) relate the amount of helicity dissipation to the retained magnetic flux.

### 14.2.2 Helicity and Reconnection in Solar Flares

Flares in a solar or stellar atmosphere predominantly arise from the release of coronal magnetic energy. Since magnetic field lines may have fixed endpoints (footpoints) in the photosphere, observations of photospheric quantities such as *shear* and *twist* become important diagnostics for energy storage in the corona.

The magnetic energy of an equilibrium field in the corona can be related to measures of its net shear and twist. For example,

the magnetic energy of a *linear* force-free field is proportional to its magnetic helicity

(see Exercise 14.2).

[Berger \(1988\)](#) presented a formula for the energy of a *non-linear* force-free field in terms of linking field lines and electric currents. This allows us to partition the magnetic energy among different current sources in a well-defined way. For example, the energy due to reconnecting current layers (RCLs) may be calculated and compared to the energy due to field-aligned currents (see Chap. 16).

Pre-flare magnetic fields are often modeled as a twisted flux tube associated with a solar prominence. Twisting can be introduced either by photospheric twisting flows (presumably due to Coriolis forces) at the locations where the base of the arch enters the photosphere ([Gold and Hoyle 1960](#)), or by *flux cancellation*, i.e. by the shear flows along the photospheric neutral line and the converging flows in direction to the neutral line (e.g., [Somov et al. 2002a](#)).

If one assumes that the magnetic field of a pre-flare prominence can be modeled as a flux tube which is uniformly twisted and force-free, then it is possible to compute a relative energy, for example, the energy difference between a twisted arch and a similar arch described by a potential field. However in order to make

realistic estimates of the energy available from a twisted tube for a flare, one must address the issue of the post-flare magnetic configuration. If it is assumed that the total helicity is conserved, it might be well that a linear force-free field, rather than a potential field, represents the post-flare configuration of the flux tube.

In general, estimates of the energy available in terms of the topological complexity of the magnetic field have been made by Berger (1994). The argument that the post-flare configuration should be a linear force-free field is based on the work of Woltjer and requires that the Taylor conjecture be true (Sect. 14.1). The key point is that, in deriving the result that a linear force-free field is the lowest energy state that can reach when helicity is conserved, Woltjer used the approximation of ideal MHD. But this means that

the constant  $\alpha$  or linear force-free state is topologically inaccessible from most initial configurations of a magnetic field.

While Taylor's conjecture, that the global helicity is conserved while finite diffusivity effects are invoked to allow the field to relax to a linear one, gives one way out of this conundrum, it is not entirely satisfactory from a theoretical point of view (Marsh 1996).

It is believed that the **excess energy**, which is the energy difference between the contained energy and the minimum energy predicted by the Taylor hypothesis, is **more rapidly dissipated than the magnetic helicity**. It is also believed that reconnection may lead to the fast MHD relaxation process to the minimum energy state, creating flares. However this theoretical preposition should be subject to careful observational examination.

In principle, there may be an application in observational models of the field structure of an active region with vector magnetogram data supplying information on the force-free field parameter  $\alpha$ . This would provide a check on the model's insight as to the true topology of the field.

Using vector magnetograms and X-ray morphology, Pevtsov et al. (1996) determine the helicity density of the magnetic field in active region NOAA 7154 during 1992 May 5–12. The observations show that a long, twisted X-ray structure retained the same helicity density as the two shorter structures, but its greater length implies a higher coronal twist. The measured length and  $\alpha$  value combine to imply a twist that exceeds the threshold for the MHD *kink instability*. It appears that such simple models, which have found that the kink instability does not lead to the global dissipation, do not adequately address the physical processes that govern coronal fields.

Numerical integration of the 3D dissipative MHD equations, in those the pressure gradient force and the density variation are neglected, shows that magnetic reconnection driven by the resistive tearing instability growing on the magnetic shear inversion layer can cause the spontaneous formation of sigmoidal structure (Kusano 2005). This process could be understood as a manifestation of the minimum energy state, which has the excess magnetic helicity compared to the bifurcation criterion for the linear force-free field (Taylor 1974). It is also numerically demonstrated that the formation of the sigmoids can be followed by an explosive energy liberation.

## 14.3 Stochastic Acceleration in Solar Flares

Modern observations of solar energetic particles (SEPs) and hard electromagnetic radiations produced by solar flares indicate that *stochastic acceleration* of charged particles by waves or wave turbulence, a second-order Fermi-type acceleration mechanism (see Part I, Sect. 7.2), may play an important role in understanding the energy release processes and the consequent plasma heating and particle acceleration. At first, this theory was applied to the acceleration of non-thermal electrons which are responsible for the microwave and hard X-ray (HXR) emissions as well as for the type III radio bursts during the impulsive phase of solar flares.

### 14.3.1 Stochastic Acceleration of Electrons

[LaRosa et al. \(1996\)](#) and [Miller et al. \(1996\)](#) presented a model for the acceleration of electrons from thermal to relativistic energies in solar flares. They assume that fast outflows from the sites of reconnection generate a cascading MHD turbulence. The ratio of the gas pressure to the magnetic one is presumably small in this cascade. Thus the MHD turbulence has a small parameter  $\beta$  (our parameter  $\gamma^2$ ) and mainly comprises of two low-amplitude wave modes: (a) Alfvén waves and (b) *fast magnetoacoustic waves* (see Part I, Sect. 15.2). The authors do not consider a possible role of slow magnetoacoustic waves in the acceleration of protons.

[LaRosa et al.](#) assume that in the reconnection-driven turbulence there is an equipartition between these two modes. About half of the energy of the turbulence resides in Alfvén waves and about half in fast magnetoacoustic waves (FMW). The threshold speed of the resonance determines the selectivity of the wave-particle interaction. Assuming  $B^{(0)} \approx 500 \text{ G}$ ,  $T^{(0)} \approx 3 \times 10^6 \text{ K}$ , and  $n^{(0)} \approx 10^{10} \text{ cm}^{-3}$ , they found that the Alfvén speed  $V_A \approx 0.036 c$ , the electron thermal speed  $V_{Te} \approx 0.032 c$ , and the proton thermal speed  $V_{Te} \approx 7.4 \times 10^{-4} c$ . Therefore the threshold speed is far in the tail of the proton distribution, and a negligible number of protons could be accelerated by FMW or Alfvén waves. Consequently protons or other ions are a negligible dissipation source for these waves, but not for slow magnetoacoustic waves (SMW) ignored by [LaRosa et al.](#).

On the other hand,  $V_A$  is only slightly above  $V_{Te}$ , and a significant number of the ambient electrons can resonate with the waves. Thus **FMW almost exclusively accelerate electrons** under the solar flare conditions accepted above. (They strongly differ from the conditions typical for the model of super-hot turbulent-current layers considered in Chap. 9.) The process under consideration could be called a *small-amplitude* Fermi acceleration or a resonant Fermi acceleration of second order ([Miller et al. 1996](#)) to denote the *resonant character* of the wave-particle interaction.

If we can ignore the gyroresonant part of the interaction, then only the parallel energy would systematically increase, leading to a velocity-space anisotropy in the electron distribution function.

So, beyond the main question of the origin and actual properties of the turbulence under consideration, an interesting question challenging electron energization by the Fermi process is pitch-angle scattering. In the absence of ancillary scattering, acceleration by FMW would lead to a systematic decrease of particle pitch-angles. Acceleration would then become less efficient, since only those waves with very high parallel phase speed would be able to resonate with the particles. However, as a tail is formed in the parallel direction, there would appear one or another instability which excites waves (for example, the fire-hose instability; see [Paesold and Benz 1999](#)) that can scatter the electrons back to a nearly isotropic state.

We should not forget, of course, that the usual Coulomb collisions (see Part I, Chaps. 8 and 4), even being very rare, can well affect formation of the accelerated-electron distribution. The Coulomb scattering of anisotropic accelerated electrons leads to their isotropization. As a result, the acceleration efficiency can significantly rise like in the case of acceleration in solar-flare collapsing magnetic traps ([Kovalev and Somov 2003](#)).

With the introduction of **isotropizing scattering of any origin**, we can average the momentum diffusion equation in spherical coordinates over the pitch-angle  $\theta$  and obtain the isotropic momentum diffusion equation

$$\frac{\partial f}{\partial t} = \frac{1}{p^2} \frac{\partial}{\partial p} \left( p^2 D(p) \frac{\partial f}{\partial p} \right). \quad (14.4)$$

Here

$$D(p) = \frac{1}{2} \int_{-1}^{+1} D_{pp} d\mu, \quad (14.5)$$

$p$  is the magnitude of the momentum vector  $\mathbf{p}$ ,  $\mu = \cos \theta$ , and  $D_{pp}$  is the  $\mu$ -dependent momentum diffusion coefficient (see [Miller et al. 1996](#)). The quantity  $f$  is the phase-space distribution function, normalized such that  $f(p, t) 4\pi p^2 dp$  equals the number of particles per unit volume with momentum in the interval  $dp$  about  $p$ .

Electron acceleration and wave evolution are thus described by the two coupled partial differential equations: Eq. (14.4) and the diffusion equation in the wave-number space (see Part I, Eq. (7.28)). Their solution allows to evaluate the bulk energization of electrons by Fermi acceleration from the MHD turbulence expected in solar flares.

[LaRosa et al. \(1996\)](#) has found that the Fermi acceleration acts fast enough to be the damping mechanism for the FMW turbulence. This means that Fermi acceleration becomes fast enough at short enough scales  $\lambda \sim \lambda_{\min}$  in the turbulent cascade of fast magnetoacoustic waves *to end* the cascade by dissipating the cascading turbulent energy into random-velocity kinetic energy of electrons. Practically all of the energy of the FMW turbulence is absorbed by the electrons while the protons get practically none.

### 14.3.2 Acceleration of Protons and Heavy Ions

As we saw above, fast magnetoacoustic waves (FMW) can cascade to higher frequencies, eventually *Landau* resonate with the thermal electrons and accelerate them by the small-amplitude Fermi-type mechanism. In this section we shall discuss the acceleration of protons and heavy ions by Alfvén waves that are assumed to be a part of the same MHD turbulent cascade but *cyclotron* resonate with particles.

Let us consider for simplicity only the Alfvén waves with phase velocities parallel and antiparallel to the background field  $\mathbf{B}^{(0)}$ . These waves have left-hand circular polarization relative to  $\mathbf{B}^{(0)}$  and occupy the frequency range below the cyclotron frequency (see Appendix C) of Hydrogen, i.e., protons:

$$\omega < \omega_{\text{B}}^{(\text{H})} = \frac{ecB}{\mathcal{E}_{\text{H}}} . \quad (14.6)$$

As the waves increase in frequency, they resonate with protons of progressively lower energies.

For simplicity we also take the low-frequency limit for the dispersion relation of the Alfvén waves under consideration:

$$\omega = V_{\text{A}} | k_{\parallel} | . \quad (14.7)$$

In a multi-ion astrophysical plasma, there are resonances and cutoffs in the dispersion relation corresponding to each kind  $i$  of ions. However, because of their small abundance, Fe and the Ne group do not affect the dispersion relation. The He group will produce a resonance at  $\omega_{\text{B}}^{(\text{He})}$  and a cutoff at a slightly higher frequency. We shall take, however, the Alfvén wave dispersion relation (14.7) for all

$$\omega < \omega_{\text{B}}^{(\text{He})} .$$

In general, a low-frequency Alfvén wave propagating obliquely with respect to the ambient field  $\mathbf{B}^{(0)}$  has a linearly polarized magnetic field  $\mathbf{B}^{(1)}$  normal to both  $\mathbf{B}^{(0)}$  and  $\mathbf{k}$  (see Part I, Fig. 15.1). The wave electric field  $\mathbf{E}^{(1)}$  is normal to  $\mathbf{B}^{(0)}$  and  $\mathbf{B}^{(1)}$ . A low-frequency FMW (Part I, Sect. 15.2.3) has a linearly polarized electric field  $\mathbf{E}^{(1)}$  normal to both  $\mathbf{B}^{(0)}$  and  $\mathbf{k}$ . In each case the electric field can be decomposed into left- and right-handed components. However, for parallel propagation, all Alfvén waves are left-handed, while all the FMWs are right-handed.

Since we consider the Alfvén waves which phase velocities are strictly *parallel and antiparallel* to the background field, there is only one resonant wave and it is the backward-moving Alfvén wave (Miller and Reames 1996). Applying the cyclotron resonance condition (see Part I, formula (7.16)) for this wave with  $s = 1$ , we find its wave number

$$k_{\parallel} = - \frac{\omega_{\text{B}}^{(\text{i})}}{\gamma_{\text{L}} (V_{\text{A}} + v_{\parallel})} . \quad (14.8)$$

Hence

when the Alfvén wave frequency becomes close to the ion-cyclotron frequency  $\omega_B^{(i)}$ , the thermal ions of the kind  $i$  would be accelerated out of the background energies.

The first kind of ions encountered by the Alfvén waves will be the one with the lowest cyclotron frequency, namely Fe. This is well visualized by Fig. 14.1 in Miller and Reames. However, due to the low Fe abundance, the waves will not be completely damped and will continue to cascade up the group of ions with the next higher cyclotron frequency, namely Ne, Mg, and Si. These ions will be also accelerated but the waves will not be totally damped again. They encounter  $^4\text{He}$ , C, N, and O. These ions do completely dissipate the waves and halt the turbulent cascade.

[Miller and Reames \(1996\)](#) showed that abundance ratios similar to those observed in the interplanetary space after solar flares can result from the stochastic acceleration by cascading Alfvén waves in impulsive flares.

### 14.3.3 Acceleration of $^3\text{He}$ and $^4\text{He}$ in Solar Flares

The most crucial challenge to the models including the stochastic acceleration arises from the extreme enhancement of  $^3\text{He}$  ions observed in some impulsive solar events. Nonrelativistic  $^3\text{He}$  and  $^4\text{He}$  ions resonate mostly with waves with frequencies close to the  $\alpha$ -particle gyrofrequency. To study the stochastic acceleration of these ions, the exact dispersion relation for the relevant wave modes must be used, resulting in more efficient acceleration than scattering that could lead to anisotropic particle distributions. [Liu et al. \(2006\)](#) have carried out a quantitative study and have showed that the interplay of the acceleration, Coulomb energy loss, and the escape processes in the stochastic acceleration of  $^3\text{He}$  and  $^4\text{He}$  by parallel-propagating waves can account for the  $^3\text{He}$  enhancement, its varied range, and the spectral shape as observed with the *Advanced Composition Explorer* (ACE).

In general, stochastic acceleration is attractive on several points. One of them is that the stochastic interaction of particles with cascading waves in astrophysical plasma offers, in principle, the opportunity to unify electron and ion acceleration within the context of a single model. Specifically the picture that is emerging is one in which resonant wave-particle interactions are able to account for acceleration of particles out of the thermal background and to relativistic energies.

### 14.3.4 Electron-Dominated Solar Flares

Hard X- and gamma-ray observations of solar flares have a wide range of energy from about 10 keV to about 10 GeV with relatively high spectral and temporal

resolutions. Photon spectra over this range show significant deviations from the simple power law (e.g., Park et al. 1997). The study of these deviations can provide information about the acceleration mechanism. There is, however, some ambiguity in the analysis of the observational data because both accelerated electrons and protons contribute to the hard electromagnetic emission. Fortunately, there exist impulsive flares which have little or no evidence of nuclear excitation lines in the gamma-ray range. Such ‘electron-dominated’ events are uncontaminated by the proton processes and provide direct insights into the nature of the electron acceleration.

Park et al. (1997) use a model consisting of a finite-size region in the solar corona near the flare-loop top which contains a high-density of turbulence. Here the electrons are accelerated. Because of the rapid scattering by waves, the electrons trapped in this region have a nearly isotropic distribution. They emit bremsstrahlung photons which can be considered in a thin-target approximation. However electrons eventually escape this region after an escape time of  $\tau_{\text{esc}}(\mathcal{E})$  and lose most of their energy  $\mathcal{E}$  in the chromosphere at the footpoints where they also emit hard X- and gamma-rays. This is called the *thick-target* source (see Part I, Sect. 4.4.2).

Instead of the simplified Eq. (14.4), the Fokker-Planck equation (Part I, Sect. 3.1.4) re-written in energy space is used to describe the spectrum of electrons assuming isotropy and homogeneity:

$$\frac{\partial N}{\partial t} = -\frac{\partial}{\partial \mathcal{E}} \{ [A(\mathcal{E}) - |B(\mathcal{E})|] N \} + \frac{\partial^2}{\partial \mathcal{E}^2} [D(\mathcal{E}) N] - \frac{N}{\tau_{\text{es}}(\mathcal{E})} + Q(\mathcal{E}). \quad (14.9)$$

Here  $N(\mathcal{E}, t) d\mathcal{E}$  is the number of electrons per unit volume in the energy interval  $d\mathcal{E}$ ,  $A(\mathcal{E})$  is the systematic acceleration rate,  $D(\mathcal{E})$  is the diffusion coefficient,  $Q(\mathcal{E})$  is a source term. The energy loss term

$$B(\mathcal{E}) = \left( \frac{d\mathcal{E}}{dt} \right)_L \quad (14.10)$$

includes both Coulomb collision and synchrotron radiation losses.

Take the Maxwellian distribution as the source term

$$Q(\mathcal{E}) = Q_0 \frac{2}{\sqrt{\pi}} \left( \frac{\mathcal{E}}{k_B T} \right)^{1/2} \exp \left( -\frac{\mathcal{E}}{k_B T} \right), \quad (14.11)$$

where  $Q_0$  is the rate at which the ambient plasma electrons of temperature  $T$  are accelerated. At steady state, the number of escaping particles is equal to the number of accelerated electrons:

$$\int \frac{N}{\tau_{\text{es}}(\mathcal{E})} d\mathcal{E} = \int Q(\mathcal{E}) d\mathcal{E} = Q_0. \quad (14.12)$$

The temperature  $T$  of about 17 MK is taken. The coefficients  $A(\mathcal{E})$ ,  $D(\mathcal{E})$ , and  $\tau_{\text{es}}(\mathcal{E})$  of the Fokker-Planck equation are determined by the particle acceleration mechanism. They can be written in the form:

$$A(\mathcal{E}) = \mathcal{D} (q + 2) (\gamma_L \beta)^{q-1}, \quad (14.13)$$

$$D(\mathcal{E}) = \mathcal{D} \beta (\gamma_L \beta)^q, \quad (14.14)$$

$$\tau_{\text{es}}(\mathcal{E}) = \mathcal{T}_{\text{es}} \frac{(\gamma_L \beta)^s}{\beta}. \quad (14.15)$$

Here  $\mathcal{D}$ ,  $\mathcal{T}_{\text{es}}$ ,  $q$ , and  $s$  are independent of the kinetic energy  $\mathcal{E} = \gamma_L - 1$  measured in units of  $m_e c^2$ , and  $\beta c$  is the velocity of electrons.

The acceleration time  $\tau_a$ , which is also the timescale for reaching the steady state in Eq. (14.9), can be estimated as

$$\tau_a(\mathcal{E}) \approx \tau_D(\mathcal{E}) \approx \frac{\mathcal{E}^2}{D(\mathcal{E})}. \quad (14.16)$$

This should be less than the rise time of a flare. For three of four flares described by Park et al. (1997), the overall rise time  $\tau_r$  of the hard X-rays is about 10 s and the total duration of the flare  $\tau_f$  is about 100 s. For the most impulsive flare  $\tau_r < 2$  s and  $\tau_f \approx 8$  s. Hence the steady state approximation is justified. After setting  $\partial/\partial t = 0$ , we can divide Eq. (14.9) by one of the parameters, say the diffusion coefficient  $\mathcal{D}$ , without changing the steady state solution.

The acceleration time for an electron with energy  $\mathcal{E} = 1$  is approximately  $\mathcal{D}^{-1}$ . Therefore, for three flares with the rise time  $\tau_r \approx 10$  s, Park et al. (1997) estimate  $\mathcal{D} \approx 0.15 \text{ s}^{-1}$ . For the shortest flare  $\mathcal{D} \approx 1 \text{ s}^{-1}$ . Shorter rise times are possible, but these require higher values of the turbulence energy density and the magnetic field. With  $\mathcal{D}$  fixed, the number of free parameters in the general stochastic model described above is reduced by one.

The numerical solutions show that the whistler wave resonant acceleration of electrons fits the observed spectra over the entire range of energy in four flares. The high-energy cutoff in the two flares can be attributed to synchrotron radiation losses in the presence of a 500 G magnetic field at the acceleration site. The observed break in the photon spectra of all four flares around 1 MeV can be attributed to a combination of the energy dependence of the escape time  $\tau_{\text{es}}(\mathcal{E})$  of particles out of the acceleration region and the change in the energy dependence of the bremsstrahlung cross-section between the nonrelativistic and relativistic regimes. Further steepening of the spectrum at even lower energies is caused by Coulomb losses.

## 14.4 Mechanisms of Coronal Heating

### 14.4.1 Heating of the Quiet Solar Corona

The high temperature of the solar corona was originally interpreted as due to the steady dissipation of various kinds of waves coming from the lower layers (see [Ulmschneider et al. 1991](#)). Later on, heating by a myriad of very small flares releasing magnetic energy by reconnection has also been proposed ([Gold 1964](#); [Priest 1982](#); [Parker 1988](#)). However these *microflares* or *nanoflares* have not yet been well identified.

It is difficult to detect the smallest flares in active regions, but in the quiet corona the background flux and stray light are smaller, and sensitive observations, for example, by the EIT (the Extreme ultraviolet Imaging Telescope) on *SOHO* can be used ([Benz and Krucker 1998](#)). The thermal radiation of the quiet corona in high-temperature iron lines is found to fluctuate significantly, even on the shortest time scale as short as 2 min and in the faintest pixels. These observations give us an evidence that

a significant fraction of the ‘steady heating’ in the quiet coronal regions is, in fact, impulsive.

The most prominent enhancements are identified with the X-ray flares above the network of the quiet chromosphere. Presumably, these X-ray flares above network elements are caused by additional plasma injected from below and heated to slightly higher temperatures than the preexisting corona.

Magnetic flux tubes in the photosphere are subject to constant buffeting by convective motions, and as a result, flux tubes experience random walk through the photosphere. From time to time, these motions will have the effect that a flux tube will come into contact with another tube of opposite polarity. We refer to this process as reconnection in weakly-ionized plasma ([Chap. 15](#)). Another possibility is the photospheric dynamo effect ([Sect. 15.5](#)) which, in an initially weak field, generates thin flux tubes of strong magnetic fields. Such tubes extend high into the chromosphere and can contribute to the mass and energy balance of the quiet corona.

*SOHO*’s MDI (the Michelson Doppler Imager) observations show that the magnetic field in the quiet network of the solar photosphere is organized into relatively small ‘concentrations’ (magnetic elements, small loops etc.) with fluxes in the range of  $10^{18}$  Mx up to a few times  $10^{19}$  Mx, and an intrinsic field strength of the order of a kilogauss. These concentrations are embedded in a superposition of flows, including the granulation and supergranulation. They *fragment* in response to sheared flows, *merge* when they collide with others of the same polarity, or *cancel* against concentrations of opposite polarity. Newly emerging fluxes replace the canceled ones.

[Schrijver et al. \(1997\)](#) present a quantitative statistical model that is consistent with the histogram of fluxes contained in concentrations of magnetic flux in the

quiet network as well as with estimated collision frequencies and fragmentation rates. Based on the model, Schrijver et al. estimate that as much flux is cancelled as is present in quiet-network elements in 1.5–3 days. This time scale is close to the timescale for flux replacement by emergence in ephemeral regions. So that this appears to be the most important source of flux for the quiet network. Schrijver et al. (1997) point out that the reconnection process appears to be an important source of outer-atmosphere heating.

Direct evidence that the ‘magnetic carpet’ (Day 1998), an ensemble of magnetic concentrations in the photosphere, really can heat the corona comes from the two other *SOHO* instruments, the Coronal Diagnostic Spectrometer (CDS) and the Extreme ultraviolet Imaging Telescope (EIT). Both instruments have recorded local brightenings of hot plasma that coincide with disappearances of the carpet’s elements. This indicates that just about all the elements reconnect and cancel, thereby releasing magnetic energy, rather than simply sick back beneath the photosphere.

The coronal transition region and chromospheric lines observed by *SOHO* together with centimeter radio emission of the quiet Sun simultaneously observed by the VLA show that the corona above the magnetic network has a higher pressure and is more variable than that above the interior of supergranular cells. Comparison of multiwavelength observations of quiet Sun emission shows good spatial correlations between enhanced radiations originating from the chromosphere to the corona. Furthermore

the coronal heating events follow the basic properties of regular solar flares

and thus may be interpreted as microflares and nanoflares (Benz and Krucker 1999). The differences seem to be mainly quantitative (Krucker and Benz 2000).

\* \* \*

What do we need to replenish the entire magnetic carpet quickly, say 1–3 days (Schrijver et al. 1997; Moore 1999)? – A rapid replenishment, including the entire cancellation of magnetic fluxes inside the carpet, requires the fundamental assumption of a two-level reconnection in the solar atmosphere (e.g., Somov 1999).

First, we may apply the concept of fast reconnection of electric currents as the source of energy for microflares to explain coronal heating in quiet regions (Somov and Hénoux 1999). Second, in addition to coronal reconnection, we need an efficient mechanism of magnetic field and current dissipation in the photosphere and chromosphere. The presence of a huge amount of neutrals in the weakly ionized plasma in the temperature minimum region makes its electrodynamical properties very different from an ideal MHD medium. Dissipative collisional reconnection is very efficient here (Litvinenko and Somov 1994b; Litvinenko 1999; Roald et al. 2000). Presumably the same mechanism can be responsible for the heating of the chromosphere.

### 14.4.2 Coronal Heating in Active Regions

The soft X-ray observations of the Sun from *Yohkoh* have revealed that roughly half of the X-ray luminosity comes from a tiny fraction ( $\sim 2\%$ ) of the solar disk (Acton 1996). Virtually all of the X-ray luminosity is concentrated within active regions, where the magnetic field is the strongest. While the corona is evidently heated everywhere, there is no question that it is heated most intensively within active regions. So this section will focus entirely on active regions.

The energy that heats the corona almost certainly propagates upward across the photosphere. Since the magnetic field plays a dominant role, the required energy flux can be expressed in terms of the electromagnetic Poynting vector in an ideal MHD medium (see Part I, Exercise 13.5):

$$\mathbf{G}_p = \frac{1}{4\pi} \mathbf{B} \times (\mathbf{v} \times \mathbf{B}) . \quad (14.17)$$

Assuming that the plasma vertical velocity  $v_z$  vanishes, we have the following expression for the vertical component of the energy flux:

$$G_z = -\frac{1}{4\pi} (\mathbf{v} \cdot \mathbf{B}) B_z . \quad (14.18)$$

A value of  $G_z \sim 10^7$  erg cm $^{-2}$  s $^{-1}$  is frequently used to account for the X-ray flux from active regions.

Detailed models of coronal heating in active regions typically invoke mechanisms belonging to one of the **two broadly defined categories**: wave (AC) or stress (DC) heating.

In wave heating, the large-scale magnetic field surveys essentially as a conductor for small-scale Alfvén waves propagating into the corona. So the average flux of wave energy can be written as

$$\langle G_z \rangle = - \sqrt{\frac{\rho}{4\pi}} \langle v^2 \rangle B_z . \quad (14.19)$$

Here  $B_z$  is the large-scale, stationary field, and  $\langle v^2 \rangle$  is the mean square velocity amplitude of the Alfvén waves. If the AC heating is the case, one expects to find some kind of correlation between the mean photospheric field strength and the heating flux.

In stress heating, the coronal magnetic field stores energy in the form of DC electric currents until it can be dissipated through, for example, nanoflares (e.g., Parker 1988). Estimating the rate of energy storage results in a Poynting flux of the form

$$G_z = c_d |v| B_z^2 . \quad (14.20)$$

Here the constant  $c_d$  describes the efficiency of magnetic dissipation, which might involve the random velocity  $v$  or the magnetic field geometry. Anyway, the Poynting flux in Eqs. (14.19) and (14.20) scales differently with the magnetic field  $B_z$ . While the constants of proportionality in each case may vary due to numerous other factors,

we might expect a large enough sample to be capable of distinguishing between the two mechanisms of coronal heating.

To analyze whether active region heating is dominated by slow (DC) or rapid (AC) photospheric motions of magnetic footpoints, the so-called reduced magnetohydrodynamic (RMHD) equations are used. They describe the dynamic evolution of the macroscopic structures of coronal loops assuming a fully turbulent state in the coronal plasma (Milano et al. 1997). The boundary condition for these equations is the subphotospheric velocity field which stresses the magnetic field lines, thus replenishing the magnetic energy that is continuously being dissipated inside the corona. In a turbulent scenario, energy is efficiently transferred by a direct cascade to the ‘microscale’, where viscous and Joule dissipation take place (see, however, Sect. 14.1.3).

Therefore, for the macroscopic dynamics of the fields, the net effect of turbulence is to produce a dramatic enhancement of the dissipation rate. Milano et al. (1997) integrated the large-scale evolution of a coronal loop and computed the effective dissipation coefficients by applying the eddy-damped closure model. They conclude that

for broadband power-law photospheric power spectra, the heating of coronal loops is DC dominated.

Nonetheless a better knowledge of the photospheric power spectrum as a function of both frequency and wavenumber will allow for more accurate predictions of the heating rate from the theory.

## 14.5 Practice: Exercises and Answers

**Exercise 14.1.** Consider two interconnected ring-tubes  $C_1$  and  $C_2$  with magnetic fluxes  $\Phi_1$  and  $\Phi_2$  inside of them but without a magnetic field outside (Fig. 14.1).

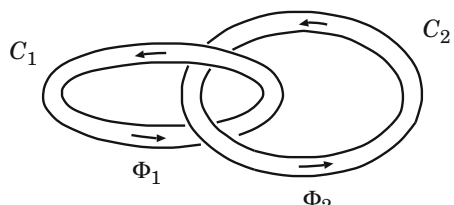


**Fig. 14.1** Two interconnected magnetic flux tubes

Show that the global magnetic helicity of the system is given by the formula (Moffatt 1978):

$$\mathcal{H} = 2\Phi_1\Phi_2. \quad (14.21)$$

**Answer.** First, we calculate the helicity of the tube  $C_1$  by integrating formula (14.1) over the volume  $V_1$  of the tube  $C_1$  and replacing  $\mathbf{B} d^3\mathbf{r}$  by  $\Phi_1 d\mathbf{r}$  where  $d\mathbf{r}$  is the length along the circuit  $C_1$ :

$$\mathcal{H}_1 = \int_{V_1} \mathbf{A} \cdot \mathbf{B} d^3\mathbf{r} = \Phi_1 \oint_{C_1} \mathbf{A} \cdot d\mathbf{r}. \quad (14.22)$$

By virtue of the Stokes theorem

$$\mathcal{H}_1 = \Phi_1 \int_{S_1} \operatorname{curl} \mathbf{A} \cdot d\mathbf{S} = \Phi_1 \int_{S_1} \mathbf{B} \cdot d\mathbf{S} = \Phi_1\Phi_2. \quad (14.23)$$

Since the other tube  $C_2$  makes the same contribution to the helicity, we obtain the Moffatt formula (14.21).

Therefore

the global magnetic helicity depends only on the fact that the two magnetic fluxes are interlinked.

The value of the helicity does not change if we deform the flux tubes as long as the linkage remains the same.

If, however, by magnetic reconnection the tubes would be cut and removed so that the linkage between them were broken, then the global helicity would go to zero. So we conclude that

as long as the topology of magnetic fluxes does not change, the magnetic helicity is an invariant.

**Exercise 14.2.** Show that for the force-free fields with constant  $\alpha$ , the magnetic energy is proportional to the global helicity (Woltjer 1959):

$$\mathcal{M} = \alpha \mathcal{H} \frac{1}{8\pi}. \quad (14.24)$$

Here

$$\mathcal{M} = \int_V \frac{B^2}{8\pi} dV, \quad (14.25)$$

$V$  is the volume of a simply connected region bounded by a magnetic surface  $S$  where  $\mathbf{B} \cdot \mathbf{n} = 0$  (see Sect. 14.1.1).

Discuss a kind of a surface integral which must be added to expression (14.24) in the case of a multiply connected volume such as a torus (see Reiman 1980).

# Chapter 15

## Reconnection in Weakly-Ionized Plasma

**Abstract** Magnetic reconnection, while being well established in the solar corona and solar wind, is also successfully invoked for explanation of many phenomena in the low-temperature weakly-ionized plasma in the solar atmosphere.

### 15.1 Early Observations and Classical Models

Magnetic reconnection, while being firmly established as a means of energy release in the high-temperature corona of the Sun during solar flares, is frequently invoked for explanation of various phenomena in the low-temperature plasma of the solar atmosphere. A particular example of these is the *prominence* phenomenon. Prominences were defined as dense ( $\approx 10^{11} \text{ cm}^{-3}$ ) and cool ( $\approx 6,000 \text{ K}$ ) plasma ‘clouds’ visible in  $H\alpha$  above the solar surface (Tandberg 1995). Pneuman (1983) suggested that both the material necessary for their formation and the magnetic field topology supporting them are the result of reconnection.

According to Pneuman (see also Syrovatskii 1982) a neutral line of the magnetic field is produced in the corona owing to some kind of plasma flow in the photosphere. Reconnection at this line gives rise to a helical magnetic field configuration. As this takes place, chromospheric material flows into the reconnection region and is then carried up by the reconnected field lines which are concave upward. The material is thereupon radiatively cooled to form a prominence that nests in the helical field topology.

An interesting modification of this model is due to van Ballegooijen and Martens (1989, 1990) who conjectured that the reconnection place is in fact located at the photospheric boundary. The point is that

if reconnection takes place *deep* enough in the solar atmosphere, a sufficient quantity of material can easily be supplied to the corona,

thus facilitating the process of prominence formation. On the observational side this conjecture is substantiated by the fact (Martin 1986) that for several hours before the formation of a filament, small-scale fragments of opposite polarity flux were seen to cancel in the region below the eventual filament.

So the model accounts for the cancelling magnetic features that are usually observed to be present in the photosphere below prominences. The scenario of the phenomenon has three phases: (a) a pre-interaction phase in which two opposite polarity photospheric magnetic fragments are unconnected magnetically, (b) an interaction phase when the fragments reconnect in the corona and create a filament, (c) a flux cancellation phase when reconnection in the photosphere produces the cancelling magnetic features.

Roumeliotis and Moore (1993) have developed a linear, analytical model for reconnection at an X-type neutral line (cf. Chap. 2). The reconnection process is assumed to be driven by converging or diverging motions applied at the photosphere. The gas pressure has been ignored (without much justifications) in the vicinity of the neutral line, and only small perturbations have been considered. The model relates the flows around the diffusion region, where dissipative effects are important, to the photospheric driving motions. The calculations based on this linear theory support the possibility of the laminar, slow reconnection occurring low in the solar atmosphere.

None of the above-mentioned authors considered the details of the reconnection process. Therefore it is still unclear whether the process can occur effectively enough in low-temperature plasma to ensure the upward flux of matter that is sufficient for prominence formation in the corona. In this chapter we shall treat the reconnection process in the chromosphere and the photosphere in greater detail.

The *reconnecting current layer* (RCL) is envisaged to be formed in consequence of centre-to-boundary flows of weakly ionized plasma in convective cells. It is in such a current layer that field lines reconnect to change the field topology in the way suggested by Syrovatskii (1982) and Pneuman (1983). As distinct from the coronal case, we treat the RCL in the chromosphere and photosphere. We shall find that the reconnection efficiency is highest in the temperature minimum region, where the classical electric conductivity of weakly ionized plasma reaches its minimum.

## 15.2 Model of Reconnecting Current Layer

### 15.2.1 Simplest Balance Equations

Let us consider a stationary reconnecting current layer (RCL) in the solar chromosphere and photosphere (Litvinenko and Somov 1994b, Litvinenko 1999). To find its characteristics, let us write down the order-of-magnitude relations stemming

from the one-fluid equations of continuity, momentum conservation (both across and along the layer) and magnetic field diffusion into the RCL:

$$n_0 v_0 b = n v_1 a, \quad (15.1)$$

$$(1 + x(T_0)) n_0 k_B T_0 + \frac{B_0^2}{8\pi} = (1 + x(T)) n k_B T, \quad (15.2)$$

$$(1 + x(T)) n k_B T = m_p n \frac{v_1^2}{2} + (1 + x(T_0)) n_0 k_B T_0, \quad (15.3)$$

$$\frac{c^2}{4\pi \sigma(T) a} = v_0. \quad (15.4)$$

Here  $a$  and  $b$  are the layer half-thickness and half-width.  $n_0$  and  $n$  are the plasma concentrations outside and inside the layer,  $x$  is the ionisation degree,  $v_0$  and  $v_1$  are the plasma inflow and outflow velocities,  $m_p$  is the proton mass (hydrogen being assumed to be the main component of the medium),  $T_0$  and  $T$  are the temperatures outside and inside the RCL.  $\sigma$  is the collisional conductivity in the layer where the magnetic field perpendicular to the electric current is zero.  $B_0$  is the field in the vicinity of the RCL.

The set of Eqs. (15.1)–(15.4) should be supplemented by the energy balance equation. However it is not an easy matter to do this. On the one hand, thermal conductivity is unlikely to play a significant role in the energy balance of the low-temperature RCL. On the other hand, there are no reliable calculations for the radiative loss function  $L(T)$  in the temperature domain  $< 10^4$  K. An attempt to solve the radiative transfer equation for such a thin layer in the dense plasma of the low solar atmosphere would be an unjustified procedure given the order-of-magnitude character of the model at hand.

Let us adhere to the simplest assumption, namely that the cooling processes are effective enough to ensure the approximate equality of plasma temperatures inside and outside the RCL. Hence we postulate that

$$T \approx T_0. \quad (15.5)$$

This means that we do not expect an abrupt temperature enhancement in the RCL as in the fully ionized case. Note that the photospheric density is about  $10^8$  times as large as that of the corona. Roughly speaking, if the same amount of magnetic free energy is released in the corona and photosphere into heat in the same volume, each particle of the photosphere would receive approximately  $10^{-8}$  of the energy given to each particle of the corona. For example, the so-called type II *white-light flares* (Mauas 1990; Fang and Ding 1995) are supposed to be the dissipation of magnetic field by reconnection in the photosphere. Such flares bring a temperature enhancement only of 150–200 K.

### 15.2.2 Solution of the Balance Equations

Now the sought-after quantities (the RCL parameters  $a$ ,  $b$  etc.) can be expressed with the aid of Eqs.(15.1)–(15.5) via the external parameters  $n_0$ ,  $T$ ,  $x$ ,  $\sigma$ ,  $v_0$ , and  $B_0$ :

$$a = \frac{c^2}{4\pi \sigma(T) v_0}, \quad (15.6)$$

$$b = (1 + \beta^{-1}) a \frac{v_1}{v_0}, \quad (15.7)$$

$$n = n_0 (1 + \beta^{-1}), \quad (15.8)$$

$$v_1 = V_{A,s} \equiv B_0 [4\pi m_p n_0 (1 + \beta^{-1})]^{-1/2}. \quad (15.9)$$

Here

$$\beta = (1 + x(T)) n_0 k_B T \frac{8\pi}{B_0^2} \quad (15.10)$$

and  $V_{A,s}$  is the Alfvén speed defined by formula (8.7).

Returning to the question posed in the introduction of this section, it is now straightforward to calculate the mass flux into the corona through the RCL, assuming the latter to be vertically orientated:

$$F = 2m_p n v_1 a l = 2m_p n_0 (1 + \beta^{-1}) \frac{c^2 l V_{A,s}}{4\pi \sigma v_0}, \quad (15.11)$$

$l \sim 10^9$  cm being a typical value of the current layer length.

To find numerical values of the current layer parameters, we make use of the chromosphere model due to (Vernazza et al. 1981). This model gives us the input parameters  $n_0$ ,  $x$  and  $T$  as functions of the height  $h$  above the lower photospheric boundary, i.e. the level where the optical column depth in continuum  $\tau_{5000} = 1$ . The collisional conductivity,  $\sigma$ , for this model was calculated by Kub and Karlický (1986). A typical value of the field is assumed to be  $B_0 \approx 100$  G. As for the inflow velocity, it is a free parameter. Its magnitude is of the order of the photospheric convective flow velocity  $\approx 100$  m/s. Table 15.1 presents the RCL characteristics predicted by our model using these data and the layer length  $l \approx 10^9$  cm.

### 15.2.3 Characteristics of the Reconnecting Current Layer

Apart from variation of the inflow velocity, we consider three levels in the solar atmosphere, in an attempt to clarify the physical picture of the reconnection process. These are the lower photosphere ( $h = 0$  km), the temperature minimum

**Table 15.1** Parameters of the reconnecting current layer in the solar chromosphere and photosphere

Height	$h$ , km	0	0	350	350	2,110	2,110
Temperature	$T$ , $10^3$ K	6.4	6.4	4.5	4.5	18.5	18.5
Conductivity	$\sigma$ , $10^{11}$ s $^{-1}$	6	6	1.5	1.5	140	140
Inflow velocity	$v_0$ , 10 m s $^{-1}$	1	10	1	10	1	10
Half-thickness	$a$ , 10 $^4$ cm	10	1	50	5	0.5	0.05
Half-width	$b$ , 10 $^7$ cm	0.8	10 $^{-2}$	10	0.1	3,000	30
Concentration	$n$ , 10 $^{16}$ cm $^{-3}$	10	10	1	1	0.02	0.02
Outflow velocity	$v_1$ , km s $^{-1}$	0.6	0.6	2	2	20	20
Mass flux	$F$ , 10 $^{10}$ g s $^{-1}$	300	30	300	30	0.4	0.04

( $h = 350$  km), and the upper chromosphere ( $h = 2,113$  km). The properties of the reconnection process drastically differ at these levels. Different regimes of *linear* reconnection (Craig and McClymont 1993, Priest et al. 1994) seem to be possible, including very slow (very small magnetic Reynolds number) reconnection.

The remarkable thing is that reconnection is predicted to effectively occur only in a thin layer of the solar atmosphere (not thicker than several 100 km), coinciding with the temperature minimum region. Here

a relatively thick reconnecting current layer (RCL) can be formed, where reconnection proceeds at a rate imposed by the converging flows of plasma.

Since the magnetic field is relatively weak, the flow is practically incompressible. Magnetic energy is transformed into the thermal and kinetic energy of the resulting plasma motion. The upward flux of matter through the RCL into the corona is capable of supplying 10 $^{16}$  g of cold chromospheric material in a time of 10 $^4$  s. This is amply sufficient for the formation of a huge prominence.

An interesting peculiarity of the solution obtained is the inverse proportionality of the mass flux to the inflow velocity. The physical reason for this is that decreasing  $v_0$  leads to a decrease of the electric current in the RCL and hence the magnetic field gradient. Since  $B_0$  is kept fixed, the layer thickness  $2a$  has to increase, thus augmenting the matter flux.

Below the temperature minimum, the RCL does not form;  $a \approx b$  because the plasma density is very high there. That diminishes the Alfvén speed and prevents the magnetic field from playing a significant role in the plasma dynamics. The overall geometry of the field is that of an X-point, so that the inflow magnetic field is highly nonuniform. This regime corresponds to the ‘nonuniform’ reconnection class according to classification given by Priest et al. (1994).

As for reconnection in the upper chromosphere, it is not efficient either. The reason for this is the relatively high temperature, resulting in the high conductivity (Table 15.1), which makes magnetic diffusion into the RCL too slow for any observable consequences related to the mass flux into the corona.

Several remarks are in order here, concerning our initial assumptions. First, we have assumed the RCL to be purely neutral, that is no magnetic field perpendicular to the RCL has been taken into account. Allowing for a non-zero transversal field  $\xi_{\perp} B_0$ , Eq. (15.1) might be rewritten as follows:

$$n_0 v_0 b = n v_1 (a + \xi_{\perp} b). \quad (15.12)$$

Since our model predicts the layer to be rather thick ( $a / b > 10^{-2}$ ) this correction is of no importance:

**|** a small transversal field does not considerably increase the effective cross-section of the plasma outflow from the RCL.

Second, formula (15.5) needs some justification. By way of example, let us suppose that the influx of magnetic energy is balanced by radiative losses (see Part I, Sect. 12.1.3):

$$\frac{B_0^2}{4\pi} v_0 b = L(T) x n^2 ab. \quad (15.13)$$

A crude estimate for the loss function  $L(T) = \chi T^{\alpha}$  has been given by, for example, [Peres et al. \(1982\)](#). Using this estimate together with the above RCL characteristics, one could find  $T \approx 10^4$  K (for  $h = 350$  km). Given the order-of-magnitude character of our model, it seems reasonable to presume that radiative energy losses can balance the Joule heating, so that (15.5) is valid as a first approximation. Anyway, although we expect the plasma heating to have some impact on our results, it is not likely to considerably alter the conclusions concerning reconnection efficiency. This is well supported by numerical results obtained in the more accurate model of the RCL by [Oreshina and Somov \(1998\)](#).

Finally, we have implicitly assumed the plasma flow in the reconnection region to be well coupled. What this means is that both neutral and charged plasma components participate in the plasma flow (see, however, Sect. 15.4). As a consequence, the total density appears in the expression for the Alfvén speed determining the outflow velocity. If the coupling were weak, the ion Alfvén speed would have to be used in Eq. (15.9), giving a faster outflow of ions.

[Zweibel \(1989\)](#) investigated reconnection in partially ionized plasmas and introduced the parameter  $Q$  defining the degree of coupling:

$$Q = \frac{v_0}{a v_{ni}}, \quad (15.14)$$

$v_{ni}$  being the frequency of neutral-ion collisions. The smaller  $Q$  is, the stronger is the coupling. It is easy to check that for the RCL in the temperature minimum region  $Q \approx 10^{-5}\text{--}10^{-1}$  for  $v_0 = 10^3\text{--}10^5$  cm s<sup>-1</sup>. This value of  $Q$  substantiates the assumption of **strong coupling for reasonably slow inflows**. In fact, a more self-consistent consideration of the reconnection region is necessary to take account of the generalized Ohm's law in a weakly-ionized plasma with a magnetic field near the temperature minimum.

## 15.3 Reconnection in Solar Prominences

The idea that magnetic reconnection in the dense cool plasma of the solar atmosphere is a mechanism of the so-called *quiescent prominence* (filament) formation was put forward many years ago. The model of prominence formation by dint of the reconnection process was shown to predict realistic field topologies near filaments. However no investigation were performed on the value of the upward flux of plasma into the corona. As were proved in the previous section, the flux can be high enough to explain the filament formation in a reasonable time:  $F \approx 10^{11}\text{--}10^{12} \text{ g s}^{-1}$ . This seems to be a strong argument in favor of the well-known Pneuman–van Ballegooijen–Martens model. However there were only circumstantial pieces of evidence in its favor.

Compared with the corona,

the solar photosphere provides us with a unique place to observe the magnetic reconnection process directly,

since the magnetic fields can be measured with high resolution.

Direct indications of reconnection in the temperature minimum have been found on the basis of the study of photospheric and chromospheric magnetograms together with dopplergrams in the same spectral lines. Liu et al. (1995) have obtained magnetograms in the H $\beta$  ( $\lambda 4861.34 \text{ \AA}$ ) and FeI ( $\lambda 5324.19 \text{ \AA}$ ) lines. A comparative study of such magnetograms has revealed the existence of **reverse polarity features**. The appearance and behavior of these features can be explained by the twisting of the magnetic flux tubes and reconnection of them in the layer between the photosphere and the chromosphere, i.e. in the temperature minimum region.

Observations show that reverse polarity *cancellation* is supposed to be a slow magnetic reconnection in the photosphere. Certainly we can adjust the parameters to account for observed flux canceling. It has been also revealed (Wang 1999) that in all well-observed events there is no connecting transversal field between two canceling component. So observations support the reconnection explanation.

We have seen that reconnecting current layers (RCLs) can be formed in the temperature minimum region in response to photospheric flows (Sect. 15.2). Here reconnection efficiency is determined by the high collisional resistivity rather than by the turbulent one, as opposed to the coronal case. As a final speculation, high-speed flows which are predicted by our model in regions of strong magnetic fields ( $B_0 > 300 \text{ G}$ ) might be identified with spicules.

\* \* \*

Optical observations reviewed by Martin (1998) confirm the following **necessary conditions** for the formation and maintenance of the filaments: (a) location of filaments at a boundary between opposite-polarity magnetic fields, (b) a system of overlying coronal loops, (c) a magnetically-defined channel beneath, (d) the convergence of the opposite-polarity network of magnetic fields towards their common boundary within the channel, and (e) cancelation of magnetic flux at the common polarity boundary.

Evidence is put forth for **three additional conditions** associated with fully developed filaments: (a) field-aligned mass flows parallel with their fine structure, (b) a multi-polar background source of a small-scale magnetic field necessary for the formation of the filament barbs, and (c) a handedness property known as *chirality* which requires them to be either of two types, dextral or sinistral.

In the northern hemisphere most quiescent filaments are *dextral*, and in the southern hemisphere most are *sinistral*.

This refers to the direction of the magnetic field when standing on the positive polarity and gives the two possible orientations for the axial field: namely to the right for a dextral structure and to the left for a sinistral one.

One-to-one relationships have been established between the chirality of filaments and the chirality of their filament channels and overlying coronal arcades. These findings reinforce either evidence that every filament magnetic field is separate from the magnetic field of the overlying arcade but both are parts of a larger magnetic field system. The larger system has *at least quadruple footprints in the photosphere* (cf. Fig. 16.1) and includes the filament channel and subphotospheric magnetic fields (Martin 1998).

To explain the hemispheric pattern, Mackay et al. (1998) consider the emergence of a sheared activity complex. The complex interacts with a remnant flux and, after convergence and flux cancellation, the filament forms in the channel. A key feature of the model is the net *magnetic helicity* of the complex (cf. Sect. 16.2.1). With the correct sign a filament channel can form, but with the opposite sign no filament channel forms after convergence because a transversal structure of the field is obtained across the polarity inversion line. This situation is quite similar to that one which will be shown in Fig. 16.3, see also DeVore (2005).

Three-dimensional dissipative MHD simulations (Galgaard and Longbottom 1999) show that a thin RCL is created above the polarity inversion line. When the current becomes strong enough, magnetic reconnection starts. In the right parameter regime,

with the correct sign of helicity, the reconnected field lines are able to lift plasma at several pressure scale heights against solar gravity.

The lifted plasma forms a region with an enhanced density above the RCL along the polarity inversion line.

## 15.4 Element Fractionation by Reconnection

It is observationally established that element abundances of the solar corona and solar wind obey a systematic fractionation pattern with respect to their original photospheric abundances. This pattern is organized in such a way that elements with a low *first ionization potential* (FIP), the so-called low-FIP elements, are enriched by a factor of about four. Apparently the elements are enriched or depleted by a

process that depends on the FIP or perhaps even more clearly on the characteristic first ionization time and the relative diffusion length for the neutrals of the minor species colliding with the dominant hydrogen atoms.

When two regions of opposite magnetic polarity come into contact with each other in a partially ionized plasma, ions drifting in response to the Lorentz force fall into the minimum of the magnetic field, i.e. a vicinity of a zeroth point of the field. Then the drifting ions force the neutrals to take part in the flow. This is the case considered by [Arge and Mullan \(1998\)](#). An essential aspect of reconnection in *weakly-ionized* plasma is that

the atoms have no trouble flowing across the magnetic-field lines; the ions are not entirely constrained to follow the field lines as this should be in ideal MHD.

Instead, they have a significant component across the field lines. The reason is **dissipation in the form of ion-atom collisions**. In view of the fact that the atoms move across field lines freely, and in the view of the fact that collisional coupling connects the atom fluid and the ion fluid, it is not surprising that ions are *not* tied strictly to the field lines. As a result, departures from ideal MHD behavior are an inevitable feature of the process that we discuss here.

Because of the finite time required for ion-atom collisions to occur, the plasma which emerges from the reconnecting current layer (RCL) has an ion/atom ratio which may be altered relative to that in the ambient medium. [Arge and Mullan \(1998\)](#) show that in chromospheric conditions, the outflow plasma exhibits enhancements in ion/atom ratios which may be as large as a factor of ten or more. The results are relevant in the context of the Sun, where the coronal abundances of elements with low FIP are systematically enhanced in certain magnetic structures.

The first ionization potential gives the energy scale of an atomic species, hence many atomic parameters and the chemical behavior of elements are closely related to it. Thus, in principle,

very different physical mechanisms could be imagined which would produce an FIP dependence of elemental abundance

(see Sect. 15.5.3). It is important that the observed FIP enhancement varies from one type of solar magnetic features to another, ranging from unity (i.e., no enhancement) in impulsive flares to as much as ten in diverging field structures. The last suggests that **magnetic field topology plays a role in creating the FIP effect in the Sun**.

If the magnetic field can trap the solar material and confine it (such as in a loop), the FIP effect apparently does not occur. On the other hand, if the field is such that a free outflow of material is allowed (e.g., in divergent field), then the FIP effect develops to a large amplitude. For this reason, when we model magnetic interactions in the chromosphere, for example the fine magnetic-flux tube formation (Sect. 15.5.3) we have to choose a topology which allows material to flow out freely.

In stars other than the Sun, EUV data have allowed to search for the FIP effect. Some stars with magnetic activity levels significantly higher than the Sun show evidence for FIP enhancement. This is consistent with a magnetic origin

of FIP enhancement. Moreover the same FIP-based compositional fractionation mechanism at work in the solar atmosphere is presumably operational in the coronae of significantly more active stars ([Laming and Drake 1999](#)).

## 15.5 The Photospheric Dynamo

### 15.5.1 Current Generation Mechanisms

In the deep photosphere, under the temperature minimum, particles are well coupled by collisions. That is why the physics of the deep photosphere, including the physics of magnetic flux tubes, is often described by the resistive *one-fluid* MHD approach. The same is valid even more for under-photospheric layers.

In the temperature minimum region, there are many neutral atoms which collide with ions and bring them into macroscopic motion. The neutrals drag the ions through a magnetic field if the ion-neutral collisional frequency  $\nu_{in}$  is much higher than the Larmor frequency of ions  $\omega_B^{(i)}$ . However the electrons can still remain well frozen in the magnetic field if the electron-neutral collisional frequency  $\nu_{en}$  is very low in comparison with the Larmor frequency of electrons  $\omega_B^{(e)}$ . Therefore a treatment of this region as

an ensemble of *three fluids* (electrons, ions and neutrals) is necessary to give a clear physical insight on the mechanisms of current generation near the temperature minimum

in the photosphere – the *photospheric dynamo* effect (e.g., [Hénoux and Somov 1987](#)).

Higher in the solar chromosphere, significant effects arise due to the density decrease that leads to a decoupling of the motions of ions and neutrals, that cannot be described by the one-fluid approximation either. However the frozen-in conditions exist, the plasma and magnetic field move together. Here, dynamo action does not occur.

The process which is similar to the photospheric dynamo takes place in the Earth ionosphere. It is well known the “*ionospheric wind dynamo*” (see [Richmond 1989](#)). In both situations, we deal with a weakly-ionized plasma and a strong magnetic field; the slippage of the plasma through the magnetic field is allowed by the dynamo inequality

$$\frac{\omega_B^{(i)}}{\nu_{in}} \ll 1 \ll \frac{\omega_B^{(e)}}{\nu_{en}}, \quad (15.15)$$

as discussed above. Thus, a dynamo mechanism can be understood, in the first approximation, on the basis of the simple three-finger rule: a conductor moving across magnetic-field lines produces an electric field perpendicular to both the magnetic field and the velocity.

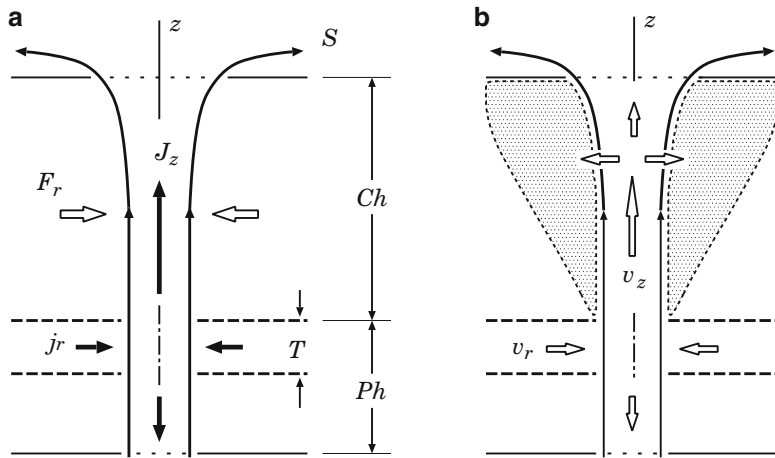


**Fig. 15.1** A simplified model of an open flux tube in the solar atmosphere. (a) The generation of electric currents and the pinch effect. (b) The motion of neutrals and their diffusion across the magnetic field lines in the chromosphere

In the solar photosphere, the horizontal velocities of electrons, ions and neutrals can be found analytically by solving the equations which describe the balance of the horizontal forces acting on each particle fluid (Hénoux and Somov 1991). The horizontal velocities of ions and neutrals derived from these equations are relative to the horizontal velocities in the convective zone, i.e. the primary source of motion. It has been shown that, in an initially weak magnetic field,

a radial inflow of neutrals can generate azimuthal DC currents, and an azimuthal velocity field can create radial DC currents leading to the circulation of vertical currents.

The effects of such velocity fields on the intensity and topology of electric currents flowing in thin magnetic flux tubes will be discussed below.

### 15.5.2 Physics of Thin Magnetic Flux Tubes

A schematic representation of an open flux tube  $S$  is given in Fig. 15.1, which shows the location of the solar chromosphere  $Ch$  and photosphere  $Ph$  with the temperature minimum region  $T$ . Such a semi-empirical model follows, for example, from the He I ( $\lambda 10830 \text{ \AA}$ ) triplet-line observations (Somov and Kozlova 1998).

Let us consider the electric currents generated by azimuthal flows with the velocity  $v_\phi$  in a partially ionized plasma in the region  $T$ . Since it is the relative azimuthal velocity between the magnetic field lines and the plasma, these currents can result either from azimuthal motions of the photospheric plasma around a

fixed magnetic field or from the rotation around the flux tube axis of the magnetic field inserted in a static partially ionized atmosphere. Anyway the azimuthal flows generate the radial currents  $j_r$ .

An inflow of the radial current density  $j_r$  is related to the vertical current density  $j_z$  by continuity equation

$$\frac{\partial j_z}{\partial z} = -\frac{1}{r} \frac{\partial (r j_r)}{\partial r}. \quad (15.16)$$

The vertical electric current

$$J_z = \int 2\pi r j_z(r) dr \quad (15.17)$$

cannot be derived locally, i.e. independently of the contribution of the other neighbouring (in height  $z$ ) layers in the solar atmosphere. Every layer in the temperature minimum region  $T$  acts as a current generator in a circuit that extends above and below this layer. So a circuit model is necessary to relate the total current  $J_z$  to the current densities. However, in all cases the contributions of every layer to the circuit regions placed above and below it are proportional to the inverse ratio of the resistances of these parts of the circuit.

The magnetic forces produced by these currents play a significant role in the structure and dynamics of flux tubes. Even for moderate values of the azimuthal photospheric velocities  $v_\varphi$ , the current  $J_z$  created is strong enough to prevent by the *pinch effect* (an action of the Lorentz force component  $F_r$ ) an opening of the flux tube with height (Hénoux and Somov 1997).

Despite the decrease of the ambient gas pressure with height, the thin magnetic flux tube extends into the solar atmosphere high above the temperature minimum.

In the internal part of the tube, the rise from the photosphere of a partially ionized plasma is found to have four effects.

First, the upflow of this plasma is associated to a leak of neutrals across the field lines as shown in Fig. 15.1b and leads to an increase of the ionization degree with altitude typical for the chromosphere. Moreover the upflow brings above the temperature minimum an energy flux comparable to the flux required for chromospheric heating.

Second, the outflow of neutrals takes place at the chromospheric level across the field lines. Here the neutrals occupy an extensive area shown by the shadow in Fig. 15.1b outside the tube. This outflow of neutrals leads to ion-neutral separation and may explain the observed abundance anomalies in the corona by enhancing in the upper part of the tube the abundances of elements of a low ionization potential (Sect. 15.5.3).

Third, the upward motion velocities are high enough to lift the matter to an altitude characteristic of spicules or even macrospicules.

Fourth, if the footpoints of the flux tubes are twisted by the photosphere, then (when they emerge into the transition region and release their magnetic energy) some rotational component is retained. Strong evidence has been found from *SOHO*'s CDS (the Coronal Diagnostic Spectrometer) observations to support the hypothesis that rotation plays a role in the dynamics of transition region features. These observations are interpreted as indicating the presence of a rotating plasma, a sort of *solar tornado* (Pike and Mason 1998).

### 15.5.3 FIP Fractionation Theory

The flux-tube model predicts the formation of closed or open structures with higher-temperature ionization state and higher low FIP to high FIP elements abundance ratios than the surrounding. A strong pressure gradient across the field lines can be present in the flux tubes where electric currents are circulating (Hénoux and Somov 1991, 1997). Since they produce **two of the ingredients that are required for ion-neutral fractionation by magnetic fields**, i.e. small scales and strong pressure gradients perpendicular to the field lines (Hénoux and Somov 1992), these currents can lead to the efficient ion-neutral fractionation.

Azimuthal motions of the partially ionized photospheric plasma, with velocity  $v_\phi$  at the boundary of the tube,  $r = r_0$ , generate a system of two current shells:  $S_{in}$  and  $S_{out}$  in Fig. 15.2 (Hénoux and Somov 1992, 1999). The vertical currents  $j_z$  in these shells flow in opposite directions, such that the azimuthal component of the field,  $B_\phi$ , vanishes at infinity. This result can be easily understood in the case of a fully ionized atmosphere where the field lines are frozen in the plasma. However the study of a partially ionized atmosphere gives insight into questions that cannot be tackled in the hypothesis of a fully ionized plasma, i.e. the possible difference in velocities perpendicular to the field lines of ions and neutrals.

The internal current system and the azimuthal component of the magnetic field,  $B_\phi$ , create an inward radial force  $B_\phi j_z$  that enhances, by the pinch effect discussed in Sect. 15.5.2, the pressure inside the internal part of the tube.

**|** The pinch effect is present from the photosphere to the chromosphere but its consequences are different in these two regions.

In the photosphere, collisions couple ions and neutrals; so they do not cross the field lines. Above the photosphere, due to the exponential decrease of the density and, as a result, of the ion-neutral friction force with height, the difference in radial velocities of neutrals and ions increases with height.

The current densities and magnetic fields in the flux tube are such that, at hydrogen densities lower than  $10^{13} \text{ cm}^{-3}$ , the collisional coupling is low enough to allow the neutrals to cross the field lines and to escape from the internal current shell with high velocities. In usual plane-parallel-atmosphere models, the fractionation starts in the temperature minimum region  $T$  in Fig. 15.2a at a temperature of about 4,000 K. So the population of ionized low FIP species begin to be enhanced

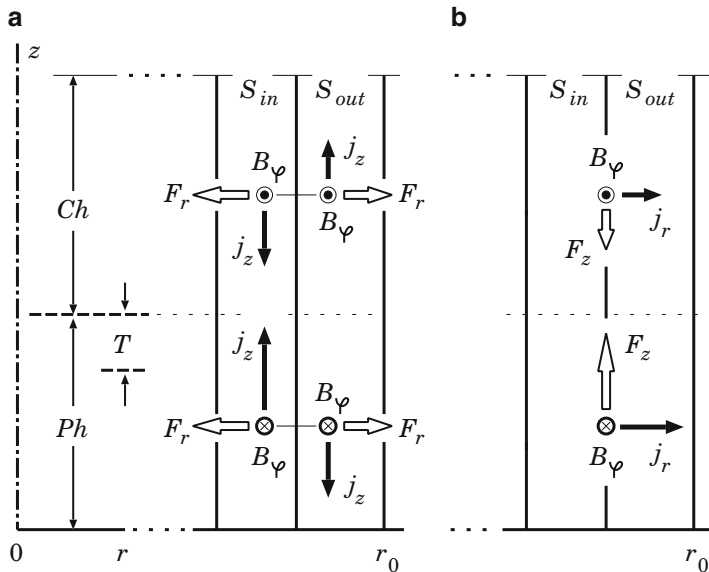


**Fig. 15.2** A simplified model of a thin magnetic flux tube in the solar atmosphere. (a) The vertical current density  $j_z$  and azimuthal component of field  $B_\varphi$  create the pinch effect in the internal part of the tube. (b) The radial current density  $j_r$  and azimuthal magnetic field  $B_\varphi$  produce the upward force in the photosphere

inside the internal current shell just at heights where the usual models place the chromospheric temperature rise and where the separation between the hot and cool components of the Ayres (1996) bifurcation model starts to take place.

Between the two opposite currents flowing vertically, the upwards Lorentz force component  $B_\varphi j_r$  is present. Since the change of the direction of the vertical currents goes with the change of direction, from the photosphere to the chromosphere, of the transversal current  $j_r$  carried by ions, the  $B_\varphi j_r$  force always produces a net ascending action. The intensity of this force is compatible with an ejection of matter up to heights of about 10,000 km, and therefore with the formation of spicules. This force acts in a shell, between the two neutralizing currents, where the gas pressure and collisional friction forces are reduced; it acts on ions and may then lead to a FIP effect in spicules by rising up preferentially the ionized low FIP species. A quantitative study of all these effects remains to be done.

## 15.6 Practice: Exercises and Answers

**Exercise 15.1.** Consider basic features of the magnetic flux-tube twist by a vortex-type motion of the fully ionized plasma.

**Answer.** Let us consider first the twisting action of a fully ionized plasma motion on a magnetic flux tube with  $B_r = 0$  everywhere as this is shown in Fig. 15.3a.

The tube consists of vertical magnetic field lines. Each surface  $r = \text{const}$  rotates with the constant velocity  $v_{\phi,0}$  but there is an excess of the azimuthal velocity  $\delta v_\phi$  in the layer  $(z_0 - \delta z, z_0 + \delta z)$  with a maximum at  $z = z_0$ . In this case, the radial component of electric current density,  $j_r$ , reverses twice with the height  $z$  according to formula

$$j_r = -\frac{1}{r} \frac{\partial}{\partial z} (rB_\phi). \quad (15.18)$$

This is shown in Fig. 15.3b in the plane  $(z, r)$ .

The existence of a maximum of the azimuthal angular velocity at a given radial distance  $r_0$  makes the vertical component of the electric current density,  $j_z$ , to reverse also with height as well as with the radial distance  $r$  because

$$j_z = +\frac{1}{r} \frac{\partial}{\partial r} (rB_\phi). \quad (15.19)$$

A Lorentz force tends to compensate for the twist of the field lines by the de-twisting motions of the plasma (Fig. 15.3c). The azimuthal and vertical components of this force are respectively:

$$f_\phi = -j_r B_z \quad \text{and} \quad f_z = +j_r B_\phi. \quad (15.20)$$

The vertical component creates some compression of the plasma in the central part of the twisting zone, but it will also act in the outer parts of the twisting zone. This will preferentially result in a propagation of the twist and plasma along the tube.

**Exercise 15.2.** Discuss basic features of the magnetic flux-tube generation by vortex-type flows of the weakly ionized plasma near the temperature minimum in the solar atmosphere.

**Answer.** Let  $V_\phi^c$  be the azimuthal component of the velocity field at the boundary between the convective zone and the photosphere as shown in Fig. 15.4.

Strong *collisional* coupling occurs in the low photosphere because of high collisional frequencies  $v_i$  and  $v_e$  in comparison with gyro-frequencies  $\omega_B^{(i)}$  and  $\omega_B^{(e)}$ . So the electric conductivity can be considered as isotropic. Moreover at the boundary with the convective zone the conductivity is so high that the ideal MHD approximation can be accepted, and the electric field acting on particles is null:

$$E_r^c - \varepsilon V_\phi^c B = 0. \quad (15.21)$$

So, in the steady case considered here, the radial electric field is continuous from the convective zone to the photosphere:

$$E_r = E_r^c = \varepsilon V_\phi^c B. \quad (15.22)$$

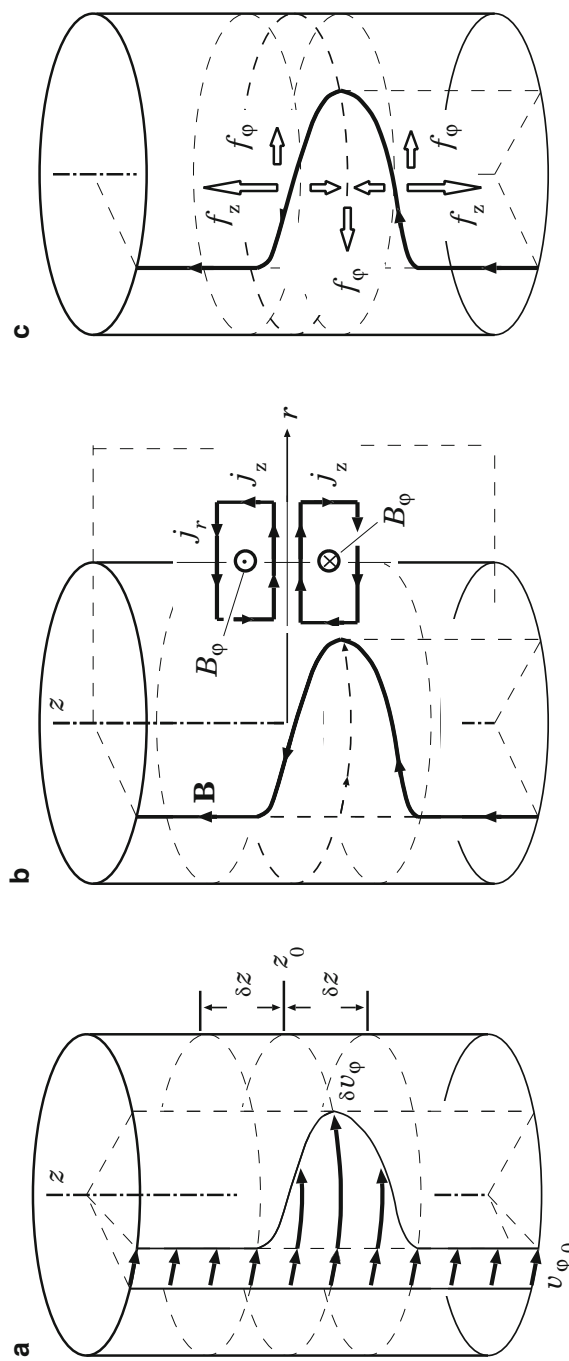


**Fig. 15.3** Twisting flow of a fully ionized plasma inside a flux-tube. (a) Azimuthal velocity distribution at the surface  $r = \text{const}$ ,  $2\delta z$  is the thickness of a twisting zone. (b) A field line on this surface and the associated radial and vertical components of electric current densities  $j_r$  and  $j_z$  in the twisting zone. (c) The vertical component  $f_z$  of the Lorentz force compresses plasma in a central part of the twisting zone, but in outer parts it makes the twisted field line move outwards

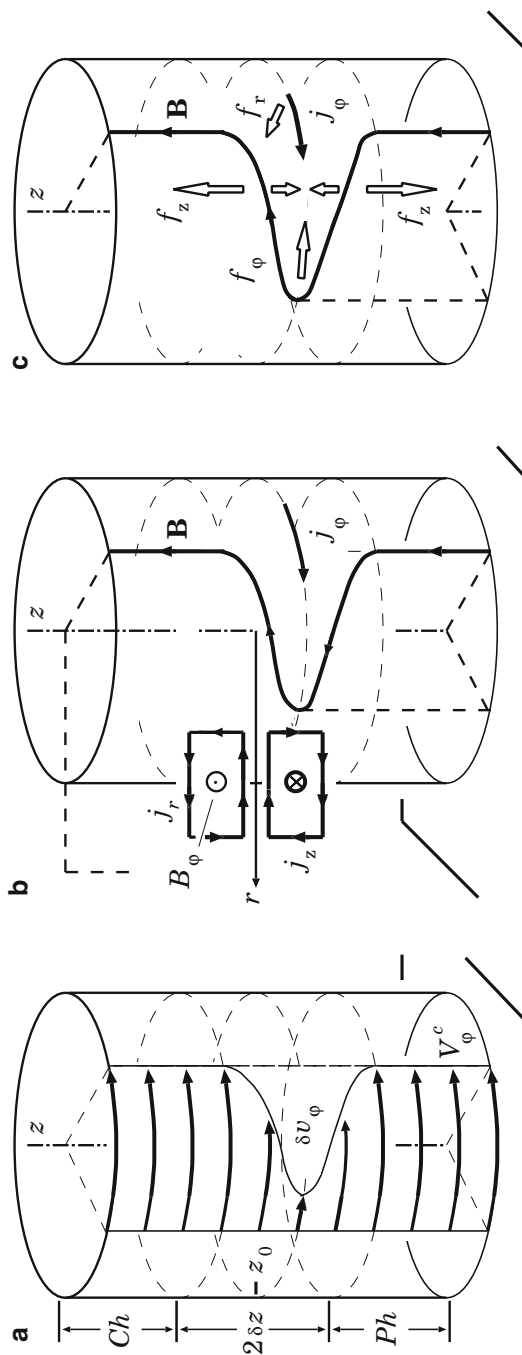


**Fig. 15.4** Twisting flow of a partially ionized plasma inside a magnetic flux-tube in the temperature minimum region, generated by a vortex flow in the convective zone under the photosphere. (a) Azimuthal velocity distribution at the surface  $r = \text{const}$ ,  $2\delta z$  is the thickness of a generator zone. (b) A field line on this surface together with the radial and vertical components of the electric current density in the generator zone. (c) The radial force component  $f_r$  is responsible for the pinch effect appears

Strong *electromagnetic* coupling between electrons and ions occurs in the upper chromosphere because of low collisional frequencies  $\nu_i$  and  $\nu_e$  in comparison with gyrofrequencies  $\omega_B^{(i)}$  and  $\omega_B^{(e)}$ . At temperatures above  $10^4$  K, the ideal MHD approximation can be taken again. So we can put the same boundary condition (15.22) in the upper chromosphere and lower layers.

This means that the upper part of the twisted tube in the steady case must rotate with the same azimuthal velocity as the lowest part at the boundary with the convective zone (see Fig. 15.4).

In the generator region, the poloidal electric current,  $j_r + j_z$ , is generated as well as in a fully ionized plasma, except with an opposite direction of circulation. Additionally, another electric current is present; this is an azimuthal current  $j_\varphi$ . In a partially ionized plasma, the difference in the amplitude of the friction forces between neutrals and ions, between neutrals and electrons (Hénoux and Somov 1991) leads to the generation of an azimuthal current  $j_\varphi$  with the same sign as the azimuthal velocity of neutrals relative to the azimuthal velocity of the electrons that are practically frozen in the magnetic fields.

The flow of neutrals across the magnetic field  $\mathbf{B}$  generates a motion of ions in the same direction. So

$$j_\varphi \approx ne \left( v_{\varphi,n} - V_\varphi^c \right) + j_\varphi^H, \quad (15.23)$$

where  $j_\varphi^H$  is the Hall current related with the electric field component  $E_r$ .

# Chapter 16

## Magnetic Reconnection of Electric Currents

**Abstract** Magnetic reconnection reconnects field lines together with field-aligned electric currents. This process may play a significant role in the dynamics of astrophysical plasma because of a topological interruption of the electric currents.

### 16.1 Introductory Comments

We shall consider the general idea of interruption and redistribution of electric currents which are aligned with magnetic-field lines (the field-aligned currents in what follows), for example in the solar atmosphere. The currents are created under the photosphere and/or inside it, as well as they are generated in the corona. However, independently of their origin, electric currents distributed in the solar atmosphere reconnect together with magnetic field lines. So the currents are interrupted and redistributed in a topological way.

This phenomenon will be discussed in the classical example of a two-dimensional (2D) configuration with four magnetic sources of interchanging polarity and with the three-dimensional (3D) topological model described in Sect. 4.2.1. Converging or diverging flows in the photosphere create a thin reconnecting current layer (RCL) at the separator – the line where separatrix surfaces are crossing. Shearing flows generate highly concentrated currents at the separatrices. We discuss their properties and point out that

the interruption of field-aligned electric currents by the magnetic reconnection process at the separator can be responsible for fast energy release in astrophysical plasma,

for example, in solar flares (e.g., Somov 2012b), in active regions with observed large shear as well as in quiet regions above the ‘magnetic carpet’ responsible for heating of the quiet corona.

## 16.2 Flare Energy Storage and Release

### 16.2.1 From Early Models to Future Investigations

It has for a long time been clear that the energy released in flares is stored originally as magnetic energy of electric currents in the solar atmosphere. At least, there do not appear to be any other sources of energy which are adequate. Simple estimates of the *free* magnetic energy content in typical active regions (e.g., Den and Somov 1989) show that it generally exceeds the observed energy of flares as well as the energy which is necessary for coronal heating in active regions. Free magnetic energy can, in principle, be converted into kinetic and thermal energy of the solar plasma with particle acceleration to high energies and other things that can be observed in the solar atmosphere and interplanetary space. This is the flare or, more exactly, the solar flare problem.

Jacobsen and Carlqvist (1964) and Alfvén and Carlqvist (1967) were the first to suggest that

the interruption of electric currents in the solar corona can create strong electric fields that accelerate particles during flares.

This mechanism of magnetic energy release and its conversion into thermal and supra-thermal energies of particles has been considered and well developed by many authors (e.g., Baum et al. 1978). The interruption of current was described as the formation of an electrostatic *double layer* within a current system – an electric circuit – storing the flare energy.

The formation of the double layer *locally* leads to a direct acceleration of particles. However, because the potential (which gives this acceleration) must be maintained by the external system, the *global* effects of the double layers are not small. In general, they lead to an MHD relaxation of the surrounding magnetic field-plasma configuration providing the influx of energy which is dissipated by the double layers (Raadu 1984).

\* \* \*

An alternative approach to the solar flare problem was introduced by Giovannelli (1946, 1947, 1948), Dungey (1958), and Sweet (1958). After them, it was believed that

the solar flare energy can be accumulated as magnetic energy of a *reconnecting current layer* (RCL)

in the place of magnetic flux interaction and redistribution, more exactly, at the *separators* (Sweet 1958). This idea was well supported by many analytical investigations, by laboratory and numerical experiments (for a review see Syrovatskii 1981; Priest 1982; Somov 1992), by observations of the reconnection process in space plasmas (Hones 1984; Berger 1989) and especially on the Sun (Tsuneta 1993; Démoulin et al. 1993; Bagalá et al. 1995).

**Fig. 16.1** A model of the coronal magnetic field in an active complex with four magnetic sources in the photosphere

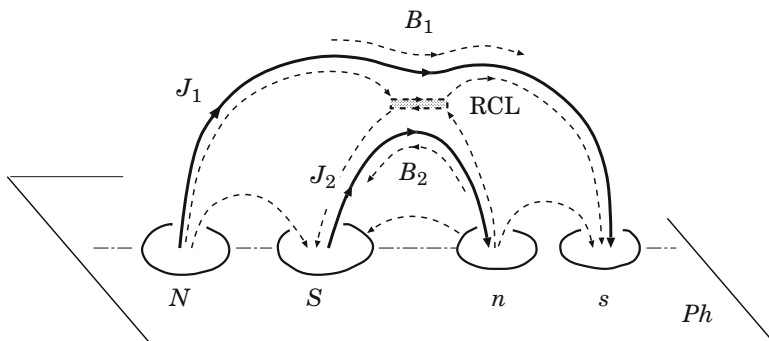
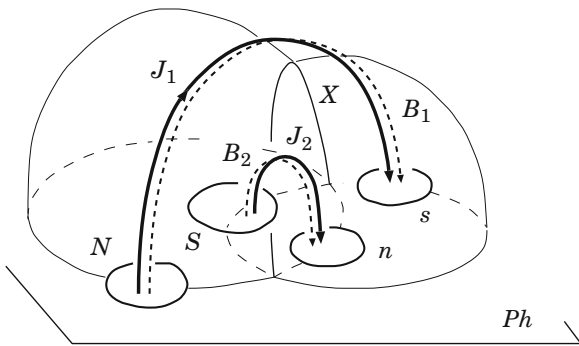


**Fig. 16.2** Coronal currents for the aligned old and new bipolar magnetic regions

In fact, the laboratory experiment by [Stenzel and Gekelman \(1984\)](#) clearly indicated the appearance of double layers in the RCL. This means that

local interruptions of the electric current, induced by reconnection, can exist in the place of magnetic-field line reconnection.

In what follows, we shall consider another effect – magnetic reconnection of electric currents – the physical phenomenon which is different from the creation of an ordinary double layer in the RCL or in the field-aligned current.

[Hénoux and Somov \(1987\)](#) considered two systems of large-scale coronal currents  $J_1$  and  $J_2$  distributed inside two different magnetic cells interacting along the separator  $X$  as shown in Fig. 16.1. Such a model for an active region complex is, in fact, the case of the magnetic topology described in Sect. 4.2.1. The two field lines  $B_1$  and  $B_2$  connect the ‘old’ ( $N, S$ ) and ‘new’ ( $n, s$ ) photospheric sources of magnetic field. The coronal currents that flow from one magnetic flux region to the other (from the old region to the new one) are distributed inside the two different cells and shown schematically as the total currents  $J_1$  and  $J_2$  along the field lines  $B_1$  and  $B_2$ .

For simplicity, in Fig. 16.2 the geometry of the same magnetic field lines and currents is illustrated in the case where the old and new bipolar regions are aligned.

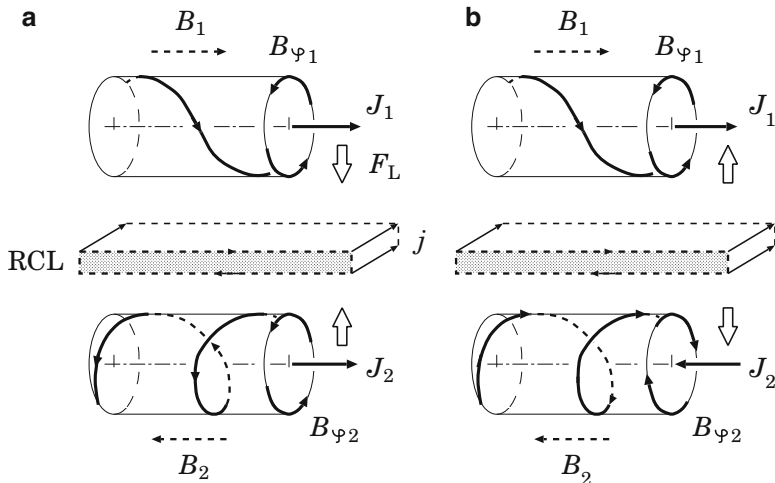


**Fig. 16.3** Two possible orientations of twist in two interacting magnetic flux-tubes with field-aligned electric currents

The field lines  $B_1$  and  $B_2$  near the RCL along the separator (cf. Fig. 4.4) have an opposite direction and can be reconnected. The two current systems  $J_1$  and  $J_2$  can be close to each other near the separator. Moreover, in the case under consideration, the currents flow in the same direction. Therefore, as in Gold and Hoyle (1960) and Sakai and de Jager (1996), they attract each other. So the field-aligned electric currents have to modify the equilibrium conditions for the RCL along the separator (Hénoux and Somov 1987).

The components of the magnetic field transversal to the separator reconnect together with electric currents flowing along them.

In this way, with a perpendicular magnetic field inside the place of interruption, magnetic reconnection creates local interruptions of the electric currents in the solar atmosphere.

If these currents are highly concentrated, their interruption can give rise to strong electric fields accelerating particles

and can contribute significantly to the flare energetics.

Let us consider the magnetic fields created by the currents. These additional or secondary fields are perpendicular to the currents; hence they are parallel to the separator. Therefore they play the role of the longitudinal magnetic field near the RCL (Sect. 8.2.2). Being superimposed on the potential magnetic field, the additional field components  $B_\varphi$  create two field line spirals: left-handed and right-handed (Fig. 16.3a). When looking along the positive direction of the main field lines  $B_1$  and  $B_2$ , we see the two opposite orientations for the spirals: namely to the right for the *dextral* structure (for example, filament) and to the left for the *sinistral* one.

When the currents flow in the same direction, as was shown in Fig. 16.2, the azimuthal components  $B_{\varphi 1}$  and  $B_{\varphi 2}$  have the same direction of rotation. Being opposite inside the RCL, they reconnect well: fully or partially. At the same time, the Lorentz force  $F_L$  pushes the parallel currents one to another. Therefore the case shown in Fig. 16.3a is the most favorable for reconnection of magnetic fields and field-aligned electric currents.

On the contrary, if the currents are antiparallel, as shown in Fig. 16.3b, the azimuthal components  $B_{\varphi 1}$  and  $B_{\varphi 2}$  cannot be reconnected. They are compressed and they decrease the reconnection rate for the main components of the magnetic fields  $B_1$  and  $B_2$ , as it was discussed in Sect. 8.2.2. Hence a handedness property known as *chirality* does influence upon the magnetic reconnection of electric currents.

This is a qualitative picture of reconnection of the field-aligned electric current according to Hénoux and Somov (1987). Physical properties of the electric current reconnection in a highly-magnetized plasma have not been investigated yet. Many of them remain to be understood, in particular, the role of Hall's and perpendicular conductivities (see Appendix C) at the place of the electric current rupture and the role of plasma motions generated there. However it is clear that magnetic reconnection changes the path of an electric current circuit. Because of large dimensions, the current circuit in the corona has a huge inductance. So a large inductive voltage can be generated locally, leading to a complex electrodynamic phenomenon with particle acceleration to high energies.

The review of the present situation in the solar flare theory will help us to understand the basic features of the electric current reconnection phenomenon in Sect. 16.4, see also Somov and Hénoux (1999).

### 16.2.2 Some Alternative Trends in the Flare Theory

A potential field in an active region contains a minimal energy which cannot be extracted from the plasma-magnetic field system. It was a question whether or not it is possible to explain the pre-flare energy storage in the force-free approximation, i.e only with electric currents aligned with the magnetic field. This idea never looked too promising, except in some investigations

(see Sturrock 1991 that suggested that the energy of a force-free field (FFF) generated by footpoint shearing flows can exceed the energy of the ‘completely open’ field having the same boundary condition (the same vertical component) in the photospheric plane. If this were true, we could expect an explosive opening of such an *force-free-field* (FFF) configuration with a fast release of excess energy. Then spontaneous eruptive opening could be a good model for *coronal transients* or *coronal mass ejections* (CMEs).

Aly (1984), by using the virial theorem (Part I, Sect. 19.1), as well as without it (Aly 1991), has shown that the energy of any FFF occupying a ‘coronal half-space’ is either infinite or smaller than the energy of the open field. So obviously

**the opening costs energy** and cannot occur spontaneously. The initial field must have free energy in excess of the threshold set by the open field limit. Only that excess is available to lift and drive the expelled plasma in CMEs or other similar phenomena ([Sturrock 1991](#)).

This conclusion seems to be natural and could actually have important consequences for our understanding of non-steady phenomena with the opening of the coronal magnetic fields. Let us mention some of these consequences, bearing in mind, however, that

| the actual coronal magnetic fields are never completely open or completely closed

(see, e.g., [Low and Smith 1993](#)).

Generally, the electric currents flowing *across* the field allow the corona to have a magnetic energy in excess of the Aly's limit. These currents can be generated by any non-magnetic forces; for example, the gravity force, the gradient of gas pressure or inertia forces. The problem arises because such forces are normally relatively weak in comparison with the magnetic force in the corona. Therefore the related effects can be considered as small corrections to the FFF (see Part I, Sect. 13.1.3).

Another possibility is that the real currents in the corona comprise two different types: (1) **smoothly distributed currents** that are necessarily parallel or nearly parallel to the magnetic-field lines, so that the field is locally force-free or nearly force-free; (2) **thin current layers** of different origin, in which the gas pressure gradient or other forces are significant. If, following [Aly \(1984, 1991\)](#), we could recognize the low efficiency of the smooth FFF (1) in energetics and dynamics of global eruptive events in the corona, we could well replace them by potential fields in evolution and action (e.g., [Syrovatskii and Somov 1980](#)). This means that, to some extent, it is possible to neglect the field-aligned current in (1); we may call this approximation the **minimum current corona**. However, at least one exception can be important. It will be discussed in the next section.

If we do not consider flares or other flare-like events that open coronal fields, and if we do not investigate how to extract the accumulated energy from the FFF, then it is easy to conclude that the free magnetic energy can well be accumulated in FFFs, even if they are smoothly distributed. The basic idea here, used by many authors, is that photospheric footpoint motions stress the coronal field lines, inflate them, thereby producing free magnetic energy. For example, [Porter et al. \(1992\)](#) have studied the energy build-up in the stressed coronal fields possessing cylindrical symmetry. In the non-linear FFF approximation ( $\alpha \neq \text{const}$ ), they have shown that

| a reasonable amount of the photospheric twist can produce enough free magnetic energy to power of a typical solar flare.

The rate of the energy build-up is enhanced if the greatest twist and/or the magnetic flux is concentrated closer to the photospheric neutral line.

### 16.2.3 Current Layers at Separatrices

Analytically, by using the *Grad-Shafranov equation* (see Part I, Sect. 19.5), and numerically, by quasi-static MHD computations, [Zwingmann et al. \(1985\)](#) have shown the occurrence of current layers near the separatrix in sheared magnetic-field structures containing an X-type neutral point – the place where the separatrices cross. They interpret the break-down of the quasi-static theory near the separatrix as evidence for the appearance of a *boundary layer* with the current flowing parallel to the *poloidal* (Sect. 16.3) magnetic field.

[Low \(1991\)](#) and [Vekstein and Priest \(1992\)](#) demonstrated analytically, in the force-free approximation, that shearing flows can produce current layers along separatrices with or without neutral points. Numerical solutions of the time-dependent MHD equations by [Karpen et al. \(1991\)](#), generally, confirmed the formation of currents in the frame of the line tying approximation. They concluded, however, that *true* (reconnecting) current layers (RCL) do not form in the solar corona when a more realistic atmospheric model is considered without a null point present in the initial potential field. These authors found more distributed currents, related to plasma inertia and the absence of a *true* static equilibrium, that cannot be considered as thin current layers.

Therefore

shearing flows in the photosphere generate highly-concentrated electric currents flowing along and near separatrices.

In this context, we suggest a new mechanism of flare energy release – the *topological interruption* of electric currents in the solar atmosphere and their redistribution (Sect. 16.4). We shall consider two stages of its development. In the first, the electric currents are produced by photospheric shearing motions and the magnetic energy is stored in the system of concentrated field-aligned currents. In the second stage, the flare energy release takes place because a strong electric current system is approaching the separator and disrupted by the magnetic-field line reconnection process in the separator region.

## 16.3 Current Layer Formation Mechanisms

### 16.3.1 Magnetic Footpoints and Their Displacements

Let us discuss the topological interruption of coronal electric currents by using the classical example of a potential field in the plane  $(x, y)$  shown in Fig. 16.4. Here  $e_i$  are the ‘magnetic charges’ placed on the  $x$  axis at the points with coordinates  $(x_i, 0)$ ,  $i = 1, 2, 3$ , and 4 at the underphotospheric plane  $y = 0$ . For simplicity we assume that they have interchanging balanced polarities:  $e_1 = -e_4 = Q$

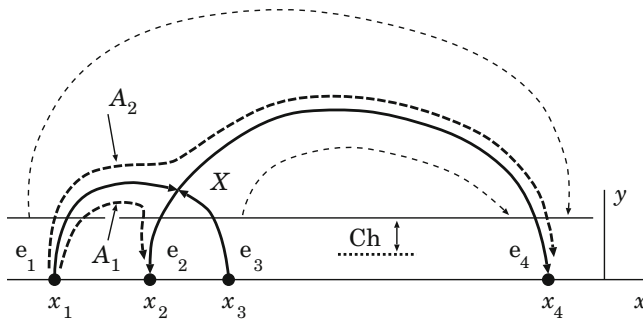


**Fig. 16.4** A 2D model of the magnetic field of four sources of interchanging polarities

and  $-e_2 = e_3 = q$ . So these are the same magnetic charges as in Fig. 4.2 but placed along a straight line – the  $x$  axis. This relative position of magnetic sources corresponds to the idealized case shown in Fig. 4.1.

The solid curves show two separatrices crossing at the neutral point  $X$  (cf. Fig. 1.3) which is the special topological line in the  $z$  direction – the separator. Two field lines are shown by the dashed curves  $A_1$  and  $A_2$ . They start from the magnetic charge  $e_1$ , go near the neutral point but arrive at different charges:  $e_2$  and  $e_4$  respectively. So they have different magnetic connectivity.

This is the *initial* configuration of a magnetic field. Just to keep the same notation as in the early works related with the controlled nuclear fusion (Morozov and Solov'ev 1966a; Shafranov 1966), we refer to a magnetic field in the plane  $(x, y)$  as the *poloidal* one. This part of the magnetic field  $\mathbf{B}_p^{(0)}(x, y)$  is described by the  $z$  component of the vector potential  $\mathbf{A}$ :

$$\mathbf{B}_p^{(0)}(x, y) = \left( \frac{\partial A^{(0)}}{\partial y}, -\frac{\partial A^{(0)}}{\partial x}, 0 \right), \quad (16.1)$$

where

$$\mathbf{A}^{(0)}(x, y) = (0, 0, A^{(0)}(x, y)).$$

In the case under consideration

$$A^{(0)}(x, y) = \sum_{i=1}^4 \ln r_i, \quad (16.2)$$

where

$$r_i = [(x - x_i)^2 + y^2]^{1/2}$$

(see Lavrent'ev and Shabat 1973, Chap. 3, Sect. 2).

Near the  $X$ -type point, where the magnetic field equals zero, the vector-potential can be written as (cf. formula (2.23)):

$$A^{(0)}(x, y) = \frac{1}{2} h_0 [-(x - x_0)^2 + (y - y_0)^2], \quad (16.3)$$

with  $x_0$  and  $y_0$  being the coordinates of the neutral point. The constant which can be added to the vector-potential is selected in such a way that  $A = 0$  on the separatrices – the lines that separate the magnetic fluxes of different linkage (or connectivity).

The main aim of our treatment is to understand the relative efficiency in generation and dissipation of electric currents of different origin. Bearing this aim in mind we will consider different motions in the photospheric plane, i.e. different displacements of field line footpoints.

Following Low (1991), we will consider **three classes of displacements**. The displacements of the first class are strictly on the line of the magnetic charges – the  $x$  axis in Fig. 16.4. These displacements model the converging, diverging or emerging motions of the magnetic sources in the photosphere. They keep the magnetic field lines in the plane of the initial field – the plane ( $x, y$ ).

Shearing flows in the  $z$  direction belong to the second and third classes. The displacements of the second class are only ‘*antisymmetric in  $x$* ’, i.e. the photospheric velocity in the  $z$  direction is an odd function of  $x$ . No symmetry is prescribed for the third class of displacements.

### 16.3.2 Classical 2D Reconnection

The displacements of the *first class* defined above do not create RCLs in the absence of a neutral point  $X$  shown in Fig. 16.4. The appearance of such a point on the boundary (for example, in the photospheric plane) is a necessary condition for the creation of a RCL. A sufficient condition is the existence of a non-zero electric field in this point (Sect. 2.1.4). The magnetic field remains potential above the photospheric plane if the boundary conditions prohibit the appearance of a neutral point. In general, however, ‘a neutral point begins to appear’ on the boundary surface (Somov and Syrovatskii 1972; Low 1991) and the reconnecting current layer is generated in it by the electric field.

Let us consider, as the simplest example, a symmetrical initial distribution of magnetic charges shown in Fig. 16.5a and the small symmetrical displacements of footpoints  $x_2$  and  $x_3$  as follows

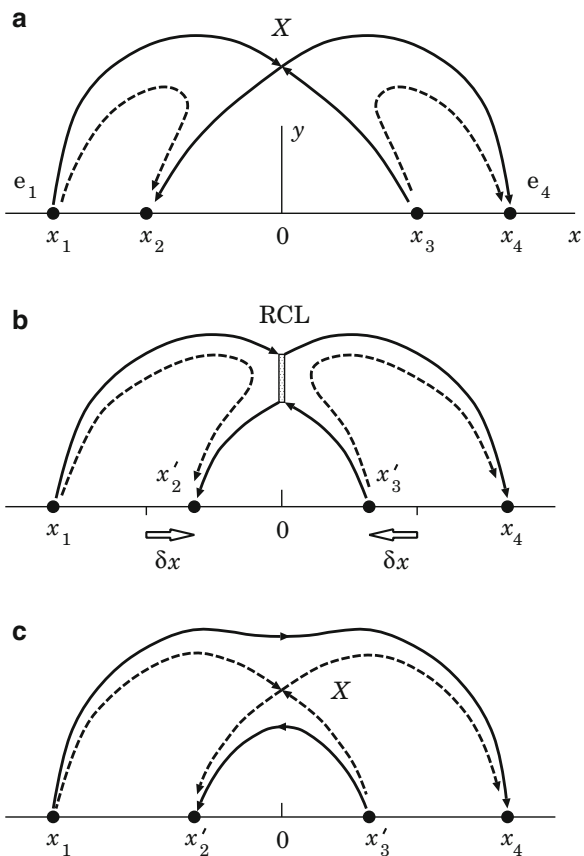
$$\delta x_2 = -\delta x_3 = \delta x(t).$$

They are shown in Fig. 16.5b. In the presence of the neutral line  $X$ , in its vicinity, the electromagnetic field can be expressed through the vector-potential (Syrovatskii 1966a, 1971)

$$A(x, y, t) = A^{(0)}(x, y) + \delta A(t). \quad (16.4)$$

Here  $\delta A(t)$  is the value of the magnetic flux which has to be reconnected in the current layer at the neutral point. Then, after the reconnection time  $\tau_r$ , the magnetic field will be potential one again, but with new positions of the footpoints  $x_2 + \delta x$ ,  $x_3 - \delta x$ . The value  $\delta A(t)$  is proportional to the displacement  $\delta x$ .

**Fig. 16.5** (a) The initial field configuration; (b) the formation of the reconnecting current layer (*RCL*) under the converging motion of footpoints  $x_2$  and  $x_3$ ; (c) the disappearance of the RCL when the field relaxes to the new potential state



It is clear from formula (16.4) that in the vicinity of the neutral line there is a uniform electric field directed along the line:

$$\mathbf{E} = -\frac{1}{c} \frac{\partial}{\partial t} \mathbf{A} = (0, 0, E_z), \quad (16.5)$$

where

$$E_z = -\frac{1}{c} \frac{\partial \delta A(t)}{\partial t}. \quad (16.6)$$

It is just this field which produces an electric current  $\mathbf{J}$  along the neutral line (Fig. 1.4b) as well as a drift motion of plasma outside the line (Fig. 1.4a). In a time of the order of the Alfvén time  $\tau_A$ , the current layer is formed along the neutral line.

Figure 16.5b schematically illustrates the process of the current layer formation induced by the photospheric displacements  $\delta x$  of the first class. The relaxation of the magnetic field which contains the current layer to the potential field corresponding to the new boundary conditions is shown in Fig. 16.5c.

### 16.3.3 Creation of Current Layers by Shearing Flows

Let us consider some general properties of the field component  $B_z$  from the initial magnetic field (Fig. 16.4) generated by a shearing displacement  $\delta z(x)$  in the *force free field* (FFF) approximation. To study plasma equilibrium and stability, it is convenient to use the so-called *specific volume* of the magnetic flux tube (see Part I, Sect. 19.3.2) or simply the specific magnetic volume. This is the ratio of the geometrical volume of the flux tube  $dV$  to the enclosed magnetic flux  $d\Phi$ , i.e.

$$U = \frac{dV}{d\Phi}. \quad (16.7)$$

For a field line specified by a given value of vector-potential  $A$ , by invoking the conservation of magnetic flux inside the tube, the specific volume is

$$U(A) = \int \frac{dl}{B}. \quad (16.8)$$

The integral in (16.8) is taken along the field line between two certain appropriate points corresponding to the beginning and the end of the tube. For the example considered in Fig. 16.4, the beginning and the end of a tube are defined by the photospheric points  $x_1$  and  $x_2$  for all field lines connecting these points above the photospheric plane:

$$U(A) = \int_{x_1}^{x_2} \frac{dl}{B_p^{(0)}(x, y)}. \quad (16.9)$$

By integrating the differential equation for a magnetic field line

$$\frac{dz}{B_z} = \frac{dl}{B_p^{(0)}(x, y)}, \quad (16.10)$$

taking account of (16.9), we see that the *toroidal* component  $B_z$  is given by the displacement of field line footpoints at the boundary plane  $y = 0$ :

$$B_z(A) = \frac{\delta z(A)}{U(A)}. \quad (16.11)$$

We see from (16.11) that, even if the displacement  $\delta z$  is a continuous function of  $x$ , a problem may arise for the following reason. In the presence of topological features like X-type points, the different field lines, by having different footpoints  $x_i$  in the photosphere and different footpoint displacements  $\delta x_i$ , may have the same values of  $A$ . Therefore discontinuities of  $B_z$  may appear above the photospheric plane.

Zwingmann et al. (1985) have illustrated this important feature of sheared magnetic fields analytically by considering the FFF locally near a hyperbolic X-point of the form (cf. formula (16.3)):

$$A^{(0)}(x, y) = -\frac{ax^2}{2} + \frac{by^2}{2} \quad \text{with } a \neq b. \quad (16.12)$$

They showed that the specific volume has a logarithmic divergence for  $A$  corresponding to the separatrices that cross at the X-point, i.e. for  $A = 0$ . This means, first of all, that one of the diverging physical quantities is the poloidal current density

$$\mathbf{j}_p = \text{rot } \mathbf{B}_z = \frac{d \mathbf{B}_z(A)}{dA} \cdot \mathbf{B}_p^{(0)} \propto \frac{1}{A \ln^2 A}. \quad (16.13)$$

The total current integrated in the direction perpendicular to the initial poloidal field  $\mathbf{B}_p^{(0)}$  is finite:

$$J_t = \int_{A_1}^{A_2} \frac{d \mathbf{B}_z(A)}{dA} dA = \mathbf{B}_z(A_2) - \mathbf{B}_z(A_1). \quad (16.14)$$

We are therefore led to the conclusion that

shearing flows do induce the current layers extending along the separatrices, with the current flowing parallel to the poloidal field.

This theoretical conclusion was also tested by numerical computations (Zwingmann et al. 1985) which take into account the physical effects that in real plasmas keep the current density from becoming infinitely large (see also Sect. 16.4).

### 16.3.4 Antisymmetrical Shearing Flows

The conclusion made above is valid even in the cases of very high symmetry, e.g. if the displacements are *antisymmetric*, and the initial potential field is symmetric (Fig. 16.5) with respect to the  $y$  axis. This is clear from the following example. Let

$$x_1 = -x_4, \quad x_2 = -x_3,$$

and

$$\delta z_1 = -\delta z_4 = \delta Z, \quad \delta z_2 = -\delta z_3 = \delta z,$$

as shown in Fig. 16.6.

The specific volume of the magnetic flux tube which goes along the field line  $A_1$  from the point  $x_1$  very near the neutral X-point to the point  $x_2$  consists of two terms

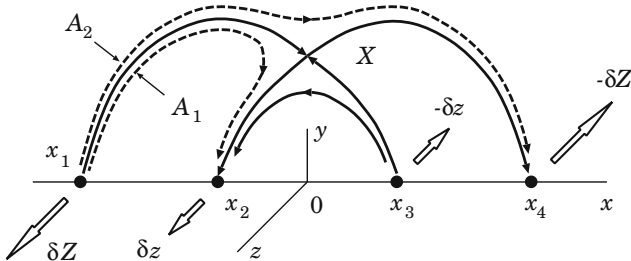


**Fig. 16.6** A 2D initial magnetic field configuration and the antisymmetric shearing motions of footpoints  $\delta Z$  and  $\delta z$

$$U(A_1) = \int_{x_1}^X \frac{dl}{B_p^{(0)}(x, y)} + \int_X^{x_2} \frac{dl}{B_p^{(0)}(x, y)} \equiv U_{1,X} + U_{X,2}. \quad (16.15)$$

According to (16.11) the toroidal (or longitudinal) component of the magnetic field is equal to

$$B_z(A_1) = \frac{\delta z_2 - \delta z_1}{U_{1,X} + U_{X,2}}. \quad (16.16)$$

For the field line  $A_2$  which goes from  $x_1$  to  $x_4$  very near the X-point, with account of the symmetry described above, we find the specific volume

$$U(A_2) = U_{1,X} + U_{X,4} = 2U_{1,X} \quad (16.17)$$

and the relative displacement  $\delta z = \delta z_4 - \delta z_1 = -2\delta z_1$ . So

$$B_z(A_2) = -\frac{\delta z_1}{U_{1X}} \neq B_z(A_1). \quad (16.18)$$

Hence an antisymmetric shear creates the discontinuity of the toroidal field, i.e. the current layer with total current (16.14) along the separatrices, in the presence of X-type point even if the initial potential field is symmetric.

Consider another example. Let the shearing motions be antisymmetric and the initial magnetic field be symmetric, but with the neutral point placed below the level of the photospheric plane (Low 1991). In this case the separatrix surface separates two ‘magnetic islands’ from each other at the point  $x = 0$  and  $y = 0$  as well as separating them from the surrounding field at the total separatrix surface in Fig. 16.7. In this way the connectivity of the magnetic field is discontinuous, and one may in principle expect the creation of magnetic field discontinuities. However, because of the symmetry, the specific volume is

$$U(A_2) = U_{1,o} + U_{o,4} = 2U_{1,o} \quad (16.19)$$

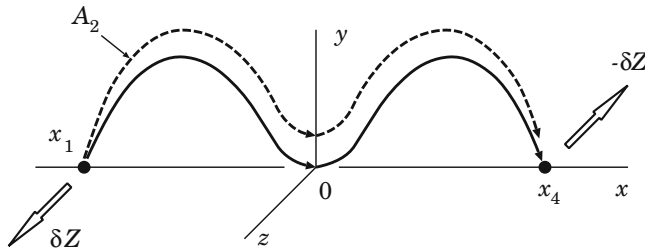


**Fig. 16.7** A 2D potential magnetic field of the quadrupole type without a neutral point above the photospheric plane

with a relative displacement

$$\delta z = \delta z_4 - \delta z_1 = -2\delta z_1.$$

Therefore

$$B_z(A_2) = B_z(A_1). \quad (16.20)$$

We see that the second class of boundary motions cannot create current layers in the absence of neutral points (Fig. 16.7). However an antisymmetric shear creates current layers with the currents flowing along separatrices in the plane  $(x, y)$  in the presence of a neutral point, even if the initial potential field is symmetrical one (Fig. 16.6).

All the other shearing boundary displacements directed in the  $z$  direction are called the *third class*, according to the classification by [Low \(1991\)](#), and will be discussed in the next section.

### 16.3.5 The Third Class of Displacements

Several examples of the third class displacements, including those which are symmetrical in  $x$ , were studied by [Low \(1991\)](#) and [Vekstein and Priest \(1992\)](#). It was shown that these shearing displacements can create discontinuities of the  $B_z$  component which are related with electric currents along separatrices. The displacements can generate such current layers even in the absence of a neutral point, but the separatrices are necessary of course.

The general boundary displacement is a superposition of displacements from all these three classes. [Titov et al. \(1993\)](#) demonstrated the existence of sections of the photospheric polarity inversion line (i.e. the photospheric neutral line) where the overlying field lines are parallel to the photosphere (like in Fig. 16.7). Such sections, called ‘bald patches’, may exist for a wide range of fields created by four concentrated sources of magnetic flux ([Gorbachev and Somov 1989, 1990; Lau 1993](#)). Bald patches appear, for example, when the photospheric neutral line is bent too much in an S-like manner, because this is the case of the separator appearance

(Somov 1985; Somov and Merenкова 1999; Somov et al. 2001). The field lines touching a patch belong to a separatrix surface along which a current layer may be formed by shearing motions of magnetic footpoints at the photosphere.

In the next section we shall discuss the mechanisms which determine the real thickness and other properties of the current layers.

## 16.4 The Shear and Reconnection of Currents

### 16.4.1 Physical Processes Related to Shear and Reconnection

Let us start by discussing the second and third classes of displacements. Since the current density  $\mathbf{j}_p$  is parallel to the poloidal field  $\mathbf{B}_p^{(0)}$  (see formula (16.13)), the plasma velocity  $\mathbf{v}_z$  and the total magnetic field

$$\mathbf{B}_t = \mathbf{B}_p^{(0)} + \mathbf{B}_z$$

are parallel to the discontinuity surface which coincides locally with the plane tangential to the separatrix. In this case, all the MHD boundary conditions are satisfied identically except one:

$$p_1 + \frac{\mathbf{B}_1^2}{8\pi} = p_2 + \frac{\mathbf{B}_2^2}{8\pi}. \quad (16.21)$$

This means that the velocity and the magnetic field may experience arbitrary jumps in magnitude and direction, being parallel to the discontinuity surface. The only requirement is that the total pressure, i.e. the sum of the gas pressure and the magnetic one, remains continuous at the discontinuity surface.

According to the general classification of MHD discontinuities given in Part I, Sect. 16.2, these discontinuities, generated by shearing flows, are usual tangential discontinuities, except that the plasma velocities in the  $z$  direction are small in comparison with the Alfvén speed in the solar corona because the magnetic field is strong there. Therefore, until we take into account the effect discussed at the end of Sect. 16.4.3,

we consider MHD tangential discontinuities as a good model for highly concentrated currents at separatrices, generated by shearing flows in the photosphere.

As treated in MHD, tangential discontinuities have several remarkable properties. One of them is important for what follows. Even in astrophysical plasma of very low resistivity, such as the solar coronal plasma, a tangential discontinuity is a *non-evolutionary* discontinuity (Part I, Sect. 17.1). In contrast to the behavior of the RCL, there is not a steady solution, the stability of which can be considered in the linear approximation.

The origin of this effect lies in the fact that the thickness of a tangential discontinuity is a continuously growing value if the electrical resistivity is finite. After its creation the  $\mathbf{B}_z$  component starts to evolve in accordance with the diffusion equation

$$\frac{\partial B_z}{\partial t} = \frac{\partial}{\partial s} \left( v_m \frac{\partial B_z}{\partial s} \right). \quad (16.22)$$

Here  $v_m$  is the magnetic diffusivity,  $s$  is the coordinate orthogonal to the discontinuity surface. By virtue of Eq. (16.22), the total magnetic flux of  $\mathbf{B}_z$  does not change:

$$\frac{\partial}{\partial t} \int_{-\infty}^{+\infty} B_z ds = v_m \frac{\partial B_z}{\partial s} \Big|_{-\infty}^{+\infty} = 0. \quad (16.23)$$

The thickness of a tangential discontinuity is increasing, but a part of the excess magnetic energy related with a tangential discontinuity is released in the continuous process in the form of Joule heating at a rate

$$\frac{\partial}{\partial t} \int_{-\infty}^{+\infty} \frac{B_z^2}{8\pi} ds = -\frac{1}{4\pi} \int_{-\infty}^{+\infty} v_m \left( \frac{\partial B_z}{\partial s} \right)^2 ds \neq 0. \quad (16.24)$$

Magnetic diffusion always acts to smooth out gradients in both the magnetic field and the electric current density, not to concentrate them. This property has been well demonstrated by many numerical computations.

In the RCL, however, the process of magnetic diffusion away from the discontinuity is compensated by the plasma drift motions into the layer. That is why the steady state for the RCL can exist with the layer width

$$a = v_m v_d^{-1}, \quad (16.25)$$

where  $v_d$  is the drift velocity, and the RCL at separator can be considered as an evolutionary discontinuity (Chap. 12). So

**|** there is a principal difference between the reconnecting current layer at the separator and the current layers at separatrices.

It is important that it is not possible to consider the RCL as a one-dimensional discontinuity because the plasma coming into the current layer has to be compensated by plasma outflow from it. These two conditions are necessary for the existence of steady states for the RCL.

As for tangential discontinuities generated by shearing flows in the photosphere, their electric currents are always spreading out in both directions from separatrix surfaces into the surrounding coronal plasma. By doing so, a part of the electric current flowing along the separatrices appears on the field lines which have already been reconnected (see Fig. 16.4), but the remaining

**|** part of the electric current will be reconnected later on together with the field lines which have not been reconnected yet.

Hence we have to consider how electric currents flowing along the magnetic field lines reconnect with them.

We shall not discuss here all other mechanisms (except presumably the most important one in Sect. 16.4.3) which make the tangential discontinuity currents more distributed rather than concentrated. Neither shall we discuss the generation of the electric currents of different origin in the solar corona, for example, currents due to variations in plasma response time (because of plasma inertia) at different heights in the solar atmosphere, nor the currents related to the absence of a *true* static equilibrium (Karpen et al. 1991). We only would like to point out that electric currents of different origin, being field-aligned after their generation (Spicer 1982), may participate in the process of magnetic field line reconnection.

### ***16.4.2 Topological Interruption of Electric Currents***

The magnetic reconnection process does the same with electric currents as with magnetic field lines, i.e. it disrupts them and connects them in a different way. Physical consequences of the phenomenon have not yet been well investigated, but some of them look clear and unavoidable.

The first of these, an interruption of the electric current, produces an electric field. It is necessary to note here that if reconnection of magnetic field lines would create symmetrical reconnection of currents, then one electric current,  $J_1$ , should replace another one,  $J_2$ , which is equal to the first current, and no electric field could be induced in such a way. Such coincidence has zero probability.

In general, the reconnected currents are not equal among themselves; hence the current ( $J_1 - J_2$ ) is actually interrupted at the  $X$  point of reconnection. This process creates an electric field at the separator.

The simplest but realistic example is the case where we neglect one of the currents; e.g.,  $J_2 = 0$ . Figure 16.8 shows such example. A new emerging magnetic flux ( $s, n$ ) moves upward together with electric current  $J$ . This current is disrupted by the magnetic reconnection process in the RCL and appears to be connected into new electric circuits.

### ***16.4.3 The Inductive Change of Energy***

The second consequence of non-symmetrical reconnection of electric currents is related to the fact that the current ( $J_1 - J_2$ ) is connected in another electric circuit which, in general, has another self-inductance  $L$ . Hence the magnetic reconnection of the current ( $J_1 - J_2$ ) changes the energy of the current system

$$W_L = \frac{LJ^2}{2} \quad (16.26)$$

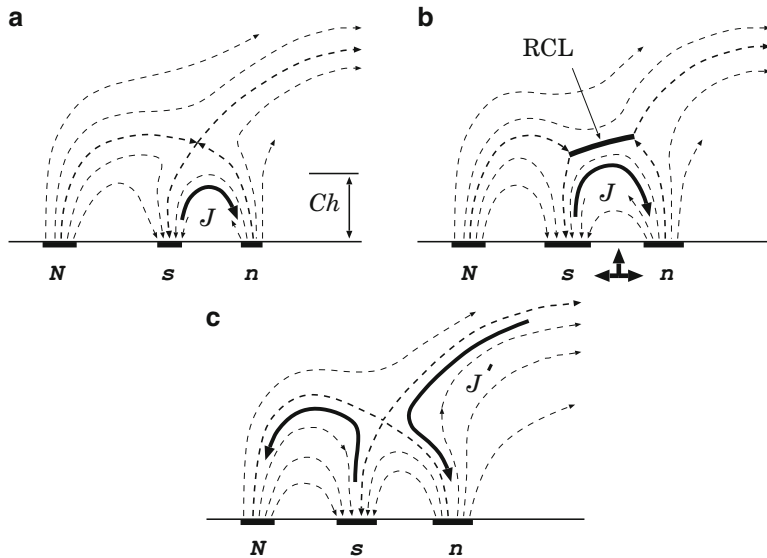


**Fig. 16.8** A reconnecting field with electric currents: (a) the initial state is mainly potential but contains a loop of emerging flux which carries a current  $J$ , (b) the pre-reconnection state, (c) the final state after reconnection of the field lines and field-aligned currents

and its inductive time scale

$$\tau_L = L/R. \quad (16.27)$$

A larger circuit implies a larger energy but a longer inductive time scale.

Zuccarello et al. (1987) pointed out that the magnetic energy release in a flare should not be attributed to current dissipation but rather to a change in the current pattern that reduces the stored magnetic energy. They introduced an example of how self-inductance and energy storage can be changed in a sheared FFF arcade. In fact, the inductive change of energy can be reversed, with the stored energy being resupplied on the inductive time scale. In terms of MHD, the inductive energy  $W_L$  is the energy of the azimuthal magnetic field  $B_\varphi$  related to the field-aligned current  $J$ .

There is an essential advantage in our model of reconnecting electric currents. The topological interruption of large-scale electric currents flowing along and near separatrix surfaces does not require an increase of the total resistivity  $R$  everywhere the currents flow but only in the place where these surfaces cross, i.e. along the separator line. More exactly, the plasma resistivity must be increased, for example by excitation of plasma turbulence, only inside the very thin RCL at the separator. Otherwise the reconnection process will be too slow and the rate of energy release insufficient for a typical flare.

Another important property of the model under consideration is that magnetic reconnection, when it is fast enough, restricts the current density  $\mathbf{j}_p$  of electric currents flowing along the separatrix surfaces and near them. The mechanism of this restriction is the same topological one.

If the characteristic time  $\tau_x$  of the  $\delta x$  displacements which drive reconnection is comparable with the reconnection time scale  $\tau_r$ , then the field lines connecting the footpoints  $x_i$  with the X-type point (see Fig. 16.5a) will not play the role of separatrices any longer after the time  $\tau_r$ . New magnetic field lines, shown by the dashed curves in Fig. 16.5c, with footpoints  $x'_i = x_i + \delta x_i$  will be the place where a new portion of shearing motions will produce a new portion of highly concentrated currents along these field lines, but not the previous ones. Therefore the real velocities of the footpoint displacements and the real reconnection rate determine the real distribution of concentrated electric currents generated by shearing flows in the photosphere.

## 16.5 Potential and Non-potential Fields

### 16.5.1 Properties of Potential Fields

To sum up what we can agree concerning the role of a magnetic field in solar flares, let us classify the magnetic fields in an active region, as shown in Fig. 16.9. The field is divided broadly into two categories: (a) the potential or current-free part and (b) the non-potential part related to electric currents flowing in an active region.

Starting from the photosphere up to some significant height in the corona, the magnetic energy density greatly exceeds that of the thermal, kinetic and gravitational energy of the solar plasma. So the magnetic field can be considered in

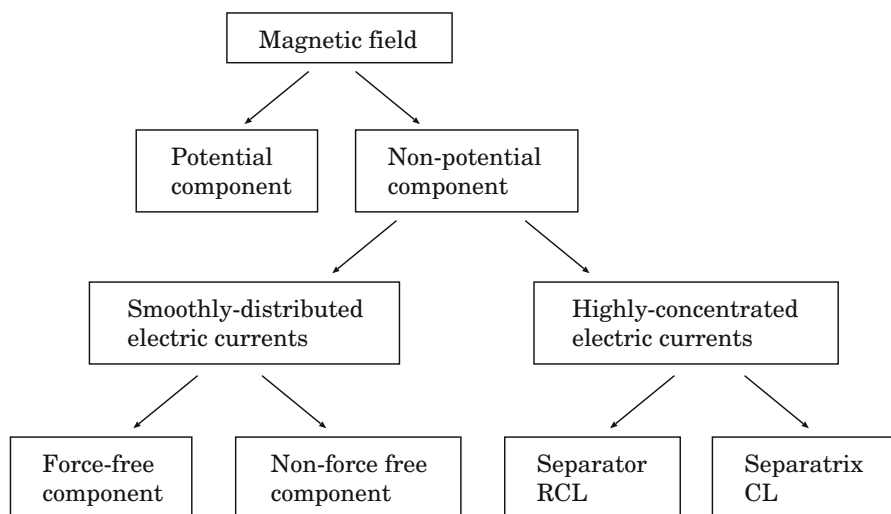


**Fig. 16.9** Main types of the magnetic field in an active region according to their physical properties

the strong field approximation. This means that the coronal field is mainly potential. At least, it is potential in a large scale, in which the field determines the *global* structure of an active region.

However the potential field, which satisfies the given boundary conditions in the photosphere and in the solar wind, has the minimum of energy because the potential field is current-free by definition. Two important consequences for the physics of large flares follow from this fact.

First, being disrupted, for example by an eruptive prominence, the field lines of the potential field are connected back again via reconnection. This behavior is important for understanding the so-called *eruptive* flares. In the strong field approximation, the magnetic field, changing in time, sets the solar plasma in motion. Such a motion can be described by the set of the ordinary differential equations. They are much simpler than the partial derivative equations of the usual MHD. This is a natural simplicity of the actual conditions in the solar atmosphere. In order to solve the simplified MHD equations, we have to find the potential field as a function of time. This is not difficult.

Second, since no energy can be taken from the current-free field, the current-carrying components have to be unavoidably introduced in the large-flare modeling to explain accumulation of energy before a flare and its release in the flare process. We assume here that the solar flare is the phenomenon which takes its energy during the flare from some volume in the corona.

### 16.5.2 Classification of Non-potential Fields

The non-potential parts of the magnetic field are related to electric currents in the solar corona. It is of principal importance to distinguish the currents of different origin (Fig. 16.9) because they have different physical properties and, as a consequence, different behaviors in the pre-flare and flare processes. The actual currents conventionally comprise two different types:

- (a) The *smoothly-distributed* currents that are necessarily parallel or nearly parallel to the field lines, so the magnetic field is locally force-free (FFF) or nearly force-free;
- (b) The *strongly-concentrated* electric currents like a RCL at separators and a current layer (CL) at separatrices.

It was a question whether or not it is possible to explain the pre-flare energy storage in a FFF, i.e. only with electric currents aligned with the magnetic field lines. If this could be true, we would expect an explosive opening of such a configuration with fast release of the excess energy. As mentioned above, the coronal fields can be considered as strong (and as a consequence the FFF or potential) only in some range of heights: starting from the photosphere up to a height in the corona where solar wind becomes fast enough to influence the magnetic field. Hence the corona has an upper boundary which is essential for the coronal field structure

([Somov and Syrovatskii 1972](#)). The coronal fields are never completely open or completely closed ([Low and Smith 1993](#)). Their energy is always lower than the Aly-Sturrock limit but higher than the energy of a potential field ([Antiochos et al. 1999](#)).

If we recognize the low efficiency of the FFF in *eruptive* solar flares, we have to assume that the currents flowing *across* the field lines allow the corona to have a magnetic energy in excess of some limit (lower than the Aly-Sturrock limit) to drive an eruptive flare. These currents can, in principle, be generated by any non-magnetic force – for example, the gravity force, the gradient of gas pressure or forces of the inertia origin.

Two problems arise, however, in this aspect: (a) in the strong magnetic field, such forces are normally relatively weak in comparison with the magnetic force in the corona, at least in large scales; (b) the smoothly-distributed currents dissipate too slowly in a low-resistivity plasma. So the highly-concentrated currents are necessary to explain an extremely high power of energy release in the impulsive phase of a flare. The RCLs may allow an active region to overcome both difficulties.

In a low-resistivity plasma, the thin CLs appear to hinder a redistribution of interacting magnetic fluxes (see the fourth line in Fig. 16.9). They appear at separators in the corona, where reconnection redistributes the fluxes so that the field remains nearly potential. Since resistivity is extremely low, only very slow reconnection proceeds in such a RCL which we call it a slowly-reconnecting RCL. The wider the layer, the larger the magnetic energy is accumulated in the region of the interacting fluxes.

There is a principal difference between the RCL at a separator and the CL at separatrices. It is impossible to consider the RCL as a one-dimensional discontinuity because the plasma coming into the RCL has to be compensated by plasma outflow from it. As for the CL generated at separatrices, it represents the current distribution typical for the MHD tangential discontinuities which are non-evolutionary; they are always spreading out in both directions from separatrix surfaces into surrounding plasma. On the contrary, the current density inside the RCL usually grows with time and reaches one or another limit. For example, wave excitation begins and wave-particle interaction becomes efficient to produce high resistivity, or the collisionless dynamic dissipation allows the fast process of collisionless reconnection.

Therefore the potential field determines a large-scale structure of the flare-active regions while the RCL at separators together with the other non-potential components of magnetic field determine energetics and dynamics of a large eruptive flare.

## 16.6 Observations by *Hinode*

Magnetic reconnection of electric currents generated by shearing flows in the photosphere may play significant role in the energetics of solar flares related to *observed* photospheric shear. Thanks to a huge database collected by *Yohkoh*, *TRACE*, *RHESSI*, and other satellites, it was found that

an active region creates the large two-ribbon flares as well as it is the most eruptive when the active region grows in size and exhibit an S-shaped loop structure or *sigmoid* structure

(see Sects. 4.3.3 and 4.3.5). On the other hand, other flares may be not so large and may not have any significant shear. So they have a different kind of electric currents related, for example, to diverging and converging flows in the photosphere near the region of a newly emerging flux, which we called the first class displacements.

To understand the relative role of different electric currents in the energetics and dynamics of an active region,

it is necessary to study the evolution of its magnetic structure in and above the photosphere.

This would allow us to determine not only the magnetic fluxes of certain magnetic links but also their changes – redistribution and reconnection. Such a study would also give us an information, at least qualitative, about the structure and evolution of the electric field in an active region.

Three experiments are flown on the Japan Institute of Space and Astronautical Science (ISAS) *Hinode* (Sunrise) mission launched in 2006 ([Kosugi et al. 2007](#)). The objective of *Hinode* is to study the origin of the corona and the coupling between the fine magnetic structure in the photosphere and the dynamic processes occurring in the corona.

The *Hinode* payload consists of three high-resolution solar telescopes in visible light, soft X-ray, and extreme ultra-violet (EUV) wavelengths: (a) a 50-cm optical telescope, the *Solar Optical Telescope* (SOT; [Tsuneta et al. 2008](#)), with sophisticated focal plane instrumentation, the *Focal Plane Package* (FPP); (b) an X-ray telescope (XRT) for imaging the high-temperature coronal plasma with a wide field of view covering the whole Sun and with an improved angular resolution, approximately 1 arcsec, i.e. a few times better than *Yohkoh*'s SXR telescope; and (c) an EUV imaging spectrometer (EIS) for diagnosing events observed.

The telescope SOT gives quantitative measurements of the magnetic fields in features as small as 100 km in size thereby providing 10 times better resolution than other space- and ground-based magnetic field measurements. So the SOT instrument gives opportunity to observe the Sun continuously with the level of resolution that ground-based observations can match only under exceptionally good conditions. SOT aims at measuring the magnetic field and the Doppler velocity field in the photosphere.

The SOT observations provide the Fraunhofer *G*-band ( $4,305 \text{ \AA}$ ,  $\delta\lambda = 0.08 \text{ \AA}$ ) images at a spatial resolution of 0.18 arcsec ([Wedemeyer 2008](#)). During the X6.5 class flare on 2006 December 6, the high-resolution *G*-band observations resolve the width of the chromospheric ribbons with values between  $\sim 0.5$  and  $\sim 1.8$  arcsec. The HXR observations of the same flare by *RHESSI* do not resolve the same ribbons but show that the main HXR footpoint has a width perpendicular to the HXR ribbon less than 1.1 arcsec. This suggests that the HXR emission comes from the sharp leading edge of the *G*-band ribbon ([Krucker et al. 2011](#)).

The *G*-band images are often used as proxy for the solar *white-light* flares. The high-resolution observations by *Hinode* and *RHESSI* of flare ribbons in the flare on 2006 December 6 show closely similar ribbon structures, strongly suggesting that the white light and HXRs have physically linked emission mechanisms. Applying the simplified thick-target model, Krucker et al. (2011) have derived the energy deposition rate  $F_{\max} > 5 \times 10^{12} \text{ erg cm}^{-2} \text{ s}^{-1}$  provided by an electron flux of  $1 \times 10^{20} \text{ electrons cm}^{-2} \text{ s}^{-1}$  above 18 keV. This requires that the beam density of electrons above 18 keV be at least  $1 \times 10^{10} \text{ cm}^{-3}$ . The dynamics of such intense beams and their return currents should be further studied.

Space-born observations of the Sun from *Hinode*, *RHESSI*, *STEREO*, and *SDO* produce stunning results that invigorate solar research and challenge existing models. Next generation of solar space missions promises to continue this ‘solar renaissance’ by providing the ability to observe and investigate the solar physical processes on their fundamental scales.

# Chapter 17

## Fast Particles in Solar Flares

**Abstract** Fast particles, the thermal ones escaping from a super-hot source of flare energy and the non-thermal ones accelerated in a flare, move with velocities larger than the mean thermal velocity in plasma in the solar atmosphere and heat it. These particles emit different radiations including the *hard X-ray* (with wavelength  $\lambda < 1 \text{ \AA}$ ) bremsstrahlung. There exist some well-known models to describe these processes that provide the observational manifestations of a solar flare. These classical models are discussed and illustrated in this chapter.

### 17.1 Hard X-Ray Radiation from Fast Electrons

One of the most important processes that takes place in the energy source of a solar flare – the *reconnecting current layer* (RCL) – is the acceleration of charged particles to high energies. For the overwhelming majority of flares that exhibit an *impulsive phase*, the accelerated particles are electrons with an energy greater than about 10–20 keV.

The fast electrons of non-thermal or thermal origin generate the bursts of *hard* (with X-ray energy  $\mathcal{E}_x = h\nu$  greater than 10 keV) X-ray radiation with a power-law spectrum of the hard X-ray (HXR) flux at the Earth orbit:

$$\frac{dI(\mathcal{E}_x)}{d\mathcal{E}_x} = K_\varphi \mathcal{E}_x^{-\varphi}, \text{ cm}^{-2} \text{ s}^{-1} \text{ keV}^{-1}. \quad (17.1)$$

Here  $\mathcal{E}_x$  is the energy of the X-rays, measured in keV, the coefficient  $K_\varphi$  is measured in  $\text{cm}^{-2} \text{ s}^{-1} \text{ keV}^{\varphi-1}$ . These bursts are interpreted as the *bremsstrahlung* produced from *non-thermal electrons* (Peterson and Winckler 1959; Korchak 1967, 1971).

Giving up the overwhelming part of their energy to the solar atmosphere, the accelerated electrons heat it locally to high ( $T > 10^6 \text{ K}$ ) temperatures. These temperatures can be so high ( $T > (3 - 4) \times 10^7 \text{ K}$ ) that the thermal X-rays of such a very hot flare plasma (the so-called *super-hot* plasma) are also hard. This circumstance makes it difficult to interpret the HXR bursts; and the interpretation is generally unambiguous in two respects.

First, the thermal HXR emission of the super-hot plasma masks the lower boundary of the non-thermal HXR spectrum,  $\mathcal{E}_{x1}$ . Moreover, the super-hot plasma is well produced by RCLs in the super-hot turbulent-current states (see Sect. 8.5.4). Thus, in order to determine the lower end of the energy spectrum of accelerated electrons, it is necessary to invoke additional arguments and observational data. For example, if one assumes that the accelerated electrons are the main contributor of heating of the super-hot plasma, then the energy balance condition in this plasma can give an estimate of a necessary power of the electron beam. If the spectral index is known, the total power is uniquely related to the lower boundary  $\mathcal{E}_1$  of the energy spectrum of the accelerated electrons. In the framework of such an approach the spectrum of fast electrons can be recovered only by using the observational data on the super-hot and hot regions: the spectra in the EUV and soft X-ray (SXR) regions, their variations in time and distributions in space.

Second, since the primary heating may not be due to electrons, in principle, there was possible an alternative point of view. Its essence was that there are no non-thermal electrons at all. This was the so-called *thermal interpretation* of the HXR bursts. In it, a flare was regarded as a purely thermal process, in contrast to a non-thermal conception, in which the hard X-ray bursts are a direct manifestation of the non-thermal phase of the flare. The thermal interpretation can be categorized as pessimistic one since it enabled us to calculate only the total amount and rate of conversion of flare energy into heat. In contrast,

by developing a theory of the HXR bursts as the bremsstrahlung of non-thermal electrons, we can obtain information about the acceleration process in a flare.

Moreover, the non-thermal interpretation is predominant since the accelerated electrons are manifested not only in the HXR bursts but as well as in radio-bursts of type III and other types and are also directly detected on spacecraft in the interplanetary space.

In the following sections, we shall briefly discuss the simplest models of the HXR emission that exist in the framework of the non-thermal interpretation. These models are of great interest since, under certain simplifying assumptions, they enable us to establish the spectra of the electrons accelerated in solar flares from the HXR spectra observed at the Earth orbit. It is also important that these models are limiting cases that must be satisfied by a more complete and adequate theory of HXR bursts.

## 17.2 Electron Spectrum and Choice of a Model

### 17.2.1 Injection Spectrum

The question of the spectrum of the electrons accelerated in a flare in connection with the solar HXR bursts was posed by Peterson and Winckler (1959). They interpreted their first registrations of HXR bursts as the Coulomb bremsstrahlung of electrons with energy higher than 10 keV and showed that the electrons accelerated

during the impulsive phase of a solar flare can contain an energy sufficient to explain the observed emission of the flare in all energy ranges. Simultaneously, it became clear that

the problem of establishing the spectrum of the accelerated electrons is neither simple nor unambiguous.

The known uncertainty in establishing the connection between the HXR and the electrons generating them appeared already in the choice of a target model.

Let us suppose that the characteristic time  $\tau_c$  of Coulomb collisions of accelerated electrons with electrons of a plasma is much shorter than the characteristic injection time  $\tau_{in}$  of the injected fast electrons. Then the injection can be regarded as stationary or *continuous*, as they say.

Suppose also that the differential energy spectrum of the flux of injected (the column depth  $\xi = 0$ ) electrons has a power law in the range of energies between  $\mathcal{E}_1$  and  $\mathcal{E}_2$ :

$$v(\mathcal{E}) N(\mathcal{E}, 0) = K_\gamma \mathcal{E}^{-\gamma} \Theta(\mathcal{E} - \mathcal{E}_1) \Theta(\mathcal{E}_2 - \mathcal{E}), \text{ cm}^{-2} \text{ s}^{-1} \text{ keV}^{-1}, \quad (17.2)$$

and accordingly the fast electron density is

$$N(\mathcal{E}, 0) = K \mathcal{E}^{-\gamma - \frac{1}{2}} \Theta(\mathcal{E} - \mathcal{E}_1) \Theta(\mathcal{E}_2 - \mathcal{E}), \text{ cm}^{-3} \text{ keV}^{-1}. \quad (17.3)$$

Here  $\Theta(x)$  is the theta function:  $\Theta(x) = 0$  for  $x < 0$  and  $\Theta(x) = 1$  for  $x \geq 0$ . The variable  $\mathcal{E}$ , measured in keV, is the energy of accelerated electrons; they are assumed non-relativistic. The coefficient  $K_\gamma$  is given by formula

$$K_\gamma = K \sqrt{\frac{2}{m}} \approx 1.87 \times 10^9 K, \text{ cm}^{-2} \text{ s}^{-1} \text{ keV}^{\gamma-1}. \quad (17.4)$$

Here  $m$  is the electron mass in  $\text{keV}/c^2$ ,  $c$  is the velocity of light in  $\text{cm/s}$ , and the coefficient  $K$  is measured in  $\text{cm}^{-3} \text{ keV}^{\gamma-1/2}$ .

### 17.2.2 Electron Spectrum and Choice of a Model

After the fast electrons have traversed a column depth  $\xi \text{ cm}^{-2}$  in an ionized plasma, the spectrum is shifted as a result of Coulomb losses to lower energies and it becomes harder [Syrovatskii and Shmeleva 1972](#):

$$N(\mathcal{E}, \xi) = K \sqrt{\mathcal{E}} (\mathcal{E}^2 + \mathcal{E}_0^2)^{-(\gamma+1)/2} \Theta(\mathcal{E} - \mathcal{E}_1) \Theta(\mathcal{E}_2 - \mathcal{E}), \text{ cm}^{-2} \text{ keV}^{-1}, \quad (17.5)$$

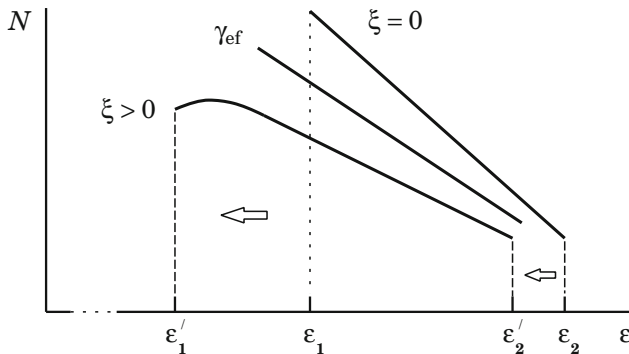


**Fig. 17.1** An injection spectrum ( $\xi = 0$ ) and the spectrum of fast electrons that have passed a column depth  $\xi$  inside a target. The straight line  $\gamma_{\text{ef}}$  represents an effective (integrated over the depth  $\xi$ ) spectrum of electrons

for more detail see Part I, Sect. 4.3. Here

$$\mathcal{E}_0 = \sqrt{2a\xi} \quad (17.6)$$

is the minimal initial energy of electrons capable of traversing the thickness  $\xi$ ; the coefficient

$$a = 1.3 \times 10^{-19} \left( \ln \frac{\mathcal{E}}{mc^2} - \frac{1}{2} \ln n + 38.7 \right), \text{ keV}^2 \text{ cm}^2, \quad (17.7)$$

characterizes the Coulomb losses:

$$\frac{d\mathcal{E}}{d\xi} = -\frac{a}{\mathcal{E}}. \quad (17.8)$$

For an electron of energy  $\mathcal{E} = 10 \text{ keV}$  and plasma density  $n = 10^{11} \text{ cm}^{-3}$  the numerical value of coefficient  $a \simeq 2.9 \times 10^{-18} \text{ keV}^2 \text{ cm}^2$ .

$$\mathcal{E}_{1(2)} = Re \left( \mathcal{E}_{1(2)}^2 - \mathcal{E}_0^2 \right)^{1/2} \quad (17.9)$$

are new boundaries of the energy spectrum of fast electrons inside a target (see the schematic Fig. 17.1).

There are two opposite limiting cases of practical interest. Let us consider them.

### 17.2.3 Thin Target

The fast electrons pass through a column depth that is so small as to allow us to ignore the change of their spectrum in the source of the HXR bremsstrahlung

emission. In this case, the differential spectrum of the HXR flux at the Earth orbit is given as

$$\begin{aligned}
 \frac{dI(\mathcal{E}_x)}{d\mathcal{E}_x} &= \frac{1}{4\pi R^2} \int_V dV \int_{\mathcal{E}_x}^{\infty} d\mathcal{E} \frac{d\sigma}{d\mathcal{E}_x} n v N(\mathcal{E}, \xi) = \\
 &= \frac{1}{4\pi R^2} \int_S dS \int_0^{s_t} n(s) ds \int_{\mathcal{E}_x}^{\infty} d\mathcal{E} \frac{d\sigma}{d\mathcal{E}_x} v N(\mathcal{E}, 0) = \\
 &= \frac{1}{4\pi R^2} \left( \frac{8 r_0^2}{3} \alpha Z^2 mc^2 \right) \int_S dS \xi_t K_\gamma = \frac{B(\gamma, 1/2)}{\gamma} \mathcal{E}_x^{-(\gamma+1)} = \\
 &= 1.74 \times 10^4 \int_S \frac{dS}{S^*} \frac{\xi_t}{\xi^*} \frac{K_\gamma}{K_\gamma^*} \frac{B(\gamma, 1/2)}{\gamma} \mathcal{E}_x^{-(\gamma+1)}, \text{ cm}^{-2} \text{ s}^{-1} \text{ keV}^{-1}.
 \end{aligned} \tag{17.10}$$

Here  $R$  is the distance from the flare to the point of observation and in (17.10) we have taken  $R = 1.5 \times 10^{13}$  cm. The integration over the volume  $V$  of the target is made under the assumption that the curvature of the magnetic-field lines can be ignored, and we can set  $dV = dS ds$ , where  $S$  is the cross-sectional area of the electron beam and  $S^* = 10^{18}$  cm $^2$  is the characteristic area of the flare taken as unit of measurement for  $S$ . The thickness of the target, i.e. its column depth

$$\xi_t = \int_0^s n(s) ds$$

is measured in units of  $\xi^* = 10^{18}$  cm $^{-2}$ . The coefficient  $K_\gamma$  is determined by formula (17.4), and its characteristic value is

$$K_\gamma^* = 6.24 \times 10^{19} \text{ cm}^{-2} \text{ s}^{-1} \text{ keV}^{\gamma-1}.$$

The differential bremsstrahlung cross-section  $d\sigma/d\mathcal{E}_x$  is taken in the Bethe-Heitler approximation,

$$r_0 = e^2/mc^2 \approx 2.8 \times 10^{-13} \text{ cm}$$

is the classical radius of an electron,  $\alpha = 1/137$  is the fine structure constant, and  $Z$  is the effective charge of the ions. The beta function

$$B(\gamma, 1/2) = 16/15, 32/35, 0.812 \text{ and } 0.738$$

for  $\gamma = 3, 4, 5$  and  $6$ , respectively.

As seen from (17.10), in the approximation of a thin target, the spectral index of the differential spectrum of the HXR flux at the Earth orbit is greater by unity than the spectral index of the differential spectrum of the flux of non-relativistic electrons on the Sun, i.e.

$$\varphi = \gamma + 1.$$

(17.11)

### 17.2.4 Thick Target

In this case all fast electrons lose their energy in the HXR source. Therefore, at all times in the source there are fast electrons with not only the injection spectrum (17.2) but also with all the harder spectra (17.3) with  $\xi$  values from 0 to  $\infty$ . This means that, in the main energy range  $\mathcal{E}_1 \leq \mathcal{E} \leq \mathcal{E}_2$  the effective (integrated over the column depth  $\chi$ ) spectrum of electrons in the HXR source is harder by two units [Syrovatskii and Shmeleva 1972](#):

$$\gamma_{\text{ef}} = \gamma - 2.$$

(17.12)

The differential spectrum of the HXR flux at the Earth orbit is

$$\begin{aligned} \frac{dI(\mathcal{E}_x)}{d\mathcal{E}_x} &= \frac{1}{4\pi R^2} \int_S dS \int_{\mathcal{E}_x}^\infty d\mathcal{E} \frac{d\sigma}{d\mathcal{E}_x} \int_0^\infty d\xi v N(\mathcal{E}, \xi) \\ &= \frac{1}{4\pi R^2} \left( \frac{8r_0^2}{3} \alpha Z^2 mc^2 \right) \frac{1}{a} \int_S dS K_\gamma \frac{B(\gamma - 2, 1/2)}{(\gamma - 1)(\gamma - 2)} \mathcal{E}_x^{-(\gamma-1)} \\ &\simeq 5.8 \times 10^3 \int_S \frac{dS}{S^*} \frac{K_\gamma}{K_\gamma^*} \frac{B(\gamma - 2, 1/2)}{(\gamma - 1)(\gamma - 2)} \mathcal{E}_x^{-(\gamma-1)}, \text{ cm}^{-2} \text{ s}^{-1} \text{ keV}^{-1}, \end{aligned} \quad (17.13)$$

or

$$\begin{aligned} \frac{dI(\mathcal{E}_x)}{d\mathcal{E}_x} &= \frac{1}{4\pi R^2} \left( \frac{8r_0^2}{3} \alpha Z^2 mc^2 \right) \frac{1}{a} \frac{B(\gamma - 2, 1/2)}{\gamma - 1} \\ &\times \mathcal{E}_1^{\gamma-2} \mathcal{E}_x^{-(\gamma-1)} \int_S dS F_0(\mathcal{E} > \mathcal{E}_1) \end{aligned}$$

$$\simeq 5.8 \times 10^3 \frac{B(\gamma - 2, 1/2)}{\gamma - 1} \mathcal{E}_1^{\gamma-2} \mathcal{E}_x^{-(\gamma-1)} \int_S \frac{dS}{S^*} \frac{F_0(\mathcal{E} > \mathcal{E}_1)}{F^*},$$

$$\text{cm}^{-2} \text{s}^{-1} \text{keV}^{-1}. \quad (17.14)$$

Here the beta function  $B(\gamma - 2, 1/2) = 2, 4/3, 16/15$  and  $32/35$  for  $\gamma = 3, 4, 5$  and  $6$ , respectively.

Therefore we see that the spectral index of the HXR spectrum is

$$\varphi = \gamma_{ef} + 1 = \gamma - 1.$$

(17.15)

In deriving formulae (17.13) and (17.14), we have assumed that the upper boundary  $\mathcal{E}_2$  of the electron spectrum is fairly high: formally  $\mathcal{E}_2 = \infty$ . Accordingly, in formula (17.14)

$$F_0(\mathcal{E} > \mathcal{E}_1) = 1.6 \times 10^{-9} K_\gamma \mathcal{E}_1^{2-\gamma} / (\gamma - 2), \text{ erg cm}^{-2} \text{s}^{-1}, \quad (17.16)$$

is the boundary energy flux of electrons with energy  $\mathcal{E} > \mathcal{E}_1$ . The characteristic flux is  $F^* = 10^{10} \text{ erg cm}^{-2} \text{s}^{-1}$ , corresponding to the above characteristic value  $K_\gamma^* = 6.24 \times 10^{19} \text{ cm}^{-2} \text{s}^{-1} \text{ keV}^{\gamma-1}$  for  $\mathcal{E}_1^* = 10 \text{ keV}$  and  $\gamma^* = 3$ .

### 17.2.5 Intermediate Cases

All the intermediate cases must be characterized by a certain thickness of a target or an effective time  $\tau_{ef}$  of emergence of the fast electrons from the emitting region. In terms of the latter, for continuous ejection the case of thin target corresponds to the following relation between the characteristic times:

$$\tau_{ef} \ll \tau_c \ll \tau_{in}, \quad (17.17)$$

while for a thick target

$$\tau_c \ll \tau_{ef} \ll \tau_{in}. \quad (17.18)$$

Nothing in fact is known about  $\tau_{ef}$  (in particular, about its dependence on the electron energy  $\mathcal{E}$ ) except that only an insignificant fraction of the electrons accelerated in solar flares reach the interplanetary space. Generally, this favors the thick target model, though it does not contradict more complicated combined models with a thick target in conjunction with a magnetic trap, etc. (see below).

The construction of a realistic and rigorous theory of the escape of the accelerated particles from the flare region is one of the most important unresolved problems

of solar physics. Many investigations concerning the diffusion escape of energetic particles from closed magnetic structures in the region of a flare can be found. Plasma turbulence effects can presumably play a role in the dynamics of the escape of electrons with energy higher than 100 keV. However, at lower energies these effects are apparently unimportant because Coulomb collisions dominates at least at low energies of about 10 keV.

## 17.3 Thick Target and Other Models

### 17.3.1 The Flux of Injected Electrons

To estimate the total energy and number of fast electrons from the observed HXR intensity, [Lin and Hudson \(1971\)](#) proposed the simplest approximate method based on calculating the average value of the ratio of the bremsstrahlung losses to the collisional and ionization losses. More quantitative models of HXR bursts in the thick-target approximation were constructed by [Brown \(1971\)](#) and [Syrovatskii \(1972\)](#). In particular, the latter obtained the solution (17.3) of the transport equation of energetic electrons with power-law spectrum in the presence of Coulomb losses in a fully ionized plasma. They showed that

the effective (integrated over the column depth) spectrum of fast emitting electrons is appreciably harder than the injection spectrum,

i.e. the spectrum of the accelerated electrons.

[Syrovatskii and Shmeleva \(1972\)](#) obtained correct expressions that enable us to calculate the slope of the spectrum of the fast electrons, their total energy, and their number from the observed spectrum of the non-thermal HXR emission of a solar flare. Namely, if the differential spectrum of the HXR flux (17.1) is known, i.e. the parameters  $K_\varphi$  and  $\varphi$  are known, then the power introduced by the electrons with energy  $\mathcal{E} > \mathcal{E}_1$  is determined by formula (see (17.13)–(17.15)):

$$\begin{aligned} \mathcal{F}(\mathcal{E} > \mathcal{E}_1) &\equiv \int_S F(\mathcal{E} > \mathcal{E}_1) dS \\ &= 4\pi R^2 \left( \frac{8r_0^2}{3} \alpha z^2 mc^2 \right)^{-1} a \frac{\gamma - 1}{B(\gamma - 2; 1/2)} K_\varphi \mathcal{E}_1^{2-\gamma} = \\ &\simeq 1.72 \times 10^{25} \frac{\gamma - 1}{B(\gamma - 2; 1/2)} K_\varphi \mathcal{E}_1^{2-\gamma}, \text{ erg s}^{-1}. \end{aligned} \quad (17.19)$$

Here

$$\gamma = \varphi + 1,$$

the low boundary energy  $\mathcal{E}_1$  is measured in keV,  $K_\varphi$  in  $\text{cm}^{-2} \text{s}^{-1} \text{keV}^{\varphi-1}$ , and the beta function  $B(\gamma - 2; 1/2) = 2, 4/3, 16/15$  and  $32/35$  for  $\gamma = 3, 4, 5$  and  $6$ , respectively.

If the total HXR flux at the Earth orbit in a certain energy range  $\mathcal{E}_{x1} \leq \mathcal{E}_x \leq \mathcal{E}_{x2}$  is known, then the power of electrons with energy  $\mathcal{E} > \mathcal{E}_1$  is determined as

$$\begin{aligned} \mathcal{F}(\mathcal{E} > \mathcal{E}_1) &= 4\pi R^2 \left( \frac{8r_0^2}{3} \alpha Z^2 mc^2 \right)^{-1} a \frac{(\gamma - 1)(\gamma - 2)}{B(\gamma - 2; 1/2)} \\ &\times \left[ 1 - \left( \frac{\mathcal{E}_{x1}}{\mathcal{E}_{x2}} \right)^{\gamma-2} \right]^{-1} \left( \frac{\mathcal{E}_{x1}}{\mathcal{E}_1} \right)^{\gamma-2} I(\mathcal{E}_{x1} < \mathcal{E}_x < \mathcal{E}_{x2}) \\ &\simeq 1.63 \times 10^{25} \frac{(\gamma - 1)(\gamma - 2)}{B(\gamma - 2; 1/2)} \frac{I(\mathcal{E}_{x1} < \mathcal{E}_x < \mathcal{E}_{x2})}{1 - (\mathcal{E}_{x1}/\mathcal{E}_{x2})^{\gamma-2}} \left( \frac{\mathcal{E}_{x1}}{\mathcal{E}_1} \right)^{\gamma-2}, \text{erg s}^{-1}. \end{aligned} \quad (17.20)$$

The total number of fast electrons per unit time of injection

$$\begin{aligned} \mathcal{N}(\mathcal{E} > \mathcal{E}_1) &\equiv \int_S dS \int d\mathcal{E} v N(\mathcal{E}, 0) = \\ &\simeq 1.02 \times 10^{34} \frac{(\gamma - 2)^2}{\mathcal{E}_1 B(\gamma - 2; 1/2)} \frac{I(\mathcal{E}_{x1} < \mathcal{E}_x < \mathcal{E}_{x2})}{1 - (\mathcal{E}_{x1}/\mathcal{E}_{x2})^{\gamma-2}} \left( \frac{\mathcal{E}_{x1}}{\mathcal{E}_1} \right)^{\gamma-2}, \text{s}^{-1}. \end{aligned} \quad (17.21)$$

In contrast to the thin-target model, the thick-target model does not require assumptions about the plasma concentration in the emitting region (or rather about the target thickness  $\xi_t$ ; see (17.10)); it is only necessary that the conditions (17.18) be satisfied. In this respect,

**|** the thick-target model requires for the description of a HXR burst the minimal number of parameters,

namely, three (see formula (17.19)): the instantaneous energy flux of the fast electrons with energy above a certain value  $\mathcal{E}_1$ , the value of this limiting energy  $\mathcal{E}_1$ , and the instantaneous slope of the spectrum.

Any other models require specification of additional parameters, for example, the plasma concentration in a magnetic trap or the escape time in the thin-target model, i.e.  $s_t/v(\mathcal{E})$  in (17.10). It is obvious that, from the point of total energy, a thick target is the most advantageous for two reasons. First, in all the remaining cases only some of the fast electrons give up their energy on bremsstrahlung and heating of the target, while the remaining electrons escape with hardly any loss into the interplanetary space.

Second, in the interpretation of a HXR burst with spectral spectral index  $\varphi$

the thick target model gives the softest (steepest) spectrum of the injected fast electrons,

which enables one to accumulate a greater part of the electron energy near the lower boundary  $\mathcal{E}_1$ . Unfortunately, it is the lower end of the electron energy spectrum that is not exactly determined since the lower end of the non-thermal HXR spectrum is unknown.

### 17.3.2 Some Combined Models

It is easy to imagine a thick-target model with impulsive injection. By this we mean, as the simplest example, the case when all the fast electrons “perish” in a target (there is no escape) but the injection time  $\tau_{in}$  is much shorter than the Coulomb collision time  $\tau_c$ :

$$\tau_{in} \ll \tau_c \ll \tau_{es}. \quad (17.22)$$

A conceivable example of such a situation could be a *magnetic trap* filled with low-density plasma into which energetic electrons are injected. Suppose that seepage of the electrons from the trap, a slow precipitation, can be ignored and that the energy losses of the electrons are determined solely by Coulomb collisions. In pure form, such a situation is clearly never realized in solar flares, but from the point of view of fundamentals it is interesting in that the characteristic time of damping of the HXR burst is here determined by the Coulomb loss time

$$\tau_c \simeq 3.3 \times 10^8 n^{-1} \mathcal{E}^{3/2}, \text{ s}, \quad (17.23)$$

where  $\mathcal{E}$  is the electron energy measured in keV.

As a rule, the observed damping time does not follow the law  $\mathcal{E}^{3/2}$ . This indicates that either the damping of the HXR burst is determined by the escape of the energetic electrons or that the electrons perish in the thick target at high plasma concentrations, i.e., the conditions (17.18) are satisfied. In the latter case, the time profile of the HXR burst is determined by the source of the accelerated particles.

The pioneering observations by means of the Utrecht solar HXR spectrometer on the satellite *ESRO TD-1A* (see [Hoyng et al. 1976](#)) with time resolution 1.2 s in the region 24–90 keV and 4.8 s at higher energies showed that frequently the HXR bursts consist of numerous short-lived spikes, or “elementary flare bursts” with rise and fall times of the order of few seconds ([de Jager and de Jonge 1978](#)). Characteristically, the fall times (sometimes 1–2 s) were practically the same in all energy channels. This indicates a very high plasma concentration in the region of the thick target. If the target is the chromosphere then obviously the lifetime of an energetic electron is comparable with the time of passage through several scale heights and is much shorter than the observed decay time of an elementary burst. In this case the time dependence of the burst will be determined by the source of the accelerated electrons.

To explain the quasi-periodic time profile of the large HXR event associated with the 3B flare on August 4, 1972, [Brown and Hoyng \(1975\)](#) proposed a model of a vibrating trap. In this model, the repeated HXR bursts are explained by betatron modulation of electrons accelerated by Alfvén oscillations of the magnetic trap. For an appropriate choice of the trap parameters, the model can be reconciled with the observations of the HXR bursts from flares behind the limb. However these observations also do not contradict the ordinary thick-target model if it is assumed that the source of energetic electrons is at an appreciable height ( $\sim 10,000$  km) in the corona and that the plasma density near the source is increased by, for example, a preliminary heating and “*evaporation*” of the upper chromosphere.

In addition, the model of a vibrating trap is hard to reconcile with the observational fact emphasized at first by [de Feiter \(1974\)](#) that individual pulses in a complicated HXR burst correspond to the appearance of bright optical  $H_{\alpha}$  kernels at different points of the chromosphere. Moreover, according to observations by means of the AC/MSFC X-ray telescope S-056 on *Skylab*, the flare energy release does not occur instantaneously and in one region (one trap) but successively in different magnetic loops that form an arcade above a zero line of the photospheric magnetic field ([Vorpahl 1976](#)).

## 17.4 Flare Heating of the Chromosphere

### 17.4.1 Chromospheric Heating by Electrons

Heating of the solar chromosphere and photosphere by particles accelerated in a flare (electrons, protons and ions of heavier elements) was assumed and discussed by many authors; for example, in connection with the chromospheric  $H_{\alpha}$ - and photospheric white-light flares. Note that fast electrons have a number of advantages as a flare heating agent. In contrast to protons, they are accelerated in almost all flares: in all large ones and about 2/3 of the smallest (with an optical importance  $\leq 1$ ), and even in small flares the energy of the accelerated electrons in the region 10–100 keV seems to be comparable with a significant part of the total flare energy.

For electrons with the injection spectrum (17.3), the energy averaged over the spectrum is

$$\bar{\mathcal{E}} = \frac{2\gamma - 1}{2\gamma - 3} \mathcal{E}_1 = \left( \frac{5}{3}, \frac{7}{5}, \frac{9}{7}, \frac{11}{9} \right) \mathcal{E}_1 \quad (17.24)$$

for  $\gamma = 3, 4, 5$ , and 6, respectively. So the averaged energy is always near the lower limit  $\mathcal{E}_1$  of the spectrum. The main energy of the fast electrons resides in the low-energy part of the spectrum.

If the spectrum is soft and the lower boundary  $\mathcal{E}_1$  is low, then this energy is absorbed in a relatively thin layer, creates a high-temperature region *HT* (Fig. 17.2), and is transformed into a heat flux. Therefore,

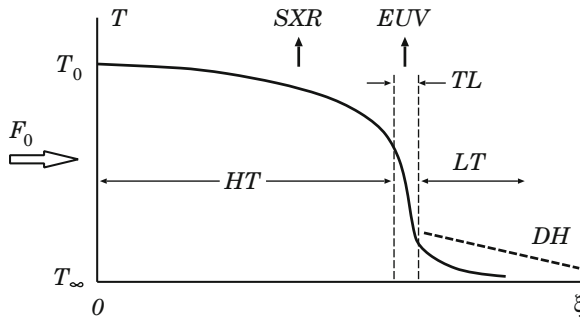


**Fig. 17.2** A temperature distribution over the column depth  $\xi$  along a magnetic flux tube. The high-temperature region  $HT$ , the narrow transition layer  $TL$  and the low-temperature region  $LT$  emit SXR, EUV and optical radiations, respectively.  $DH$  is a region of direct heating by the fast electrons penetrating through the transition layer into the  $LT$  region

in both the impulsive and gradual phase of a flare, its temperature structure is determined primarily by heat conduction.

This enables us to explain the high-temperature part  $HT$  of a flare, which is responsible for the thermal soft X-rays (SXR), and the transition layer  $TL$  which emits mainly in the EUV range. However only a small part (less than 1%) of the original heat flux penetrates to the low-temperature region  $LT$  where temperatures  $T < 2 \times 10^4$  K, and the Hydrogen lines are formed.

For a sufficiently hard spectrum, an appreciable number of fast particles (with high initial energies) can penetrate below the transition layer  $TL$  and thus contribute to the flux of energy supplied to the low-temperature region  $LT$  of a flare. Here they produce the so-called *direct heating* (see  $DH$  in Fig. 17.2), i.e. the heating of the chromosphere by fast particle due to collisional losses of energy. Shmeleva and Syrovatskii (1973) ignored this contribution. In contrast, Brown (1973) determined the temperature structure of this region, taking into account only the direct heating by fast particles but ignoring heat conduction. Let us emphasize here that the direct heating by particles can again become important at great depths only as a result of a rapid decrease of the thermal conductivity at  $T \lesssim 10^4$  K, which is partly compensated by the thermal conductivity of the neutrals  $\kappa_H$  (see Shmeleva and Syrovatskii), which was not taken into account by Brown.

We can readily find the conditions under which the decisive factor is direct heating of the low-temperature region  $LT$  by fast electrons and not by heat fluxes. It is obvious that

the harder is the electron spectrum, the greater the fraction of their energy flux that penetrates into the optical region of a flare.

It is therefore simply necessary to compare this part of the flux for different spectral indexes of the spectrum with the corresponding heat flux that penetrates below the transition layer  $TL$ .

We shall assume that in both the compared situations the heating is stationary and leads to temperature and density distributions corresponding to equality of the pressure along a magnetic flux tube, i.e.  $p = \text{const}$ . However it is obvious that this is a very restricted approach, especially in view of the pioneering observations that show that

the injection of the fast electrons during the impulsive phase of a solar flare and therefore the heating do not have a continuous but an impulsive nature in spatially separated regions

([Zirin and Tanaka 1973](#); [Vorpahl 1976](#)).

Bearing this observational fact in mind, following [Shmeleva and Syrovatskii \(1973\)](#), we give the similar results of calculations corresponding to the case when the pressure in a heated region does not have time to be equalized, i.e. in the opposite limiting case  $n = \text{const}$ . Of course, this is in no way a substitute for consistent treatment of non-stationary two-temperature hydrodynamical phenomena (see Chap. 2 in [Somov 1992](#)). Here we only emphasize that,

in the case of rapid heating, the approximation  $n = \text{const}$  may be more adequate for describing the real distributions of the temperature and density than the approximation  $p = \text{const}$ .

This applies particularly to the case of heating of the low-temperature region  $LT$  by particles since the characteristic time of the observed changes in the HXR,  $H\alpha$  and microwave emissions is frequently of the order of one to several seconds. Therefore, in general, the radiative hydrodynamic simulations ([Allred et al. 2005](#)) of physical processes in the region  $LT$  is needed.

Thus let us consider the heating of the chromosphere by a beam of non-relativistic electrons with the power-law injection spectrum (17.3). The energy flux of the electrons at the column depth  $\xi$  in the chromosphere is

$$F(\xi) = \int_{\varepsilon'_1}^{\varepsilon'_2} \mathcal{E} v N(\mathcal{E}, \xi) d\mathcal{E}, \text{ erg cm}^{-2} \text{ s}^{-1}. \quad (17.25)$$

In particular, the energy flux at the boundary of a heated region, i.e. at  $\xi = 0$ , is

$$F(0) = \int_{\varepsilon_1}^{\varepsilon_2} \mathcal{E} v N(\mathcal{E}, 0) d\mathcal{E} = K \sqrt{\frac{2}{m}} \frac{\varepsilon_1^{2-\gamma} - \varepsilon_2^{2-\gamma}}{\gamma - 2}, \text{ erg cm}^{-2} \text{ s}^{-1} \quad (17.26)$$

for  $\gamma > 2$ . For integral values of  $\gamma$  the ratio  $F(\xi)/F(0)$  was calculated.

As [Petrosian \(1973\)](#) showed at first, the dip observed around  $\sim 100 \text{ keV}$  in the HXR spectrum could be a consequence of the relativistic directivity of the bremsstrahlung of energetic electrons. Therefore there was no reliable grounds for cutting off the electron spectrum at energies  $\simeq 100 \text{ keV}$ . In what follows we consider

the case  $\mathcal{E}_2 = \infty$ . Note that this assumption was also made by Brown (1973) but on the basis of the conjecture that the electrons with energy above 100 keV do not play a role in the heating of an optical flare. Brown assumes a Hydrogen concentration  $n_H < 7 \times 10^{13} \text{ cm}^{-3}$  (i.e. the column depth  $\xi < 10^{21} \text{ cm}^{-2}$ ) in the region of the flare. In fact, however, as Svestka (1973) has shown, in flares with  $n_e \simeq 3 \cdot 10^{13} \text{ cm}^{-3}$  and real ionization of Hydrogen, one can expect a Hydrogen concentration  $n_H$  from  $5 \times 10^{13}$  to  $2 \times 10^{15} \text{ cm}^{-2}$  in the low-temperature region  $LT$ . At such concentration, heating of the low-temperature region can be achieved only by electrons with energy  $\mathcal{E} > 80 \text{ keV}$ .

In the case when the upper limit of the spectrum is infinite, we can use the simpler expression for the energy flux of the electron beam

$$\frac{F(\xi)}{F(0)} = \frac{\gamma - 2}{2} B \left( \frac{3}{2}, \frac{\gamma - 2}{2} \right) \left( \frac{\mathcal{E}_1}{\mathcal{E}_0} \right)^{\gamma - 2}, \quad (17.27)$$

where  $B/2 = 0.785, 0.333, 0.196$  and  $0.137$  for  $\gamma = 2, 4, 5$  and  $6$ , respectively.

### 17.4.2 Protons or Electrons Heat White-Light Flares?

The low-energy protons accelerated in the flare do not give rise to the bremsstrahlung HXR radiation. We obtained the first information about them from interplanetary observations (e.g., van Hollebeke et al. 1975) and also from observations of solar gamma-rays (Chupp et al. 1973). The first gamma-ray observations showed that

the nuclear reactions leading to the gamma-ray emission began simultaneously with the HXR emission

and continued for not less than 10 min. The ratios of the gamma lines at, for example, 2.23 and 4.43 MeV enable one to estimate the slope of the spectrum of the accelerated protons under certain assumptions about the  $\text{He}^3$  abundance in the photosphere.

Ramaty et al. (1975) calculated lines for power-law and exponential spectra of the accelerated particles (mainly protons and  $\alpha$  particles) and showed that in the energy interval 10–100 MeV the differential spectrum of the particles satisfies a power law with exponent  $1.8 \pm 0.2$  and  $2.7 \pm 0.2$  in the thin and thick target models, respectively. Thus the slope of the proton spectrum agrees in general with the data of the interplanetary observations. For the thick target model, the total number of protons with energy  $\geq 30 \text{ MeV}$  was found to be  $\sim 10^{33} \text{ erg}$ .

In connection with optical flares, heating by energetic protons was considered on many occasions. For comparison of the penetrating capacity of thermal electrons (more precisely, of the stationary heat-conductive flux), the energetic electrons and protons, Table 17.1

contains the calculated values of the initial energy of particles that is needed to traverse a column thickness  $\xi$  (measured in  $\text{cm}^{-2}$ ) into the chromosphere.

**Table 17.1** Flare heating of the chromosphere

Model of the quiet chromosphere	$h$ , km	$n_{\text{H}}$ , $\text{cm}^{-3}$	$T$ , $10^3 \text{ K}$	$\xi$ , $\text{cm}^{-2}$	Region		Heating agent		Radiation <sup>a</sup>		
					emission in a flare	$p = \text{const}$	$n = \text{const}$		$\varepsilon_e$ , keV	$\varepsilon_p$ , MeV	$\xi_{\text{x-ray}}$ , keV
							Heat flux	$T_0, 10^7 \text{ K}$			
1,250	$5 \times 10^{12}$	6.4	$8.7 \times 10^{19}$			1			23	1.2	0.17
1,150	$10^{13}$	6.3	$1.7 \times 10^{20}$						32	1.7	0.21
1,050	$2 \times 10^{13}$	6.1	$3.8 \times 10^{20}$			2			48	2.5	0.29
1,000	$3 \times 10^{13}$	6.0	$4.6 \times 10^{20}$						53	2.8	0.31
950	$5 \times 10^{13}$	5.8	$5.3 \times 10^{20}$						56	3.0	0.33
880	$8 \times 10^{13}$	5.6	$9.0 \times 10^{20}$	H $\alpha$		3			73	3.9	0.42
820	$10^{14}$	5.3	$1.7 \times 10^{21}$	H $\alpha$					100	5.3	0.68
600	$10^{15}$	4.3	$1.1 \times 10^{22}$	H $\alpha$					260	14	1.4
550	$2 \times 10^{15}$	4.2	$1.8 \times 10^{22}$	H $\alpha$					330	17	1.7
510	$3 \times 10^{15}$	4.1	$2.7 \times 10^{22}$						400	22	2.1

<sup>a</sup> According to Somov (1975)

The model of the quiet chromosphere is taken from [Vernazza et al. \(1973\)](#): in the first column the height  $h$  measured in km above the photosphere, in the second column the Hydrogen concentration  $n_{\text{H}}$  ( $\text{cm}^{-3}$ ), in the third column the temperature  $T$  ( $10^3 \text{ K}$ ).

It is clear that the non-relativistic protons with an energy approximately  $\sqrt{m_p/m_e} \approx 50$  times higher than the energy of the non-relativistic electrons penetrate to the same depth as the electrons. The energy losses of such protons per unit thickness of matter is approximately the same number of times greater than for the corresponding electrons. Therefore

a proton flux  $\sqrt{m_p/m_e}$  times smaller in number than the electron flux but with proton energy  $\sqrt{m_p/m_e}$  times greater carries the same total energy and gives rise to the same heating of the chromosphere as the electron flux.

The following difference is however important. Beginning at a depth corresponding to a column thickness of  $\sim 3 \times 10^{22} \text{ cm}^{-2}$  or to a concentration  $n_{\text{H}} \approx 3 \times 10^{15} \text{ cm}^{-3}$  and below, the heating of the chromosphere requires electrons with an energy above 400 keV, i.e., electrons for which a relativistic behavior of the losses becomes important. Protons that have penetrated to the same depth have essentially non-relativistic energies  $\mathcal{E}_p \geq 20 \text{ MeV}$ . It could be this that explains why all *white light flares*, i.e. the flares having an enhanced optical continuum which can be due to thermal emission presumably in the upper photosphere, were observed to be proton flares ([McIntosh et al. 1972](#)).

However a correlation between the optical continuum, HXR and microwave bursts, which are due to non-thermal emission processes ([Rust and Hegwer 1975](#)) suggested that the white-light emission could be due to heating of the chromosphere by the same energetic electrons as generated the HXR and the microwave radio emission. White-light and HXR emissions, as observed in our days, are well correlated in time (e.g., [Fletcher et al. 2007](#)), intensity (e.g., [Watanabe et al. 2010](#)), and space (e.g., [Xu et al. 2006](#)). Therefore, to explain a white light flare, there is no principal need to invoke the heating by energetic protons. Moreover, one can get the impression that, in contrast to electrons, energetic protons escape virtually freely from an acceleration region into the interplanetary space and cannot guarantee the heating of the chromosphere necessary for a white-light flare.

The general picture of a chromospheric response to an impulsive heating by energetic electrons is not simple (see Chap. 2 in [Somov 1980, 1992](#)). The electrons rapidly heat the upper chromosphere up to high temperatures ( $\gtrsim 10^7 \text{ K}$ ). The heat-conductive flux goes deep into the chromosphere and forms a flare transition layer  $TL$  as illustrated by Fig. 17.2. Below this layer the temperature rise during the direct heating  $DH$  by electrons is limited by radiative energy losses rather than heat conduction.

Radiative cooling soon establishes a quasi-equilibrium distribution of temperature, which is characterized by energy balance (heating by electrons is balanced by radiative cooling) and by the absence of hydrostatic equilibrium because of pressure gradient due to the heating. As shown by the calculations (for more detail see

Somov 1992), when the plasma heated under the transition layer starts expanding, the more rapid process of its radiative cooling and small-scale compression results in a formation of a *cold dense condensation*.

Motion of the condensation into the chromosphere is accompanied by the formation of a shock wave which causes additional compression. In its turn the density rise behind the shock front increases the rate of radiative cooling of the plasma heated by electrons and therefore promotes the condensation mode of the *thermal instability* (Somov et al. 1981). The result is that the condensation mass grows quickly. The condensation emission in EUV lines can be larger than the emission of the flare transition layer. Moreover, after a short EUV flash in a given point,

the condensation can be a powerful source of optical continuum emission, i.e. a white light flare.

The harder the electron spectrum, the greater part of the electron energy is transformed into optical emission.

Krucker et al. (2011) compare high-resolution optical and HXR observations of the two-ribbon X6.5-class flare on 2006 December 6. The data consist of images at 4,300 Å (the Fraunhofer *G* band) taken by the Solar Optical Telescope (SOT; Tsuneta et al. 2008) on board *Hinode* (Kosugi et al. 2007) with HXR images obtained from the *Reuven Ramaty High Energy Solar Spectroscopic Imager* (RHESSI; Lin et al. 2002). These two sets of data show closely similar ribbon structures, strongly suggesting that

the flare white light and HXRs have physically linked emission mechanisms.

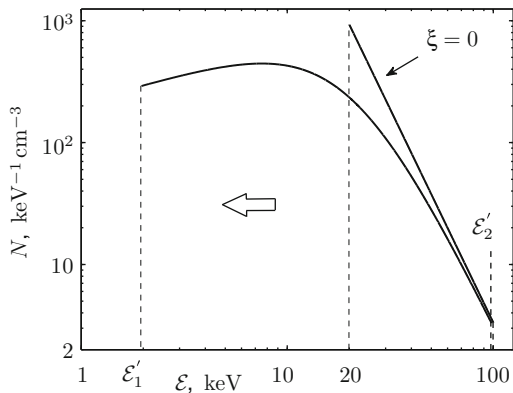
The source structure along the ribbons is resolved at both wavelengths. However only the *G*-band observations resolve their width, with values between  $\sim 0.5$  and 1.8 arcsec. The unresolved HXR observations reveal an even narrow ribbon in HXRs, suggesting that the HXR emission comes from the sharp leading edge of the *G*-band ribbon.

Applying the simplest thick-target model (Part I, Sect. 4.3.4), the derived energy deposition rate is huge:  $F_{\max} > 5 \times 10^{12}$  erg cm $^{-2}$  s $^{-1}$  provided by an electron flux of  $> 1 \times 10^{20}$  electrons cm $^{-2}$  s $^{-1}$  above 18 keV. This requires that the beam density of electrons above 18 keV be at least  $> 1 \times 10^{20}$  electrons cm $^{-3}$  (Krucker et al. 2011). The dynamics of such intensive beams and their *reverse currents* (Part I, Sect. 4.5; see also Gritsyk and Somov 2011) should be further studied in detail.

## 17.5 Practice: Exercises and Answers

**Exercise 17.1 (Sect. 17.2.2).** By using the thick-target model, find the energy spectrum of fast electrons, passing in an ionized solar plasma a column depth  $\xi$ . The power-low injection spectrum ( $\xi = 0$ ) has the boundaries  $\mathcal{E}_1 = 20$  keV and  $\mathcal{E}_2 = 100$  keV, the spectral index  $\gamma = 3$ ; the energy flux of fast electrons  $F_0 = 10^{11}$  erg cm $^{-2}$  s $^{-1}$ .

**Fig. 17.3** The energy spectrum of fast electrons in an ionized plasma on the column depth  $\xi = 0$  (the right straight line) and on the column depth  $\xi = 6.7 \times 10^{19} \text{ cm}^{-2}$  (left curve). Here  $\mathcal{E}'_1 \simeq 2 \text{ keV}$  and  $\mathcal{E}'_2 \simeq 98 \text{ keV}$  according to (17.9)



**Answer.** At first, by using formulae (17.5)–(17.9), we find the coefficient  $K$ . With this aim, let us write expression for the energy flux

$$\begin{aligned} F_0 &= \int_{\mathcal{E}_1}^{\mathcal{E}_2} \mathcal{E} v N(\mathcal{E}, 0) d\mathcal{E} \\ &= K \left( \frac{m}{2} \right)^{1/2} \times \begin{cases} (\mathcal{E}_2^{2-\gamma} - \mathcal{E}_1^{2-\gamma}) / (2 - \gamma), & \text{if } \gamma \neq 2, \\ \ln(\mathcal{E}_2/\mathcal{E}_1), & \text{if } \gamma = 2. \end{cases} \quad (17.28) \end{aligned}$$

Thus

$$K = F_0 \left( \frac{m}{2} \right)^{1/2} \times \begin{cases} (2 - \gamma) / (\mathcal{E}_2^{2-\gamma} - \mathcal{E}_1^{2-\gamma}), & \text{if } \gamma \neq 2, \\ [\ln(\mathcal{E}_2/\mathcal{E}_1)]^{-1}, & \text{if } \gamma = 2. \end{cases} \quad (17.29)$$

From here, with  $\gamma = 3$ , we calculate coefficient

$$K \simeq 3.3 \times 10^7 \text{ cm}^{-3} \text{ keV}^{2.5}.$$

The energy spectrum is presented on Fig. 17.3.

**Exercise 17.2 (Sect. 17.3.1).** As one of the first classic examples, let us consider the well-known impulsive flare on 1972 August 2 at 18:38 UT. According to the UCSD X-ray telescope on *OSO-7* the HXR flux at the Earth orbit averaged over 10.2 s at the maximum of the HXR (20–30 keV) burst at 18:39:52 UT had a power-law spectrum with  $K_\varphi \approx 10^7 \text{ cm}^{-2} \text{ s}^{-1} \text{ keV}^{\varphi-1}$  and  $\varphi = 3.7$ . Estimate the power of the fast electrons on the Sun in this flare.

**Answer.** Using formula (17.19), we calculate the power of the fast electrons  $\mathcal{F}(\mathcal{E} > 20 \text{ keV}) \simeq 7.6 \times 10^{28} \text{ erg s}^{-1}$ .

If we take the area

$$S_{fk} = \int_S dS \simeq 5 \times 10^{17} \text{ cm}^2$$

of the flare bright HXR kernels at this time, then the value of the power correspond to boundary energy flux

$$F_0(\mathcal{E} > 20 \text{ keV}) \simeq 1.5 \times 10^{11} \text{ erg cm}^{-2} \text{ s}^{-1}.$$

Recall that, according to the modern *RHESSI* observations (e.g., Krucker et al. 2011), the accelerated-electron energy deposition rate can be even higher. For example, in the X6.5-class flare on 2006 December 6,

$$F_{\max} > 5 \times 10^{12} \text{ erg cm}^{-2} \text{ s}^{-1}$$

provided by an electron flux of  $> 1 \times 10^{20}$  electrons  $\text{cm}^{-2} \text{ s}^{-1}$  above 18 keV.

**Exercise 17.3 (Sect. 17.3.1).** For the same solar flare on 1972 August 2 at 18:38 UT estimate the power of the fast electrons under assumption that the lower boundary of the non-thermal electrons  $\mathcal{E}_1 = 10 \text{ keV}$ .

**Answer.** Using the same formula (17.19), we find the power of the fast electrons  $\mathcal{F}(\mathcal{E} > 10 \text{ keV}) \simeq 6 \times 10^{29} \text{ erg s}^{-1}$ . If the flare HXR kernel area  $S_{fk} \simeq 5 \times 10^{17} \text{ cm}^2$ , then the boundary energy flux would be  $F_0(\mathcal{E} > 10 \text{ keV}) \simeq 10^{12} \text{ erg cm}^{-2} \text{ s}^{-1}$ .

# Epilogue

Most of the known matter in the Universe is in an ionized state. And many naturally occurring plasmas, such as the atmosphere of the Sun and magnetic stars, the magnetospheres of the Earth and other planets, the magnetospheres of pulsars and other relativistic objects, galactic and extragalactic jets, exhibit distinctively plasma-dynamical phenomena arising from the effects of strong magnetic and electric forces. The science of **plasma astrophysics** was born and developed to provide an understanding of these plasmas and those which will be discovered and investigated in future space observations. With this aim, from the very beginning, **many of the conceptual tools** and many different approaches were introduced and developed in the course of general fundamental research on the plasma state or independently. How can we understand the interconnection between different descriptions of astrophysical plasma behavior?

I was frequently asked by my students to give them a quick introduction to the theory of astrophysical plasma. It turned out that it is not easy to do for many reasons. The most important of them is that the usual way of such an introduction is generalization. This means that we go from simple well-known things to more complicated ones, for example, we generalize the ordinary hydrodynamics to magnetohydrodynamics. Though this way certainly makes a textbook easier to read, it does not give the reader complete knowledge of the subject, the tools especially. For a long time, my goal was to write a book which I would myself had liked when I first took up the subject, plasma astrophysics, and which I could recommend to my students to provide them an **accessible introduction** to plasma astrophysics at least at an intuitive level of the basic concepts.

We began a long journey together, when we first started such a book, “Plasma Astrophysics. I. Fundamentals and Practice” (referred in the text as Part I), and we are now almost at that journey’s end, book “Plasma Astrophysics. 2. Reconnection and Flares”.

A unifying theme of the first book (vol. 1) was the attempt at a deeper understanding of the underlying physics. Starting from the most general physical principles, we have seen the consecutive simplifications of them and of simplifying

assumptions which allowed us to obtain a simpler description of plasma under cosmic conditions. In so doing, the boundaries of the domain of applicability for the approximation at hand were well outlined from the viewpoint of physics and possible applications.

On the basis of this approach we can find the answers to the key questions: (1) what approximation is the simplest but a sufficient one for a description of a phenomenon in astrophysical plasma; (2) how to build an adequate model for the phenomenon, for example, a solar flare.

*Practice is really important in the theory of astrophysical plasma;* related exercises (problems and answers supplemented to each chapter) served to better understanding of its physics. Most of the problems for students have been used as homework in the lecture course. A particular feature of the problems is that they widely range in difficulty from fairly straightforward (useful for an exam) to quite challenging. This property is not an advantage or disadvantage of the book but rather **a current state of modern astrophysics**.

As for applications, evidently preference was given to physical processes in the solar plasma. The Sun is unique in the astrophysical realm for the great diversity of the diagnostic data that are available. Much attention to solar plasma physics was and will be conditioned by the possibility of the all-round observational test of theoretical models.

About fifty years ago it was still possible, as [Alfvén and Fälthammar \(1963\)](#) so ably demonstrated, to write a single book on cosmic plasma theory concerning practically everything that is worth knowing of the subject. The subsequent development has been explosive, and today a corresponding comprehensive coverage would require a hole library. The present book is an earnest attempt to a general overview of the whole area but big gaps unavoidably appear. Important and interesting effects and problems have been skipped because I either felt to go too far beyond an introductory text for students or, worse, I have not been aware of them.

There would be infinitely more to say about new space observations, modern numerical simulations, and analytical investigations of astrophysical plasma.

Any reader who, after having read this book, would like to become acquainted with profound results of astrophysical plasma should keep this fact in mind. I hope, however, that he/she, having learned sufficiently many topics of this textbook, will willingly and easily fill the gaps. Good luck!

## Appendix A

### Acronyms

<i>Acronym</i>	<i>Meaning</i>
ACE	Advanced Composition Explorer
CME	coronal mass ejection
CDS	Coronal Diagnostic Spectrometer
EIT	Extreme ultraviolet Imaging Telescope
FFF	force free (magnetic) field
FIP	first ionization potential
GLE	ground level enhancement
GOES	Geostationary Operational Environmental Satellite
GONG	Global Oscillation Network Group
GRB	gamma ray burst
HSOS	Huairou Solar Observing Station
HXIS	Hard X-ray Imaging Spectrometer
IVM	Imaging Vector Magnetograph
LASCO	Large Angle and Spectrometric Coronagraph on board <i>SOHO</i>
LDE	long duration event
MDI	Michelson Doppler Imager on board <i>SOHO</i>
PNL	photospheric neutral line (polarity inversion line)
RCL	reconnecting current layer
RHESSI	Reuven Ramaty High Energy Solar Spectroscopic Imager
SDO	Solar Dynamics Observatory
SEPs	solar energetic particles
SHTCL	super-hot turbulent-current layer
SMFT	Solar Magnetic Field Telescope
SMM	Solar Maximum Mission
SNL	simplified neutral line (of the photospheric magnetic field)
SOHO	Solar and Heliospheric Observatory
SOT	Solar Optical Telescope on board <i>Hinode</i>
TRACE	Transition Region and Coronal Explorer
VLA	Very Large Array

## Appendix B

### Notation

#### Latin Alphabet

<i>Symbol</i>	<i>Description</i>	<i>Introduced in section</i>
<b>A</b>	vector potential of a magnetic field	1.1.2
<i>a</i>	half-thickness of a reconnecting current layer (RCL)	1.1.3
<b>B</b>	vector of a magnetic field	1.1.2
<i>b</i>	half-width of a reconnecting current layer	1.1.3
<i>d</i>	thickness of non-adiabatic region	1.1.1
<b>E</b>	vector of a electric field	1.1.2
<i>h</i>	magnetic field gradient inside a reconnecting current layer	1.2.1
<i>h</i> <sub>0</sub>	magnetic field gradient near a zeroth line (point)	2.1.5
<i>H</i>	Hamiltonian	11.2
$\mathcal{H}$	magnetic helicity	14.1
<i>K</i>	curvature of a magnetic field line	11.2
<i>l</i>	current layer length	15
<i>L</i> ( <i>T</i> )	radiative loss function	15
<b>u</b>	electric current velocity	2.3
<i>V</i>	velocity of a plasma flow	15
<i>V</i> <sub>a</sub>	gradient of the Alfvén speed	2.1
<i>v</i> <sub>d</sub>	drift velocity	1.1.3
<i>x</i>	ionisation degree	15

## Greek Alphabet

<i>Symbol</i>	<i>Description</i>	<i>Introduced in Section</i>
$\varepsilon$	dimensionless electric field	11.1
$\varepsilon_\alpha$	small parameter of expansion	12.3
$v_{ni}$	neutral-ion mean collisional frequency	15
$\xi$	displacement of a current layer	12.3
$\xi_{\parallel}$	dimensionless longitudinal magnetic field	11.1
$\xi_{\perp}$	dimensionless transverse magnetic field	11.1
$\xi$	displacement of the medium	2.1
$\Pi$	work against the Lorentz force	13.4
$\tau_r$	reconnection time scale	16.4

## Appendix C

### Useful Formulae

The most important characteristics of astrophysical plasmas (for more detail see Part I, Plasma Astrophysics: Fundamental and Practice)

Alfvén speed

$$V_A = \frac{B}{\sqrt{4\pi\rho}} \approx 2.18 \times 10^{11} \frac{B}{\sqrt{n}} , \text{ cm s}^{-1} .$$

Conductivity of magnetized plasma

$$\sigma_{\parallel} = \sigma = \frac{e^2 n}{m_e} \tau_{ei} \approx 2.53 \times 10^8 n (\text{cm}^{-3}) \tau_{ei} (\text{s}) , \text{ s}^{-1} ,$$

$$\sigma_{\perp} = \sigma \frac{1}{1 + \left( \omega_B^{(e)} \tau_{ei} \right)^2} , \quad \sigma_{\perp} = \sigma \frac{\omega_B^{(e)} \tau_{ei}}{1 + \left( \omega_B^{(e)} \tau_{ei} \right)^2} .$$

Coulomb logarithm

$$\ln \Lambda = \ln \left[ \left( \frac{3k_B^{3/2}}{2\pi^{1/2} e^3} \right) \left( \frac{T_e^3}{n_e} \right)^{1/2} \right] \approx \ln \left[ 1.25 \times 10^4 \left( \frac{T_e^3}{n_e} \right)^{1/2} \right] .$$

Cyclotron frequency (or gyrofrequency)

$$\omega_B = \frac{ecB}{\mathcal{E}} .$$

Debye radius ( $T_e = T$ ,  $T_i = 0$  or  $T_e \gg T_i$ )

$$r_D = \left( \frac{k_B T}{4\pi n e^2} \right)^{1/2} .$$

Debye radius in electron-proton thermal plasma ( $T_e = T_p = T$ )

$$r_{\text{D}} = \left( \frac{k_B T}{8\pi e^2 n} \right)^{1/2} \approx 4.9 \left( \frac{T}{n} \right)^{1/2} , \text{ cm.}$$

Dreicer electric field

$$E_{\text{Dr}} = \frac{4\pi e^3 \ln \Lambda}{k_B} \frac{n_e}{T_e} \approx 6.54 \times 10^{-8} \frac{n_e}{T_e} , \text{ V cm}^{-1} .$$

Drift velocity

$$\mathbf{v}_d = \frac{c}{e} \frac{\mathbf{F} \times \mathbf{B}}{B^2} . \quad (\text{C.1})$$

Electric drift velocity

$$\mathbf{v}_d = c \frac{\mathbf{E} \times \mathbf{B}}{B^2} . \quad (\text{C.2})$$

Electric field in a magnetized plasma

$$E \approx \frac{1}{c} v B \approx 10^{-8} v (\text{cm s}^{-1}) B (\text{G}) , \text{ V cm}^{-1} .$$

Electron plasma frequency

$$\omega_{pl}^{(e)} = \left( \frac{4\pi e^2 n_e}{m_e} \right)^{1/2} \approx 5.64 \times 10^4 \sqrt{n_e} , \text{ rad s}^{-1} .$$

Electron-ion collision (energy exchange) time

$$\tau_{ei} (\mathcal{E}) = \frac{m_e m_i [3k_B (T_e/m_e + T_i/m_i)]^{3/2}}{e_e^2 e_i^2 (6\pi)^{1/2} 8 \ln \Lambda} .$$

Gradient drift velocity

$$\mathbf{v}_d = \frac{\mathcal{M}c}{eB} \mathbf{n} \times \nabla B .$$

Larmor frequency of a non-relativistic electron

$$\omega_B^{(e)} = \frac{eB}{m_e c} \approx 1.76 \times 10^7 B (\text{G}) , \text{ rad s}^{-1} .$$

Larmor frequency of a non-relativistic proton

$$\omega_B^{(p)} \approx 9.58 \times 10^3 B (\text{G}) , \text{ rad s}^{-1} .$$

Larmor radius of a relativistic electron

$$r_{\text{L}}^{(\text{e})} = \frac{c p_{\perp}}{eB} .$$

Larmor radius of a non-relativistic electron

$$r_{\text{L}}^{(\text{e})} = \frac{m_e c}{e} \frac{v_{\perp}}{B} \approx 5.69 \times 10^{-8} \frac{v_{\perp} (\text{cm s}^{-1})}{B (\text{G})} , \text{ cm} .$$

Larmor radius of a non-relativistic proton

$$r_{\text{L}}^{(\text{p})} \approx 1.04 \times 10^{-4} \frac{v_{\perp} (\text{cm s}^{-1})}{B (\text{G})} , \text{ cm} .$$

Larmor radius of a non-relativistic *thermal* electrons

$$r_{\text{L}}^{(\text{e})} = \frac{V_{\text{Te}}}{\omega_{\text{B}}^{(\text{e})}} \approx 3.83 \times 10^{-2} \frac{\sqrt{T_{\text{e}} (\text{K})}}{B (\text{G})} , \text{ cm} .$$

Larmor radius of a non-relativistic *thermal* protons

$$r_{\text{L}}^{(\text{p})} = \frac{V_{\text{Tp}}}{\omega_{\text{B}}^{(\text{p})}} \approx 1.64 \frac{\sqrt{T_{\text{p}} (\text{K})}}{B (\text{G})} , \text{ cm} .$$

Lundquist number

$$N_{\text{L}} = \text{Re}_{\text{m}}(V_{\text{A}}, L) = \frac{V_{\text{A}} L}{v_{\text{m}}} .$$

Magnetic diffusivity (or viscosity)

$$\nu_{\text{m}} = \frac{c^2}{4\pi\sigma} \approx 7.2 \times 10^{19} \frac{1}{\sigma} , \text{ cm}^2 \text{ s}^{-1} .$$

Magnetic moment of a particle on the Larmor orbit

$$\mathcal{M} = \frac{1}{c} JS = \frac{e \omega_{\text{B}} r_{\text{L}}^2}{2c} = \frac{p_{\perp}^2}{2mB} = \frac{\mathcal{E}_{\perp}}{B} .$$

Magnetic Reynolds number

$$\text{Re}_{\text{m}} = \frac{L^2}{v_{\text{m}} \tau} = \frac{vL}{v_{\text{m}}}$$

Mean thermal velocity of electrons

$$V_{Te} = \left( \frac{3k_B T_e}{m_e} \right)^{1/2} \approx 6.74 \times 10^5 \sqrt{T_e \text{ (K)}}, \text{ cm s}^{-1}.$$

Mean thermal velocity of protons

$$V_{Tp} \approx 1.57 \times 10^4 \sqrt{T_p \text{ (K)}}, \text{ cm s}^{-1}.$$

Sound speed in electron-proton plasma

$$V_s = \left( \gamma_g \frac{p}{\rho} \right)^{1/2} \approx 1.66 \times 10^4 \sqrt{T \text{ (K)}}, \text{ cm s}^{-1}.$$

Thermal electron collisional time

$$\tau_{ee} = \frac{m_e^2}{0.714 e^4 8\pi \ln \Lambda} \frac{V_{Te}^3}{n_e} \approx 4.04 \times 10^{-20} \frac{V_{Te}^3}{n_e}, \text{ s}.$$

Thermal proton collisional time

$$\tau_{pp} = \frac{m_p^2}{0.714 e^4 8\pi \ln \Lambda} \frac{V_{Tp}^3}{n_p} \approx 1.36 \times 10^{-13} \frac{V_{Tp}^3}{n_p}, \text{ s}.$$

Time of energy exchange between electrons and protons

$$\tau_{ep}(\mathcal{E}) \approx 22 \tau_{pp} \approx 950 \tau_{ee}.$$

# Appendix D

## Constants

### Fundamental Physical Constants

Speed of light	$c$	$2.998 \times 10^{10} \text{ cm s}^{-1}$
Electron charge	$e$	$4.802 \times 10^{-10} \text{ CGSE}$
Electron mass	$m_e$	$9.109 \times 10^{-28} \text{ g}$
Proton mass	$m_p$	$1.673 \times 10^{-24} \text{ g}$
Boltzmann constant	$k_B$	$1.381 \times 10^{-16} \text{ erg K}^{-1}$
Gravitational constant	$G$	$6.673 \times 10^{-8} \text{ dyne cm}^2 \text{ g}^{-2}$
Planck's constant	$h$	$6.625 \times 10^{-27} \text{ erg s}$

### Some Useful Constants and Units

Ampere (current)	$\text{A}$	$3 \times 10^9 \text{ CGSE}$
Angström (length)	$\text{Å}$	$10^{-8} \text{ cm}$
Electron Volt (energy)	$\text{eV}$	$1.602 \times 10^{-12} \text{ erg}$
	$\text{eV}$	$1,1605 \text{ K}$
Gauss (magnetic induction)	$\text{G}$	$3 \times 10^{10} \text{ CGSE}$
Henry (inductance)	$\text{H}$	$1.111 \times 10^{-12} \text{ s}^2 \text{ cm}^{-1}$
Ionization potential of hydrogen		$13.60 \text{ eV}$
Joule (energy)	$\text{J}$	$10^7 \text{ erg}$
Maxwell (magnetic flux)	$\text{M}$	$3 \times 10^{10} \text{ CGSE}$
Ohm (resistance)	$\Omega$	$1.111 \times 10^{-12} \text{ s cm}^{-1}$
Tesla (magnetic induction)		$10^4 \text{ Gauss}$
Volt (potential)	$\text{V}$	$3.333 \times 10^{-3} \text{ CGSE}$
Watt (power)	$\text{W}$	$10^7 \text{ erg s}^{-1}$
Weber (magnetic flux)	$\text{Wb}$	$10^8 \text{ Maxwell}$

## Some Astrophysical Constants

Astronomical unit	$AU$	$1.496 \times 10^{13}$ cm
Mass of the Sun	$M_{\odot}$	$1.989 \times 10^{33}$ g
Mass of the Earth	$M_E$	$5.98 \times 10^{27}$ g
Solar radius	$R_{\odot}$	$6.960 \times 10^{10}$ cm
Solar surface gravity	$g_{\odot}$	$2.740 \times 10^4$ cm s <sup>-2</sup>
Solar luminosity	$L_{\odot}$	$3.827 \times 10^{33}$ erg s <sup>-1</sup>
Mass loss rate	$\dot{M}_{\odot}$	$10^{12}$ g s <sup>-1</sup>
Rotation period of the Sun	$T_{\odot}$	26 days (at equator)

# Bibliography

- Abbasi, R., Ackermann, M., Adams, J., et al.: Solar energetic particle spectrum on 2006 December 13 determined by IceTop. *Astrophys. J.* **689**(1), L65–L68 (2008) [Sect. 11.4.3]
- Acton, L.: Coronal structures, local and global. In: Uchida, Y., Kosugi, T., Hudson, H. (eds.) *Magnetohydrodynamic Phenomena in the Solar Atmosphere: Prototypes of Stellar Magnetic Activity*, pp. 3–11. Kluwer, Dordrecht (1996) [Sect. 14.4]
- Acton, L., Tsuneta, S., Ogawara, Y., et al.: The *Yohkoh* mission for high-energy solar physics. *Science* **258**(5082), 618–625 (1992) [Intr., Sects. 4.3.5 and 6.1]
- Akimov, V.V., Ambroz, P., Belov, A.V., et al.: Evidence for prolonged acceleration in the solar flare of June 15, 1991. *Sol. Phys.* **166**(1), 107–134 (1996) [Sect. 11.4]
- Alfvén, H., Carlqvist, P.: Currents in the solar atmosphere and a theory of flares. *Sol. Phys.* **1**(2), 220–228 (1967) [Sects. 5.2.4 and 16.2]
- Alfvén, H., Fälthammar, C.-G.: *Cosmic Electrodynamics, Fundamental Principles*, 2nd edn., p. 228. Clarendon Press, Oxford (1963)
- Allred, J.C., Hawley, S.L., Abbott, W.P., Carlsson, M.: Radiative hydrodynamic models of the optical and ultraviolet emission from solar flares. *Astrophys. J.* **630**(1), 573–586 (2005) [Sect. 17.4.1]
- Altyntsev, A.T., Krasov, V.I., Tomozov V.M.: Magnetic field dissipation in neutral current sheets. *Sol. Phys.* **55**(1), 69–81 (1977) [Sect. 5.1.2]
- Aly, J.J.: On some properties of force-free fields in infinite regions of space. *Astrophys. J.* **283**(1), 349–362 (1984) [Sect. 16.2]
- Aly, J.J.: How much energy can be stored in a force-free field? *Astrophys. J.* **375**(1), L61–L64 (1991) [Sect. 16.2]
- Anderson, J.E.: *Magnetohydrodynamic Shock Waves*, p. 226. M.I.T. Press, Cambridge (1963) [Sect. 12.2]
- Anosov, D.V.: *Geodesic Flows on Closed Riemannian Manifolds with Negative Curvature*, p. 235. American Mathematical Society, Providence (1969) [Sect. 11.2]
- Antiochos, S.K.: The magnetic topology of solar eruptions. *Astrophys. J.* **502**, L181–L184 (1998) [Sects. 4.3.4, 5.3.2 and 8.6]
- Antiochos, S.K., Karpen, J.T., DeVore, C.R.: The nature of magnetic reconnection in the corona. In: Bentley, R.D., Mariska, J.T. (eds.) *Magnetic Reconnection in the Solar Atmosphere*. Astronomical Society of the Pacific Conference Series, vol. 111, p. 79–81. Astronomical Society of the Pacific, San Francisco (1997) [Sects. 5.1.2 and 12.1]
- Antiochos, S.K., DeVore, C.R., Klimchuk, J.A.: A model for solar coronal mass ejections. *Astrophys. J.* **510**(1), 485–493 (1999) [Sects. 7.6 and 16.5.2]
- Antonova, E.E., Tverskoi, B.A.: On the nature of electric fields in the Earth's inner magnetosphere (A review). *Geomagn. Aeron. Int.* **1**(1), 9–21 (1998) [Sect. 10.2.2]

- Antonucci, E., Benna, C., Somov, B.V.: Interpretation of the observed plasma ‘turbulent’ velocities as a result of reconnection in solar flares. *Astrophys. J.* **456**(2), 833–839 (1996) [Sects. 8.5.5 and 14.1]
- Anwar, B., Acton, L.W., Hudson, H.S., et al.: Rapid sunspot motion during a major solar flare. *Sol. Phys.* **147**(2), 287–303 (1993) [Sect. 7.1.2]
- Apatenkov, S.V., Sergeev, V.A., Kubyshkina, M.V., et al.: Multi-spacecraft observation of plasma dipolarization/injection in the inner magnetosphere. *Ann. Geophys.* **25**(3), 801–814 (2007) [Sect. 9.8]
- Archontis, V., Moreno-Insertis, F., Galsgaard, K., et al.: The three-dimensional interaction between emerging magnetic flux and a large-scale coronal field: reconnection, current sheets, and jets. *Astrophys. J.* **635**(2), 1299–1318 (2005) [Sect. 5.2.1]
- Arge, C.N., Mullan, D.J.: Modeling of magnetic interactions in partially-ionized gas. *Sol. Phys.* **182**(2), 293–332 (1998) [Sect. 15.4]
- Artsimovich, L.A., Sagdeev, R.Z.: Plasma Physics for Physicists, p. 320. Atomizdat, Moscow (1979) [Sect. 8.4.1]
- Asai, A., Ishii, T.T., Kurokawa, H., et al.: Evolution of conjugate footpoints inside flare ribbons during a great two-ribbon flare on 2001 April 10. *Astrophys. J.* **586**, 624–629 (2003) [Sect. 7.4.1]
- Aschwanden, M.J., Alexander, D.: Flare plasma cooling from 30 MK down to 1 MK modeled from *Yohkoh*, GOES, and TRACE observations during the Bastille day event (14 July 2000). *Sol. Phys.* **204**(1), 93–121 (2001) [Sects. 6.2.3, 6.2.4 and 7.1.1]
- Aschwanden, M.J., Kliem, B., Schwarz, U., et al.: Wavelet analysis of solar flare hard X-rays. *Astrophys. J.* **505**(2), 941–956 (1998) [Sect. 9.2.3]
- Aschwanden, M.J., Kosugi, T., Hanaoka, Y., et al.: Quadrupole magnetic reconnection in solar flares. I. Three-dimensional geometry inferred from *Yohkoh* observations. *Astrophys. J.* **526**, 1026–1045 (1999) [Sects. 8.6 and 9.1.3]
- Aulanier, G., DeLuca, E.E., Antiochos, S.K., et al.: The topology and evolution of the Bastille day 1998 flare. *Astrophys. J.* **540**(2), 1126–1142 (2000) [Sects. 5.3.2 and 7.6]
- Ayres, T.R.: Thermal bifurcation of the solar chromosphere. In: Strassmeier, K.G., Linsky, J.L. (eds.) Stellar Surface Structure. IAU Symposium, vol. 176, p. 371–384. Kluwer, Dordrecht (1996) [Sect. 15.5]
- Bagalá, L.G., Mandrini, C.H., Rovira, M.G., et al.: A topological approach to understand a multi-loop flare. *Sol. Phys.* **161**(1), 103–121 (1995) [Intr., Sects. 5.3.2, 8.6 and 16.2]
- Bai, T., Sturrock, P.A.: Classification of solar flares. *Ann. Rev. Astron. Astrophys.* **27**, 421–467 (1989) [Sects. 11.1 and 11.4]
- Bai, T., Hudson, H.S., Pelling, R.M., et al.: First-order Fermi acceleration in solar flares as a mechanism for the second-step acceleration of protons and electrons. *Astrophys. J.* **267**(1), 433–441 (1983) [Sect. 9.2.3]
- Barnes, G.: On the relationship between coronal magnetic null points and solar eruptive events. *Astrophys. J.* **670**(1), L53–L56 (2007) [Sects. 6.3.1, 7.1.3 and 8.6]
- Barnes, G., Longcope, D.W., Leka, K.D.: Implementing a magnetic charge topology model for solar active regions. *Astrophys. J.* **629**(1), 561–571 (2005) [Sect. 4.3.4]
- Barret, D., Olive, J.F., Boirin, L., et al.: Hard X-ray emission from low-mass X-ray binaries. *Astrophys. J.* **533**, 329–351 (2000) [Sect. 10.3]
- Batchelor, G.K.: On the spontaneous magnetic field in a conducting liquid in turbulent motion. *Proc. Royal Soc. A* **201**, 405–416 (1950) [Sect. 14.1]
- Bateman, G., Erdelyi, A.: Higher Transcendental Functions. McGraw-Hill, New York (1953) [Sect. 3.4.1]
- Baum, P.J., Bratenahl, A., Kamin, G.: Current interruption and flux transfer solar flare models. *Astrophys. J.* **226**(1), 286–300 (1978) [Sects. 5.1.3 and 16.2]
- Bazilevskaya, G.A.: Solar cosmic rays in the near Earth space and the atmosphere. *Adv. Space Res.* **35**(3), 458–464 (2005) [Sect. 11.4.3]
- Becker, W. (ed.): Neutron Starts and Pulsars, p. 997. Springer, Berlin/Heidelberg (2009) [Intr., Sects. 10.3.2 and 11.5]

- Bednarek, W., Protheroe, R.J.: Gamma-ray and neutrino flares produced by protons accelerated on an accretion disc surface in active galactic nuclei. *Mon. Not. Royal Astron. Soc.* **302**, 373–380 (1999) [Sect. 10.3]
- Begelman, M.C., Blandford, R.D., Rees, M.J.: Theory of extragalactic radio sources. *Rev. Mod. Phys.* **56**(2), 255–351 (1984) [Intr.]
- Bentley, R.D., Klein, K.-L., van Driel-Gesztelyi, L., et al.: Magnetic activity associated with radio noise storms. *Sol. Phys.* **193**(1–2), 227–245 (2000) [Sect. 5.3.2]
- Benz, A.: Plasma Astrophysics: Kinetic Processes in Solar and Stellar Coronae, 2nd edn., p. 299. Kluwer, Dordrecht (2002) [Sects. 6.2.6, 9.3.4 and 9.7]
- Benz, A., Krucker, S.: Heating events in the quiet solar corona. *Sol. Phys.* **182**(2), 349–363 (1998) [Sect. 14.4]
- Benz, A., Krucker, S.: Heating events in the quiet solar corona: multiwavelength correlations. *Astron. Astrophys.* **341**(1), 286–295 (1999) [Sect. 14.4]
- Benz, A.O., Lin, R.P., Sheiner, O.A., et al.: The source regions of impulsive solar electron events. *Sol. Phys.* **203**(1), 131–144 (2001) [Sect. 11.4]
- Berestetskii, V.B., Lifshitz, E.M., Pitaevskii, L.P.: Quantum Electrodynamics. Fizmatlit, Moscow (2001) (in Russian) [Sect. 9.5.3]
- Berger, M.A.: Rigorous limits on magnetic helicity dissipation in the solar corona. *Geophys. Astrophys. Fluid Dyn.* **30**(1), 79–104 (1984) [Sect. 14.1]
- Berger, M.A.: An energy formula for nonlinear force-free fields. *Astron. Astrophys.* **201**(1), 355–361 (1988) [Sects. 14.1 and 14.2]
- Berger, M.A.: Three-dimensional reconnection from a global viewpoint. In: Guyenne, T.D., Hunt, J.J. (eds.) *Reconnection in Space Plasma*. ESA SP-285, vol. 2, p. 83–86. European Space Agency, Paris (1989) [Sects. 14.1 and 16.2]
- Berger, M.A.: Coronal heating by dissipation of magnetic structure. *Space Sci. Rev.* **68**(1), 3–14 (1994) [Sect. 14.2]
- Bezrodnykh, S.I., Vlasov, V.I., Somov, B.V.: Analytical model of magnetic reconnection in the presence of shock waves attached to a current sheet. *Astron. Lett.* **33**(2), 130–136 (2007) [Sects. 3.2 and 3.4.1]
- Bezrodnykh, S.I., Vlasov, V.I., Somov, B.V.: Generalized analytical models of Syrovatskii's current sheet. *Astron. Lett.* **37**(2), 113–130 (2011) [Sects. 3.2, 3.4.3 and 3.6]
- Bhattacharjee, A.: Impulsive magnetic reconnection in the Earth's magnetotail and the solar corona. *Ann. Rev. Astron. Astrophys.* **42**(1), 365–384 (2004) [Sect. 2.4.4]
- Birk, G.T., Otto, A.: The resistive tearing instability for generalized resistivity models. *Phys. Fluids* **3**(B7), 1746–1754 (1991) [Sect. 13.1.2]
- Biskamp, D.: Magnetic reconnection via current sheets. *Phys. Fluids* **29**(5), 1520–1531 (1986) [Sects. 3.2, 3.4.3 and 4.2.4, 12.1 and 12.5]
- Biskamp, D.: Resistive and collisionless magnetic reconnection. In: Chiudery, C., Einaudi, G. (eds.) *Plasma Astrophysics*, pp. 1–29. Springer, Berlin (1994) [Sect. 8.6]
- Biskamp, D.: Nonlinear Magnetohydrodynamics, p. 392. Cambridge University Press, Cambridge, UK (1997) [Sects. 3.1, 3.4.3, 4.2.4, 8.1.3, 12.1 and 12.5]
- Bogachev, S.A., Somov, B.V.: Comparison of the Fermi and betatron acceleration efficiencies in collapsing magnetic traps. *Astron. Lett.* **33**(1), 54–62 (2005) [Sects. 9.4.2 and 9.4.3, 9.4.4 and 9.4.5]
- Bogachev, S.A., Somov, B.V.: Formation of power-law electron spectra in collapsing magnetic traps. *Astron. Lett.* **33**(1), 54–62 (2007) [Sects. 9.5.1 and 9.5.3]
- Bogachev, S.A., Somov, B.V.: Effect of Coulomb collisions on the particle acceleration in collapsing magnetic traps. *Astron. Lett.* **35**(1), 57–69 (2009) [Sects. 9.2.2, 9.6.2, 9.6.3, 9.6.4 and 9.7]
- Bogachev, S.A., Somov, B.V., Masuda, S.: On the velocity of a hard X-ray source in the solar corona. *Astron. Lett.* **24**(4), 543–548 (1998) [Sects. 9.2.4 and 9.4.1]
- Bogachev, S.A., Somov, B.V., Kosugi, T., et al.: The motions of the hard X-ray sources in solar flares: images and statistics. *Astrophys. J.* **630**(1), 561–572 (2005) [Sect. 7.4.5]

- Bogdanov, S.Yu., Frank, A.G., Kyrei, N.P., and Markov, V.S.: Magnetic reconnection, generation of plasma fluxes and accelerated particles in laboratory experiments. In: *Plasma Astrophys.* ESA SP-251, pp. 177–183. ESA Publications Division, Noordwijk (1986) [Sect. 5.1.2]
- Bogdanov, S.Yu., Kyrei, N.P., Markov, V.S., and Frank, A.G.: Current sheets in magnetic configurations with singular X-lines. *JETP Lett.* **71**(2), 78–84 (2000) [Sect. 5.1.2]
- Borovsky, J.E., Funsten, H.O.: Role of the solar wind turbulence in coupling of the solar wind to the Earth's magnetosphere. *J. Geophys. Res.* **108**(A6), pp. SMP 13–1, CiteID 1246 (2003a) [Sects. 10.2.2 and 14.1.3]
- Borovsky, J.E., Funsten, H.O.: MHD turbulence in the Earth's plasma sheet: dynamics, dissipation, and driving. *J. Geophys. Res.* **108**(A7), pp. SMP 9–1, CiteID 1284 (2003b) [Sects. 10.2.2 and 14.1.3]
- Brandenburg, A.: An inverse cascade and nonlinear  $\alpha$ -effect in simulations of isotropic helical hydromagnetic turbulence. *Astrophys. J.* **550**(2), 824–840 (2001) [Sect. 14.1]
- Brandenburg, A., Subramanian, K.: Large scale dynamos with ambipolar diffusion nonlinearity. *Astron. Astrophys.* **361**, L33–L36 (2000) [Sect. 14.1]
- Brissaud, A., Frisch, U., Leorat, J., et al.: Helicity cascades in fully developed isotropic turbulence. *Phys. Fluid* **16**, 1366–1367 (1973) [Sect. 14.1]
- Brown, J.C.: The deduction of energy spectra of non-thermal electrons in flares from the observed dynamic spectra of hard X-ray bursts. *Sol. Phys.* **18**(3), 489–502 (1971) [Sect. 17.3.1]
- Brown, J.C.: The temperature structure of chromospheric flares heated by non-thermal electrons. *Sol. Phys.* **31**(1), 143–169 (1973) [Sect. 17.4.1]
- Brown, J.C., Hoyng, P.: Betatron acceleration in a large solar hard X-ray burst. *Astrophys. J.* **200**(1), 734–746 (1975) [Sect. 17.3.2]
- Browning, P.K.: Helicity injection and relaxation in a coronal magnetic loop with a free surface. *J. Plasma Phys.* **40**(2), 263–280 (1988) [Sect. 14.2]
- Brushlinskii, K.V., Zaborov, A.M., Syrovatskii, S.I.: Numerical analysis of the current sheet near a magnetic null line. *Sov. J. Plasma Phys.* **6**(2), 165–173 (1980) [Sects. 3.2, 3.4.3, 4.2.4, 5.1.2, 12.1 and 12.5]
- Büchner, J., Zelenyi, L.: Regular and chaotic particle motion in magnetotail field reversal. *J. Geophys. Res.* **94**(A9), 11821–11842 (1989) [Sect. 11.2]
- Bykov, A.M., Chevalier, R.A., Ellison, D.C., et al.: Non-thermal emission from a supernova remnant in a molecular cloud. *Astrophys. J.* **538**(1), 203–216 (2000) [Sect. 9.6.1]
- Canfield, R.C., Hudson, H.S., McKenzie, D.E.: Sigmoidal morphology and eruptive solar activity. *Geophys. Res. Lett.* **26**(6), 627–630 (1999) [Sect. 4.3.5]
- Carrington, R.C.: Description of a singular appearance seen in the Sun on September 1, 1859. *Mon. Not. R. Astron. Soc.* **20**(1), 13–15 (1859) [Sect. 4.1.1]
- Casolino, M., Picozza, P., Altamura, F., et al.: Launch of the space experiment PAMELA. *Adv. Space Res.* **42**(3), 455–466 (2008) [Sect. 11.4.3]
- Casolino, M., Bongue, D., De Pascale, M.P., et al.: The Pamela cosmic ray space observatory: detector, objectives and first results. E-print [arXiv:0904.4692v1](https://arxiv.org/abs/0904.4692v1) [astro-ph.HE] (2009) [Sect. 11.4.3]
- Cassak, P.A., Drake, J.F., Shay, M.A., et al.: Onset of fast magnetic reconnection. *Phys. Rev. Lett.* **98**(21), id. 215001 (2007) [Sect. 4.2.4]
- Cattaneo, F.: On the origin of magnetic fields in the quiet photosphere. *Astrophys. J.* **515**, L39–L42 (1999) [Sect. 14.1]
- Chae, J., Wang, H., Qiu, J., et al.: The formation of a prominence in active region NOAA 8668. 1. SOHO/MDI observations of magnetic field evolution. *Astrophys. J.* **560**(1), 476–489 (2001) [Sect. 7.3]
- Chandra, R., Pariat, E., Schmieder, B., et al.: How can a negative magnetic helicity active region generate a positive helicity magnetic cloud? *Sol. Phys.* **261**(1), 127–148 (2010) [Sect. 6.4.1]
- Chapman, S., Kendall, P.C.: Liquid instability and energy transformation near magnetic neutral line. A soluble non-linear hydromagnetic problem. *Proc. Roy. Soc. Lond.* **A271**, 435–448 (1963) [Sects. 2.4.1 and 2.4.2]

- Chen, J., Palmadesso, P.J.: Chaos and nonlinear dynamics of single particle orbits in a magnetotail field. *J. Geophys. Res.* **91**(A2), 1499–1508 (1986) [Sect. 11.2]
- Chen, P.F., Fang, C., Tang, Y.H., Ding, M.D.: Simulation of magnetic reconnection with heat conduction. *Astrophys. J.* **513**(1), 516–523 (1999a) [Sect. 3.4.3]
- Chen, P.F., Fang, C., Ding, M.D., Tang, Y.H.: Flaring loop motion and a unified model for solar flares. *Astrophys. J.* **520**(2), 853–858 (1999b) [Sects. 3.4.3 and 8.5.2]
- Cheng, K.S., Romero, G.E. (eds.): *Cosmic Gamma-Ray Sources*, p. 402 Kluwer, Dordrecht (2004) [Sect. 11.5]
- Cho, J., Vishniac, E.T.: The anisotropy of magnetohydrodynamic Alfvénic turbulence. *Astrophys. J.* **539**(1), 273–282 (2000a) [Sect. 14.1]
- Cho, J., Vishniac, E.T.: The generation of magnetic fields through driven turbulence. *Astrophys. J.* **538**(1), 217–225 (2000b) [Sect. 14.1]
- Chupp, E.L.: In: Ramaty, R., Mandzhavidze, N., Hua, X.-M. (eds.) *High Energy Solar Physics*. AIP conference proceedings, vol. 374, pp. 3–9 AIP, Woodbury (1996) [Sect. 11.4]
- Chupp, E.L., Forrest, D.J., Higbie, P.R., et al.: Solar gamma ray lines observed during the solar activity of August 2 to August 11. *Nature* **241**, 333 (1973) [Sect. 17.4.2]
- Colgate, S.A.: Relationship between high-energy phenomena on the Sun and in astrophysics. *Sol. Phys.* **118**(1), 1–15 (1988) [Sect. 11.4]
- Colgate, S.A., Furth, H.P.: Stabilization of pinch discharges. *Phys. Fluid* **3**(6), 982–1000 (1960) [Sect. 13.1.2]
- Colpi, M., Casella, P., Gorini, V., et al. (eds.): *Physics of Relativistic Objects in Compact Binaries: From Birth to Coalescence*, p. 378 Springer, Dordrecht (2009) [Sect. 11.5]
- Contopoulos, G.: *Order and Chaos in Dynamical Astronomy*, Springer, Berlin (2002) [Sect. 11.2]
- Coppi, B., Laval, G., Pellat, R.: Dynamics of the geomagnetic tail. *Phys. Rev. Lett.* **6**(26), 1207–1210 (1966) [Sects. 13.1.2 and 13.6]
- Cowley, S.W.H.: Magnetic reconnection. In: Priest, E.R. (ed.) *Solar System Magnetic Fields*, p. 121–134 D. Reidel Publishing, Dordrecht (1986) [Sect. 1.2.2]
- Cox, D.P., Tucker, W.H.: Ionization equilibrium and radiative cooling of a low-density plasma. *Astrophys. J.* **157**(3), 1157–1167 (1969) [Sect. 8.1.2]
- Craig, I.J.D., McClymont, A.N.: Linear theory of reconnection at an X-type neutral point. *Astrophys. J.* **405**(1), 207–215 (1993) [Sect. 15.2.3]
- Crooker, N., Joselyn, J.A., Feynman, J. (eds.): *Coronal Mass Ejections*, p. 299. American Geophysical Union, Washington (1997) [Intr.]
- Crooker, N.U., Gosling, J.T., Kahler, S.W.: Reducing heliospheric magnetic flux from coronal mass ejections without disconnection. *J. Geophys. Res.* **107**(A2), SSH 3–1 (2002) [Sect. 7.2.2]
- Day, C.: SOHO observations implicate ‘magnetic carpet’ as source of coronal heating in quiet Sun. *Physics Today*, March issue, 19–21 (1998) [Sect. 14.4]
- de Feiter, L.D.: Solar flares as source of energetic particles. *Space Sci. Rev.* **16**(1), 3–43 (1974) [Sect. 17.3.2]
- de Jager, C.: Solar flares and particle acceleration. *Space Sci. Rev.* **44**(1), 43–90 (1986) [Sect. 14.1]
- de Jager, C.: Solar forcing of climate. 1: solar variability. *Space Sci. Rev.* **120**(1), 197–241 (2005) [Intr., Sect. 10.2.3]
- de Jager, C., de Jonge, G.: Properties of elementary flare bursts. *Sol. Phys.* **58**(1), 127–137 (1978) [Sect. 17.3.2]
- de Kluiver, H., Perepelkin, N.F., Hirose, A.: Experimental results on current-driven turbulence in plasmas – A survey. *Phys. Rep. (Review Section of Physics Letters)* **199**(6), 281–381 (1991) [Sect. 10.1]
- Démoulin, P., van Driel-Gesztelyi, L., Schmieder, B., et al.: Evidence for magnetic reconnection in solar flares. *Astron. Astrophys.* **271**(1), 292–307 (1993) [Intr., Sects. 5.3.2, 8.6 and 16.2]
- Den, O.G., Somov, B.V.: Magnetic field dissipation in a high-temperature plasma as a mechanism of energy release in a solar flare. *Sov. Astron. – AJ* **33**(2), 149–155 (1989) [Sects. 4.3.3, 5.1.1, 8.5.5 and 16.2]
- Deng, Y., Wang, J., Yan, Y., et al.: Evolution of magnetic non-potentiality in NOAA AR 9077. *Sol. Phys.* **204**(1), 13–28 (2001) [Sects. 6.2.4, 7.1.1 and 7.6]

- Dennis, B.R.: Solar hard X-ray bursts. *Sol. Phys.* **100**(2), 465–490 (1985) [Sect. 8.5.5]
- Dennis, B.R.: Solar flare hard X-ray observations. *Sol. Phys.* **118**(1), 49–94 (1988) [Sect. 8.5.5]
- DeVore, C.R., Antiochos, S.K., Guillaume, A.: Solar prominence interactions. *Astrophys. J.* **629**(2), 1122–1134 (2005) [Sect. 15.3]
- Dobrowolny, M.: Instability of a neutral sheet. *Nuovo Cimento* **B55**(1), 427–438 (1968) [Sect. 11.3]
- Domingo, V., Fleck, B., Poland, A.A.: SOHO: the solar and heliospheric observatory. *Space Sci. Rev.* **72**(1), 81–84 (1995) [Intr., Sect. 6.1]
- Drake, J.F., Biskamp, D., Zeiler, A.: Breakup of the electron current layer during 3-D collisionless reconnection. *Geophys. Res. Lett.* **24**(2), 2921–2924 (1997) [Sect. 3.5]
- Dreicer, H.: Electron and ion runaway in a fully ionized gas. *Phys. Rev.* **115**(2), 238–249 (1959) [Sect. 8.1.1]
- Dubrovin, B.A., Novikov, S.P., Fomenko, A.T.: Modern Geometry, p. 515. Nauka, Moscow (1986) (in Russian) [Sects. 4.2.2 and 4.2.3]
- Duijveman, A., Hoyng P., Ionson, J.A.: Fast plasma heating by anomalous and inertial resistivity effects in the solar atmosphere. *Astrophys. J.* **245**(2), 721–735 (1981) [Sect. 8.4.1]
- Duijveman, A., Somov, B.V., Spektor, J.A.: Evolution of a flaring loop after injection of energetic electrons. *Sol. Phys.* **88**(1), 257–273 (1983) [Sect. 4.3.1]
- Duncan, R.C., Thompson, C.: Formation of very strongly magnetized neutron stars: implications for gamma-ray bursts. *Astrophys. J.* **392**(1), L9–L13 (1992) [Intr.]
- Dungey, J.W.: Cosmic Electrodynamics, p. 183. Cambridge University Press, England (1958) [Intr., Sects. 1.1.1, 2.1.1, 13.1.2 and 16.2]
- Dungey, J.W.: Interplanetary magnetic field and the auroral zones. *Phys. Rev. Lett.* **6**(2), 47–48 (1961) [Sect. 10.2]
- Efthymiopoulos, C., Gontikakis, C., Anastasiadis, A.: Particle dynamics in 3D reconnecting current sheets in the solar atmosphere. *Astron. Astrophys.* **443**(2), 663–678 (2005) [Sect. 11.1.5]
- Ermolaev, Yu.I., Zelenyi, L.M., Zastenker, G.N., et al.: Solar and heliospheric disturbances that resulted in the strongest magnetic storm of November 20, 2003. *Geomag. Aeron.* **45**(1), 20–34 (2005) [Sect. 6.4.1]
- Fang, C., Ding, M.D.: On the spectral characteristics and atmosphere models of the two types of white-light flares. *Astron. Astrophys. Suppl.* **110**(1), 99–106 (1995) [Sect. 15.2.1]
- Field, G.B.: Thermal instability. *Astrophys. J.* **142**(2), 531–567 (1965) [Sects. 5.1.2 and 8.1.2]
- Fletcher, L.: On the generation of loop-top impulsive hard X-ray sources. *Astron. Astrophys.* **303**(1), L9–L12 (1995) [Sect. 9.2.1]
- Fletcher, L., Hudson, H.: The magnetic structure and generation of EUV flare ribbons. *Sol. Phys.* **204**(1), 71–91 (2001) [Sects. 6.1, 6.2.3, 6.2.4 and 7.1.2]
- Fletcher, L., Hudson, H.: Spectral and spatial variations of flare hard X-ray footpoints. *Sol. Phys.* **210**(1), 307–321 (2002) [Intr., Sect. 7.4.1]
- Fletcher, L., Hannah, I.G., Hudson, H.S., Metcalf, T.R.: A TRACE white light and RHESSI hard X-ray study of flare energetics. *Astrophys. J.* **656**(2), 1187–1196 (2007) [Sect. 17.4.2]
- Forbes, T.G., Acton, L.W.: Reconnection and field line shrinkage in solar flares. *Astrophys. J.* **459**(1), 330–341 (1996) [Sects. 6.1, 6.2.4 and 7.4.1]
- Frank, A.G., Bugrov, S.G., Markov, V.S.: Hall currents in a current sheet: structure and dynamics. *Phys. Plasma* **15**, 092102 (2008) [Sect. 2.4.4]
- Frank, A., Bugrov, S., Markov, V.: Enhancement of the guide field during the current sheet formation in the three-dimensional magnetic configuration with an X line. *Phys. Lett. A* **373**, 1460–1464 (2009) [Sect. 8.2.2]
- Froyland, J.: Introduction to Chaos and Coherence, p. 156. Institute of Physics Publishing, Bristol/Philadelphia/Tokyo (1992) [Sect. 11.2]
- Furth, H.P.: Sheet pinch instabilities caused by finite conductivity. *Bull. Am. Phys. Soc.* **6**(2), 193 (1961) [Sect. 13.1.2]
- Furth, H.P.: In: Proceedings of ESRW Conference of the Stability of Plane Plasmas, pp. 22–25. European Space Research Institute, Frascaty (1967) [Sect. 13.1.2]

- Furth, H.P., Killen, J., Rosenbluth, M.N.: Finite-resistivity instabilities of a sheet pinch. *Phys. Fluids* **6**(4), 459–484 (1963) [Sects. 3.2, 6.2.4, 13.1.2, 13.2 and 13.3]
- Gal'per, A.M., Zemskov, V.M., Luchkov, B.I., et al.: Temporal fine structure in hard  $\gamma$  radiation in solar flares. *JETP Lett.* **59**(3), 153–157 (1994) [Sect. 11.4]
- Galeev, A.A., Zelenyi, L.M.: Tearing instability in plasma configurations. *Sov. Phys. – JETP* **43**(6), 1113–1123 (1976) [Sects. 13.1.2 and 13.6.2]
- Galeev, A.A., Rosner, R., Vaiana, G.S.: Structured coronae of accretion discs. *Astrophys. J.* **229**(1), 318–326 (1979) [Intr., Sect. 10.3]
- Galsgaard, K., Longbottom, A.W.: Formation of solar prominences by flux convergence. *Astrophys. J.* **510**(1), 444–459 (1999) [Sect. 15.3]
- Giovanelli, R.G.: A theory of chromospheric flares. *Nature* **158**(4003), 81–82 (1946) [Intr., Sects. 1.1.1 and 16.2]
- Giovanelli, R.G.: Magnetic and electric phenomena in the sun's atmosphere associated with sunspots. *Mon. Not. R. Astron. Soc.* **107**(4), 338–355 (1947) [Sects. 2.1 and 16.2]
- Giovanelli, R.G.: Chromospheric flares. *Mon. Not. R. Astron. Soc.* **108**(2), 163–176 (1948) [Sect. 16.2]
- Giuliani, P., Neukirch, T., Wood, P.: Particle motion in collapsing magnetic traps in solar flares. 1. Kinematic theory of collapsing magnetic traps. *Astrophys. J.* **635**(1), 636–646 (2005) [Sects. 9.2.2 and 9.3.2]
- Glover, A., Ranns, N.D.R., Harra, L.K., et al.: The onset and association of CMEs with sigmoidal active regions. *Geophys. Res. Lett.* **27**(13), 2161–2164 (2000) [Sect. 4.3.5]
- Gold, T.: Magnetic energy shedding in the solar atmosphere. In: Hess, W.N. (ed.) *AAS-NASA Symposium in the Physics of Solar Flares*. NASA-SP 50, pp. 389–396. NASA, Scientific and Technical Information Division, Washington (1964) [Sect. 14.4]
- Gold, T., Hoyle, F.: On the origin of solar flares. *Mon. Not. R. Astron. Soc.* **120**(2), 89–105 (1960) [Sects. 4.3.3, 14.2 and 16.2]
- Goldreich, P., Sridhar, S.: Magnetohydrodynamic turbulence revisited. *Astrophys. J.* **485**(2), 680–688 (1997) [Sect. 14.1]
- Golub, L., Bookbinder, J., DeLuca, E., et al.: A new view of the solar corona from the transition region and coronal explorer (TRACE). *Phys. Plasma* **6**(5), 2205–2212 (1999) [Intr.]
- Gontikakis, C., Efthymiopoulos, C., Anastasiadis, A.: Regular and chaotic dynamics in 3D reconnecting current sheets. *Mon. Not. R. Astron. Soc.* **368**(1), 293–304 (2006) [Sect. 11.2.5]
- Gopasyuk, S.I.: Solar magnetic fields and large-scale electric currents in the active regions. *Adv. Space Res.* **10**(9), 151–160 (1990) [Sect. 5.1.1]
- Gorbachev, V.S., Somov, B.V.: Photospheric vortex flows as a cause for two-ribbon flares: a topological model. *Sol. Phys.* **117**(1), 77–88 (1988) [Sects. 4.2.1, 4.3.5, 5.3.1, 5.3.2 and 7.2.3]
- Gorbachev, V.S., Somov, B.V.: Solar flares of November 5, 1980, as the result of magnetic reconnection at a separator. *Sov. Astron. – AJ* **33**(1), 57–61 (1989) [Intr., Sects. 4.2.1, 4.2.4, 4.3.2, 5.3.2, 7.4.2, 8.6 and 16.3]
- Gorbachev, V.S., Somov, B.V.: Magnetic reconnection on the separator as a cause of a two-ribbon flare. *Adv. Space Res.* **10**(9), 105–108 (1990) [Intr., Sects. 4.2.1, 4.3.1, 4.3.4, 5.3.1, 5.3.2, 6.2.3, 8.6 and 16.3]
- Gorbachev, V.S., Kel'ner, S.R., Somov, B.V., et al.: New topological approach to the question of solar flare trigger. *Sov. Astron. – AJ* **32**(3), 308–314 (1988) [Sects. 4.2.1, 4.2.2 and 7.1.3]
- Gosling, J.T., Birn, J., Hesse, M.: Three-dimensional magnetic reconnection and the magnetic topology of coronal mass ejection events. *Geophys. Res. Lett.* **22**(8), 869–872 (1995) [Sect. 7.2.2]
- Greco, A., Taktakishvili, A.L., Zimbardo, G., et al.: Ion dynamics in the near-Earth magnetotail: magnetic turbulence versus normal component of the average magnetic field. *J. Geophys. Res.* **107**(A10), CiteID 1267 (2002). doi: [10.1029/2002JA009270](https://doi.org/10.1029/2002JA009270) [Sect. 11.1.3]
- Greene, J.M.: Geometrical properties of three-dimensional reconnecting magnetic fields with nulls. *J. Geophys. Res.* **93**, 8583–8590 (1988) [Sect. 4.2.5]
- Gritsyk, P.A., Somov, B.V.: The kinetic description of the accelerated-electron flux in solar flares. *Mosc. Univ. Phys. Bull.* **66**(5), 466–472 (2011) [Sect. 17.4.2]

- Groth, C.P.T., De Zeeuw, D.L., Gombosi, T.I., et al.: Global three-dimensional MHD simulation of a space weather event: CME formation, interplanetary propagation, and interaction with the magnetosphere. *J. Geophys. Res.* **105**(A11), 25053–25078 (2000) [Sect. 10.2.3]
- Guckenheimer, J., Holmes, P.: Nonlinear Oscillations, Dynamical Systems and Bifurcations of Vector Fields. Springer, New York (1983) [Sect. 13.6]
- Gurevich, A.V.: On the theory of runaway electrons. *Sov. Phys. – JETP* **12**(5), 904–912 (1961) [Sect. 8.1.1]
- Gurevich, A.V., Zhivlyuk, Y.N.: Runaway electrons in a non-equilibrium plasma. *Sov. Phys. – JETP* **22**(1), 153–159 (1966) [Sect. 8.1.1]
- Haisch, B.M., Strong, K.T., Rodonò M.: Flares on the Sun and other stars. *Ann. Rev. Astron. Astrophys.* **29**, 275–324 (1991) [Intr.]
- Haken, H.: Synergetics. Springer, New York (1978) [Sect. 13.6]
- Hanslmeier, A.: The Sun and Space Weather, 2nd edn., p. 315. Springer, Dordrecht (2007) [Intr., Sect. 10.2.3]
- Hargreaves, J.K.: The Solar-Terrestrial Environment, p. 420. Cambridge University Press, Cambridge (1992) [Intr.]
- Harra-Murnion, L.K., Schmieder, B., van Driel-Gestelyi, L., et al.: Multi-wavelength observations of post flare loops in two long duration solar flares. *Astron. Astrophys.* **337**, 911–920 (1998) [Sect. 9.1.2]
- Harris, E.G.: On a plasma sheath separating regions of oppositely directed magnetic field. *Nuovo Cimento* **23**(1), 115–121 (1962) [Sects. 11.1.3, 11.3.2, 11.3.3, 11.4 and 13.6]
- Hénoux, J.-C., Somov, B.V.: Generation and structure of the electric currents in a flaring activity complex. *Astron. Astrophys.* **185**(1), 306–314 (1987) [Sects. 7.2.3, 15.5.1 and 16.2.1]
- Hénoux, J.-C., Somov, B.V.: The photospheric dynamo. 1. Magnetic flux-tube generation. *Astron. Astrophys.* **241**(2), 613–617 (1991) [Sects. 15.5 and 15.6]
- Hénoux, J.-C., Somov, B.V.: First ionization potential fractionation. In: Coronal Streamers, Coronal Loops, and Coronal and Solar Wind Composition. Proceedings of the First SOHO Workshop, ESA SP-348, pp. 325–330. European Space Agency, Noordwijk (1992) [Sect. 15.5]
- Hénoux, J.-C., Somov, B.V.: The photospheric dynamo. 2. Physics of thin magnetic flux tubes. *Astron. Astrophys.* **318**(3), 947–956 (1997) [Sect. 15.5]
- Hénoux, J.-C., Somov, B.V.: Physics of thin flux tubes in a partially ionized atmosphere. In: Schmieder, B., Hofmann, A., Staude, J. (eds.) Third Advances in Solar Physics Euroconference: Magnetic Fields and Oscillations. ASP Conference Series, vol. 184, pp. 55–59. Astronomical Society of the Pacific, San Francisco (1999) [Sect. 15.5]
- Hesse, M., Birn, J., Baker, D.N., Slavin, J.A.: MHD simulation of the transition of reconnection from closed to open field lines. *J. Geophys. Res.* **101**(A5), 10805–10816 (1996) [Sect. 8.2.1]
- Heyvaerts, J., Priest, E.R.: Coronal heating by reconnection in DC current systems. A theory based on Taylor's hypothesis. *Astron. Astrophys.* **137**(1), 63–78 (1984) [Sect. 14.2]
- Hirano, Y., Yagi, Y., Maejima, Y., et al.: Self-organization and its effect on confinement in a reversed field pinch plasma. *Plasma Phys. Control. Fusion* **39**(5A), A393–A400 (1997) [Sect. 14.1]
- Hirose, S., Uchida, Y., Uemura, S., et al.: A quadruple magnetic source model for arcade flares and X-ray arcade formations outside active regions. II. Dark filament eruption and the associated arcade flare. *Astrophys. J.* **551**(1), 586–596 (2001) [Sect. 7.2.2]
- Hodgson, R.: On a curious Appearance seen in the Sun. *Mon. Not. R. Astron. Soc.* **20**(1), 15–16 (1859) [Sect. 4.1.1]
- Hoh, F.C.: Stability of sheet pinch. *Phys. Fluid* **9**, 277–284 (1966) [Sect. 11.3]
- Hones, E.W.Jr. (ed.): Magnetic Reconnection in Space and Laboratory Plasmas, p. 386. American Geophysical Union, Washington (1984) [Sect. 16.2]
- Horiuchi, R., Sato, T.: Particle simulation study of driven reconnection in a collisionless plasma. *Phys. Plasma* **1**(11), 3587–3597 (1994) [Sect. 8.1.3]
- Horiuchi, R., Sato, T.: Particle simulation study of collisionless driven reconnection in a sheared magnetic field. *Phys. Plasma* **4**(2), 277–289 (1997) [Sects. 8.2.1, 8.6, 8.5.6 and 11.2]

- Horiuchi, R., Pei, W., Sato, T.: Collisionless driven reconnection in an open system. *Earth Planet Space* **53**(6), 439–445 (2001) [Sects. 8.2.1 and 8.6]
- Horwitz, J.L., Gallagher, D.L., Peterson, W.K. (eds): *Geospace Mass and Energy Flow*, p. 393. American Geophysical Union, Washington (1998) [Intr.]
- Hoyng, P., Brown, J.C., van Beek, H.F.: High time resolution analysis of solar hard X-ray flares observed on board the ESRO TD-1A satellite. *Sol. Phys.* **48**(1), 197–254 (1976) [Sect. 17.3.2]
- Hudson, H., Ryan, J.: High-energy particles in solar flares. *Ann. Rev. Astron. Astrophys.* **33**, 239–282 (1995) [Sects. 9.2.1 and 11.1]
- Hudson, H.S., Lemen, J.R., St. Cyr, O.C., et al.: X-ray coronal changes during halo CMEs. *Geophys. Res. Lett.* **25**(14), 2481–2484 (1998) [Sect. 4.3.5]
- Hurford, G.J., Schwartz, R.A., Krucker, S., et al.: First gamma-ray images of a solar flare. *Astrophys. J.* **595**(2), L77–L80 (2003) [Intr.]
- Hurley, K., Boggs, S.E., Smith, D.M., et al.: An exceptionally bright flare from SGR 1806-20 and the origins of short-duration gamma-ray bursts. *Nature* **434**(7037), 1098–1103 (2005) [Intr.]
- Ichimoto, K., Hirayama, T., Yamaguchi, A., et al.: Effective geometrical thickness and electron density of a flare of 1991 December 2. *Publ. Astron. Soc. Jpn.* **44**(5), L117–L122 (1992) [Intr.]
- Imshennik, V.S., Syrovatskii, S.I.: Two-dimensional flow of an ideally conducting gas in the vicinity of the zero line of a magnetic field. *Sov. Phys. – JETP* **25**(4), 656–664 (1967) [Sects. 2.4.1 and 2.4.2]
- Ip, J.T.C., Sonnerup, B.U.: Resistive tearing instability in a current sheet with coplanar viscous stagnation-point flow. *J. Plasma Phys.* **56**(2), 265–284 (1996) [Sect. 13.5]
- Iroshnikov, P.S.: Turbulence of a conducting fluid in a strong magnetic field. *Sov. Astron. – AJ* **7**(4), 566–571 (1964) [Sect. 14.1]
- Isliker, H.: Structural properties of the dynamics in flares. *Sol. Phys.* **141**(2), 325–334 (1992) [Sect. 11.2]
- Jacobsen, C., Carlqvist, P.: Solar flares caused by circuit interruptions. *Icarus* **3**(3), 270–272 (1964) [Sect. 16.2]
- Jahnke, E., Emde, F., Losch, F.: Tables of Higher Functions. McGraw-Hill, New York (1960) [Sect. 9.5.1]
- Jain, R., Pradhan, A.K., Joshi, V., et al.: The Fe-like feature of the X-ray spectrum of solar flares: first results from the SOXS Mission. *Sol. Phys.* **239**(1), 217–237 (2006) [Sect. 8.6]
- Janicke, L.: The resistive tearing mode in weakly two-dimensional neutral sheets. *Phys. Fluid* **23**(9), 1843–1849 (1980) [Sect. 13.1.2]
- Janicke, L.: Resistive tearing mode in coronal neutral sheets. *Sol. Phys.* **76**(1), 29–43 (1982) [Sect. 13.1.2]
- Ji, H., Huang, G., Wang, H., et al.: Converging motion of  $H\alpha$  conjugate kernels: the signature of fast relaxation of a sheared magnetic field. *Astrophys. J.* **636**(2), L173–L174 (2006) [Sects. 7.2.2 and 7.5.1]
- Ji, H., Huang, G., Wang, H.: The relaxation of sheared magnetic fields: a contracting process. *Astrophys. J.* **660**(1), 893–900 (2007) [Sects. 7.2.2 and 7.5.1]
- Joshi, B., Veronig, A., Cho, K.-S., et al.: Magnetic reconnection during the two-phase evolution of a solar eruptive flare. *Astrophys. J.* **707**(2), 1435–1450 (2009) [Sect. 7.5.1]
- Kadomtsev, B.B.: Hydrodynamic stability of a plasma. In: Leontovich, M.A. (ed.) *Reviews of Plasma Physics*, vol. 2, pp. 153–198. Consultants Bureau, New York (1966) [Sect. 5.1.2]
- Kadomtsev, B.B.: *Collective Phenomena in Plasma*, p. 238. Nauka, Moscow (1976) (in Russian) [Sect. 8.4.1]
- Kan, J.R., Akasofu, S.I., Lee, L.C.: A dynamo theory of solar flares. *Sol. Phys.* **84**(1), 153–167 (1983) [Sect. 5.1.3]
- Karpen, J.T., Antiochos, S.K., De Vore, C.R.: Coronal current sheet formation: the effect of asymmetric and symmetric shears. *Astrophys. J.* **382**(1), 327–337 (1991) [Sects. 16.2 and 16.4]
- Karpen, J.T., Antiochos, S.K., De Vore, C.R., et al.: Dynamic responses to reconnection in solar arcades. *Astrophys. J.* **495**(1), 491–501 (1998) [Sects. 4.1.2 and 12.1]
- Kivelson, M.G., Russell, C.T. (eds): *Introduction to Space Physics*, p. 568. Cambridge University Press, Cambridge (1995) [Intr., Sect. 10.2.3]

- Klein, K.-L., Chupp, E.L., Trottet, G., et al.: Flare-associated energetic particles in the corona and at 1 AU. *Astron. Astrophys.* **348**(1), 271–285 (1999) [Sect. 11.4]
- Klein, K.-L., Trottet, G., Lantos, P., et al.: Coronal electron acceleration and relativistic proton production during the 14 July 2000 flare and CME. *Astron. Astrophys.* **373**, 1073–1082 (2001) [Sect. 7.2.2]
- Kokubun, S., Kamide, Y. (eds): Substorms-4, p. 823. Kluwer, Dordrecht/Terra Scientific Publishing, Tokyo (1998) [Intr., Sect. 13.6]
- Kontorovich, V.M.: On the interaction between small perturbations and the discontinuities in MHD and the stability of shock waves. *Sov. Phys. – JETP* **8**(5), 851–858 (1959) [Sect. 12.2]
- Kopp, R.A., Pneuman, G.W.: Magnetic reconnection in the corona and the loop prominence phenomenon. *Sol. Phys.* **50**(1), 85–94 (1976) [Sect. 7.4.1]
- Koppenfels, W., Stallmann, F.: *Praxis der Konformen Abbildung*. Springer, Berlin/Goettingen/Heidelberg (1959) [Sect. 3.3]
- Korchak, A.A.: Possible mechanisms for generating hard X-rays in solar flares. *Sov. Astron. – AJ* **11**(2), 258–263 (1967) [Sect. 17.1]
- Korchak, A.A.: On the origin of solar flare X-rays. *Sol. Phys.* **18**(2), 284–304 (1971) [Sect. 17.1]
- Korchak, A.A.: Coulomb losses and the nuclear composition of the solar flare accelerated particles. *Sol. Phys.* **66**(1), 149–158 (1980) [Sect. 9.6.1]
- Kosovichev, A.G., Zharkova, V.V.: Magnetic energy release and transients in the solar flare of 2000 July 14. *Astrophys. J.* **550**(Part 2), L105–L108 (2001) [Sects. 7.1.2 and 7.3]
- Kosugi, T.: Solar flare energy release and particle acceleration as revealed by *Yohkoh* HXT. In: Ramaty, R., Mandzhavidze, N., Hua, X.-M. (eds.) *High Energy Solar Physics*, pp. 267–276. American Institute of Physics, New York (1996) [Sects. 9.2.1 and 11.4.2]
- Kosugi, T., Somov, B.: Magnetic reconnection and particle acceleration in solar flares. In: Watanabe, T., Kosugi, T., Sterling, A.C. (eds.) *Observational Plasma astrophysics: Five Years of Yohkoh and Beyond*, pp. 297–306. Kluwer, Dordrecht (1998) [Intr., Sect. 11.4.2]
- Kosugi, T., Dennis, B.R., Kai, K.: Energetic electrons in impulsive and extended solar flares as deduced from flux correlation between hard X-rays and microwaves. *Astrophys. J.* **324**, 1118–1127 (1988) [Sects. 6.2.6 and 9.7]
- Kosugi, T., Makishima, K., Murakami, T., et al.: The hard X-ray telescope (HXT) for the Solar-A mission. *Sol. Phys.* **136**(1), 17–36 (1991) [Intr., Sect. 6.1]
- Kosugi, T., Sakao, T., Masuda, S., et al.: Hard and soft X-ray observations of a super-hot thermal flare of 6 February, 1992. In: Enome, S., Hirayama, T. (eds.) *New Look at the Sun with Emphasis on Advanced Observations of Coronal Dynamics and Flares*, pp. 127–129 (1994) (*Proceedings of Kofu Symposium, Kofu, 6–10 Sept 1993*) [Sect. 9.1.1]
- Kosugi, T., Matsuzaki, K., Sakao, T., et al.: The Hinode (Solar-B) mission: an overview. *Sol. Phys.* **243**(1), 3–17 (2007) [Intr., Sects. 16.6 and 17.4.2]
- Kovalev, V.A., Somov, B.V.: The role of collisions in the particle acceleration in solar-flare magnetic traps. *Astron. Lett.* **29**(6), 465–472 (2003) [Sect. 14.3.1]
- Kraichnan, R.H.: Inertial-range spectrum of hydromagnetic turbulence. *Phys. Fluid* **8**(7), 1385–1389 (1965) [Sect. 14.1]
- Krause, F., Rädler, K.-H.: *Mean-Field Magnetohydrodynamics and Dynamo Theory*. Pergamon Press, Oxford (1980) [Sect. 14.1]
- Krucker, S., Benz, A.O.: Are heating events in the quiet solar corona small flares? Multiwavelength observations of individual events. *Sol. Phys.* **191**(2), 341–358 (2000) [Sect. 14.4]
- Krucker, S., Benz, A.O., Aschwanden, M.J.: *Yohkoh* observation of the source regions of solar narrowband, millisecond spike events. *Astron. Astrophys.* **317**(2), 569–579 (1997) [Sect. 11.4]
- Krucker, S., Hurford, G.J., Lin, R.P.: Hard X-ray source motions in the 2002 July 23 gamma-ray flare. *Astrophys. J.* **595**, L103–L106 (2003) [Intr., Sects. 6.2.6, 7.4.1 and 9.1.2]
- Krucker, S., Hudson, H.S., Jeffrey, N.L.S., et al.: High-resolution imaging of solar flare ribbons and its implication on the thick-target beam model. *Astrophys. J.* **739**(2), id. 96 (7pp) (2011) [Sects. 6.2.6, 16.6, 17.4.2 and 17.5]
- Kubát, J., Karlický, M.: Electric conductivity in the solar photosphere and chromosphere. *Bull. Astron. Inst. Czechosl.* **37**(3), 155–163 (1986) [Sect. 15.2.2]

- Kundt, W.: Astrophysics: A Primer, p. 183. Springer, New York/Berlin/Heidelberg/Tokyo (2001) [Intr.]
- Kurths, J., Herzel, H.: Can a solar pulsation event be characterized by a low-dimensional chaotic attractor? *Sol. Phys.* **10**(1), 39–45 (1986) [Sect. 11.2]
- Kurths, J., Benz, A., Aschwanden, M.J.: The attractor dimension of solar decimetric radio pulsations. *Astron. Astrophys.* **248**(1), 270–276 (1991) [Sect. 11.2]
- Kusano, K.: Simulation study of the formation mechanism of sigmoidal structure in the solar corona. *Astrophys. J.* **631**(2), 1260–1269 (2005) [Sects. 7.6 and 14.2.2]
- Kusano, K., Nishikawa, K.: Bifurcation and stability of coronal arcades in a linear force-free field. *Astrophys. J.* **461**(1), 415–423 (1996) [Sects. 4.1.2 and 5.1.1]
- Laming, J.M., Drake, J.J.: Stellar coronal abundances. VI. The FIP effect and  $\xi$  Bootis A – Solar-like anomalies. *Astrophys. J.* **516**(1), 324–334 (1999) [Sect. 15.4]
- Landau, L.D., Lifshitz, E.M.: Mechanics, 3rd edn., p. 165. Pergamon Press, Oxford/London/Paris (1976) [Sects. 5.2.4 and 11.2]
- Landau, L.D., Lifshitz, E.M., Pitaevskii, L.P.: Electrodynamics of Continuous Media, p. 460. Pergamon Press, Oxford/New York (1984) [Sect. 12.2.2]
- LaRosa, T.N., Moore, R.L.: A mechanism for bulk energization in solar flares: MHD turbulent cascade. *Astrophys. J.* **418**(2), 912–918 (1993) [Sect. 14.1]
- LaRosa, T.N., Moore, R.L., Miller, J.A., et al.: New promise for electron bulk energization in solar flares: preferential Fermi acceleration of electrons over protons in reconnection-driven MHD turbulence. *Astrophys. J.* **467**(1), 454–464 (1996) [Sect. 14.3.1]
- Lau, Y.-T.: Magnetic nulls and topology in a class of solar flare models. *Sol. Phys.* **148**(2), 301–324 (1993) [Sects. 4.2.1 and 16.3]
- Lau, Y.-T., Finn, J.M.: Three-dimensional kinematic reconnection in the presence of field nulls and closed field lines. *Astrophys. J.* **350**, 672–691 (1990) [Sect. 4.2.5]
- Lavrent'ev, M.A., Shabat, B.V.: Methods of the Theory of Complex Variable Functions, p. 736. Nauka, Moscow (1973) (in Russian) [Sects. 3.3, 3.4.1 and 16.3]
- Leamon, R.J., Smith, C.W., Ness, N.F., et al.: Observational constraints on the dynamics of the interplanetary magnetic field dissipation range. *J. Geophys. Res.* **103**(A3), 4775–4787 (1998) [Sect. 14.1]
- Ledentsov, L.S., Somov, B.V.: On discontinuous plasma flows in the vicinity of reconnecting current layers in solar flares. *Astron. Lett.* **37**(2), 131–140 (2011) [Sect. 3.4.3]
- Lembege, B., Pellat R.: Stability of a thick two-dimensional quasi-neutral sheet. *Phys. Fluid* **25**(11), 1995–2004 (1982) [Sects. 11.1.3 and 13.6]
- Lesch, H., Pohl, M.: A possible explanation for intraday variability in active galactic nuclei. *Astron. Astrophys.* **254**(1), 29–38 (1992) [Sect. 10.3]
- Li, Y.P., Gan, W.Q.: The shrinkage of flare radio loops. *Astrophys. J.* **629**(2), L137–L139 (2005) [Sects. 7.5.1 and 9.7]
- Li, C., Tang, Y.H., Dai, Y., et al.: The acceleration characteristics of solar energetic particles in the 2000 July 14 event. *Astron. Astrophys.* **461**(3), 1115–1119 (2007) [Sect. 6.2.5]
- Lichtenberg, A.J., Lieberman, M.A.: Regular and Stochastic Motion, p. 314. Springer, New York (1983) [Sect. 11.2]
- Lilensten, J. (ed.): Space Weather, Research Towards Applications in Europe, p. 330. Springer, Dordrecht (2007) [Intr., Sect. 10.2.3]
- Lin, R.P., Hudson, H.S.: 10–100 keV electron acceleration and emission from solar flares. *Sol. Phys.* **17**(2), 412–435 (1971) [Sect. 17.3.1]
- Lin, R.P., Schwartz, R.A., Pelling, R.M., et al.: A new component of hard X-rays in solar flares. *Astrophys. J.* **251**(2), L109–L114 (1981) [Sect. 8.5.5]
- Lin, Y., Wei, X., Zhang, H.: Variations of magnetic fields and electric currents associated with a solar flare. *Sol. Phys.* **148**(1), 133–138 (1993) [Sect. 4.1.1]
- Lin, R.P., Larson, D., McFadden, J., et al.: Observations of an impulsive solar electron event extending down to  $\sim 0.5$  keV energy. *Geophys. Res. Lett.* **23**(10), 1211–1214 (1996) [Sect. 11.4]
- Lin, R.P., Dennis, B.R., Hurford, G.J., et al.: The reuven ramaty high-energy solar spectroscopic imager (RHESSI). *Sol. Phys.* **210**(1), 3–32 (2002) [Intr., Sects. 9.1.1 and 17.4.2]

- Lin, R.P., Krucker, S., Hurford, G.J., et al.: *RHESSI* observations of particle acceleration and energy release in an intense solar gamma-ray line flare. *Astrophys. J.* **595**(2), L69–L76 (2003a) [Intr., Sects. 6.2.6, 9.1.2 and 9.7]
- Lin, R.P., Krucker, S., Holman, G.D., et al.: In: Kajita, T., Asaoka, Y., Kawachi, A., et al. (eds.) *Proceedings of the 28th International Cosmic Ray Conference*, p. 3207. Universal Academy Press, Tokyo (2003b) [Sect. 9.5.3]
- Litvinenko, Y.E.: Regular versus chaotic motion of particles in non-neutral current sheets. *Sol. Phys.* **147**(2), 337–342 (1993) [Sect. 11.2]
- Litvinenko, Y.E.: Interpretation of particle acceleration in a simulation study of collisionless reconnection. *Phys. Plasma* **4**(9), 3439–3441 (1997) [Sect. 11.2]
- Litvinenko, Y.E.: Photospheric reconnection and cancelling magnetic features on the Sun. *Astrophys. J.* **515**(1), 435–440 (1999) [Sects. 14.4 and 15.2.1]
- Litvinenko, Y.E., Somov, B.V.: Electron acceleration in current sheets in solar flares. *Sov. Astron. Lett.* **17**(5), 353–356 (1991) [Sect. 11.1]
- Litvinenko, Y.E., Somov, B.V.: Particle acceleration in reconnecting current sheets. *Sol. Phys.* **146**(1), 127–133 (1993) [Sects. 11.2 and 11.3]
- Litvinenko, Y.E., Somov, B.V.: Electromagnetic expulsion force in cosmic plasma. *Astron. Astrophys.* **287**(1), L37–L40 (1994a) [Sect. 7.3]
- Litvinenko, Y.E., Somov, B.V.: Magnetic reconnection in the temperature minimum and prominence formation. *Sol. Phys.* **151**(2), 265–270 (1994b) [Sects. 7.3, 14.4 and 15.2.1]
- Litvinenko, Y.E., Somov, B.V.: Relativistic acceleration of protons in current sheets of solar flares. *Sol. Phys.* **158**(1), 317–330 (1995) [Sects. 11.3.3 and 11.4]
- Litvinenko, Y.E., Somov, B.V.: Aspects of the global MHD equilibria and filament eruptions in the solar corona. *Space Sci. Rev.* **95**(1), 67–77 (2001) [Sect. 7.3]
- Liu, Y., Zhang, H.: Relationship between magnetic field evolution and major flare event on July 14, 2000. *Astron. Astrophys.* **372**(3), 1019–1029 (2001) [Sects. 6.1, 6.2.3, 6.2.4, 6.2.6, 7.2.3 and 7.3]
- Liu, Y., Zhang, H.: Analysis of a delta spot. *Astron. Astrophys.* **386**(2), 648–652 (2002) [Sect. 6.1]
- Liu, Y., Srivastava, N., Prasad, D., et al.: A possible explanation of reversed magnetic field features observed in NOAA AR 7321. *Sol. Phys.* **158**(1), 249–258 (1995) [Sect. 15.3]
- Liu, C., Deng, N., Liu, Y., et al.: Rapid change of  $\delta$  spot structure associated with seven major flares. *Astrophys. J.* **622**(1), 722–736 (2005) [Sects. 4.1.1 and 4.1.3]
- Liu, S., Petrosian, V., Mason, G.M.: Stochastic acceleration of  $^3\text{He}$  and  $^4\text{He}$  in solar flares by parallel-propagating plasma waves: general results. *Astrophys. J.* **636**(1), 462–474 (2006) [Sect. 14.3.2]
- Liu, W., Petrosian, V., Dennis, B.R., et al.: Double coronal hard and soft X-ray source observed by *RHESSI*: evidence of magnetic reconnection and particle acceleration in solar flares. *Astrophys. J.* **676**(1), 704–716 (2008) [Sects. 7.2.2, 7.4.4 and 9.1.4]
- Liu, W., Petrosian, V., Dennis, B.R., et al.: Conjugate hard X-ray footpoints in the 2003 29 X10 flare: unshearing motions, correlations, and asymmetries. *Astrophys. J.* **693**(1), 847–867 (2009) [Sects. 7.4.4, 7.5.1 and 7.5.2]
- Longcope, D.W.: Topology and current ribbons: a model for current, reconnection and flaring. *Sol. Phys.* **169**(1), 91–121 (1996) [Sects. 5.3.2, 6.2.3 and 6.2.4]
- Longcope, D.W., Beveridge, C.: A quantitative topological model of reconnection and flux rope formation. *Astrophys. J.* **669**(1), 621–635 (2007) [Sect. 8.6]
- Longcope, D.W., Cowley, S.C.: Current sheet formation along 3D magnetic separators. *Phys. Plasma* **3**(8), 2885–2897 (1996) [Sects. 4.2.4, 5.1.1 and 6.2.3]
- Longcope, D.W., Silva, A.V.R.: A current ribbon model for energy storage and release with application to the flare of 7 January 1992. *Sol. Phys.* **179**(2), 349–377 (1998) [Intr., Sects. 5.3.2 and 8.6]
- Longcope, D.W., McKenzie, D.E., Curtin, J., et al.: Observations of separator reconnection to an emerging active region. *Astrophys. J.* **630**(1), 596–614 (2005) [Sects. 5.1.3 and 5.3.3]
- Longmire, C.L.: *Elementary Plasma Physics*, p. 296. Interscience Publishing, New York/London (1963) [Sect. 11.3]

- Low, B.C.: Electric current sheet formation in a magnetic field induced by footpoint displacements. *Astrophys. J.* **323**(1), 358–367 (1987) [Sect. 2.1.4]
- Low, B.C.: On the spontaneous formation of current sheets above a flexible solar photosphere. *Astrophys. J.* **381**(1), 295–305 (1991) [Sects. 16.2 and 16.3]
- Low, B.C., Smith, D.F.: The free energies of partially open coronal magnetic fields. *Astrophys. J.* **410**(1), 412–425 (1993) [Sect. 16.2]
- Low, B.C., Wolfson, R.: Spontaneous formation of current sheets and the origin of solar flares. *Astrophys. J.* **324**(1), 574–581 (1988) [Sect. 2.1.4]
- Lu, E.T., Hamilton, R.J.: Avalanches and distribution of solar flares. *Astrophys. J.* **380**(2), L89–L92 (1991) [Sect. 14.1]
- Lyon J.G.: The solar wind-magnetosphere-ionosphere system. *Science* **288**, 1987–1991 (2000) [Sect. 10.2.3]
- Mackay, D.H., Priest, E.R., Gaizauskas, V. et al.: Role of helicity in the formation of intermediate filaments. *Sol. Phys.* **180**(1), 299–312 (1998) [Sect. 15.3]
- Mandrini, C.H., Machado, M.E.: Large-scale brightenings associated with flares. *Sol. Phys.* **141**(1), 147–164 (1993) [Sect. 5.3.2]
- Mandrini, C.H., Demoulin, P., Hénoux, J.C., et al.: Evidence for the interaction of large scale magnetic structures in solar flares. *Astron. Astrophys.* **250**(2), 541–547 (1991) [Intr., Sect. 5.3.2]
- Mandrini, C.H., Rovira, M.G., Demoulin, P., et al.: Evidence for reconnection in large-scale structures in solar flares. *Astron. Astrophys.* **272**(2), 609–620 (1993) [Intr., Sect. 5.3.2]
- Manoharan, P.K., Tokumaru, M., Pick, M., et al.: Coronal mass ejection of 2000 July 14 flare event: imaging from near-sun to Earth environment. *Astrophys. J.* **559**(2), 1180–1189 (2001) [Sects. 7.1.1, 7.1.2 and 7.2.2]
- Markovskii, S.A., Skorokhodov, S.L.: Disintegration of trans-Alfvénic shocks due to variable viscosity and resistivity. *J. Geophys. Res.* **105**(A6), 12702–12711 (2000) [Sect. 3.4.3]
- Markovskii, S.A., Somov, B.V.: A model of magnetic reconnection in a current sheet with shock waves. In: *Fizika Solnechnoi Plasmy* (Physics of Solar Plasma), pp. 456–472. Nauka, Moscow (1989) (in Russian) [Sect. 3.2]
- Markovskii, S.A., Somov, B.V.: A criterion for splitting of a reconnecting current sheet into MHD discontinuities. *J. Plasma Phys.* **55**(3), 303–325 (1996) [Sect. 12.2]
- Marsh, G.E.: Force-Free Magnetic Fields: Solutions, Topology and Applications, River Edge, p. 159. World Scientific Publishing, London (1996) [Sect. 14.2]
- Martens, P.C.H.: The generation of proton beams in two-ribbon flares. *Astrophys. J.* **330**(2), L131–L133 (1988) [Sects. 11.3 and 11.4]
- Martin, S.F.: Recent observations of the formation of filaments. In: *Coronal and Prominence Plasmas*, NASA CP-2442, pp. 73–80. National Aeronautics and Space Administration, Scientific and Technical Information Branch, Washington (1986) [Sects. 7.3 and 15.1]
- Martin, S.F.: Conditions for the formation and maintenance of filaments. *Sol. Phys.* **182**(1), 107–137 (1998) [Sects. 7.3 and 15.3]
- Martin, S.F., Livi, S.H.B., Wang, J.: The cancellation of magnetic flux. II. In a decaying active region. *Aust. J. Phys.* **38**, 929–959 (1985) [Sect. 7.3]
- Masuda, S.: Ph.D. thesis, University of Tokyo (1994) [Sect. 9.1.3]
- Masuda, S.: Hard X-ray solar flares revealed with *Yohkoh* HXT - A review. In: Martens, P.C.H., Cauffman, D.P. (eds.) *Multi-wavelength Observations of Coronal Structure and Dynamics, Yohkoh 10th Anniversary Meeting*, pp. 351–359. Pergamon, Amsterdam (2002) [Sect. 9.1.1]
- Masuda, S., Kosugi, T., Hara, H., et al.: A loop-top hard X-ray source in a compact solar flare as evidence for magnetic reconnection. *Nature* **371**, 495–497 (1994) [Intr., Sect. 9.1.1]
- Masuda, S., Kosugi, T., Hara, H., et al.: Hard X-ray sources and the primary energy-release site in solar flares. *Publ. Astron. Soc. Jpn.* **47**, 677–689 (1995) [Intr.]
- Masuda, S., Kosugi, T., Sakao, T., et al.: Coronal hard X-ray sources in solar flares observed with *Yohkoh*/HXT. In: Watanabe, T., Kosugi, T., Sterling, A.C. (eds.) *Observational Plasma Astrophysics: Five Years of Yohkoh and Beyond*, pp. 259–267. Kluwer, Dordrecht (1998) [Sect. 9.1.1]

- Masuda, S., Kosugi, T., Hudson, H.S.: A hard X-ray two-ribbon flare observed with *Yohkoh/HXT*. *Sol. Phys.* **204**(1), 57–69 (2001) [Intr., Sects. 6.1, 6.2.3, 6.2.6, 7.1.2, 7.4.1 and 9.7]
- Mathieu, J., Scott, J.: An Introduction to Turbulent Flow. Cambridge University Press, New York (2000) [Sect. 14.1.2]
- Mauas, P.J.: The white-light flare of 1982 June 15 – Observations. *Astrophys. J. Suppl.* **74**, 609–646 (1990) [Sect. 15.2.1]
- McIntosh, P.S., Donnelly, R.F.: Properties of white light flares. I: association with H $\alpha$  flares and sudden frequency deviations. *Sol. Phys.* **23**(2), 444–456 (1972) [Sect. 17.4.2]
- McKenzie, D.E., Hudson, H.S.: X-ray observations of motions and structure above a solar flare arcade. *Astrophys. J.* **519**, L93–L96 (1999) [Sects. 9.2.2 and 9.2.5]
- Mikhailovskii, A.B.: The Theory of Plasma Instabilities, p. 272. Atomizdat, Moscow (1975) (in Russian) [Sect. 8.4.1]
- Milano, L.J., Gómez, D.O., Martens, P.C.H.: Solar coronal heating: AC versus DC. *Astrophys. J.* **490**(1), 442–451 (1997) [Sect. 14.4]
- Miller, J.A., Reames, D.V.,: Heavy ion acceleration by cascading Alfvén waves in impulsive solar flares. In: Ramaty, R., Mandzhavidze, N., Hua, X.-M. (eds.) High Energy Solar Physics, pp. 450–460. AIP, Woodbury/New York (1996) [Sect. 14.3.2]
- Miller, J.A., LaRosa, T.N., Moore, R.L.: Stochastic electron acceleration by cascading fast mode waves in impulsive solar flares. *Astrophys. J.* **461**(1), 445–464 (1996) [Sect. 14.3.1]
- Miroshnichenko, L.I.: Solar Cosmic Rays, p. 480. Kluwer, Dordrecht/Boston/London (2001) [Intr., Sect. 11.1]
- Moffatt, H.K.: Magnetic Field Generation in Electrically Conducting Fluids, p. 343. Cambridge University Press, London/New York/Melbourne (1978) [Sects. 14.1 and 14.5]
- Moiseev, S.S., Chkhetiani, O.G.: Helical scaling in turbulence. *JETP* **83**(1), 192–198 (1996) [Sect. 14.1]
- Moore, R.L., Falconer, D.A., Porter, J.G., et al.: On heating the Sun's corona by magnetic explosions: feasibility in active regions and prospects for quiet regions and coronal holes. *Astrophys. J.* **526**(1), 505–522 (1999) [Sect. 14.4]
- Moreton, G.E., Severny, A.B.: Magnetic fields and flares. *Sol. Phys.* **3**(2), 282–297 (1968) [Sect. 5.1.1]
- Morita, S., Uchida, Y., Hirose, S., et al.: 3D structure of arcade-type flares derived from the homologous flare series. *Sol. Phys.* **200**(1), 137–156 (2001) [Sects. 7.1.2 and 8.6]
- Morozov, A.I., Solov'ev, L.S.: The structure of magnetic fields. In: Leontovich M.A. (ed.) Reviews of Plasma Physics, vol. 2, pp. 1–101. Consultans Bureau, New York (1966a) [Sect. 16.3]
- Mukerjee, K., Agrawal, P., Paul, B., et al.: Pulse characteristics of the X-ray pulsar 4U1907+09. *Astrophys. J.* **548**(1), 368–376 (2001) [Sect. 10.3]
- Murty, G.S.: Instabilities of a conducting fluid slab carrying uniform current in the presence of a magnetic field. *Ark. Fys.* **19**(6), 499–510 (1961) [Sect. 13.1.2]
- Nagai, T., Fujimoto, M., Saito, Y., et al.: Structure and dynamics of magnetic reconnection for substorm onsets with Geotail observations. *J. Geophys. Res.* **103**, 4419–4428 (1998) [Intr., Sect. 13.6]
- Nakar, E., Piran, T., Sari, R.: Pure and loaded fireballs in Soft Gamma-Ray repeater giant flares. *Astrophys. J.* **635**(1), 516–521 (2005) [Sect. 10.4]
- Newkirk, G., Altschuler, M.D.: Magnetic fields and the solar corona. III: the observed connection between magnetic fields and the density structure of the corona. *Sol. Phys.* **13**(1), 131–152 (1970) [Sect. 3.7]
- Nishida, A., Nagayama, N.: Synoptic survey for the neutral line in the magnetotail during the substorm expansion phase. *J. Geophys. Res.* **78**(19), 3782–3798 (1973) [Intr.]
- Nishida, A., Baker, D.N., Cowley, S.W.H. (eds): New Perspectives on the Earth's Magnetotail, p. 339. American Geophysical Union, Washington (1998) [Intr.]
- Nishikawa, K.I., Sakai, J.: Stabilizing effect of a normal magnetic field on the collisional tearing mode. *Phys. Fluid* **25**(8), 1384–1387 (1982) [Sect. 13.4]
- Ogawara, Y., Takano, T., Kato, T., et al.: The Solar-A mission: an overview. *Sol. Phys.* **136**(1), 1–16 (1991) [Intr., Sect. 6.1]

- Ono, Y., Yamada,M., Akao, T., et al.: Ion acceleration and direct ion heating in three-component magnetic reconnection. *Phys. Rev. Lett.* **76**(18), 3328–3331 (1996) [Sects. 8.2.1 and 8.5.6]
- Oreshina, A.V., Somov, B.V.: Slow and fast magnetic reconnection. I. Role of radiative cooling. *Astron. Astrophys.* **331**, 1078–1086 (1998) [Sects. 8.1.2 and 15.2.3]
- Oreshina, A.V., Somov, B.V.: Analytical description of charged particle motion in a reconnecting current layer. *Astron. Lett.* **35**(3), 195–206 (2009a) [Sect. 11.1.2]
- Oreshina, I.V., Somov, B.V.: Evolution of photospheric magnetic field and coronal zeroth points before solar flares. *Astron. Lett.* **35**(3), 207–213 (2009b) [Sects. 6.3.2 and 6.4.4]
- Oreshina, A.V., Oreshina, I.V., Somov, B.V.: Magnetic-topology evolution in NOAA AR 10501 on 2003 November 18. *Astron. Astrophys.* **538**, A138 (2012) [Sects. 6.4.1, 6.4.2, 6.4.3 and 6.4.4]
- Ott, E.: Chaotic flows and kinematic magnetic dynamos. *Phys. Plasma* **5**(5), 1636–1646 (1998) [Sect. 14.1]
- Otto, A.: The resistive tearing instability for generalized resistive models: theory. *Phys. Fluid* **3B**(7), 1739–1745 (1991) [Sect. 13.1.2]
- Ozernoy, L.M., Somov, B.V.: The magnetic field of a rotating cloud and magneto-rotational explosions. *Astrophys. Space Sci.* **11**(2), 264–283 (1971) [Intr.]
- Paesold, G., Benz, A.O.: Electron firehose instability and acceleration of electrons in solar flares. *Astron. Astrophys.* **351**, 741–746 (1999) [Sect. 14.3.1]
- Paesold, G., Benz, A.O., Klein, K.-L., et al.: Spatial analysis of solar type III events associated with narrow band spikes at metric wavelengths. *Astron. Astrophys.* **371**, 333–342 (2001) [Sect. 11.4]
- Pallavicini, R., Serio, S., Vaiana, G.S.: A survey of soft X-ray limb flare images – The relation between their structure in the corona and other physical parameters. *Astrophys. J.* **216**(1), 108–122 (1977) [Sects. 6.1.1 and 8.5.2]
- Palmer, I.D., Smerd, S.F.: Evidence for a two-component injection of cosmic rays from the solar flare of 1969, March 30. *Sol. Phys.* **26**(2), 460–467 (1972) [Sect. 11.4]
- Park, B.T., Petrosian, V., Schwartz, R.A.: Stochastic acceleration and photon emission in electron-dominated solar flares. *Astrophys. J.* **489**(1), 358–366 (1997) [Sect. 14.3.4]
- Parker, E.N.: Suprathermal particle generation in the solar corona. *Astrophys. J.* **128**(2), 677–685 (1958) [Sect. 3.7]
- Parker, E.N.: Topological dissipation and the small-scale fields in turbulent gases. *Astrophys. J.* **174**(1), 499–510 (1972) [Sects. 2.1.4 and 14.1]
- Parker, E.N.: Cosmic Magnetic Fields. Their Origin and Their Activity, p. 841. Clarendon Press, Oxford (1979) [Sects. 8.1 and 14.1]
- Parker, E.N.: Nanoflares and the solar X-ray corona. *Astrophys. J.* **330**(1), 474–479 (1988) [Sects. 14.1 and 14.4]
- Parker, E.N.: A solar dynamo surface wave at the interface between convection and nonuniform rotation. *Astrophys. J.* **408**(2), 707–719 (1993) [Sect. 14.1]
- Parnell, C.E.: Multiply connected source and null pairs. *Sol. Phys.* **242**(1), 21–41 (2007) [Sect. 4.3.4]
- Pellat, R., Coroniti, F.V., Pritchett, P.L.: Does ion tearing exist? *Geophys. Res. Lett.* **18**(2), 143–146 (1991) [Sect. 13.1.2]
- Peratt, A.L.: Physics of the Plasma Universe, p. 342. Springer, New York/Berlin/Heidelberg (1992) [Intr.]
- Peres, G., Rosner, R., Serio, S., et al.: Coronal closed structures. 4. Hydrodynamical stability and response to heating perturbations. *Astrophys. J.* **252**(2), 791–799 (1982) [Sect. 15.2.3]
- Peterson, L.E., Winckler, J.B.: Gamma-ray burst from a solar flare. *J. Geophys. Res.* **64**(7), 697–707 (1959) [Sects. 17.1 and 11.1.3]
- Petrosian, V.: Impulsive solar X-ray bursts: bremsstrahlung radiation from a beam of electrons in the solar chromosphere and the total energy of solar flares. *Astrophys. J.* **186**(1), 291–304 (1973) [Sect. 17.4.1]
- Petrosian, V., Donaghy, T.Q., McTiernan, J.M.: Loop top hard X-ray emission in solar flares: images and statistics. *Astrophys. J.* **569**(1), 459–473 (2002) [Sects. 9.1.1 and 9.1.3]
- Petrovskii, I.G.: Lectures on the Theory of Ordinary Differential Equations, p. 272. Nauka, Moscow (1964) (in Russian) [Sect. 4.2.3]

- Petschek, H.E.: Magnetic field annihilation. In: Hess, W.N. (ed.) AAS-NASA Symposium on the Physics of Solar Flares, NASA SP-50, pp. 425–439. NASA, Scientific and Technical Information Division, Washington (1964) [Sects. 3.1, 3.4.3, 12.1 and 12.6]
- Pevtsov, A.A.: Transequatorial loops in the solar corona. *Astrophys. J.* **531**(1), 553–560 (2000) [Sect. 5.3.3]
- Pevtsov, A.A., Longcope, D.W.: NOAA 7926: a kinked  $\Omega$ -loop? *Astrophys. J.* **508**(2), 908–915 (1998) [Sect. 4.3.3]
- Pevtsov, A.A., Canfield, R.C., Zirin, H.: Reconnection and helicity in a solar flare. *Astrophys. J.* **473**(1), 533–538 (1996) [Sects. 4.3.3 and 14.2]
- Pike, C.D., Mason, H.E.: Rotating transition region features observed with the SOHO CDS, coronal diagnostic spectrometer. *Sol. Phys.* **182**(2), 333–348 (1998) [Sect. 15.5]
- Pneuman, G.W.: Magnetic structure responsible for coronal disturbances. In: Newkirk, G. (ed.) Coronal Disturbances, (IAU Symposium. 57), pp. 35–68. D. Reidel Publishing, Dordrecht/Boston (1974) [Sect. 13.1.2]
- Pneuman, G.W.: The formation of solar prominences by magnetic reconnection and condensation. *Sol. Phys.* **88**(2), 219–239 (1983) [Sect. 15.1]
- Podgornii, A.I., Syrovatskii, S.I.: Formation and development of a current sheet for various magnetic viscosities and gas pressures. *Sov. J. Plasma Phys.* **7**(5), 580–584 (1981) [Sects. 12.1 and 12.5]
- Pollard, R.K., Taylor, Y.B.: Influence of equilibrium flows on tearing modes. *Phys. Fluid* **22**(1), 126–131 (1979) [Sect. 13.5]
- Pope, S.B.: Turbulent Flows. Cambridge University Press, Cambridge (2000) [Sect. 14.1.2]
- Porter, L.J., Klimchuk, J.A., Sturrock, P.A.: Cylindrically symmetric force-free magnetic fields. *Astrophys. J.* **385**(2), 738–745 (1992) [Sect. 16.2]
- Priest, E.R.: Solar Magnetohydrodynamics, p. 472. D. Reidel Publishing, Dordrecht/Boston/London (1982) [Sects. 3.1, 14.4 and 16.2]
- Priest, E.R., Forbes, T.: Magnetic Reconnection: MHD Theory and Applications. Cambridge University Press, Cambridge (2000) [Intr., Sects. 3.1 and 8.6]
- Priest, E.R., Titov, V.S., Vekstein, G.E., et al.: Steady linear X-point magnetic reconnection. *J. Geophys. Res.* **99**(A11), 21467–21479 (1994) [Sect. 15.2.3]
- Qiu, J., Lee, J., Gary, D.E.: Impulsive and gradual nonthermal emissions in an X-class flare. *Astrophys. J.* **603**(1), 335–347 (2004) [Sects. 6.2.6 and 9.7]
- Raadu, M.A.: Global effects of double layers. In: Schrittwieser, R., Eder, G. (eds.) Second Symposium on Plasma Double Layers and Related Topics, p. 3–27. University of Innsbruck, Institute of Theoretical Physics, Innsbruck (1984) [Sect. 16.2]
- Ramaty, R., Kozlovsky, B., Lingefelter, R.E.: Solar gamma rays. *Space Sci. Rev.* **18**, 341–388 (1975) [Sect. 17.4.2]
- Ranns, N.D.R., Harra, L.K., Matthews, S.A., et al.: Emerging flux as a driver for homologous flares. *Astron. Astrophys.* **360**, 1163–1169 (2000) [Sect. 5.3.2]
- Reiman, A.: Minimum energy state of a toroidal discharge. *Phys. Fluid* **23**(1), 230–231 (1980) [Sect. 14.5]
- Ren, Y., Yamada, M., Gerhardt, S., et al.: Experimental verification of the Hall effect during magnetic reconnection in a laboratory plasma. *Phys. Rev. Lett.* **95**(5), id. 055003 (2005) [Sect. 2.4.4]
- Richmond, A.D.: Modeling the ionosphere wind dynamo: a review. *Pure Appl. Geophys.* **131**(2), 413–435 (1989) [Sect. 15.5.1]
- Roald, C.B., Sturrock, P.A., Wolfson, R.: Coronal heating: energy release associated with chromospheric magnetic reconnection. *Astrophys. J.* **538**(2), 960–967 (2000) [Sect. 14.4]
- Roikhvarger, Z.B., Syrovatskii, S.I.: Evolutionarity of MHD discontinuities with allowance for dissipative waves. *Sov. Phys. – JETP* **39**(4), 654–656 (1974) [Sects. 3.4.3 and 12.2]
- Romanova, M.M., Ustyugova, G.V., Koldoba, A.V., et al.: Three-dimensional simulations of disk accretion to an inclined dipole. II. Hot spots and variability. *Astrophys. J.* **610**(2), 929–932 (2004) [Sect. 10.3]

- Rose, W.K.: Advanced Stellar Astrophysics, p. 494. Cambridge University Press, Cambridge (1998) [Intr.]
- Roumeliotis, G., Moore, R.L.: A linear solution for magnetic reconnection driven by converging or diverging footpoint motions. *Astrophys. J.* **416**(1), 386–391 (1993) [Sect. 15.1]
- Runov, A., Angelopoulos, V., Sitnov, M.I., et al.: THEMIS observations of an earthward-propagating dipolarization front. *Geophys. Res. Lett.* **36**, L14106 (2009). doi: [10.1029/2009GL038980](https://doi.org/10.1029/2009GL038980) [Sect. 9.2.5]
- Russell, C.T.: A brief history of solar-terrestrial physics. In: Kivelson, M.G., Russel, C.T. (eds.) *Introduction to Space Physics*, pp. 1–26. Cambridge University Press, Cambridge (1995) [Sect. 10.2.2]
- Rust, D.M., Hegwer, F.: Analysis of the August 7, 1972 white light flare: light curves and correlation with hard X-rays. *Sol. Phys.* **40**(1), 141–157 (1975) [Sect. 17.4.2]
- Rust, D.M., Kumar, A.: Evidence for helically kinked magnetic flux ropes in solar eruptions. *Astrophys. J.* **464**(2), L199–L202 (1996) [Sect. 4.3.5]
- Rust, D.M., Somov, B.V.: Flare loops heated by thermal conduction. *Sol. Phys.* **93**(1), 95–104 (1984) [Sect. 4.3.1]
- Ryan, J.M.: Long-duration solar gamma-ray flares. *Space Sci. Rev.* **93**(3/4), 581–610 (2000) [Sect. 11.4.3]
- Ryan, J.M., Lockwood, J.A., Debrunner, H.: Solar energetic particles. *Space Sci. Rev.* **93**(1/2), 35–53 (2000) [Sect. 11.4.3]
- Sakai, J.I., de Jager, C.: Solar flares and collisions between current-carrying loops. *Space Sci. Rev.* **77**(1), 1–192 (1996) [Sects. 4.3.3 and 16.2]
- Sakao, T.: Ph.D. thesis, The University of Tokyo (1994) [Sect. 7.4.2]
- Sakao, T., Kosugi, T., Masuda, S.: Energy release in solar flares with respect to magnetic loops. In: Watanabe, T., Kosugi, T., Sterling, A.C. (eds.) *Observational Plasma Astrophysics: Five Years of Yohkoh and Beyond*, pp. 273–284 Kluwer Academic Publishing, Dordrecht (1998) [Sects. 5.3.1, 6.1 and 7.4.2]
- Sato, J.: Ph.D. thesis, Graduate University of Advanced Science, Tokyo (1997) [Sect. 9.1.1]
- Sato, J.: Observation of the coronal hard X-ray sources of the 1998 April 23 flare. *Astrophys. J.* **558**, L137–L140 (2001) [Sect. 9.1.1]
- Sato, J., Kosugi, T., Makishima, K.: Improvement of Yohkoh hard X-ray imaging. *Publ. Astron. Soc. Jpn.* **51**, 127–150 (1999) [Sects. 9.1.1 and 9.1.2]
- Sato, J., Sawa, M., Yoshimura, K., et al.: The Yohkoh HXT/SXT Flare Catalogue. Montana State University, Montana/Institute of Space and Astronautical Science, Sagamihara (2003) [Sect. 9.1.3]
- Schabansky, V.P.: Some processes in the magnetosphere. *Space Sci. Rev.* **12**(3), 299–418 (1971) [Sect. 11.3]
- Scherrer, P.H., Bogart, R.S., Bush, R.I., et al.: The solar oscillations investigation – Michelson Doppler Imager. *Sol. Phys.* **162**(1), 129–188 (1995) [Intr., Sect. 6.1]
- Schindler, K.: A theory of the substorm mechanism. *J. Geophys. Res.* **79**(19), 2803–2810 (1974) [Sects. 13.1.2 and 13.6.2]
- Scholer, M., Sidorenko, I., Jaroschek, C.H., et al.: Onset of collisionless magnetic reconnection in thin current sheets: three-dimensional particle simulations. *Phys. Plasma* **10**(9), 3521–3527 (2003) [Sects. 1.2.1 and 3.5]
- Schrijver, C.J., Title, A.M., van Ballegooijen, A.A., et al.: Sustaining the quiet photospheric network: the balance of flux emergence, fragmentation, merging, and cancellation. *Astrophys. J.* **487**(1), 424–436 (1997) [Sect. 14.4]
- Schrijver, C.J., DeRosa M.L., Title, A.M., et al.: The nonpotentiality of active-region coronae and the dynamics of the photospheric magnetic field. *Astrophys. J.* **628**(1), 501–513 (2005) [Sects. 5.1.3 and 7.2.3]
- Schuster, H.G.: Deterministic Chaos. An Introduction, p. 220. Physik-Verlag, Weinheim (1984) [Sect. 11.2]

- Sergeev, V., Kubyshkina, M., Alexeev, I., et al.: Study of near-Earth reconnection events with Cluster and Double Star. *J. Geophys. Res.* **113**, A07S36 (2008). doi: [10.1029/2007JA012902](https://doi.org/10.1029/2007JA012902) [Sect. 9.2.5]
- Severny, A.B.: The stability of plasma layer with a neutral-point magnetic field. *Sov. Astron. – AJ* **6**(6), 770–773 (1962) [Sect. 2.1.1]
- Severny, A.B.: Solar flares. *Ann. Rev. Astron. Astrophys.* **2**, 363–400 (1964) [Sect. 4.1.1]
- Shafranov, V.D.: Plasma equilibrium in a magnetic field. In: Leontovich, M.A. (ed.) *Reviews of Plasma Physics*, vol. 2, pp. 103–151. Consultants Bureau, New York (1966) [Sect. 16.3]
- Share, G.H., Murphy, R.J., Tulka, A.J., et al.: Gamma-ray line observations of the 2000 July 14 flare and SEP impact on the Earth. *Sol. Phys.* **204**(1), 43–55 (2001) [Sects. 6.2.5 and 7.1.1]
- Shay, M.A., Drake, J.F., Denton, R.E., Biskamp, D.: Structure of the dissipative region during collisionless magnetic reconnection. *J. Geophys. Res.* **103**(A5), 9165–9176 (1998) [Sect. 3.5]
- Sheeley, N.R. Jr., Bohling, J.D., Brueckner, G.E., et al.: XUV observations of coronal magnetic fields. *Sol. Phys.* **40**(1), 103–121 (1975) [Sect. 5.3.3]
- Shibasaki, K.: High-beta disruption in the solar atmosphere. *Astrophys. J.* **557**(1), 326–331 (2001) [Sect. 7.6]
- Shibata, K., Masuda, S., Shimojo, M., et al.: Hot-plasma ejections associated with compact-loop solar flares. *Astrophys. J.* **451**(2), L83–L86 (1995) [Sect. 7.1.2]
- Shimizu, T., Ugai, M.: Magnetohydrodynamic study of adiabatic supersonic and subsonic expansion accelerations in spontaneous fast magnetic reconnection. *Phys. Plasma* **10**(4), 921–929 (2003) [Sect. 3.6]
- Simnett, G.M.: Studies of the dynamic corona from SOHO. In: Ramaty, R., Mandzhavidze, N. (eds.) *High Energy Solar Physics: Anticipating HESSI*. ASP Conference Series, Greenbelt, Maryland, vol. 206, pp. 43–53 (2000) [Sect. 9.2.2]
- Sitnov, M.I., Sharma, A.S.: Role of transient electrons and microinstabilities in the tearing instability of the geomagnetotail current sheet, and the general scenario of the substorms as a catastrophe. In: Kokubun, S., Kamide, Y. (eds.) *Substorms-4*, pp. 539–542. Kluwer, Dordrecht/Terra Scientific Publishing, Tokyo (1998) [Sect. 13.6]
- Sitnov, M.I., Malova, H.V., Lui, A.T.Y.: Quasi-neutral sheet tearing instability induced by electron preferential acceleration from stochasticity. *J. Geophys. Res.* **102**(A1), 163–173 (1997) [Sect. 13.6]
- Shmeleva, O.P., Syrovatskii, S.I.: Distribution of temperature and emission measure in a steadily heated solar atmosphere. *Sol. Phys.* **33**(2), 341–362 (1973) [Sect. 17.4.1]
- Smets, R., Delcourt, D., Sauvad, J.A., et al.: Electron pitch angle distributions following the dipolarization phase of a substorm: interball-tail observations and modeling. *J. Geophys. Res.* **104**(A7), 14571–14576 (1999) [Sects. 9.7 and 9.8]
- Smith, H.J., Smith, E.V.P.: *Solar Flares*, p. 426. Macmillan, New York (1963) [Sect. 4.1.1]
- Somov, B.V.: X-ray heating of a low-temperature region in chromospheric flares. *Sol. Phys.* **42**(1), 235–246 (1975) [Sect. 17.4.2]
- Somov, B.V.: Comments on hydrodynamic models for the influence of flares upon the chromosphere. *Sov. Astron. Lett.* **6**(5), 312–315 (1980) [Sect. 17.4.2]
- Somov, B.V.: Fast reconnection and transient phenomena with particle acceleration in the solar corona. *Bull. Acad. Sci. USSR, Phys. Ser.* **45**(4), 114–116 (1981) [Sects. 8.1.1, 10.1 and 11.4.2]
- Somov, B.V.: New theoretical models of solar flares. *Sov. Phys. Usp.* **28**(3), 271–272 (1985) [Sects. 4.3.5, 8.6 and 16.3]
- Somov, B.V.: Non-neutral current sheets and solar flare energetics. *Astron. Astrophys.* **163**(1), 210–218 (1986) [Sects. 4.3.5 and 8.6]
- Somov, B.V.: A scenario for the large-scale magnetic field evolution in CMEs. *J. Geomag. Geoelectr.* **43** (Suppl), 31–36 (1991) [Sect. 9.2.2]
- Somov, B.V.: Physical Processes in Solar Flares, p. 248. Kluwer, Dordrecht/Boston/London (1992) [Sects. 3.1, 4.2.4, 4.3.3, 6.1, 8.2.1, 8.2.2, 8.3.1, 8.3.2, 8.3.3, 8.4.1, 8.4.2, 8.5.3, 10.1, 11.1, 11.2, 11.3, 12.1, 13.5, 13.6, 16.2, 17.4.1 and 17.4.2]
- Somov, B.V.: Cosmic electrodynamics and solar physics. *Bull. Russ. Acad. Sci. Phys.* **63**(8), 1157–1162 (1999) [Sect. 14.4]

- Somov, B.V.: Cosmic Plasma Physics, p. 652. Kluwer, Dordrecht/Boston/London (2000) [Intr., Sects. 8.5.2 and 8.6]
- Somov, B.V.: On the topological trigger of large eruptive solar flares. *Astron. Lett.* **34**(9), 635–645 (2008a) [Sects. 4.2.3, 6.3.1, 6.3.2 and 6.4.1]
- Somov, B.V.: Magnetic reconnection and topological trigger in physics of large solar flares. *Asian J. Phys.* **17**(2–3), 421–454 (2008b). [Sects. 4.2.3, 6.3.1, 6.3.2 and 6.4.1]
- Somov, B.V.: Interpretation of the observed motions of hard X-ray sources in solar flares. *Astron. Lett.* **36**(7), 514–519 (2010) [Sect. 7.5.2]
- Somov, B.V.: A new scenario for impulsive bursts of hard electromagnetic radiation in space plasma. *Astron. Lett.* **37**(10), 679–691 (2011) [Sect. 11.5]
- Somov, B.V.: Plasma Astrophysics, Part I, Fundamentals and Practice, p. 498. Springer Science+Business Media, New York (2012a) [Intr.]
- Somov, B.V.: On the magnetic reconnection of electric currents in solar flares. *Astron. Lett.* **38**(2), 128–138 (2012b) [Sect. 16.1]
- Somov, B.V., Bogachev, S.A.: The betatron effect in collapsing magnetic trap. *Astron. Lett.* **29**, 621–628 (2003) [Sects. 9.3.1, 9.3.2, 9.3.3, 9.3.4, 9.5.1, 9.4.3, 9.4.4, 9.4.5 and 9.7]
- Somov, B.V., Hénoux J.C.: Generation and interaction of electric currents in the quiet photospheric network. In: Magnetic Fields and Solar Processes. Proceedings of the 9th European Meeting on Solar Physics, ESA SP-448, pp. 659–663. European Space Agency, Noordwijk (1999) [Sects. 14.4 and 16.2]
- Somov, B.V., Kosugi, T.: Collisionless reconnection and high-energy particle acceleration in solar flares. *Astrophys. J.* **485**(2), 859–868 (1997) [Sects. 6.1, 6.2.6, 7.5.2, 8.6, 9.2.1, 9.2.2, 9.2.3, 9.7, 9.8 and 10.1]
- Somov, B.V., Kozlova, L.M.: Fine structure of the solar chromosphere from infrared He I line observations. *Astron. Rep.* **42**(6), 819–826 (1998) [Sect. 15.5]
- Somov, B.V., Litvinenko, Yu.E.: Magnetic reconnection and particle acceleration in the solar corona. In: Linsky, J., Serio, S. (eds.) *Physics of Solar and Stellar Coronae*, pp. 603–606. Kluwer, Dordrecht (1993) [Sect. 11.1]
- Somov, B.V., Merenkova, E.Yu.: Model computations of magnetic fields in solar flares. *Bull. Russ. Acad. Sci. Phys.* **63**(8), 1186–1188 (1999) [Sects. 5.3.1, 11.2 and 16.3]
- Somov, B.V., Oreshina, A.V.: Slow and fast magnetic reconnection. II. High-temperature turbulent-current sheet. *Astron. Astrophys.* **354**, 703–713 (2000) [Sects. 8.1.2 and 8.3.2]
- Somov, B.V., Syrovatskii, S.I.: Appearance of a current sheet in a plasma moving in the field of a two-dimensional magnetic dipole. *Sov. Phys. – JETP* **34**(5), 992–997 (1972) [Sects. 2.1.4, 3.4.1, 3.7, 6.3.2, 8.1.1, 10.3 and 16.3]
- Somov, B.V., Syrovatskii, S.I.: Electric and magnetic fields arising from the rupture of a neutral current sheet. *Bull. Acad. Sci. USSR Phys. Ser.* **39**(2), 109–111 (1975) [Sects. 3.2, 3.6 and 5.1.2]
- Somov, B.V., Syrovatskii, S.I.: Physical processes in the solar atmosphere associated with flares. *Sov. Phys. Usp.* **19**(10), 813–835 (1976a) [Sects. 8.1.2 and 17.4.2]
- Somov, B.V., Syrovatskii, S.I.: Hydrodynamic plasma flows in a strong magnetic field. In: Basov, N.G. (ed.) *Neutral Current Sheets in Plasma*. Proceedings of the P.N. Lebedev Physics Institute, vol. 74, pp. 13–71. Consultants Bureau, New York/London (1976b) [Sects. 2.2.1, 3.1 and 12.1]
- Somov, B.V., Syrovatskii, S.I.: Current sheets as the source of heating for solar active regions. *Solar Phys.* **55**(2), 393–399 (1977) [Sect. 5.1.1]
- Somov, B.V., Syrovatskii, S.I.: Thermal trigger for solar flares and coronal loops formation. *Solar Phys.* **75**(1), 237–244 (1982) [Sect. 8.1.2]
- Somov, B.V., Titov, V.S.: Magnetic reconnection as a mechanism for heating the coronal loops. *Sov. Astron. Lett.* **9**(1), 26–28 (1983) [Sect. 10.1]
- Somov, B.V., Titov, V.S.: Effect of longitudinal magnetic field in current sheets on the Sun. *Sov. Astron. – AJ* **29**(5), 559–563 (1985a) [Sects. 8.2.2 and 14.2]
- Somov, B.V., Titov, V.S.: Magnetic reconnection in a high-temperature plasma of solar flares. 2. Effects caused by transverse and longitudinal magnetic fields. *Sol. Phys.* **102**(1), 79–96 (1985b) [Sects. 8.2.2, 8.3.1, 13.5 and 14.2]

- Somov, B.V., Verneta, A.I.: Magnetic reconnection in a high-temperature plasma of solar flares. 3. Stabilization effect of a transverse magnetic field in non-neutral current sheets. *Sol. Phys.* **117**(1), 89–95 (1988) [Sects. 13.1.2 and 13.6.2]
- Somov, B.V., Verneta, A.I.: Magnetic reconnection in a high-temperature plasma of solar flares. 4. Resistive tearing mode in non-neutral current sheets. *Sol. Phys.* **120**(1), 93–115 (1989) [Sects. 13.1.2 and 13.4]
- Somov, B.V., Verneta, A.I.: Tearing instability of reconnecting current sheets in space plasmas. *Space Sci. Rev.* **65**(3), 253–288 (1993) [Sects. 13.1.2, 13.5.2 and 13.6.2]
- Somov, B.V., Syrovatskii, S.I., Spektor, A.R.: Hydrodynamic response of the solar chromosphere to elementary flare burst. 1. Heating by accelerated electrons. *Sol. Phys.* **73**(1), 145–155 (1981) [Sect. 17.4.2]
- Somov, B.V., Kosugi, T., Sakao, T.: Collisionless 3D reconnection in impulsive solar flares. *Astrophys. J.* **497**(2), 943–956 (1998) [Sects. 5.3.1, 6.1, 7.1.3, 7.2.3, 7.4.1, 7.6, 8.6, 10.1 and 11.2]
- Somov, B.V., Litvinenko, Y.E., Kosugi, T., et al.: Coronal hard X-rays in solar flares: *Yohkoh* observations and interpretation. In: *Magnetic Fields and Solar Processes*. Proceedings of the 9th European Meeting on Solar Physics, ESA SP-448, pp. 701–708. European Space Agency, Noordwijk (1999) [Sects. 9.2.4 and 9.8]
- Somov, B.V., Kosugi, T., Litvinenko, Y.E., et al.: Collisionless reconnection in the structure and dynamics of active regions. In: Brekke, P., Fleck, B., Gurman, J.B. (eds.) *Recent Insight into the Physics of the Sun and Heliosphere: Highlights from SOHO and Other Space Missions*. Proceedings of the IAU Symposium, vol. 203, pp. 558–561. Sheridan Books, Chelsea (2001) [Sects. 4.3.3 and 16.3]
- Somov, B.V., Kosugi, T., Hudson, H.S., et al.: Magnetic reconnection scenario of the Bastille day 2000 flare. *Astrophys. J.* **579**(2), 863–873 (2002a) [Sects. 6.1.1, 7.2.3, 7.4.1, 7.4.4, 7.5.1, 7.5.2, 7.6, 8.6 and 14.2]
- Somov, B.V., Kosugi, T., Litvinenko, Y.E., et al.: Three-dimensional reconnection at the Sun: Space observations and collisionless models. *Adv. Space Res.* **29**(7), 1035–1044 (2002b) [Sect. 4.3.3]
- Somov, B.V., Hénoux, J.C., Bogachev, S.A.: Is it possible to accelerate ions in collapsing magnetic trap? *Adv. Space Res.* **30**(1), 55–60 (2002c) [Sect. 9.8]
- Somov, B.V., Oreshina, A.V., Oreshina, I.V., et al.: Flares in accretion disk coronae. *Adv. Space Res.* **32**(6), 1087–1096 (2003a) [Intr., Sect. 10.3]
- Somov, B.V., Kosugi, T., Hudson, H.S., et al.: Modeling large solar flares. *Adv. Space Res.* **32**(12), 2439–2450 (2003b) [Sects. 7.4.4 and 7.4.5]
- Somov, B.V., Kosugi, T., Bogachev, S.A., et al.: Motion of the HXR sources in solar flares: *Yohkoh* images and statistics. *Adv. Space Res.* **35**(10), 1700–1706 (2005a) [Sects. 7.4.2, 7.4.5 and 7.5.2]
- Somov, B.V., Kosugi, T., Bogachev, S.A., et al.: On upward motions of coronal hard X-ray sources in solar flares. *Adv. Space Res.* **35**(10), 1690–1699 (2005b) [Sect. 9.1.3]
- Somov, B.V., Kosugi, T., Oreshina, I.V., et al.: Large-scale reconnection in a large flare. *Adv. Space Res.* **35**(10), 1712–1722 (2005c) [Sects. 6.2.1, 6.2.4, 6.2.5 and 6.2.6]
- Somov, B.V., Oreshina, I.V., Kovalenko, I.A.: Magnetic reconnection, electric field, and particle acceleration in the July 14, 2000 solar flare. *Astron. Lett.* **34**(5), 327–336 (2008) [Sect. 4.1.3]
- Sotirelis, T., Meng, C.-I.: Magnetopause from pressure balance. *J. Geophys. Res.* **104**(A4), 6889–6898 (1999) [Sect. 10.2]
- Speiser, T.W.: Particle trajectories in model current sheets. 1. Analytical solutions. *J. Geophys. Res.* **70**(17), 4219–4226 (1965) [Sects. 1.2.3, 11.1, 11.2, 11.3 and 11.4]
- Speiser, T.W.: On the uncoupling of parallel and perpendicular particle motion in a neutral sheet. *J. Geophys. Res.* **73**(3), 1112–1113 (1968) [Sect. 11.2]
- Speiser, T.W., Lyons, L.R.: Comparison of an analytical approximation for particle motion in a current sheet with precise numerical calculations. *J. Geophys. Res.* **89**(A1), 147–158 (1984) [Sect. 11.3]
- Spicer, D.S.: Magnetic energy storage and conversion in the solar atmosphere. *Space Sci. Rev.* **31**(1), 351–435 (1982) [Sects. 5.1.3 and 16.4]

- Srivastava, N., Mathew, S.K., Louis, R.E. et al.: Source region of the 18 November 2003 coronal mass ejection that led to the strongest magnetic storm of cycle 23. *J. Geophys. Res.* **114**(A3), CiteID A03107 (2009) [Sect. 6.4.1]
- Stenzel, R.L., Gekelman, W.: Particle acceleration during reconnection in laboratory plasmas. *Adv. Space Res.* **4**(2), 459–470 (1984) [Sects. 5.1.2, 5.1.3 and 16.2]
- Sterling, A.C., Hudson, H.S.: Yohkoh SXT observations of X-ray “dimming” associated with a halo coronal mass ejection. *Astrophys. J.* **491**(1), L55–L58 (1997) [Sect. 4.3.5]
- Stewart, R.T., Labrum, N.R.: Meter-wavelength observations of the solar radio storm of August 17–22, 1968. *Sol. Phys.* **27**(1), 192–202 (1972) [Sect. 11.4]
- Strong, K.T., Saba, J.L.R., Haisch, B.M., et al. (eds): *The Many Faces of the Sun*, p. 610. Springer, New York/Berlin/Heidelberg/Tokyo (1999) [Intr., Sect. 6.1]
- Sturrock, P.A.: Maximum energy of semi-infinite magnetic field configurations. *Astrophys. J.* **380**(2), 655–659 (1991) [Sect. 16.2]
- Sturrock, P.A.: *Plasma Physics: An Introduction to the Theory of Astrophysical, Geophysical and Laboratory Plasmas*, p. 335. Cambridge University Press, Cambridge (1994) [Intr.]
- Sudol, J.J., Harvey, J.W.: Longitudinal magnetic field changes accompanying solar flares. *Astrophys. J.* **635**(1), 647–658 (2005) [Sects. 4.1.1 and 4.1.3]
- Sui, L., Holman, G.D.: Evidence for the formation of a large-scale current sheet in a solar flare. *Astrophys. J.* **596**, L251–L254 (2003) [Sects. 7.5.1, 9.1.2 and 9.1.3]
- Sui, L., Holman, G.D., Dennis, B.R.: Evidence for magnetic reconnection in three homologous solar flares observed by RHESSI. *Astrophys. J.* **612**(1), 546–556 (2004) [Sects. 7.5.1, 9.1.2 and 9.1.3]
- Svestka, Z.: The H $\alpha$  flare as a secondary product of a coronal instability. *Sol. Phys.* **31**(2), 389–400 (1973) [Sect. 17.4.1]
- Svestka, Z.: *Solar Flares*. D. Reidel Publishing, Dordrecht (1976) [Sects. 6.1, 7.1.2 and 7.4.3]
- Sweet, P.A.: The production of high energy particles in solar flares. *Nuovo Cimento Suppl.* **8**(Serie 10), 188–196 (1958) [Intr., Sect. 16.2]
- Sweet, P.A.: Mechanisms of solar flares. *Ann. Rev. Astron. Astrophys.* **7**, 149–176 (1969) [Sects. 2.1.1, 4.2.4, 4.3.1, 8.1.1 and 11.1]
- Syrovatskii, S.I.: Some properties of discontinuity surfaces in MHD. *Proc. P.N. Lebedev Phys. Inst.* **8**, 13–64 (1956) (in Russian) [Sect. 12.3]
- Syrovatskii, S.I.: The stability of plasma in a nonuniform magnetic field and the mechanism of solar flares. *Sov. Astron. – AJ* **6**(6), 768–769 (1962) [Sect. 2.1.1]
- Syrovatskii, S.I.: Dynamical dissipation of a magnetic field and particle acceleration. *Sov. Astron. – AJ* **10**(2), 270–276 (1966a) [Sects. 2.1.1, 2.2.1, 2.3.2, 3.1, 4.2.4, 5.3.2, 8.6, 8.5.6 and 16.3]
- Syrovatskii, S.I.: Dynamical dissipation of magnetic energy in the vicinity of a neutral line. *Sov. Phys. – JETP* **23**(4), 754–762 (1966b) [Sects. 2.1.6, 2.1.7, 2.3.2 and 8.6]
- Syrovatskii, S.I.: MHD cumulation near a zero field line. *Sov. Phys. – JETP* **27**(5), 763–766 (1968) [Sect. 2.4.2]
- Syrovatskii, S.I.: On the mechanism of solar flares. In: de Jager, C., Svestka, Z. (eds.) *Solar Flares and Space Research. 11th COSPAR Symposium*, pp. 346–355. North-Holland Publishing, Amsterdam (1969) [Sects. 5.2.3 and 5.2.4]
- Syrovatskii, S.I.: Formation of current sheets in a plasma with a frozen-in strong field. *Sov. Phys. – JETP* **33**(5), 933–940 (1971) [Sects. 3.1, 12.1 and 16.3]
- Syrovatskii, S.I.: Particle acceleration and plasma ejection from the Sun. In: Dryer, E.R. (ed.) *Solar-Terrestrial Physics 1970*, Part 1, pp. 119–133. D. Reidel Publishing, Dordrecht (1972) [Sects. 5.2.1, 5.2.4, 7.1.2 and 8.4.1]
- Syrovatskii, S.I.: Neutral current sheets in laboratory and space plasmas. In: Basov, N.G. (ed.) *Neutral Current Sheets in Plasmas. Proceedings of the P.N. Lebedev Physics Institute*, vol. 74, pp. 2–10. Consultants Bureau, New York/London (1976a) [Sects. 3.1, 8.1.1 and 12.1]
- Syrovatskii, S.I.: Current-sheet parameters and a thermal trigger for solar flares. *Sov. Astron. Lett.* **2**(1), 13–14 (1976b) [Sects. 5.1.1, 5.1.3 and 8.1.2]
- Syrovatskii, S.I.: Pinch sheets and reconnection in astrophysics. *Ann. Rev. Astron. Astrophys.* **19**, 163–229 (1981) [Sects. 4.2.4, 5.1.1, 5.3.2, 8.1.1, 8.4.1, 11.1, 11.4, 13.5.2 and 16.2]

- Syrovatskii, S.I.: Model for flare loops, fast motions, and opening of magnetic field in the corona. *Sol. Phys.* **76**(1), 3–20 (1982) [Sects. 4.3.5, 6.3.1, 11.1 and 15.1]
- Syrovatskii, S.I., Shmeleva, O.P.: Heating of plasma by high-energy electrons, and the non-thermal X-ray emission in solar flares. *Sov. Astron. – AJ* **16**(2), 273–283 (1972) [Sects. 17.2.2, 17.2.4 and 17.3.1]
- Syrovatskii, S.I., Somov, B.V.: Physical driving forces and models of coronal responses. In: Dryer, M., Tandberg-Hanssen, E. (eds.) *Solar and Interplanetary Dynamics*. IAU Symposium, vol. 91, pp. 425–441. Reidel, Dordrecht (1980) [Sects. 4.3.5, 6.3.1 and 16.2]
- Tanaka, K.: Impact of X-ray observations from the Hinotori satellite on solar flare research. *Publ. Astron. Soc. Jpn.* **39**(1), 1–45 (1987) [Sect. 8.5.5]
- Tandberg-Hanssen, E.: The Nature of Solar Prominences, p. 308. Kluwer, Dordrecht/Boston/London (1995) [Sect. 15.1]
- Tarbell, T.D.: Early results from the atmospheric imaging assembly (AIA) on the solar dynamics observatory (SDO). *Bull. Am. Astron. Soc.* **43**, AAS Meeting 217, No. 115.09, p. 122 (2011) [Intr.]
- Taylor, J.B.: Relaxation of toroidal plasma and generation of reverse magnetic fields. *Phys. Rev. Lett.* **33**(19), 1139–1141 (1974) [Sects. 14.1 and 14.2.2]
- Taylor, J.B.: Relaxation and magnetic reconnection in plasmas. *Rev. Mod. Phys.* **58**(3), 741–763 (1986) [Sect. 14.11]
- Tian, L., Wang, J., Wu, D.: Non-potentiality of the magnetic field beneath the eruptive filament in the Bastille event. *Sol. Phys.* **209**, 375–389 (2002) [Sect. 6.2.4]
- Titov, V.S., Priest, E.R., Démoulin, P.: Conditions for the appearance of ‘bald patches’ at the solar surface. *Astron. Astrophys.* **276**(2), 564–570 (1993) [Sect. 16.3]
- Tsalas, M., Chapman, S.C., Rowlands, G.: The stability of charged-particle motion in sheared magnetic reversals. *J. Plasma Phys.* **65**(4), 331–352 (2001) [Sect. 11.1.2]
- Tsuneta, S.: Solar flares as an ongoing magnetic reconnection process. In: Zirin, H., Ai, G., Wang, H. (eds.) *ASP Conference Series*, vol. **46**, pp. 239–248. Astronomical Society of the Pacific, San Francisco (1993) [Intr, Sect. 16.2]
- Tsuneta, S.: Structure and dynamics of reconnection in a solar flare. *Astrophys. J.* **456**(2), 840–849 (1996) [Sects. 6.1, 7.1.2, 8.1.1, 8.6 and 8.5.5]
- Tsuneta, S., Naito, T.: Fermi acceleration at the fast shock in a solar flare and the impulsive loop-top hard X-ray source. *Astrophys. J.* **495**, L67–L70 (1998) [Sect. 9.3.1]
- Tsuneta, S., Nitta, N., Ohki, K., et al.: Hard X-ray imaging observations of solar hot thermal flares with the *Hinotori* spacecraft. *Astrophys. J.* **284**(2), 827–832 (1984) [Sect. 8.5.5]
- Tsuneta, S., Acton, L., Bruner, M., et al.: The soft X-ray telescope for the Solar-A mission. *Solar Phys.* **136**(1), 37–67 (1991) [Intr, Sect. 6.1]
- Tsuneta, S., Hara, H., Shimuzu, T., et al.: Observation of a solar flare at the limb with the *Yohkoh* soft X-ray telescope. *Publ. Astron. Soc. Jpn.* **44**(5), L63–L69 (1992) [Intr.]
- Tsuneta, S., Masuda, S., Kosugi, T., et al.: Hot and super-hot plasmas above an impulsive-flare loop. *Astrophys. J.* **478**(2), 787–796 (1997) [Sects. 8.1.1, 8.5.4, 8.6, 9.2.3 and 9.6.4]
- Tsuneta, S., Ichimoto, K., Katsukawa, Y., et al.: The Solar Optical Telescope for the Hinode mission: an overview. *Solar Phys.* **249**(2), 167–196 (2008) [Intr, Sects. 16.6 and 17.4.2]
- Tsurutani, B.T., Gonzalez, W.D., Kamide, Y., et al. (eds): *Magnetic Storms*, p. 266. American Geophysical Union, Washington (1997) [Intr.]
- Tsyganenko, N.A.: Effects of the solar wind conditions on the global magnetospheric configuration as deduced from data-based field models. In: Proceedings of 3rd International Conference on Substorms (ICS-3), ESA SP-389, pp. 181–190. European Space Agency Publications Division, Noordwijk (1996) [Sect. 10.2]
- Uchida, Y., Hirose, S., Morita, S., et al.: Observations of flares and active regions from *Yohkoh*, and magnetohydrodynamic models explaining them. *Astrophys. Space Sci.* **264**(1), 145–169 (1998) [Sects. 7.1.2 and 7.6]
- Ugai, M.: The evolution of fast reconnection in a three-dimensional current sheet system. *Phys. Plasma* **15**(8), 082306–082306-10 (2008) [Sect. 3.4.3]

- Ugai, M.: Impulsive magnetic pulsations and electrojets in the loop footpoint driven by the fast reconnection jet. *Phys. Plasma* **16**(11), 112902–112902-8 (2009) [Sect. 3.4.3]
- Ugarte-Urra, I., Warren, H.P., Winebarger, A.R.: The magnetic topology of coronal mass ejection sources. *Astrophys. J.* **662**(2), 1293–1301 (2007) [Sects. 6.3.1 and 8.6]
- Ulmschneider, P., Rosner, R., Priest, E.R. (eds): *Mechanisms of Chromospheric and Coronal Heating*. Springer, Berlin (1991) [Sect. 14.4]
- Uzdensky, D.A.: Self-regulation of solar coronal heating process via the collisionless reconnection condition. *Phys. Rev. Lett.* **99**(26), id. 261101 (2007a) [Sect. 4.2.4]
- Uzdensky, D.A.: Fast collisionless reconnection condition and self-organization of solar coronal heating. *Astrophys. J.* **671**(2), 2139–2153 (2007b) [Sect. 8.3.1]
- Uzdensky, D.A., Kulsrud, R.M.: Physical origin of the quadrupole out-of-plane magnetic field in Hall-magnetohydrodynamic reconnection. *Phys. Plasma* **13**(66), 062305–062305-14 (2006) [Sect. 2.4.4]
- van Ballegooijen, A.A., Martens, P.C.H.: Formation and eruption of solar prominences. *Astrophys. J.* **343**(3), 971–984 (1989) [Sects. 7.3 and 15.1]
- van Ballegooijen, A.A., Martens, P.C.H.: Magnetic fields in quiescent prominences. *Astrophys. J.* **361**(1), 283–289 (1990) [Sect. 15.1]
- van Hollebeke, M.A.I., Ma Sung, L.S., McDonald, F.B.: The variation of solar proton energy spectra and size distribution with heliolatitude. *Solar Phys.* **41**(1), 189–223 (1975) [Sect. 17.4.2]
- Vekstein, G.E., Priest, E.R.: Magnetohydrodynamic equilibria and cusp formation at an X-type neutral line by footpoint shearing. *Astrophys. J.* **384**(1), 333–340 (1992) [Sects. 16.2 and 16.3]
- Veltri, P., Zimbardo, G., Taktakishvili, A.L., et al.: Effect of magnetic turbulence on the ion dynamics in the distant magnetotail. *J. Geophys. Res.* **103**(A7), 14897–14910 (1998) [Sect. 11.1.3]
- Vernazza, J.E., Avrett, E.H., Loeser, R.: Structure of the solar chromosphere. Basic computations and summary of results. *Astrophys. J.* **184**, 605–632 (1973) [Sect. 17.4.2]
- Vernazza, J.E., Avrett, E.H., Loeser, R.: Structure of the solar chromosphere. 3. Models of the EUV brightness components of the quiet Sun. *Astrophys. J. Suppl.* **45**, 635–725 (1981) [Sect. 15.2.2]
- Verneta, A.I., Somov, B.V.: Effect of compressibility on the development of the tearing instability in a non-neutral current sheet in the solar atmosphere. *Astron. Rep.* **37**(3), 282–285 (1993) [Sect. 13.5.2]
- Vladimirov, V.S.: *Equations of Mathematical Physics*, p. 418. M. Dekker, New York (1971) [Sect. 13.6]
- Voronov, G.S., Kyrie, N.P., Markov, V.S., et al.: Spectroscopic measurements of the electron and ion temperatures and effective ion charge in current sheets formed in two- and three-dimensional magnetic configurations. *Plasma Phys. Rep.* **34**(12), 999–1015 (2008) [Sect. 5.1.2]
- Vorpahl, J.A.: The triggering and subsequent development of a solar flare. *Astrophys. J.* **205**(1), 868–873 (1976) [Sects. 17.3.2 and 17.4.1]
- Wang, J.: Vector magnetic fields and magnetic activity of the Sun. *Fundam. Cosm. Phys.* **20**(3), 251–382 (1999) [Sects. 4.1.1 and 15.3]
- Wang, H., Qiu, J.: Relationship between flare kernels in H $\alpha$  far-blue wing and magnetic fields. *Astrophys. J.* **568**(1), 408–412 (2002) [Sect. 6.1]
- Wang, Y.M., Sheeley, N.R.: Observations of core fallback during coronal mass ejections. *Astrophys. J.* **567**(2), 1211–1224 (2002) [Sect. 9.2.5]
- Wang, J., Shi, Z.: The flare-associated magnetic changes in an active region. II. Flux emergence and cancellation. *Sol. Phys.* **143**(1), 119–139 (1993) [Sects. 6.2.4 and 7.6]
- Wang, J.X., Shi, Z.X., Wang, H., et al.: Flares and the magnetic non-potentiality. *Astrophys. J.* **456**(2), 861–878 (1996) [Sect. 5.1.1]
- Wang, H., Qiu, J., Jing, J., et al.: Study of ribbon separation of a flare associated with a quiescent filament eruption. *Astrophys. J.* **593**(1), 564–570 (2003) [Sect. 7.4.5]
- Wang, H., Liu, C., Deng, Y., et al.: Reevaluation of the magnetic structure and evolution associated with the Bastille day flare on 2000 July 14. *Astrophys. J.* **627**(2), 1031–1039 (2005) [Sects. 4.1.1, 4.1.3, 7.1.1 and 7.1.2]

- Watanabe, K., Krucker, S., Hudson, H., et al.: G-band and hard X-ray emissions of the 2006 December 14 flare observed by Hinode/SOT and RHESSI. *Astrophys. J.* **715**(1), 651–655 (2010) [Sect. 17.4.2]
- Wedemeyer-Böhm, S.: Point spread functions for the Solar optical telescope onboard Hinode. *Astron. Astrophys.* **487**(1), 399–412 (2008) [Sect. 16.6]
- Woltjer, L.: A theorem on force-free magnetic fields. *Proc. Nat. Acad. Sci. USA* **44**(6), 489–491 (1958) [Sect. 14.1]
- Woltjer, L.: Hydromagnetic equilibrium: II. Stability in the variational formulation. *Proc. Nat. Acad. Sci. USA* **45**(6), 769–771 (1959) [Sect. 14.5]
- Wright, J.M.: National Space Weather Program: The Implementation Plan, FCM-P31. Office of the Federal Coordinator for Meteorological Services and Supporting Research, Washington (1997) [Intr., Sect. 10.2.3]
- Wright, A.N., Berger, M.A.: The effect of reconnection upon the linkage and interior structure of magnetic flux tubes. *J. Geophys. Res.* **94**(A2), 1295–1302 (1989) [Sect. 14.1]
- Wright, A.N., Berger, M.A.: A physical description of magnetic helicity evolution in the presence of reconnection lines. *J. Plasma Phys.* **46**(1), 179–199 (1991) [Sect. 14.2]
- Xiao, C.J., Wang, X.G., Pu, Z.Y., et al.: Satellite observations of separator-line geometry of three-dimensional magnetic reconnection. *Nature Phys.* **3**(9), 609–613 (2007) [Intr., Sect. 4.2.1]
- Xu, Y., Cao, W., Liu, C., et al.: High-resolution observations of multiwavelength emissions during two X-class white-light flares. *Astrophys. J.* **641**(2), 1210–1216 (2006) [Sect. 17.4.2]
- Yamada, M., Ren, Y., Ji, H., et al.: Identification of two-scale diffusion layer during magnetic reconnection in a laboratory plasma. *Bull. Am. Phys. Soc.* **52**(11), abstract ID: BAPS.2007.DPP.TP8.6 (2007) [Sect. 4.2.4]
- Yan, Y., Deng, Y., Karlicky, M., et al.: The magnetic rope structure and associated energetic processes in the 2000 July 14 solar flare. *Astrophys. J.* **551**(Part 2), L115–L118 (2001) [Sects. 6.1 and 7.2.3]
- Yokoyama, T., Shibata, K.: Magnetic reconnection coupled with heat conduction. *Astrophys. J.* **474**(1), L61–L64 (1997) [Sect. 3.6]
- Yokoyama, T., Akita, K., Morimoto, T., et al.: Clear evidence of reconnection inflow of a solar flare. *Astrophys. J.* **546**(1), L69–L72 (2001) [Sect. 8.1.1]
- Zeiler, A., Biskamp, D., Drake, J.F., et al.: Three-dimensional particle simulation of collisionless magnetic reconnection. *J. Geophys. Res.* **107**(A9), SPM 6-1, CiteID 1230 (2002) [Sects. 3.4.3 and 3.5]
- Zel'dovich, Ya.B., Raizer, Yu.P.: Physics of Shock Waves and High-Temperature Hydrodynamic Phenomena, vol. 1, p. 464; vol. 2, p. 452. Academic, New York/San Francisco/London (1966) [Sect. 2.4.1]
- Zel'dovich, Ya.B., Raizer, Yu.P.: In: Hayes, W.D., Probstein, R.F. (eds.) Physics of Shock Waves and High-Temperature Hydrodynamic Phenomena. Dover, Mineola (2002) [Sect. 2.4.1]
- Zelenyi, L.M., Dolgonosov, M.S., Grigorenko, E.E., et al.: Universal properties of the nonadiabatic acceleration of ions in current sheets. *JETP Lett.* **85**(4), 187–193 (2007) [Sect. 11.1.3]
- Zelenyi, L.M., Artemyev, A.V., Petrukovich, A.A., et al.: Low frequency eigenmodes of thin anisotropic current sheets and Cluster observations. *Ann. Geophys.* **27**(2), 861–868 (2009) [Sects. 11.1.3 and 13.1.1]
- Zhang, H.: Configuration of magnetic shear and vertical current in the active region NOAA 5395 in 1989 March. *Astron. Astrophys. Suppl.* **111**(1), 27–40 (1995) [Sect. 5.1.1]
- Zhang, H.: Magnetic field, helicity and the 2000 July 14 flare in solar active region 9077. *Mon. Not. R. Astron. Soc.* **332**(2), 500–512 (2002) [Sects. 6.2.4 and 7.1.1]
- Zhang, H.-Q., Chupp, E. L.: Studies on post-flare prominence of 1981 April 27. *Astrophys. Space Sci.* **153**(1), 95–108 (1989) [Sect. 11.4]
- Zhang, J., Wang, J., Deng, Y., et al.: Magnetic flux cancelation associated with the major solar event on 2000 July 14. *Astrophys. J.* **548**(Part 2), L99–L102 (2001) [Sects. 6.1, 7.2.2, 7.2.3 and 7.3]

- Zhang, J., Li, L., Song, Q.: Interaction between a fast rotating sunspot and ephemeral regions as the origin of the major solar event on 2006 December 13. *Astrophys. J.* **662**(1), Part 2, L35–L38 (2007) [Sect. 11.4.3]
- Zhou, T., Ji, H., Huang, G.: Converging motion of conjugate flaring kernels during two large solar flares. *Adv. Space Res.* **41**(8), 1195–1201 (2008) [Sects. 7.2.2 and 7.5.1]
- Zirin, H.: *Astrophysics of the Sun*. D. Reidel, Dordrecht (1988) [Sects. 6.1 and 7.1.2]
- Zirin, H., Tanaka, K.: The flare of August 1972. *Sol. Phys.* **32**(1), 173–207 (1973) [Sect. 17.4.1]
- Zirker, J.B., Cleveland, F.M.: Avalanche models of active region heating and flaring. *Sol. Phys.* **145**(1), 119–128 (1993) [Sect. 14.1]
- Zuccarello, F., Burm, H., Kuperus, M., et al.: Varying self-inductance and energy storage in a sheared force-free arcade. *Astron. Astrophys.* **180**(1), 218–222 (1987) [Sect. 16.4]
- Zweibel, E.G.: Magnetic reconnection in partially ionized gases. *Astrophys. J.* **340**(2), 550–557 (1989) [Sect. 15.2.3]
- Zwingmann, W., Schindler, K., Birn, J.: On sheared magnetic field structures containing neutral points. *Sol. Phys.* **99**(1), 133–143 (1985) [Sects. 13.1, 16.2 and 16.3]

# Index

## A

- abundance
  - elements, 404, 409
- acceleration
  - betatron, 213
  - by electric field, 15, 35, 43, 179, 317, 418
  - by Langmuir turbulence, 317
  - by shock waves, 315
  - electrons, viii, 15, 293, 300, 306, 307, 386, 390
  - Fermi, 213, 223, 386
  - first-step, 221
  - in current layer, 15, 35, 293
  - in solar flares, 307, 315
  - ions, viii, 15, 221, 309
  - particle, vii, 9, 35, 93, 208, 294
  - regular, 35, 307
  - stochastic, 307, 386
  - two-step, 128, 221
- accretion disk, vii, 285
- ACE, 319
- active complex, 145, 157
- active galaxy, vii
- active region, ix, 2, 327, 377
- adiabatic invariant
  - second or longitudinal, 224
- afterglow, 291
- Alfvén-Mach number, 183
- alpha-effect, 380, 382
- anomalous resistivity, 187, 205
- anomalous thermal flux, 189, 209
- approximation
  - adiabatic or drift, 4, 302
  - collisionless, 4, 187, 369
  - dissipative MHD, 187
  - electron MHD, 59
  - force free, 174, 425
- ideal MHD, 25, 186
- large mag. Reynolds number, 378
- line tying, 421
- magnetostatic, 326
- non-relativistic, 12
- one-fluid, 399, 406
- small mag. Reynolds number, 384, 401
- stationary, 398
- strong magnetic field, 20, 45, 190, 199, 202, 286
- strong-field-cold-plasma, 21, 28
- three-fluid, 406
- two-dimensional, 421
- WKB, 327, 340, 375

## atmosphere

- solar, 1, 15

## B

- bald patch, 428
- Bastille day flare
  - electric field, 126
  - energy, 146
  - gamma-rays, 127
  - hard X-rays, 109
  - magnetic field, 112
  - plasma motions, 147
  - soft X-rays, 109
  - sunspot structure, 71, 128
  - topological portrait, 119
- bifurcation, 6, 92, 321, 375
  - global, 133
- black hole, 320
- boundary conditions
  - on current layer, 52, 343
- boundary layer, 421
- bremsstrahlung, 213, 220, 253, 439, 441

- C**
- cascade
    - direct, 381
    - inverse, 381
  - catastrophe theory, 375
  - Cherenkov detector, 319
  - chirality, 404, 419
  - chromospheric evaporation, 85
  - Cluster, x
  - CME, 109, 136, 141, 319
  - collapse
    - magnetic, 42
  - collapsing magnetic trap, 128, 213, 220, 317
  - collision
    - between neutrals and ions, 402
  - collisional relaxation, 204, 207
  - compact object, 320
  - condensation mode, 182
  - conditions
    - initial, 22
  - conductivity
    - anomalous, 43, 189, 198, 277
    - classical, 180, 198, 210, 276
    - electric, 352, 400
    - Hall, 419
    - perpendicular, 419
  - conform mapping, 289
  - conservation law
    - magnetic flux, 425
    - magnetic helicity, 379
  - continuity equation
    - for plasma, 29
    - Lagrangian form, 29
  - cooling
    - heat conductive, 189
    - radiative, 182, 397
  - coordinates
    - generalized, 303
    - Lagrangian, 29
  - Coriolis force, 384
  - corona
    - accretion disk, 285
    - solar, 285
  - coronal heating, 377, 383, 392
  - coronal hole, 90
  - coronal mass ejection, viii, 1, 90, 154, 221, 284, 310, 315, 419
  - coronal streamer, 23, 63, 221
  - coronal transient, viii, 1, 90, 318, 419
  - cosmic rays, 319
  - coupling
    - electrodynamic, 94
  - cumulative effect, 20, 27, 36
- D**
- current
    - conductive, 34
    - cross-tail, 284
    - direct, 6
    - displacement, 34
    - field-aligned, 415
    - interruption, 416
    - magnetopause, 282
    - reverse, 6, 31, 324
  - current layer
    - actual thickness, 205
    - at separator, ix, 78
    - at separatrices, 174
    - cold dense, 178, 210
    - collisionless, 204, 209
    - disrupting, 50, 60
    - disruption, 93
    - electron, 59
    - energy, 78
    - evolutionarity, 347
    - formation, 78
    - interplanetary, 184
    - neutral, 6, 9, 15, 23, 47, 51, 124, 177, 210, 289, 351, 366, 402
    - non-adiabatic thickness, 302
    - non-neutral, 353
      - electrically, 15, 311
      - magnetically, 15, 185, 199, 294, 306
    - non-reconnecting, 8
    - reconnecting, 6, 23, 47, 78, 182, 207, 321, 351
    - slowly-reconnecting, 71, 78, 92, 174
    - splitting, 321
    - super-hot turbulent-current, 59, 147, 174, 177, 182, 185, 208, 209, 213, 216, 221, 267, 273, 277, 293
    - Sweet-Parker, 178, 182
    - Syrovatskii, 182, 211
    - thin, 194, 282

- discontinuity  
 evolutionary, 323, 430  
 non-evolutionary, 59, 323, 429  
 rotational, 101  
 tangential, 101, 429
- dispersion equation, 327, 359, 365
- displacement  
 antisymmetric, 423  
 magnetic footpoints, 377, 423
- dissipation  
 dynamic, 35, 43, 125, 207, 209, 435  
 Joule, 35  
 magnetic helicity, 384
- dissipative wave, 329
- double layer, 95, 125, 416
- Dreicer field, 43
- drift  
 electric, 4, 9, 188, 298  
 gradient, 9
- Dungey, 19
- dynamic chaos, 303
- dynamic dissipation, 33, 43, 125, 207, 209
- dynamo  
 ionospheric, 406  
 photospheric, 406  
 solar, 382  
 turbulent, vii, 380
- E**
- Earth  
 ionosphere, x, 406  
 magnetosphere, viii, 320  
 plasma sheet, 381
- eddy viscosity, 379
- ejection, vii  
 coronal mass (CME), viii, 284
- electric circuit, 94, 416
- electric conductivity  
 isotropic, 352
- electric drift, 4, 9, 188
- electric field, 15  
 Dreicer, 43, 179, 276  
 generation, 4, 77  
 impulsive, 94, 100  
 quasi-stationary, 100
- electric runaway, 43, 94
- electron resonance, 372
- elementary flare bursts, 448
- emission measure, 253
- energy conservation law, 188, 372
- energy losses  
 collisional, 179
- energy surface, 305
- entropy wave, 329
- equation  
 continuity, 29, 188  
 diffusion, 430  
 dispersion, 327, 359  
 Fokker-Planck, 390  
 freezing-in, 29  
 Grad-Shafranov, 421  
 kinetic, 369  
 linear oscillator, 15  
 motion, 6, 12  
 oscillator, 298  
 Vlasov, 369  
 wave, 26
- equations  
 ideal MHD  
 linearized, 25  
 magnetic field line, 425  
 resistive MHD, 182
- equipartition, 380
- ESRO TD-1A, 448
- evaporation  
 chromospheric, 85, 449
- evolutionarity  
 conditions, 323  
 criterion, 343  
 current layer, 207, 324, 347  
 fast shock wave, 324  
 slow shock wave, 324
- F**
- Fermi acceleration, 223, 319, 386
- filament  
 channel, 403  
 dextral, 404, 418  
 formation, 398  
 sinistral, 404, 418
- fireball, 291
- flare  
 avalanche model, 377  
 central part, 143, 156  
 chromospheric, ix  
 electron-dominated, 390  
 eruptive, 110, 434, 436  
 giant, 291  
 gradual, 203  
 gradual phase, 100, 213  
 homologous, 106  
 impulsive, 203  
 impulsive phase, 100, 213, 439  
 in astrophysical plasma, vii  
 less impulsive, 102, 157  
 more impulsive, 102, 156

- flare (*cont.*)  
 non-thermal, 204  
 rainbow reconnection, 156, 165, 169  
 Sakao-type, 156  
 solar, vii, 1, 19, 43, 78, 177, 197, 284, 293,  
   300, 384, 386, 389, 435  
 spaghetti model, 377  
 standard model, 114, 148, 149, 160, 163,  
   169, 177, 214, 218  
 stellar, vii  
 thermal, 204, 206  
 topological model, 129, 156  
 topological trigger, 129, 307  
 turbulent cascade, 377, 386  
 two-ribbon, 84, 110  
 white light, 67, 399, 454
- flow  
 converging, 158  
 shear, 70, 174  
 vortex, 209
- fluid particle, 29
- flux cancellation, 125, 158, 384, 398, 403
- Fokker-Planck equation, 390
- force  
 Coriolis, 384  
 electromotive, 94  
 magnetic, 15  
 non-magnetic, 174
- force-free field  
 helicity, 378  
 linear, 175, 379, 384, 385, 428  
 non-linear, 384
- fractionation  
 elements, 404  
 FIP effect, 404, 409
- free magnetic energy, 8, 68, 78, 92, 416
- freezing-in condition  
 generalized, 100
- freezing-in equation, 29
- frequency  
 Larmor, 199  
 neutral-ion collisions, 402  
 plasma, 199
- G**
- galaxy  
 spiral, vii
- gamma ray burst, 127, 320
- geomagnetic storm, 136
- geomagnetic tail, 4, 308, 310, 373, 374
- geospace, x
- giant flare, 291
- Giovanelli, 19
- GOES, 135, 319
- GONG, 71
- gradient drift, 9
- ground level enhancement, 319
- group velocity, 329
- H**
- Hall current, 414
- Hamilton equations, 100
- Hamiltonian  
 transformed, 304  
 usual, 303
- heating  
 coronal, 377
- helicity  
 global, 396  
 sign, 86
- helioseismology, 383
- Hinode, viii, 96, 174, 436, 455
- Hinotori, 207
- hodograph, 54
- I**
- IceTop, 319
- ideal MHD, 25
- inductance, 94
- initial conditions, 22
- instability  
 current, 43, 208  
 fire-hose, 387  
 ion-acoustic, 194, 197  
 ion-cyclotron, 194, 197  
 kink, 385  
 lower hybrid drift, 60  
 overheating, 92  
 resistive, 352  
 structural, 93, 323  
 tearing, 6, 50, 93, 351  
 thermal, 92, 181, 210  
 two-stream, 93, 208
- interacting loops, 86
- interaction  
 magnetic fluxes, 1  
 wave-particle, 43, 188, 208, 296
- Interball, 268
- interface dynamo, 383
- invariant  
 adiabatic, 224  
 motion, 303
- inverse cascade, 381
- involution, 304
- ion resonance, 374
- ion viscosity, 208

**J**

jet, vii, 101  
Joule heating, 182, 187, 402, 430

**K**

kinematic problems, 382  
kinetic energy, 372  
kink instability, 385  
Kolmogorov turbulence, 382

**L**

Lagrangian coordinates, 29  
Landau resonance, 372  
Larmor frequency, 199  
Larmor radius, 6, 12, 302, 370  
LASCO, 90  
law  
  conservation, 188, 209  
  Ohm's, 189, 362  
  scaling, 182  
layer  
  boundary, 421  
  double, 416  
long duration event, 90, 109, 203, 214  
Lundquist number, 183, 210

**M**

magnetar, vii, 320  
magnetic collapse, 42  
magnetic diffusivity, 178, 326, 355, 430  
magnetic dynamo, 380  
magnetic energy  
  free, 92  
magnetic field  
  bald patch, 428  
  completely open, 419  
  cumulative effect, 27  
  force free, 174, 378, 419  
  galactic, vii  
  guide, 45, 185  
  less-ideal, 104  
  linkage, 77, 378, 423  
  longitudinal, 15, 44, 45, 60, 79, 102, 184,  
    185, 199, 294, 303, 427  
  more-ideal, 104  
  non-force-free, 174  
  poloidal, 382, 422  
  potential or current free, 2, 71, 105, 107,  
    419  
  separator, ix, 185  
separatrix, ix  
  strong, 379  
  toroidal, 382, 425  
  transversal, 15, 44, 184, 294, 303, 353  
  weak, 379  
zeroth point  
  isolated, 73  
  non-degenerate, 73  
zeroth point or line, 1, 19, 22, 74, 321, 352,  
  421  
  peculiar, 22, 321  
magnetic field line  
  equations, 425  
  separator, ix, 416, 422  
  separatrix, 3, 352, 421, 422  
magnetic flux, 423  
  emerging, 1, 96  
magnetic flux conservation, 425  
magnetic flux tube  
  closely packed, 377  
  specific volume, 425  
magnetic force, 15  
magnetic helicity, 86, 384, 404  
  change, 382  
  conservation, 379  
  dissipation, 384  
  global, 378, 396  
magnetic mirror, 224  
magnetic moment, 10  
magnetic obstacle, 221  
magnetic reconnection, ix, 3, 19, 47, 282, 320,  
  351, 377  
  collisionless, 188  
  of electric currents, 417  
  Petschek's regime, 321, 348  
magnetic Reynolds number, 382  
magnetic storm, vii  
magnetic stresses, 383  
magnetic trap, 448  
magnetoacoustic wave  
  fast, 329  
  slow, 329  
magnetopause, 282, 286  
magnetosphere  
  Earth, vii, 221, 282, 381  
magnetospheric substorm, vii, 268, 373, 374  
magnetospheric tail, 184, 284, 299  
Masuda's flare, 213  
mean field, 380  
MHD turbulence, 286, 379  
minimum current corona, 92, 106, 420  
moment  
  magnetic, 10

momentum  
 conservation law, 188  
 generalized, 303  
 longitudinal, 224

motion  
 invariant, 303  
 shear, 421  
 vortex, 209

**N**

nanoflare, 392  
 near space, ix  
 neutron star, vii, 320

**O**

Ohm's law  
 generalized, 43, 402  
 in MHD, 362

orbit  
 sticky, 308

OSO-7, 456

**P**

PAMELA, 319

particle  
 fluid, 29

peculiar zeroth point, 22, 321

Petschek, 49, 58, 178

phase space, 305

phase trajectory, 305

photospheric dynamo, 406

pinch effect, 408

pitch-angle, 224

plasma  
 collisional, 4  
 collisionless, 35, 59, 187, 209, 221  
 fusion, 4  
 super-hot, 94, 189, 206, 213, 220, 281, 439  
 weakly-ionized, 397, 405

plasma layer, 202

plasma motion  
 continuous, 22

plasma sheet, 381

plasma turbulence, 93, 125  
 marginal regime, 194  
 saturated regime, 195

Poisson brackets, 304

potential  
 magnetic field, 2, 71, 107  
 vector, 4, 21

Poynting vector, 394

problem  
 self-similar  
 first type, 38

prominence, 397  
 filament, 398  
 quiescent, 403

pseudo-phase space, 307

pulsar  
 magnetosphere, 286  
 millisecond, 291

**Q**

quasar, vii

**R**

radiative energy losses, 402

rainbow reconnection, 89

reconnecting current layer, 6, 9, 19, 23, 33, 43,  
 47, 67, 78, 93, 96, 124, 178, 207,  
 215, 317, 398, 416, 439

reconnection  
 collisionless, 4, 35, 43, 59, 125, 175, 187,  
 208, 209, 221, 435

coronal, 67, 175

day-side, 282

fast, 43, 60, 70, 93, 107, 175, 320, 349

in vacuum, 4

inflow velocity, 178

large-scale, 114

linear, 28, 398, 401

magnetic, ix, 3, 19, 47, 67, 282

night-side, 282

Petschek-type, 178

photospheric, 67, 158, 174

pile-up, 146

rainbow, 89, 156, 209

relativistic, 320

slow, 69, 78, 107, 403

Sweet-Parker, 182

two-level, 174, 393

weakly-ionized plasma, 67, 392, 397, 405

resistivity

anomalous, 187

Coulomb, 95

resonance  
 Landau, 372

Resurs-DK1, 319

reverse current, 6, 31, 47, 64, 320, 324, 455

RHESSI, viii, 128, 164, 169, 189, 209, 214,  
 219, 267, 281, 435, 455, 457

Riemann–Hilbert problem, 52, 62

rigidity, 100

ring current, 284

runaway

  electric, 36, 43, 94

## S

SAMPLEX, 319

scaling law, 183

SDO, ix, 63, 437

self-inductance, 91, 95

self-organization, 379

self-similar solution, 36, 42

separator, ix, 72, 191

  resistance, 94

separatrix, ix, 3, 72, 421

shear, 70, 151, 174, 384, 421, 429

shear relaxation, 153, 165, 167

shock wave

  collisional, 207

  collisionless, 220

  oblique

    fast, 56, 207, 220, 222

    slow, 56

  switch-on, 58

  trans-Alfvénic, 56

sigmoidal structure, 90, 175, 436

skin thickness

  electron, 59

  ion, 60

Skylab, 110, 449

SMM, 206

SOHO, viii, 90, 95, 96, 106, 110, 111, 136,  
  144, 174, 221, 392, 409

solar activity, 67, 382

solar atmosphere, 1

solar corona, 4, 286, 390, 404

solar cycle, 382

solar energetic particles, 318

solar flare, 300, 309

  standard model, 177, 191, 210

  topological model, ix, 84, 210

solar tornado, 409

solar wind, x, 23, 64, 282, 379, 404

SOT, 455

SOXS, 209

space

  near, ix

  phase, 305

  pseudo-phase, 307

space weather, x, 284

specific magnetic volume, 425

Speiser, 15, 293

splitting

  current layer, 321

star

  cataclysmic variable, 291

  magnetar, 291

  neutron, vii, 285, 289, 291

  Sun, vii

  supernova, vii

  T Tauri, 291

STEREO, ix, 319, 437

stickiness, 308

stochastic acceleration, 386

stochasticity, 43

stress heating, 394

structural instability, 323

Sun

  active region, ix, 2, 327, 377

  atmosphere, vii

  chromosphere, ix, 2, 181, 398

  corona, 4, 286, 327

  photosphere, viii, 2, 398, 415

  prominence, 158, 174

surface wave, 331

Syrovatskii, 20, 47, 96, 179, 182

## T

tachocline, 383

tangential discontinuity, 325, 429

Taylor hypothesis, 379

tearing instability, 6, 50, 93, 124, 351

  electron, 372

  ion, 373

  nonlinear, 375

theorem

  virial, 419

  Woltjer, 378

thermal instability, 181

  condensation mode, 455

thick target, 220, 390

thin target, 390

tokamak, 275

topological index, 74

topological interruption, 421, 431

topological model

  exact-quadrupole, 81

  many charges, 107

  quadrupole, 72, 81

topological portrait, 83, 119, 137

topological trigger, 93, 141, 150

topologically critical state, 141

TRACE, viii, 95, 96, 107, 110, 111, 144, 148,

  160, 169, 174, 435

trans-Alfvénic shock wave, 56

trap

  collapsing, 213, 221

- trigger  
 tearing instability, 351  
 thermal, 182  
 topological, 93, 141, 150, 307
- turbulence  
 current-driven, 275  
 fluid, 379  
 helical, 383  
 ion-acoustic, 195, 293, 296  
 ion-cyclotron, 195  
 Langmuir, 317  
 MHD, 286, 379  
 plasma, 190, 296  
 reconnection-driven, 386  
 strong, 379  
 turbulent heating, 275  
 twist, 384, 410, 420  
 two-ribbon structure, 84, 104, 110, 177
- V**  
 vector potential, 4, 7, 21  
 velocity  
 group, 329  
 virial theorem, 419  
 viscosity  
 eddy, 379  
 ion, 208  
 Vlasov equation, 369
- W**  
 wave  
 dissipative, 329
- X**  
 X-ray emission  
 hard, 79, 102  
 chromospheric, 220  
 coronal, 169, 213, 220, 253  
 non-thermal, 220, 255, 439  
 thin target, 443  
 soft, 79  
 X-type zeroth point, 3, 19, 77, 185, 191, 324, 352, 421
- Y**  
 Yohkoh, viii, 90, 96, 101, 102, 106, 109, 144, 148, 161, 174, 178, 189, 206, 209, 213, 221, 226, 266, 281, 394, 435